Faculty of Science
Department of Applied Physics

The Measurement of Underwater Acoustic Noise Radiated by a Vessel Using the Vessel's Own Towed Array

Alexander John Duncan

This thesis is presented for the Degree of
Doctor of Philosophy
of
Curtin University of Technology

November 2003

Abstract

The work described in this thesis tested the feasibility of using a towed array of hydrophones to: 1. localise sources of underwater acoustic noise radiated by the tow-vessel, 2. determine the absolute amplitudes of these sources, and 3. determine the resulting far-field acoustic signature of the tow-vessel. The concept was for the tow-vessel to carry out a U-turn manoeuvre so as to bring the acoustic section of the array into a location suitable for beamforming along the length of the tow-vessel. All three of the above were shown to be feasible using both simulated and field data, although no independent field measurements were available to fully evaluate the accuracy of the far-field acoustic signature determinations.

A computer program was written to simulate the acoustic signals received by moving hydrophones. This program had the ability to model a variety of acoustic sources and to deal with realistic acoustic propagation conditions, including shallow water propagation with significant bottom interactions. The latter was accomplished using both ray and wave methods and it was found that, for simple fluid half-space seabeds, a modified ray method gave results that were virtually identical to those obtained with a full wave method, even at very low frequencies, and with a substantial saving in execution time.

A field experiment was carried out during which a tug towing a 60-hydrophone array carried out a series of U-turn manoeuvres. The signals received by the array included noise radiated by the tow-vessel, signals from acoustic tracking beacons mounted on the tow-vessel, and transient signals generated by imploding sources deployed from a second vessel. Algorithms were developed to obtain snapshots of the vertical plane and horizontal plane shapes of the array from the transient data and to use range data derived from the tracking beacon signals to track the hydrophones in the horizontal plane. The latter was complicated by a high proportion of dropouts and outliers in the range data caused by the directionality of the hydrophones at the high frequencies emitted by the beacons. Despite this, excellent tracking performance was obtained.

Matched field inversion was used to determine the vertical plane array shapes at times when no transient signals were available, and to provide information about the

geoacoustic properties of the seabed. There was very good agreement between the inversion results and array shapes determined using transient signals.

During trial manoeuvres the array was moving rapidly relative to the vessel and changing shape. A number of different array-processing algorithms were developed to provide source localisation and amplitude estimates in this situation: a time-domain beamformer; two frequency-domain, data independent beamformers; an adaptive frequency-domain beamformer; and an array processor based on a regularised least-squares inversion. The relative performance of each of these algorithms was assessed using simulated and field data.

Data from three different manoeuvres were processed and in each case a calibrated source was localised to within 1 m of its known position at the source's fundamental frequency of 112 Hz. Localisation was also successful in most instances at 336 Hz, 560 Hz and 784 Hz, although with somewhat reduced accuracy due to lower signal to noise ratios. Localisation results for vessel noise sources were also consistent with the positions of the corresponding items of machinery.

The estimated levels of the calibrated source obtained during the three manoeuvres were all within 4.1 dB of the calibrated value, and varied by only 1.3 dB between manoeuvres. Results at the higher frequencies had larger errors, with a maximum variation of 3.8 dB between serials, and a maximum deviation from the calibrated value of 6.8 dB.

An algorithm was also developed to predict the far-field signature of the tow-vessel from the measured data and results were produced. This algorithm performed well with simulated data but no independent measurements were available to compare with the field results.

Acknowledgements

I would firstly like to acknowledge the assistance and support provided by my supervisors, Dr Robert McCauley (Curtin University), Emeritus Professor John Penrose (Curtin University), Dr Darryl McMahon (Defence Science and Technology Organisation) and, in the early stages of the project, Dr Alexander Kritski (Curtin University).

The planning, preparation and execution of the field experiments described in this project involved a large number of people. I would particularly like to mention the contributions of the late Mr Harry Protoolis from Nautronix Ltd., who was tragically killed in a recent light aircraft crash, and Mr Mike Knubley, also from Nautronix, who was critically injured in the same accident. The contributions of these two men were vital to the success of the experiments.

I would also like to thank the following for their contributions:

- Dr Darryl McMahon, Mr Robert Hendrie, Mr Vlatko Cuculoski, Mr Damien Killeen and Ms Jennifer Schahinger from the Maritime Operations Division of the Defence Science and Technology Organisation (DSTO);
- Mr Alessandro Ghiotto and Mr Cheong Chong from Nautronix Ltd;
- Dr Alexander Kritski and Mr Malcolm Perry from the Centre for Marine Science and Technology (CMST) at Curtin University, and
- the skippers and crews of *Tammar* and *Sea Witch* from Defence Maritime Services Pty Ltd (DMS).

I would also like to thank Mr Mark Savage from the Maritime Operations Division of DSTO for carrying out the initial calibration of the UW30 sound source, acknowledge the technical support provided by Mr Malcolm Perry from CMST throughout the project, and thank the other individuals who have provided me with useful advice and feedback on this thesis.

This project would not have been possible without the financial support provided by DSTO and the involvement of Nautronix Ltd, who provided the acoustic tracking and data acquisition systems used during the experiments. Nautronix Ltd participated under a DSTO-Nautronix project agreement to cooperate on acoustic sound ranging.

Table of Contents

List of Figures

List of Tables

Table of Symbols

All symbols are defined in the text where they are first used. Symbols that only appear in the text in the immediate vicinity of their definition have been omitted from this table.

Symbol	Meaning	Units	Used in chapters	Defined on page
a	Snell invariant.	$s.m^{-1}$	2	16
a	Array steering vector. Each element represents the expected acoustic field at the corresponding hydrophone computed for a source of unit amplitude and zero phase.	-	6, 7, 8	173
A	Area of acoustic piston source.	m^2	3	40
A_c	Area of cavitation on propeller blade surface.	m^2	3	36
A_n	Amplitude of the n^{th} harmonic of the propeller cavitation volume.	m^3	3	34
A	Array steering matrix (each column is a steering vector).	-	7	208
Ai	Airy function.	-	2	18
b	Array bow.	m	6	180
$b(q_s, f_s, f)$	Source beam pattern function.	-	3	49
B	Number of propeller blades.	-	3	32
B_j	Normalised Bartlett power for frequency j.	-	6	173
c	Sound speed in a medium.	$m.s^{-1}$	2	6
c_0	Sound speed in water.	$m.s^{-1}$	2, 3, 5, 6, 7	11
c_1	Sound speed in half-space seabed.	$m.s^{-1}$	2	11
c_p	Compressional sound speed in a sediment.	$m.s^{-1}$	6, 8	181
c_s	Shear wave speed in a sediment.	$m.s^{-1}$	6, 8	182

Symbol	Meaning	Units	Used in chapters	Defined on page
$\tilde{C}_T$	Oscillating thrust coefficient.	-	3	37
$\tilde{C}_{Tm}$	Oscillating thrust coefficient at the frequency of the mth harmonic.	-	3	37
$\mathbf{C}_\mathbf{X}$	Covariance matrix of estimated parameters (transient position fixing).	various	5	119
$\mathbf{C}_\mathbf{Y}$	Covariance matrix of observation errors (transient position fixing).	various	5	114
D	Propeller diameter.	m	3	32
E	Cost (energy) function for matched field inversion.	-	6	173
$\mathrm{E}\{\ \}$	Expectation operator.	-	6, 7	176
f	Frequency .	Hz	2, 3, 6, 7	6
f_{lp}	Low-pass cut-off frequency.	Hz	3	42
f_{hp}	High-pass cut-off frequency.	Hz	3	42
f_m	Frequency of maximum in broadband cavitation noise spectrum.	Hz	3	31
f_n	Frequency of nth harmonic. Frequency of frequency step *n*.	Hz	3	35
$\mathbf{f}()$	General function returning a vector of values.	-	5	114
$\Im^{-1}$	Inverse Fourier transform.	-	3	52
g	Rayleigh roughness parameter.	-	2, 8	26
h	Propeller depth.	m	3	35
h	Root mean square surface height.	m	2	26
h	Sediment layer thickness	m	6	182
$h(\mathbf{r},t)$	Source term in the inhomogeneous acoustic wave equation.	m^{-1}	2	6
H (super-script)	Hermitian transpose of a matrix (complex conjugate of transpose).	-	6, 7	173

Symbol	Meaning	Units	Used in chapters	Defined on page
$H(\mathbf{r},w)$	Source term in the inhomogeneous Helmholtz equation.	m^{-1}	2	6
$H(f;t)$	Filter transfer function at time t.	-	3	51
$H_0^{(1)}$	Zero order Hankel function of the first kind.	-	2	19
$H_0^{(2)}$	Zero order Hankel function of the second kind.	-	2	23
i	square root of –1.	-	2, 3, 6, 7	6
I_0	Acoustic intensity referred to a distance of 1 m from the source.	$W.m^{-2}$	3	32
I_m	Acoustic intensity of m^{th} harmonic.	$W.m^{-2}$	3	37
J	Propeller advance ratio – the distance the propeller advances in one revolution divided by its diameter.	-	3	32
J_0	Bessel function of the first kind of order 0.	-	2, 3	22
k	Acoustic wavenumber.	m^{-1}	2, 3, 7	6
k_r	Horizontal component of acoustic wavenumber.	m^{-1}	2, 3	11
k_z	Vertical component of acoustic wavenumber.	m^{-1}	2, 3	12
K	Number of snapshots (blocks) array data is broken into.	-	6, 7, 8	173
K_t	Propeller tip cavitation index.	-	3	31
K_{ti}	Propeller tip cavitation index at cavitation inception.	-	3	32
L_{pm}	Peak source spectral level.	dB re 1 μPa^2/ Hz @ 1 m	3	34
L_S'	Overall source level for broad-band cavitation integrated over frequencies above 100 Hz.	dB re 1μPa at 1m	3	33

Symbol	Meaning	Units	Used in chapters	Defined on page
L()	Likelihood function.	-	6	176
M	Number of frequencies.	-	6, 7	173
n_b	Number of seabed reflections along a ray path.	-	3	62
n_p	Propeller shaft rotation rate.	rev-olutions per second	3	32
n_s	Number of sea surface reflections along a ray path.	-	3	62
N	Number of hydrophones in array.	-	6, 7	173
p	Acoustic pressure.	Pa	2, 3	5
p_0	Hydrostatic pressure.	Pa	3	31
p_h	Acoustic pressure received at hydrophone.	Pa	3	50
p_n	Acoustic pressure of nth harmonic.	Pa	3	35
$p_s(t)$	Source acoustic pressure waveform at a distance of 1 m from the source.	Pa @ 1 m	3	49
p_v	Fluid vapour pressure.	Pa	3	31
$\left\langle p^2_{>100} \right\rangle$	Mean-square acoustic source pressure for frequencies above 100 Hz.	Pa^2 @ 1 m	3	43
P_d	Dipole source strength.	Pa @ 1m	3	35
$P_s(f)$	Fourier transform of source waveform $p_s(t)$.	Pa.s	3	51
$P_{s,n}$	Discrete Fourier transform of source waveform $p_s(t)$.	Pa	3	52
P	Kalman filter / smoother covariance matrix of estimated state vector.	various	5	134
Pr()	Probability of.	-	6	176

Symbol	Meaning	Units	Used in chapters	Defined on page
$\mathbf{Q}_k$	Kalman filter / smoother dynamic model covariance matrix.	various	5	133
r	Distance from acoustic source to receiver.	m	2, 3	7
r_h	Horizontal range coordinate in cylindrical coordinate system.	m	2, 3, 5	8
r_i	Slant range from image source to hydrophone.	m	2, 3	8
r_s	Slant range from physical source to receiver.	m	2, 3	8
$\mathbf{r}$	Position vector.	m	2	5
$\mathbf{r}_{sh}$	Position vector of hydrophone relative to source.	m	3	49
R	Plane wave pressure reflection coefficient.	-	2	12
R_b	Seabed plane wave pressure reflection coefficient.	-	3	62
R_{coh}	Equivalent plane wave reflection coefficient for coherent scattering.	-	2	26
R_{eff}	Effective plane wave reflection coefficient for multiple reflections.	-	3	62
R_s	Sea surface plane wave pressure reflection coefficient.	-	3	62
$\mathbf{R}_k$	Kalman filter / smoother observation model covariance matrix.	various	5	133
$\mathbf{R}_\mathbf{x}$	Array population covariance matrix.	Pa^2	7	210
$\hat{\mathbf{R}}$	Array sample covariance matrix.	Pa^2	6, 7	178
s	Propeller blade mean chord length.	m	3	31
s	Distance along ray path.	m	2	10
s	Distance along array.	m	5	116
s	Array slope.	-	6	180
$\mathbf{s}$	Vector of signals emitted by different sources.	Pa	7	215

Symbol	Meaning	Units	Used in chapters	Defined on page
S_w	Acoustic source strength.	$m^2.Pa^{-1}$	2	7
SL	Acoustic source level.	dB re 1 µPa @1 m	4	98
t	Time.	s	2	5
t_k	Time at time-step k.	s	3	52
t_r	Time at which signal is received at a hydrophone.	s	3	50
$\widetilde{T}_{rms}$	Root mean square of the oscillating component of the thrust force.	N	3	37
T	Array output transformation matrix.	-	7	212
TL	Transmission loss.	dB	3	58
u	Acoustic particle displacement vector.	m	2	5
U_t	Propeller tip speed.	$m.s^{-1}$	3	32
U_{ti}	Propeller tip speed at cavitation inception.	$m.s^{-1}$	3	32
v	Acoustic particle velocity vector.	$m.s^{-1}$	2	5
$\mathbf{v}_k$	Kalman filter/ smoother innovation vector. (Vector of differences between predicted and actual observations.)	various	5	142
V_c	Volume of propeller cavitation.	m^3	3	34
$V_{\max}$	Maximum propeller cavitation volume during a revolution.	m^3	3	35
w	Beamformer complex weight vector.	-	7, 8	207
x	Tow-vessel x coordinate (positive forward).	m	2, 4, 5, 6	5
x_s	X coordinate of acoustic source (tow-vessel coordinates).	m	6	182
x	Array output vector at a specific frequency. (One complex element per hydrophone.)	Pa	6, 7	173

Symbol	Meaning	Units	Used in chapters	Defined on page
$\tilde{\mathbf{x}}$	Kalman filter / smoother true state vector.	various	5	132
$\hat{\mathbf{x}}$	Kalman filter / smoother estimated state vector.	various	5	134
X	Global coordinate system X coordinate (Northing).	m	2, 5	4
X_s	Source centred X coordinate	m	3	49
$\mathbf{X}$	Vector of parameters (transient position fixing).	various	5	114
y	Tow-vessel y coordinate (positive to starboard).	m	2, 4, 5, 6	5
y_s	Y coordinate of acoustic source (tow-vessel coordinates).	m	6	182
$\mathbf{y}_d$	Vector of desired beamformer outputs.	-	7	208
Y	Global coordinate system Y coordinate (Easting).	m	2, 5	4
Y_s	Source centred Y coordinate.	m	3	49
$\mathbf{Y}$	Vector of observations (transient position fixing).	various	5	113
z	Depth coordinate (positive down with origin at sea surface). Same for global, tow-vessel and cylindrical coordinate systems.	m	2, 3, 4, 5, 6	4
z_0	Height of the source above a reflecting interface.	m	2, 3	20
z_a	Array depth.	m	6	180
z_h	Height of the receiver above reflecting interface.	m	2, 3	20
z_r	Depth of acoustic receiver.	m	2	8
z_s	Depth of acoustic source.	m	2, 5, 6	8
z_w	Water depth.	m	5, 6	115

Symbol	Meaning	Units	Used in chapters	Defined on page
$\mathbf{z}$	Transformed array output vector.	-	7	212
$\tilde{\mathbf{z}}$	Kalman filter / smoother observation vector.	various	5	133
Z	Tow-vessel Z coordinate (positive down).	m	2, 4	5
Z_s	Source centred Z coordinate.	m	3	49
a_p	Compressional wave attenuation in a sediment.	dB per wave-length	6, 8	182
a_s	Shear wave attenuation in a sediment.	dB per wave-length	6, 8	182
b'	Normalised array white noise gain weighting factor.	-	7	240
g'	Normalised regularisation weight.	-	7	243
$d()$	Dirac delta function.	-	2	7
dt	Sampling interval.	s	3	52
$ds_{n,n-1}$	Measured distance along the array between hydrophones n and $n-1$.	m	5	117
Δ	Beam displacement distance.	m	2	11
e'	Normalised covariance matrix diagonal loading.	-	7	241
$\mathbf{e}$	Vector of observation errors.	various	5	114
q	Angle between source-receiver line and direction of applied force.	rad	3	37
q_c	Critical angle of incidence.	rad	2	12
q_i	Angle of incidence relative to normal to boundary.	rad	2	11
q_s	Elevation angle of hydrophone relative to source.	rad	3	49

Symbol	Meaning	Units	Used in chapters	Defined on page
$k_{x,n}$, $k_{y,n}$	Second derivatives of x and y hydrophone coordinates with respect to distance along the array at hydrophone n.	m^{-1}	5	117
$k_{z,n}$	Second derivative of the hydrophone depth at hydrophone n with respect to the distance along the array.	m^{-1}	5	116
l	Acoustic wavelength in a medium.	m	6, 7	182
l_0	Acoustic wavelength in water.	m	3	40
r	Density of a medium.	$kg.m^{-3}$	2, 6, 8	5
r_0	Water density.	$kg.m^{-3}$	2, 3, 6	11
r_1	Density of half-space seabed.	$kg.m^{-3}$	2	11
s^2	Variance.	various	5	114
$f(\mathbf{r},t)$	Acoustic velocity potential (space - time domain).	$m^2.s^{-1}$	2	5
f_R	Phase of the plane-wave reflection coefficient.	rad	2	11
f_s	Azimuth angle of hydrophone relative to source.	rad	3	49
$j(k_r)$	Saddle point method phase function.	rad	2, 3	20
Φ	Kalman filter / smoother dynamic model coefficient matrix.	various	5	133
c^2	Sum of the squared observation residuals weighted by the reciprocal of the corresponding noise variances.	-	5	114
$y(\mathbf{r},t)$	Acoustic displacement potential (space-time domain).	m^2	2	5
$y_s(t)$	Displacement potential source waveform.	m^2	2	7
$\Psi(\mathbf{r},w)$	Acoustic displacement potential (space-frequency domain).	m^2	2	6

Symbol	Meaning	Units	Used in chapters	Defined on page
Ψ_0	Acoustic displacement potential amplitude.	m^2	2, 3	7
$\hat{\Psi}(k_r, z)$	Acoustic displacement potential wavenumber spectrum (wavenumber-frequency domain).	m^2	2, 3	22
w	Angular frequency.	$rad.s^{-1}$	2, 3	6
w_n	Angular frequency at frequency step n.	$rad.s^{-1}$	3	52
w_p	Propeller angular velocity.	$rad.s^{-1}$	3	35

1 Introduction

Ships and submarines radiate sound into the water as an inevitable by-product of the mechanical energy required to propel them. For military surface vessels the characteristics of the radiated underwater sound can be a critical factor in determining the vulnerability of the vessel to detection, and consequently considerable effort is put into characterising and minimising the radiation from these vessels.

The task of characterising the acoustic radiation is usually carried out using a fixed or portable acoustic range (Mathews et al. 2000), but these require either travelling to a fixed location or some form of outside assistance (for example the use of aircraft to drop sonobuoys). It is highly desirable for a vessel to have a means of autonomously measuring its own acoustic signature and localising noise sources so that changes due to machinery wear can be monitored and steps can be taken to rectify emerging problems.

Military surface vessels and submarines commonly tow arrays of hydrophones for the detection and tracking of other vessels. These arrays are streamed behind the vessel, may have a total length of more than 800 m and are typically populated with around 100 hydrophones. By carrying out an appropriate manoeuvre it is possible for a vessel towing such an array to bring the acoustic section of the array into a position that is favourable for imaging noise sources on the vessel.

The aim of this project was to determine the feasibility of using such a technique to:

- localise underwater acoustic noise sources on the tow-vessel,
- quantify the strength of these sources, and
- determine the resultant far-field acoustic signature of the tow-vessel.

The project included theoretical work, algorithm development, numerical simulations and a field experiment in which a 60-hydrophone array was towed by a tug, which performed a number of U-turn manoeuvres.

During the initial stages of the project it was unclear whether data from a field experiment would be available within the required timeframe, and considerable effort was therefore devoted to the development of algorithms to simulate acoustic radiation from realistic vessel noise sources, and the propagation of signals from

sources to moving hydrophones in shallow water. A simple hydrodynamic simulation of a towed array was also written to provide realistic hydrophone tracks for test purposes and this is described in Appendix A.

In the event, good quality field data were obtained, and the full capability of the simulation was not required. However, the simulation proved extremely useful for generating data for testing and developing processing techniques before applying them to field data. These techniques included algorithms to determine array shape and depth using transient signals, track the array in the horizontal plane using signals from acoustic beacons, carry out matched field inversion to determine vertical plane array shape and seabed geoacoustic properties, and process the signals from the array in order to localise the sources, determine their strengths and determine the tow-vessel's far-field signature.

The candidate has carried out the majority of this work. Contributions of others are noted in the Acknowledgements and are specifically mentioned in the text.

Because of the very broad scope of the project, which covered a number of distinct areas of research, each with its own substantial body of literature, a separate literature review chapter has not been provided, but rather the literature relevant to the work covered in each chapter has been reviewed within that chapter.

This thesis is organised as follows:

Chapter 2 presents the theoretical background on acoustic propagation required by the work presented in later chapters.

Chapter 3 deals with the development of an acoustic simulation that was used to simulate the acoustic signals received by a moving array of hydrophones. These simulated signals were then used to test the matched-field inversion and array-processing algorithms discussed in Chapters 6 and 7. As mentioned previously, the availability of good quality field data changed the direction of the project away from one based solely on simulated data, and only some of the capability of the acoustic simulation was utilised in the work reported on in later chapters.

Chapter 4 gives details of the field experiment that was carried out using a 60 hydrophone array towed by a surface vessel. Acoustic tracking beacons were used to provide range measurements between several points on the tow-vessel and the array

hydrophones, and transient sources deployed from a second vessel were used to obtain “snapshots” of the array shape.

Chapter 5 covers the development of the algorithms that were used to track the hydrophone positions during manoeuvres based on the recorded transient signals and range measurements, and shows the results of their application to both simulated and field data.

Chapter 6 deals with the application of matched-field inversion techniques to simulated and measured data in order to estimate vertical-plane array shape and seabed acoustic parameters.

Chapter 7 describes the algorithms that were used to estimate vessel noise source locations and source levels and presents the results of applying these algorithms to both simulated and field data.

Chapter 8 contains a detailed discussion of the results presented in the earlier chapters.

Finally, Chapter 9 presents the conclusions and recommendations for future work.

2 Background Theory

This chapter provides the theoretical background for the acoustic propagation modelling that forms an essential part of this project. Section 2.1 defines coordinate systems that are used throughout this thesis. Section 2.2 introduces the acoustic wave equation and proceeds with a short derivation of the Helmholtz equation. The properties of some general acoustic sources are described in Section 2.3, and Section 2.4 summarises some important numerical techniques for acoustic propagation modelling.

The scenario considered in this thesis involved horizontal separations between sources and receivers comparable to the water depth, and angles of incidence at the seabed close to the critical angle, which led to a requirement to deal accurately with seabed interactions. Ray methods offered the potential for more efficient simulation of broadband signals than wave methods, at least for relatively simple seabeds, and therefore considerable space is devoted to techniques for improving the accuracy of the treatment of seabed interactions in these models through the use of beam displacement and saddle point integration methods (see Section 2.4.1).

Wave methods are also included because of their ability to deal with seabeds of arbitrary layering (see Section 2.4.2).

Scattering at the rough sea surface is dealt with in Section 2.5 and a brief summary of the main points raised in this chapter is given in Section 2.6.

2.1 Coordinate systems

Several different coordinate systems are referred to in this thesis. Two of these are used throughout the thesis and are defined here, whereas the others had specific applications and are defined in the context in which they are used.

2.1.1 Global coordinates

(X, Y, z). This coordinate system was fixed to the earth. X was positive towards true north, Y positive towards true east and z positive down. Azimuth and heading angles were measured clockwise from due north looking downwards. The origin was chosen with $z = 0$ at the sea surface. For simulations the origin in the horizontal plane was chosen arbitrarily whereas when dealing with field data it was chosen so that the coordinate system coincided with Zone 50 of the Universal

Transverse Mercator (UTM) projection (ICSM 1998). With this latter definition X corresponded to Northing and Y to Easting.

2.1.2 Tow-vessel coordinates

(x, y, z). This coordinate system moved with the tow-vessel and was oriented with its x and y axes in the horizontal plane. x was positive towards the bow of the vessel, y positive towards the starboard (right hand) side of the vessel and z positive vertically downwards. Azimuth angles were measured clockwise from the x axis when looking downward. The origin was level with the sea surface directly below the attachment point of the towed array.

Note that with these definitions the z coordinates of a point were identical in the two coordinate systems and so the same symbol was used.

2.2 The acoustic wave equation

The starting point for this work is the acoustic wave equation, which may be specified as a function of position, $\mathbf{r}$, and time, t, in a similar form for pressure, $p(\mathbf{r},t)$, particle velocity, $\mathbf{v}(\mathbf{r},t)$, velocity potential, $f(\mathbf{r},t)$, or displacement potential, $y(\mathbf{r},t)$. The velocity and displacement potentials are defined by the equations:

$$\mathbf{v}(\mathbf{r},t) = \nabla f(\mathbf{r},t) \qquad \textbf{(2.1)}$$

and

$$\mathbf{u}(\mathbf{r},t) = \nabla y(\mathbf{r},t) \qquad \textbf{(2.2)}$$

where $\mathbf{u}$ is the particle displacement.

The acoustic pressure is given by:

$$p(\mathbf{r},t) = -r\,\frac{\partial f(\mathbf{r},t)}{\partial t} = -r\,\frac{\partial^2 y(\mathbf{r},t)}{\partial t^2} \qquad \textbf{(2.3)}$$

where r is the density of the medium (kg.m^{-3}).

In a region free of sources and where the medium density is constant, the homogeneous wave equation for displacement potential is given by (Jensen et al. 2000):

$$\nabla^2 y(\mathbf{r},t) - \frac{1}{c(\mathbf{r})^2}\frac{\partial^2 y(\mathbf{r},t)}{\partial t^2} = 0 \qquad \textbf{(2.4)}$$

where c is the sound speed.

A slightly more complicated form of the wave equation can be derived that does not require the constant density assumption, but in many numerical modelling schemes changes in density are dealt with by solving Equation 2.4 in regions of constant density subject to boundary conditions that deal with the density discontinuities.

The inclusion of sources results in the inhomogeneous wave equation:

$$\nabla^2 y(\mathbf{r},t) - \frac{1}{c(\mathbf{r})^2}\frac{\partial^2 y(\mathbf{r},t)}{\partial t^2} = h(\mathbf{r},t) \qquad \textbf{(2.5)}$$

where $h(\mathbf{r},t)$ represents the source in terms of the equivalent volume injection.

The approximate methods outlined below all start by assuming a solution of the form:

$$y(\mathbf{r},t) = \Psi(\mathbf{r},w)e^{-iwt} \qquad \textbf{(2.6)}$$

where $i = \sqrt{-1}$, $w = 2pf$ and f is frequency (Hz). Similarly, for the source signal:

$$h(\mathbf{r},t) = H(\mathbf{r},w)e^{-iwt} \qquad \textbf{(2.7)}$$

Substituting these into equations 2.4 and 2.5 results in the homogeneous and inhomogeneous Helmholtz equations:

$$\left[\nabla^2 + k(\mathbf{r})^2\right]\Psi(\mathbf{r},w) = 0 \qquad \textbf{(2.8)}$$

and

$$\left[\nabla^2 + k(\mathbf{r})^2\right]\Psi(\mathbf{r},w) = H(\mathbf{r},w) \qquad \textbf{(2.9)}$$

where $k(\mathbf{r}) = \dfrac{w}{c(\mathbf{r})}$.

Time domain solutions can be synthesized from solutions of the Helmholtz equation at many different frequencies by using the inverse Fourier transform:

$$y(\mathbf{r},t) = \frac{1}{2p}\int_{-\infty}^{\infty}\Psi(\mathbf{r},w)e^{-iwt}dw \qquad \textbf{(2.10)}$$

Although simple in principle care must be taken in implementing Equation 2.10 via the Fast Fourier Transform in order to avoid inaccuracies. This is covered in detail in Chapter 8 of Jensen et al. (2000).

By expressing ∇^2 in spherical coordinates (Spiegel 1968) and assuming spherical symmetry about a source at the origin, it can be shown by substitution that Equation 2.11 is a solution of the homogeneous wave equation (Equation 2.4).

$$y(r,t) = \frac{1}{r} y_s\left(t - \frac{r}{c}\right) \qquad \textbf{(2.11)}$$

where y_s is any function and r is the distance from the origin. Similarly, Equation 2.12 is a solution of the homogeneous Helmholtz equation (Equation 2.8).

$$\Psi(r,w) = \frac{\Psi_0 e^{ikr}}{r} \qquad \textbf{(2.12)}$$

where Ψ_0 is a constant.

2.3 Acoustic sources

Acoustic sources are often physically small compared to the wavelength of the sound they emit, and radiate sound by virtue of changes in volume. Such sources radiate uniformly in all directions and are often referred to as acoustic monopole sources. In such cases the right hand side of Equation 2.9 can be written

$$H(r,w) = S_w d(\mathbf{r} - \mathbf{r}_0) \qquad \textbf{(2.13)}$$

where d is the Dirac delta function, and S_w is the source strength. A pressure of unit amplitude at a range of 1 m from the source corresponds to $S_w = -\frac{4p}{w^2}$ (Jensen et al. 2000, Chapter 2).

In the absence of boundaries the displacement potential due to a monopole source drops off with range, r, according to Equation 2.12 with $\Psi_0 = \frac{-S_w}{4p}$.

The dipole source is another important source class. A dipole can be treated as being made up of two spatially separated monopole sources of equal source strength radiating 180° out of phase. There are a number of physical situations that produce dipole sources, but of particular importance is the situation where a monopole source is placed close to the sea surface. A dipole arises because the reflected signal can be

treated as if it were coming from an image source above the sea surface radiating 180° out of phase with the physical source (see Figure 2.1).

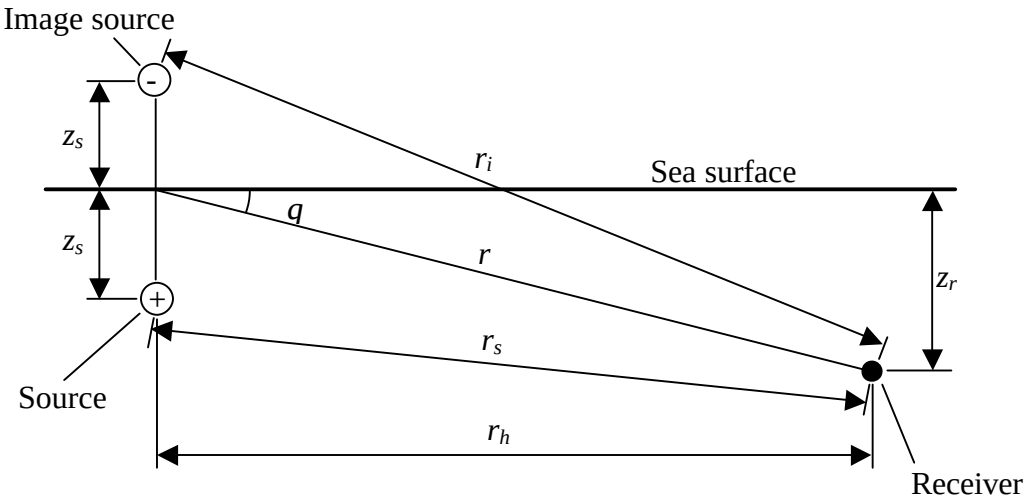

Figure 2.1 Geometry for dipole source comprising a physical source and its reflection in sea surface.

The displacement potential at the receiver can be determined by computing the contribution of each source separately using Equation 2.12, giving

$$\Psi(r,w) = \Psi_0\left(\frac{e^{ikr_s}}{r_s} - \frac{e^{ikr_i}}{r_i}\right) \qquad \textbf{(2.14)}$$

where the symbols are defined in the figure.

If $r >> 2z_s$ this can be approximated by

$$\Psi(r,w) \approx \frac{2\Psi_0}{r} e^{ikr} \sin(kz_s \sin q) \qquad \textbf{(2.15)}$$

Making the additional assumption that $r_h >> z_r$ so that $\sin q \approx \frac{z_r}{r_h}$ and $r_h \approx r$ gives

$$\Psi(r,w) \approx \frac{2\Psi_0}{r_h} e^{ikr} \sin\left(\frac{kz_s z_r}{r_h}\right), \qquad \textbf{(2.16)}$$

and finally, if $\frac{kz_s z_r}{r_h} << 1$, which is the case when the source depth is less than the acoustic wavelength,

$$\Psi(r,w) \approx \frac{2\Psi_0 kz_s z_r e^{ikr}}{r_h^{\,2}}. \qquad \textbf{(2.17)}$$

The last equation implies that when the horizontal separation between the source and receiver is much greater than the source and receiver depths, and in addition the

source depth is less than the acoustic wavelength, then the displacement potential at the receiver is proportional to the source and receiver depths and inversely proportional to the square of their horizontal separation.

2.4 Shallow water acoustic propagation modelling

The wave equation, Equation 2.5, can be solved numerically using finite difference methods, finite element methods or boundary element methods but for most problems in underwater acoustics the computational requirements are prohibitive. Considerable effort has been expended on the development of numerical models for predicting shallow water acoustic propagation since the pioneering theoretical work of C L Pekeris in the 1940s (Pekeris 1948). These efforts have focused on developing suitable approximations to the wave equation in order to make it amenable to efficient numerical solution. The various approximations all have their limitations and in general each is applicable to a particular class of problems. The mathematical backgrounds of these various techniques are covered in a number of texts, see for example Etter (1996) and Jensen et al. (2000), and only a brief summary will be given here.

The primary requirement for acoustic propagation prediction in this work is for the case of a receiver at a horizontal range of only a few water depths from the source. Over these short distances the acoustic environment can be considered to be effectively independent of range and so in the following discussion the emphasis is placed on methods for modelling range independent environments. Methods for improving the accuracy of ray theory are considered in detail in Section 2.4.1 because of ray theory's potential to form the basis of a computationally efficient algorithm for simulating the propagation of broadband acoustic signals for simple seabeds, and the inaccuracies of conventional ray theory at low frequency, especially when dealing with incidence angles near the critical angle. Wave methods appropriate to short-range, range independent situations are also considered (see Section 2.4.2) because, unlike the modified ray methods, they can deal with seabeds of arbitrary layering.

2.4.1 Ray methods

Ray methods are based on the assumption that

$$\Psi(\mathbf{r},w) = A(\mathbf{r},w)e^{iP(\mathbf{r},w)} \qquad \textbf{(2.18)}$$

where $A(\mathbf{r},w)$ represents an amplitude term that varies slowly with position and $P(\mathbf{r},w)$ represents a more rapidly varying phase term. Substituting Equation 2.18 into Equation 2.8, equating real and imaginary parts, and invoking the assumption of slowly varying amplitude results in the following two equations:

$$(\nabla P)^2 = k^2 \qquad \textbf{(2.19)}$$

and

$$2\nabla A.\nabla P + A\nabla^2 P = 0 \qquad \textbf{(2.20)}$$

Equation 2.19 can be further manipulated (see Jensen et al. 2000), to produce a pair of second order differential equations that can be integrated to obtain the ray path. In cylindrical coordinates these are:

$$\frac{d}{ds}\left(\frac{1}{c(r_h,z)}\frac{dr_h(s)}{ds}\right) = -\frac{1}{c(r_h,z)^2}\frac{dc(r_h,z)}{dr_h} \qquad \textbf{(2.21)}$$

and

$$\frac{d}{ds}\left(\frac{1}{c(r_h,z)}\frac{dz(s)}{ds}\right) = -\frac{1}{c(r_h,z)^2}\frac{dc(r_h,z)}{dz} \qquad \textbf{(2.22)}$$

where:

z is depth (m)

r_h is horizontal range (m), and

s is the distance along the ray path (m).

Equation 2.20 can be solved to obtain the signal amplitude along the ray. Boundaries and ray turning points need to be incorporated in the model as special cases.

The assumptions inherent in the ray method mean that it does not deal correctly with caustics and shadow zones where there is a rapid spatial variation of $A(\mathbf{r},w)$, nor is it accurate at low frequencies where the wavelength becomes comparable to the water depth. Etter (1996) gives the following approximate criterion that for the ray method to be applicable: the wavelength should be less than one tenth of the water depth. The first of these problems has been largely overcome by the introduction of

a formalised Gaussian beam model (Porter & Bucker 1987) which replaces the rays, which theoretically have zero width, with beams with a Gaussian intensity profile. This approach has the effect of smoothing the abrupt intensity changes predicted by the ray method and gives very good agreement with theory.

Attempts have been made to extend the low frequency limit of the ray method by including a more accurate model of the interaction between the sound wave and the seabed. Brekovskikh (1960) showed that when a narrow beam of sound waves reflects from a fluid-fluid interface it undergoes a horizontal displacement given by:

$$\Delta(q_i) = -\frac{\partial f_R(q_i)}{\partial k_r} \qquad \textbf{(2.23)}$$

where:

f_R is the phase of the plane-wave reflection coefficient at angle of incidence q_i,

$k_r = k_0 \sin(q_i)$ is the horizontal component of the wavenumber (m^{-1}),

$k_0 = \frac{w}{c_0}$, and

c_0 is the sound speed in the water column (see Figure 2.2).

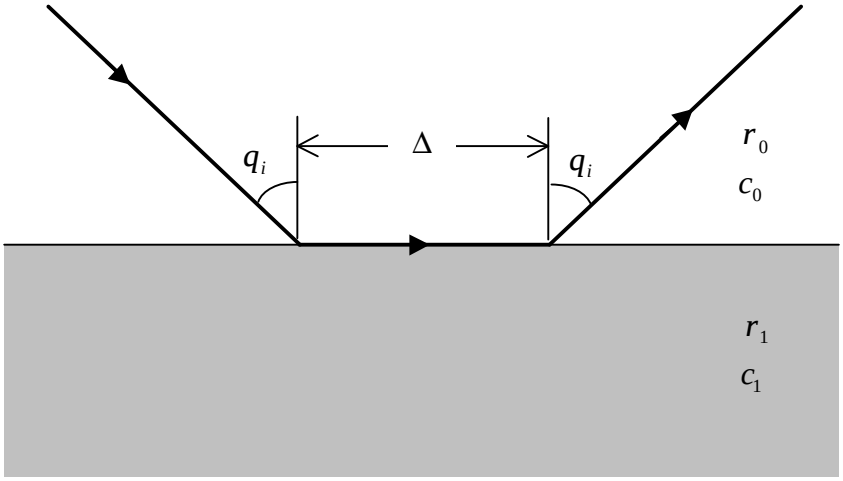

Figure 2.2 Geometry for reflection at a fluid-fluid interface with beam displacement

For the fluid-fluid interface the plane-wave reflection coefficient is given by (Jensen et al. 2000):

$$R = \frac{r_1 k_{z,0} - r_0 k_{z,1}}{r_1 k_{z,0} + r_0 k_{z,1}} \qquad \textbf{(2.24)}$$

where $k_{z,n}$ is the vertical component of the wavenumber in medium n.

In underwater acoustics the sound speed in the seabed is usually greater than that in the water column and in this case for angles of incidence, q_i, less than the critical angle, $q_c = \sin^{-1}\left(\frac{c_0}{c_1}\right)$, the reflection coefficient given by Equation 2.24 is real, and therefore the beam displacement is zero. However, for $q_i > q_c$ the magnitude of the reflection coefficient is 1 but the phase varies from zero at $q_i = q_c$ to 180° at grazing incidence (q_i = 90°). The most rapid change in phase, and hence the greatest beam displacement, occurs just beyond the critical angle and close to grazing incidence (for example, see Figure 2.3). Note that for a given incidence angle the beam displacement is proportional to the wavelength of the incident sound.

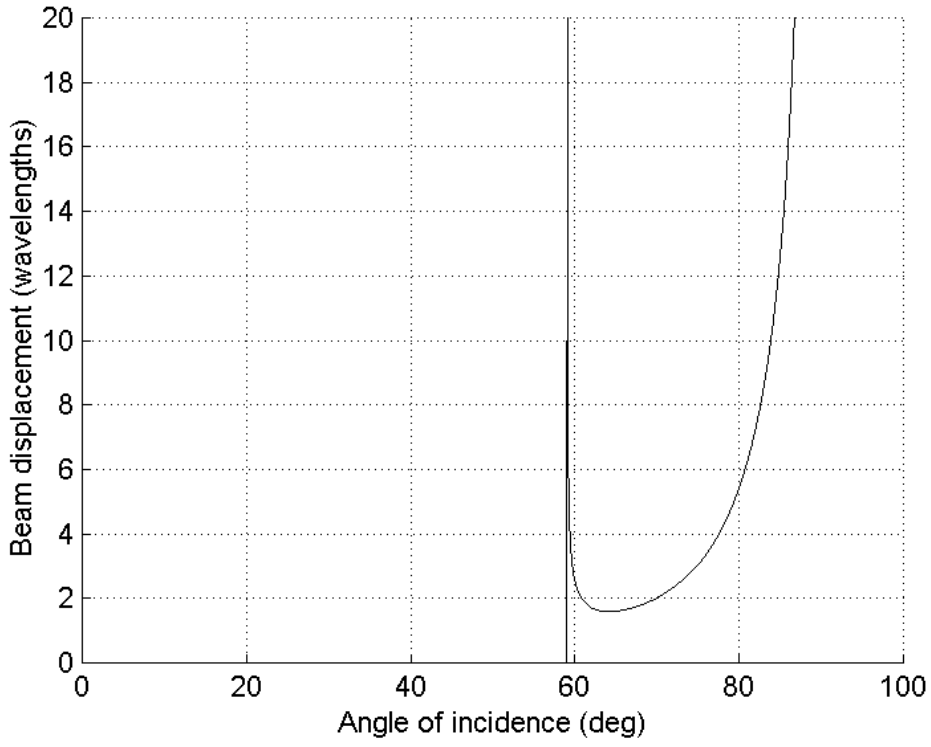

Figure 2.3 Beam displacement (in wavelengths in medium 0) as a function of angle of incidence for a fluid-fluid interface with c_0 = 1500 m/s, r_0 = 1024 kgm^{-3}, c_1 = 1749 m/s, and r_1 = 1941 kgm^{-3}. The critical angle is 59°.

The physical interpretation of this phenomenon is that the beam enters the lower medium where it propagates as an evanescent wave at speed c_1, and then re-emerges into the upper medium at the mirror image of the original angle of incidence. Rays with incidence angles just beyond critical undergo large displacements, with those closest to the critical angle being displaced furthest, and emerge at angles very close to the critical angle forming a plane wave front. This is the ray explanation for the lateral-wave or head-wave (Brekovskikh 1960) utilised in seismic refraction studies.

Figure 2.4 illustrates the ray paths for a narrow bundle of diverging rays incident on a fluid-fluid interface at angles very close to the critical angle. One ray is incident just below the critical angle and is geometrically reflected. The remaining rays are incident above the critical angle, undergo varying displacements, and emerge very nearly parallel forming the plane wave front of the lateral-wave. The increasing spacing of the displaced rays with range is indicative of the attenuation of the lateral-wave.

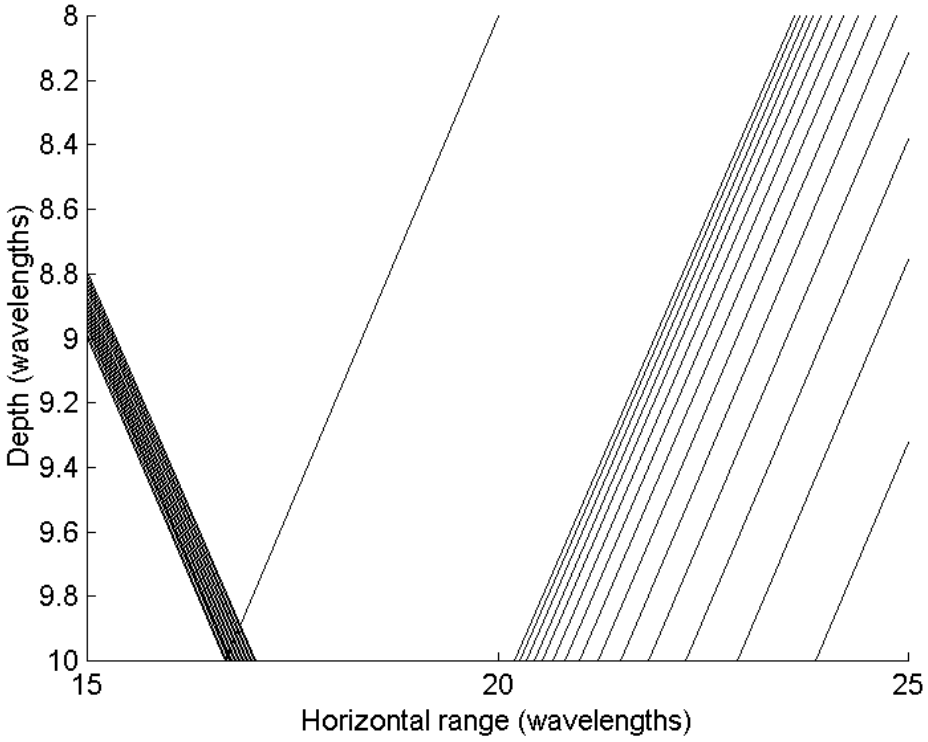

Figure 2.4 Ray diagram for a narrow diverging beam of rays incident from the left and reflecting from a fluid-fluid interface. The angles of incidence are very close to the critical angle. The media properties are the same as in Figure 2.3, the source is at (0,0) and the interface is at a depth of 10 wavelengths below the source.

Tindle and co-workers at the University of Auckland have published a number of papers in which beam displacement has been incorporated into ray models and tested for simple acoustic environments. In Tindle & Bold (1981) beam displacement was applied to a simple Pekeris environment (iso-velocity fluid waveguide bounded above by a vacuum and below by a fluid half-space of constant sound speed and density). The model was used to predict the received waveforms for transmit signals comprising band-pass filtered four-cycle cosine waves of various centre frequencies. Comparisons were made both with normal mode predictions and experimental results for various receiver depths and a fixed horizontal range of just over 100 water depths. The results for the ray theory with beam displacement agreed very well with the normal mode solution, even for a frequency at which the water depth was only three wavelengths, and both models agreed reasonably well with experiment.

Tindle (1983) presented a theoretical derivation of ray theory in which, unlike the derivation given above, beam displacement arose naturally. The derivation was based on the approximate evaluation of an exact integral form of the wave equation. The results showed good agreement with normal mode theory except at relatively short range (< 15 water depths) and at very low frequency where only a single mode existed. These discrepancies were explained as being due to a breakdown in the approximations used to evaluate the exact integral.

In the same paper the author expanded the technique to include attenuation in the fluid half-space and introduced techniques to deal with the shadow zones and caustics caused by beam displacement. The caustics and shadow zones arise because of the behaviour of the displacement as a function of incidence angle shown in Figure 2.3, and can be seen in the ray diagram given in Figure 2.5.

As pointed out in Tindle (1983), further insight into the formation of the shadow zone and caustic is provided by plotting the horizontal range at which the reflected ray crosses the receiver depth as a function of angle of incidence. Such a plot is shown in Figure 2.6 for the parameters stated in the caption. Similar plots can be generated for rays undergoing multiple reflections.

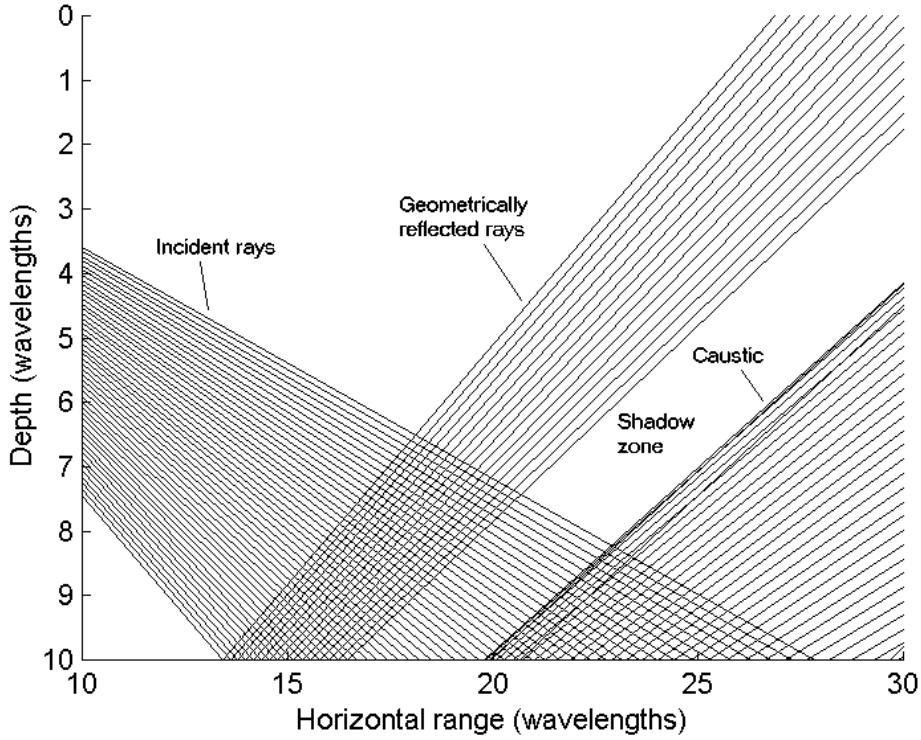

Figure 2.5 Ray diagram showing shadow zone and caustic formed by beam displacement on reflection at a fluid-fluid interface. The media properties are the same as in Figure 2.3, the source is at (0,0) and the interface is at a depth of 10 wavelengths below the source.

For angles less than the critical angle of 59° the range increases smoothly with increasing angle of incidence. Once the critical angle is reached the range jumps discontinuously to infinity and then reduces to a local minimum after which it again increases smoothly. Note that there is no incidence angle that results in a ray crossing the receiver depth at a horizontal range between 500 m and 560 m - this is the shadow zone. A receiver at a range greater than 560 m would receive two rays corresponding to two different launch angles. As discussed above the ray launched at the smaller of these two angles corresponds to the lateral-wave or head-wave. The ray launched at the larger angle corresponds to a displaced, reflected ray. As the receiver range is reduced towards the local minimum these two rays merge to form the caustic.

In a pure ray treatment the amplitude of the received signal is inversely proportional to the slope of this curve, implying an infinite amplitude at the caustic and a zero amplitude in the shadow zone. This is a problem that occurs in other situations with

ray theory. Tindle avoided the problem by applying a standard asymptotic expansion involving Airy functions.

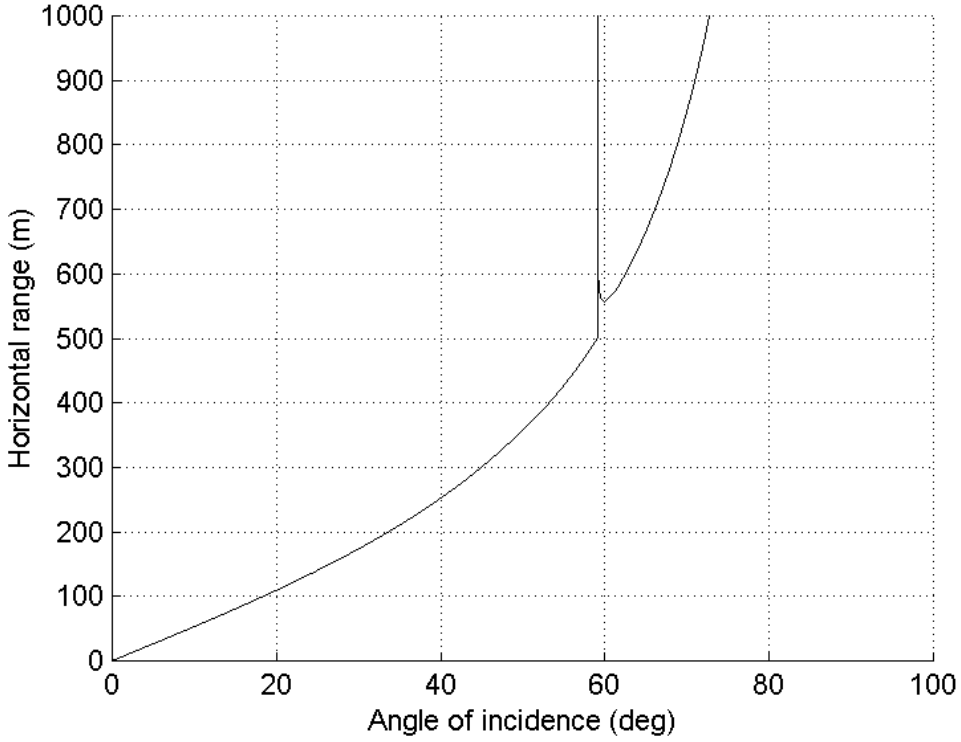

Figure 2.6 Horizontal range at which the reflected ray crosses the depth of the receiver plotted against angle of incidence. Both the source and receiver are 150 m above the seabed. Media properties are as in Figure 2.3.

Tindle & Deane (1985) applied the modified ray model to the prediction of sound propagation over a sloping bottom and found good agreement with adiabatic normal mode theory.

Two papers from the University of Texas build on this work. Westwood & Vidmar (1987) dealt with the problem of finding eigenrays (rays that pass from the source to a receiver at a given location) and simulating time series in an ocean with a layered bottom, and Westwood & Tindle (1987) dealt with the simulation of time series in a Pekeris environment. In both cases the approach taken was to generate a function for each possible ray path similar to that plotted in Figure 2.6. The Snell invariant, $a = \frac{\sin(q_i)}{c}$ was used as the independent variable rather than q_i itself. The value(s) of a at which the curve crossed the actual receiver range was (were) then

determined and the corresponding signal magnitude and phase determined according to whether the receiver range was:

- in the sub-critical region, in which the plane-wave reflection coefficient was used,
- in the shadow zone, in which case an Airy function approximation was used,
- at or just above the caustic, in which case a different Airy function approximation was used, or
- well above the caustic, in which case the contributions of the two eigenrays were computed separately and summed.

For a receiver in the shadow zone the received pressure was calculated using:

$$\frac{p_s}{p_0} = \left[V_s \,\mathrm{Ai}(-x_s) + iW_s \,\mathrm{Ai}'(-x_s)\right] e^{i\{f_s + w[t_c + a(r_h - r_{h,c})]\}} \qquad \textbf{(2.25)}$$

where:

the subscript c denotes the caustic ray,

p_s is the received pressure for a receiver in the shadow zone,

p_0 is the reference pressure,

$x_s = \mathrm{sgn}(r''_{h,c}) w^{2/3} \left| r''_{h,c} / 2 \right|^{-1/3} (r_h - r_{h,c})$,

$V_s = \sqrt{2p}\, w^{1/6} \left| r''_{h,c} / 2 \right|^{-1/3} |C_c| G_s$,

$W_s = \frac{1}{2} \mathrm{sgn}(r''_{h,c}) \sqrt{2p}\, w^{-1/6} \left| r''_{h,c} / 2 \right|^{-2/3} |C_c| G_s \left(2 - \hat{g}_0^2 c_0^2\right) / \left(a \hat{g}_0^2 c_0^2\right)$,

$G_s = \sqrt{a / \left(g_0^2 r_h\right)}$,

$f_s = f_c + p/4$,

r_h is the horizontal range from the source to the receiver,

$r_{h,c}$ is the horizontal range at which the caustic ray crosses the receiver depth,

$r''_{h,c}$ is the second derivative of the horizontal range at which the caustic ray crosses the receiver depth with respect to a,

t_c is the accumulated travel time along the caustic ray,

f_c is the accumulated reflection coefficient phase along the caustic ray,

$|C_c|$ is the accumulated reflection coefficient along the caustic ray,

$\hat{g}_0 = \dfrac{\sqrt{1-a^2c_0^2}}{c_0}$,

c_0 is the sound speed in the upper medium,

Ai denotes the Airy function, and

Ai′ denotes the first derivative of the Airy function with respect to its argument.

In the insonified zone the received pressure was calculated using:

$$\frac{p_i}{p_0} = \left[V_i \,\mathrm{Ai}(-x_i) + iW_i \,\mathrm{Ai}'(-x_i)\right] e^{i\{f_i + w[t_- + t_+]/2\}} \qquad \textbf{(2.26)}$$

where:

symbol definitions are as above except that the subscript c is replaced by - for the ray with a smaller Snell invariant than the caustic ray and by + for the ray with a larger Snell invariant than the caustic ray,

$x_i = \left\{\dfrac{3}{4}\left[w(t_+ - t_-) + (f_+ - f_-)\right]\right\}^{2/3}$,

$V_i = \sqrt{p}\left(|C_+|G_{n+} + |C_-|G_{n-}\right)x_i^{1/4}$,

$W_i = \mathrm{sgn}(t_+ - t_-)\sqrt{p}\left(|C_+|G_{n+} - |C_-|G_{n-}\right)x_i^{-1/4}$,

$G_n = \sqrt{\dfrac{a}{\hat{g}_0^2 r_h \left|r'_{h,0}\right|}}$,

$r'_{h,0}$ is the first differential with respect to a of the horizontal range at which the ray crosses the receiver depth.

$f_i = (f_- + f_+)/2 + p/4$.

Well beyond the caustic range, where only the t_+ ray is significant, the received pressure was calculated using:

$$\frac{p_n}{p_0} = |C_+| G_{n+} e^{i(f_n + w t_+)} \qquad \textbf{(2.27)}$$

where:

$$f_n = f_+ + \frac{p}{4}\left(1 - \mathrm{sgn}\left(r'_{h,0}\right)\right).$$

Because of the frequency dependence of the beam displacement the signal had to be decomposed into its frequency components using the Fourier transform, the ray path calculation carried out at a range of frequencies, and then the received signal reconstructed via the inverse Fourier transform. The authors explicitly located the frequency at which the caustic corresponded to the receiver range and exploited the relatively smooth change in range with frequency on either side of this to minimise the number of calculations required.

Although this technique gave excellent results at ranges that were very long compared to the water depth it did not correctly predict the field close to the critical angle. Methods to deal with this problem were published independently by Tindle's group (Plumpton & Tindle 1989 and Tindle & Plumpton 1990) and by Westwood (Westwood 1989a, Westwood 1989b and Westwood 1992). Similar approaches were taken with the central idea being to express the reflection process as an integral over plane waves travelling at different incidence angles. For a single reflection, the reflected field is given by:

$$p(r_h, z_h) = \frac{i}{2} \int_{-\infty}^{\infty} \frac{R(k_r)}{k_z} e^{i k_z (z_0 + z_h)} \mathrm{H}_0^{(1)}\left(k_r r_h\right) k_r \, dk_r \qquad \textbf{(2.28)}$$

where:

$\mathrm{H}_0^{(1)}$ represents the zero order Hankel function of the first kind,

$k_r = \frac{w}{c_1}\sin(q_i)$ is the horizontal component of the wavenumber,

$R(k_r)$ is the complex plane-wave reflection coefficient,

$k_z = \sqrt{\left(\frac{w}{c_0}\right)^2 - k_r^2}$ is the vertical component of the wavenumber in the upper medium,

z_0 is the height of the source above the interface, and

z_h is the height of the receiver above the interface.

More than a few wavelengths from the source an asymptotic approximation to the Hankel function was used to simplify the integral to:

$$p(r_h, z_h) = \frac{e^{ip/4}}{\sqrt{2pr_h}} \int_{-\infty}^{\infty} \frac{R(k_r)}{k_z} e^{i[k_r r_h + k_z(z_0+z_h)]} k_r^{1/2} dk_r \qquad \textbf{(2.29)}$$

Including the phase of the reflection coefficient in the exponential term allowed the integral in Equation 2.29 to be evaluated approximately by the method of stationary phase (Tindle & Plumpton 1990), which effectively states that the major contributions to the integral are due to those points at which the phase of the exponential is constant. This led to the beam displacement equations given in equations 2.25 to 2.27, which therefore inherently assume that the magnitude of the reflection coefficient varies slowly with incidence angle, which is clearly not the case in the vicinity of the critical angle. The alternative approach, which overcame this limitation, was to include the entire reflection coefficient in the exponential term, which was done by writing:

$$p(r_h, z_h) = e^{ip/4} \int_{-\infty}^{\infty} f(k_r) e^{ij(k_r)} dk_r \qquad \textbf{(2.30)}$$

where:

$f(k_r) = \frac{1}{k_z}\sqrt{\frac{k_r}{2pr_h}}$, and

$$j(k_r) = k_r r_h + k_z(z_0 + z_h) - i\ln(R(k_r)). \qquad \textbf{(2.31)}$$

The major contributions to the integral are now from the saddle points, which correspond to $\frac{dj}{dk_r} = 0$ and which, unlike in the method of stationary phase, may be complex. For a Pekeris environment with no attenuation in the lower medium there are two saddle points which are complex conjugates at ranges less than the caustic range. They join on the real axis at the caustic range and for larger ranges are both real, approaching w/c_0 and w/c_1 as the range approaches infinity. For ranges greater than the caustic range the saddle points correspond exactly with the beam

displacement eigenrays described above. When attenuation is included in the lower medium the saddle points are complex at all ranges.

When the saddle points are widely separated the reflected field contributed by each can be evaluated using an explicit formula, but note that at short range the position of the integration path dictates that only the lower saddle point should be included. The reflected field contributed by each saddle point is given by:

$$p_s(r_h, z_h) = \sqrt{\frac{i2p}{j''(k_s)}} e^{i\left(\frac{p}{4} + j(k_s)\right)} f(k_s) \qquad \textbf{(2.32)}$$

where:

k_s is the complex horizontal wavenumber at the saddle point, and

$j''(k_s)$ is the second derivative of the phase function, j , evaluated at the saddle point.

When the saddle points are close together other techniques must be used and it is here that the main difference occurs between the methods described by Plumpton & Tindle (1989) and by Westwood (1989a). Plumpton and Tindle once again used an explicit formula based on Airy functions:

$$p(r_h, z_h) = 2pe^{i\left(\frac{p}{4} + \frac{j_1 + j_2}{2}\right)} \left[P\,\mathrm{Ai}(-s) + iQ\,\mathrm{Ai}'(-s)\right] \qquad \textbf{(2.33)}$$

where:

$$\sqrt{s} = \left|\frac{3}{4}(j_2 - j_1)\right|^{1/3} e^{i[\arg(j_2 - j_1) + 2p]/3},$$

$$P = (g_1 f_1 + g_2 f_2)/2,$$

$$Q = (g_2 f_2 - g_1 f_1)/\left(2\sqrt{s}\right)$$

$$g_1 = \left(\frac{2\sqrt{s}}{j_1''}\right)^{1/2}, \text{ and}$$

$$g_2 = \left(\frac{-2\sqrt{s}}{j_2''}\right)^{1/2}.$$

The subscript 1 indicates the quantity is to be evaluated at saddle point 1, which has a value of k_r with a negative imaginary part at short range and asymptotes to w/c_1 at very long range. The subscript 2 indicates that the quantity is to be evaluated at the other saddle point.

By contrast, Westwood performed numerical integration along the steepest descent path in the vicinity of the saddle point. Each approach has its advantages: the explicit formula is efficient to evaluate but requires an explicit formulation for the reflection coefficient, whereas the numerical integration, while being slower, is more generally applicable. Westwood (1992) went on to generalise the technique to the case of multiple reflections from horizontal and sloping interfaces in order to carry out acoustic propagation predictions in a variety of environments.

2.4.2 Integral transform techniques for horizontally stratified media

If the medium properties depend only on depth the inhomogeneous Helmholtz equation (Equation 2.9) can be reduced to the depth separated wave equation (Jensen et al. 2000, Chapter 2). In cylindrical coordinates this is done by substituting the inverse Hankel transform representation of the displacement potential:

$$\Psi(r_h, z) = \int_0^\infty \hat{\Psi}(k_r, z)\, \mathrm{J}_0(k_r r_h) k_r dk_r \,, \qquad \textbf{(2.34)}$$

into Equation 2.9, resulting in:

$$\frac{d^2\hat{\Psi}(k_r, z)}{dz^2} + (k^2 - k_r^2)\hat{\Psi}(k_r, z) = \frac{S_w d(z - z_s)}{2p} \qquad \textbf{(2.35)}$$

where:

J_0 represents the Bessel function of the first kind of order 0,

$\hat{\Psi}(k_r, z)$ is the wavenumber spectrum expressed in terms of displacement potential,

z_s is the source depth, and

S_w is the source strength.

Two steps are now required to determine the acoustic field:

1. solve Equation 2.35 for $\hat{\Psi}(k_r, z)$ subject to the appropriate boundary conditions, and

2. carry out the inverse Hankel transform specified in Equation 2.34 to determine the acoustic field.

2.4.2.1 Normal modes

When all the energy is trapped in the waveguide, $\hat{\Psi}(k_r, z)$ is dominated by poles on the real wavenumber axis and the inverse Hankel transform can be carried out in the complex k_r plane as a summation over the residues associated with each pole. Each pole corresponds to a so-called normal mode of the waveguide. In this case Equation 2.35 can be reduced to an eigenvalue problem, with each real eigenvalue corresponding to a normal mode.

The resulting expression for the received pressure is (Jensen et al. 2000, Chapter 5):

$$p(r_h, z) = \frac{i}{4\rho(z_s)} \sum_{m=1}^{\infty} \hat{\Psi}_m(z_s)\hat{\Psi}_m(z)\, \mathrm{H}_0^{(1)}(k_{rm} r_h) \qquad \textbf{(2.36)}$$

where:

$\hat{\Psi}_m$ is the modal shape function for mode *m* obtained by solving the eigenvalue problem, and

k_{rm} is the horizontal wavenumber for mode m.

The result is a very efficient method for computing the acoustic field in horizontally stratified media. The main limitation of the normal mode method is that it does not account for the energy that is lost into the seabed. This is most important at short range where the incident angle at the seabed may be less than the critical angle, resulting in partial reflection. At long range propagation is dominated by totally reflected waves and the normal mode method gives good results.

2.4.2.2 Wavenumber integration

Methods that carry out direct numerical integration of the inverse Hankel transform are known as wavenumber integration methods. The most common of these is the so-called fast-field method which first simplifies Equation 2.34 by the substitution:

$$\mathrm{J}_0(k_r r_h) = \left[\mathrm{H}_0^{(1)}(k_r r_h) + \mathrm{H}_0^{(2)}(k_r r_h)\right]/2 \qquad \textbf{(2.37)}$$

where $\mathrm{H}_0^{(1)}$ and $\mathrm{H}_0^{(2)}$ are zero order Hankel functions of the first and second kind respectively. Retaining only the $\mathrm{H}_0^{(1)}$ term, as the $\mathrm{H}_0^{(2)}$ term represents incoming

waves, which are generally not important, and using the asymptotic approximation to the Hankel function, which is valid more than a few wavelengths from the source, yields:

$$\Psi(r_h, z) = \sqrt{\frac{1}{2pr}} e^{-i\frac{p}{4}} \int_0^\infty \hat{\Psi}(k_r, z) \sqrt{k_r} e^{ik_r r_h} dk_r \qquad \textbf{(2.38)}$$

This integral can be evaluated very efficiently by means of the Fast Fourier Transform.

$\Psi(k_r, z)$ is usually found by dividing the environment up into layers for which the depth-separated wave equation (Equation 2.35) can be solved analytically. Other approaches are also possible and the reader is referred to Chapter 4 of Jensen et al. (2000) for a complete description.

For an isovelocity water column, $\hat{\Psi}(k_r, z)$ may be expressed in terms of $R(k_r)$, the plane wave reflection at the seabed (Brekovskikh & Lysanov 1982):

$$\hat{\Psi}(k_r, z) = \begin{cases} \dfrac{2\sin(k_z z)\left(e^{ik_z(z_s - z_w)} + R(k_r)e^{-ik_z(z_s - z_w)}\right)}{k_z\left(e^{-ik_z z_w} + R(k_r)e^{ik_z z_w}\right)}, z < z_s \\ \dfrac{2\sin(k_z z)\left(e^{ik_z(z - z_w)} + R(k_r)e^{-ik_z(z - z_w)}\right)}{k_z\left(e^{-ik_z z_w} + R(k_r)e^{ik_z z_w}\right)}, z > z_s \end{cases} \qquad \textbf{(2.39)}$$

where $k_z = \sqrt{k^2 - k_r^2}$ is the vertical component of the wavenumber in the water column.

2.4.2.3 <u>*Moving receiver*</u>

The case of both a source and receiver moving in a horizontally stratified waveguide is dealt with in Chapter 8 of Jensen et al. (2000). Under the assumptions that the velocities of the source and receiver, and the angles between their velocity vectors and the range vector connecting the source and receiver are effectively constant over the duration of the signal the result is given by:

$$\begin{aligned} y(\mathbf{r}_0 + \mathbf{v}_r t, z, t) = \int_0^\infty & \hat{\Psi}(k_r, z; w_0 + k_r v_s \cos q_s) \\ & \times e^{-i[w_0 + k_r(v_s \cos q_s - v_r \cos q_r)]t} \\ & \times \mathrm{J}_0(k_r r_0) k_r dk_r \end{aligned} \qquad \textbf{(2.40)}$$

where:

$\mathbf{r}_0$ is the horizontal range vector to the receiver at time $t = 0$,

r_0 is the magnitude of $\mathbf{r}_0$,

$\mathbf{v}_r$ is the velocity vector of the receiver,

v_r is the magnitude of $\mathbf{v}_r$,

v_s is the magnitude of the source velocity vector,

q_r is the angle in the horizontal plane between the range vector connecting the source and receiver and the receiver velocity vector,

q_s is the angle in the horizontal plane between the range vector connecting the source and receiver and the source velocity vector,

w_0 is the angular frequency of the signal transmitted by the source, and

$\hat{\Psi}(k_r, z; w)$ represents the solution of the depth dependent wave equation (Equation 2.35) for angular frequency w.

Note that the exponential term in Equation 2.40 implies that source and/or receiver motion will cause a single frequency source waveform to be spread in frequency at the receiver. The spreading occurs because each horizontal wavenumber corresponds to a different propagation angle and therefore has a different component of the source and/or receiver velocity in the direction of propagation. Consequently each horizontal wavenumber experiences a different Doppler shift.

2.4.3 Parabolic equation methods

The parabolic equation (PE) methods for modelling acoustic propagation are based on an approximation to the homogeneous Helmholtz equation (Equation 2.8) that is valid for energy propagating at relatively small angles to the horizontal. The methods have now been developed to the point where the small angle requirement is no longer a limitation in most practical cases. For range independent problems PE methods are more computationally demanding than the integral transform techniques discussed above but they have become the method of choice for range dependent problems, as they do not rely on an assumption of horizontal stratification. The reader is referred to Chapter 6 of Jensen et al. (Jensen et al. 2000) for further details.

2.5 Rough surface reflection and scattering

Scattering from rough surfaces is an important problem in underwater acoustics as it relates to the interaction of sound with both the sea surface and the seabed, both of which often have to be considered acoustically rough. A number of texts devote considerable space to the theory of rough surface scattering, for example Medwin & Clay (1998) and Ogilvy (1991).

The sound scattered from a rough surface can be considered to be made up of two components:

1. a component with a fixed phase relationship to the incident wave (the coherent component) and
2. a component with a random phase relative to the incident wave (the incoherent component).

Medwin & Clay (1998, Chapter 13) gave the following formula for the effective reflection coefficient of the coherently scattered component:

$$R_{coh} = Re^{-g/2} \qquad \textbf{(2.41)}$$

where:

R is the plane wave reflection coefficient of a flat interface,

$g = 4k^2h^2\cos^2 q_i$ is the Rayleigh roughness parameter,

$k = 2pf / c_0$ is the wavenumber,

h is the RMS surface height, and

q_i is the angle of incidence relative to the normal to the surface.

This formula applies for $g < 1$, and assumes a Gaussian probability density function for the surface height. For rougher surfaces departures from the Gaussian pdf and shadowing of parts of the surface can cause fluctuations both above and below this.

For reflections from relatively smooth surfaces ($g < 1$) the coherent component tends to dominate whereas for $g >> 1$ the incoherent component dominates. Prediction of the incoherent component is complicated by the fact that many locations on the surface may contribute to the received signal and the result thus depends on how the incident signal varies over the surface. Equations for evaluating

the mean square scattered pressure (which includes both the coherent and incoherent components) are given in Chapter 13 of Medwin & Clay (1998) in terms of integrals over the insonified area of the surface. For surfaces with a Gaussian height distribution the result depends on both the RMS surface height and the spatial correlation properties of the surface.

2.6 Summary

This chapter presented the theoretical background that will be used in subsequent chapters to derive methods for simulating acoustic signals and for processing both simulated and measured acoustic data.

Extensions to ray theory were discussed which improve its accuracy when applied to the geometries encountered in this work, making ray theory appropriate for simulating acoustic propagation in regions that can be modelled as having acoustically simple half-space seabeds. Methods of dealing with more complicated, layered seabeds using integral transform methods were also discussed.

3 Acoustic Simulation

An acoustic simulation program was written to allow the signals received by a moving array of hydrophones to be realistically modelled in situations where the exact source characteristics and propagation conditions were known. These simulated signals were then used to test the performance of matched-field inversion and beamforming algorithms as described in chapters 6 and 7.

The simulation was written at a time when it was unclear whether field experiment data would be available within the timescale of the project. The program was therefore given wide ranging capabilities so that, in the absence of field data, simulated data could be used to test, as fully as possible, the feasibility of carrying out tow-vessel noise localisation and measurement. It was also felt that adequate tests could, in most cases, be carried out using relatively simple half-space fluid seabed models and consequently considerable effort was expended on developing an efficient acoustic propagation simulation that could be used with such seabeds, based on modified ray theory. An integral transform based computation method was also developed in order to deal with more complicated layered seabeds.

As described in Chapter 4, good quality field data were obtained, which resulted in a shift in emphasis away from the use of simulated data, and therefore only some of the capabilities of the simulation were required. In particular, at the low tow-vessel speeds used during the field experiment the vessel noise was dominated by machinery noise, and no cavitation noise was detectable. Also, the seabed in the area of the experiment could not be adequately modelled as a simple fluid half-space and therefore the wave theory version of the simulation was eventually used to generate test data.

However, for completeness, this chapter describes the full capabilities of the simulation.

Section 3.1 describes the simulation of acoustic sources with realistic characteristics. Background information about the characteristics of various sources of acoustic radiation from ships and submarines is given in Section 3.1.1 and a description of how these sources were simulated is given in Section 3.1.2, together with some typical results.

Section 3.2 describes the methods used to simulate the propagation of these signals from the sources to the moving hydrophones and gives examples of results obtained using these methods. A program was written that could simulate signals in an unbounded medium (Section 3.2.1), a deep ocean taking sea surface reflections into account (Section3.2.2), and a shallow ocean taking both sea surface and seabed reflections into account (Section 3.2.3). The shallow ocean case was the most challenging, for the reasons described in Section 2.4, and four different techniques of varying complexity and accuracy were derived to deal with it.

A short summary of the main results of this chapter is given in Section 3.3.

3.1 Acoustic source simulation

3.1.1 Background

The physics of the various sources of underwater noise radiated by ships and submarines is described in detail in Ross (1987). The acoustic noise of surface vessels tends to be dominated by propeller cavitation noise at normal cruising speeds and by machinery noise at lower speeds. For submarines at depth the greater hydrostatic pressure tends to reduce or eliminate cavitation noise at low to moderate speeds and a great deal of effort goes into minimising machinery noise so that other noise sources, such as the noise generated by fluctuating forces acting on the propeller, become important.

A considerable body of literature exists which deals with radiated noise from merchant vessels and there is some data available on the noise radiated by World War II submarines and warships but data for more modern military vessels is invariably classified. Despite this, the basic physics of the various noise production mechanisms is well understood and so it is possible to establish the general characteristics of the radiated noise even if the absolute levels are unknown.

3.1.1.1 Cavitation noise

Propeller cavitation is the dominant source of radiated noise from surface vessels at normal operating speeds and is discussed in a number of underwater acoustics texts. (See for example Urick 1983, and Loeser 1992). A particularly extensive account is given in Ross (1987), which devotes several chapters to this mechanism. The following discussion is based on that reference except where otherwise noted.

Cavitation noise is usually broken up into two categories: broadband cavitation noise, which has a broad spectrum with no distinct peaks, and narrowband cavitation noise which has distinct spectral peaks at the propeller blade rate (the product of the shaft rotation rate and the number of propeller blades) and its harmonics.

When the pressure in a fluid drops below its vapour pressure, bubbles of vapour can form – the fluid effectively boils. If the bubbles then move into a region of higher pressure they collapse very rapidly and the volume changes associated with the formation and collapse of the bubbles give rise to high levels of acoustic noise.

For marine vessels the required pressure drop most commonly occurs in the vicinity of the propeller and can take the form of blade surface cavitation, tip vortex cavitation or hub vortex cavitation. Blade surface cavitation may occur either on the suction (forward) face of the blade, or on the driving (aft) face, depending on the local flow conditions. Of these, blade surface cavitation on the suction face is the most noisy because bubbles transition quickly from negative to positive pressure regions, so there is insufficient time for gas to diffuse into them. This mechanism is shown schematically in Figure 3.1 and Figure 3.2 (after Matusiak 1992). Sheet cavitation forms a cavity that remains attached to the blade surface, although its volume fluctuates due to varying flow conditions and hydrostatic pressure as the blade rotates. It is these fluctuations in cavity volume that give rise to narrowband cavitation noise (see Section 3.1.1.2). The trailing edge of the cavity is unstable and breaks up into bubbles which convect with the flow into regions of higher pressure where they collapse, giving rise to broadband cavitation noise.

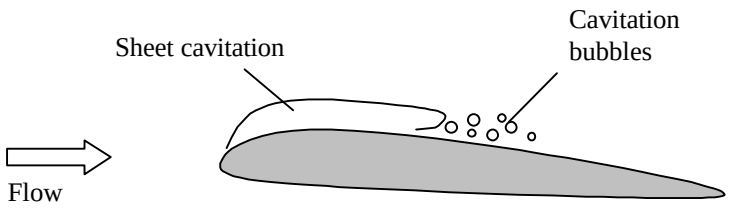

Figure 3.1 Section through propeller blade showing suction face cavitation (after Matusiak 1992)

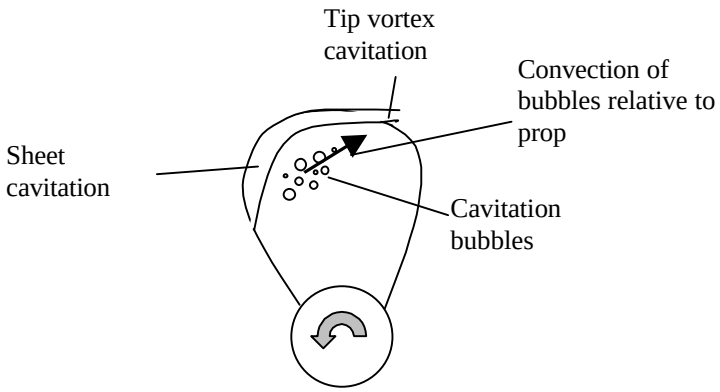

Figure 3.2 Suction face view of propeller blade showing suction face cavitation (after Matusiak 1992)

Tip vortex and hub vortex cavitation noise has received relatively little attention but Latorre (1981) presents the results of noise measurements made on model scale propellers in a cavitation tunnel and a comparison with a numerical model. Unfortunately no information is given on scaling these results to full scale.

Broadband cavitation noise

Ross (1987) presents the results of a simplified model of blade surface cavitation based on a combination of theory and the results of experiments on rotating rods in still water. The model predicts a broad spectrum with a peak frequency that varies according to:

$$f_m \propto \frac{1}{s}\sqrt{\frac{p_0 - p_v}{r_0}}K_t^{3/2} \qquad \textbf{(3.1)}$$

Here

p_v is the fluid vapour pressure,

p_0 is the static pressure,

r_0 is the fluid density,

s is the chord length of the propeller blade (the chord is a line on the blade of constant radius from the shaft), and

K_t is the tip cavitation index (see Equation 3.3).

The model predicts that below the spectral peak the noise spectrum increases with frequency at about 9 dB/ octave, and above the spectral peak it drops at about 6 dB/ octave.

The model also predicts the following relationship for the total acoustic intensity referred to a distance of 1 m from the source:

$$I_0 \propto r_0 BsDK_{ti}U_{ti}^3\left[\left(\frac{U_t}{U_{ti}}\right)\left(\frac{U_t}{U_{ti}}-1\right)^2\right] \qquad \textbf{(3.2)}$$

B is the number of blades

U_t is the propeller tip speed

U_{ti} is the tip speed at cavitation inception

D is the propeller diameter, and

K_{ti} is the cavitation index at cavitation inception.

The characteristics of the cavitation noise depend on the ratio of the propeller tip speed to the tip speed when cavitation just begins: U_t / U_{ti}. Experiments on rotating rods in lakes have indicated that for $1 \le U_t / U_{ti} \le 1.27$ the noise is dominated by transients as individual bubbles collapse and has a spectrum with a rounded peak. In the region $1.27 < U_t / U_{ti} \le 1.55$ the individual events merge together and the spectrum develops a sharp peak. At larger values of U_t / U_{ti} the spectrum becomes flatter as the low frequency noise increases with speed faster than that at high frequencies.

A useful measure of the likelihood of a propeller cavitating is the tip cavitation index which is defined as:

$$K_t = \frac{p_0 - p_v}{\frac{1}{2} r_0 (pn_p D)^2\left(1+\left(\frac{J}{p}\right)^2\right)} \approx \frac{p_0 - p_v}{\frac{1}{2} r_0 (pn_p D)^2} \qquad \textbf{(3.3)}$$

where

n_p is the propeller rotational speed in revolutions per second,

J is the advance ratio which is the ratio of the distance the propeller advances in one revolution to its diameter.

Cavitation will occur if K_t is less than the critical inception cavitation index, K_{ti}, which is in turn a function of the advance ratio, J. For a propeller operating in

uniform flow at the design advance ratio K_{ti} may be as low as 0.5 for suction surface and tip vortex cavitation. At lower advance ratios the inception cavitation indices for tip vortex and suction surface cavitation become larger and may get as high as 5 at stall. Higher advance ratios, corresponding to negative angles of attack, result in reduced inception cavitation indices for tip vortex and suction surface cavitation but the driving face cavitation inception index now becomes the significant factor as the propeller is operating at a negative angle of attack.

Radial variations in wake can cause an earlier onset of cavitation on parts of the propeller that aren't operating at their optimum angle of attack. Circumferential variations in inflow velocity are extremely important as each blade experiences time varying cavitation, which gives rise to narrowband cavitation noise.

The wake often has more effect on cavitation inception than the propeller design. As a general rule:

$K_t > 5$ cavitation is unlikely

$2 < K_t \leq 5$ cavitation may start to occur in a poor (highly non-uniform) wake

$1 < K_t \leq 2$ cavitation may start to occur in a good (reasonably uniform) wake

$0.5 < K_t \leq 1$ cavitation may start to occur in an ideal uniform wake

$0.2 < K_t \leq 0.5$ moderate cavitation

$K_t \leq 0.2$ heavy cavitation

A number of empirically derived prediction formulae are given in the literature for estimating the broadband cavitation noise from surface vessels. Ross (1987) summarises several and presents his conclusion that equivalent results are obtained from:

$$L_S' \approx 175 + 60\log\left(\frac{U_t}{25}\right) + 10\log\left(\frac{B}{4}\right) \qquad \textbf{(3.4)}$$

where:

L_S' is the overall source level integrated over frequencies above 100 Hz (dB re 1μPa at 1m).

Heine (1982) gives formulae for the frequency of the peak in the broadband cavitation spectrum and for the source spectral level at that frequency which can be expressed as:

$$f_m = 120\left(\frac{U_{ti}}{U_t}\right)^{0.7} \qquad \textbf{(3.5)}$$

$$L_{pm} = 91 + 10\log\left[DB\frac{U_t}{U_{ti}}\left(\frac{U_t}{U_{ti}} - 1\right)^2\right] + 25\log\left(\frac{30}{\sqrt{p^2 + J^2}}\right) - 17\log(f_m) \qquad \textbf{(3.6)}$$

Here the peak source spectral level, L_{pm}, is in units of dB re 1 μPa^2/Hz @ 1m. Heine's model uses a spectral level that drops off at 6 dB per octave above the peak frequency, although he also states that some full-scale measurements indicate a faster roll-off than this.

Matusiak (1992) presents a numerical model of cavitation noise which simulates the collapse of discrete cavitation bubbles as they move into regions of higher pressure. The simulation results compare favourably with full-scale noise measurements made on several vessels.

3.1.1.2 *Narrowband cavitation noise*

In addition to the broadband cavitation noise discussed above, measured ship noise spectra show evidence of narrowband noise at harmonics of the propeller blade rate. A detailed discussion and analysis of a proposed mechanism for narrowband cavitation noise is given in Gray & Greeley (1980). The proposed mechanism is gross changes in the cavitating volume on the surface of each propeller blade as the blade encounters varying wake inflow velocities and hydrostatic pressures during each revolution. This fluctuating cavitating volume acts as an acoustic monopole source which radiates at the propeller blade rate and its harmonics.

The authors express the cavitation volume as a function of time as a Fourier series:

$$V_c(t) = \sum_{n=1}^{\infty} A_n e^{iBnw_p t} \qquad \textbf{(3.7)}$$

where:

A_n is the Fourier coefficient for the nth harmonic,

B is the number of propeller blades, and

w_p is the angular velocity of the propeller.

In the absence of boundaries the radiated pressure at a distance r from the propeller at frequency $f_n = \frac{nBw_p}{2p}$ is:

$$p_n = \frac{r_0 p f_n^2 A_n}{r} \qquad \textbf{(3.8)}$$

An estimate of the radiation at the fundamental blade rate frequency was obtained by assuming the cavitating volume fluctuated according to:

$V_c(t) = \frac{1}{2} V_{\max}(1 + \cos Bwt)$

This yielded a mean square pressure at range *r* of:

$$\left\langle p_1^2 \right\rangle \approx \left(\frac{p f_1^2 r_0 V_{\max}}{2\sqrt{2} r} \right)^2 \qquad \textbf{(3.9)}$$

By treating the fluctuating volume source and its surface reflected image as a dipole source the following formula for the dipole source strength was derived:

$$P_d = 4p^2 r_0 f_1^3 h V_{\max} \qquad \textbf{(3.10)}$$

where:

P_d is the dipole source strength (Pa @ 1m), and

h is the propeller depth (m).

Note that there is an error in the equation given in the reference which shows a multiplier of 8, rather than 4 in the above equation. The error does not appear in the dB version which is given correctly as:

$$10\log\left(P_d^2\right) = 140 + 10\log\left(f^6 h^2 V_{\max}^2\right) \qquad \textbf{(3.11)}$$

dB re 1μPa @ 1m

In a later paper Gray (1981) presented comparisons between cavitation volumes predicted from model scale wake measurements and full scale measurements obtained using stereo photography. A graph of cavitation volume against cavitation area was presented which shows that model scale measurements and 2-D foil theory generally under-predict the full-scale cavitation volume. The line of best fit to the full-scale data was given by:

$$\frac{V_c}{D^3} = 0.08\left(\frac{A_c}{D^2}\right)^{1.5} \qquad \textbf{(3.12)}$$

where:

V_c is the volume of the cavitation (m^3) and

A_c is the area of the blade on which cavitation is occurring (m^2).

In the same paper the results of acoustic measurements on two other ships obtained using reciprocity techniques were presented. The primary conclusion was that cavitation volumes are extremely variable with small changes in inflow velocity causing large changes in cavitation volume, and that this results in correspondingly large changes in the radiated acoustic signal at the blade rate and its harmonics.

Measurements of the amplitude of the blade rate vessel vibration of three different ships (measured using an accelerometer mounted on the vessel) showed similar characteristics with variations of 8 to 20 dB occurring with characteristic time scales of a few seconds. Gray (1981) directly related these variations to changes in the acoustic radiation at blade rate.

Arveson & Vendittis (2000) presented a detailed set of noise measurements that were made on the bulk carrier *M/V Overseas Harriette* in 1980. In this paper a comparison was made between the predicted and measured source strengths of the acoustic dipole formed by the combination of the propeller noise source and its surface reflected image. In deriving their prediction formula the authors unfortunately used the incorrect version of Equation 10 given in Gray & Greeley (1980), and therefore computed dipole source levels 6dB higher than they should have. Their predicted source levels at the fundamental blade rate frequency were 3dB lower than their measured values and would have been 9dB lower if the correct formula was used. The authors did not indicate the value of $V_{\max}$ that was used in the prediction formula.

Heine (1982) used the results of Gray & Greeley (1980) and an estimate of the maximum cavitation volume of $V_{\max} = 0.00012D^3$ to predict the dipole radiation from the combination of the fluctuating volume source located at the propeller of a merchant ship and its surface reflected image. His result, for a depression angle of 30°, over-estimated the radiation by about 6 dB. The name of the ship was not stated

in this paper but from the parameters given it appears to be the *M/V Overseas Harriett.*

3.1.1.3 Fluctuating hydrodynamic forces

As discussed in Ross (1987) a fluctuating force acting on a surface radiates acoustic energy as an acoustic dipole source. This is because a fluctuating force gives rise to a fluctuating pressure which then acts as an acoustic source. This is a much less efficient form of radiation than the monopole radiation due to cavitation but can be significant when cavitation is absent. The largest fluctuating forces are usually due to the propeller, and a summary of the treatment of fluctuating propeller forces as given by Ross (1987) follows.

Propellers operating in non-uniform flows produce unsteady forces which then radiate as dipole sources. The forces can also couple to the hull via either pressure fluctuations in the fluid or via the propeller shaft and result in radiation from the hull or appendages. Fluid coupled forces reduce rapidly as the gap between the propeller and the hull or appendage is increased.

The oscillating thrust coefficient is defined as:

$$\tilde{C}_T = \frac{\tilde{T}_{rms}}{r_0 n_p{}^2 D^4} \qquad \textbf{(3.13)}$$

where

$\tilde{T}_{rms}$ is the RMS of the oscillating component of the thrust force,

n_p is the propeller rotation rate (revolutions per second), and

The intensity of the sound radiated directly by the propeller at the m^{th} harmonic of the blade rate, received at a distance r is:

$$I_m(q) \approx \frac{m^2 B^2}{4 r^2 c_0^2} r_0 n_p{}^6 D^8 \tilde{C}_{Tm}^2 \cos^2 q \qquad \textbf{(3.14)}$$

where

$\tilde{C}_{Tm}$ is the fluctuating thrust coefficient at the frequency of the m^{th} harmonic, and

q is the angle between the propeller shaft and the line between the propeller and receiver.

This intensity is generally quite small and it is often hull resonances excited by the oscillating forces transmitted by the propeller shaft that dominate. Note, however, that the oscillating forces can also excite resonances of the propeller itself with a subsequent increase in acoustic output at particular frequencies.

Shaft rate force fluctuations are generally much smaller than blade rate fluctuations but when they occur they result in harmonics, separated by the shaft rate, either side of each of the blade rate harmonic peaks.

3.1.1.4 Machinery noise

A number of different mechanical noise sources can cause structural vibrations within a vessel that are transmitted to the hull and radiated into the water as sound. A detailed discussion is given in Ross (1987), a summary of which is given here.

- The sound power radiated by rotating machinery with a mechanical unbalance increases with the 4^{th} power of the rotational speed and has a spectrum which is dominated by a single tone at the rotational frequency. Harmonics and sub-harmonics may also be present if there is movement within the bearings.

- Reciprocating machines such as diesel engines, pumps etc. produce unbalanced forces and moments that occur at low harmonics of the reciprocation rate. However in most cases the dominant noise source is the impact of the piston with the cylinder wall, which occurs several times each cycle, but is not evenly spaced. The resultant spectrum for a multiple cylinder engine has a fundamental frequency at the crankshaft revolution rate, with harmonics that are multiples of the number of cylinders being emphasised. The latter are called firing rate tonals. Impact noise produces a spectrum of harmonics separated by $1/T$ where T is the period between impacts. The envelope of the harmonics is given by:

  $$w(w) \approx \frac{t w_0}{\sqrt{1+(wt)^2}}$$

  where

  w_0 is the peak amplitude of the impact velocity, t is the decay time constant, and w is angular frequency (rad/s).

- Gear noise is usually dominated by impact noise at the tooth impact frequency and its harmonics, although sub-harmonics are also sometimes observed. The noise power is proportional to the power being transmitted.
- Transformers can produce transformer hum, due to magnetostriction, at twice power line frequency.
- AC electric motors produce noise at power line frequency, twice power line frequency and at a frequency given by the number of rotor slots times the rotational speed. Rotor slot noise is also produced by DC machines whereas in AC machines there are also components at the rotor slot frequency +/- twice the line frequency.
- Ball bearings can generate noise due to resonances of the outer ring being excited by impacts of the balls. Axial pre-loading largely eliminates this noise source and is common practice. In most cases bearing noise is only important when the bearing is nearing the end of its life.

All of the above mechanical noise sources can be characterised by a fundamental frequency and a series of harmonics, in some cases with further modulation.

In general flexural vibration of structural members is the most important means of transmitting the mechanical source vibrations to the hull, and flexural vibration of the hull is the primary mechanism of sound radiation. Ross (1987) deals with these mechanisms in considerable detail. Both serve to markedly change the relative phases and amplitudes of the mechanical source vibration harmonics.

3.1.1.5 Other noise sources

A number of other noise sources are described in Ross (1987), Urick (1983), and Loeser (1992) but, except for occasional cases, are generally of lesser importance than the sources dealt with above. These sources include:

Vortex shedding sounds, especially where periodic vortex shedding excites a structural resonance, or a cavity resonance. A singing propeller is an example of the former where vortices shed from the trailing edge of a propeller blade excite a blade vibration mode.

Radiation from underwater pipe openings where there is an oscillating flow in the pipe (eg an underwater exhaust or pump inlet/outlet).

Noise due to pressure fluctuations in turbulent flow. This form of noise is a very inefficient radiator of sound and consequently is only of importance for hydrophones mounted in the immediate vicinity of the flow, such as inside a sonar dome.

3.1.2 Simulation of vessel noise

A vessel noise simulation was written so that a number of different types of physical noise source could be modelled, including propeller noise, machinery noise, and general broadband and narrowband noise sources. The simulation could also add isotropic noise with a realistic spectrum to the hydrophone signals. Generally the approach taken was to produce signals with properties representative of the types of sources likely to be encountered in practice rather than attempting to produce detailed models of the underlying physical processes.

Each source was represented as a point source with a specified beam pattern, which could be frequency dependent or frequency independent. The signature of an entire vessel was modelled by placing sources of the required types at appropriate locations and independently computing the received signal at each hydrophone due to each source. The resultant hydrophone signals were then calculated by summing the contributions from each source.

The point source model is a good approximation to the reality of spatially extended sources providing the individual hydrophones are in the far-field of the sources which, for a circular piston source, equates to the requirement that (Urick 1983):

$$r >> A / l_0 \qquad \textbf{(3.15)}$$

where:

A is the area of the piston,

l_0 is the acoustic wavelength, and

r is the distance between the source and the hydrophone

Similar relationships can be derived for sources of other geometries.

As a numerical example consider a maximum acoustic frequency of interest of 1000 Hz (an acoustic wavelength of approximately 1.5 m), and a circular piston source of 10 m diameter. At this frequency the source can be treated as a point

source provided the hydrophone is much more than 52 m away, and at lower frequencies or with smaller sources a shorter distance would suffice.

The source simulations were implemented using object oriented programming techniques with each type of source being represented by a different class. This approach facilitated the simulation of arbitrary numbers of sources of the same and different types.

3.1.2.1 Propeller noise model

Propeller noise was modelled as a combination of three sources at the same location: a broadband cavitation source with monopole radiation characteristics and a broad spectrum, a narrowband cavitation source with a monopole radiation characteristics and a spectrum comprising a number of spectral lines, and a fluctuating force source with dipole radiation characteristics and a spectrum comprising a number of spectral lines.

Broadband cavitation source

A signal generation flow-chart for the broadband cavitation source is shown in Figure 3.3. A Gaussian white noise generator was used to generate a time-series, $x(t)$, with a flat spectrum. This time-series was then transformed into the frequency domain using a Fast Fourier Transform (FFT) where it was filtered to obtain an amplitude spectrum with a 9 dB per octave roll-off below a specified peak frequency and a 6 dB per octave roll-off above the peak frequency. The filter transfer function used was based on a Butterworth response (Tietze & Schenk 1991), although it was necessary to use a fractional order filter to obtain the 9 dB per octave response and, unlike a true Butterworth filter, only the amplitude of the spectrum was altered; the phase was left unchanged.

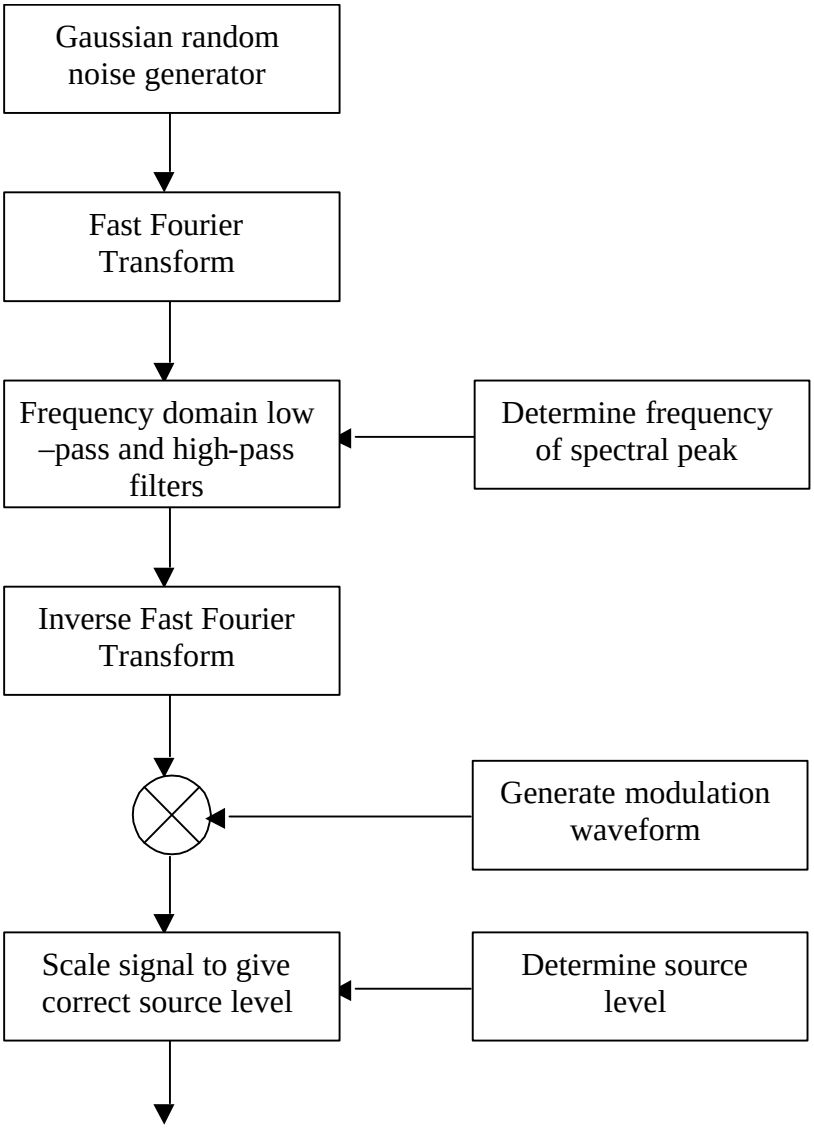

Figure 3.3 Signal generation flow-chart for broadband cavitation source.

The filtered spectrum was calculated according to:

$$Y(f) = X(f)\frac{1}{\sqrt{\left[1+\left(\frac{f}{f_{lp}}\right)^{2}\right]\left[1+\left(\frac{f_{hp}}{f}\right)^{3}\right]}} \qquad \textbf{(3.16)}$$

where:

f_{lp} is the low-pass cut-off frequency (Hz),

f_{hp} is the high-pass cut-off frequency (Hz),

$X(f)$ is the Fourier transform of the original white noise time-series, and

$Y(f)$ is the Fourier transform of the filtered time-series.

The two cut-off frequencies were related to the expected peak cavitation frequency, f_m, according to the following formulae which were chosen to give an appropriate spectral shape:

$f_{lp} = f_m$, and

$f_{hp} = 0.5 f_m$.

f_m was computed using an equation based on Equation 3.5, but modified to include a depth dependence. Substituting Equation 3.3 into Equation 3.1 implied that $f_m \propto (p_0 - p_v)^2$. By assuming Equation 3.5 applies to a mean propeller depth of 4 m and noting that it already contains a pressure dependence of $(p_0 - p_v)^{0.35}$ because of the dependence of U_{ti} on pressure for a constant K_{ti}, the following expression for f_m was derived:

$$f_m = 3.91 \times 10^{-7} (p_0 - p_v)^{1.65} \left(\frac{U_{ti}}{U_t} \right)^{0.7} \qquad \textbf{(3.17)}$$

The mean square source level for frequencies above 100 Hz was estimated by using Equation 3.2 and determining the constant of proportionality that provided the best fit between equations 3.2 and 3.4 for $K_{ti} = 2$ and $U_{ti} = 11\,\text{m/s}$, typical values for surface vessels. The fit was carried out in the log-log domain to give improved accuracy at the low speeds that this simulation is required for. The resulting equation for the mean square pressure above 100 Hz was:

$$\left\langle p_{>100}^2 \right\rangle = 8.25 \times 10^{-9}\, r_0^2 c_0 B K_{ti} U_{ti}^3 \left[\left(\frac{U_t}{U_{ti}} \right) \left(\frac{U_t}{U_{ti}} - 1 \right)^2 \right] \qquad \textbf{(3.18)}$$

Scaling of the simulated signal was carried out by high-pass filtering the signal with a sixth order Butterworth filter with a 100 Hz cut-off and then calculating the mean square of this filtered signal, $\left\langle y_{>100}^2 \right\rangle$. The original signal was then multiplied by $\sqrt{\frac{\left\langle p_{>100}^2 \right\rangle}{\left\langle y_{>100}^2 \right\rangle}}$, resulting in the final simulated waveform.

Radiation from the broadband cavitation source was assumed to be omni-directional. This assumption was made because of the lack of consistency of horizontal beam patterns given in the literature and because the variations that were quoted were primarily in the forward and aft directions. Since the technique developed here was concerned primarily with acoustic noise levels abeam of the vessel, fore and aft beam patterns were of little importance.

Narrowband cavitation source

The narrowband cavitation source time series was simulated by summing sine waves with specified relative amplitudes and phases, and frequencies corresponding to the propeller blade rate and its harmonics. The amplitude variation observed by Gray (1981) was simulated by combining this deterministic signal with a random signal generated by passing Gaussian random noise through a bank of bandpass filters at the blade rate frequency and its harmonics. The filtering was carried out in the frequency domain in a manner analogous to that described previously for the broadband cavitation source, with each filter having a raised cosine frequency response, a 0.6 Hz 3 dB bandwidth and an amplitude response proportional to the specified harmonic relative amplitude. The filter bandwidth was chosen to give a similar time variation envelope to that shown in Gray's plots, and the random component was added to the deterministic signal in the ratio 0.43:1 to give a similar range of amplitudes.

For surface vessels at normal operating speed the source level of narrowband cavitation at the fundamental frequency (propeller blade rate) could be estimated from Equation 3.9 with $r = 1$ m and, following Heine (1982), by using a maximum cavitation volume of $V_{\max} = 0.00012D^3$.

Heine's formula for $V_{\max}$ does not apply to vessels operating well below their normal operating speed nor was any information found in the literature on the effect of propeller depth on $V_{\max}$. In order to give realistic predictions over a range of operating conditions a simple theoretical model was therefore developed based on the assumption of a triangular pressure distribution over the suction surface of the propeller blade. Heine's formula was then used to calibrate the model.

Fluctuating force source

The fluctuating force time series was simulated by combining deterministic sinusoidal signals at the blade rate and its harmonics with band-pass filtered random signals in the same manner as for narrowband cavitation noise. The random signals were included to simulate the effect of turbulence on the propeller thrust. In the absence of any better information the same filter band-widths and proportions of deterministic to random signals were used as for narrowband cavitation noise. The time series was also amplitude modulated at the propeller shaft rate. Equation 3.14 was used to determine the intensity of each harmonic of the blade rate.

Radiation from the fluctuating force source was assumed to have a dipole (cosine) beam pattern with maxima in the fore and aft directions and no radiation at right angles to the propeller's axis of rotation.

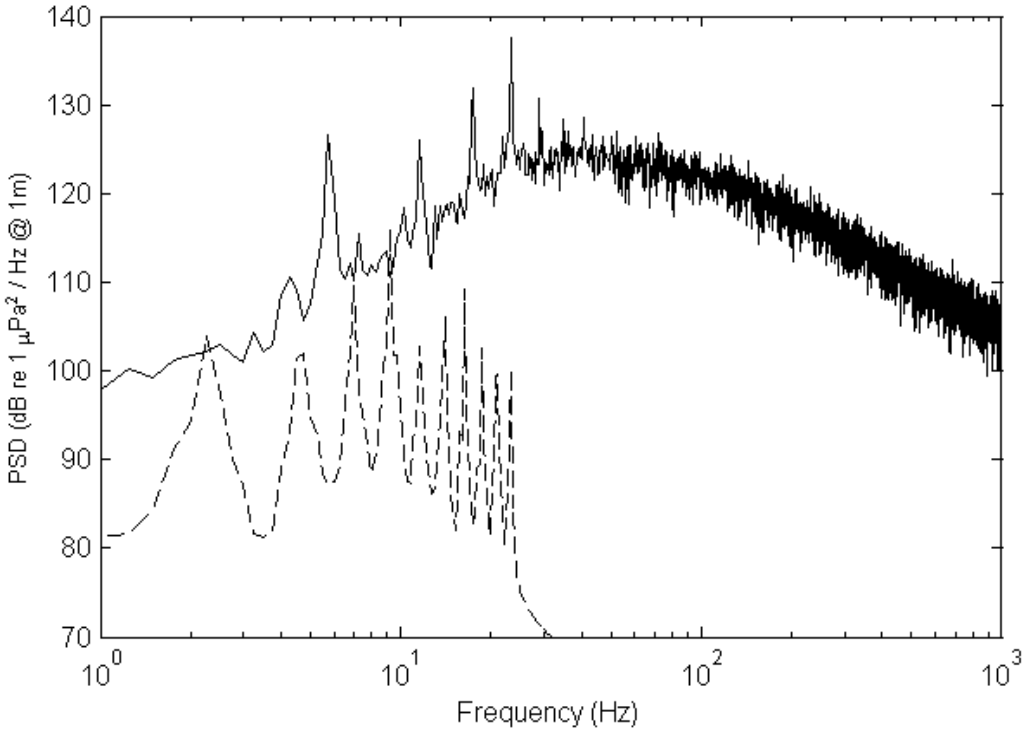

Figure 3.4 Power density spectra of simulated propeller noise for a vessel with a cavitating propeller (solid line) and a non-cavitating propeller (broken line). Analysis bandwidth is 0.25 Hz. These plots were generated using parameters appropriate to the tug *Tammar* (see Chapter 4) operating on a single propeller at 10 knots and 4 knots respectively.

Spectra of two examples of simulated propeller noise are shown in Figure 3.4. In one case the propeller was cavitating and the spectrum included contributions due to both broadband and narrowband cavitation. The fluctuating force source was also

present but produced levels much lower than the cavitation sources. In the second case the propeller wasn't cavitating and only the fluctuating force source was present.

3.1.2.2 Machinery noise model

As discussed in Section 3.1.1.4 the spectrum of machinery vibration typically consists of a sequence of harmonics of the fundamental frequency, each of which will have side-bands if modulation is present. The relative amplitudes and phases of these harmonics are then modified by the transmission path to the radiating surface, and by the radiation process itself.

Because of the difficulty of simulating this complete physical process in a realistic manner for given items of machinery the noise was simply modelled as the sum of a specified number of harmonics of given relative amplitudes and phases. In addition the waveform could be amplitude modulated at a specified frequency. The source level, source location, beam pattern and beam axis orientation could all be arbitrarily specified.

3.1.2.3 General broadband sources

General broadband noise sources were included in the simulation to allow for both near-field (vessel located) and far-field broadband sources of arbitrary location and beam pattern.

Near-field

Near-field broadband sources were simulated by generating Gaussian random noise and then filtering this with a fourth order high-pass filter and a fourth order low-pass filter of specified cut-off frequencies. The location of each source on the vessel, its source level, beam pattern (omnidirectional, dipole, circular piston, or rectangular piston) and the orientation of its beam axis could all be arbitrarily specified.

Far-field

Far-field broadband sources were included to allow the simulation of interfering sources a long way from the array that were not moving with the vessel. The signals were generated in a similar way to those of near-field broadband sources but were normalised to achieve a specified RMS pressure level at the origin of the tow-vessel

coordinate system. The location of each source was specified in terms of its azimuth and elevation from the vessel.

The spectral characteristics of the far-field broadband source were effectively the same as those of the near-field broadband source except for the normalisation of the vertical axis.

3.1.2.4 General tone-burst source

Tone burst sources were simulated to provide the capability of including arbitrary narrowband sources such as pingers. Each source was specified in terms of its location, frequency, start and stop times, source level, beam pattern, and the orientation of its beam axis.

3.1.2.5 Isotropic noise

For the purposes of this simulation noise at the hydrophones was assumed to be isotropic and therefore uncorrelated between hydrophones. The noise spectrum was determined by adding the appropriate noise power spectral densities for wind dependent noise and traffic noise as determined from the curves given in Cato (1995), which are shown here in Figure 3.5.

The wind dependent noise spectra were extrapolated down to lower frequencies by assuming that the slope of the spectrum remained constant at the 30 Hz level, whereas the traffic noise was extrapolated to lower frequencies by assuming the levels remained constant at the 20 Hz levels.

For each hydrophone a Gaussian random noise sequence was generated and then Fourier transformed, filtered in the frequency domain with the noise spectrum, and inverse transformed back to the time domain to give the required signal.

An example spectrum is shown in Figure 3.6 for Indian Ocean traffic noise and a wind speed of 7.5 m/s.

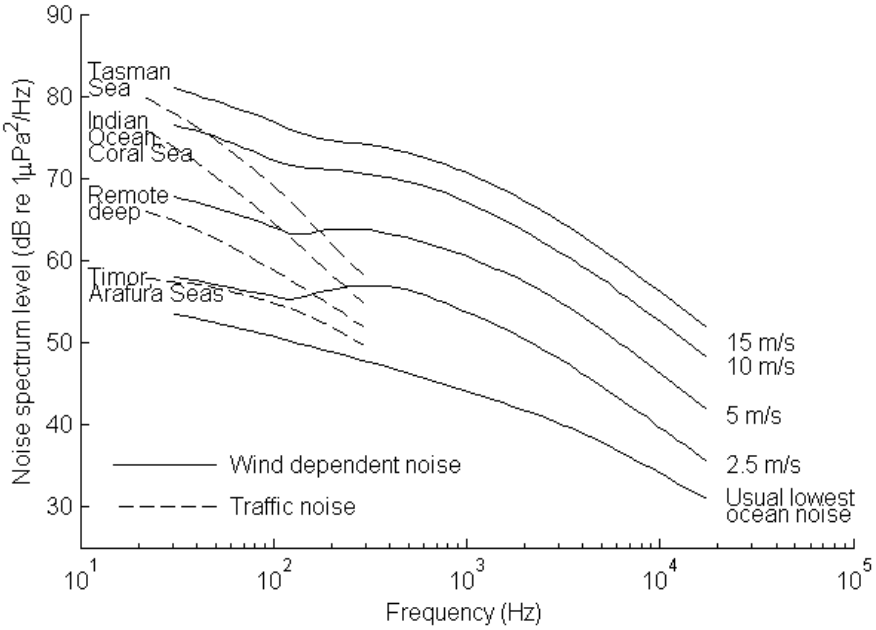

Figure 3.5 Ambient sea noise prediction curves from Cato (1995).

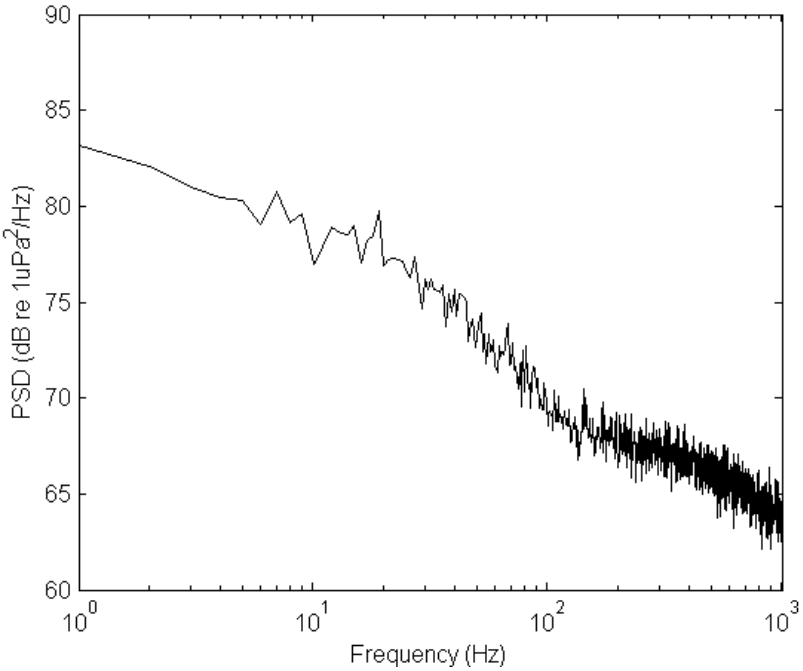

Figure 3.6 Example power density spectrum of simulated sea noise in the Indian Ocean for a wind speed of 7.5 m/s – note that these are received signal levels rather than source levels.

3.2 Acoustic propagation simulation

3.2.1 Unbounded ocean

The vessel noise source simulations described in Section 3.1 treated each noise source as a point source that produced a specified acoustic pressure time-series, $p_s(t)$, at a reference distance of 1 m in the direction of the source's beam axis. Propagation in any other direction modified the time series by a beam pattern function, which could either be frequency dependent, $b(q_s, f_s, f)$, or frequency independent $b(q_s, f_s)$. The coordinate system (X_s, Y_s, Z_s) used to calculate the signal received by the hydrophone due to a single source in the absence of boundaries is shown in Figure 3.7. This coordinate system had the same orientation as the tow-vessel coordinate system but its origin was translated to the source location.

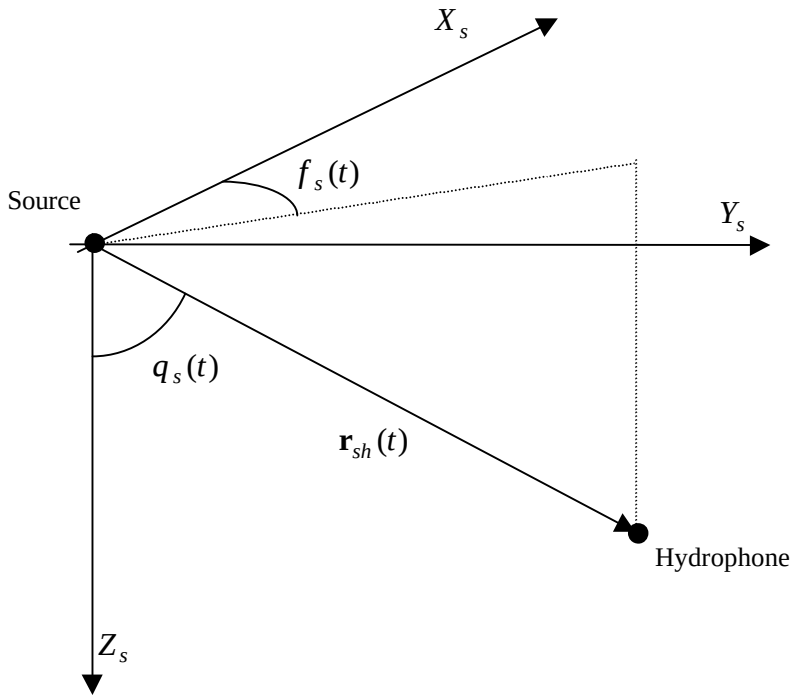

Figure 3.7 Coordinate system for calculating signal received by hydrophone for unbounded propagation

3.2.1.1 Sources with frequency independent beam patterns

An equation for the acoustic pressure at a moving hydrophone due to a source in an infinite, isotropic medium was derived by analogy with Equation 2.11, with

displacement potential replaced by pressure and the inclusion of a term to account for the directionality of the source.

$$p_h(t_r) = \frac{p_s\left(t_r - \frac{r(t_r)}{c_0}\right) b(q_s(t_r), f_s(t_r))}{r(t_r)} \qquad \textbf{(3.19)}$$

where

t_r is the time of reception of the signal (s) and

$r(t_r) = |\mathbf{r}_{sh}(t_r)|$ is the distance from the source to the hydrophone.

Equation 3.19 was implemented in the simulation by firstly linearly interpolating hydrophone locations to the desired hydrophone sampling times and then calculating the corresponding azimuth and elevation angles and ranges of the hydrophone relative to the source. These values were then used to compute the appropriate values of $b(q_s, f_s)$ with due allowance being made for the orientation of the source beam axis relative to the coordinate system. $p_s\left(t - \frac{r(t)}{c_0}\right)$ was then calculated by cubic interpolation (Keys 1981) of the source pressure time series.

3.2.1.2 *Sources with frequency dependent beam patterns*

The inclusion of a frequency dependent beam made the calculation of the received signal at a moving hydrophone considerably more complicated. This was because the frequency spectrum of the received signal was then different at different locations in the beam, and thus for a moving hydrophone the beam pattern acted as a time varying filter.

Winder & Loda (1981) gave the following formula for the output of a time-varying filter:

$$y(t) = \frac{1}{2p} \int_{-\infty}^{\infty} X(f) H(f;t) e^{iwt} dw \qquad \textbf{(3.20)}$$

where

$y(t)$ is the output of the filter at time t,

$X(f)$ is the Fourier transform of the input signal, $x(t)$,

$H(f;t)$ is the transfer function of the filter at time t,

$w = 2pf$ is angular frequency (rad.s^{-1}), and

i represents the square-root of –1.

Applying Equation 3.20 to the acoustic radiation from a source with a frequency dependent beam pattern yielded

$$p_h(t_r) = \frac{1}{r(t_r)} p_s'\left(t_r - \frac{r(t_r)}{c} \right) \qquad \textbf{(3.21)}$$

where

$$p_s'(t) = \frac{1}{2p} \int_{-\infty}^{\infty} P_s(f) b[q(t_r(t)), f(t_r(t)), f] e^{iwt} dw \qquad \textbf{(3.22)}$$

is the effective source waveform in the direction of the hydrophone. In this equation $P_s(f)$ is the Fourier transform of the source waveform $p_s(t)$.

The signal receive time at the hydrophone was then given by

$$t_r(t) = t + \frac{r(t_r(t))}{c} \qquad \textbf{(3.23)}$$

which could not, in general, be solved explicitly but was amenable to simple numerical solution.

There were two situations which resulted in a simplification of Equation 3.22. If the beam pattern was independent of frequency the equation reduced to

$$\begin{aligned} p_s'(t) &= b[q(t_r(t)), f(t_r(t))] \frac{1}{2p} \int_{-\infty}^{\infty} P_s(f) e^{iwt} dw \\ &= b[q(t_r(t)), f(t_r(t))] p_s(t) \end{aligned} \qquad \textbf{(3.24)}$$

which led directly to Equation 3.19.

If the beam pattern was independent of time, for example if the hydrophone was stationary or moved only through a range of angles where the beam pattern was constant then

$$\begin{aligned} p_s'(t) &= \frac{1}{2p} \int_{-\infty}^{\infty} P_s(f) b(f) e^{iwt} dw \\ &= \Im^{-1}\{P_s(f) b(f)\} \end{aligned} \qquad \textbf{(3.25)}$$

where

$\Im^{-1}$ represents the inverse Fourier transform.

Equation 3.22 was then discretised by analogy with the derivation of the discrete inverse Fourier transform to yield

$$p'_{s,k} = \frac{1}{N}\sum_{n=0}^{N-1} P_{s,n} b_{k,n} e^{2pikn/N} \qquad \textbf{(3.26)}$$

where

$P_{s,n} = P_s(f_n)$,

$b_{k,n} = b[q(t_r(t_k)), f(t_r(t_k)), f_n]$,

$$f_n = \begin{cases} \dfrac{n}{Ndt}, & 0 \le n \le N/2 \\ \dfrac{n-N}{Ndt}, & N/2+1 \le n \le N-1 \end{cases},$$

$w_n = 2pf_n$,

$t_k = kdt$, and

dt is the sampling interval.

The operation count for direct implementation of Equation 3.26 increased with the square of the number of points, making it impractical to use this method for generating long time series. For example a Matlab implementation of Equation 3.26 took just over 8 minutes to generate 8.2 seconds of data at a sampling rate of 1 kHz on a 220 MHz Pentium PC. An approximate implementation was therefore developed which relied on the assumption that the beam pattern varied slowly with time and frequency.

The algorithm was as follows:

1. The raw source signal was divided into a series of segments that overlapped by 50%.
2. Each segment was Fourier transformed.
3. The resulting spectrum for each segment was multiplied by the beam pattern, as a function of frequency, appropriate for the time corresponding to the centre of the segment.

4. The result was inverse Fourier transformed giving a modified time domain waveform for each segment.

5. The segments were reassembled into a single waveform by performing a weighted average of the overlapping sections. The triangular weighting functions shown in Figure 3.8 were used to eliminate jumps in the signal at the segment boundaries.

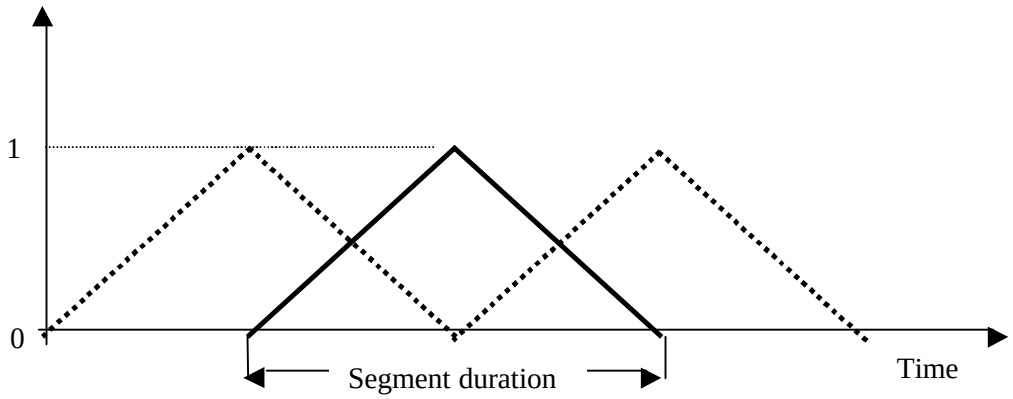

Figure 3.8 Triangular weighting functions used for recombining segments

The operation count for this method was of order $N\log_2(NSeg)$ where N is the total number of points in the time series and $NSeg$ is the number of points in each segment. This resulted in far fewer operations than the exact method for long time series. The same example that took 8 minutes using the exact method took only 0.5 seconds using the approximate method with 256 point segments.

The assumption of a slow change in beam pattern over time equated to the requirement that the change over the segment duration, $NSegdt$, was insignificant. The assumption of a slow change with frequency required the change in beam pattern over the frequency interval $1/(NSegdt)$ to be insignificant. Note that when choosing the segment length there was a direct trade-off between these two requirements.

To test the method a point source was simulated with a beam pattern equivalent to the far-field beam-pattern of a 100m square piston in an infinite baffle. This represented a very large source, with a narrow beam pattern and provided a worst-case test of the method. The maximum in the beam pattern was at an azimuth of 0 degrees and the azimuth of the hydrophone relative to the source as a function of time was as shown Figure 3.9. The source waveform was Gaussian random noise

and 8.192 seconds of data were simulated with a sampling interval of 0.001 seconds. A segment length of 256 points was used for the calculation by the approximate method.

The hydrophone signals computed by the two different methods are shown in Figure 3.10, and Figure 3.11 shows the difference between them. Note that the signals were normalised by the root mean square (RMS) of the signal computed by the exact method. The differences between them were mainly at low frequency, which can also be seen in their spectra, which are shown in Figure 3.12. A plot of the spectrum of the differences between the two signals is given in Figure 3.13 and shows that most of the error is at frequencies below 5 Hz.

The reason for the low frequency error was the frequency limit of the approximate method, which in this case was 3.9 Hz. Increasing the segment length improved the low frequency response at the expense of the speed of response to changes with time. Because of this effect the minimum frequency of interest was used to determine the appropriate segment length in the full simulation.

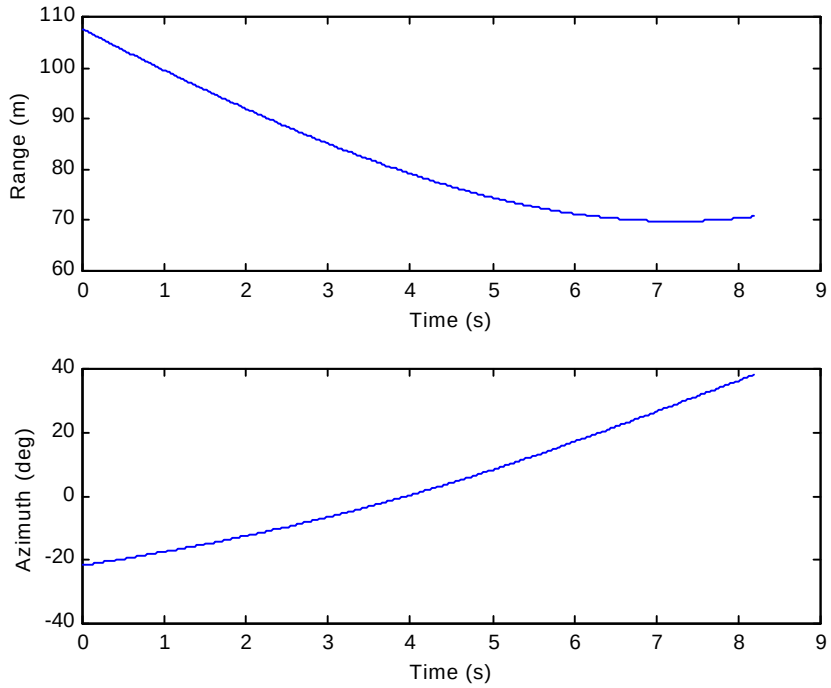

Figure 3.9 Range and azimuth of the hydrophone relative to the source as a function of time

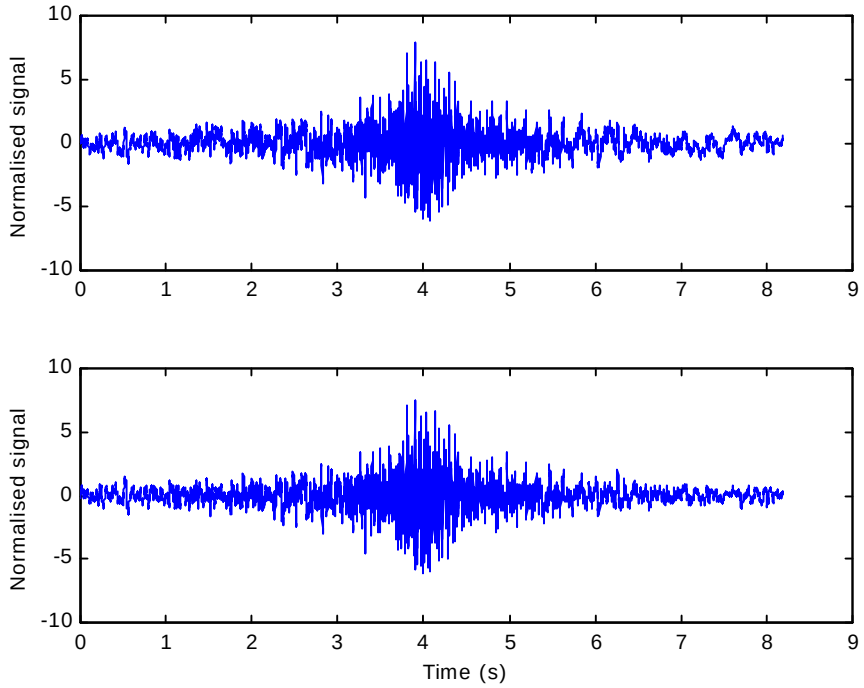

Figure 3.10 Simulated hydrophone signal calculated using exact method (top) and approximate method (bottom). Signals are normalised to a RMS level of 1.

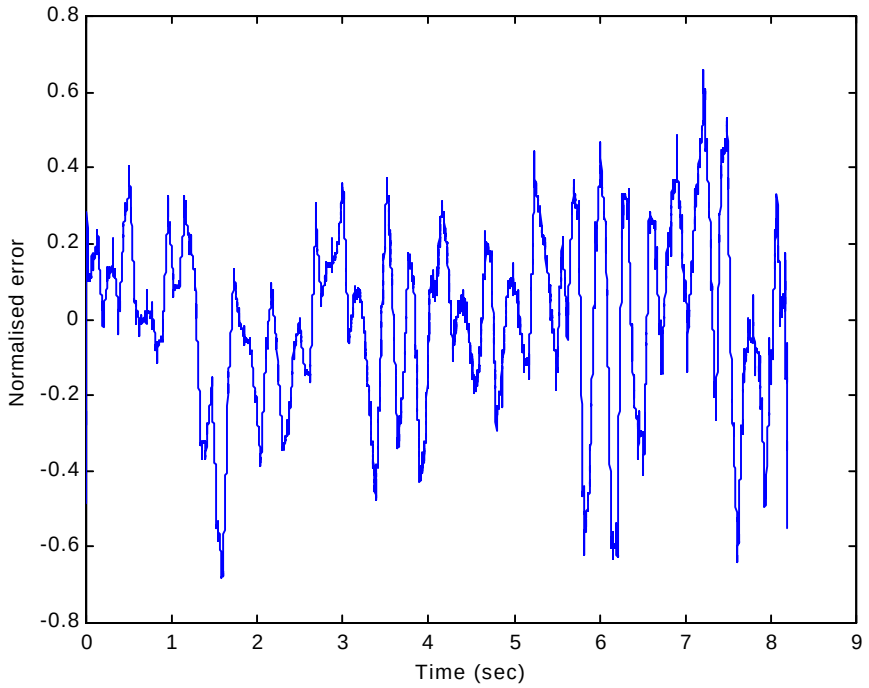

Figure 3.11 Difference between normalised hydrophone signals shown in Figure 3.10 (approximate – exact).

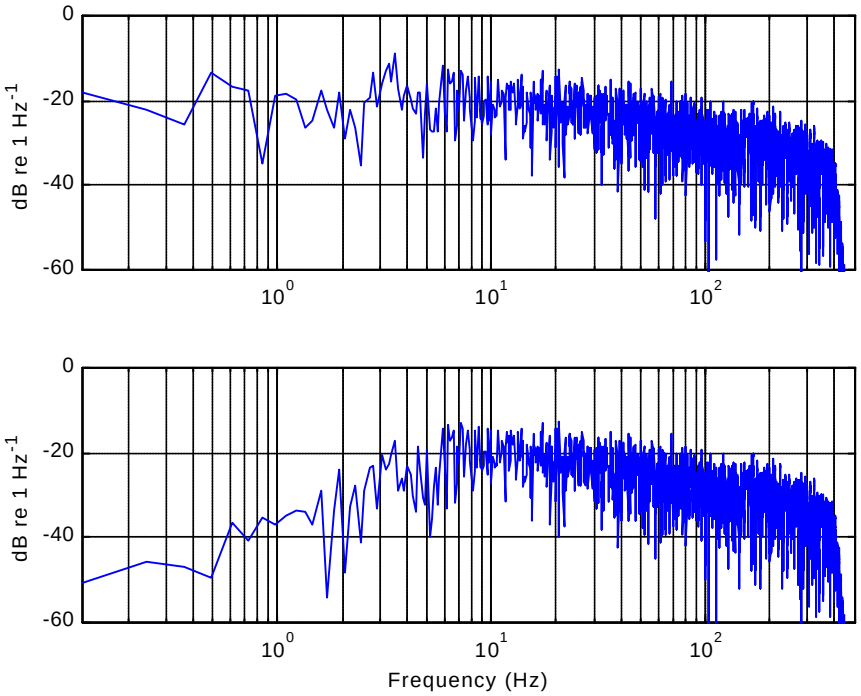

Figure 3.12 Spectral densities of normalised hydrophone signals shown in Figure 3.10. Top is exact method, bottom is approximate method.

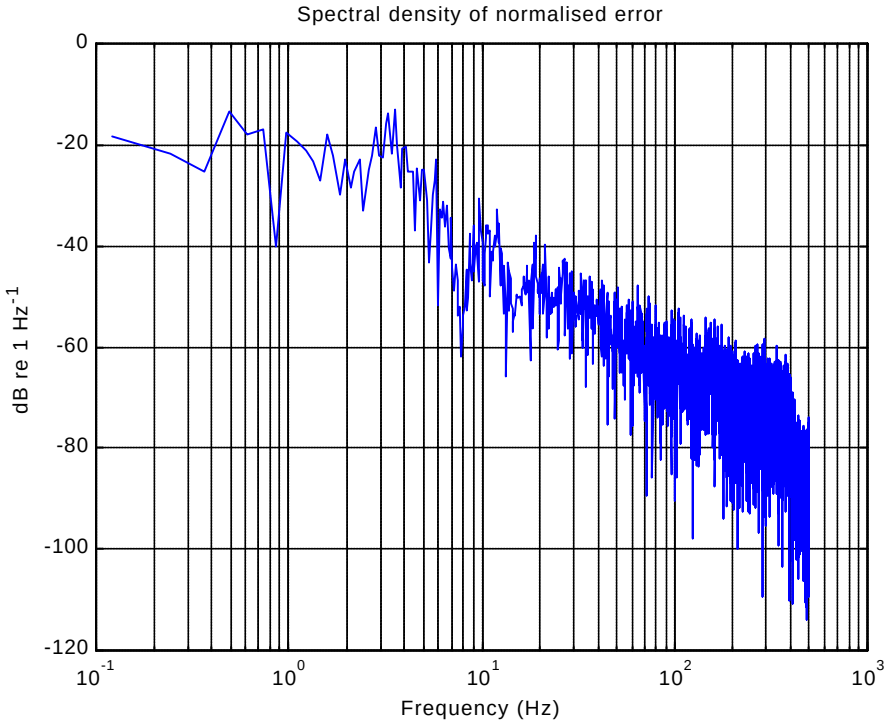

Figure 3.13 Spectral density of difference between normalised signals generated by approximate and exact methods shown in Figure 3.11

3.2.2 Deep ocean

The deep ocean case was dealt with by the method described in Section 3.2.1 but with the addition of image sources to account for the reflection at the sea surface. One image source was created for each real source on the vessel and was placed the same distance above the water surface as the real source was below it. The signal generated by the image source was the signal generated by the real source multiplied by a reflection coefficient which was taken as -1 for a flat sea surface.

Rough sea surfaces were accounted for by modifying the reflection coefficient according to Equation 2.41. Note that the resulting reflection coefficient was frequency dependent and therefore was handled by the method used for frequency dependent beam patterns (see Section 3.2.1.2). No attempt was made to model the incoherent scatter from the rough surface as this was considered to be too computationally demanding to incorporate in the simulation.

To investigate the effect of sea surface roughness, the transmission loss was computed from the simulation output by running the simulation with a mechanical noise source with a fundamental frequency of 5 Hz and with all harmonics up to 450 Hz having the same amplitude. The results were computed as follows:

1. The received signal was broken up into segments 0.512 seconds long with 50% overlap of adjacent segments.
2. The power density spectrum of each received signal segment was computed without averaging (see Chapter 12 of Press et al. 1988).
3. The power density spectrum of each segment of the transmit signal was computed in the same way and then the spectra of these segments were averaged.
4. The transmission loss as a function of frequency was computed for each received signal segment by dividing the received segment spectra computed in 2 by the source spectrum computed in 3 and then taking $10\log_{10}$ of the result.
5. The transmission loss at the required frequency was then calculated for each segment by cubic interpolation in the frequency domain.

6. The result of 5 was plotted against the horizontal spacing between the source and receiver at the centre time of the corresponding receive signal segment.

A comparison between transmission loss versus range plots computed from the simulation output for various values of sea surface roughness and frequencies of 200 Hz and 400 Hz are shown in figures 3.14 and 3.15. The source depth was 40 m and the receiver depth was 20 m. The theoretical curve for a perfectly reflecting sea surface is also plotted. This was calculated by combining the spherical waves from the source and its image according to Equation 3.27:

$$TL = -20\log\left(\left|\frac{e^{ikr_s}}{r_s} - \frac{e^{ikr_i}}{r_i}\right|\right) \qquad \textbf{(3.27)}$$

where:

TL is the transmission loss (dB)

r_s is the slant range between the source and hydrophone (m),

r_i is the slant range between the image source and hydrophone (m), and

k is the wavenumber (m^{-1}).

The plots in figures 3.14 and 3.15 showed excellent agreement between the theoretical and simulated curves for the flat sea surface although there was a slight discrepancy at 400 Hz which was due to errors introduced when interpolating the received signal when there were only a few samples per cycle.

The influence of sea surface roughness followed the expected behaviour of smoothing out the fluctuations due to the interference between the two paths, an effect that was most apparent at high frequencies and at short ranges where the ray paths were steeper.

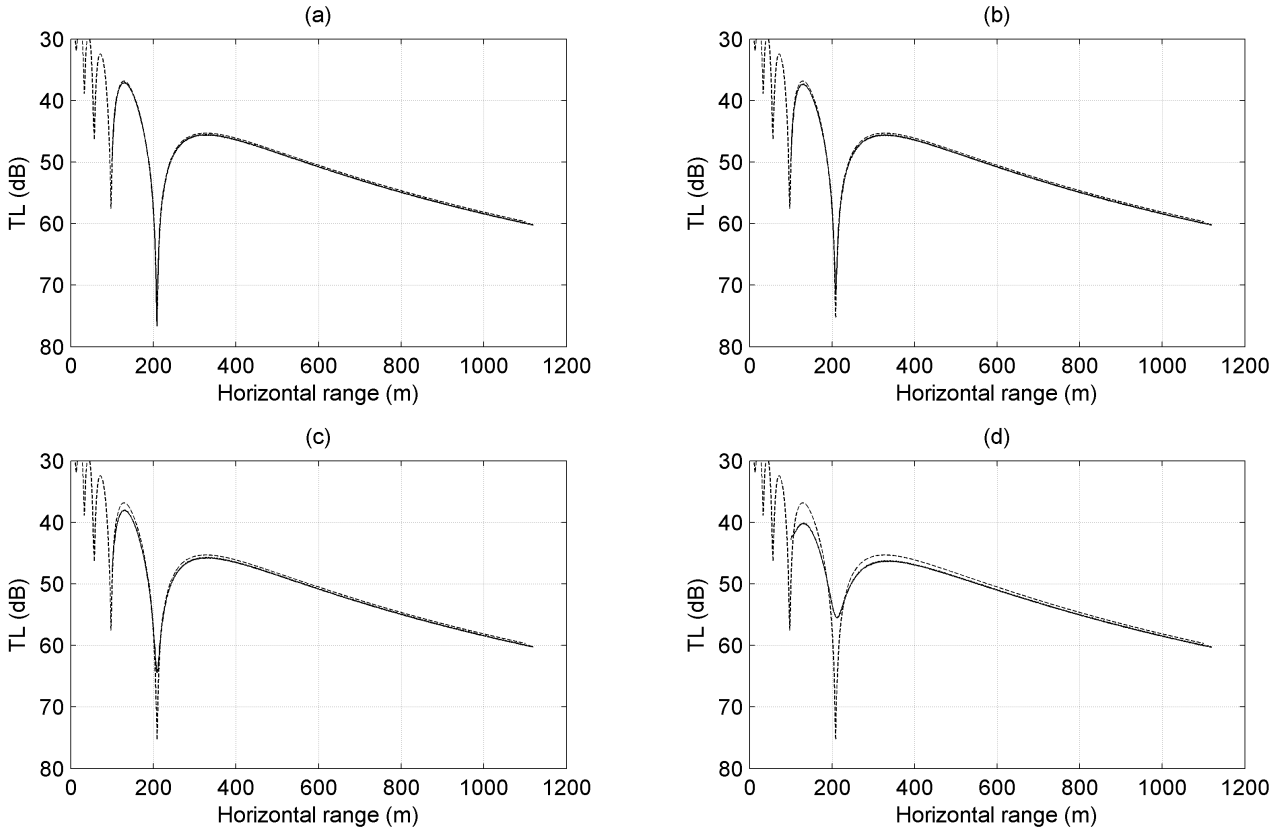

Figure 3.14 Transmission loss vs. horizontal range in deep water at 200 Hz. Source depth was 40 m, hydrophone depth was 20 m. Dashed line is theoretical curve for a flat sea surface, solid line was computed from simulation output for RMS surface roughness of: (a) 0 m, (b) 0.5 m, (c) 1 m and (d) 2 m.

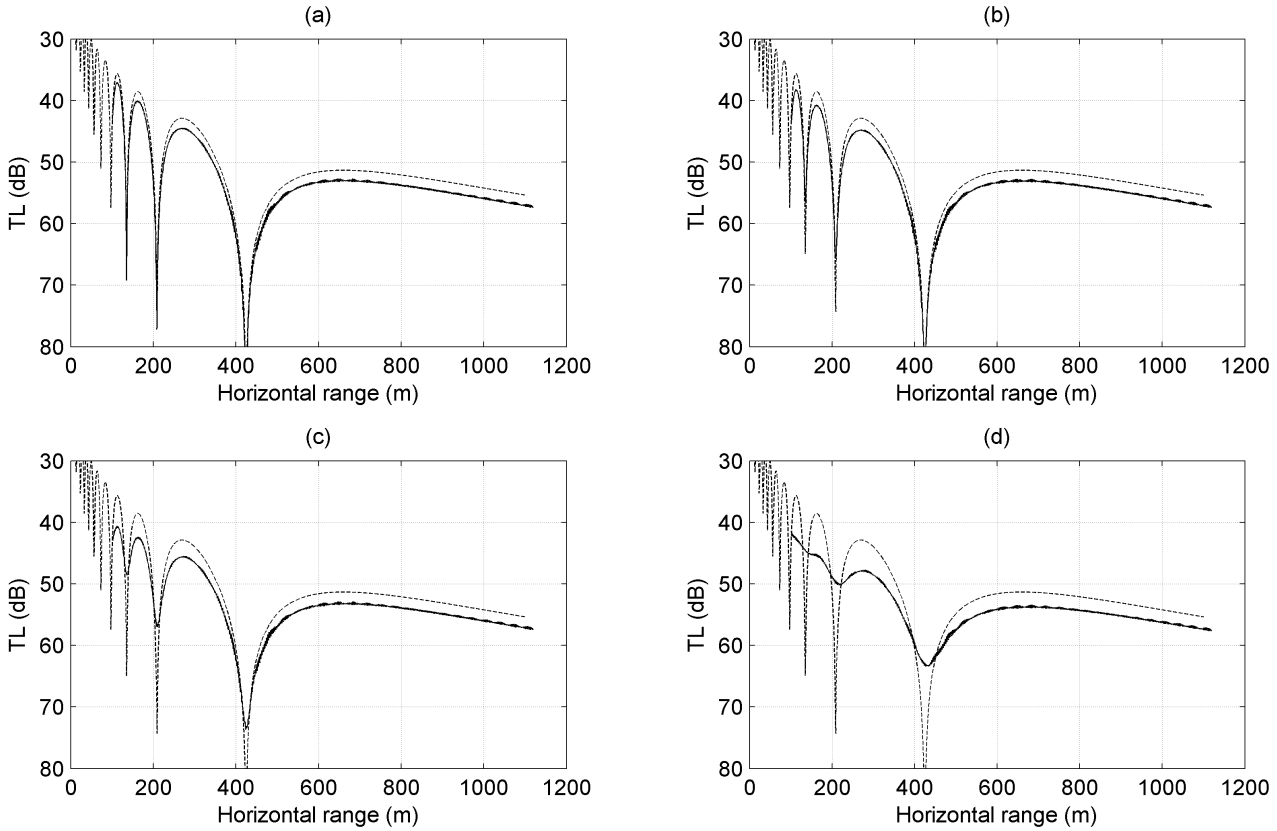

Figure 3.15 Transmission loss vs. horizontal range in deep water at 400 Hz. Source depth was 40 m, hydrophone depth was 20 m. Dashed line is theoretical curve for a flat sea surface, solid line was computed from simulation output for RMS surface roughness of: (a) 0 m, (b) 0.5 m, (c) 1 m and (d) 2 m.

3.2.3 Shallow ocean

Two different approaches were taken to simulating acoustic propagation in shallow water. In the first the image method described in Section 3.2.2 was extended to deal with reflections at both the sea surface and the seabed. This is described in Section 3.2.3.1.

The second approach was to use a well-established acoustic propagation program based on the wavenumber integration technique to generate transfer functions from which the time domain waveforms were computed by Fourier synthesis. (See Section 3.2.3.2.)

3.2.3.1 Extension of image method

The presence of the seabed complicated the image method in two ways. Firstly, as is shown in Figure 3.16 there were now an infinite number of image sources, each corresponding to a different ray path. At the relatively short ranges being dealt with here the contributions from image sources well away from the axis were small because the signals from these sources underwent multiple reflections from the seabed at incidence angles less than the critical angle and were consequently attenuated rapidly. A relatively small number of image sources were therefore sufficient to give accurate results.

A second complication was that in order to obtain accurate results at low frequencies it was necessary to incorporate the complicated physics of the reflection of a spherical wave at the seabed as described in Section 2.4.1. The simulation was therefore written so that reflections at the seabed could be dealt with in any of the following ways:

1. by simply using the plane-wave reflection coefficient,
2. by including the effects of beam displacement through equations 2.25 to 2.27, or
3. by implementing the saddle point method (equations 2.32 and 2.33).

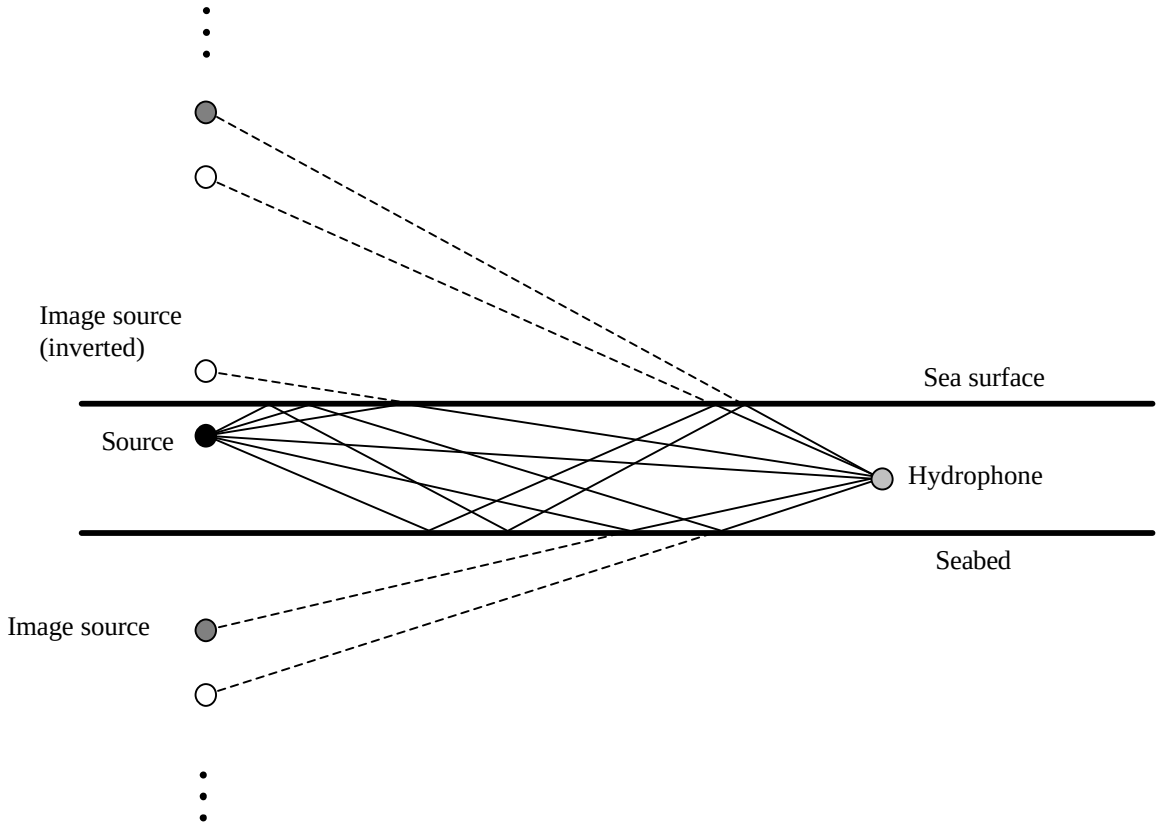

Figure 3.16 Shallow water image source geometry

These different methods of dealing with seabed reflections were incorporated in the simulation by computing an effective multiple reflection coefficient for each ray path that incorporated the losses and phase shifts associated with all reflections along the path. For the plane wave method this was simply given by:

$$R_{eff} = R_s^{n_s} R_b^{n_b} \qquad \textbf{(3.28)}$$

where

R_s is the sea surface plane wave reflection coefficient (including rough surface effects),

R_b is the seabed plane wave reflection coefficient,

n_b is the number of seabed reflections, and

n_s is the number of surface reflections.

For the other two methods the procedure was to compute the ratio of the received pressure to the source pressure, p / p_0, for sinusoidal signals at the required

frequencies using equations 2.25 to 2.27 or equations 2.32 and 2.33 and then calculate the effective multiple reflection coefficient from:

$$R_{eff} = \frac{p}{p_0} re^{-ikr} \qquad \textbf{(3.29)}$$

where r is the slant range between the image source and the hydrophone.

Note that the resulting effective reflection coefficient was, in most cases, frequency dependent.

To implement the beam displacement method the incidence angle at the seabed was first computed for the ray path assuming no beam displacement. If this angle was less than the critical angle the plane-wave reflection coefficient was used in Equation 3.28. Otherwise, the beam displacement caustic for the ray path was located by means of a golden section search (Press et al. 1988) and the receiver range was compared to the caustic range. If the receiver range was less than the caustic range the shadow zone formula (Equation 2.25) was used to compute the received pressure. If the receiver range was greater than the caustic range the method of bisection (Press et al. 1988) was used to locate the two eigenrays and the received pressure was computed using the insonified zone formula (Equation 2.26).

In order to implement the saddle point method it was first necessary to generalise the phase function, Equation 2.31, to the case of multiple surface and seabed reflections. Using the approach given in Westwood (1992), the following function was derived:

$$j(k_r) = k_r r_h + g_1(z_0 + z_h) - in_b \ln(R_b(k_r)) + n_s p \qquad \textbf{(3.30)}$$

Calculation of the received pressure by the saddle point method was straightforward apart from finding a robust method for determining the saddle point locations in complex wavenumber space. Following Westwood (1992), this was done by using Newton-Raphson iteration (Press et al. 1988, Chapter 9) to find locations corresponding to $j' = \frac{dj}{dk_r} = 0$. This was an iterative procedure that changed k_r by $dk_r = -j'/j''$ on each iteration. Different starting locations were used to select between the two saddle points. To make the method robust it was found necessary to include a number of bounds checks and to keep halving the computed value of dk_r until $|j'(k_r + dk_r)| < |j'(k_r)|$.

3.2.3.2 Wavenumber integration (fast-field) method

An alternative shallow water simulation was implemented based on the SCOOTER fast-field program (Porter 1999). In order to apply this program to the case of a moving receiver it was necessary to make the assumptions that the source depth was constant, and that the source velocity was sufficiently small relative to the environment that the dependence of the integration kernel, $\hat{\Psi}(k_r, z; w_0 + k_r v_s \cos q_s)$ in Equation 2.40, on source velocity could be ignored. Under these assumptions the equation for the received field at a moving receiver was obtained by substituting $r_h = r_h(t)$ and $z = z(t)$ into Equation 2.34, giving:

$$\Psi(r_h(t), z(t), w_0) = \int_0^\infty \hat{\Psi}(k_r, z(t)) \mathrm{J}_0[k_r r_h(t)] k_r dk_r \qquad \textbf{(3.31)}$$

where $r_h(t)$ is the horizontal range of the receiver relative to the source. Except for the time dependence of the range and depth this was the same as the standard inverse Hankel transform equation that SCOOTER and its associated integration program FIELDS were designed to solve.

The time dependence in Equation 3.31 complicated the process of Fourier synthesising the time domain waveform. The approach taken here was to separately compute a portion of the time domain waveform at each receiver location and then sample this at the required signal reception time. This was accurate but slow. Other approaches such as directly implementing Equation 2.40 would also have been possible but would have required modifying FIELDS and/or SCOOTER to deal with Doppler shifts in the wavenumber domain.

The final algorithm developed for the wavenumber integration simulation was as follows:

1. The minimum and maximum horizontal separation between source and receiver, and the minimum and maximum receiver depth were determined.
2. The required frequency spacing was determined (see below).
3. SCOOTER and FIELDS were run at each required frequency with receiver locations spanning the required horizontal separation and depth ranges. Spacings between receiver locations were chosen small enough to avoid the

possibility of phase ambiguities when interpolating between locations. To this end the horizontal and vertical spacings were taken as just less than one half of the wavelength in the water column at the highest frequency of interest (actually minimum wavelength divided by 2.1).

4. For each receive time, t_r:
    - The hydrophone location relative to the source was determined.
    - The appropriate block of the transmit signal was selected.
    - This block was Fourier transformed.
    - The resulting spectrum was multiplied by the beam pattern appropriate for the hydrophone location. (This may be a function of frequency.)
    - The output of FIELDS was interpolated at each frequency to produce a frequency domain transfer function appropriate to the hydrophone location. The transfer function is complex and was interpolated by linear interpolation of its magnitude and phase.
    - The transfer function was multiplied by the product of the transfer function and beam pattern.
    - The result was multiplied by e^{iwt} where $t = t_r - t_{tx,end}$ and $t_{tx,end}$ is the transmit time of the last point in the transmit signal block.
    - This was inverse Fourier transformed and the last point was selected. This value corresponded to the instantaneous received pressure at t_r.

A critical parameter in generating time domain waveforms by this method was the length of the signal segments that had to be Fourier transformed. The required frequency spacing was the inverse of the segment duration and therefore the longer the segment the more runs of the propagation code that were necessary. The minimum segment length was determined by the requirement to avoid wrap-around of the signal components, a phenomenon referred to in Chapter 8 of Jensen et al. (Jensen et al. 2000) as time domain aliasing.

This phenomenon is illustrated in Figure 3.17 which shows the regions of the transmit signal block that contribute to the received signal computed for a given time. In this plot t_0 is the time of transmission of the beginning of a signal block of

duration T, and $t_{\min}$ and $t_{\max}$ are the minimum and maximum transmission delays from the source to the hydrophone. If $t_r - t_0 < t_{\max}$ then, as shown in Figure 3.17(b), the received signal will include contributions from the wrong end of the transmit block. This problem could have been avoided by taking the received signal as the last point in the receive transform block and taking both transmit and receive transform blocks to run from $t_r - t_{\max}$ to t_r, giving a required block duration of $T = t_{\max}$.

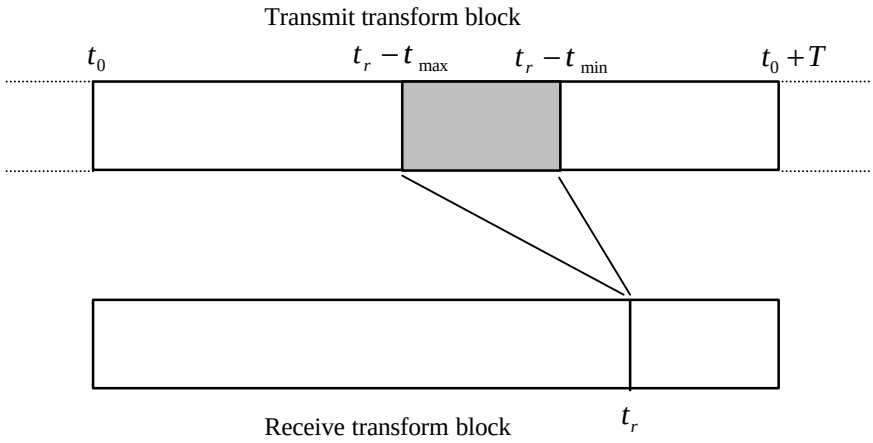

(a)

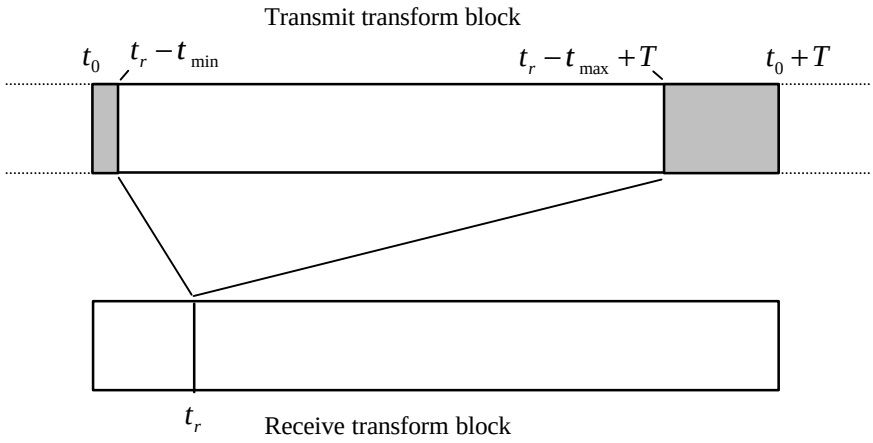

(b)

Figure 3.17 Relationship between transmit and receive transform blocks. (a) is for a receive time near the end of the receive block and (b) is for a receive time near the beginning of the block. In both cases the shaded area in the transmit transform block contributes to the calculated receive signal at time t_r.

Introducing a time delay of $t_{\min}$ between transmit and receive transform blocks by performing a frequency domain multiplication by $e^{iwt_{\min}}$ resulted in the situation shown in Figure 3.18. Again the block length was minimised by taking the last point in the receive block, but now the transmit block ran from $t_r - t_{\max}$ to $t_r - t_{\min}$, and the required block duration was reduced to $T = t_{\max} - t_{\min}$, with a corresponding frequency spacing $df = 1/T$.

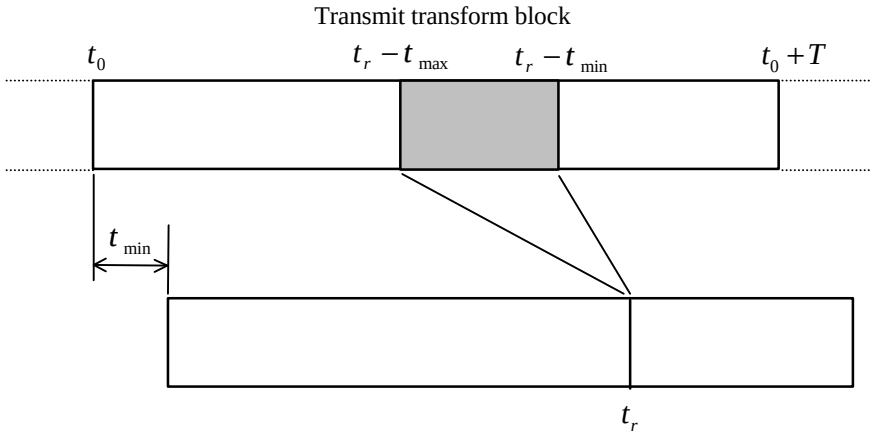

(a)

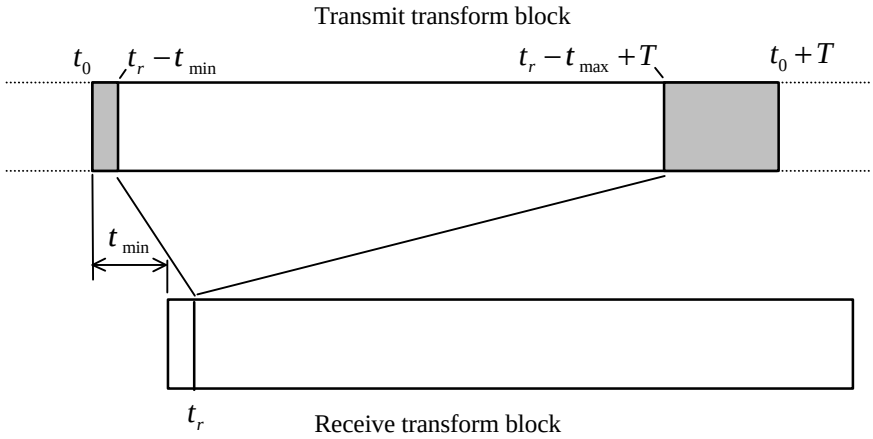

(b)

Figure 3.18 As for Figure 3.17 but in this case a delay has been introduced between the transmit and receive blocks by a frequency domain multiplication by $e^{iwt_{\min}}$

The minimum time delay was taken as the minimum horizontal separation between the source and receiver divided by the maximum sound speed in the environment. The maximum time delay was estimated by using the image method to compute the arrival time of the shallowest angled ray with an angle of incidence at the seabed greater than the critical angle, and having at least three bottom reflections. The block length was then increased so as to contain a number of samples that was an integer power of two.

There were a number of parameters that had to be specified when running SCOOTER and FIELDS. The following criteria for determining the parameter values were found to give reliable results:

- Minimum horizontal phase speed, $c_{p\min}$. This controlled the upper limit for the wavenumber integration according to $k_{r\max} = w / c_{p\min}$ and was calculated from the relationship: $c_{p\min} = f.dr$ where dr was the required range interval. $c_{p\min}$ was limited to a maximum value of 90% of the minimum sound speed (compressional or shear) in the environment.
- Maximum horizontal phase speed, $c_{p\max}$. This controlled the incidence angle of the steepest ray according to $q_{i\min} = \sin^{-1}(c_0 / c_{p\max})$ and was set to a large value (10^9) to include rays travelling close to normal incidence.
- The maximum horizontal range, $r_{h\max}$, controlled the sampling interval in the wavenumber domain according to $dk_r = 2p / r_{h\max}$ and had to be set large enough to obtain sufficiently fine wavenumber sampling. This was accomplished by setting $r_{h\max} \geq 2000dr$ which guaranteed at least 2000 samples in the wavenumber domain.
- The number of vertical mesh points in each layer was determined by requiring at least ten points per vertical wavelength and a total of at least 20 points in the layer. The minimum wavelength in the layer was used for this calculation (compressional or shear).

3.2.3.3 Comparison of shallow water methods

The various simulation methods were tested using the Pekeris environment shown in Figure 3.19 with a source depth of 10 m and a hydrophone depth of 20 m. Each simulation generated 350 seconds of simulated data at a sampling interval of 1 ms and during this time the hydrophone moved at a constant speed and direction of 3 m/s away from the source, commencing at a separation of 100 m and ending at a separation of 1150 m.

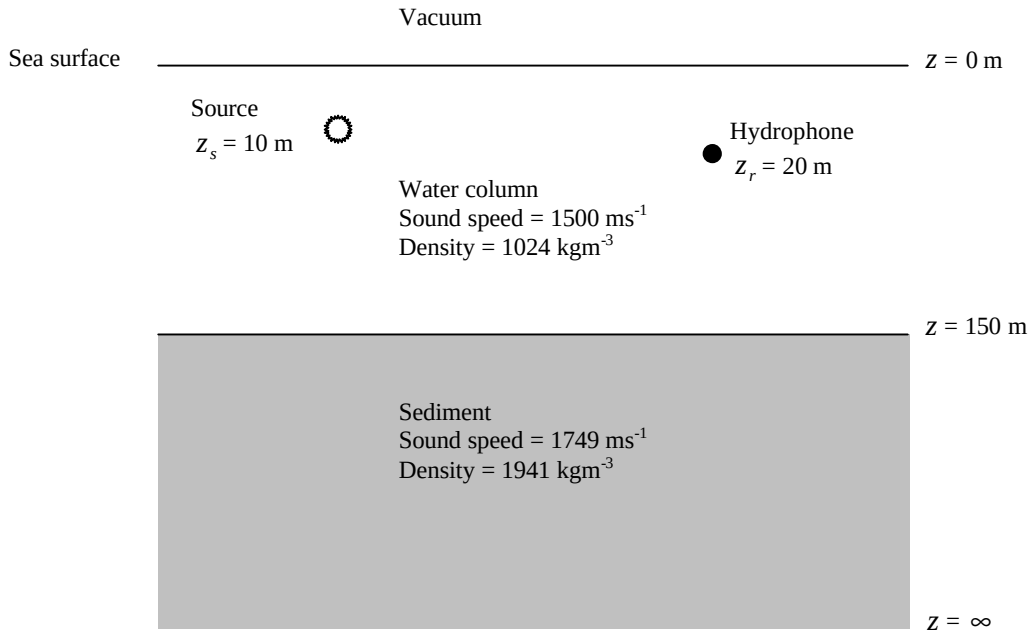

Figure 3.19 Pekeris environment used for simulation comparisons

Continuous wave comparisons

Transmission loss versus range plots were generated from the simulation output by the method described in Section 3.2.2. For comparison purposes SCOOTER was used to directly calculate the transmission loss as a function of range for continuous wave (CW) signals at the same frequencies. In all the image method simulations, 15 image sources were used.

The results of these comparisons are plotted in figures 3.20 to 3.26 for frequencies of 5 Hz, 10 Hz, 20 Hz, 50 Hz, 100 Hz, 200 Hz and 400 Hz.

The image simulation based on the saddle point reflection method and the simulation that used the SCOOTER fast-field program to compute transfer functions both produced results which agreed extremely well with the CW results over the full range

of frequencies. The largest discrepancies in the fast-field simulation result were at 5 Hz and were due to errors introduced in interpolating the 5 Hz result from the closest computed frequencies (3.91 Hz and 5.87 Hz).

Not surprisingly, the image simulations based on the plane-wave reflection coefficient and the beam-displacement reflection coefficient both performed poorly at low frequencies. The beam displacement method produced marginally better results than the plane-wave method away from the critical angle crossings, which occurred at ranges of about 500 m and again at about 1000 m. However, the beam displacement method produced large errors in the vicinity of the critical angle crossings. As the frequency was increased the discrepancies between the results produced by the different methods reduced until by 200 Hz they were almost indistinguishable. This was in accordance with the fact that the assumptions of standard ray theory become more valid as the wavelength becomes much smaller than the dimensions of the problem.

Table 3.1 lists the execution times of the different methods and also summarises the applicability and restrictions on each method as implemented.

Table 3.1 Summary of simulation method applicability

Method		**Time to generate 340 s of data (min)**	**Restrictions/ Comments**
Image method	Plane wave	16.3	Poor accuracy at low frequencies. Can, in principle, be applied to any environment for which the complex bottom reflection coefficient is known or can be computed but this has not been fully implemented.
	Beam displacement	29.2	Poor accuracy near critical angle. Can, in principle, be applied to multi-layer seabeds but this has not been implemented.
	Saddle point	42.5	Accurate at all frequencies. Only applicable to Pekeris environment (with or without attenuation in lower half-space).
Wavenumber integration (fast-field)		102	Accurate at all frequencies. Applicable to complex environments.

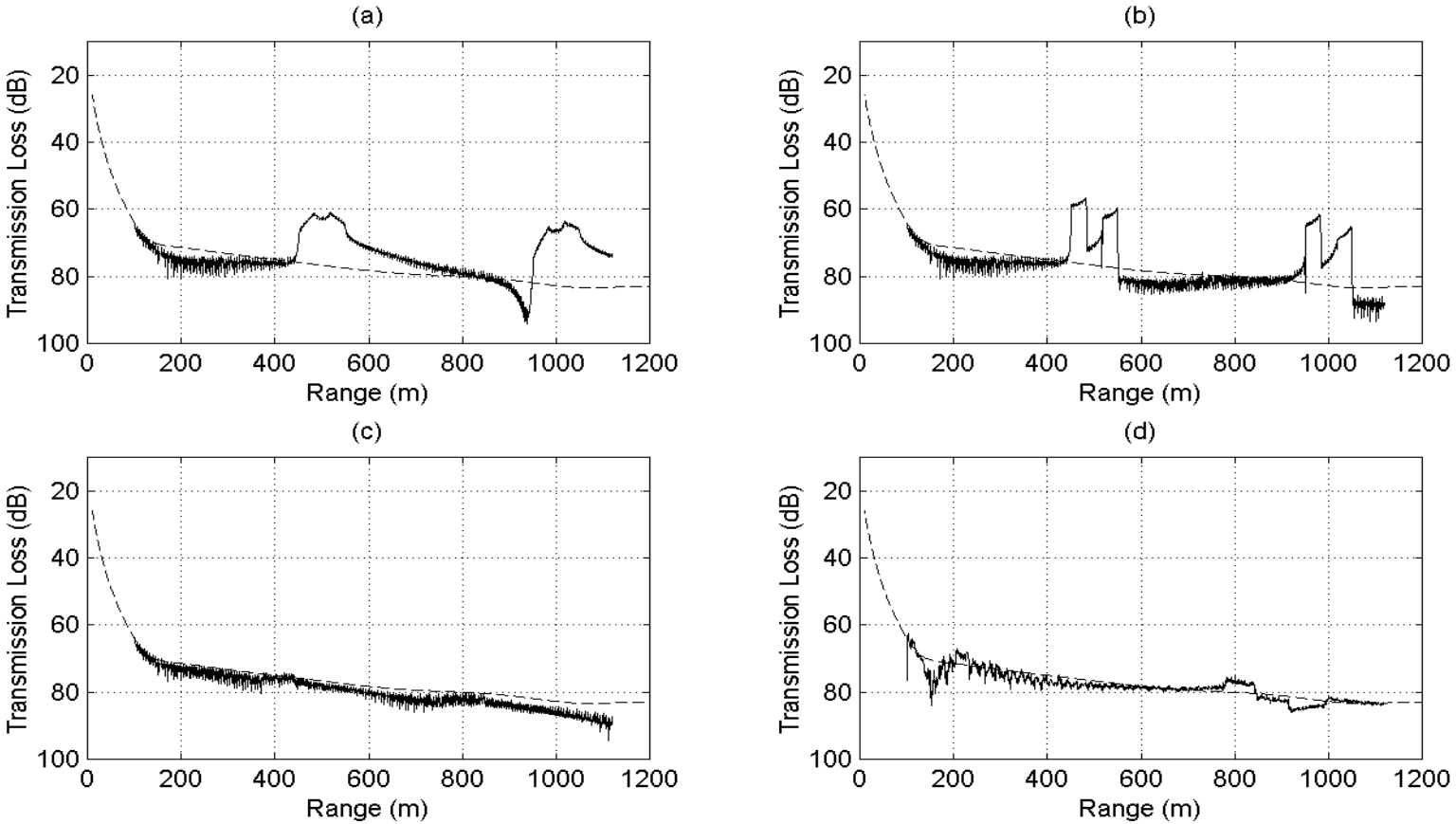

Figure 3.20 Transmission loss comparison at 5 Hz. In each case broken line is continuous wave transmission loss computed directly by SCOOTER. Solid line is transmission loss computed from simulation output for (a) image method, plane wave reflection coefficient, (b) image method, beam displacement reflection coefficient, (c) image method, saddle point reflection coefficient, and (d) fast-field method

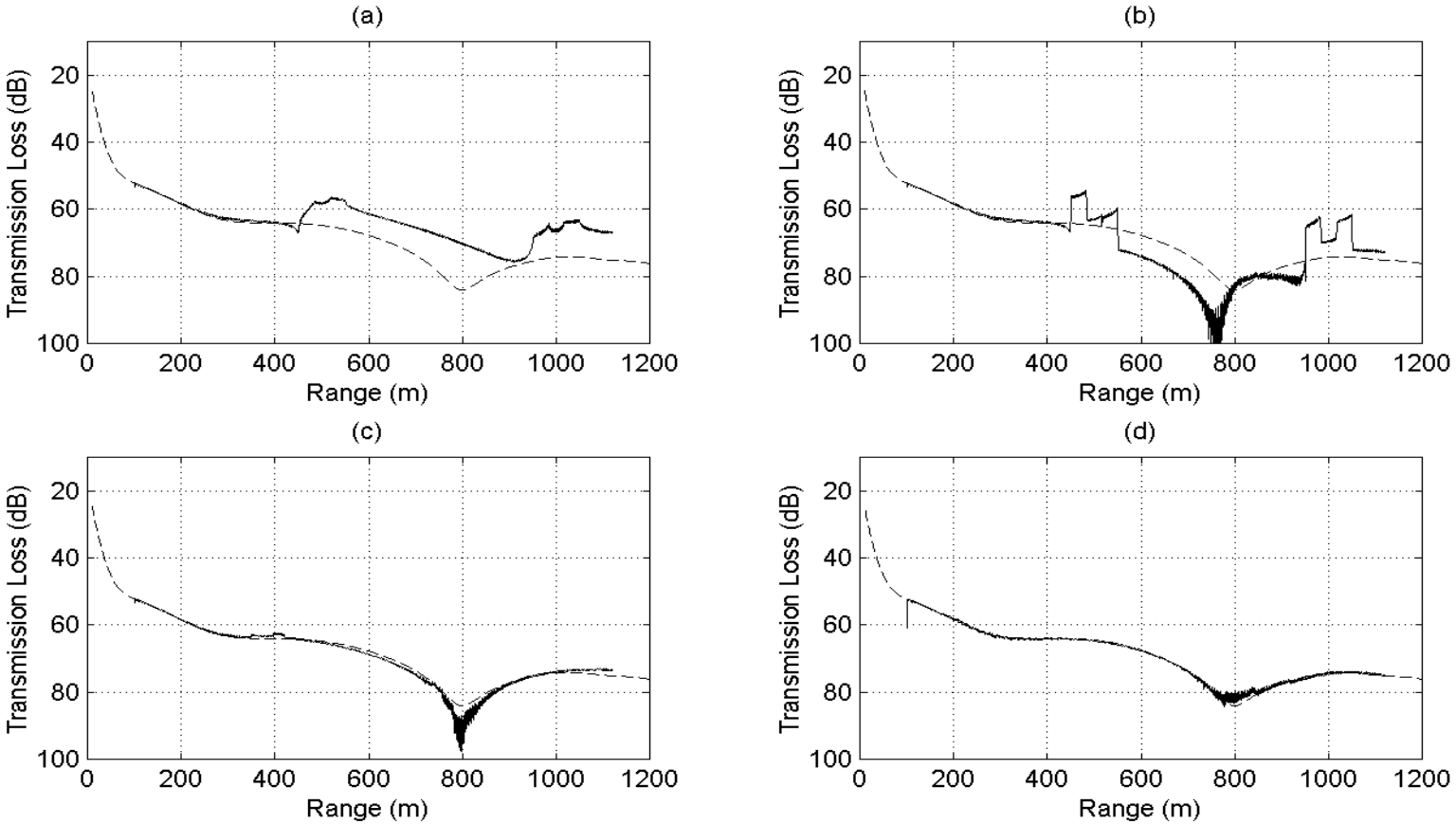

Figure 3.21 Transmission loss comparison at 10 Hz. In each case broken line is continuous wave transmission loss computed directly by SCOOTER. Solid line is transmission loss computed from simulation output for (a) image method, plane wave reflection coefficient, (b) image method, beam displacement reflection coefficient, (c) image method, saddle point reflection coefficient, and (d) fast-field method

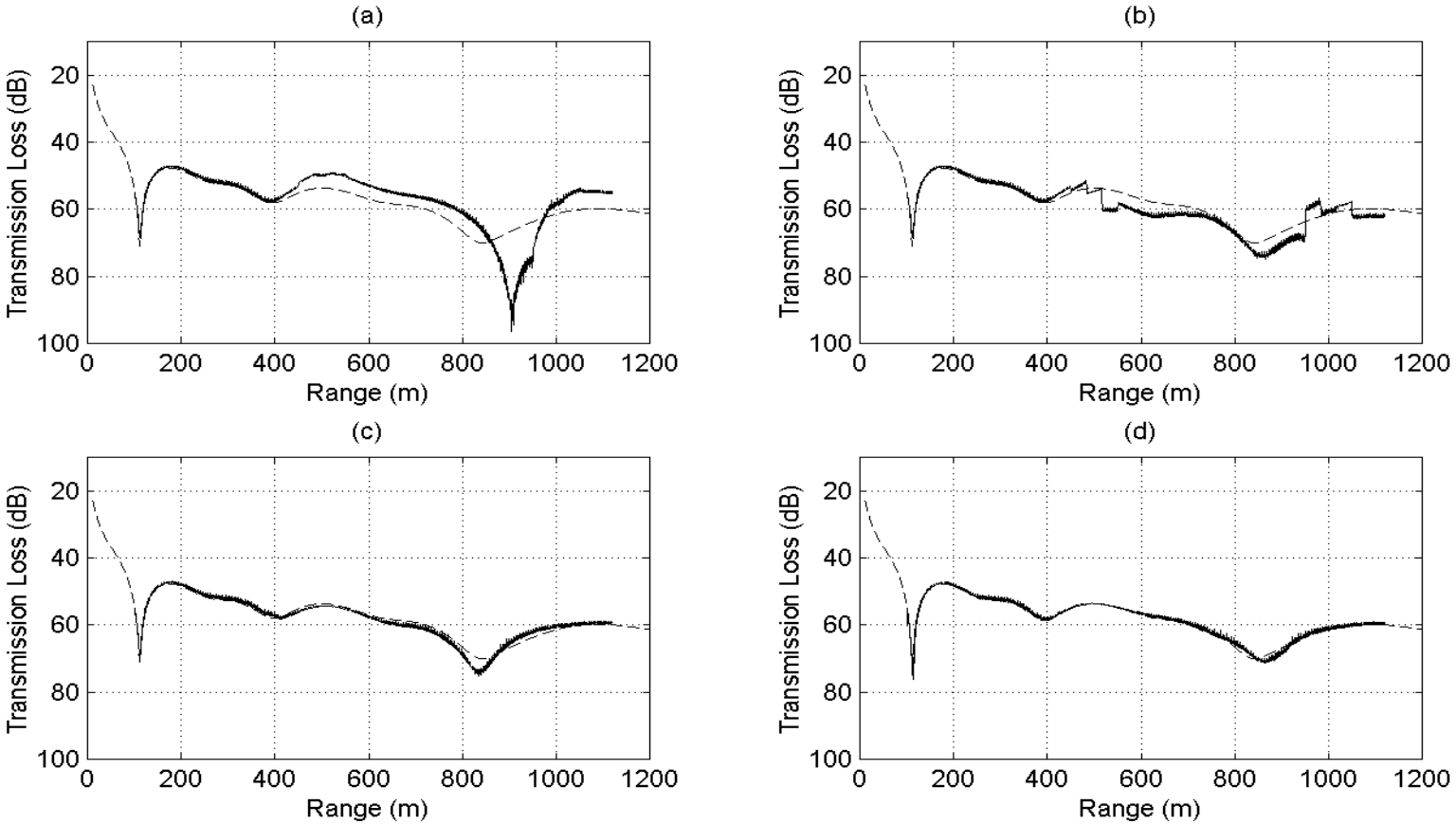

Figure 3.22 Transmission loss comparison at 20 Hz. In each case broken line is continuous wave transmission loss computed directly by SCOOTER. Solid line is transmission loss computed from simulation output for (a) image method, plane wave reflection coefficient, (b) image method, beam displacement reflection coefficient, (c) image method, saddle point reflection coefficient, and (d) fast-field method

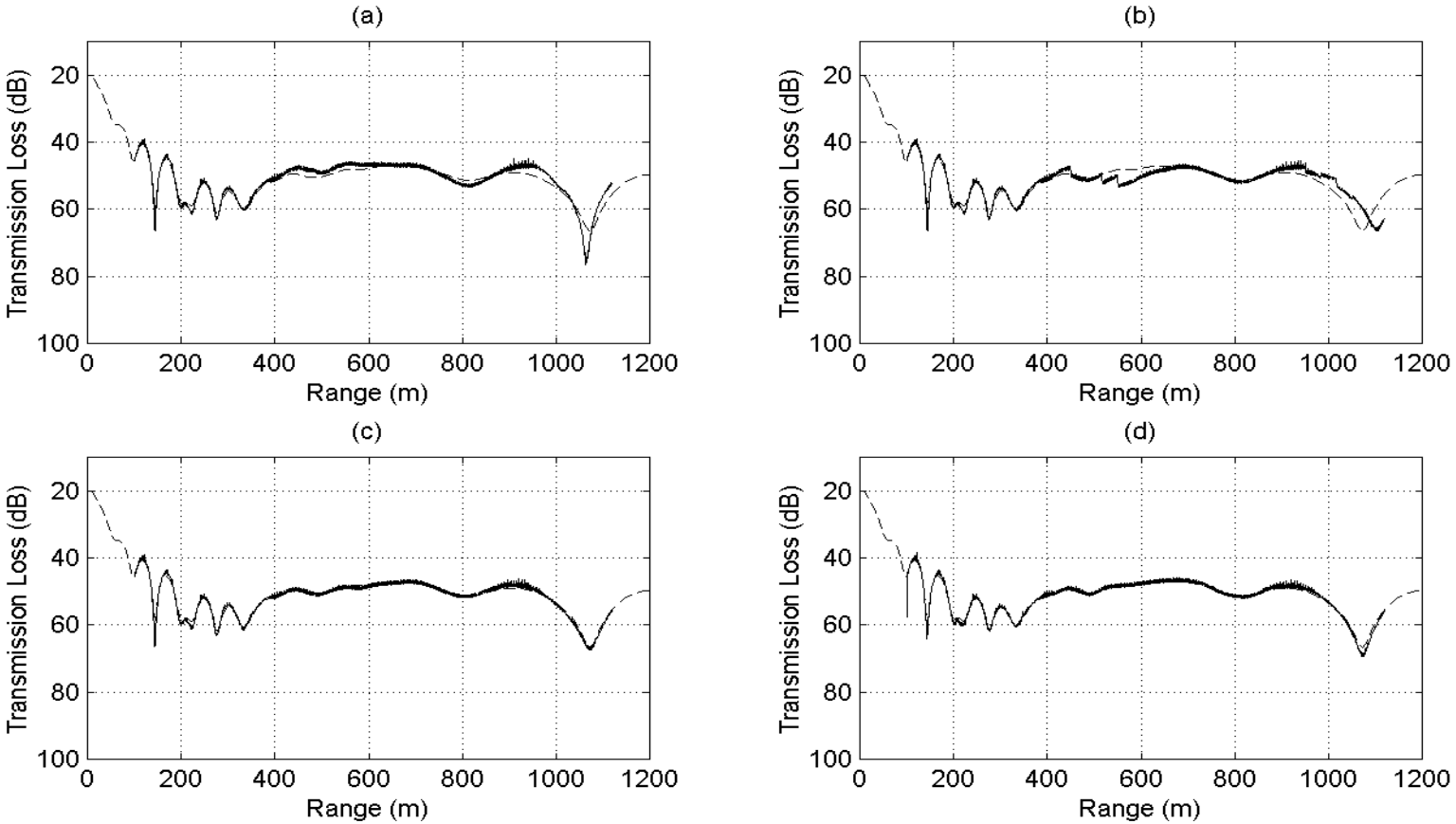

Figure 3.23 Transmission loss comparison at 50 Hz. In each case broken line is continuous wave transmission loss computed directly by SCOOTER. Solid line is transmission loss computed from simulation output for (a) image method, plane wave reflection coefficient, (b) image method, beam displacement reflection coefficient, (c) image method, saddle point reflection coefficient, and (d) fast-field method

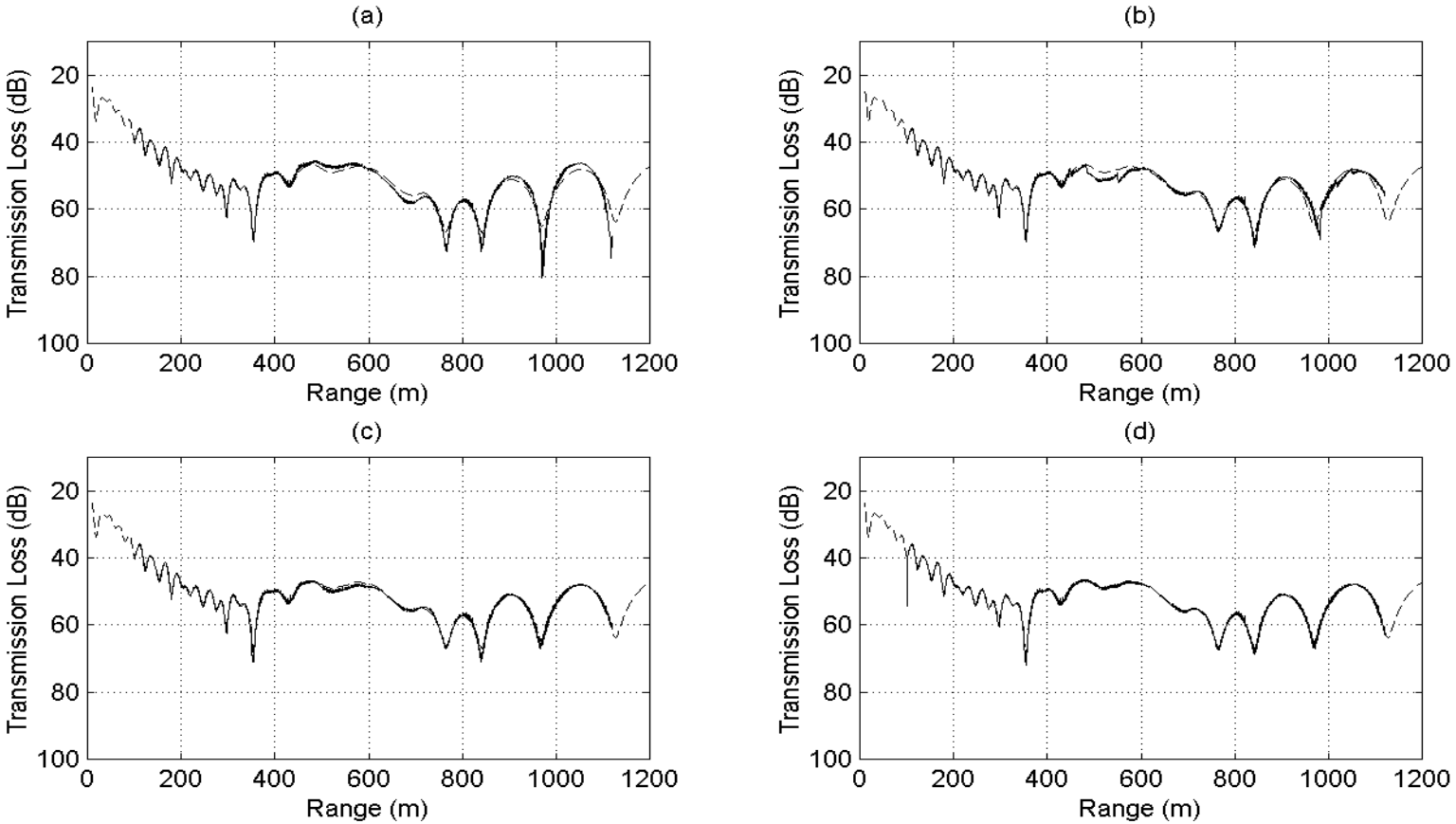

Figure 3.24 Transmission loss comparison at 100 Hz. In each case broken line is continuous wave transmission loss computed directly by SCOOTER. Solid line is transmission loss computed from simulation output for (a) image method, plane wave reflection coefficient, **(b) image** method, beam displacement reflection coefficient, (c) image method, saddle point reflection coefficient, and (d) fast-field method

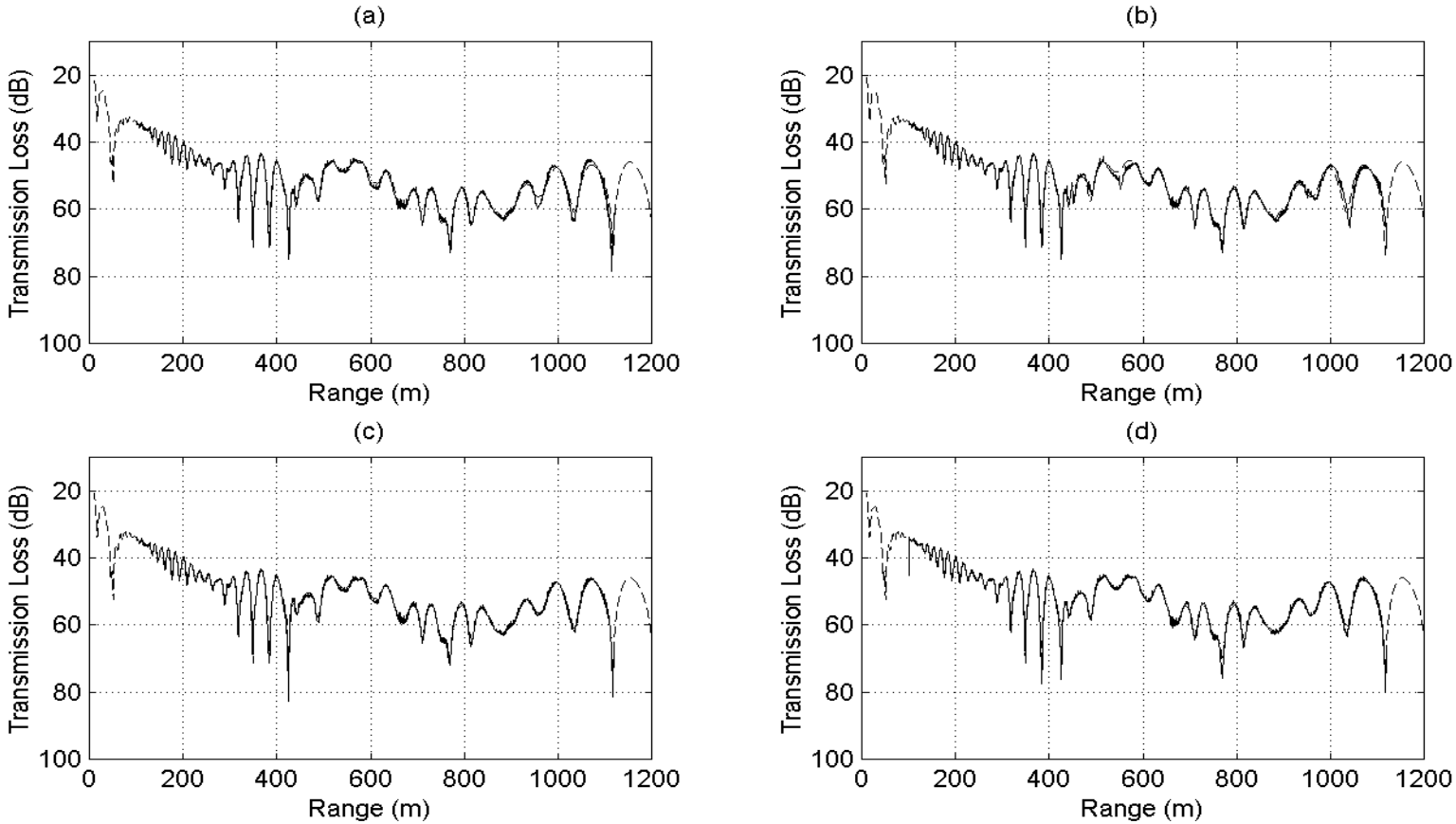

Figure 3.25 Transmission loss comparison at 200 Hz. In each case broken line is continuous wave transmission loss computed directly by SCOOTER. Solid line is transmission loss computed from simulation output for (a) image method, plane wave reflection coefficient, (b) image method, beam displacement reflection coefficient, (c) image method, saddle point reflection coefficient, and (d) fast-field method

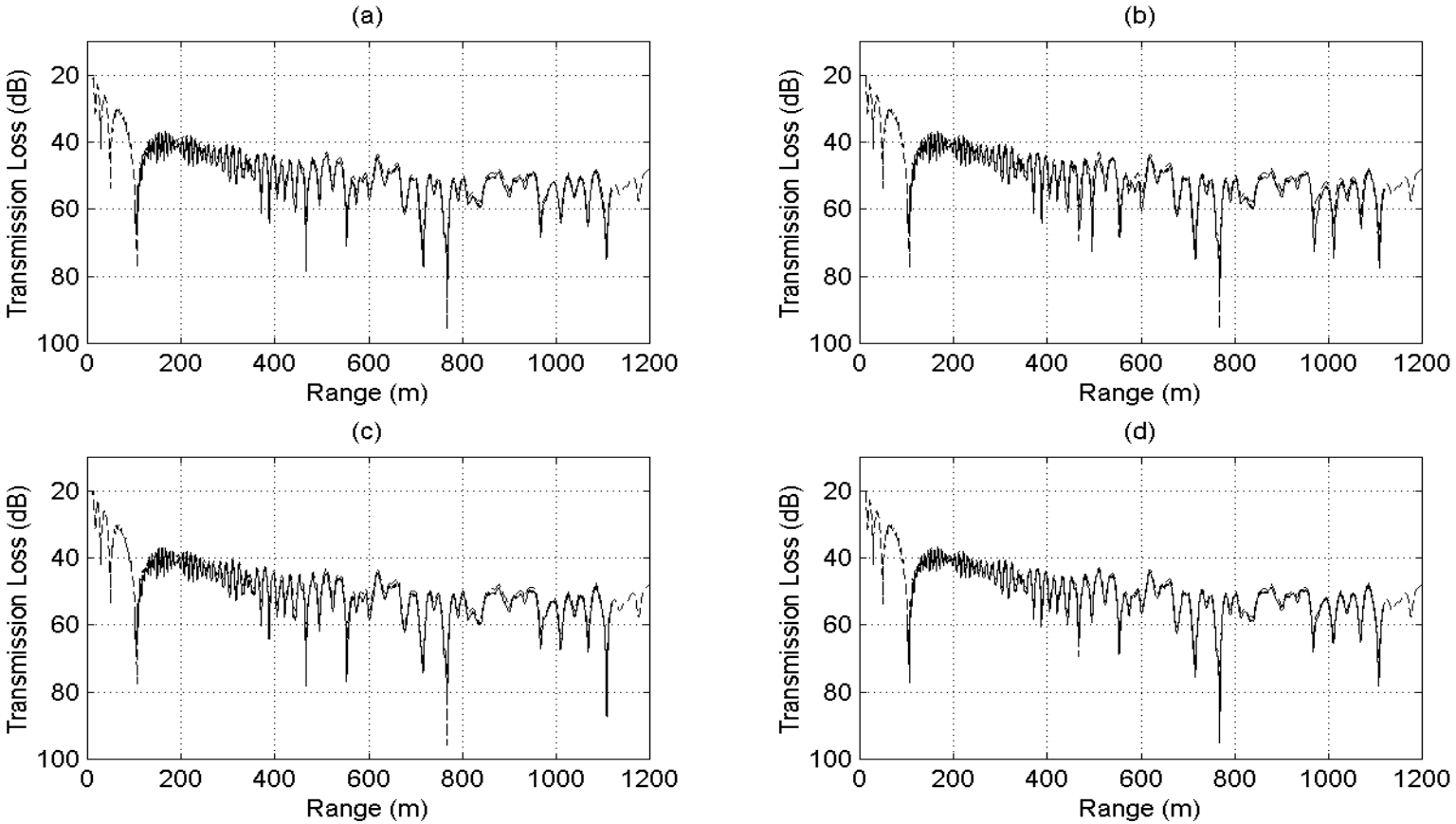

Figure 3.26 Transmission loss comparison at 400 Hz. In each case broken line is continuous wave transmission loss computed directly by SCOOTER. Solid line is transmission loss computed from simulation output for (a) image method, plane wave reflection coefficient, (b) image method, beam displacement reflection coefficient, (c) image method, saddle point reflection coefficient, and (d) fast-field method

Transient signal comparisons

The different simulation methods were also compared using transient source signals. Figure 3.27 shows the simulated received signals for a transmit signal consisting of an ideal impulse. The impulse was transmitted at 133.0 seconds at which time the horizontal separation between the source and hydrophone was 499 m, which was in the region of the first set of critical angle crossings.

Arrivals due to the various propagation paths were clearly visible, commencing with the direct path, which was immediately followed by the inverted signal from the surface reflected path. The arrivals in the following group all underwent one bottom reflection and either 0, 1 (two paths) or 2 surface reflections. Arrivals in the third group underwent 2 bottom reflections and 1, 2 (two paths) or 3 surface reflections, and so on. The high frequency ringing that is apparent in all traces was an artefact caused by truncating the flat frequency spectrum of the ideal impulse at the Nyquist frequency of 500 Hz.

The signals calculated by the four different methods were virtually indistinguishable in Figure 3.27, although careful inspection of trace (d) showed some very small additional arrivals, which were an artefact due to wrap-around in the time domain as discussed in Section 3.2.3.2. A frequency domain comparison of the four different methods (Figure 3.28) did, however, show significant differences at low frequencies.

This was born out by Figure 3.29 which shows the received signals for a transmit waveform which consisted of two cycles of a 10 Hz sine wave, commencing at 133.0 s. The plane wave reflection coefficient method clearly overestimated the signal amplitude and there were less obvious but still significant differences between the signal calculated using the beam displacement method and that calculated using the saddle point and fast-field methods. These last two were virtually identical.

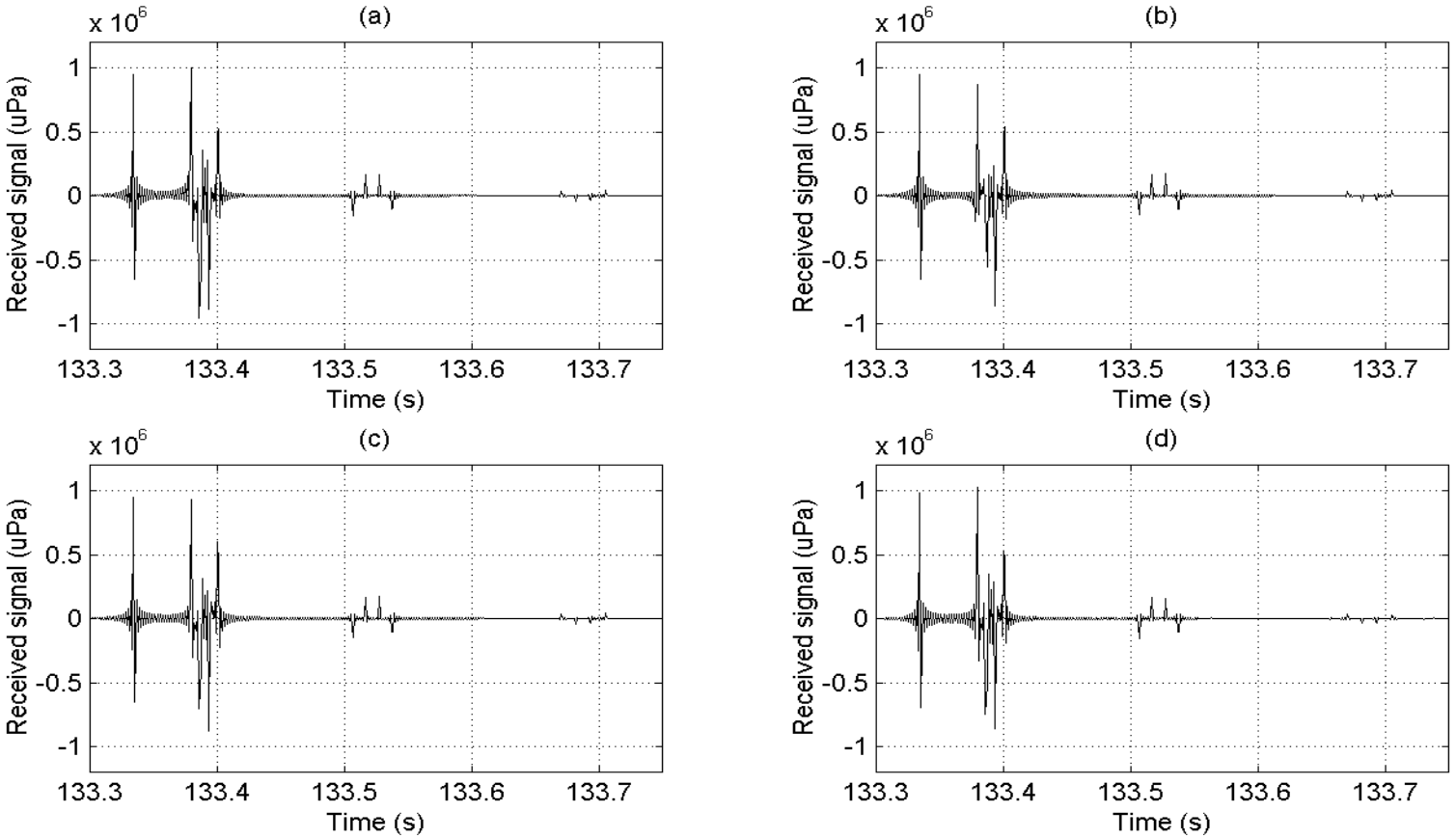

Figure 3.27 Simulated received signals for an ideal impulse transmitted at 133.0 s: (a) image method, plane wave reflection coefficient, (b) image method, beam displacement reflection coefficient, (c) image method, saddle point reflection coefficient, and (d) fast-field method

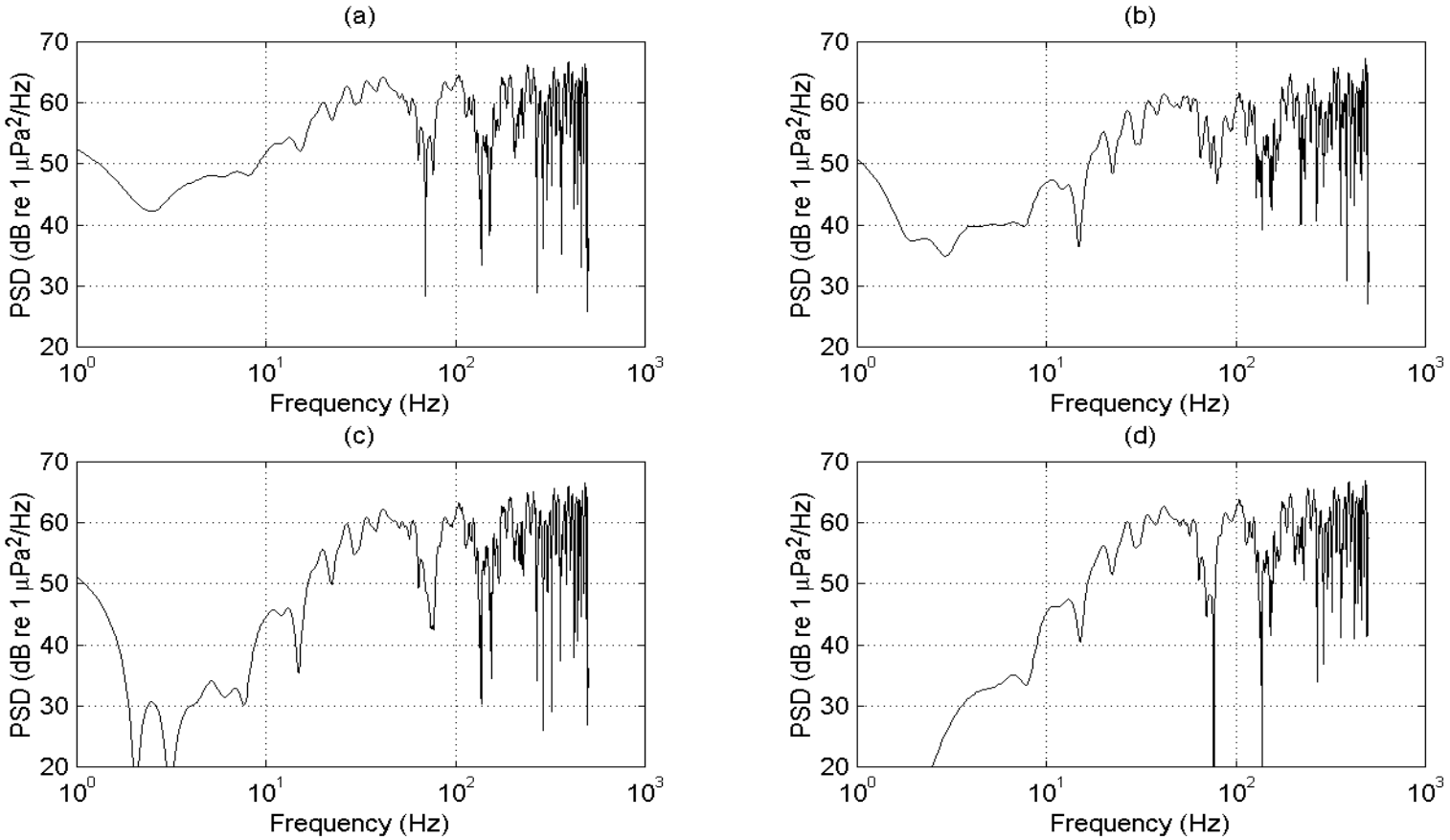

Figure 3.28 Spectra of the signals shown in Figure 3.27

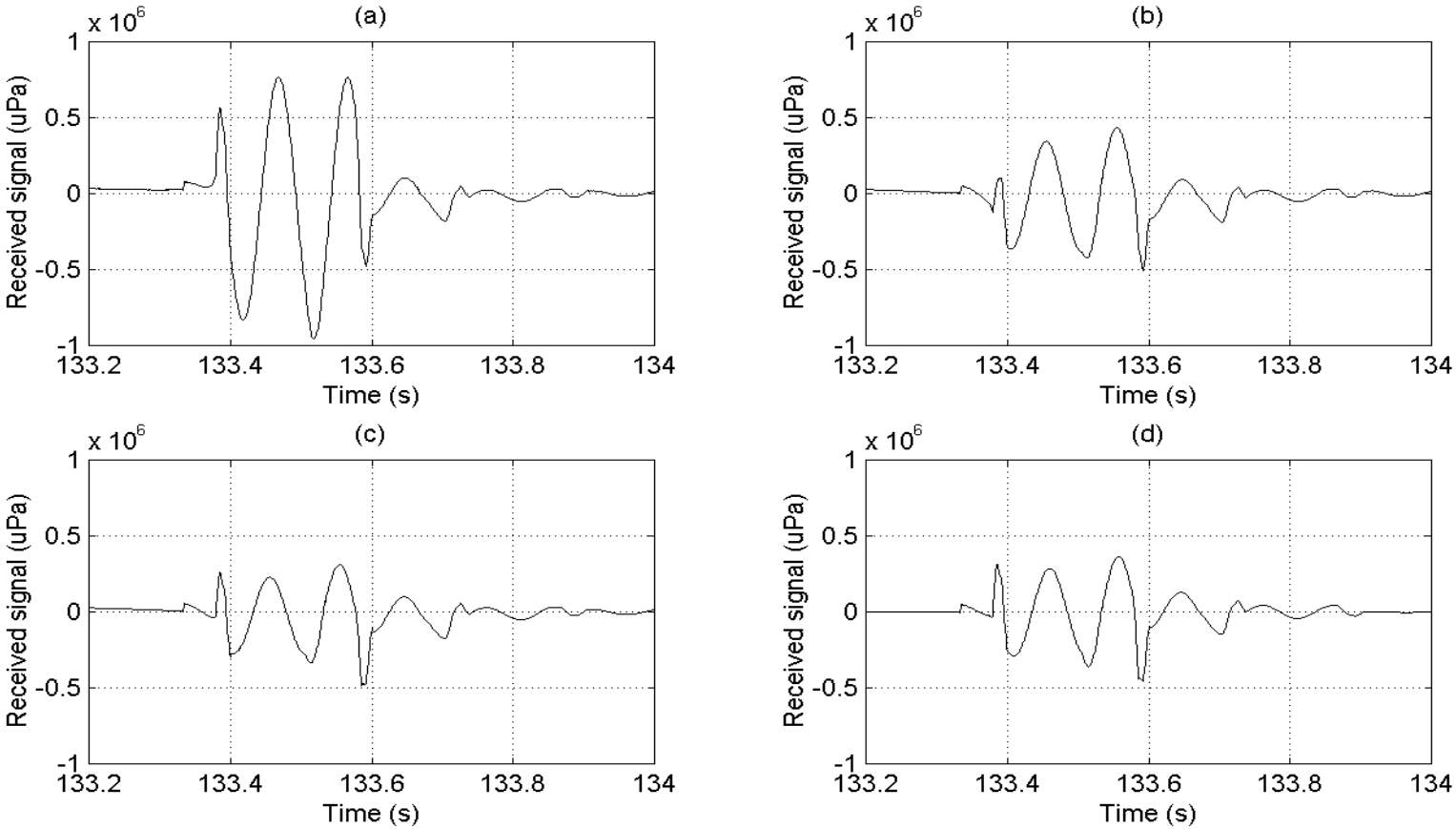

Figure 3.29 Simulated received signals for a source signal comprising a two cycle, 10 Hz burst transmitted at 133.0 s: (a) image method, plane wave reflection coefficient, (b) image method, beam displacement reflection coefficient, (c) image method, saddle point reflection coefficient, and (d) fast-field method.

3.3 Summary

An acoustic simulation was implemented with the capability to simulate a variety of acoustic sources, including both narrowband and broadband cavitation, machinery noise, tone burst sources, generalised broadband sources and isotropic sea noise. Sources could be omnidirectional or could have one of several frequency dependent or frequency independent beam patterns.

The program was capable of simulating the signals received at rapidly moving hydrophones although a slight compromise in accuracy was necessary to bring the execution times down to reasonable levels.

Several different techniques for dealing with shallow water propagation were implemented and it was found that for a Pekeris (fluid) seabed the results obtained using a modified ray theory based on a saddle point integration treatment of the seabed reflection process were virtually identical to those obtained using wavenumber integration, even at very low frequencies, and the ray method was significantly faster. However, the wavenumber integration method was capable of dealing with a greater variety of seabeds than the modified ray method.

4 Field Experiment

This chapter describes an experiment that was carried out to test the feasibility of using a towed array to localise and quantify sources of underwater noise radiated by the tow-vessel.

A general description of the experiment is given in Section 4.1. The recorded signals were dominated by machinery noise, so Section 4.2 provides details of the tow-vessel machinery characteristics and layout. Details of the equipment used during the experiment are provided in Section 4.3. This section provides descriptions of the methods used to calibrate the towed array hydrophones and a sound source that was mounted over the side of the tow-vessel at a known position. This source was used to provide a means of quantifying the accuracy with which sources on the tow-vessel could be located and their amplitudes measured. Detailed descriptions of the manoeuvres carried out during the experiment are given in Section 4.4 and a brief summary is given in Section 4.5.

4.1 General description

On the 14th September 2001 an experiment was carried out off the Western Australian coast to test the feasibility of using a towed array to localize sources of radiated acoustic noise on the tow-vessel. The location of the experiment is shown in Figure 4.1. The water depth in the area was approximately 100 m. Two vessels were used, the 27 m tug *Tammar*, shown in Figure 4.2, which was used to tow the hydrophone array, and the 14 m vessel *Sea Witch*, shown in Figure 4.3, which was used to deploy transient acoustic sources and to recover and retrieve sonobuoys. During the experiment the tow-vessel executed four U-turn manoeuvres designed to bring the array into a favourable position for localising acoustic sources on the tow-vessel.

The experiment involved personnel from the Maritime Operations Division of the Defence Science and Technology Organisation (DSTO), Nautronix Ltd, the Centre for Marine Science and Technology at Curtin University, and Defence Maritime Services (DMS).

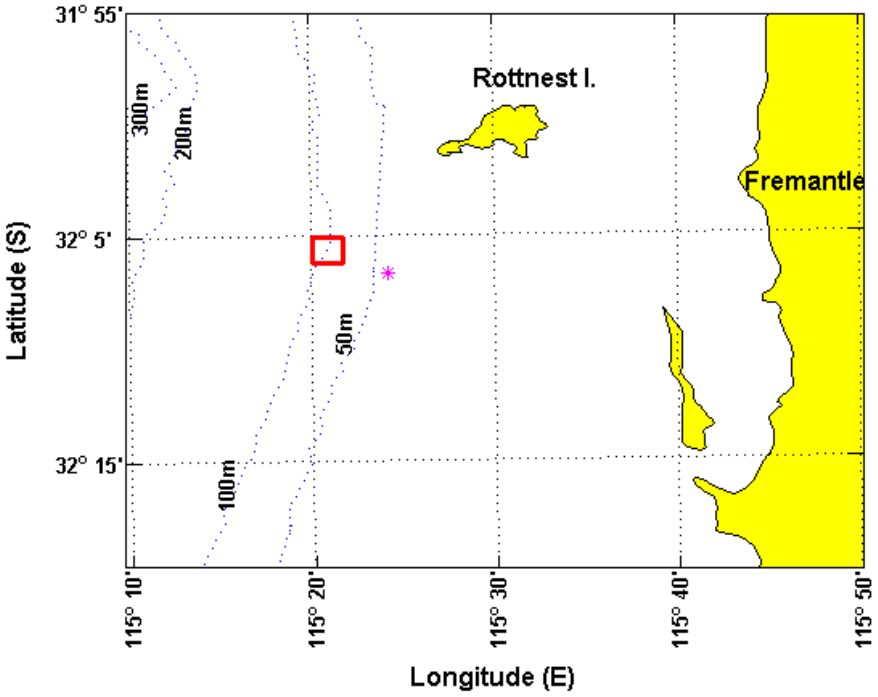

Figure 4.1 Experiment location (red box) and location of the waverider buoy operated by the Department of Planning and Infrastructure (magenta asterisk).

Figure 4.2 *Tammar*

Figure 4.3 *Sea Witch*

4.2 Tow-vessel machinery description

The aim of this experiment was to measure the acoustic noise radiated by the tow-vessel, *Tammar*, and so the details of her propulsion system and machinery are important. These are listed in Table 4.1. The location of Tammar's engine room is shown in Figure 4.4 and the machinery layout is shown in Figure 4.5.

Table 4.1 Tow-vessel specifications

Length overall	27 m
Beam	8.86 m
Draft	3.52 m
Displacement	270 tonnes
Main engines	2 x Detroit 16v149 16 cylinder diesels
Main transmission	Twin disc gearboxes with 8.86:1 reduction ratio
Propellers	2 x 2.3 m diameter, four-blade counter-rotating propellers
Alternator	1 x Detroit 3-71 3 cylinder diesel operating at 1500 rpm
Air conditioning pump	Continuous, 2800 rpm
Vane steering pumps	2x continuous, 1425 rpm
Air compressor	Intermittent, 1420 rpm
Fuel transfer pump	Intermittent, 920 rpm
Fresh water pump	Intermittent, rpm not logged
Air conditioning unit	Intermittent, rpm not logged

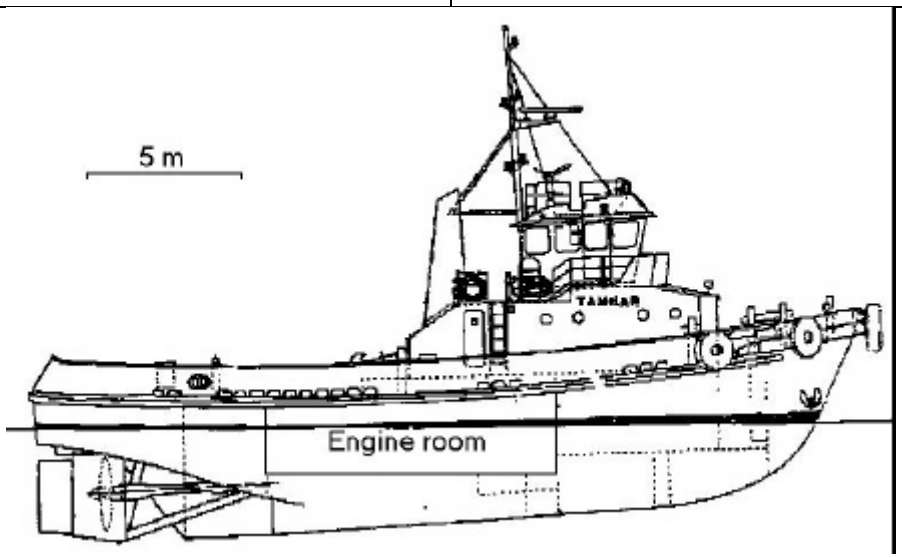

Figure 4.4 Side view of *Tammar* showing engine room location

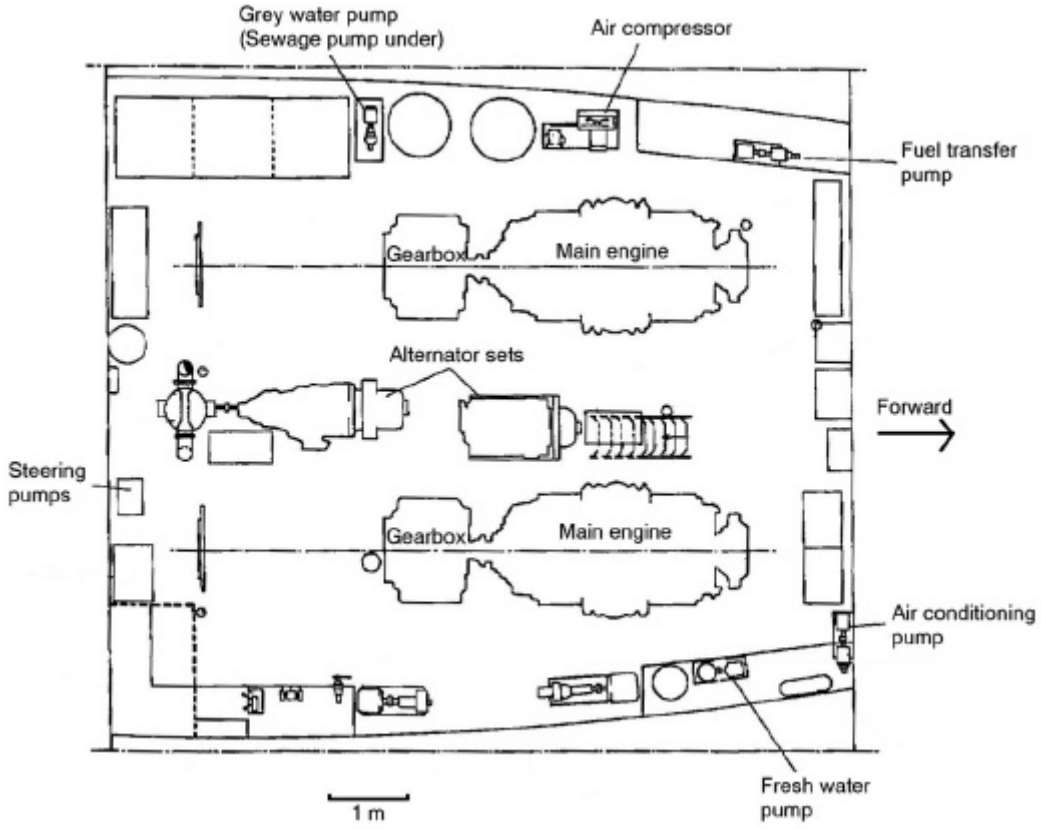

Figure 4.5 Plan of *Tammar's* engine room showing locations of the machinery that was operational during the experiment

4.3 Equipment description

4.3.1 Towed array

A schematic diagram of the towed array used for this experiment is shown in Figure 4.6. Starting from the forward end there was a tow cable, an interchangeable instrumentation module known as a DA module, the forward vibration isolation module (VIM), another DA module, the acoustic module that contained the bulk of the hydrophones, a third DA module and finally the aft vibration isolation module. The DA modules could be configured for various types of measurements but in this case each of them contained three high-frequency omnidirectional hydrophones.

The acoustic module had an overall length of 135 m and contained 60 hydrophones arranged in four octaves designated X, Y, Z and U (see Figure 4.6). The spacing between the centres of the outermost hydrophones was 112 m. The array was designed so that four different 24 element equally spaced arrays could be synthesised by using various combinations of hydrophones. For example, the highest frequency octave (U) used the 24 central hydrophones, the next lowest frequency octave (Z)

used the six hydrophones on either side of these and also combined adjacent pairs of hydrophones from the central 24 to give the remaining 12 array elements. To reduce flow noise each hydrophone was itself made up of several individual elements, with the number of hydrophone elements, and hence the effective length of the hydrophone, being a function of the design frequency of the corresponding octave. The hydrophones in the lowest frequency octave (X) had a length of 2.2 m, and the length halved for each subsequent octave.

The signal processing within the array was purely analog, and consisted of a preamplifier with a differential output for each hydrophone. A deck cable connected between the tow-cable and a top-end interfacing unit, which buffered the hydrophone signals and provided an analog output for each hydrophone.

The array was also fitted with two pressure sensors, one at each end of the acoustic module, but these were not functioning at the time of the experiment.

Figure 4.7 shows the towed array being deployed. The array was sufficiently light and flexible that it could be deployed and recovered manually without the need for a winch.

All sixty acoustic module hydrophones and four of the DA module hydrophones were recorded using the data acquisition system described in Section 4.3.9. The quality of the data recorded on the acoustic module hydrophones was excellent, but the DA module hydrophone signals were very noisy and did not produce useful results.

Calibration of the towed array hydrophones and associated data acquisition system was carried out during a separate experiment and is described in Section 4.3.10.

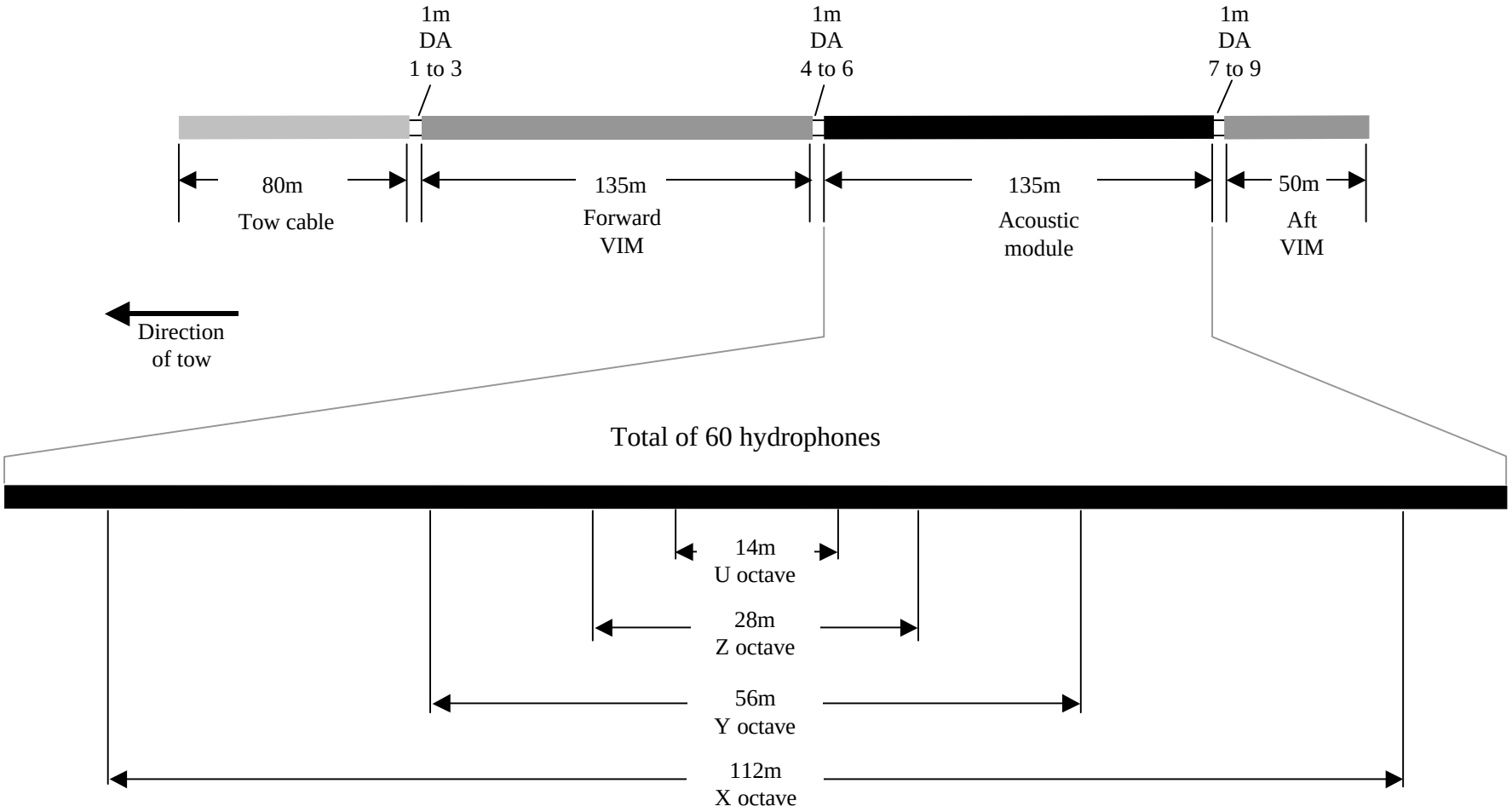

Figure 4.6 Schematic of towed array

Figure 4.7 The towed array (green cable) being deployed from the aft deck of *Tammar*. The signal conditioning electronics, data acquisition system and vessel motion sensor were housed in the blue shipping container on the left hand side of the photo. The GPS antennas on the roof of the shipping container were used for synchronisation and vessel position logging.

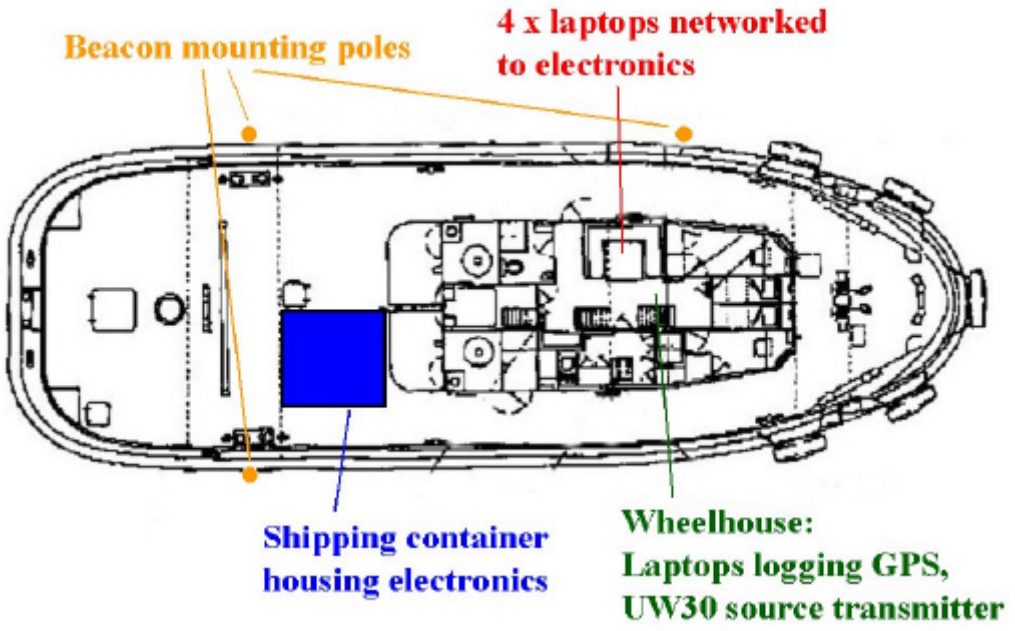

Figure 4.8 Plan view of *Tammar* showing locations of various items of equipment.

4.3.2 Tracking system

The array hydrophones were tracked during the manoeuvres by a system consisting of six acoustic beacons mounted on three poles. Two beacon poles were mounted on the port side of the tow-vessel and one on the starboard side (see Figure 4.8 and Figure 4.9). A low frequency (3.8 kHz to 8.9 kHz) and a high frequency (16.6 kHz to 19.2 kHz) beacon were mounted on each pole to reduce the detrimental effects of dropouts due to the directionality of the towed array hydrophones.

Details of beacon locations and frequencies are given in Table 4.2, and the beacon locations are plotted in figures 4.10 to 4.12. Note that the beacon poles were originally designed for mounting on a shallower draft vessel, and that a late change of vessel resulted in the beacons being above the bottom of the keel. The positions of the beacons and other items on each pole were measured prior to deployment using a tape-measure, and the pole locations and orientations were measured using a tape measure and spirit level with the vessel tied up to a wharf and the poles deployed. Standard coordinate transformations were then used to convert these measurements to the required coordinate system.

Each beacon transmitted a broadband pseudo-noise modulated signal with a bandwidth of 2.55 kHz. The modulation was precisely synchronized to a rubidium oscillator slaved to GPS time. Signals from the tracking beacons were received by the towed array hydrophones along with the lower frequency noise generated by the tow-vessel, and were recorded using the data acquisition system described in Section 4.3.9.

The tracking system determined the range between each acoustic beacon and each hydrophone by band-pass filtering the received signal to only include that beacon's spectrum, and then replica correlating with the transmitted pseudo-noise modulation. The location of the peak in the correlator output was then used to determine the elapsed time between transmission and reception of the signal and hence the distance between beacon and hydrophone. A limited number of beacon-hydrophone ranges were computed in real-time to allow data quality checking, but the bulk of the computations were done in post processing.

An additional tracking beacon was deployed from the support-vessel, *Sea Witch*, to allow it to be tracked by the towed array hydrophones but did not function correctly during the experiment.

Figure 4.9 Forward port beacon pole showing the high frequency tracking beacon (left), the low frequency tracking beacon (right), and the monitor hydrophone (top).

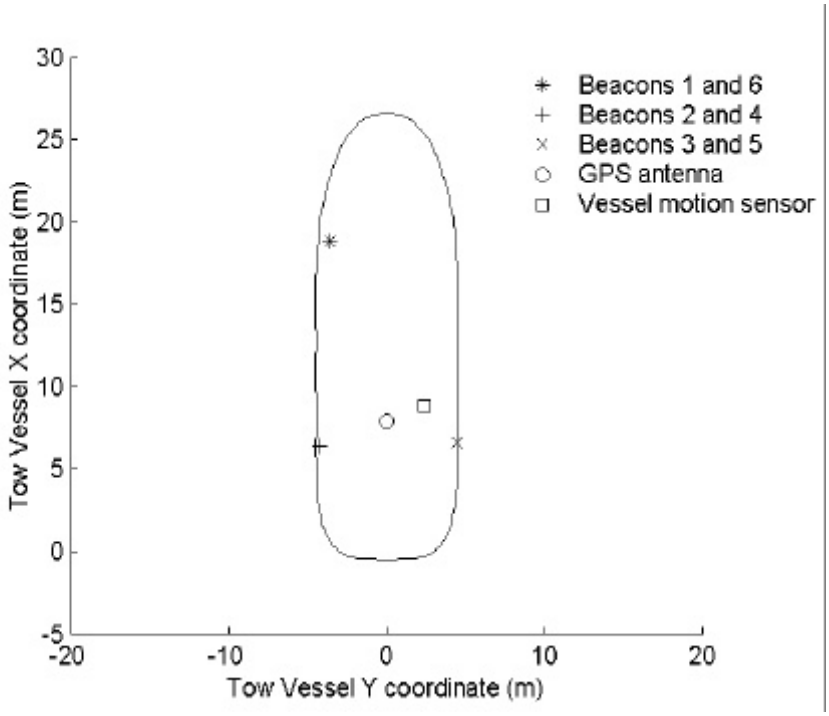

Figure 4.10 Plan view of tow-vessel (*Tammar*) showing beacon positions, GPS antenna position, and motion sensor position. Coordinate system origin is at tow point.

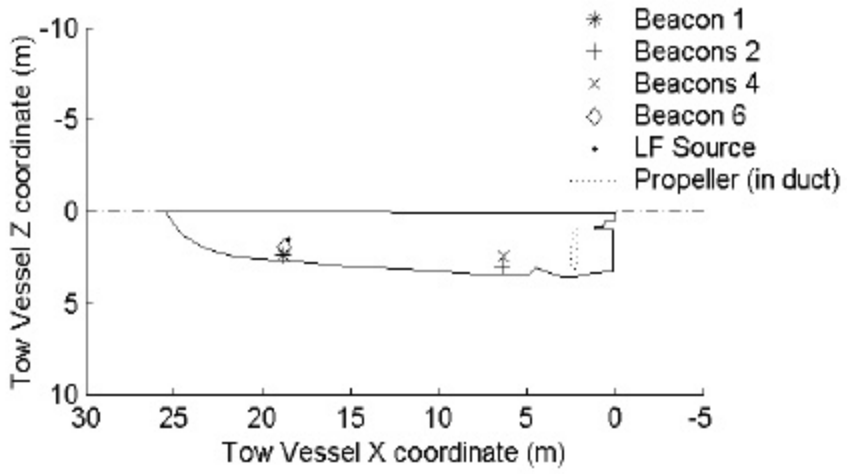

Figure 4.11 Port view of underwater profile of tow-vessel showing acoustic tracking beacon and low frequency source positions. Dash-dot line is still waterline.

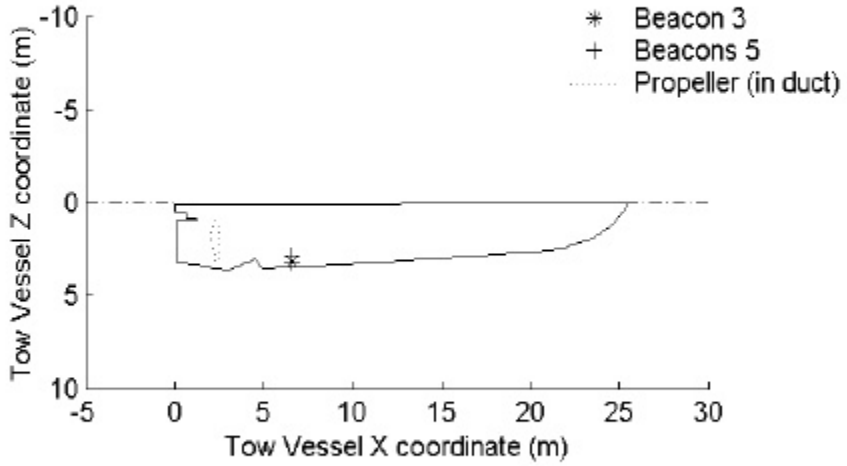

Figure 4.12 Starboard view of underwater profile of tow-vessel showing acoustic tracking beacon positions. Dash-dot line is still waterline.

Table 4.2 Tow-vessel beacon and sensor locations. Positions are given in tow-vessel coordinates with origin at waterline below tow-point, *x* positive forward, *y* positive to starboard and *z* positive down.

Item	***x* (m)**	***y* (m)**	***z* (m)**
Aft port pole			
Beacon 2 6387 Hz	6.42	-4.24	3.02
Beacon 4 16607 Hz	6.34	-4.24	2.43
Forward port pole			
Beacon 1 3832 Hz	18.79	-3.57	2.37
Beacon 6 19162 Hz	18.76	-3.67	1.96
UW30 source	18.53	-3.62	1.50
Monitor hydrophone	17.81	-3.61	2.37
Aft starboard pole			
Beacon 3 8942 Hz	6.61	4.42	3.16
Beacon 5 17885 Hz	6.59	4.41	2.86
GPS antenna	7.90	0.00	-5
Vertical reference unit	8.80	2.40	-1.5

4.3.3 Monitor hydrophone

A Reson type TC – 4032 hydrophone was mounted on the forward port beacon pole (Figure 4.9) at the location specified in Table 4.2, and was used to monitor the tracking beacon output levels. This hydrophone had an inbuilt preamplifier and a receive sensitivity of -170 dB re 1V/μPa (calibration provided by manufacturer).

4.3.4 UW30 moving coil source

A University Sound type UW30 moving coil underwater sound source (Figure 4.13) was mounted on the forward port pole, above the high frequency beacon shown in

Figure 4.9 and 1.5 m below the waterline (see Table 4.2). This source was used to generate a 112 Hz square wave, resulting in useable harmonics at 112 Hz, 336 Hz, 560 Hz and 784 Hz. The signal source was a portable CD player set to auto-repeat mode resulting in 60 second continuous transmissions separated by 1.5 second gaps. The signal from the CD player was fed into a power amplifier and the output level adjusted to give 6.0 V RMS at the amplifier output.

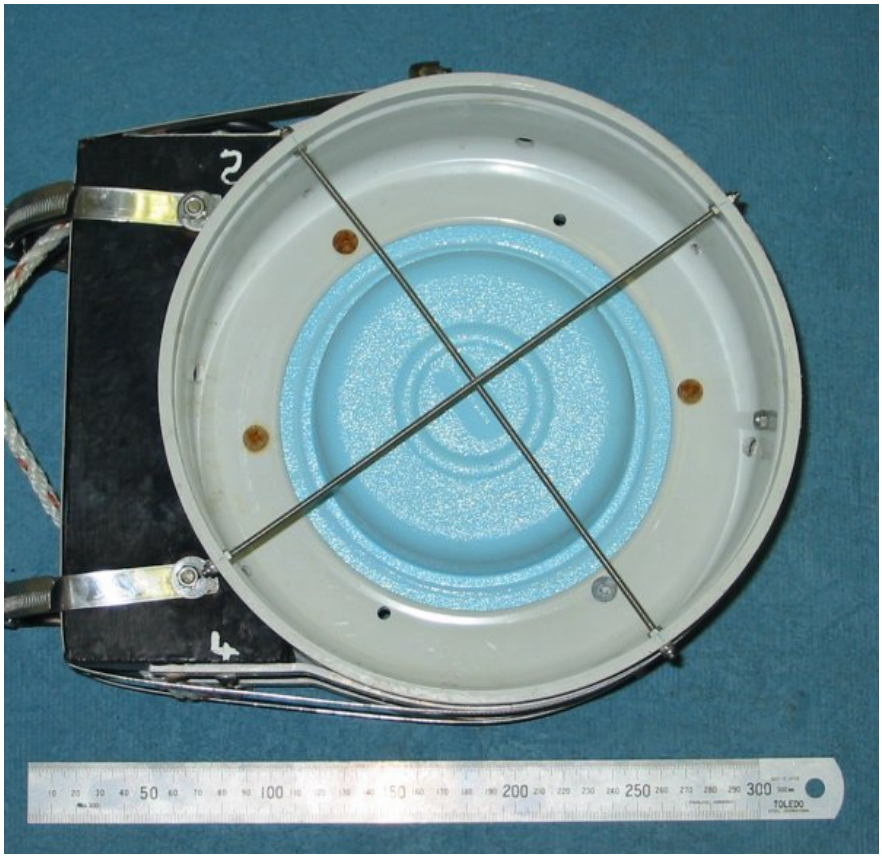

Figure 4.13 UW30 moving coil sound source

The UW30 was used to provide an acoustic source of known amplitude at a known location that could then be used to quantify the performance of the source localisation and amplitude estimation algorithms described in later chapters. It was therefore vital that its characteristics were accurately known and to this end several calibrations were carried out. DSTO performed a calibration at their facility at Woronora Dam, NSW, with the source at a depth of 3.0 m. During this calibration the transmit voltage response of the source was measured at discrete frequencies between 40 Hz and 20 kHz, a recording was made on a calibrated hydrophone of the same source signal used in the sea experiment, and the beam pattern of the

transducer was measured at 100 Hz, 200 Hz, 500 Hz, 1 kHz, 2 kHz, 5 kHz, and 10 kHz. The beam pattern results showed that the source was omnidirectional to within 1.5 dB for frequencies up to and including 1 kHz (Duncan & Savage 2002).

An additional calibration experiment was carried out by the author at the Armaments Wharf, Garden Island, WA to check the depth dependence of the UW30 source level. During this experiment the 112 Hz square wave signal was transmitted by the UW30 and received on a calibrated MASSA TR1025C hydrophone at 1 m horizontal separation. The depth of both the hydrophone and the source were changed from 0.5 m to 3.0 m in 0.5 m steps. Additionally, a swept frequency signal was transmitted with the source and hydrophone at a depth of 1.5 m and at a depth of 3.0 m. It took 60 seconds for the signal to sweep from 10 Hz to 20 kHz at a rate that increased with increasing frequency.

The hydrophone signals were recorded via a preamplifier on a Sony DAT tape deck. A calibrated white noise signal was recorded on the same channel via the same preamplifier, with all tape deck settings unchanged.

The swept frequency recordings made at the Armaments Wharf were processed to compute the transmit voltage response of the source as follows:

1. The recorded white noise and hydrophone signals were digitised using a Data Physics DP430 spectrum analyser.
2. The power density spectrum of the white noise signal was computed and used, together with the known hydrophone sensitivity, to compute the gain of the overall system, including the hydrophone, preamplifier, recording system and playback system.
3. The power density spectrum of the recorded hydrophone signal was then calculated and converted to pressure units using the results of step 2.
4. The transmit voltage waveform was not recorded during the experiment, but was obtained by using the DP430 to directly digitise the transmit waveform with the source suspended in a 1.5 m by 1.5 m by 2.5 m laboratory tank filled with fresh water. Changing the position of the source in the tank did not affect the voltage waveform or its spectrum, and no resonance effects were observed in the spectrum. It was therefore unlikely that the change in radiation impedance between the tank and the free field conditions of the

Armaments Wharf experiment had a significant effect on the transmit voltage waveform.

5. The power density spectra of the recorded hydrophone signal and the voltage waveform were computed for a single sweep.
6. The resulting spectra were smoothed by applying a running average, and outliers corresponding to electrical interference were removed.
7. The smoothed hydrophone signal spectrum was corrected for the source-hydrophone separation and the surface reflection by modelling the received signal as being due to the combination of the true source and its image in the sea surface, transmitting 180° out of phase. This inherently assumed that the water surface acted as a perfect reflector.
8. The smoothed pressure spectrum was then divided by the voltage spectrum and the square root taken to yield the transmit voltage response.

The results of applying this procedure to the signals recorded at source depths of 1.5 m and 3.0 m are shown in Figure 4.14, together with the measurements made at Woronora dam at 3.0 m depth, which have also been corrected for the surface reflection. At frequencies below 1 kHz the source had a higher transmit voltage response at a depth of 1.5 m than at 3.0 m. The Woronora dam results agreed with the sweep calibration to within a few dB over most of the frequency range, but there was a slight offset in the frequency of the extremely sharp resonant peak at around 150 Hz. The reason for this offset is unknown, but may indicate that some components of the source were temperature dependent. Discrepancies at frequencies above 1 kHz were due to orientation effects (the source was free to rotate during the Armaments Wharf calibration) and the decreasing accuracy of the surface reflection correction when the perfect reflector assumption broke down as the acoustic wavelength became comparable to the scale of the surface roughness.

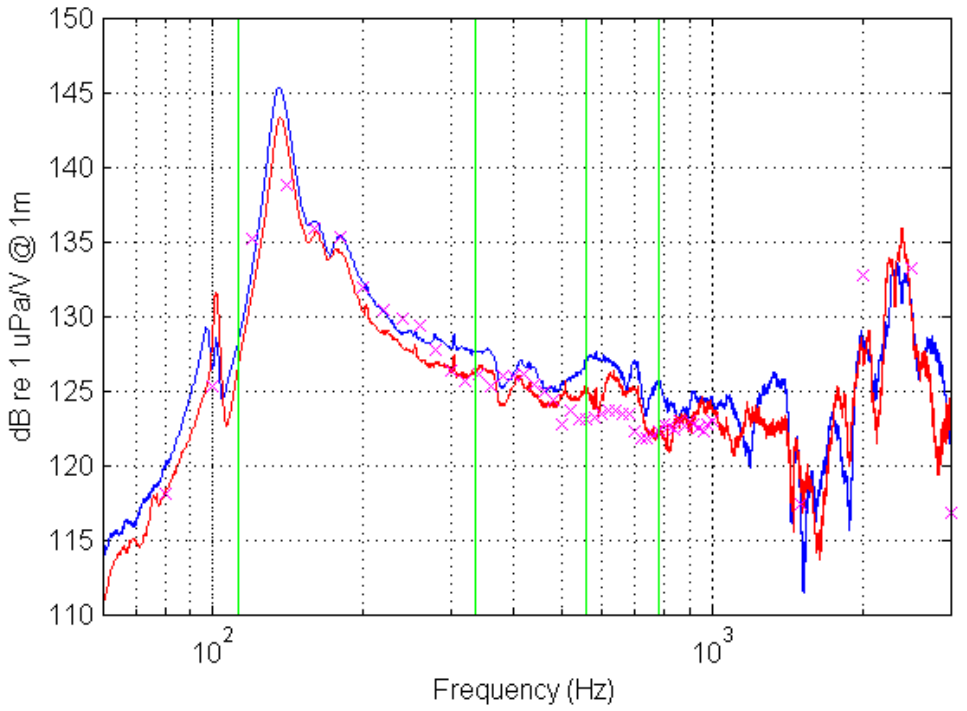

Figure 4.14 UW30 transmit voltage response versus frequency. Lines are from Armaments Wharf sweep calibration at depths of 1.5 m (blue) and 3.0 m (red). Crosses are from Woronora dam calibration. Vertical green lines are the square wave frequencies of 112 Hz, 336 Hz, 560 Hz and 784 Hz.

Source levels estimates were made using the DAT recordings of the square wave signal made at the armaments wharf, and the similar recordings made by DSTO at Woronora dam. This was done as follows:

1. The signals were recovered from tape and converted to pressure levels using the procedure used for the swept frequency recordings.
2. The peaks in the power density spectra were integrated to give mean square pressure levels.
3. The mean square pressure levels were corrected for the source-hydrophone separation and for the surface reflection in the same manner as for the swept frequency signals.

Figure 4.15 shows the resulting source levels as a function of depth. It is apparent that at all four frequencies the source level decreased with increasing depth. The Woronora Dam results agreed with the Armaments Wharf results to within experimental uncertainty at 336 Hz, 560 Hz and 784 Hz, but there was a discrepancy of about 6 dB at 112 Hz. The discrepancy at 112 Hz was due to the previously noted

slight shift in frequency of the resonant peak between the Woronora Dam and Armaments Wharf calibrations. The transmit voltage response had a very steep slope at 112 Hz due to the close proximity of the resonant peak, and the resulting source level was thus very sensitive to the frequency of the resonance.

Source levels were also computed from the transmit voltage response data. The required voltage levels were obtained by sampling the square wave transmit voltage waveform with the source suspended in the laboratory tank, computing its power density spectrum, and then integrating each peak and taking the square root to obtain the corresponding root mean square voltage. This was done using both the Armaments Wharf data and the Woronora Dam data. The results are plotted in Figure 4.15 and in each case were consistent with the corresponding square wave data.

As a final check, effective source levels were also computed from sea experiment recordings of monitor hydrophone signals. This hydrophone was located 1.13 m from the centre of the source. The source levels were calculated by integrating the power density spectrum as described above, after subtracting background noise levels and making due allowance for the hydrophone sensitivity and data acquisition system gain. These results were corrected for the surface reflected path but not for reflections from the ship's hull and, as can be seen in Figure 4.15, agreed reasonably well with the other calibration results. The discrepancies are likely to have been due to reflections from the ship's hull, the much rougher sea surface during the sea experiment, and the changes in source depth that occurred as the vessel rolled.

The Armaments Wharf calibration square wave source levels at 1.5 m depth were adopted as the appropriate values to be used for the sea experiment. These are listed in Table 4.3.

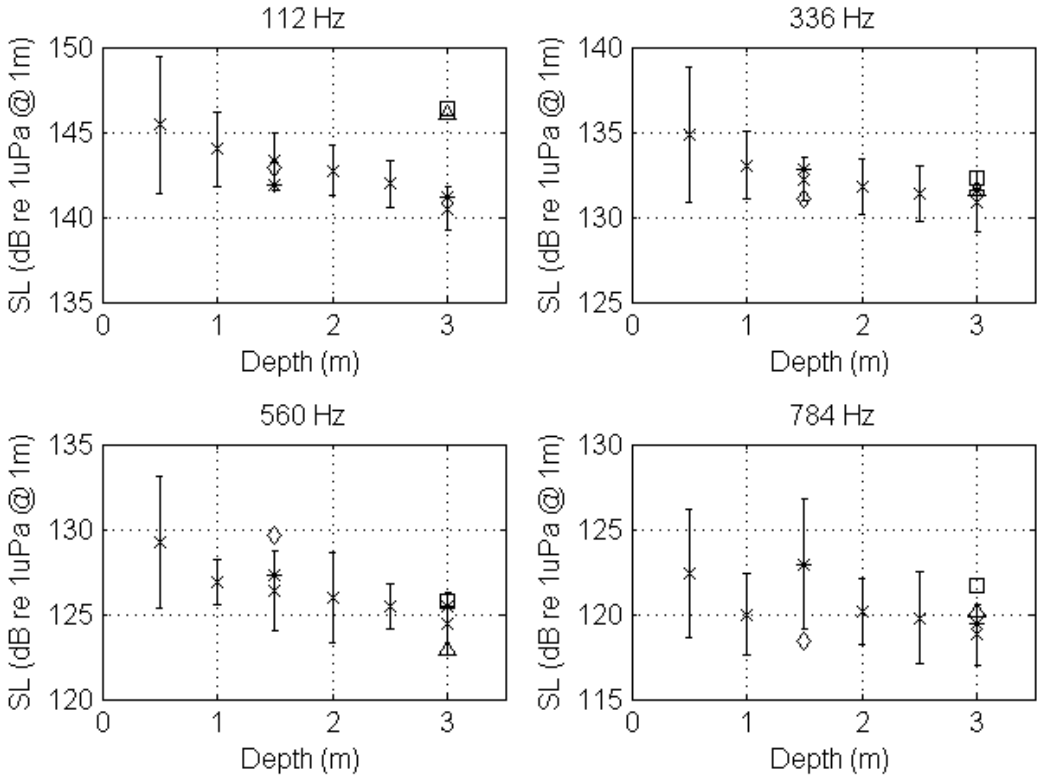

Figure 4.15 Summary of UW30 source level calibrations. The crosses and their associated error bars (95% confidence intervals) are the results of the Armaments Wharf square wave calibration; asterisks are from the Armaments Wharf sweep calibration; triangles are from the Woronora dam transmit voltage response measurements; squares are from the Woronora dam square wave calibration; and diamonds are from the measurements made on the monitor hydrophone during the sea experiment.

Table 4.3 UW30 source levels at 1.5 m depth.

Frequency (Hz)	112	336	560	784
Source level (dB re 1 µPa RMS @ 1 m)	143.3	132.2	126.3	122.9
Uncertainty (dB)	1.7	1.3	2.3	3.9

4.3.5 Transient source

Transient sound sources were deployed from the support-vessel, *Sea Witch*, at approximately one-minute intervals while *Tammar* was carrying out the U-turn manoeuvres. The signals from these sources as received by the array to provide snapshots of the array shape. Two types of sources were used: standard light globes

and 50 mm diameter evacuated glass spheres. In each case the source was mechanically imploded using the device shown in Figure 4.16. To operate the device a light globe or evacuated sphere was mounted in the imploder, which was then lowered to the required depth (10 m in this case). A weight slid down the rope activated a plunger, which broke the globe or sphere, resulting in a short impulsive sound signal.

Figure 4.16 A light globe mounted in the imploder

During the experiment a sonobuoy hydrophone was suspended 1 m below the imploder and connected to a standard SSQ-57A sonobuoy transmitter mounted on the mast of the support-vessel. This signal was received on board *Tammar* and recorded on the data acquisition system along with the towed array hydrophone signals, with the intention of using it to obtain the exact time of each implosion and therefore allow absolute range measurements to be made. There were two problems with this arrangement: the cable to the sonobuoy hydrophone tended to twist around the rope, slowing the weight down and resulting in a number of misfires where the sphere or globe cracked or punctured but did not implode completely, and also the

sonobuoy signals received on board *Tammar* had such high noise levels that the implosions could not be detected. Despite these problems the relative arrival time data provided by the transients provided very useful data on array shape and will be discussed in detail in Chapter 5.

4.3.6 Sonobuoys

Two standard SSQ-57A sonobuoys were deployed about 100 m apart so that *Tammar* could steam between them before commencing each U-turn manoeuvre. The signals from these sonobuoys were received on board *Tammar* and recorded on the data acquisition system along with the towed array hydrophone signals. The purpose of the sonobuoys was to provide an independent measurement of *Tammar's* noise signature at the beginning of each manoeuvre. The signals from these sonobuoys had very high noise levels and did not produce any useful data.

4.3.7 Vessel motion sensor

A vertical reference unit was mounted in the shipping container on the *Tammar's* aft deck and provided vessel roll, pitch and heave data which was logged by the data acquisition system at 1.8 Hz. The position of the motion sensor is given in Table 4.2.

4.3.8 GPS

Tow-vessel position was measured by a True Time GPS receiver which was also used to synchronise the acoustic beacons and the various components of the data acquisition system. The GPS antenna was mounted on top of the shipping container on the aft deck at the location given in Table 4.2.

Support-vessel position was measured using a Garmin 45 GPS receiver with the NMEA output logged on a notebook computer.

4.3.9 Data acquisition system

The data acquisition system used in this experiment was provided and operated by Nautronix Ltd., and is described in detail by Ghiotto (2002), so only a brief description is given here.

To cope with the required data rates three computers were used for data logging, each fitted with a 24-channel Hammerfall analog to digital converter sampling at 48 kHz. Each logging computer recorded data directly to hard disk and also made

data available over an Ethernet network so that other networked computers could carry out real-time monitoring and ranging calculations. Precise synchronisation was achieved by using the same sampling clock for all converters and also by recording an IRIG-B synchronisation signal generated by the True Time GPS receiver on one channel of each converter.

The 72 analog channels were allocated as specified in Table 4.4.

Table 4.4 Analog channel allocations

Signal	**Number of channels**
IRIG-B synchronisation signal	3
Sonobuoy receivers	4
Monitor hydrophone	1
Towed array hydrophones	60
Towed array DA module hydrophones (1, 2, 3 and 9)	4

Vessel position and motions data were input to the data acquisition system via RS232 serial links and were logged at 1 Hz (position) and 1.8 Hz (motions).

A total of 110 Gigabytes of data were recorded during the experiment.

4.3.10 Towed array and data acquisition system calibration

A separate experiment was carried out at the Armaments Wharf, Garden Island, on the 26th and 27th of April 2001 with the primary aim of determining whether towed array hydrophones could be successfully tracked using the tracking system described above. This opportunity was also used to carry out a calibration of several of the hydrophone channels. Note that a different array was used for this experiment, albeit with the same specifications as the array used for the sea experiment. The calibration was carried out as follows:

The towed array was positioned on the seabed in about 12 m of water parallel to and roughly 100 m south of the jetty. A reference hydrophone was slid down a line tied onto the array at the position of the appropriate hydrophone. The signal from this hydrophone was recorded from a small outboard-motor powered boat. The recording system comprised a pre-amp and Sony DAT walkman. Prior to making the hydrophone recordings the DAT's clock was synchronised to within 1 second of

the data acquisition system's clock and a one minute signal from a calibrated white noise generator was recorded on the DAT tape via the pre-amp.

While the reference hydrophone signal was being recorded the towed array hydrophone output was being recorded by the data acquisition system. It was later found that the array hydrophone signals were corrupted by significant electrical interference at 50 Hz and its harmonics. Each recording lasted for five minutes and during this time a 30 second exponential sweep spanning the frequency range 50 Hz to 10 kHz was transmitted from an underwater loudspeaker suspended from the jetty. Analysis of the data from each hydrophone comprised the following steps:

1. The reference hydrophone recordings were converted to equivalent input pressure using the parameters given in Table 4.5.
2. The array hydrophone recordings were converted to equivalent pre-amp output voltages using the analog to digital converter input sensitivity specified in Table 4.5.
3. The two recordings were time aligned.
4. A spectrogram of the reference signal was inspected to determine a suitable time period for analysis. The main criterion was that the signal should be as free as possible of impulsive noise caused by the reference hydrophone hitting the seabed.
5. Spectrograms of the chosen sections of the reference and array signals were compared to ensure that the time alignment was adequate. This could be judged from the position of the exponential sweep waveform.
6. The power density spectra of the two waveforms were computed using a one second FFT, a Hanning time domain window, and 50% overlap.
7. The array hydrophone spectrum was divided by the reference hydrophone spectrum to yield the combined sensitivity of the hydrophone and its associated preamplifier.
8. A correction for the high frequency directivity of the array hydrophone was made as follows:

- The theoretical directivity index of the hydrophone was computed as a function of frequency using the equations given in Table 3.2 of Urick (1983) and the parameters given in Table 4.5.
- The hydrophone sensitivity computed in 7 was then expressed in dB and added to the directivity index.
- Note that this correction assumed that the noise field was omnidirectional.

Table 4.5 Parameters array hydrophone calibration calculations:

Parameter	**Value**	**How obtained**
LC57 hydrophone sensitivity	-196 dB re 1V/μPa	Calibration by DSTO
Electrical gain of pre-amp / DAT / playback system	+39.1 dB	Spectral analysis of recorded white noise calibration signal
Array hydrophone length (hydrophones 42 and 21)	0.51 m	In-air measurements made on the array at DSTO
Nautronix data acquisition system A/D converter input sensitivity	3276.4 counts/Volt	Measured by Nautronix

Attempts were made to calibrate hydrophones from all four octaves and the DA modules but it was discovered after the event that a number of the hydrophones were connected to the wrong analog to digital converter channel due to a wiring problem within the towed array signal-conditioning unit. There were consequently a number of occasions on which the array hydrophone next to the reference hydrophone was not recorded. Successful recordings were made for hydrophones 21, 42, 49, DA5 and DA6 but the reference signal for hydrophone 49 had too much impact noise for it to be successfully analysed.

Calibration results for hydrophones 21 and 42, which are both high frequency U octave hydrophones, are plotted in Figure 4.17 and Figure 4.18. It can be seen from these figures that despite the problems caused by impact noise at low frequencies and electrical interference the results provided a useful calibration result between

120 Hz and 2500 Hz. At higher frequencies the effect of the anti-aliasing filter on the analyser used to digitise the reference hydrophone signal is apparent.

The most notable feature of the calibration data for these two hydrophones is that the response increased with frequency at 20 dB per decade up to about 800 Hz. The uncorrected results also showed evidence of a high frequency roll-off above 1200 Hz but correcting for hydrophone directivity significantly reduced this.

A reasonable fit to the corrected results for hydrophones 42 and 21 was provided by a transfer function comprising a first-order high-pass filter. This gave an amplitude response given by:

$$|A(f)| = \frac{A_0 f}{f_1 \sqrt{\left(1 + \left(\frac{f}{f_1}\right)^2\right)}} \qquad \textbf{(4.1)}$$

where:

$|A(f)|$ is the magnitude of the voltage at the output of the preamp divided by the magnitude of the received pressure (V/Pa)

f is frequency (Hz)

A_0 is the midband gain (V/Pa)

f_1 is the highpass cut-off frequency (Hz), and

The values A_0 = 0.38 V/Pa and f_1 = 900 Hz were found to give good fits to the data for both hydrophones.

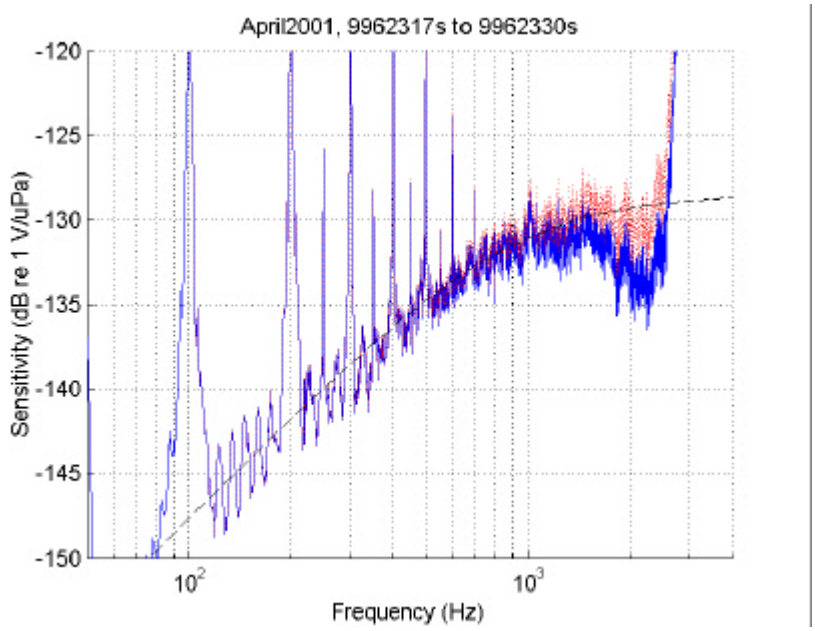

Figure 4.17 Overall sensitivity of Hydrophone 21 and its associated preamp - first data set. Blue solid line is measured data, dotted red line includes directivity correction, broken line is Equation 4.1 with A0 = 0.38 V/Pa and f1=900 Hz. (Spikes at integer multiples of 50 Hz are due to electrical interference.)

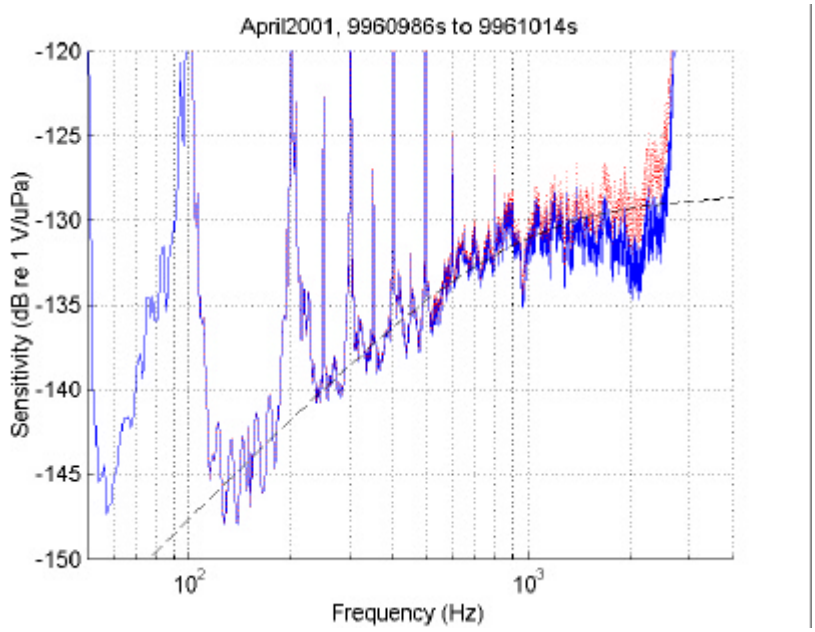

Figure 4.18 Overall sensitivity of Hydrophone 42 and its associated preamp - first data set. Blue solid line is measured data, dotted red line includes directivity correction, broken line is Equation 4.1 with A0 = 0.38 V/Pa and f1=900 Hz. (Spikes at integer multiples of 50 Hz are due to electrical interference.)

4.4 Manoeuvre descriptions

The weather on the day of the sea experiment was fine, with a moderate to fresh south-westerly wind and a significant wave height of 2 metres as measured at the waverider buoy operated by the Department of Planning and Infrastructure, which is located close to the experiment site at 32° 06' 41'' S, 115°24'07'' E (see Figure 4.1).

A number of manoeuvres were carried out during the experiment for a variety of purposes, but of these only the four U-turn manoeuvres designated Serial 1A, Serial 1B, Serial 1C and Serial 1D are relevant to this project and will be discussed here.

Each of these serials commenced with the tow-vessel (*Tammar*) steaming in a generally northerly direction at 4 knots on a course chosen to pass between the two drifting sonobuoys, and with the support-vessel (*Sea Witch*) drifting from an initial position approximately150 m to the east of the easternmost sonobuoy. The tow-vessel steamed about 500 m past the sonobuoys before commencing a 180° turn to port. The support-vessel commenced firing transient sources when the tow-vessel passed between the sonobuoys and continued firing them as rapidly as possible until the support-vessel was abeam the tow-vessel with the tow-vessel heading south. Different combinations of engines and rpm were used for each serial and these are detailed in Table 4.6.

GPS track plots showing the tow-vessel tracks during all four U-turn manoeuvres are shown in Figure 4.19, and the positions of the two vessels during each serial are given in figures 4.20 to 4.23. These plots clearly show the influences of the wind and sea on the vessel positions.

Table 4.6 Tow-vessel engine rpm for U-turn manoeuvres as displayed on bridge tachometers.

Serial	Nominal speed (knots)	Port engine rpm	Port engine in gear	Starboard engine rpm	Starboard engine in gear	Nominal turn radius (m)
1A	4	770	N	800	Y	50
1B	5	770	N	1100	Y	50
1C	4	775	Y	775	Y	100
1D	4	750	Y	750	Y	100

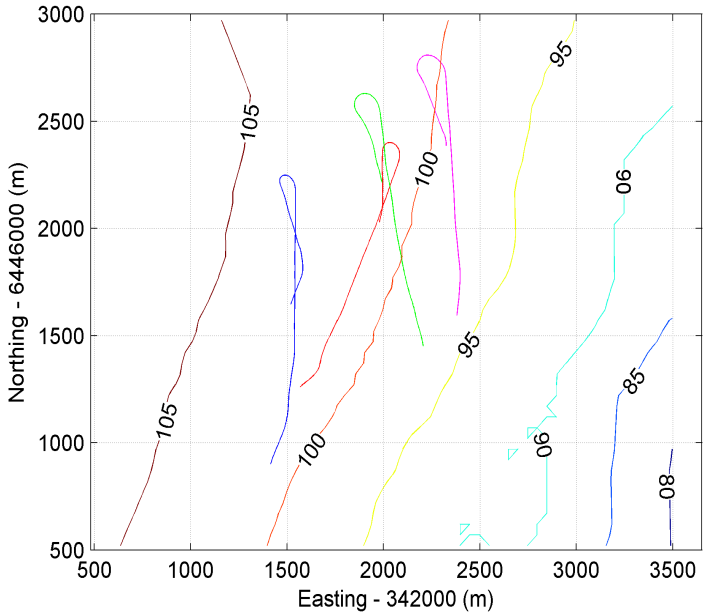

Figure 4.19 Track plots for the tow-vessel for all four U-turn manoeuvres. Mid-blue, Serial 1A; red, Serial 1B; green, Serial 1C; magenta, Serial 1D. Other lines are bathymetry contours with water depths marked in metres. Coordinates are for zone 50 of the Universal Transverse Mercator (UTM) projection.

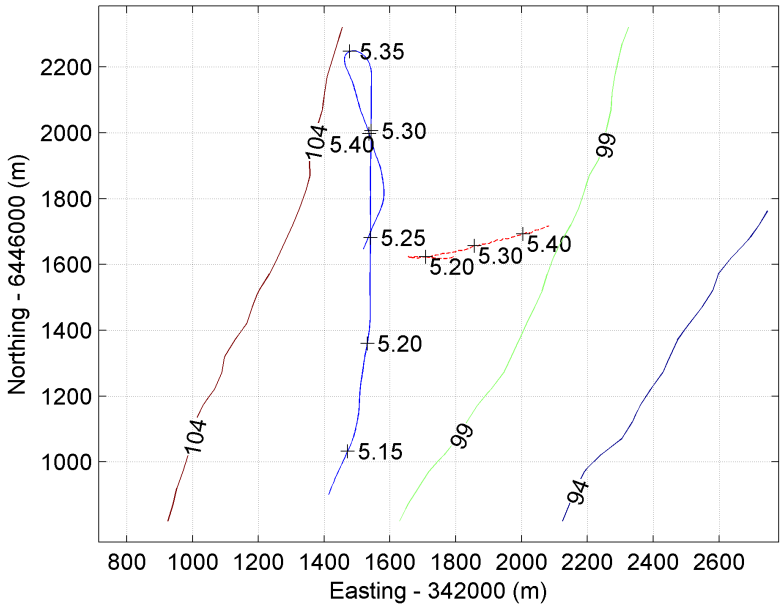

Figure 4.20 Serial 1A vessel tracks and bathymetry. Mid-blue line is tow-vessel track, red dashed line is support-vessel track (drifting). Time-markers on these tracks are in decimal hours UTC. Other lines are bathymetry contours with water depths marked in metres. Coordinates are for zone 50 of the Universal Transverse Mercator (UTM) projection.

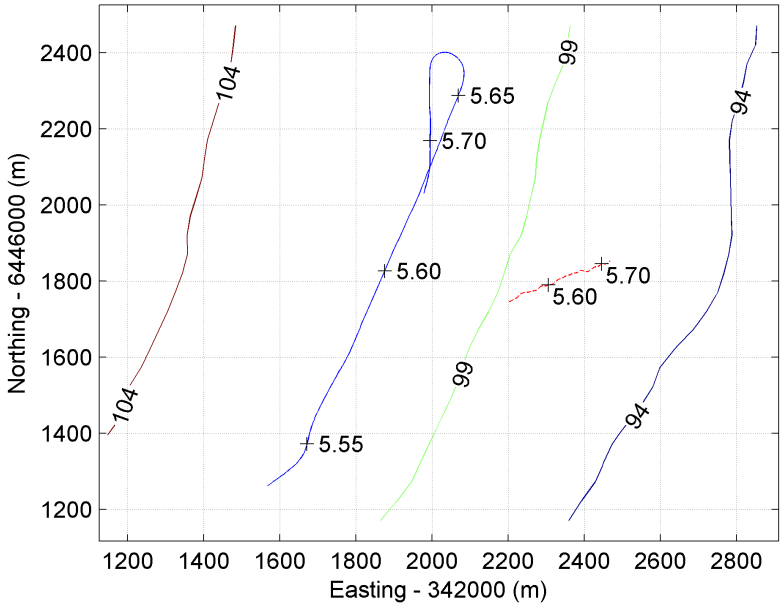

Figure 4.21 Serial 1B vessel tracks and bathymetry. Light blue line is tow-vessel track, red dashed line is support-vessel track (drifting). Time-markers on these tracks are in decimal hours UTC. Other lines are bathymetry contours with water depths marked in metres. Coordinates are for zone 50 of the Universal Transverse Mercator (UTM) projection.

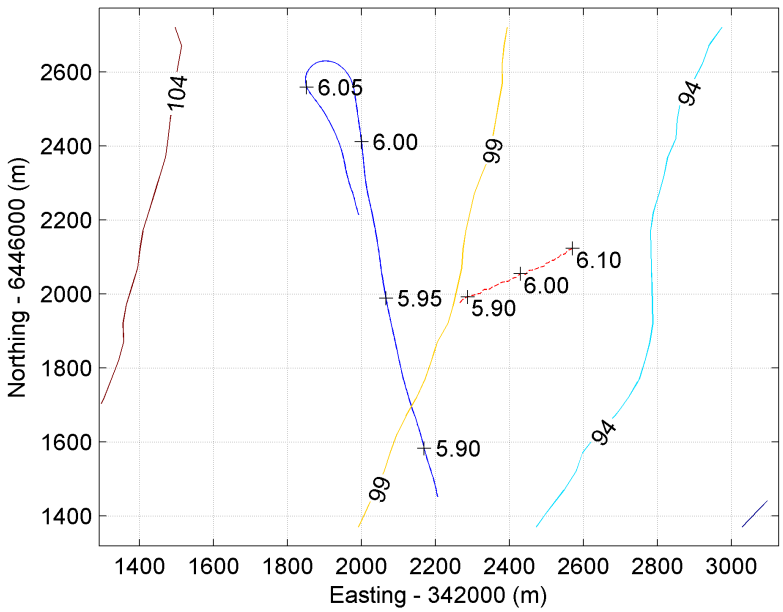

Figure 4.22 Serial 1C vessel tracks and bathymetry. Mid blue line is tow-vessel track, red dashed line is support-vessel track (drifting). Time-markers on these tracks are in decimal hours UTC. Other lines are bathymetry contours with water depths marked in metres. Coordinates are for zone 50 of the Universal Transverse Mercator (UTM) projection.

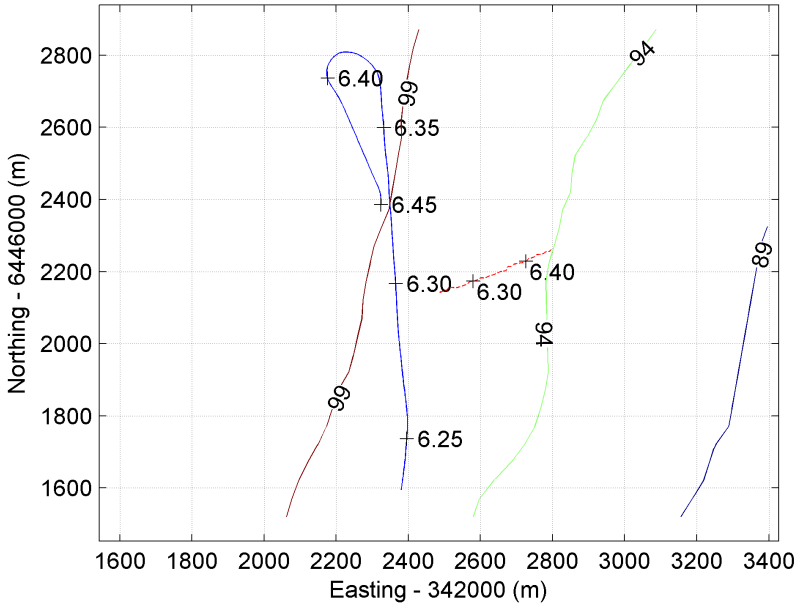

Figure 4.23 Serial 1D vessel tracks and bathymetry. Mid blue line is tow-vessel track, red dashed line is support-vessel track (drifting). Time-markers on these tracks are in decimal hours UTC. Other lines are bathymetry contours with water depths marked in metres. Coordinates are for zone 50 of the Universal Transverse Mercator (UTM) projection.

4.5 Summary

An experiment was carried out to test the feasibility of using a towed array to localise and quantify sources of underwater noise radiated by the tow-vessel. During the experiment a 27 m tug towing a 60-hydrophone array carried out a series of four U-turn manoeuvres.

The tow-vessel was fitted with a calibrated source mounted at a known location to allow the performance of source localisation and amplitude determination algorithms to be quantified.

The array hydrophones were tracked during the manoeuvres using signals from 6 acoustic beacons mounted on the tow-vessel and transient sources deployed from a second vessel were used to obtain snapshots of the array shape.

Several towed array hydrophones were calibrated during a separate experiment but high levels of electrical interference and impact noise reduced the accuracy of the calibration results.

5 Hydrophone localisation

This chapter describes the processing of data from the two different acoustic systems used during the sea experiment to provide information about the location of the towed array hydrophones during tow-vessel manoeuvres (see Chapter 4).

Section 5.1 describes the processing of transient signals from imploding spheres and light globes deployed from the support vessel. These signals were used to provide snapshots of the array shape in the horizontal and vertical planes. Processing of tracking beacon data to provide horizontal plane hydrophone positions as a function of time is described in Section 5.2, and a comparison between horizontal plane array shapes determined using the two different methods is given in Section 5.3. A short summary of the main results is given in Section 5.4.

5.1 Localisation using transient signals

Transient acoustic signals were generated at the support-vessel by imploding evacuated glass spheres and light globes at a depth of 10 m. This section describes the processing of the resulting signals received on the towed array in order to obtain information about the array hydrophone depths and horizontal plane array shape.

In many cases up to five multi-path arrivals in addition to the direct arrival could be identified which allowed the hydrophone depths to be determined unambiguously. An example is shown in Figure 5.1, which clearly shows a strong initial signal made up of the direct and surface reflected arrivals, followed about 0.04 seconds later by the bottom reflected arrival. The bottom-surface reflected arrival comes next and in most cases the surface-bottom and surface-bottom-surface arrivals can also be seen. The pronounced S shape is due to the increased hydrophone spacing towards the ends of the array, and the increased signal lengths at the extremities of the array are due to the greater lengths of the outer hydrophones.

The received signals from a single source did not allow the horizontal shape of the array at the time of each shot to be determined unambiguously, but by estimating the relative positions of the array and source from GPS data and applying element separation and array curvature constraints reasonable estimates of the array shapes were obtained.

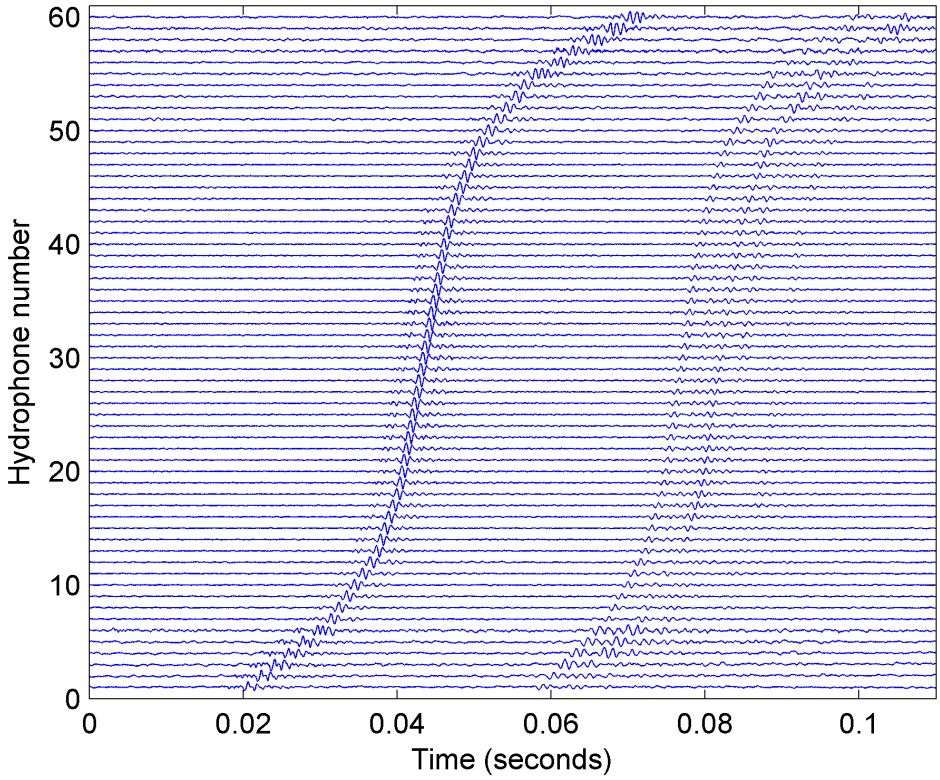

Figure 5.1 Transient signals received on all 60 hydrophones for Serial 1A, Shot 2.

5.1.1 Theory

The method used to determine array element locations from transient arrival times was a somewhat modified version of that described in Dosso et al. (1998) and Dosso & Riedel (2001). As in the method described in these references curvature and hydrophone separation constraints were used as part of a non-linear least-squares inversion procedure to obtain the smoothest array shape consistent with the measured arrival times. These constraints were implemented in a slightly different, but numerically equivalent, way in order to make use of the standard Levenberg-Marquadt method for solving non-linear least-squares problems (see Chapter 14 of Press et al. 1988). The Levenberg-Marquadt method had the advantage of having a high probability of achieving convergence even for highly non-linear problems.

In order to use this method it was necessary to set the problem up in the form:

$$\mathbf{Y} = \mathbf{f(X)} + \mathbf{e} \qquad (\ 5.1\ )$$

where:

$\mathbf{Y}$ is a column vector of observations,

$\mathbf{X}$ is a column vector of parameters to be determined,

$\mathbf{f}$ is a function which specifies how the observations depend on the parameters, and

$\mathbf{e}$ is a vector of zero-mean random noise with known covariance matrix $\mathbf{C_Y}$.

Equation 5.1 is often referred to as the observation equation. Given an initial estimate of the parameter vector, the Levenberg-Marquadt method iteratively solves for the parameter values that minimise:

$$c^2 = \left(\left(\hat{\mathbf{Y}} - \mathbf{Y} \right)^T \mathbf{C}_\mathbf{y}^{-1} \left(\hat{\mathbf{Y}} - \mathbf{Y} \right) \right) \qquad \textbf{(5.2)}$$

where $\hat{\mathbf{Y}}$ is the vector of measured observations.

If the noise is uncorrelated between observations $\mathbf{C_Y}$ is a diagonal matrix, and

$$\mathbf{C}_\mathbf{Y}^{-1} = \begin{bmatrix} 1/s_1^2 & 0 & \cdots & 0 \\ 0 & 1/s_2^2 & & 0 \\ \vdots & & \ddots & \vdots \\ 0 & 0 & \cdots & 1/s_N^2 \end{bmatrix} \qquad \textbf{(5.3)}$$

where s_n^2 is the variance of the error in observation n. In this case c^2 is the sum of the squared observation errors weighted by the reciprocal of the corresponding noise variances, the usual least-squares criterion.

The Levenberg-Marquadt method also requires the partial derivative of each observation with respect to each parameter in order to determine the manner in which to alter the parameters to improve the fit. To maximise execution speed it is best if the derivatives are computed analytically but as speed was not an issue in this case numerical derivatives were used and only the function $\mathbf{f}$ in Equation 5.1 and the inverse covariance matrix $\mathbf{C}_\mathbf{Y}^{-1}$ had to be specified.

Three different implementations of this method are described in detail below: 1. inversion for hydrophone depths with a curvature constraint; 2. inversion for the horizontal positions of the hydrophones including curvature and hydrophone spacing constraints; and 3. simultaneous inversion for hydrophone depth and horizontal position including curvature and hydrophone spacing constraints.

The observation vector included not only the arrival times but also such parameters as water depth, source depth, and the approximate position of the array relative to the

source, which was determined by combining GPS support-vessel and tow-vessel fixes with the hydrodynamic simulation described in Appendix A and the geometric parameters appropriate to the array used in the sea experiment (see Chapter 4). Hydrophone spacing constraints were included as additional observations, as were curvature constraints. In the latter case the "observed" curvature was set to zero to provide the straightest array consistent with the measured arrival times. The variances of the curvature observations were then used to control the trade-off between the straightness of the array and the fit to the arrival times.

5.1.1.1 Depth-only inversion with curvature constraint

For the depth-only inversion the following parameter vector was used:

$$\mathbf{X} = \begin{bmatrix} d_0 & z_s & z_w & r_{h,1} & \cdots & r_{h,N} & z_1 & \cdots & z_N \end{bmatrix}^T \qquad \textbf{(5.4)}$$

where:

d_0 is the product of the sound speed and the time of transmission of the transient in seconds relative to the digitisation reference time (m),

z_s is the source depth (m),

z_w is the water depth (m),

$r_{h,n}$ is the horizontal distance between the source and hydrophone n (m), and

z_n is the depth of hydrophone n (m).

Note that expressing all parameters in the same units and ensuring they were of similar magnitude improved the numerical stability of the algorithm.

The observation vector was:

$$\begin{aligned} \mathbf{Y} = \begin{bmatrix} t_{1,1} \cdots & t_{A,1} & t_{1,2} & \cdots & t_{A,2} & \cdots & t_{1,N} & \cdots & t_{A,N} \\ & r_{gps,1} & \cdots & r_{gps,N} & k_{z,2} & \cdots & k_{z,N-1} & z_{s,rope} & z_{w,chart} \end{bmatrix}^T \end{aligned} \qquad \textbf{(5.5)}$$

where:

$t_{a,n}$ is the arrival time for arrival $a \in \{1 \cdots A\}$ at hydrophone $n \in \{1 \cdots N\}$ measured in seconds relative to an arbitrary digitisation reference time. $a = 1$ corresponds to the direct path arrival, $a = 2$ to the surface reflected arrival, $a = 3$ to the bottom

reflected arrival, $a = 4$ to the surface-bottom reflected arrival, $a = 5$ to the bottom-surface reflected arrival, and $a = 6$ to the surface-bottom-surface reflected arrival.

$r_{gps,n}$ is the horizontal spacing between the source and hydrophone n estimated by combining GPS support-vessel and tow-vessel fixes with a hydrodynamic model of the array,

$k_{z,n} = \left.\frac{\partial^2 z}{\partial s^2}\right|_{s=s_n}$ is the second derivative of the hydrophone depth at hydrophone n with respect to s, the distance along the array. This was set to zero to minimise the curvature of the calculated array shape.

$z_{s,rope}$ is the depth of the source as determined from the length of the rope used to deploy the source, and

$z_{w,chart}$ is the water depth estimated from the appropriate nautical chart, corrected for the measured tidal height at the port of Fremantle.

The observation equation was defined by equations 5.6 to 5.10:

$$t_{a,n} = \frac{d_0 + \sqrt{r_{h,n}^2 + (z_n - z_a)^2}}{c_0} \qquad \textbf{(5.6)}$$

where:

c_0 is the sound speed (m/s), and

$$z_a = \begin{cases} z_s, & a = 1 \\ -z_s, & a = 2 \\ 2z_w - z_s, & a = 3 \\ 2z_w + z_s, & a = 4 \\ z_s - 2z_w, & a = 5 \\ -(z_s + 2z_w), & a = 6 \end{cases}$$

is the depth of the corresponding image source.

$$r_{gps,n} = r_{h,n}. \qquad \textbf{(5.7)}$$

$$k_{z,n} = 2\left(\frac{z_{n-1}}{(s_n - s_{n-1})(s_{n+1} - s_{n-1})} - \frac{z_n}{(s_n - s_{n-1})(s_{n+1} - s_n)} + \cdots \right.$$
$$\left. \frac{z_{n+1}}{(s_{n+1} - s_n)(s_{n+1} - s_{n-1})} \right) \qquad \textbf{(5.8)}$$

is a finite difference approximation to the second derivative of the hydrophone depth with respect to distance along the array.

$$z_{s,rope} = z_s \qquad \textbf{(5.9)}$$

$$z_{w,chart} = z_w \qquad \textbf{(5.10)}$$

5.1.1.2 Horizontal-plane only inversion

For the horizontal-plane only inversion the parameter vector was:

$$\mathbf{X} = \begin{bmatrix} d_0 & X_1 & \cdots & X_N & Y_1 & \cdots & Y_N \end{bmatrix}^T \qquad \textbf{(5.11)}$$

where:

X_n and Y_n are the global X and Y coordinates of hydrophone n relative to the source location (relative northing and easting respectively).

The observation vector was:

$$\mathbf{Y} = \begin{bmatrix} t_{1,1} & t_{1,2} & \cdots & t_{1,N} & X_{gps,ref} & Y_{gps,ref} & ds_{2,1} & ds_{3,2} & \cdots & ds_{N,N-1} \\ k_{x,2} & \cdots & k_{x,N-1} & k_{y,2} & \cdots & k_{y,N-1} \end{bmatrix}^T \qquad \textbf{(5.12)}$$

where:

$X_{gps,ref}$ and $Y_{gps,ref}$ are the X and Y coordinates of one of the array hydrophones (the central hydrophone) relative to the source as determined from a combination of GPS data and a hydrodynamic model of the array,

$ds_{n,n-1}$ is the measured distance along the array between hydrophones n and $n-1$, and

$k_{x,n}$ and $k_{y,n}$ are the second derivatives of the x and y coordinates with respect to distance along the array at hydrophone n. These were set to zero to minimise the curvature of the calculated array shape.

Note that only the times of the first arrivals were incorporated in the observation vector.

The observation equation was defined by equations 5.13 to 5.18:

$$t_{1,n} = \frac{d_0 + \sqrt{X_n^2 + Y_n^2}}{c_0} \quad \textbf{(5.13)}$$

$$X_{gps,ref} = X_{ref} \quad \textbf{(5.14)}$$

$$Y_{gps,ref} = Y_{ref} \quad \textbf{(5.15)}$$

$$ds_{n,n-1} = \sqrt{(X_n - X_{n-1})^2 + (Y_n - Y_{n-1})^2} \quad \textbf{(5.16)}$$

$$k_{x,n} = 2\left(\frac{X_{n-1}}{(s_n - s_{n-1})(s_{n+1} - s_{n-1})} - \frac{X_n}{(s_n - s_{n-1})(s_{n+1} - s_n)} + \cdots \right.$$
$$\left. \frac{X_{n+1}}{(s_{n+1} - s_n)(s_{n+1} - s_{n-1})} \right) \quad \textbf{(5.17)}$$

$$k_{y,n} = 2\left(\frac{Y_{n-1}}{(s_n - s_{n-1})(s_{n+1} - s_{n-1})} - \frac{Y_n}{(s_n - s_{n-1})(s_{n+1} - s_n)} + \cdots \right.$$
$$\left. \frac{Y_{n+1}}{(s_{n+1} - s_n)(s_{n+1} - s_{n-1})} \right) \quad \textbf{(5.18)}$$

5.1.1.3 *Combined horizontal plane / vertical plane inversion*

This inversion solved for the complete three-dimensional array shape and the other unknown parameters using the following parameter vector:

$$\mathbf{X} = \begin{bmatrix} d_0 & z_s & z_w & X_1 & \cdots & X_N & Y_1 & \cdots & Y_N & z_1 & \cdots & z_n \end{bmatrix}^T \quad \textbf{(5.19)}$$

and observation vector:

$$\mathbf{Y} = \begin{bmatrix} t_{1,1} & \cdots & t_{A,1} & t_{1,2} & \cdots & t_{A,2} & \cdots & t_{1,N} & \cdots & t_{A,N} \\ X_{gps,ref} & Y_{gps,ref} & ds_{2,1} & ds_{3,2} & \cdots & ds_{N,N-1} & k_{x,2} & \cdots & k_{x,N-1} \\ k_{y,2} & \cdots & k_{y,N-1} & k_{z,2} & \cdots & k_{z,N-1} & z_{s,rope} & z_{w,chart} \end{bmatrix}^T \quad \textbf{(5.20)}$$

The observation equation was defined by equations 5.7 to 5.10, 5.14, 5.15, 5.17, 5.18, 5.21 and 5.22.

$$t_{a,n} = \frac{d_0 + \sqrt{X_n^2 + Y_n^2 + (z_n - z_a)^2}}{c_0} \quad \textbf{(5.21)}$$

$$ds_{n,n-1} = \sqrt{(X_n - X_{n-1})^2 + (Y_n - Y_{n-1})^2 + (z_n - z_{n-1})^2} \quad \textbf{(5.22)}$$

5.1.1.4 Estimation of uncertainty

In addition to providing estimates of the parameter values, the Levenberg-Marquadt method provides an estimate of the uncertainties in the fitted parameters in the form of a covariance matrix $\mathbf{C_X}$. The diagonal elements of this matrix are the estimated variances of the corresponding parameters and the off-diagonal elements are the covariances between pairs of parameters. Note that these estimates are dependent on the covariance matrix of the observations, $\mathbf{C_Y}$, so it is important that the observation uncertainties are quantified as well as possible.

For the geometry used in this experiment there was a relatively large uncertainty in the horizontal position of the array as a whole, but a much smaller uncertainty in the relative positions of the hydrophones within the array. $\mathbf{C_X}$ contained information about the uncertainties in the absolute positions of the hydrophones from which the relative position uncertainties could be calculated as follows.

The relative and absolute positions were related by:

$$\mathbf{?}_n = \mathbf{M}\mathbf{X}'_n \qquad \textbf{(5.23)}$$

where:

$\mathbf{?}_n = \begin{bmatrix} dX_n \\ dY_n \end{bmatrix}$ is the vector of coordinates relative to the reference hydrophone at X_{ref}, Y_{ref},

$\mathbf{M} = \begin{bmatrix} -1 & 1 & 0 & 0 \\ 0 & 0 & -1 & 1 \end{bmatrix}$, and $\mathbf{X}'_n = \begin{bmatrix} X_{ref} & X_n & Y_{ref} & Y_n \end{bmatrix}^T$.

By Gauss's propagation of error law for linear equations (Cross 1983) the covariance matrix of the relative parameters was therefore:

$$\mathbf{C}_{\Delta_n} = \mathbf{M}\mathbf{C}_{\mathbf{X}'_n}\mathbf{M}^T \qquad \textbf{(5.24)}$$

where $\mathbf{C}_{\mathbf{X}'_n}$ contains the appropriate elements extracted from $\mathbf{C_X}$:

$$\mathbf{C}_{\mathbf{X}'_n} = \begin{bmatrix} s^2_{xref} & s_{xref,xn} & s_{xref,yref} & s_{xref,yn} \\ s_{xref,xn} & s^2_{xn} & s_{xn,yref} & s_{xn,yn} \\ s_{xref,yref} & s_{xn,yref} & s^2_{yref} & s_{yref,yn} \\ s_{xref,yn} & s_{xn,yn} & s_{yref,yn} & s^2_{yn} \end{bmatrix}$$

Single parameter uncertainty regions could be plotted simply by plotting error bars that extended the appropriate number of standard deviations from the estimated parameter value. For example, there was a 68.3% probability that the true parameter was within $\pm s$ of the estimated value.

For the estimated horizontal plane hydrophone positions it was more instructive to plot the joint uncertainty region for the x and y coordinate which was, in general, elliptical (see Chapter 14 of Press et al. 1988). The radius of the ellipse as a function of q, the angle anticlockwise from the x axis, was:

$$a = \sqrt{\frac{\Delta c^2 \left(s_X^2 s_Y^2 - s_{X,Y}^2 \right)}{s_Y^2 \cos^2 q + s_X^2 \sin^2 q - 2 s_{X,Y} \sin q \cos q}} \qquad \textbf{(5.25)}$$

where:

Δc^2 is the change in c^2 corresponding to the desired uncertainty ($\Delta c^2 = 2.3$ for a 68.3% uncertainty region). By using the appropriate variances and covariances this formula could be used to plot the boundary of the uncertainty region for either the absolute or relative coordinates.

5.1.2 Data analysis

A summary of the methods used to determine the observed quantities and their standard deviations is given in Table 5.1. The observation errors were assumed to be uncorrelated and consequently Equation 5.3 was used to compute $\mathbf{C}_\mathbf{Y}^{-1}$.

The procedure used to compute the final estimate of the hydrophone locations and the associated uncertainties for each transient was as follows:

1. Using the depth only inversion the standard deviation of the vertical plane array curvature, k_z, was adjusted until the value of c^2, calculated over the arrival times only, was approximately equal to its statistically expected value (the number of arrival time measurements included in the observation vector). In order to avoid numerical instability the standard deviation was not reduced below 0.001 m^{-1}.

2. Using the horizontal-plane only inversion the standard deviations of k_x and k_y were adjusted until the value of c^2, calculated over the arrival times only, was approximately equal to its statistically expected value (the number

of first arrivals). The standard deviations of the two horizontal plane curvatures, k_x and k_y, were given the same value and in order to avoid numerical instability were not reduced below 0.001 m^{-1}.

3. A combined horizontal plane / vertical plane inversion was then carried out using these curvature standard deviations, and the results of this were used as the final estimates of the parameter values and uncertainties.

For some transients only the first arrival could be unambiguously identified and only step 2 was carried out.

Table 5.1 Transient array localisation parameter values and standard deviations

Parameter	**Value**	**How obtained**	**Standard deviation**	**How obtained**
Arrival times	Various	Manual digitisation of stacked time-series.	≥ 100 μs	Minimum value represents estimate of best accuracy to which transient peaks could be localised. Larger values were input as part of digitisation procedure where peaks were poorly defined.
GPS relative positions	Various	Calculated from support-vessel and two-vessel GPS data and hydrodynamic model of array.	30 m	Estimate from standard GPS accuracy plus allowance for model error.
Hydrophone spacing	Various	From in-air element localisation experiment.	X: 0.2 m Y: 0.15 m Z: 0.1 m U: 0.1 m	Estimated accuracies of localisation experiment for hydrophones in X, Y, Z and U octaves.
Curvature	0 m^{-1}	Chosen to obtain straightest array shape consistent with other measurements.	Various	Adjusted to obtain appropriate c^2 for arrival times. See text.
Source depth	10 m	Measured length of rope used to deploy implosion device.	0.5 m	Estimated effect of surface waves and rope slant to vertical on source depth.
Water depth	Various	Estimated for each shot by interpolating charted depths and applying tidal correction.	2 m	Estimated uncertainty in interpolation and correction process.

5.1.3 Results

Typical results of applying the inversion process are plotted in Figure 5.2 and Figure 5.3, in this case for Serial 1A, Shot 2. The results for all other implosions that produced sufficient signal to noise ratio at the array to be processed are given in Appendix B. The multi-path arrivals could not be unambiguously identified for Serial 1A, Shot 1 and Serial 1C, Shot 3, and consequently these shots were processed using horizontal plane inversions. Combined horizontal plane / vertical plane inversions were carried out for all other shots.

On the hydrophone position plots the error bars and ellipses are 68.3% confidence regions for the hydrophone locations relative to the central hydrophone. For the central hydrophone the 68.3% confidence region of the absolute position is plotted.

It will be noted that the horizontal plane uncertainty in the absolute array position was much greater than the uncertainties in the relative hydrophone positions whereas in the vertical plane the absolute position uncertainty was of similar magnitude or smaller than the relative uncertainties. This is because in the vertical plane the multiple arrivals at each hydrophone provided an estimate of that hydrophone's absolute depth whereas in the horizontal plane arrival times only provided relative range information. The only constraints on the absolute position in the horizontal plane were provided by the relatively imprecise GPS derived positions and the somewhat improved source to hydrophone ranges provided by the multiple arrivals, resulting in an error ellipse with its major axis perpendicular to the source-array direction (recall that the source is at (0,0).

The error ellipses plotted in the plan views included a component due to the uncertainty in the absolute array position. This is because moving the central hydrophone in a direction perpendicular to the source-array direction would also have required a rotation of the array about the source position in order to maintain the same relative arrival times.

The only shots showing large amounts of horizontal plane curvature were Serial 1A, Shot 9 and Serial 1C, Shot 6. In most other cases, however, there seemed to be some slight curvature although this was not always statistically significant.

With the exception of Serial 1A, Shot 7 and Serial 1C shots 2 and 6, the vertical plane results showed that the forward end of the array was shallower than the aft end, which was consistent with the array being negatively buoyant. In many of the shots the results showed significant curvature of the array in the vertical plane, particularly when there was also large horizontal plane curvature, and there was considerable variation in array depth and shape from shot to shot.

Correctly identifying the order of arrival of the bottom-surface and surface-bottom reflected paths proved to be important when determining the vertical plane array shape. This was done by carrying out the least-squares inversion for both possibilities, and choosing the result that gave the smaller c^2 error. In most cases this showed that the bottom-surface reflected signal arrived first, which implied that the hydrophones were shallower than the source, but for Serial 1A, Shot 7 the array was deeper and the surface-bottom reflected signal arrived first. The arrival order was assumed to be the same for all hydrophones for a given shot, which may have led to errors in situations where the array depth crossed the source depth.

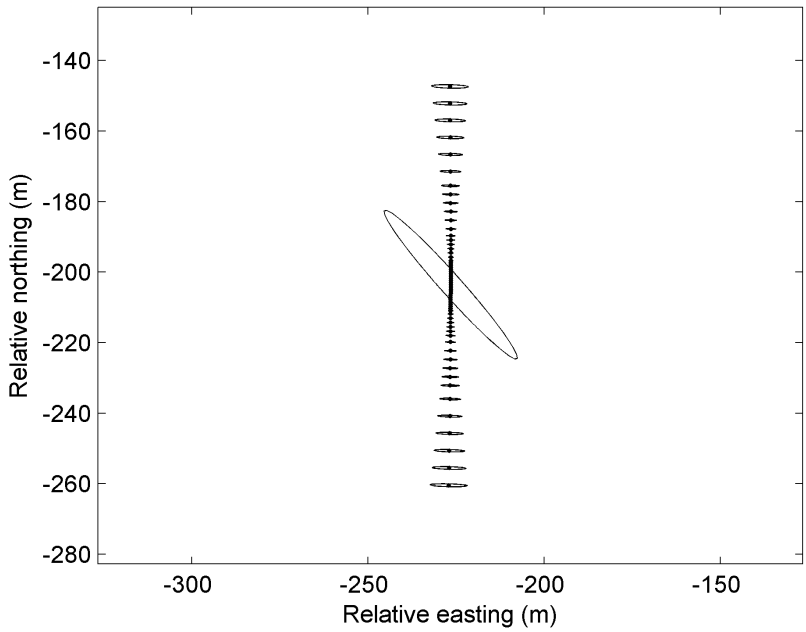

Figure 5.2 Serial 1A, Shot 2 (5.257 h) horizontal plane array shape. Large ellipse is 68.3% uncertainty region for overall array position. Ellipses on individual hydrophones are 68.3% uncertainty regions for relative positions.

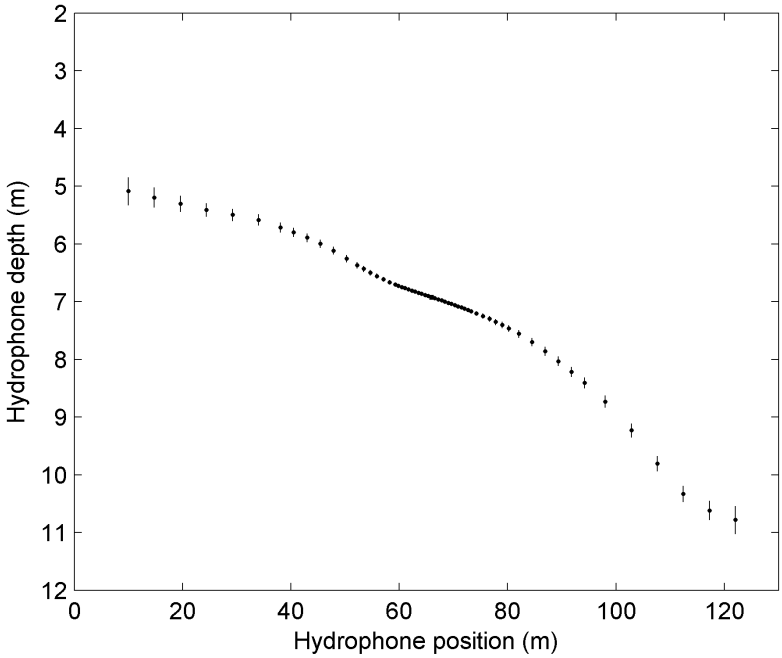

Figure 5.3 Serial 1A, Shot 2 (5.257 h) vertical plane array shape. Error bars are 68.3% uncertainty regions for relative positions.

5.2 Localisation using acoustic tracking beacons

An acoustic tracking system provided and operated by Nautronix Ltd was used to track the towed array hydrophones during the sea experiment and was described in Chapter 4. The output of the tracking system was a series of range measurements between the acoustic beacons mounted on the tow-vessel and the towed-array hydrophones. The directionality of the towed array hydrophones at the high frequencies used by the tracking beacons, and the siting of the tracking beacons above the bottom of the tow-vessel's keel because of a late change of vessel, resulted in raw range measurements with a high proportion of dropouts and outliers. The methods used to deal with these problems and produce accurate hydrophone positions during tow-vessel manoeuvres are detailed in the following subsections.

5.2.1 Measured Range Data

Plots of three examples of the raw range data provided by Nautronix Ltd. are given in figures 5.4 to 5.6. The effect of the U-turn manoeuvre, which took place between 5.32 hours and 5.42 hours, was to produce the pronounced reduction in range that can be clearly seen in these plots.

Figure 5.4 shows ranges from the six beacons to Hydrophone 1, a low frequency hydrophone at the forward end of the array. Very few ranges were measured from beacon 3, and those that were gave virtually constant readings at just over 300 m. The pseudo-noise modulation used by the ranging system was cyclic with a period corresponding to a range of 300 m, so these readings were likely to be due to electrical pickup which was incorrectly assigned to a range of just over 300 m instead of just over 0 m. No physically realistic ranges were obtained from Beacon 3 during the entire experiment and it appears that this was due to this beacon having an unfavourable conical beam pattern directed vertically downwards.

Ranges measured to Hydrophone 1 from the other beacons exhibited varying numbers of dropouts and outliers. Between 5.16 hours and 5.34 hours, and again between 5.40 hours and 5.44 hours the measured ranges from Beacon 6 corresponded to a seabed reflected path rather than the direct path. Another point to note is that no valid range measurements were made from either of the beacons on the aft starboard pole (beacons 3 and 5) during the straight-tow portion of the manoeuvre (5.17 to 5.32 hours). This was also true for the other U-turn serials (1B,

1C and 1D) and appears to have been due to shielding of the Beacon 5 signal by the underwater shape of the hull and/or the wake from the starboard propeller (the port propeller was out of gear) and the previously mentioned problem with Beacon 3.

Figure 5.5 is an example of the best data quality that was achieved during the experiment. The ranges plotted here are for Hydrophone 31, which was in the centre of the array and was a high frequency hydrophone. Generally the high frequency hydrophones gave the most reliable tracking results, which is to be expected given that they were physically shorter and therefore less directional at high frequencies than the lower frequency hydrophones.

The data plotted in Figure 5.6 is for Hydrophone 60, which was the low frequency hydrophone at the aft end of the array, and produced the least reliable range data for this Serial.

Range data for Serial 1B was much worse than that shown here and proved to be unusable. This appears to be because the tow-vessel was running at higher engine revolutions in Serial 1B than in Serial 1A (1100 rpm on the starboard engine rather than 800 rpm) and produced much more noise. (In both cases the port engine was idling with the port propeller out of gear.) Data for serials 1C (775 rpm on both engines) and 1D (750 rpm on both engines) was only marginally worse than that for Serial 1A.

5.2.2 Pre-processing of range data

Figure 5.6 clearly demonstrates the issues that had to be dealt with when pre-processing the range data:

- Seabed reflections being tracked instead of the direct path (e.g. Beacon 5 from 5.17 to 5.32 hours).
- Range dropouts being incorrectly interpreted as 300 m ranges (e.g. Beacon 6 from 5.25 to 5.35 hours).
- 300 m jumps in valid ranges (e.g. Beacon 1 at 5.37 hours).
- Outliers with no particular relationship to the true range.

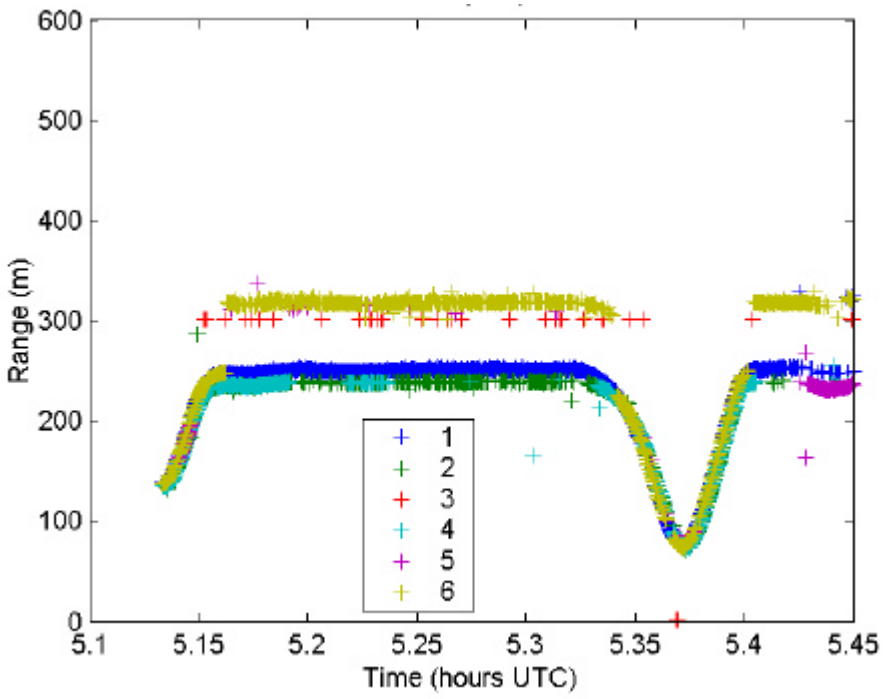

Figure 5.4 Raw range measurements from tow-vessel mounted beacons to Hydrophone 1 for Serial 1A. Legend shows beacon number.

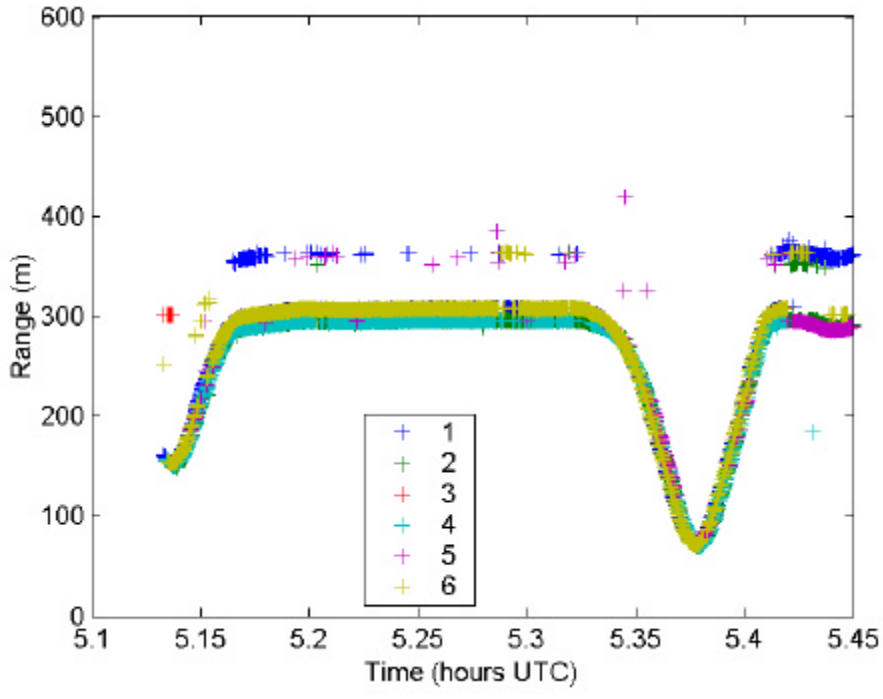

Figure 5.5 Raw range measurements from tow-vessel mounted beacons to Hydrophone 31 for Serial 1A. Legend shows beacon number.

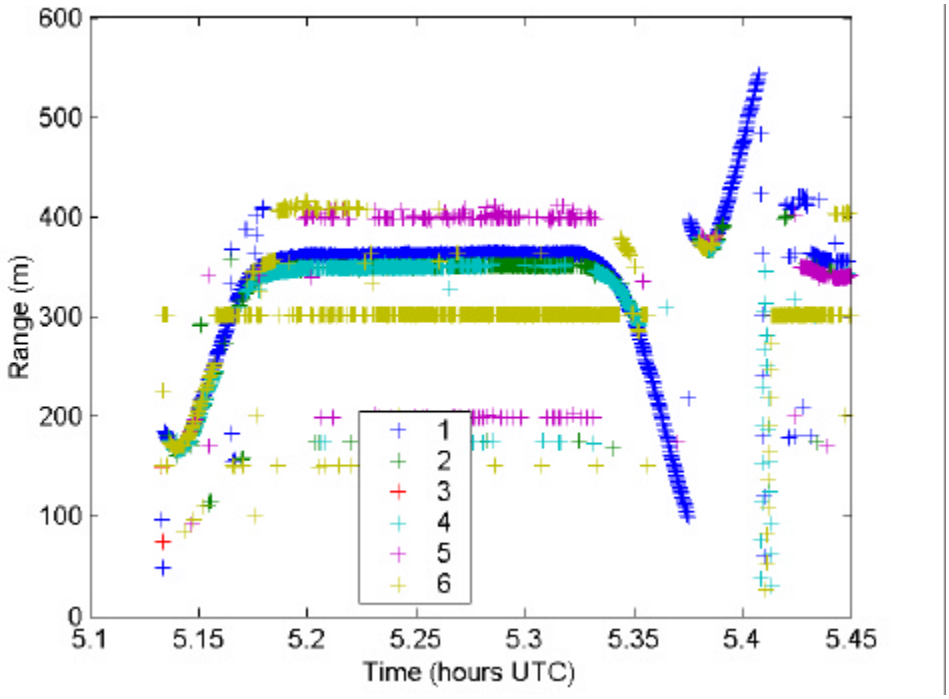

Figure 5.6 Raw range measurements from tow-vessel mounted beacons to Hydrophone 60 for Serial 1A. Legend shows beacon number.

In order to remove these erroneous data points while retaining the maximum number of valid range measurements a pre-processing algorithm was devised based on requiring consistency between ranges measured between all combinations of beacons and hydrophones. Two consistency criteria were used:

1. To be valid it was necessary that a range measurement be shorter than the sum of the distances of the corresponding beacon and hydrophone from the tow-point.
2. Valid range measurements from two different beacons to the same hydrophone could not differ by more than the spacing between the beacons, and similarly valid range measurements from the same beacon to two different hydrophones could not differ by more than the hydrophone spacing.

The second criterion was generalised to the requirement that:

$$\left| r_{m,n} - r_{i,j} \right| \le d_{m,i} + d_{n,j} + e \qquad \textbf{(5.26)}$$

where:

$r_{m,n}$ is the measured range from Beacon m to Hydrophone n,

$d_{m,i}$ is the distance between Beacon m and Beacon i,

$d_{n,j}$ is the distance between Hydrophone n and Hydrophone j, and

e is an additional term to account for the uncertainty in the range measurement. e was taken as $4\sqrt{2}s_r$ where s_r is the range measurement standard deviation which, under the assumption of normally distributed range errors, would result in 99.994% of valid ranges satisfying Equation 5.26.

Using these two criteria the algorithm processed range data for all beacon-hydrophone combinations at each time-step as follows:

1. An offset of 300 m was subtracted from any ranges that failed to meet criterion 1. (300 m was the range interval corresponding to the pseudo-random modulation repeat period.)
2. Any negative ranges were rejected.
3. A $N_r \times N_r$ square matrix **L** was formed, where N_r is the number of remaining ranges. $L_{p,q}$ was set to one if ranges p and q satisfied Equation 5.26, otherwise it was set to zero. Note that by this definition **L** was symmetric.
4. While there were still zeros in **L**:
5. The row and column containing the greatest number of zeros were removed, keeping track of which ranges corresponded to the remaining elements.
6. The remaining elements of **L** corresponded to the largest mutually consistent set of ranges for this time-step.

Figures 5.7 to 5.9 show the results of applying this algorithm to the raw ranges plotted in figures 5.4 to 5.6. The few remaining outliers were dealt with in the next stage of processing (see Section 5.2.3).

5.2.3 Hydrophone position estimation algorithm

The computation of hydrophone positions from the pre-processed ranges was complicated by the need to obtain realistic positions for all 60 hydrophones throughout each U-turn manoeuvre in the presence of a significant proportion of dropouts in the range data. Because of this requirement it was necessary to make full use of all available information, including a realistic model of the motion of the

hydrophones, a knowledge of the array hydrophone spacing, and also to find the array shape with minimum curvature consistent with the range measurements.

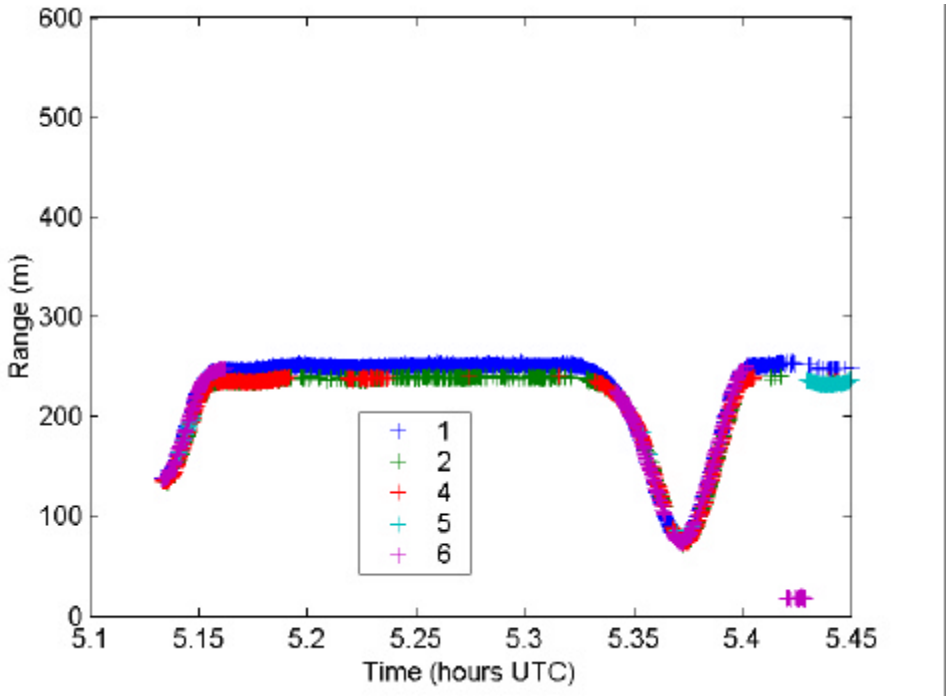

Figure 5.7 Screened range measurements from tow-vessel mounted beacons to Hydrophone 1 for Serial 1A. Legend shows beacon number.

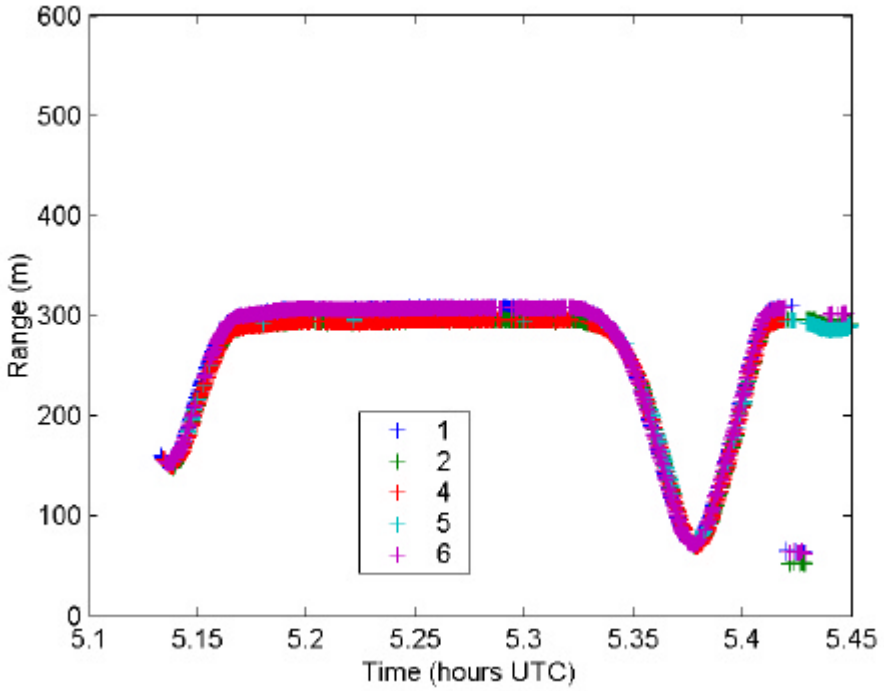

Figure 5.8 Screened range measurements from tow-vessel mounted beacons to Hydrophone 31 for Serial 1A. Legend shows beacon number.

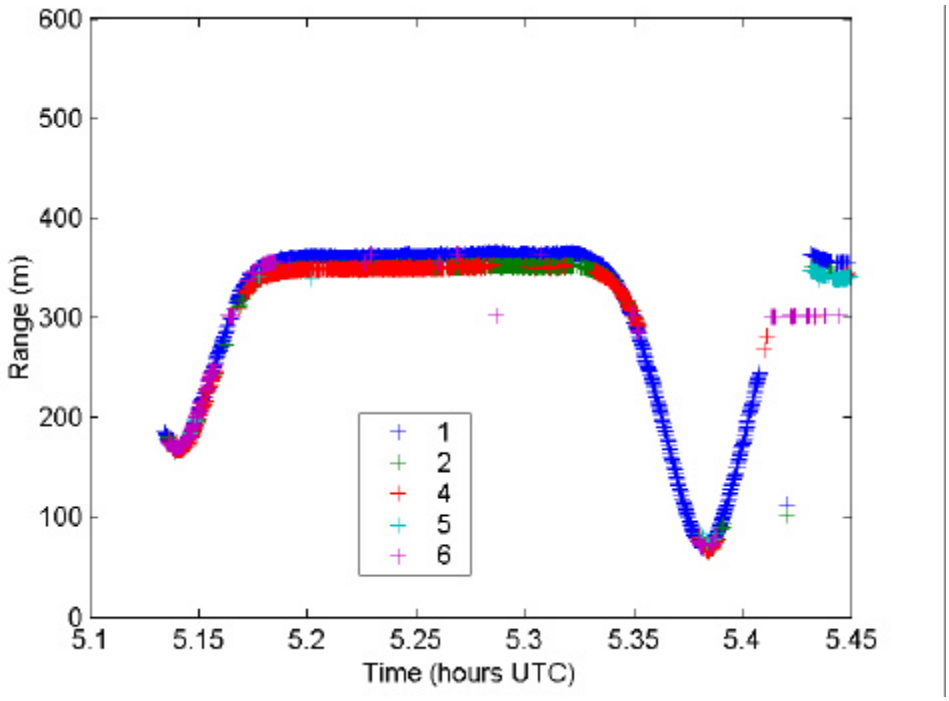

Figure 5.9 Screened range measurements from tow-vessel mounted beacons to Hydrophone 60 for Serial 1A. Legend shows beacon number.

A standard method of combining dynamic information with observations is provided by the Kalman filter, or in the case of post-processing, the Kalman smoother (Grewel & Andrews 1993). The Kalman filter and Kalman smoother algorithms require the problem to be specified in terms of an equation, called the dynamic equation, that relates the state of a system at one time step to its state at the next time step, and an equation, called the observation equation, that relates the measurements to the system state.

In this case the observations (ranges) depended nonlinearly on the system state (hydrophone coordinates) and it was necessary to use the extended Kalman filter for real-time processing and the extended Kalman smoother for post-processing. The dynamic model equation, including an additional linear dependence on a vector of known inputs, was therefore given by:

$$\tilde{\mathbf{x}}_k = \Phi_{k-1}\tilde{\mathbf{x}}_{k-1} + \mathbf{B}_{k-1}\mathbf{u}_{k-1} + \mathbf{w}_{k-1}, \qquad \textbf{(5.27)}$$

and the observation equation was given by:

$$\tilde{\mathbf{z}}_k = \mathbf{f}_k(\tilde{\mathbf{x}}_k) + \mathbf{v}_k. \qquad \textbf{(5.28)}$$

In these equations:

$\tilde{\mathbf{x}}$ is a vector of system states,

$\mathbf{u}$ is a vector of known inputs,

$\tilde{\mathbf{z}}$ is a vector of observations,

$\mathbf{w}$ is a vector of dynamic model errors which are assumed random and uncorrelated in time, with zero mean and covariance matrix $\mathbf{Q}_k$,

$\mathbf{v}$ is a vector of observation errors which are also assumed random and uncorrelated in time, with zero mean and covariance matrix $\mathbf{R}_k$,

Φ and $\mathbf{B}$ are coefficient matrices,

$\mathbf{f}_k$ is a vector valued function of the state vector, and

the subscript k refers to the sampling instant.

The extended Kalman filter estimate of the state vector was then computed iteratively as follows:

1. Initial estimates of the state vector, $\hat{\mathbf{x}}_0$, and the state vector covariance matrix, $\mathbf{P}_0$, were set up.

2. The time-step count, k, was set to 1.

3. The dynamic model equation was used to predict the new state vector:

$$\hat{\mathbf{x}}_{k|k-1} = \Phi_{k-1}\hat{\mathbf{x}}_{k-1} + \mathbf{B}_{k-1}\mathbf{u}_{k-1}. \qquad \textbf{(5.29)}$$

4. The covariance matrix of the predicted state vector was calculated:

$$\mathbf{P}_{k|k-1} = \Phi_{k-1}\mathbf{P}_{k-1}\Phi_{k-1}^T + \mathbf{Q}_{k-1}. \qquad \textbf{(5.30)}$$

5. The coefficient matrix of the linearised observation equation was calculated. This was given by the Jacobian of $\mathbf{f}_k$:

$$\mathbf{H}_k = \begin{bmatrix} \frac{\partial f_1}{\partial \tilde{x}_1} & \cdots & \frac{\partial f_1}{\partial \tilde{x}_p} \\ \vdots & \ddots & \vdots \\ \frac{\partial f_q}{\partial \tilde{x}_1} & \cdots & \frac{\partial f_q}{\partial \tilde{x}_p} \end{bmatrix} \qquad \textbf{(5.31)}$$

evaluated at the predicted state $\hat{\mathbf{x}}_{k|k-1}$. Here p is the number of states and q is the number of observations.

6. The Kalman gain matrix was calculated:

$$\mathbf{K}_k = \mathbf{P}_{k|k-1}\mathbf{H}_k^T\left[\mathbf{H}_k\mathbf{P}_{k|k-1}\mathbf{H}_k^T + \mathbf{R}_k\right]^{-1}. \qquad \textbf{(5.32)}$$

7. The state vector estimate was corrected:

$$\hat{\mathbf{x}}_k = \hat{\mathbf{x}}_{k|k-1} + \mathbf{K}_k\left[\tilde{\mathbf{z}}_k - \mathbf{f}_k\left(\hat{\mathbf{x}}_{k|k-1}\right)\right]. \qquad \textbf{(5.33)}$$

8. The covariance matrix of the corrected state vector was computed:

$$\mathbf{P}_k = \left[\mathbf{I} - \mathbf{K}_k\mathbf{H}_k\right]\mathbf{P}_{k|k-1} \qquad \textbf{(5.34)}$$

9. The time-step count was incremented, $k = k+1$, and the process was repeated from step 3.

The Kalman filter only uses observations made up to and including the current time to estimate the current state, and is therefore suitable for real-time processing. However, when carrying out post-processing, all recorded observations (past present and future) can be used in the computation of the state at each time-step, resulting in significantly better estimates. A convenient algorithm to carry out this post-processing is the Kalman smoother algorithm first proposed in Rauch et al. (1965), and also described in Grewel & Andrews (1993). To apply this algorithm the data is first processed using the standard Kalman filter, the results of which are then run in reverse order through the smoother defined by the following equations:

1. The smoother estimates of the state vector and its covariance matrix for the final time-step ($k = K$) were the same as the filter estimates, i.e.:

$$\hat{\mathbf{x}}_{K|K} = \hat{\mathbf{x}}_K \qquad \textbf{(5.35)}$$

and

$$\mathbf{P}_{k|K} = \mathbf{P}_K \qquad \textbf{(5.36)}$$

2. The time-step counter was initialised to $k = K - 1$.

3. The predicted state vector for time-step $k+1$ was calculated (alternatively this information could be stored when running the filter):

$$\hat{\mathbf{x}}_{k+1|k} = \Phi_k\hat{\mathbf{x}}_k + \mathbf{B}_k\mathbf{u}_k, \qquad \textbf{(5.37)}$$

as was the covariance matrix of the predicted state vector:

$$\mathbf{P}_{k+1|k} = \Phi_k\mathbf{P}_k\Phi_k^T + \mathbf{Q}_k, \qquad \textbf{(5.38)}$$

4. The smoother gain matrix was calculated:

$$\mathbf{A}_k = \mathbf{P}_k \mathbf{F}_k^T \mathbf{P}_{k+1|k}^{-1}, \qquad (5.39)$$

and used to compute the smoothed state vector estimate for time-step k:

$$\hat{\mathbf{x}}_{k|K} = \hat{\mathbf{x}}_k + \mathbf{A}_k \left(\hat{\mathbf{x}}_{k+1|K} - \hat{\mathbf{x}}_{k+1|k} \right), \qquad (5.40)$$

and its covariance matrix:

$$\mathbf{P}_{k|K} = \mathbf{P}_k + \mathbf{A}_k \left(\mathbf{P}_{k+1|K} - \mathbf{P}_{k+1|k} \right) \mathbf{A}_k^T \qquad (5.41)$$

5. The time-step counter was decremented, $k = k - 1$, and the procedure was repeated from step 3.

Note that the smoother algorithm did not require any information about the observations or the observation equation and was thus unchanged whether linear or non-linear observations were used.

5.2.3.1 Dynamic models

A dynamic model for a towed array suitable for incorporating into a Kalman filter was proposed by Gray et al. (1993) and tested at sea (Riley & Gray 1993) with an array instrumented with heading and depth sensors. The model was based on the observation that disturbances in the array shape caused by vessel motion propagated down the array at approximately the tow-speed, and with very little damping. The dynamic model thus calculated the motion of a segment of the array at one time-step from the motion of a segment further towards the head of the array at a previous time-step.

An alternative, and somewhat simpler model to implement, was the Taylor series approximation given in Cross & Prichett (1986). As applied here this model assumed each hydrophone had a constant acceleration over a time-step and treated the rate of change of acceleration as a random variable. The position, velocity, and acceleration were all estimated by the filter. Results obtained by Cross & Prichett, for the case of estimating survey vessel position, were comparable to those obtained using much more complex hydrodynamic models.

It would have been possible to implement the dynamic model in several coordinate frames:

1. the moving coordinate frame of the tow-vessel,
2. an earth-fixed global coordinate system, or

3. a hybrid coordinate system that moves with the tow-vessel but maintains a fixed orientation relative to the earth.

Option 1 had the advantage of not requiring any coordinate transformations as the range measurements were also made relative to fixed points on the tow-vessel, whereas option 2 required knowledge of the tow-vessel position and heading, and option 3 required knowledge of tow-vessel heading only. To apply Gray's model it would have been necessary to use option 3.

Unfortunately tow-vessel heading was not measured during the experiment and the only heading information available was the tow-vessel course derived from the GPS data, which could be significantly different from the vessel heading during tight turns.

Two different dynamic models were implemented, the first approximating the motion of each hydrophone as having a constant acceleration in tow-vessel coordinates, and the second assuming a constant acceleration in the global reference frame. These models are described in detail in the next two subsections. Gray's model was not implemented as it was felt that the added complexity was not justified given the errors involved in translating between coordinate systems in the absence of accurate heading data.

Tow-vessel coordinates

This model effectively assumed that the array hydrophones moved with a constant acceleration in tow-vessel coordinates. It had the advantage of simplicity and required no information about the heading and velocity of the tow-vessel as all calculations were carried out in a coordinate system fixed relative to the vessel.

The state vector was as follows:

$$\tilde{\mathbf{x}} = \begin{bmatrix} x_1 & \cdots & x_N & \dot{x}_1 & \cdots & \dot{x}_N & \ddot{x}_1 & \cdots & \ddot{x}_N \cdots \\ y_1 & \cdots & y_N & \dot{y}_1 & \cdots & \dot{y}_N & \ddot{y}_1 & \cdots & \ddot{y}_N \end{bmatrix}^T \qquad \textbf{(5.42)}$$

where (x_n, y_n), $(\dot{x}_n, \dot{y}_n)$, and $(\ddot{x}_n, \ddot{y}_n)$ are respectively the position, velocity, and acceleration of hydrophone $n \in \{1 \cdots N\}$, relative to the tow-vessel.

The dynamic model equations were based on a third order Taylor expansion of the hydrophone motion (Cross & Prichett 1986). In the x direction this gave:

$$x_{k+1} = x_k + dt\dot{x}_k + \frac{dt^2}{2}\ddot{x}_k + \frac{dt^3}{6}\dddot{x}_k, \qquad \textbf{(5.43)}$$

$$\dot{x}_{k+1} = \dot{x}_k + dt\ddot{x}_k + \frac{dt^2}{2}\dddot{x}_k, \qquad \textbf{(5.44)}$$

and

$$\ddot{x}_{k+1} = \ddot{x}_k + dt\dddot{x}_k \qquad \textbf{(5.45)}$$

with an analogous set of equation for the y direction. Here dt is the time interval between time-step k and time-step $k+1$.

In each of the above equations the last term involving the rate of change of acceleration was modelled as zero mean Gaussian noise, uncorrelated in time, uncorrelated between hydrophones, and uncorrelated with the observations. As is often the case when implementing Kalman filters, the first two assumptions were at best dubious, but the algorithm still performed well.

These equations were linear in the states and could readily expressed in the form of Equation 5.27 with $\mathbf{B}_k = \mathbf{0}$ and

$$\mathbf{F}_k = \begin{bmatrix} \mathbf{T}_1 & \mathbf{Z}_1 \\ \mathbf{Z}_1 & \mathbf{T}_1 \end{bmatrix} \qquad \textbf{(5.46)}$$

where:

$\mathbf{Z}_1$ is a $3N \times 3N$ matrix of zeros, and $\mathbf{T}_1$ is a $3N \times 3N$ block diagonal matrix:

$$\mathbf{T}_1 = \begin{bmatrix} 1 & & dt & & dt^2/2 & & \\ & \ddots & & \ddots & & \ddots & \\ & & 1 & & dt & & dt^2/2 \\ & & & 1 & & dt & \\ & & & & \ddots & & \ddots \\ & & & & & 1 & & dt \\ & & & & & & 1 & \\ & & & & & & & \ddots \\ & & & & & & & & 1 \end{bmatrix}. \qquad \textbf{(5.47)}$$

The elements not shown are zero.

The dynamic model covariance matrix was given by:

$$\mathbf{Q}_k = \mathbf{G}\mathbf{S}\mathbf{G}^T \qquad \textbf{(5.48)}$$

where $\mathbf{S} = s_j^2\mathbf{I}$ is a $2N \times 2N$ diagonal matrix with the variance of the rate of change of acceleration, s_j^2, on the diagonal, and

$$\mathbf{G} = \begin{bmatrix} \mathbf{T}_2 & \mathbf{Z}_2 \\ \mathbf{Z}_2 & \mathbf{T}_2 \end{bmatrix}. \qquad \textbf{(5.49)}$$

Here $\mathbf{Z}_2$ is a $3N \times N$ matrix of zeros, and $\mathbf{T}_2$ is the $3N \times N$ matrix:

$$\mathbf{T}_2 = \begin{bmatrix} dt^3/6 & & \\ & \ddots & \\ & & dt^3/6 \\ dt^2/2 & & \\ & \ddots & \\ & & dt^2/2 \\ dt & & \\ & \ddots & \\ & & dt \end{bmatrix}. \qquad \textbf{(5.50)}$$

Again, the elements not shown are zero.

In this case there was no dependence on known inputs, and so $\mathbf{B} = \mathbf{0}$.

Global coordinates

The global dynamic model assumed that the hydrophones had a constant acceleration in a global coordinate system with its origin fixed relative to the earth, its X axis positive north, its Y axis positive east and its Z axis positive down. For convenience the origin was chosen so that these coordinates correspond to Zone 50 of Universal Transverse Mercator (UTM) projection, MGA94 (ICSM 1998). This would be expected to be a more realistic model of the true motion of the hydrophones but required knowledge of the tow-vessel heading and velocity in order to carry out the necessary coordinate transformations.

The state vector contained a mixture of parameters expressed in global and tow-vessel coordinates:

$$\begin{aligned} \tilde{\mathbf{x}} = \lfloor & x_1 \quad \cdots \quad x_N \quad \dot{X}_1 \quad \cdots \quad \dot{X}_N \quad \ddot{X}_1 \quad \cdots \quad \ddot{X}_N \cdots \\ & y_1 \quad \cdots \quad y_N \quad \dot{Y}_1 \quad \cdots \quad \dot{Y}_N \quad \ddot{Y}_1 \quad \cdots \quad \ddot{Y}_N \rfloor^T \end{aligned} \qquad \textbf{(5.51)}$$

where lower case letters represent tow-vessel coordinates and capital letters represent global coordinates.

With this definition of the state vector the equations for velocity and acceleration were analogous to equations 5.44 and 5.45 with the velocities, accelerations, etc. replaced by their global equivalents. The dynamic equations for position were, however, more complex, as they now included the coordinate transformation (See Appendix C for derivation):

$$\begin{aligned} x_{k+1} = x_k + dqy_k + \ldots \\ \left(dt\left(\dot{X}_k - \dot{X}_{0,k}\right) + dt^2\ddot{X}_k/2 + dt^3\dddot{X}_k/6\right)\cos q_{k+1} + \ldots \\ \left(dt\left(\dot{Y}_k - \dot{Y}_{0,k}\right) + dt^2\ddot{Y}_k/2 + dt^3\dddot{Y}_k/6\right)\sin q_{k+1} \end{aligned} \qquad \textbf{(5.52)}$$

$$\begin{aligned} y_{k+1} = y_k - dqx_k - \ldots \\ \left(dt\left(\dot{X}_k - \dot{X}_{0,k}\right) + dt^2\ddot{X}_k/2 + dt^3\dddot{X}_k/6\right)\sin q_{k+1} + \ldots \\ \left(dt\left(\dot{Y}_k - \dot{Y}_{0,k}\right) + dt^2\ddot{Y}_k/2 + dt^3\dddot{Y}_k/6\right)\cos q_{k+1} \end{aligned} \qquad \textbf{(5.53)}$$

where:

X, Y are the global coordinates of a hydrophone (X is northing, Y is easting),

X_0, Y_0 are the global coordinates of the origin of the tow-vessel coordinate system (i.e. the tow-point),

x, y are the coordinates of the hydrophone in tow-vessel coordinates

q is the vessel heading (radians clockwise from north), and

the subscript k refers to the time-step.

Expressing these equations in matrix form resulted in the matrices given in Appendix C.

5.2.3.2 *Observation model*

The observation model consisted of equations dealing with three types of observations: measured distances between beacons and hydrophones, distances between adjacent hydrophones, and pseudo-observations used to minimise the curvature of the array.

Slant ranges measured by the acoustic tracking system were first converted to horizontal ranges using the known beacon depths, and an assumed hydrophone depth of 8 m. The observation equation for the horizontal range from beacon m, located at (x_m, y_m), to hydrophone n, located at (x_n, y_n), was then:

$$r_{m,n} = \sqrt{(x_m - x_n)^2 + (y_m - y_n)^2} \qquad \textbf{(5.54)}$$

Partial derivatives of this equation with respect to x_n and y_n were required for the $\mathbf{H}_k$ matrix, and were given by:

$$\frac{\partial r_{m,n}}{\partial x_n} = \frac{x_n - x_m}{\sqrt{(x_m - x_n)^2 + (y_m - y_n)^2}} \qquad \textbf{(5.55)}$$

and

$$\frac{\partial r_{m,n}}{\partial y_n} = \frac{y_n - y_m}{\sqrt{(x_m - x_n)^2 + (y_m - y_n)^2}} \qquad \textbf{(5.56)}$$

Partial derivatives with respect to the other parameters were zero.

The observation equation for the distance between hydrophones n and $n+1$, assuming a horizontal array, was given by:

$$ds_{n,n+1} = \sqrt{(x_{n+1} - x_n)^2 + (y_{n+1} - y_n)^2}\ . \qquad \textbf{(5.57)}$$

The non-zero partial derivatives of this equation were:

$$\frac{\partial s_{n,n+1}}{\partial x_{n+1}} = -\frac{\partial s_{n,n+1}}{\partial x_n} = \frac{x_{n+1} - x_n}{\sqrt{(x_{n+1} - x_n)^2 + (y_{n+1} - y_n)^2}} \qquad \textbf{(5.58)}$$

and

$$\frac{\partial s_{n,n+1}}{\partial y_{n+1}} = -\frac{\partial s_{n,n+1}}{\partial y_n} = \frac{y_{n+1} - y_n}{\sqrt{(x_{n+1} - x_n)^2 + (y_{n+1} - y_n)^2}}\ . \qquad \textbf{(5.59)}$$

The curvature of the estimated array shape was minimised using the same technique that was used for transient array shape determination (see Section 5.1): the introduction of a set of pseudo-observation equations for array curvature, with the corresponding "observations" set to zero. The curvature equation in the x direction was:

$$k_{x,n} = 2\left(\frac{x_{n-1}}{ds_{n-1,n} ds_{n-1,n+1}} - \frac{x_n}{ds_{n-1,n} ds_{n,n+1}} + \frac{x_{n+1}}{ds_{n,n+1} ds_{n-1,n+1}} \right) \qquad \textbf{(5.60)}$$

with an analogous equation in the y direction.

The non-zero partial derivatives with respect to the parameters were:

$$\frac{\partial k_{x,n}}{\partial x_{n-1}} = \frac{\partial k_{y,n}}{\partial y_{n-1}} = \frac{2}{ds_{n-1,n} ds_{n-1,n+1}}, \qquad \textbf{(5.61)}$$

$$\frac{\partial k_{x,n}}{\partial x_n} = \frac{\partial k_{y,n}}{\partial y_n} = \frac{-2}{ds_{n-1,n} ds_{n,n+1}}, \qquad \textbf{(5.62)}$$

and

$$\frac{\partial k_{x,n}}{\partial x_{n+1}} = \frac{\partial k_{y,n}}{\partial y_{n+1}} = \frac{2}{ds_{n-1,n+1} ds_{n,n+1}} \qquad \textbf{(5.63)}$$

5.2.3.3 Determination of variances

The Kalman filter and smoother algorithms required estimates of the uncertainties in the dynamic model equations and observations, which were input via the corresponding covariance matrices **S** and **R**. The statistics of the observation errors were often known in advance or could be estimated from the data, whereas satisfactory values of the dynamic model uncertainties usually had to be obtained by tuning the performance of the filter with simulated data. Too large a value for the dynamic model uncertainty (in this case the variance of the rate of change of acceleration) resulted in very noisy hydrophone tracks whereas setting the uncertainty too small produced smooth tracks but also introduced systematic errors.

The beacon-hydrophone range measurement variances and covariances were calculated for segments of data where the array was streaming directly behind the tow-vessel, and consequently the true ranges were known to be constant. Variances for ranges to the lower frequency hydrophones were systematically larger than those for ranges to the higher frequency hydrophones and so the variances were averaged over all hydrophones in each octave. There was no systematic trend in the calculated covariances and therefore these were averaged over all beacon-hydrophone combinations. The results are given in Table 5.2. The values used in the hydrophone position calculation algorithm were the averages over serials 1A, 1C and 1D given in the last row of the table.

The variances in the inter-hydrophone spacing observations were taken as 0.04 m^2 for octave X hydrophones, 0.0225 m^2 for octave Y, and 0.01 m^2 for octaves Z and U. These values were derived from the estimated accuracy of the in-air hydrophone localisation experiment.

Table 5.2 Beacon-hydrophone range measurement variances and covariances computed from straight-tow portions of data

	Average range measurement variance (m^2) for octave:				Average covariance (m^2)
Serial	X	Y	Z	U	
1A	0.54	0.23	0.16	0.15	0.11
1C	1.15	0.17	0.19	0.11	0.036
1D	0.79	0.29	0.17	0.25	0.041
All serials	0.83	0.23	0.17	0.17	0.062

A dynamic model variance, s_j^2, of 0.01 m^2s^{-6} was found to give satisfactory results using the simulated range data discussed in Section 5.2.4.1.

The simulation was also used to tune the variance of the curvature pseudo-observations. A value of 10^{-4} m^{-2} was found to give a sufficiently smooth array shape without unduly affecting the statistics of the range innovations (differences between actual and predicted range measurements) discussed in the next section.

5.2.3.4 *Gross error screening*

Beacon-hydrophone range data were screened for any remaining gross errors by computing the innovation, $\mathbf{v}_k$, which was the difference between the actual and predicted range measurements, i.e.

$$\mathbf{v}_k = \tilde{\mathbf{z}}_k - \mathbf{f}_k\left(\hat{\mathbf{x}}_{k|k-1}\right) \qquad \textbf{(5.64)}$$

The covariance matrix for $\mathbf{v}_k$ was (Candy 1988, Chapter 9):

$$\mathbf{C}_\mathbf{v} = \mathbf{R}_k + \mathbf{H}_k\mathbf{P}_{k|k-1}\mathbf{H}_k^T \qquad \textbf{(5.65)}$$

Before applying step 6 of the Kalman filter algorithm each innovation was compared to its corresponding standard deviation (square root of the appropriate diagonal element of $\mathbf{C}_\mathbf{v}$) and rejected if its magnitude was larger than the standard deviation by more than a factor a. A range was rejected by setting its corresponding variance in $\mathbf{R}_k$ to a very large value.

Choosing an appropriate value of a required some experimentation: setting it too large resulted in erroneous ranges being accepted whereas setting it too small

resulted in the filter rejecting valid ranges, which in extreme cases caused the filter to diverge. A value of $a = 10$ was found to generally give good results.

The innovations were also a useful diagnostic of Kalman filter performance. If the filter was working correctly the sequence of innovations for each observation should have had zero mean and been statistically white (i.e. uncorrelated in time), with a variance close to the expected variance given by the appropriate diagonal element of $\mathbf{C}_v$ (Candy 1988, Chapter 9). Conversely, if the filter was not tracking the observations the innovations would become highly correlated in time. Candy gave the following test for statistical whiteness:

If a sequence, v, of N samples is spectrally white then 95% of the values of the autocorrelation of v will lie in the range

$$\pm \frac{1.96 \mathrm{R}_{vv}(0)}{\sqrt{N}}, \qquad \textbf{(5.66)}$$

where $\mathrm{R}_{vv}(0)$ is the autocorrelation at zero lag.

5.2.3.5 *Generating simulated range data*

Testing and tuning the hydrophone position estimation algorithm required the generation of a set of realistic hydrophone positions and corresponding simulated range measurements. This was achieved as follows:

1. The hydrodynamic simulation described in Appendix A was used to generate simulated hydrophone tracks using the tow-vessel GPS positions recorded during serials 1A, 1C and 1D.
2. Ranges between the tracking system beacons and the simulated hydrophones were computed.
3. Gaussian random noise with the appropriate variance for each hydrophone (see Table 5.2) was added to the computed ranges. Simulations were run with noise that was uncorrelated in time (spectrally white) and also with coloured noise. The coloured noise was obtained by filtering uncorrelated noise with a frequency domain filter with a spectral response corresponding to the spectrum of the noise in the measured data. The noise spectrum was obtained by calculating the power spectral density of the ranges measured during the straight-tow section of the serial, after first subtracting the mean

and de-trending the data (Figure 5.10). In this figure the dominant peaks just below 0.1 Hz corresponded to the dominant swell frequency as measured by the Department of Planning and Infrastructure waverider buoy, and the higher frequency peaks just below 0.2 Hz corresponded to the dominant frequency of the wind generated waves. Note that the same filter was used for all beacon-hydrophone combinations but the input noise sequences, and consequently the coloured noise sequences, were independent. The output sequences were scaled to give the required variance.

4. Dropouts were introduced into the simulated ranges for the same times and same beacon-hydrophone combinations as the dropouts in the measured range data.

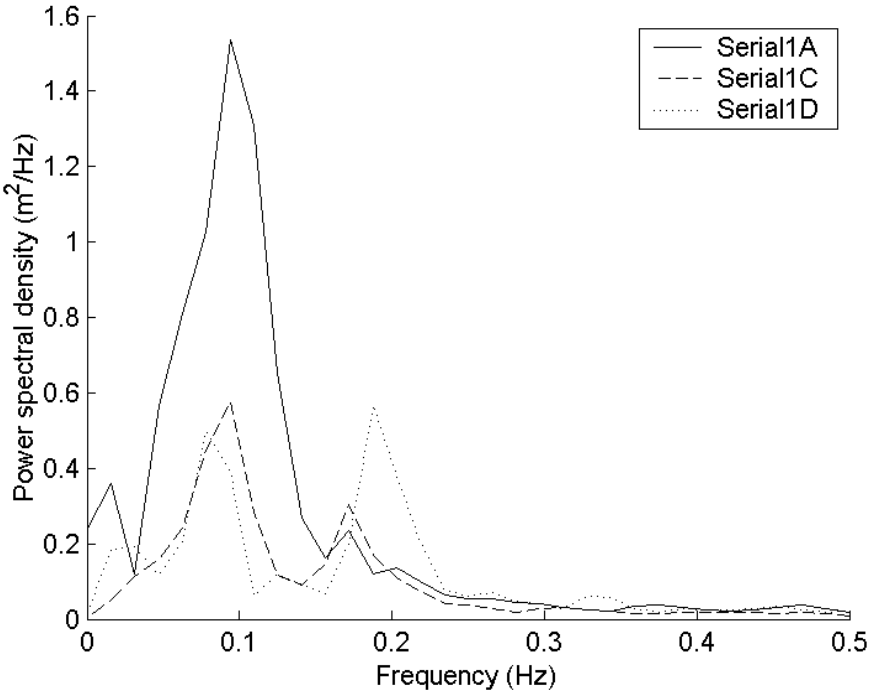

Figure 5.10 Range noise spectra computed from initial straight tow sections of the U-turn manoeuvres.

5.2.4 Results

5.2.4.1 Simulated range data

Figure 5.11 shows the simulated hydrophone positions, in tow-vessel coordinates, for Serial 1D at various times during the manoeuvre. This serial was chosen for verifying the operation of the hydrophone position estimation algorithm because the minimum ranges computed from the simulation of this serial were closer to those obtained from the corresponding measured data than for serials 1A and 1C.

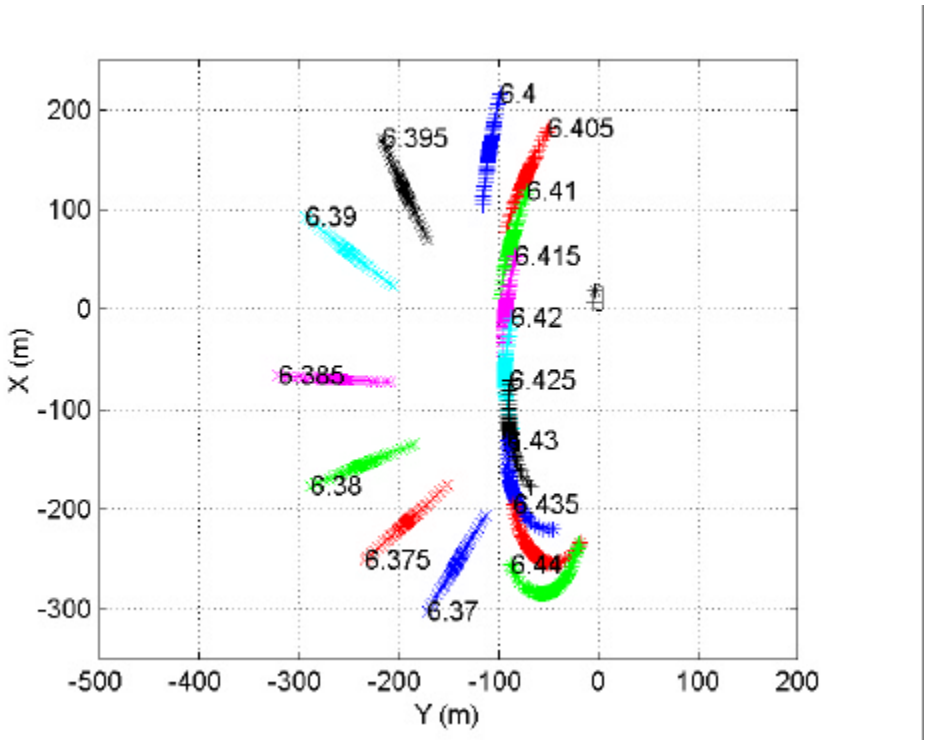

Figure 5.11 Simulated array positions at specified times (decimal hours UTC) for Serial 1D. Vessel outline and port side beacon positions are shown to scale near (0,0).

Figure 5.12 shows the relative innovation (ratio of innovation to its expected standard deviation - see Section 5.2.3.4) and its autocorrelation for ranges from Beacon 1 to Hydrophone 1. This result was for the local (tow-vessel coordinate) dynamic model described in Section 5.2.3.1, and for white range noise. A summary of the innovation statistics for this situation, and for various other combinations of

hydrophone, dynamic model and noise type is given in Table 5.3.

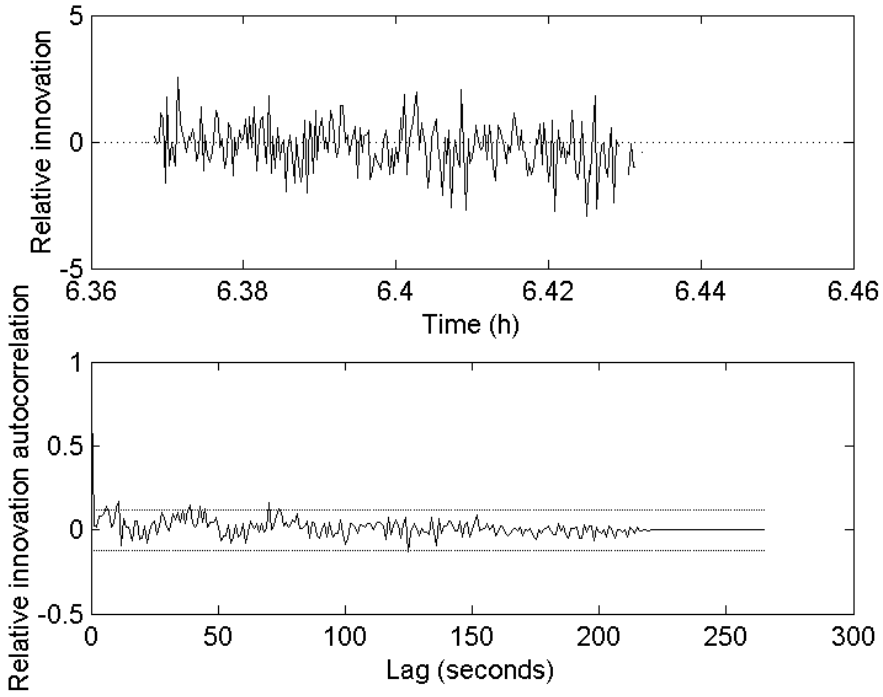

Figure 5.12 Serial 1D, Beacon 1, Hydrophone 1, relative innovation vs. time (top) and whiteness test (bottom) for hydrophone position estimation using simulated range data with white noise and local dynamic model. For a statistically white innovation sequence at least 95% of relative autocorrelation values should be between horizontal dotted lines.

Table 5.3 Innovation statistics for ranges from Beacon 1 to hydrophones 1, 31 and 60. Asterisk in last column denotes coloured innovation sequence.

Hydrophone	Dynamic model type	Noise type	Standard deviation of relative innovation	% of innovation autocorrelation inside limits defined by Equation 5.66
1	Local	White	0.95	97.2
31			0.91	87.6 *
60			1.05	96.2
1	Local	Coloured	1.0	96.2
31			0.93	92.1 *
60			0.93	92.5 *
1	Global	Coloured	0.96	96.6
31			0.86	95.1
60			0.91	95.5

The whiteness test described in Section 5.2.3.4 implied that 95% or more of the autocorrelation values should be inside the limits defined by Equation 5.66. Note, however, that it was necessary to compute the autocorrelation after first removing gross errors and dropouts from the data, and the whiteness test was therefore not definitive.

All the innovation sequences listed in Table 5.3 had relative standard deviations close to the expected value of 1.0, but in several cases the sequences failed the whiteness test. This was not surprising for cases where the observation noise was coloured, which violates one of the assumptions of the Kalman filter, but it was also true for Hydrophone 31 with white range noise. Figure 5.13, which shows the innovation sequence and autocorrelation for Hydrophone 31, reveals that the autocorrelation had a distinct oscillatory component which was due to an oscillatory component in the innovation sequence. Very similar results were obtained using coloured range noise. This oscillation was also apparent in the first half of the data plotted in Figure 5.15, which shows the errors in the Kalman filter estimates of the hydrophone positions. The oscillatory autocorrelation function did not occur when the global dynamic model was used (see Figure 5.14).

Comparing Figure 5.15 with Figure 5.16 shows the effect of applying the Kalman smoother to the estimates computed by the filter. The smoothed tracks had much less high frequency noise and there was also a reduction in the low frequency errors, especially around 6.4 hours where the relative array motion changed from circular to approximately linear.

Figure 5.17 is a vector plot of the errors in the hydrophone positions calculated using the smoother with the local dynamic model. This shows that the position errors were almost exclusively due to errors in the azimuths of the hydrophones relative to the tracking beacon baseline. This was to be expected given the short baseline available (12.3 m). During the section of the manoeuvre when the array was moving approximately linearly past the vessel, and the position fixing geometry was good (6.405 to 6.42 hours), the magnitudes of the position errors were less than 2 m.

A plot of the errors in the hydrophone positions calculated using the global dynamic model is given in Figure 5.18 and Figure 5.19 is the corresponding vector error plot. Note that the magnitudes of the errors in the positions calculated using the global

coordinate dynamic model were very similar to those in the positions calculated using the local coordinate dynamic model. The oscillatory autocorrelation that occurred in the local coordinate case seems to have been due to the position errors having been approximately periodic in the early part of the manoeuvre, rather than being an indicator of larger errors.

The differences between positions calculated using the two different dynamic models are plotted in Figure 5.20, which shows that the results were almost identical in regions where the position fixing geometry was good.

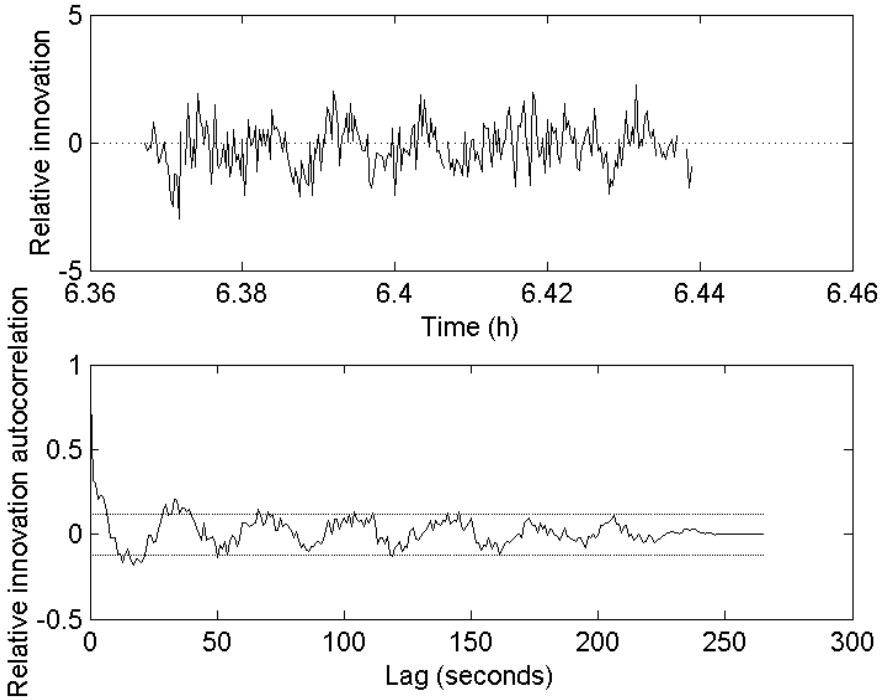

Figure 5.13 As for Figure 5.12, but Hydrophone 31.

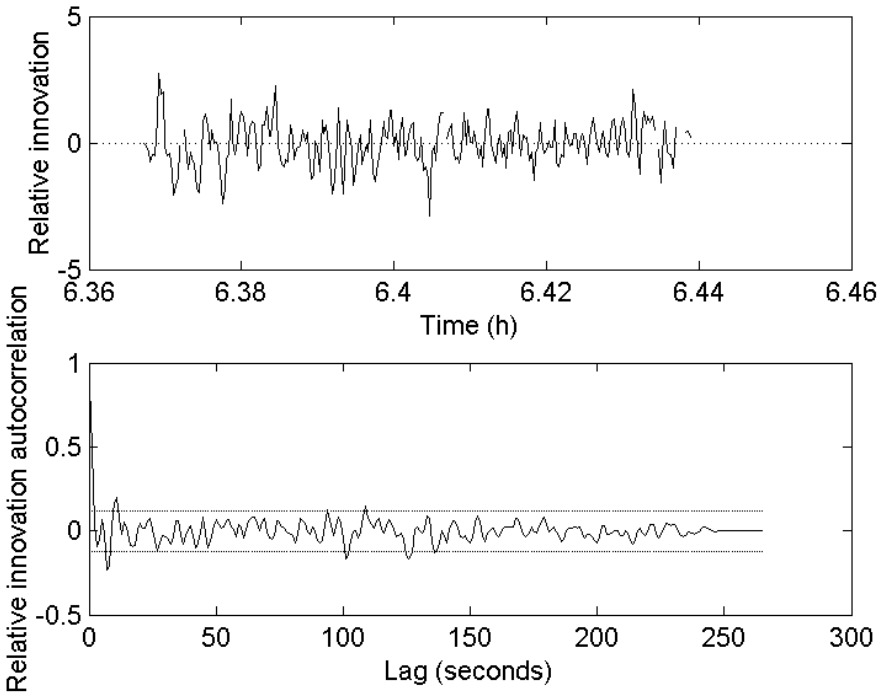

Figure 5.14 As for Figure 5.13, but global dynamic model and coloured range noise.

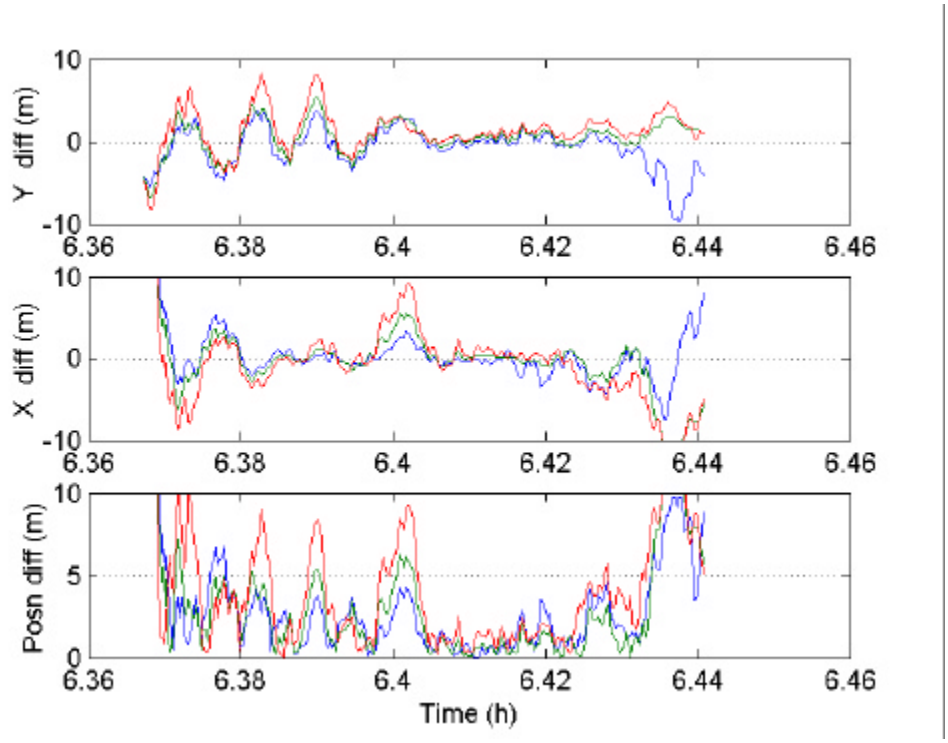

Figure 5.15 Simulated Serial 1D hydrophone position errors for Kalman filter with local dynamic model (coloured range noise). Hydrophones are: blue = 1, green = 31, red = 60.

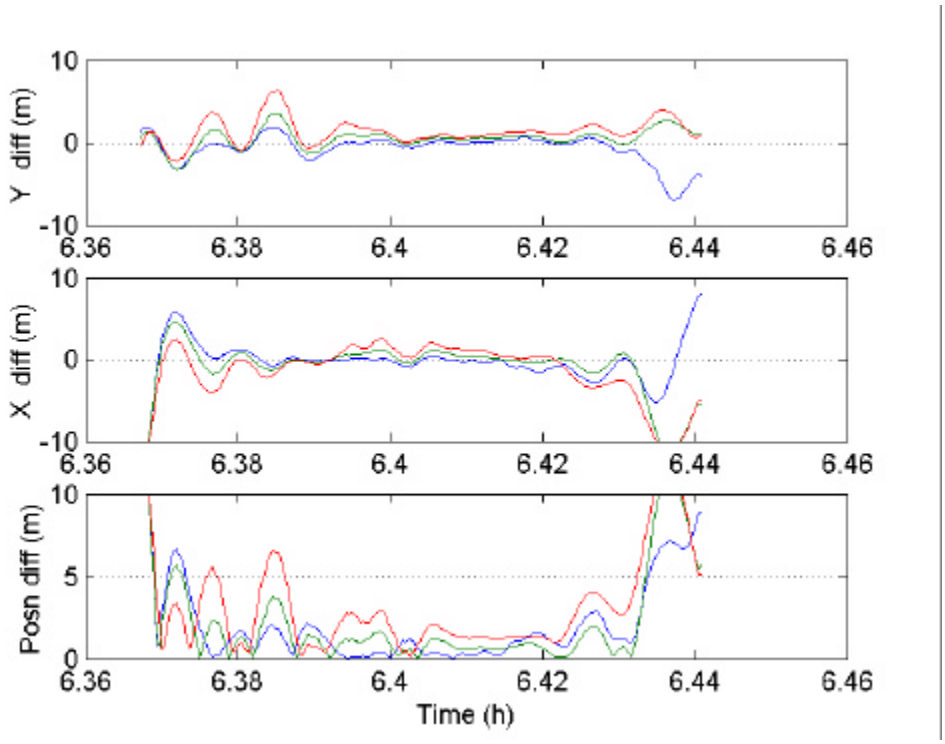

Figure 5.16 Hydrophone position errors for Kalman smoother with local dynamic model. (Coloured range noise.) Hydrophones are: blue = 1, green = 31, red = 60.

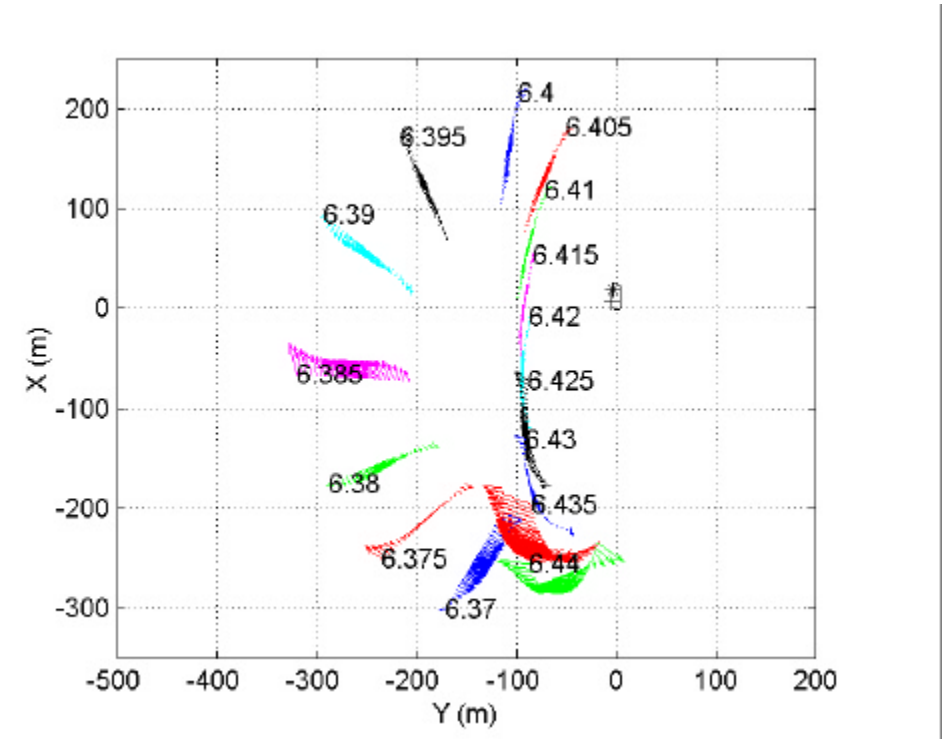

Figure 5.17 Vector plot of hydrophone position errors for Kalman smoother with local dynamic model. (Coloured range noise.) Vectors start at true hydrophone positions and vector lengths are five times position error.

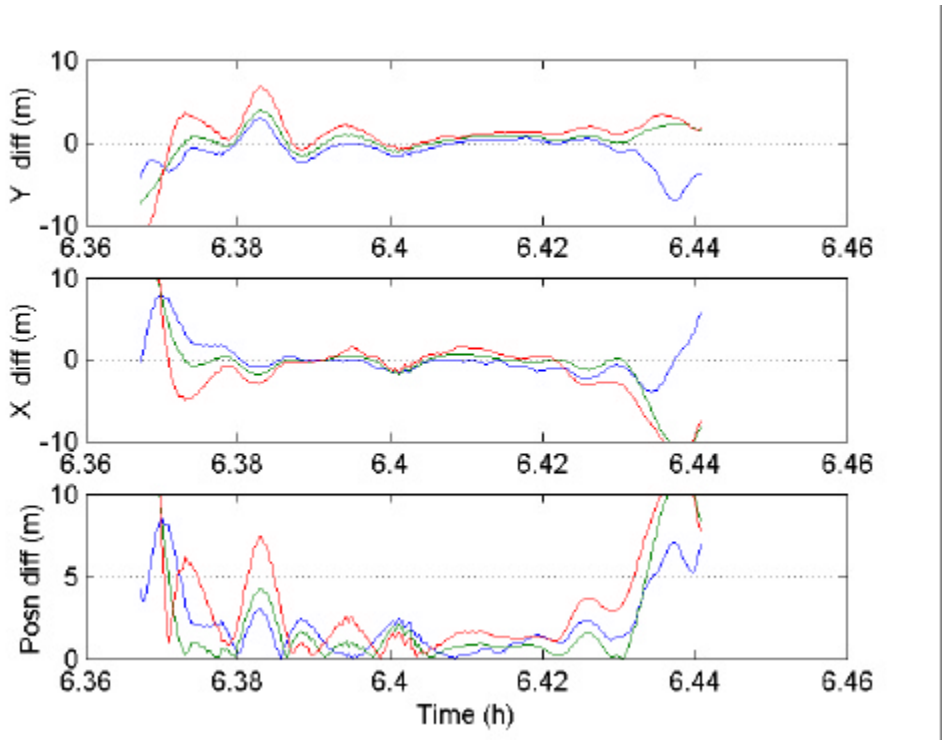

Figure 5.18 Hydrophone position errors for Kalman smoother with global dynamic model. (Coloured range noise.) Hydrophones are: blue = 1, green = 31, red = 60.

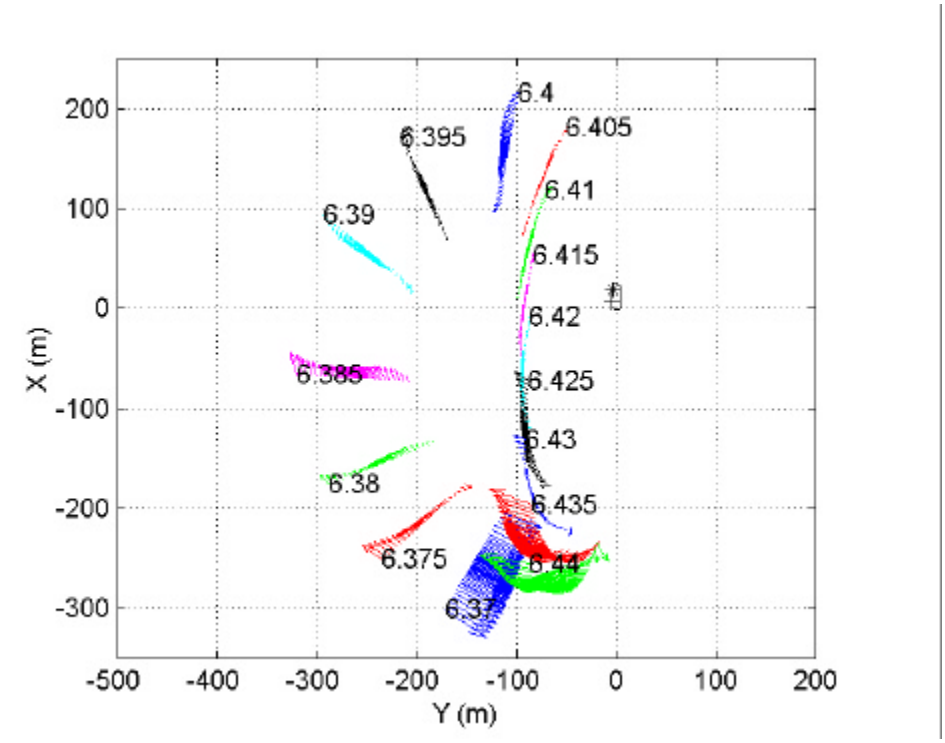

Figure 5.19 Vector plot of hydrophone position errors for Kalman smoother with global dynamic model. (Coloured range noise.) Vectors start at true hydrophone positions and vector lengths are five times position error.

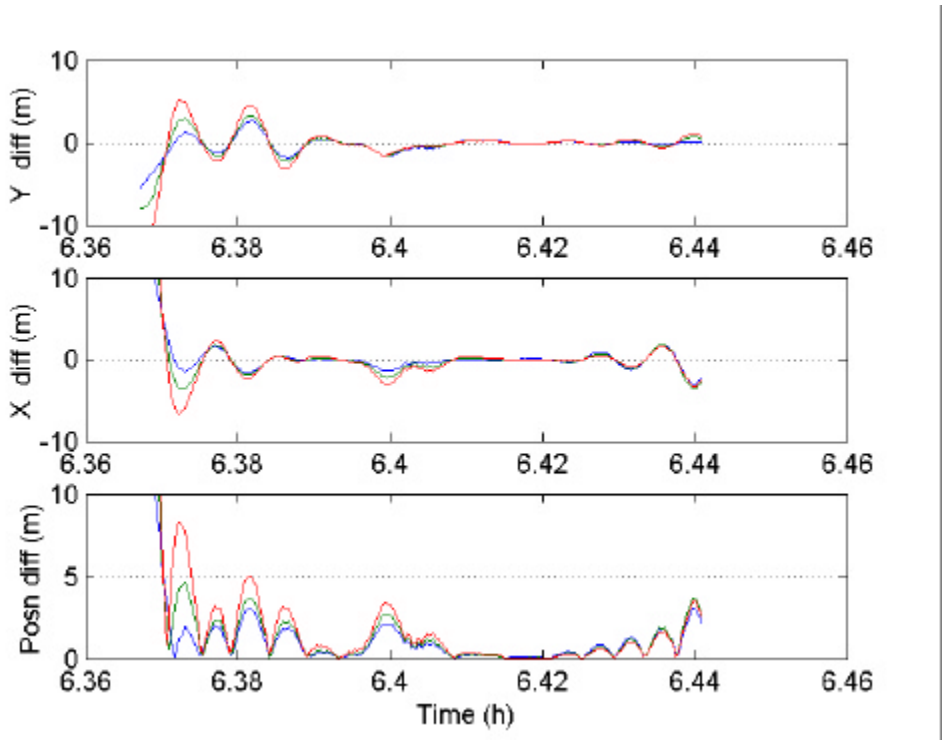

Figure 5.20 Differences between Kalman smoother outputs for global and local dynamic models for hydrophones 1 (blue), 31 (green), and 60 (red).

The Kalman filter and Kalman smoother algorithms provided estimates of the uncertainties in the calculated parameters by way of the parameter covariance matrices $\mathbf{P}_k$ and $\mathbf{P}_{k|K}$ respectively. Figure 5.21 shows a plot of the errors in the coordinates of Hydrophone 31 calculated by the smoother together with the 95.4% ($\pm 2s$) confidence interval derived from the corresponding diagonal elements of $\mathbf{P}_{k|K}$. The standard deviation of the position difference was obtained from the relation:

$$s_{dr}^2 = \frac{1}{dr^2}\left(dx^2 s_{dx}^2 + 2dxdy\, s_{dxdy} + dy^2 s_{dy}^2\right) \qquad \textbf{(5.67)}$$

where dx is the error in the x coordinate, dy is the error in the y coordinate, and $dr = \sqrt{dx^2 + dy^2}$ is the distance of the estimated position from the true position.

Although the errors followed trends in the confidence intervals, there were far fewer points within the intervals than predicted (see Table 5.4). These results are in accordance with a general tendency for Kalman filters and smoothers to produce overoptimistic uncertainty estimates (Uhlmann 1996) that results from the statistical

assumptions inherent in the dynamic model not being justified in practice (see Section 5.2.3.1).

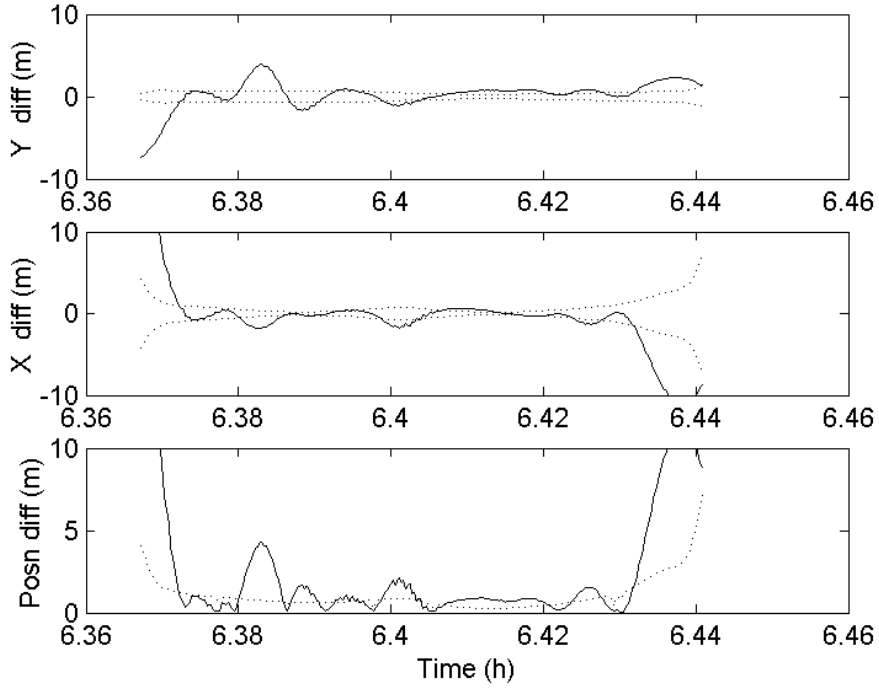

Figure 5.21 Comparison of actual position error (solid line) and $\pm 2s$ Kalman smoother uncertainty estimate (dotted line) for hydrophone 31. Global dynamic model, coloured range noise.

Table 5.4 Percentage of position errors within estimated 95.4% confidence interval

Dynamic model	Hydrophone	Percentage of points within 95.4% confidence interval		
		X Coordinate	Y Coordinate	Position error
Local	1	62	60	42
Local	31	29	35	26
Local	60	23	35	17
Global	1	50	55	30
Global	31	33	45	33
Global	60	20	35	20

5.2.4.2 Measured range data

Figure 5.22 shows the result of applying the hydrophone position estimation algorithm (local dynamic model) to the measured range data recorded during Serial 1D. These results were similar to the simulated hydrophone positions plotted in

Figure 5.11, although there were differences in detail. These differences were to be expected given that the simulation made no allowance for errors in tow-vessel heading estimates or for the effects of currents, and that accurate hydrodynamic coefficients were not available for the array.

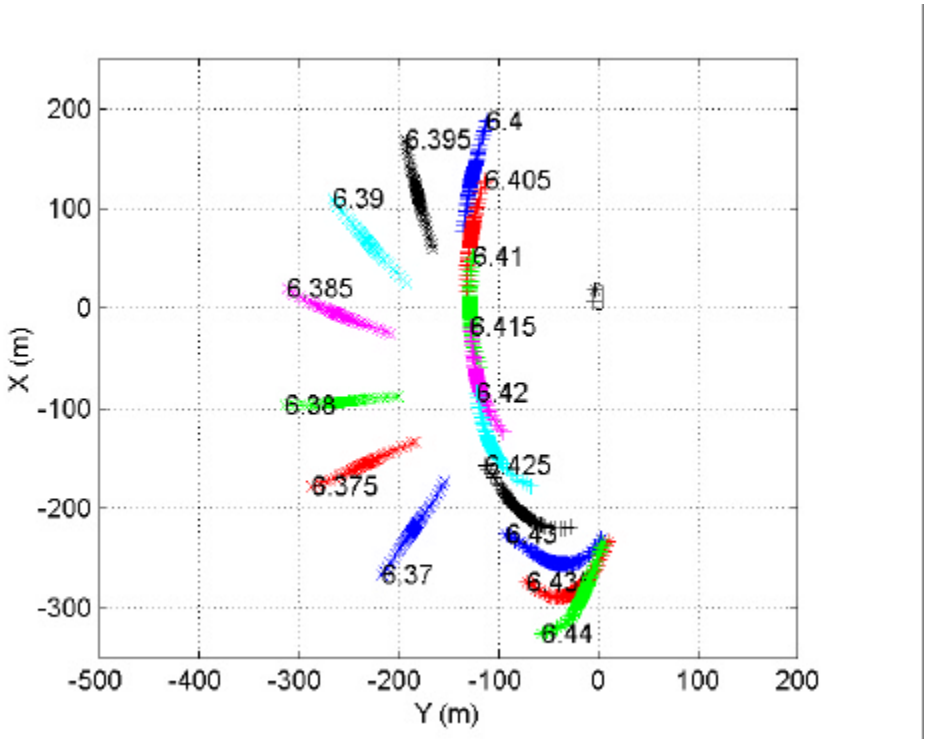

Figure 5.22 Array positions at specified times (decimal hours UTC) for Serial 1D estimated using measured range data and local dynamic model. Vessel outline and port side beacon positions are shown to scale near (0,0).

Relative innovation plots for the ranges from beacon 1 to hydrophones 1 and 31 are given in figures 5.23 and 5.24, and show that the innovations were generally larger and more highly correlated than in the simulated data case. The corresponding statistics for hydrophones 1, 31 and 60 for all three processed serials are summarised in Table 5.5. These results implied that the range data for Serials 1C and 1D were somewhat noisier than for Serial 1A, and that the innovations showed no clear preference between the local and global dynamic models.

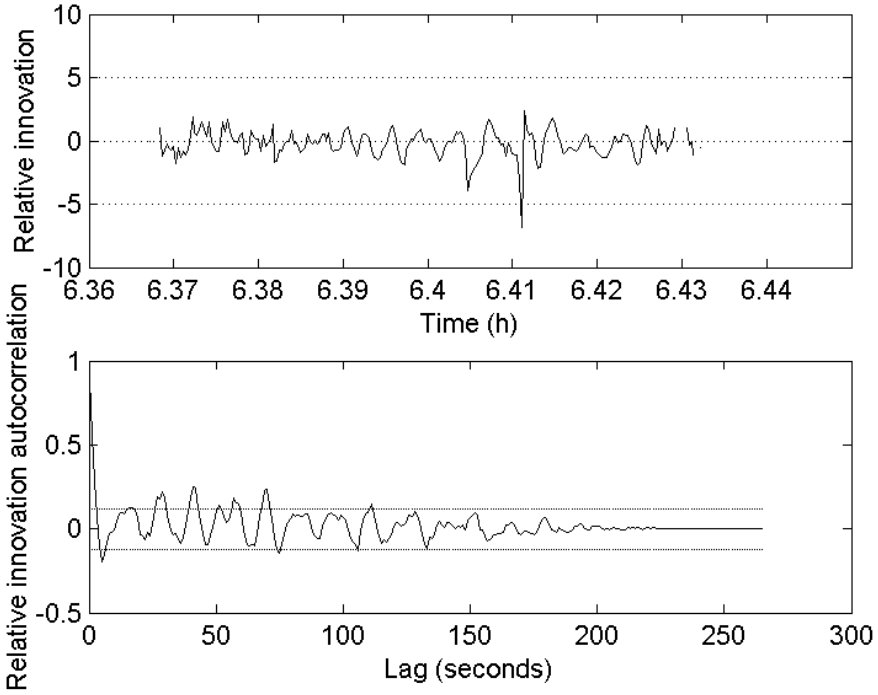

Figure 5.23 Relative innovation vs. time (top) and whiteness test (bottom) for measured beacon 1 to hydrophone 1 range (local dynamic model).

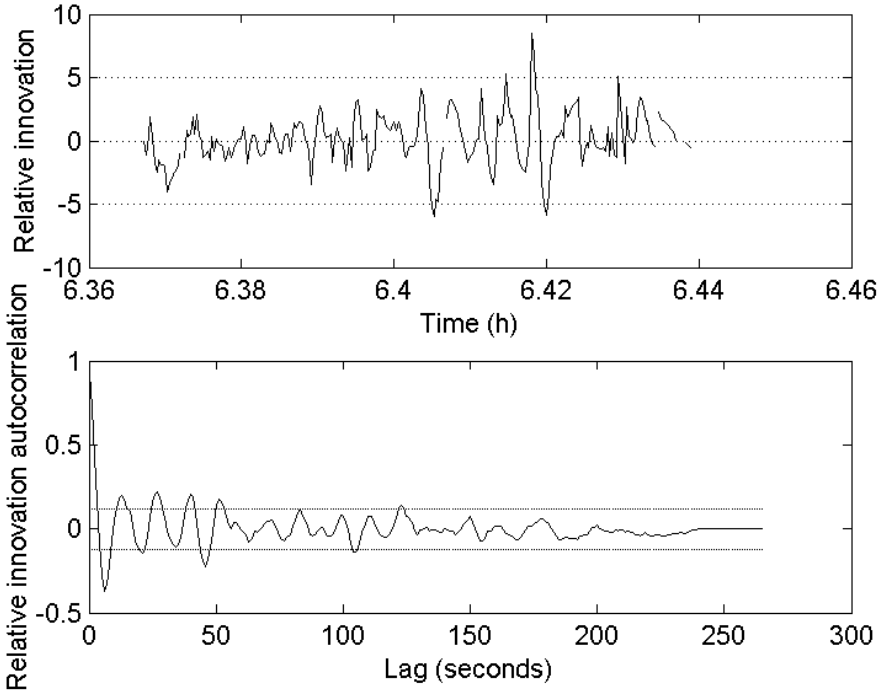

Figure 5.24 Relative innovation vs. time (top) and whiteness test (bottom) for measured beacon 1 to hydrophone 31 range (local dynamic model).

Table 5.5 Measured data innovation statistics for ranges from Beacon 1 to hydrophones 1, 31 and 60. Asterisk in last column denotes coloured innovation sequence.

Serial	Hydrophone	Dynamic model type	Standard deviation of relative innovation	% of innovation autocorrelation inside limits defined by Equation 5.66
1A	1	Local	0.78	72.8 *
		Global	0.78	77.7 *
	31	Local	1.3	86.1 *
		Global	1.22	83.2 *
	60	Local	0.95	65.9 *
		Global	0.94	59.4 *
1C	1	Local	1.3	86.8 *
		Global	1.9	92.7 *
	31	Local	2.4	87.7 *
		Global	2.7	85.9 *
	60	Local	4.9	97.7
		Global	5.0	97.7
1D	1	Local	1.0	90.2 *
		Global	1.1	90.6 *
	31	Local	2.0	86.1 *
		Global	2.0	84.6 *
	60	Local	1.5	95.9
		Global	2.0	97.4

The whiteness test results are given in the same table and showed that virtually all innovation sequences failed the test. Those that passed (e.g. Serial 1C, Hydrophone 60) were actually anomalous because there were a large number of dropouts in the corresponding range data. This was also the reason for the large standard deviation in the relative innovation for this hydrophone.

The primary implication of the correlated innovations was that the estimated uncertainties of the state estimates were likely to be inaccurate. The lack of any

trends or divergence in the innovation sequences implied that the estimated states themselves were consistent with the measured data.

Figure 5.25 is a plot of the differences between the positions of hydrophones 1, 31 and 60 calculated using the local and global dynamic models, and Figure 5.26 is a vector plot of the same information for all hydrophones. From these figures it can be seen that, as was the case with the simulated data, the choice of dynamic model had very little influence on the computed hydrophone positions when the geometry was favourable for position fixing (i.e. the array was abeam of the vessel), but that there were significant differences elsewhere. These differences were primarily differences in azimuth rather than range, which was again consistent with the geometry.

Corresponding sets of results for serials 1A and 1C are plotted in figures 5.27 to 5.31 and showed very similar trends to those for Serial 1D.

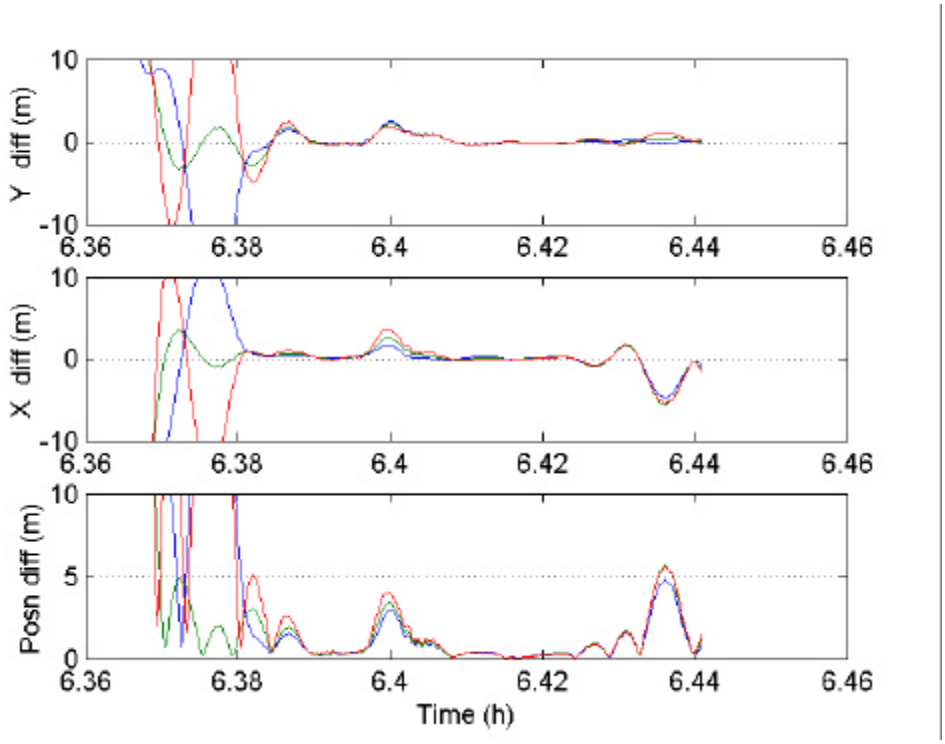

Figure 5.25 Differences between Kalman smoother outputs for global and local dynamic models for Serial 1D measured data, hydrophones 1 (blue), 31 (green), and 60 (red).

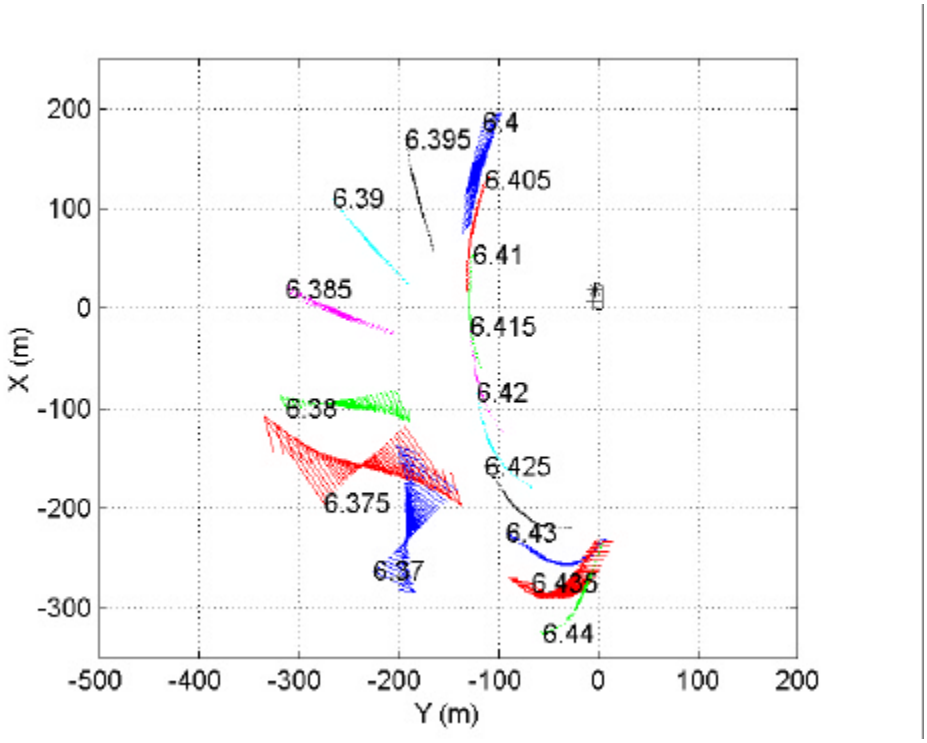

Figure 5.26 Vector plot of differences between Kalman smoother estimates of hydrophone positions obtained from Serial 1D measured ranges using global and local dynamic models. Vectors start at hydrophone positions calculated using global model and vector lengths are five times position differences.

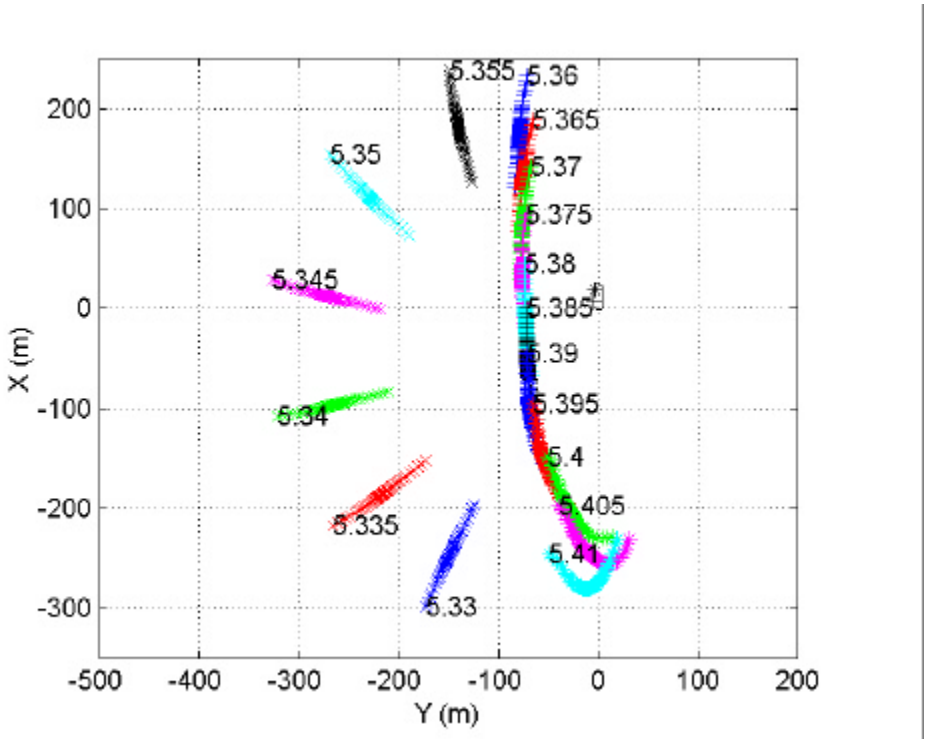

Figure 5.27 Array positions at specified times (decimal hours UTC) for Serial 1A estimated using measured range data and local dynamic model. Vessel outline and port side beacon positions are shown to scale near (0,0).

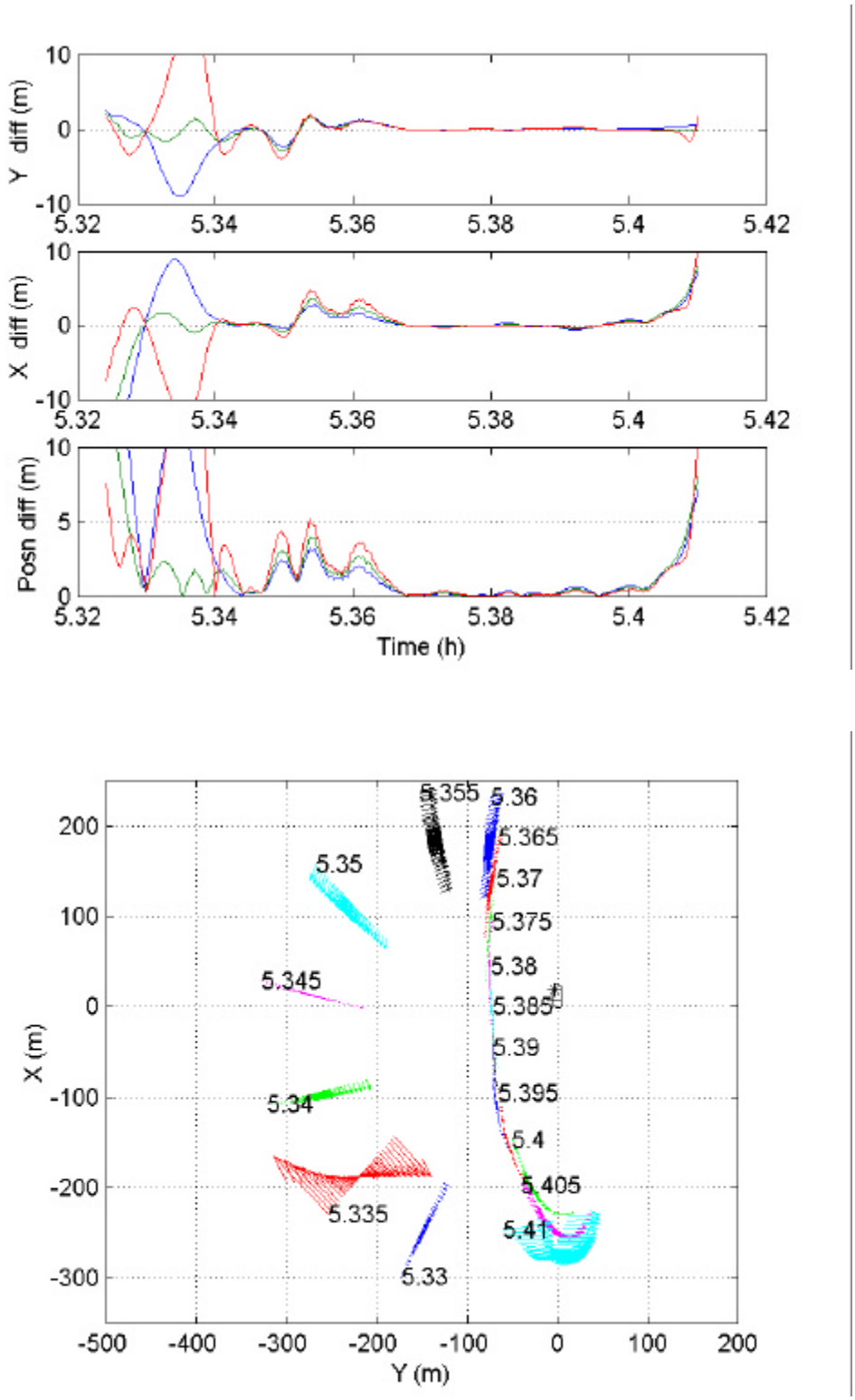

Figure 5.28 Vector plot of differences between Kalman smoother estimates of hydrophone positions obtained from Serial 1A measured ranges using global and local dynamic models. Vectors start at hydrophone positions calculated using global model and vector lengths are five times position differences.

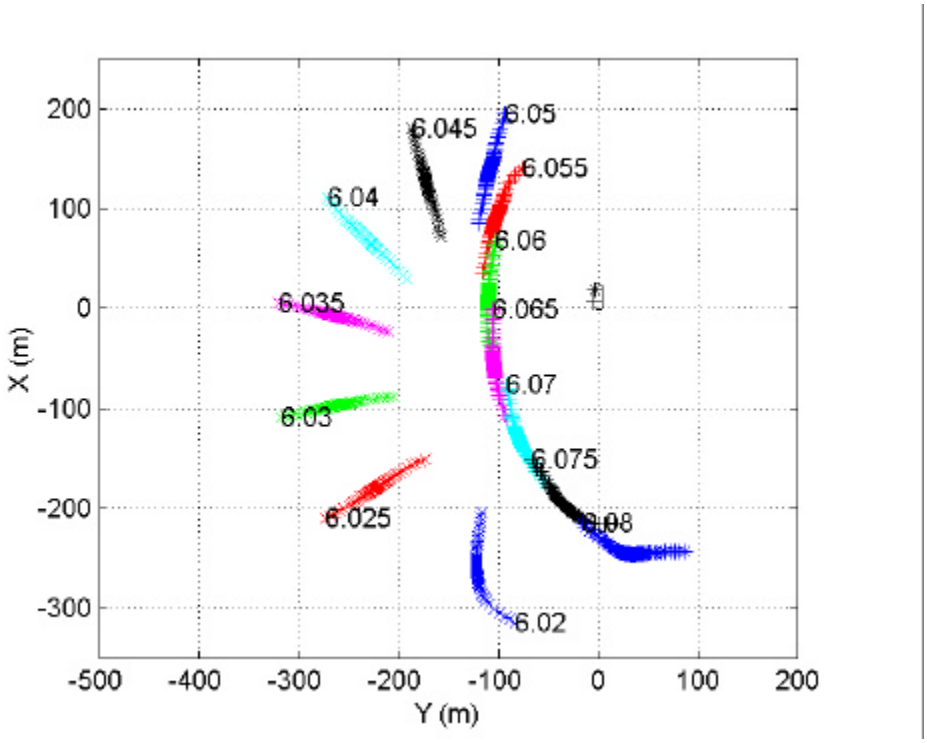

Figure 5.29 Array positions at specified times (decimal hours UTC) for Serial 1C estimated using measured range data and local dynamic model. Vessel outline and port side beacon positions are shown to scale near (0,0).

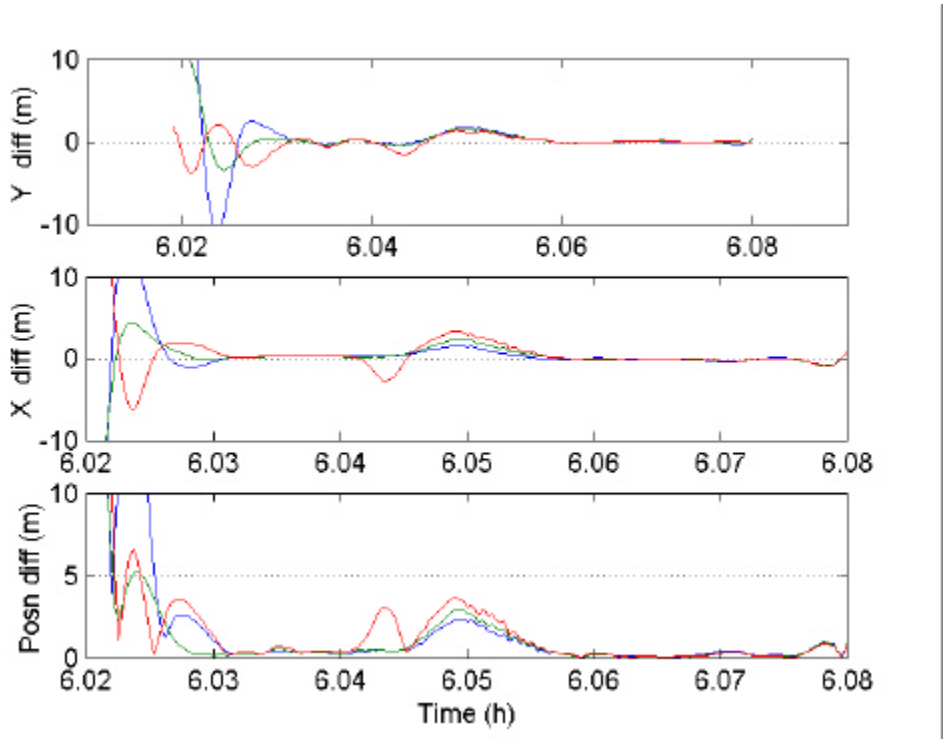

Figure 5.30 Differences between Kalman smoother outputs for global and local dynamic models for Serial 1C measured data, hydrophones 1 (blue), 31 (green), and 60 (red).

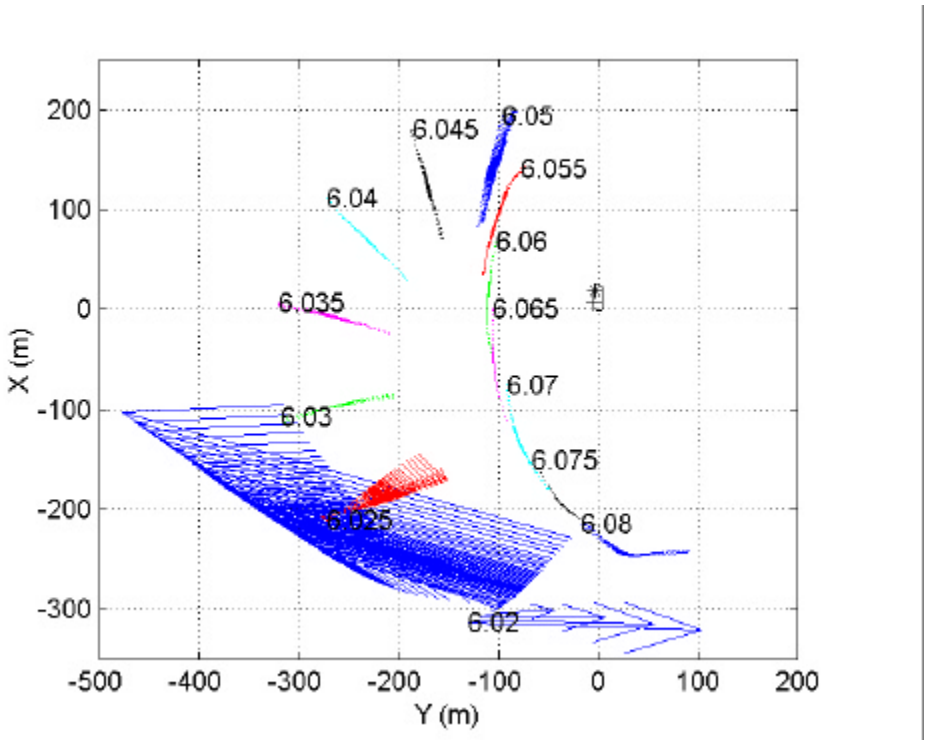

Figure 5.31 Vector plot of differences between Kalman smoother estimates of hydrophone positions obtained from Serial 1C measured ranges using global and local dynamic models. Vectors start at hydrophone positions calculated using global model and vector lengths are five times position differences.

The estimated Serial 1D array positions shown in Figure 5.22 were transformed to global coordinates using the vessel heading and position derived from the GPS data. The results are plotted in Figure 5.32 and show that from 6.4 hours on the array followed the expected path, cutting slightly inside the tow-vessel track, but prior to this it was offset to the west. This position offset was almost certainly due to the vessel heading not corresponding to the vessel's direction of motion while the vessel was turning. The evidence for this is that the offset only occurred during the period when the vessel was turning, and its direction was consistent with the vessel heading being offset towards the centre of the turning circle.

Corresponding plots for Serials 1A and 1C showed exactly the same trends with the tightest turn (Serial 1A) having the largest offset, again consistent with the effect being due to a vessel heading offset during the turn.

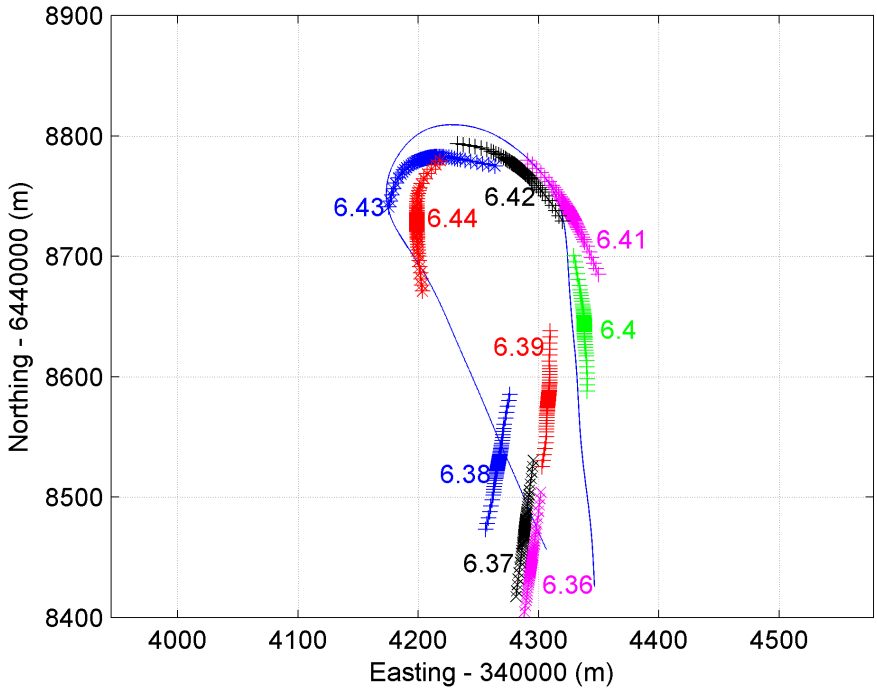

Figure 5.32 Points are Serial 1D estimated array positions transformed to global coordinates. Numbers indicate time in decimal hours UTC. Solid line is vessel track from GPS.

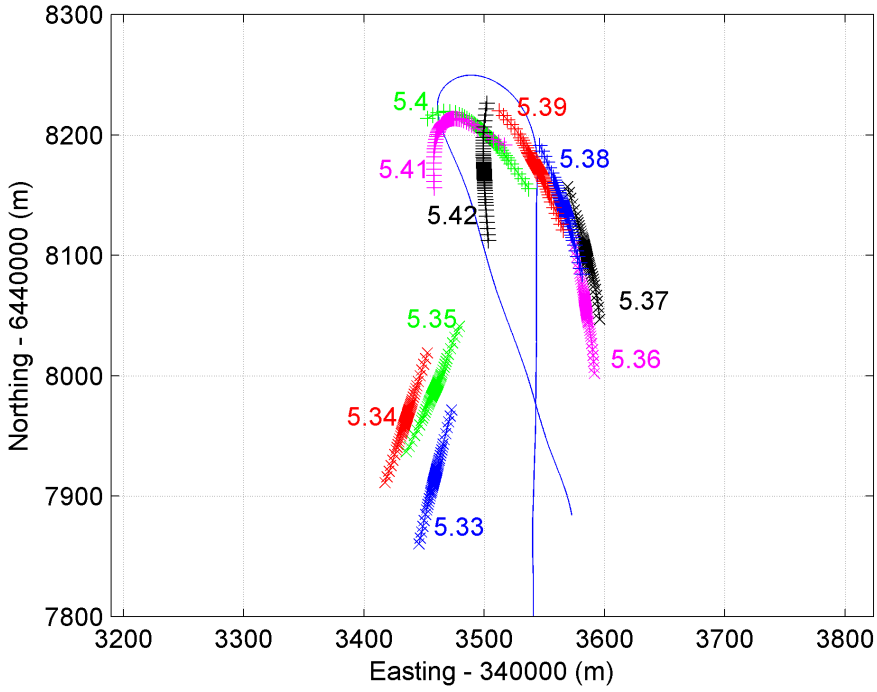

Figure 5.33 Points are Serial 1A estimated array positions transformed to global coordinates. Solid line is vessel track from GPS.

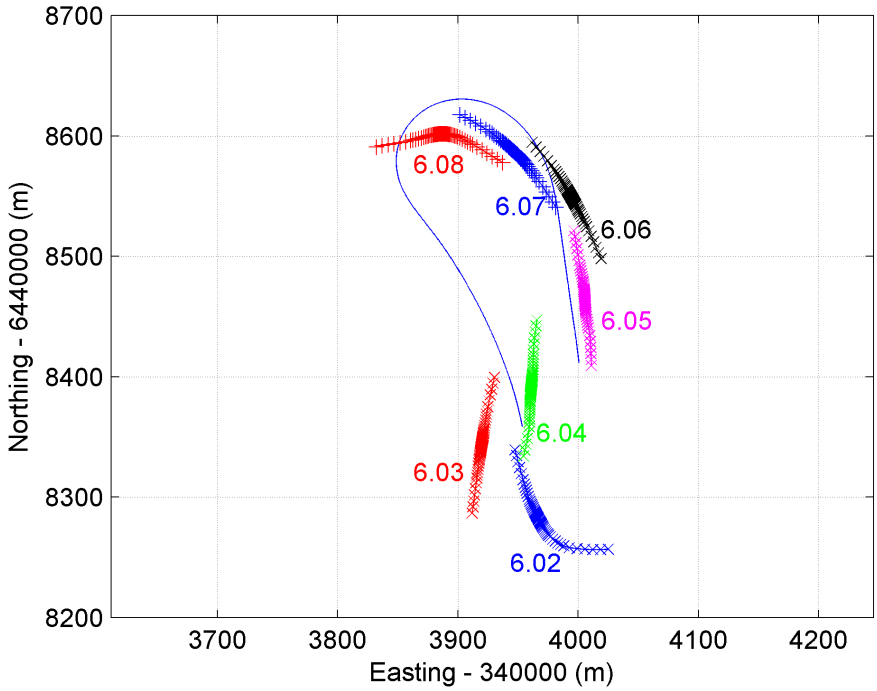

Figure 5.34 Points are Serial 1C estimated array positions transformed to global coordinates. Solid line is vessel track from GPS.

5.3 Comparisons between array shapes derived from acoustic tracking system and transient data

On three occasions transient data from light globe or evacuated sphere implosions were received during periods when the array was also being successfully tracked by the acoustic tracking beacons mounted on the tow-vessel. Figures 5.35 to 5.37 show the array shapes computed by the two different methods. Note that the absolute positions and orientations of the array derived from the transient data had a large uncertainty and so to facilitate comparison the transient array shapes plotted in these figures were translated and rotated to obtain the minimum mean square difference between the hydrophone positions computed by the two different methods. The amount of translation and rotation required for each transient is tabulated in Table 5.6 which also gives the statistics of the differences.

The hydrophone positions for Serial 1A, Shot 7 obtained by the two different methods (Figure 5.35) were in excellent agreement and those for Serial 1A, Shot 9 (Figure 5.36) agreed well except for one section of the array where it was aligned directly towards the transient source, which gave very poor position fixing geometry and ambiguous positions in the transient case. The transient results for Serial 1D, Shot 6 (Figure 5.37) suffered from the same problem, as in this case the entire array was aligned with the source, which resulted in substantial discrepancies.

These results showed, however, that when the transient geometry was good the two position fixing methods gave consistent results.

Table 5.6 Position shifts and rotations applied to transient hydrophone positions and statistics of comparisons between transient and tracking system results

Serial	Shot	Time (h)	Required shift (m)	Required rotation (deg)	RMS hydrophone position difference (m)	Maximum hydrophone position difference (m)
1A	7	5.363	86	1.9	0.7	2.8
1A	9	5.409	82	-8.0	2.1	4.5
1D	6	6.415	48	7.7	2.8	9.5

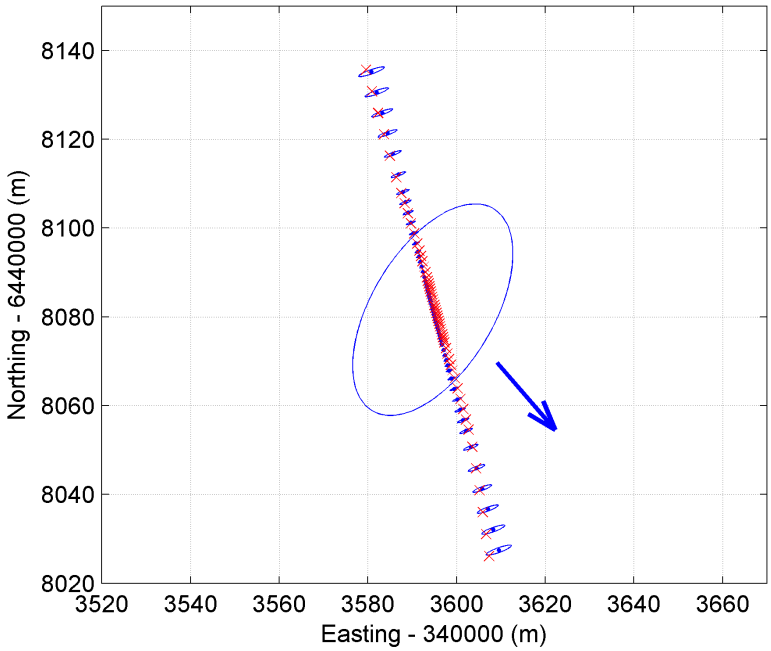

Figure 5.35 Comparison of array shapes derived from transient data (blue dots) and acoustic tracking system data (red crosses) for Serial 1A, Shot 7. Transient array shape has been shifted and rotated to obtain minimum mean square position difference. Large error ellipse is 68.3% confidence region for the central hydrophone absolute position (transient), small ellipses are 68.3% confidence regions for relative hydrophone positions (transient). The Arrow points in the direction of the transient source.

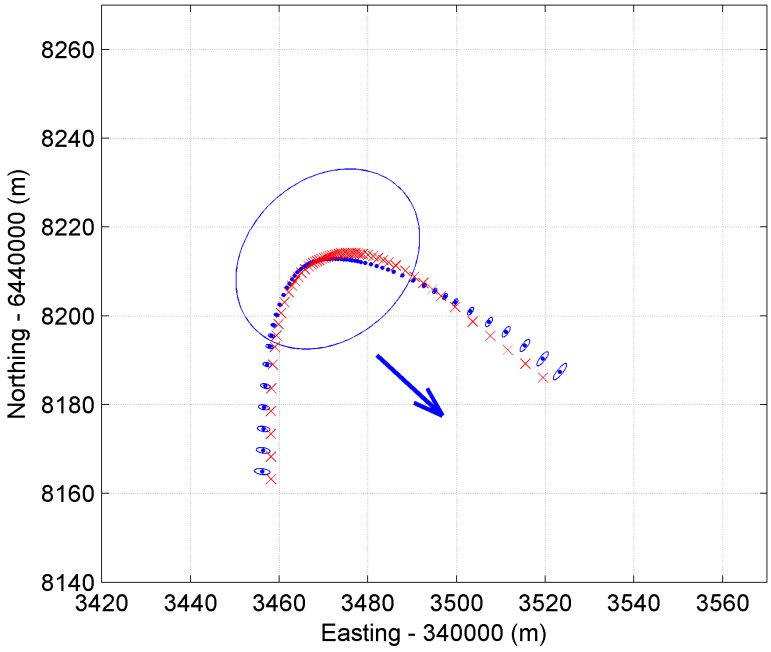

Figure 5.36 As for Figure 5.35, but Serial 1A, Shot 9.

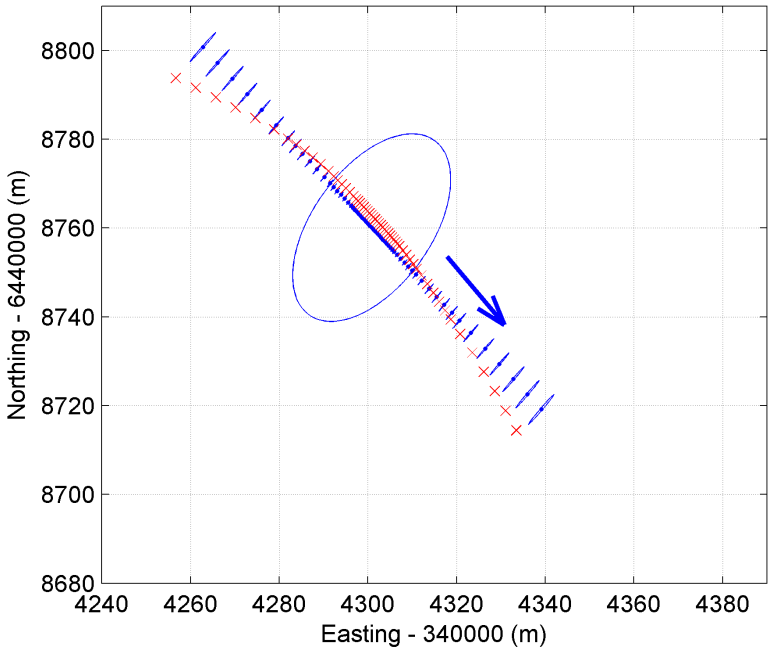

Figure 5.37 As for Figure 5.35, but Serial 1D, Shot 6.

5.4 Summary

Hydrophone positions were calculated using signals received on the towed array hydrophones due to both transient source and tracking beacon signals.

Transient data were processed using a non-linear least squares inversion technique that included constraints on the hydrophone spacings and a penalty on array curvature by way of pseudo observations. In the majority of cases multiple reflections of the transient signals from the seabed and water surface allowed the vertical plane array shape to be determined, and in all cases an estimate of the horizontal plane array shape was obtained, albeit with some ambiguity.

The tracking beacon signals were first pre-processed to remove outliers and then a Kalman smoother was used to compute the horizontal plane hydrophone positions as a function of time. The Kalman smoother algorithm included constraints on the hydrophone spacings and a penalty on array curvature in a similar manner to the non-linear least squares algorithm used to process the transient data. Two different dynamic models were implemented and were found to produce very similar results where the position fixing geometry was good. The performance of this algorithm was studied using both simulated and field data. This included an analysis of the innovation sequences, which failed a statistical whiteness test in some instances, indicating that some of the statistical assumptions inherent in the derivation of the algorithm were not being met. However, the innovation sequences also showed that the smoother was tracking correctly and not diverging.

Horizontal plane positions produced using the transient data and tracking beacon data were consistent in the three instances where a direct comparison was possible.

6 Matched-field inversion for environmental and geometric parameters

A number of parameters important for modelling acoustic propagation were either not measured at all or were measured with limited accuracy during the sea experiment described in Chapter 4. In particular, the lack of functioning pressure sensors on the array meant that the hydrophone depths were only available at the times the implosive source was fired and the occurrence of a number of misfires and the high noise levels from the tow-vessel meant that a number of these implosions could not be processed, resulting in very sparse hydrophone depth data. In addition, the water depth was only known to within a few metres and the acoustic parameters of the seabed were uncertain.

It was therefore decided to investigate whether matched-field inversion techniques could be used to obtain better estimates of these uncertain parameters using the recorded acoustic data itself.

Section 6.1 provides some background to matched-field inversion techniques and includes a survey of some of the more relevant literature. This is a fairly mature area with a large literature and consequently this survey is by no means exhaustive. The development of the particular algorithm used in this work is detailed in Section 6.2, which included the use of simulated data to determine how the problem should be parameterised, and the results of applying this algorithm to field data are presented in Section 6.3. A brief summary of the main results of this chapter is provided in Section 6.4.

6.1 Background

Matched-field inversion is a technique for determining unknown acoustic and geometric parameters of the environment and/or the measurement system using measurements of the acoustic field generated by a known source. Geoacoustic inversion is strictly a subset of matched-field inversion where the unknown parameters are restricted to the geoacoustic parameters of the environment, but the two terms are used almost interchangeably in the literature. The related term matched-field processing (MFP) usually refers to the determination of the location of a source by matching the measured acoustic field at a hydrophone array to the field computed using a known environment, although it is also sometimes used to

encompass all array-processing techniques that make use of information about the environment.

Most applications of matched-field inversion have been to long-range data using sources such as CW projectors, air guns and explosives (e.g. Collins et al. 1992, Chapman & Lindsay 1996, Hermand & Gerstoft 1996, Hermand 1999, Hoffman 2002), but the technique has also been successful in obtaining limited seabed sound-speed information where a horizontal towed array has been used to receive signals from a CW source towed by the same vessel (Caiti et al. 1996), a broadband swept frequency source (Siderius & Nielsen 2002), or tow-vessel machinery noise (Battle et al. 2003). In the latter two cases the inversion also included parameters defining the vertical-plane shape of the array. Successful determinations of hydrophone locations via matched-field inversion, this time for a vertical line array, have also been reported (Hodgkiss et al. 1996).

Matched-field inversion proceeds as follows:

1. An estimate of the parameters of interest is made, usually based on prior knowledge of the geology, bathymetry etc.
2. These parameter values are used in an appropriate propagation model to compute the acoustic field at the measurement locations at one or more frequencies.
3. The computed field is compared to the measured field by means of an appropriate cost function.
4. The parameter values are then varied and the process is repeated until the set of parameters that produces the best match between the measured and computed fields is found.

A number of decisions must be made before this procedure can be carried out:

- What method should be used to model the acoustic propagation? This is usually a straightforward decision based on the relative merits of the different acoustic propagation models available.
- Which frequencies should be used? As a general rule the more measured data that can be included, the better the chance of avoiding a situation where two or more quite different sets of parameter values give computed fields that

match the measured data nearly as well. Unfortunately the acoustic propagation model must be run at each frequency each time the cost function is evaluated, so adding frequencies does slow down the execution of the inversion process.

- Which cost function to use? A number of cost functions are proposed in the literature and can be specified in terms of either the acoustic pressure field or the wavenumber spectrum. Cost functions based on the acoustic pressure field include the normalised cross-correlation between the array output and the modelled field (Collins et al. 1992) and the normalised Bartlett power (Gerstoft 1994), which is proportional to the square of the cross-correlation. Some authors use a likelihood function, which is in turn based on the Bartlett power (e.g. Dosso 2002). Cost functions specified in the wavenumber domain are usually based on a cross-correlation in wavenumber space. Examples may be found in Collins et al. (1992) and Collins & Fishman (1995).

- How should the parameters be varied in order to efficiently search the parameter space? An exhaustive search of the parameter space is usually impractical when there are more than two or three parameters to be determined, so a more efficient algorithm is required. The algorithms that have been used for matched-field inversion include classical downhill optimisation methods (Hodgkiss et al. 1996, Yang & Yates 1996, Hermand 1999) which are relatively fast but have a tendency to become trapped in local minima, and the slower but more robust guided random search methods such as simulated annealing (Collins et al. 1992, Lindsay & Chapman 1993, Collins & Fishman 1995, Chapman & Lindsay 1996) and genetic algorithms (Gerstoft 1994, Hermand & Gerstoft 1996, Caiti et al. 1996, Battle et al. 2003). Various hybrid algorithms that combine classical and stochastic techniques have also been used. For example, an algorithm that combines simulated annealing with a downhill simplex technique is described in Dosso et al. (2001). Bayesian inversion techniques are another alternative and have the advantage that they quantify the uncertainties and ambiguities in the parameter estimates but at the cost of increased computational effort. Particular implementations can be based on genetic algorithms (Gerstoft

1994, Gerstoft & Mecklenbrauker 1998) or on a technique called fast Gibbs sampling which is closely related to simulated annealing (Dosso 2002, Dosso & Nielsen 2002, Dosso & Wilmut 2002b, Dosso & Wilmut 2002a, Gillard et al. 2002).

- How should the problem be parameterised? This is particularly an issue when choosing a seabed model and deciding which parameters to fix and which to vary during the inversion. Parameters that have little effect on the measured data need to be excluded from the inversion whereas the failure to include a parameter that has a significant effect will result in a poor match between the final model and reality.

The particular choices made in order to apply matched-field inversion to the sea experiment data in the present work are described in the next section.

6.2 Matched-field inversion algorithm

6.2.1 Forward propagation model

Due to the short distances between the tow-vessel and the towed array hydrophones involved in this work the water column was considered to be isovelocity and constant depth. As discussed in Section 2.4.2.2, the wavenumber integration method was the method of choice for modelling acoustic propagation in this situation. The fast-field program SCOOTER (Porter 1999) implements this method and was used for the simulation of the received hydrophone signals, however thousands of runs of the forward propagation model were typically required when performing an inversion and it was felt that a more efficient approach was desirable.

The main opportunity for an improvement was to avoid running the full propagation model when only the water depth changed or a larger range of receiver depths was required. To this end another program, BOUNCE (Porter 1999), was used to compute the plane wave reflection coefficient of the seabed as a function of incidence angle, which was then used in Equation 2.39 to compute the wavenumber spectrum. The wavenumber spectrum was then integrated numerically using a simple fast-field integration program written in Matlab that implemented Equation 2.38. This procedure was found to give identical results to SCOOTER when used to compute transmission loss curves in environments with an isovelocity water column.

6.2.2 Choice of frequencies

The criteria used to choose the frequencies to use in the inversion were as follows:

- The frequencies were chosen in the range 50 Hz to 250 Hz. The lower limit was chosen so that the array had useful directionality (it was 4 wavelengths long at 50 Hz), and the upper limit was chosen as the highest frequency at which the effects of sea surface roughness could safely be ignored, and also to avoid the computational load becoming excessive.
- Frequencies were chosen that corresponded to strong spectral lines in the tow-vessel's acoustic noise spectrum in order to maximise the signal to noise ratio.

- A preliminary beamforming step was carried out so that only frequencies corresponding to spatially co-located sources were chosen.

It was found that using four frequencies in the range 50 Hz to 250 Hz was sufficient.

6.2.3 Choice of cost-function

The cost-function used for this work was the frequency averaged, normalised Bartlett power, which was chosen because it had the advantage of being independent of the amplitudes and phases of the source signals. The cost function had to be suitably modified to minimise the effects of the rapid motion of the hydrophones relative to the source, which resulted in:

$$E = 1 - \frac{1}{M}\sum_{j=1}^{M} B_j \qquad \textbf{(6.1)}$$

where M is the number of frequencies, and

$$B_j = \frac{1}{K}\sum_{i=1}^{K} \frac{\mathbf{a}_{i,j}^H \mathbf{x}_{i,j} \mathbf{x}_{i,j}^H \mathbf{a}_{i,j}}{\mathbf{x}_{i,j}^H \mathbf{x}_{i,j} \mathbf{a}_{i,j}^H \mathbf{a}_{i,j}} \qquad \textbf{(6.2)}$$

is the normalised Bartlett power at frequency f_j. Here $\mathbf{x}_{i,j}$ is the N element array output vector for snapshot i and frequency f_j, where N is the number of hydrophones. Each element of $\mathbf{x}_{i,j}$ was calculated by breaking the data from the corresponding hydrophone into K blocks (called snapshots), Fourier transforming snapshot i, and then selecting the result in the frequency bin corresponding to f_j. Note that in the final algorithm each snapshot was Doppler compensated by re-sampling (see Section 7.2.1) before Fourier transforming.

$\mathbf{a}_{i,j}$ is the N element array steering vector corresponding to snapshot i and frequency j. Each element of $\mathbf{a}_{i,j}$ represents the acoustic field at the corresponding hydrophone computed by the propagation model for a source of unit amplitude and zero phase.

The superscript H denotes the Hermitian transpose (complex conjugate of the transpose).

The difference between this expression for the normalised Bartlett power and the conventional expression found in the literature arose because the constantly changing ship-array geometry resulted in a steering vector that was different for each snapshot

and therefore couldn't be brought outside the summation in Equation 6.2, as is usually done.

Note that these definitions resulted in $0 \le E \le 1$ with $E = 0$ corresponding to a perfect match between the modelled and measured signals.

The inversions described in this thesis were carried out using eighteen blocks of data, each one second long.

6.2.4 Optimisation strategy

6.2.4.1 Simulated annealing

Simulated annealing (SA) was chosen as the primary optimisation strategy for this work because of its relative ease of implementation. The final set of parameters produced by the SA algorithm was then refined further by Powell's direction-set method (see Press et al. 1988, chapter 10), a deterministic downhill optimisation method.

A general description of the SA algorithm can also be found in Press et al (1988, chapter 10). As its name implies, the procedure is analogous to the annealing process that occurs when a metal is heated and then slowly cooled and the terminology reflects this. The algorithm is defined in terms of a parameter called the temperature, which is slowly lowered during the procedure. The particular variant of SA used here operated as follows:

1. An initial value for the temperature, T_0, and an initial parameter vector were chosen. $T_0 = 1.44$ was found to give good results.
2. The initial value of the cost function, E_0, (termed the energy in SA parlance) was computed.
3. The iteration count was initialised, $k = 1$.
4. One element of the parameter vector was perturbed and the energy, E_k, computed.
5. If $E_k < E_{k-1}$, the new set of parameters was accepted.

6. If $E_k \geq E_{k-1}$, the new set of parameters was accepted with probability $e^{(E_k - E_{k-1})/T_j}$ where T_j is the current temperature.

7. The iteration count was incremented, $k = k + 1$.

8. This process was repeated from step 4, perturbing each parameter in turn until either the number of accepted perturbations equalled the number of parameters, in which case the algorithm moved on to the next step, or the number of rejections in a row exceeded a stopping criterion (20 rejections), in which case the algorithm entered the quenching phase.

9. A new temperature was computed using $T_{j+1} = bT_j$, where b is a constant between 0 and 1. The inversions described here used $b = 0.98$.

10. If less than a specified number of temperatures (280) had been used, this process was repeated from step 4, otherwise the algorithm entered the quenching phase.

In the quenching phase the temperature was set to zero and only perturbations that lowered the energy were accepted until a specified number of rejections occurred in a row (5 in this case), at which point the procedure terminated.

The method chosen to perturb the parameters was important in terms of optimising the algorithm to ensure that a lot of effort wasn't wasted evaluating cost functions for parameter sets that were ultimately rejected. This was achieved by using a technique similar to that used in the so-called fast simulated annealing algorithm (Szu & Hartley 1987). Parameter perturbations were drawn from a random variable, x, with a Cauchy probability distribution:

$$p(x) = \frac{c}{p\left(x^2 + c^2\right)} \qquad \textbf{(6.3)}$$

where c, which is a parameter which defines the width of the distribution, is taken as being proportional to the temperature. The value of c corresponding to the starting temperature was taken as being equal to five times the range of the parameter, resulting in a very broad initial distribution.

A random variable with this distribution was conveniently generated from a variable, g, with a uniform distribution in the range $-1 < g < 1$ using the formula:

$$x = c\tan\left(\frac{pg}{2}\right) \qquad \textbf{(6.4)}$$

The Cauchy distribution had the desirable property of being strongly peaked around $x = 0$, but extending to infinity in both directions. When used for parameter perturbation this resulted in sampling being concentrated in the vicinity of the current best solution, but with some sampling still occurring over the entire parameter space. As the temperature decreased the sampling became more and more concentrated, but there was always the chance of a large jump to escape from a local minimum.

Perturbations that took the parameter values outside their limits were dealt with by reflection in the parameter boundaries using the formulae given by Collins et al. (1992). This was done to avoid over-sampling the boundaries relative to the remainder of the parameter space, which would have happened if the parameters had simply been set to their limiting values.

6.2.4.2 Gibbs sampling

The SA algorithm provided an efficient means of finding the global minimum of the cost function but gave only a qualitative picture of the uncertainties and ambiguities in the inverted parameters.

A more rigorous approach to dealing with this problem was provided by Bayesian inversion, which sets up the problem in terms of the likelihood function, $\mathrm{L}(\mathbf{x}\,|\,\mathbf{p})$, which is the probability of the measured array output, $\mathbf{x}$, given the parameter vector, $\mathbf{p}$. Bayes rule (Walpole & Myers 1985) is then used to convert this to the *a posteriori* probability of the parameters given the observations, which can be shown to be (Dosso 2002): $\Pr(\mathbf{p}\,|\,\mathbf{x}) \propto \mathrm{L}(\mathbf{x}\,|\,\mathbf{p})\Pr(\mathbf{p})$. Here $\Pr(\mathbf{p})$ is the *a priori* probability distribution of the parameters, which represents the previously known information about them.

$\Pr(\mathbf{p}\,|\,\mathbf{x})$ is a multidimensional probability density function which must be integrated numerically in order to compute quantities that can be readily interpreted, such as the mean parameter values:

$$\mathrm{E}\{\mathbf{p}\} = \int \mathbf{p}' \Pr(\mathbf{p}'|\,\mathbf{x})\,d\mathbf{p}', \qquad \textbf{(6.5)}$$

(here $\mathrm{E}\{\ \}$ represents expectation), the parameter covariance matrix:

$$\mathrm{E}\left\{(\mathbf{p}'-\mathrm{E}\{\mathbf{p}\})(\mathbf{p}'-\mathrm{E}\{\mathbf{p}\})^T\right\}=\int(\mathbf{p}'-\mathrm{E}\{\mathbf{p}\})(\mathbf{p}'-\mathrm{E}\{\mathbf{p}\})^T\,\Pr(\mathbf{p}'|\,\mathbf{x})d\mathbf{p}' \qquad \textbf{(6.6)}$$

and the marginal probability distribution for parameter p_i:

$$\Pr(p_i\,|\,\mathbf{x})=\int d\,(m_i'-m_i)\Pr(\mathbf{p}'|\,\mathbf{x})d\mathbf{p}' \qquad \textbf{(6.7)}$$

It is usually assumed that $\Pr(\mathbf{p})$ is uniformly distributed within specified parameter limits and zero elsewhere, in which case $\Pr(\mathbf{p}'|\,\mathbf{x})$ can be replaced by $\mathrm{L}(\mathbf{x}\,|\,\mathbf{p}')$ in the above integrals, which are then evaluated over the region defined by the specified parameter limits. The main computational workload is in adequately sampling the likelihood function so that the integrals can be evaluated with sufficient accuracy.

The algorithm used in this project to quantify the parameter uncertainties was based on Dosso's fast Gibbs sampling (FGS) algorithm but incorporated some modifications. A detailed justification for the FGS algorithm is given in Dosso (2002) and only a brief outline is presented here.

The basis for the procedure is to sample a likelihood function of the form $\mathrm{L}(\mathbf{x}\,|\,\mathbf{p})=Ae^{-E(\mathbf{x}|\mathbf{p})}$ according to the Metropolis criterion with unit temperature, i.e.:

If $E_k<E_{k-1}$, accept the new set of parameters.

If $E_k\geq E_{k-1}$, accept the new set of parameters with probability $e^{(E_k-E_{k-1})}$.

(This is almost the same acceptance criterion used in the SA algorithm, the only difference being that in SA the energy difference is scaled inversely with temperature.) It can be shown (Dosso 2002) that the accepted samples are distributed according to $\mathrm{L}(\mathbf{x}\,|\,\mathbf{p})$, and the above integrals can therefore be approximated by summations over the R accepted samples:

$$\int f(\mathbf{p}')\Pr(\mathbf{p}'|\,\mathbf{x})d\mathbf{p}'\approx\frac{1}{R}\sum_{i=1}^{R}f(\mathbf{p}_i) \qquad \textbf{(6.8)}$$

with the function $f(\mathbf{p}')$ chosen appropriately for the desired integral.

$E(\mathbf{x}\,|\,\mathbf{p})$ is given by:

$$E(\mathbf{x}\,|\,\mathbf{p})=\sum_{j=1}^{M}\frac{1-B_j(\mathbf{x}\,|\,\mathbf{p})}{1-B_j(\mathbf{x}\,|\,\hat{\mathbf{p}})}N_{e,j} \qquad \textbf{(6.9)}$$

where $B_j(\mathbf{x}\,|\,\mathbf{p})$ is the normalised Bartlett power at frequency bin j defined in Equation 6.2, $N_{e,j}$ is the equivalent number of independent hydrophones at

frequency bin j (see below), and $\hat{\mathbf{p}}$ is the optimum parameter vector calculated using the SA algorithm. The parameter vector, $\mathbf{p}$, does not appear explicitly in Equation 6.2 but is used implicitly in the calculation of the steering vectors, $\mathbf{a}_{i,j}$. In practice modelling errors tend to be correlated between hydrophones and $N_{e,j}$ is therefore significantly less than the number of physical hydrophones. Dosso & Nielsen (2002) used principal component analysis of the array covariance matrix, $\hat{\mathbf{R}} = \frac{1}{K}\sum_{t=1}^{K}\mathbf{x}(t)\mathbf{x}^H(t)$, to estimate $N_{e,j}$, but again this approach had to be modified because of the rapid motion of the tow-vessel relative to the array. The approach taken here was to carry out principal component analysis of the error covariance matrix, rather than the array covariance matrix. To do this the received signal vector at snapshot i and frequency j was modelled according to:

$$\mathbf{x}_{i,j} = \hat{\mathbf{a}}_{i,j} s_{i,j} + \mathbf{e}_{i,j}, \qquad \textbf{(6.10)}$$

where $s_{i,j}$ is the source signal and $\mathbf{e}_{i,j}$ is an error vector which includes both modelling errors and noise. The estimated array steering vector, $\hat{\mathbf{a}}_{i,j}$, was calculated from the inverted parameters obtained using the preliminary SA inversion run.

The least squares estimate of the source signal was then given by:

$$\hat{s}_{i,j} = \frac{\hat{\mathbf{a}}_{i,j}^H \mathbf{x}_{i,j}}{\hat{\mathbf{a}}_{i,j}^H \hat{\mathbf{a}}_{i,j}}, \qquad \textbf{(6.11)}$$

which could then be substituted for $s_{i,j}$ in Equation 6.10 and rearranged to give:

$$\mathbf{e}_{i,j} = \mathbf{x}_{i,j} - \frac{\hat{\mathbf{a}}_{i,j}\hat{\mathbf{a}}_{i,j}^H \mathbf{x}_{i,j}}{\hat{\mathbf{a}}_{i,j}^H \hat{\mathbf{a}}_{i,j}}. \qquad \textbf{(6.12)}$$

The covariance matrix of the error vector was then estimated using:

$$\hat{\mathbf{C}}_{e,j} = \frac{1}{K}\sum_{i=1}^{K}\mathbf{e}_{i,j}\mathbf{e}_{i,j}^H. \qquad \textbf{(6.13)}$$

The effective number of hydrophones was then calculated as in Dosso & Nielsen (2002) by computing the eigenvalues, l_k, of $\hat{\mathbf{C}}_{e,j}$, arranging them in order of decreasing magnitude, and computing their normalised cumulative sum:

$$h_n = \frac{\sum_{k=1}^{n} l_k}{\sum_{k=1}^{N_{pc}} l_k} \qquad \textbf{(6.14)}$$

where N_{pc} is the number of non-zero eigenvalues. N_e was then taken as the smallest value of n for which $h_n > 0.9$, in other words the smallest number of principal components that together accounted for 90% of the energy.

The differences between Dosso's algorithm and the algorithm developed for this work are as follows:

- In order to ensure that sampling commences in a region of relatively high probability, Dosso's algorithm started with a cooling phase, identical to simulated annealing. This phase was not necessary in this work because an estimate of the optimum parameter vector was already available from the SA inversion and the algorithm could be started from there.
- Dosso's algorithm also obtained estimates of appropriate parameter perturbation magnitudes during the cooling phase whereas in this work the parameters were randomly perturbed over their allowed range.
- Dosso's algorithm incorporated a rotation of the parameter space in order to obtain more efficient sampling in cases where parameters were strongly correlated. This was tried but it was found that including a parameter space rotation had little effect on the time taken to accumulate the samples.

6.2.5 Parameterisation

The problem was set up in terms of a set of geometric parameters defining the water depth, array shape and source location, and the geoacoustic parameters of the seabed (see Table 6.1).

Following Battle et al. (2003), the vertical-plane array shape was approximated by a quadratic function of the horizontal distance along the array and was described by three parameters depth, z_a; bow, b; and slope, $s = \tan q$ (see Figure 6.1).

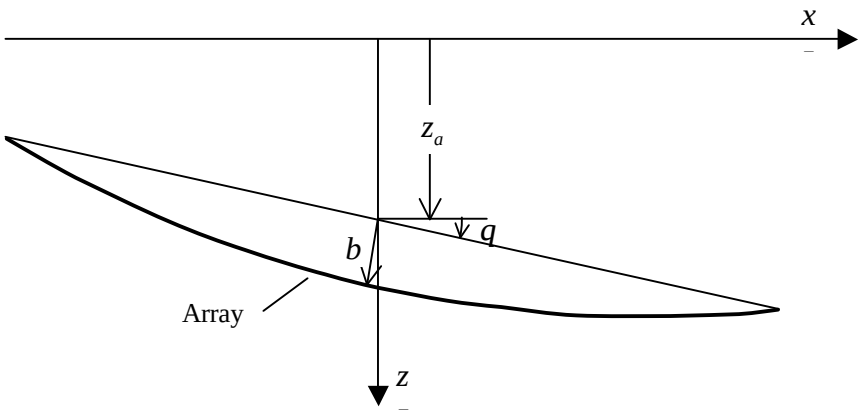

Figure 6.1 Definitions of array shape parameters

Providing the slope of the array is sufficiently small, the depth of a point on the array a horizontal distance x from its centre is given by:

$$\begin{aligned} z(x) &= z_a + x\tan q + d(x)\cos q \\ &= z_a + \left(sx + \frac{d(x)}{\sqrt{1+s^2}} \right) \end{aligned} \qquad \textbf{(6.15)}$$

where $d(x) = b\left(1 - 4\frac{x^2}{L^2}\right)$ is the perpendicular offset of a point on the array from the straight line through the array's end-points and L is the length of the array.

Preliminary propagation model runs indicated that the seabed layer densities had very little effect on the acoustic field and consequently the densities were computed from the compressional wave sound speeds according to an algorithm provided in Hall (2002), which is based on the work of Hamilton (1978) and Richardson & Briggs (1993).

For sound speeds less than 6100 ms^{-1} the algorithm made two estimates of the density, the first obtained using a regression fit to Hamilton's data:

$$r_1 = 1734 + 0.224c_p - 1.18\times10^{-5}c_p^2, \qquad \textbf{(6.16)}$$

and the second obtained by solving the following quadratic equation due to Richardson and Briggs:

$$\frac{c_p}{c_0} = 1.623 - 0.936\frac{r_2}{1000} + 0.3417\left(\frac{r_2}{1000}\right)^2. \qquad \textbf{(6.17)}$$

The smaller of these two densities was then used. In these equations c_p is the sound speed in the sediment (ms^{-1}), c_0 is the sound speed in the water column immediately above the bottom (ms^{-1}), and r_1 and r_2 represent the density of the sediment in $kg.m^{-3}$.

Simulated hydrophone signals were generated using the acoustic simulation described in Chapter 3 and the parameters shown in Table 6.2, and included two sources, one intended to simulate the UW30 sound source used in the experiment, and the other intended to simulate engine/ gear noise. Simulations were run using two acoustic environments, the half-space seabed shown in Figure 6.2, and the layered seabed shown in Figure 6.3, which is a geoacoustic model for the location of the experiment derived in a previous study by inversion of transmission loss versus range data (Hoffman 2002). The simulated acoustic signals did not include any noise.

Two sets of data were generated for each environment, one with the vessel in the endfire of the array (5.342 h to 5.347 h) and one with the vessel near array broadside (5.378 h to 5.383 h). These data sets were then used to generate parameter sensitivity plots: plots of the cost function as one parameter is varied, with all other parameters being fixed at their true values. These plots served as a guide to the parameters that were to be allowed to vary during the inversion process. The cost was calculated at frequencies corresponding to four of the harmonics of the simulated engine noise source: 96, 106, 117, and 213 Hz.

Table 6.1 Matched-field inversion parameter descriptions

Symbol	**Description**
z_w	Water depth (m)
z_a	Array depth (m)
s	Array slope
b	Array bow (m)
x_s, y_s, z_s	Source position on vessel relative to sea surface directly under tow-point (x +ve forward, y +ve to starboard, z +ve down).
c_{p1}	Layer 1 compressional wave speed in seabed (ms^{-1})
c_{s1}	Layer 1 shear wave speed in seabed (ms^{-1})
a_{p1}	Layer 1 compressional wave attenuation in seabed (dB/λ)
a_{s1}	Layer 1 shear wave attenuation in seabed (dB/λ)
h_1	Layer 1 thickness (m)
c_{p2}	Layer 2 compressional wave speed in seabed (ms^{-1})
c_{s2}	Layer 2 shear wave speed in seabed (ms^{-1})
a_{p2}	Layer 2 compressional wave attenuation in seabed (dB/λ)
a_{s2}	Layer 2 shear wave attenuation in seabed (dB/λ)

Table 6.2 Parameters used when generating simulated acoustic data for testing inversion and beamforming algorithms

Parameter	**Value and/or how determined**
Hydrophone horizontal plane positions	Computed from Serial 1A field data using the dynamic tracking algorithm described in Section 5.2.
Hydrophone depths	All 8 m
Hydrophone noise	None
Source 1 type	Mechanical noise source (simulates UW30 sound source)
Source 1 position (m)	x_s = 18.5, y_s = -3.6, z_s = 1.5
Source 1 frequencies (Hz)	112, 336, 560, 784
Source 1 source levels (dB re 1 μPa RMS @ 1 m)	219.2, 209.6, 205.3, 202.3
Source 1 beam pattern	Omni-directional
Source 2 type	Mechanical noise source (simulates engine and gear noise)
Source 2 position (m)	x = 12.4, y = -3.0, z = 2.0
Source 2 fundamental frequency (Hz)	10.636
Source 2 number of harmonics	20
Source 2 source levels (dB re 1 μPa RMS @ 1 m)	206.9 (each harmonic)
Source 2 beam pattern	Omni-directional
Propagation simulation	Wavenumber integration using the environments shown in Figure 6.2 and Figure 6.3

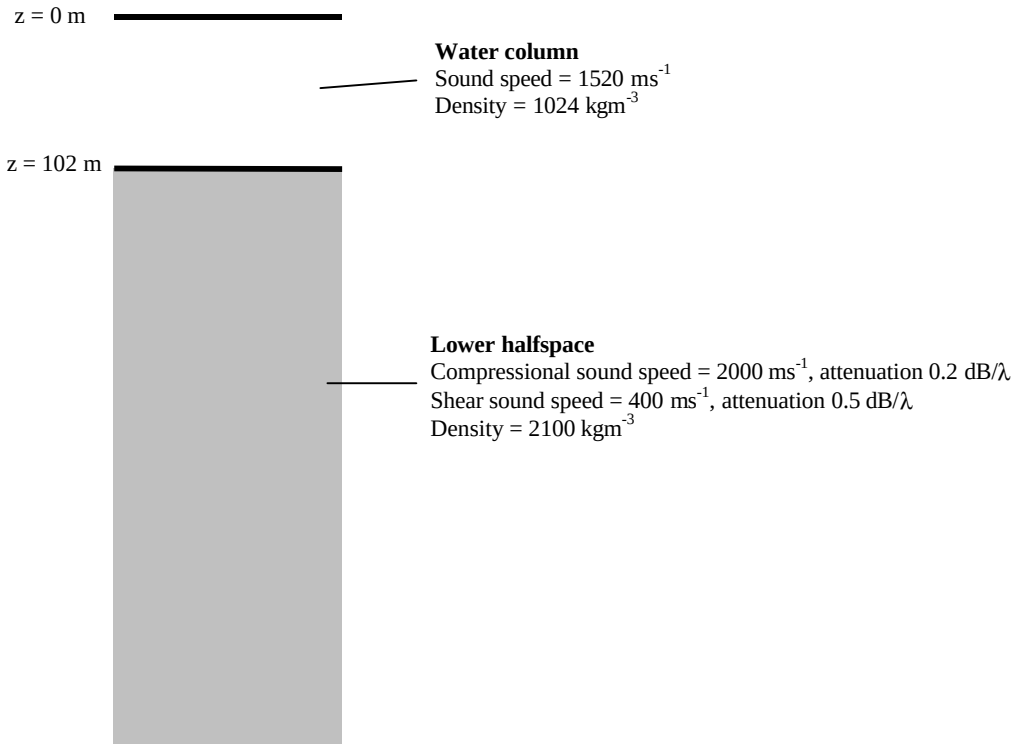

Figure 6.2 Half-space seabed acoustic environment used for generation of simulated acoustic data for inversion.

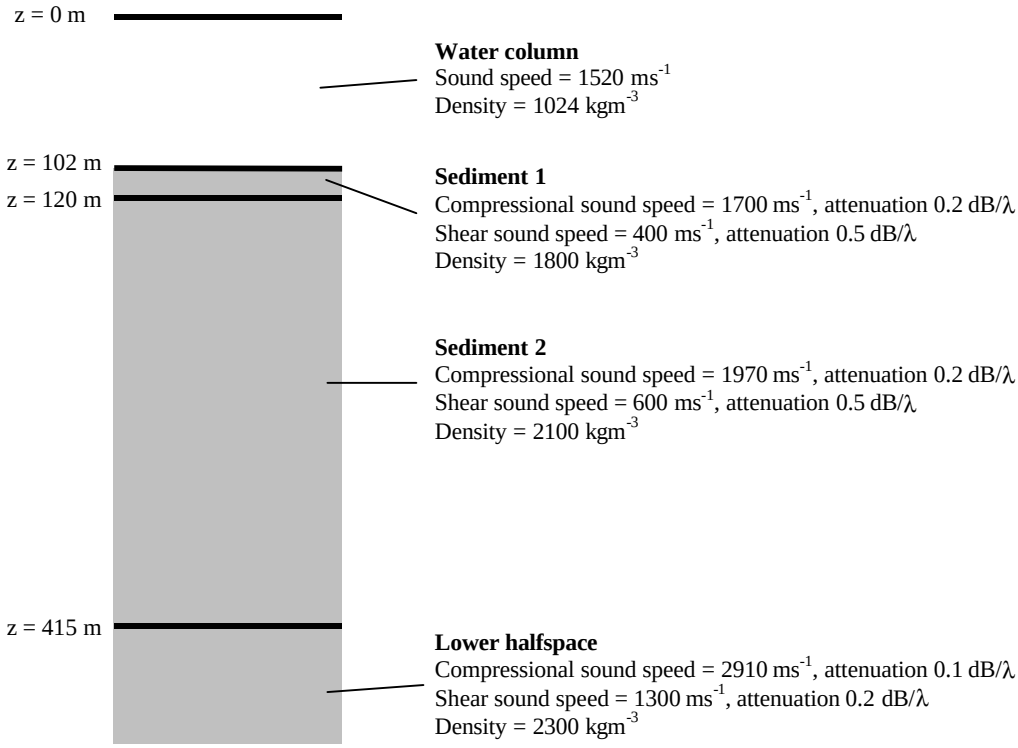

Figure 6.3 Layered seabed acoustic environment used for generation of simulated acoustic data for inversion and beamformer tests.

Parameter sensitivity plots with the vessel in the array endfire direction are shown for the half-space seabed in Figure 6.4 and for the layered seabed in Figure 6.5. In both cases the cost was insensitive to the position of the source (x_s, y_s, z_s) and the compressional and shear wave attenuations in the seabed $(a_{p1}, a_{p2}, a_{s1}, a_{s2})$, and only weakly dependent on the shear speeds (c_{s1}, c_{s2}). By contrast, the cost depended strongly on the parameters defining the array shape (z_a, s, b). The water depth (z_w) was also reasonably well localised, although the cost did not vary as strongly with this parameter.

Somewhat surprisingly the cost was only weakly dependent on the compressional wave speed in the half-space seabed but in the layered seabed the compressional wave speeds in the two layers (c_{p1}, c_{p2}) and the thickness of the first seabed layer (h_1) were all well localised. The reflection coefficient versus seabed grazing angle plots shown in Figure 6.6 revealed the reason for this: over the range of grazing angles corresponding to single bottom-bounce signals the reflection coefficient for the layered seabed was a more complex function of grazing angle than for the half-space seabed and was also frequency dependent. The resulting acoustic field therefore depended more strongly on the seabed's detailed characteristics in the layered case.

The situation changed dramatically for the broadside geometry (Figure 6.7 and Figure 6.8) with the cost now being virtually independent of the geoacoustic parameters of the seabed, but strongly dependent on the horizontal source location (x_s, y_s), the water depth (z_w), and the array shape parameters (z_a, s, b). The reflection coefficient plots in Figure 6.6 showed that, over the range of incidence angles involved at broadside, the bottom reflection coefficient had a smaller magnitude, and therefore the bottom bounce paths contributed less to the received signals, than at endfire. There was also much less structure in the reflection coefficient over this angle range, resulting in the weak dependence of the cost on the seabed parameters.

Although the parameter sensitivity plots shown here were useful for eliminating parameters that only weakly affect the cost, they only sampled a small fraction of the total parameter space and therefore did not prove whether the remaining parameters

could be uniquely determined by the data. As an example, Figure 6.9 shows the cost plotted against both the thickness and compressional wave sound speed of the top seabed layer, and clearly shows several minima of almost equal depth, which indicated that several combinations of these parameters provided equally good fits to the data.

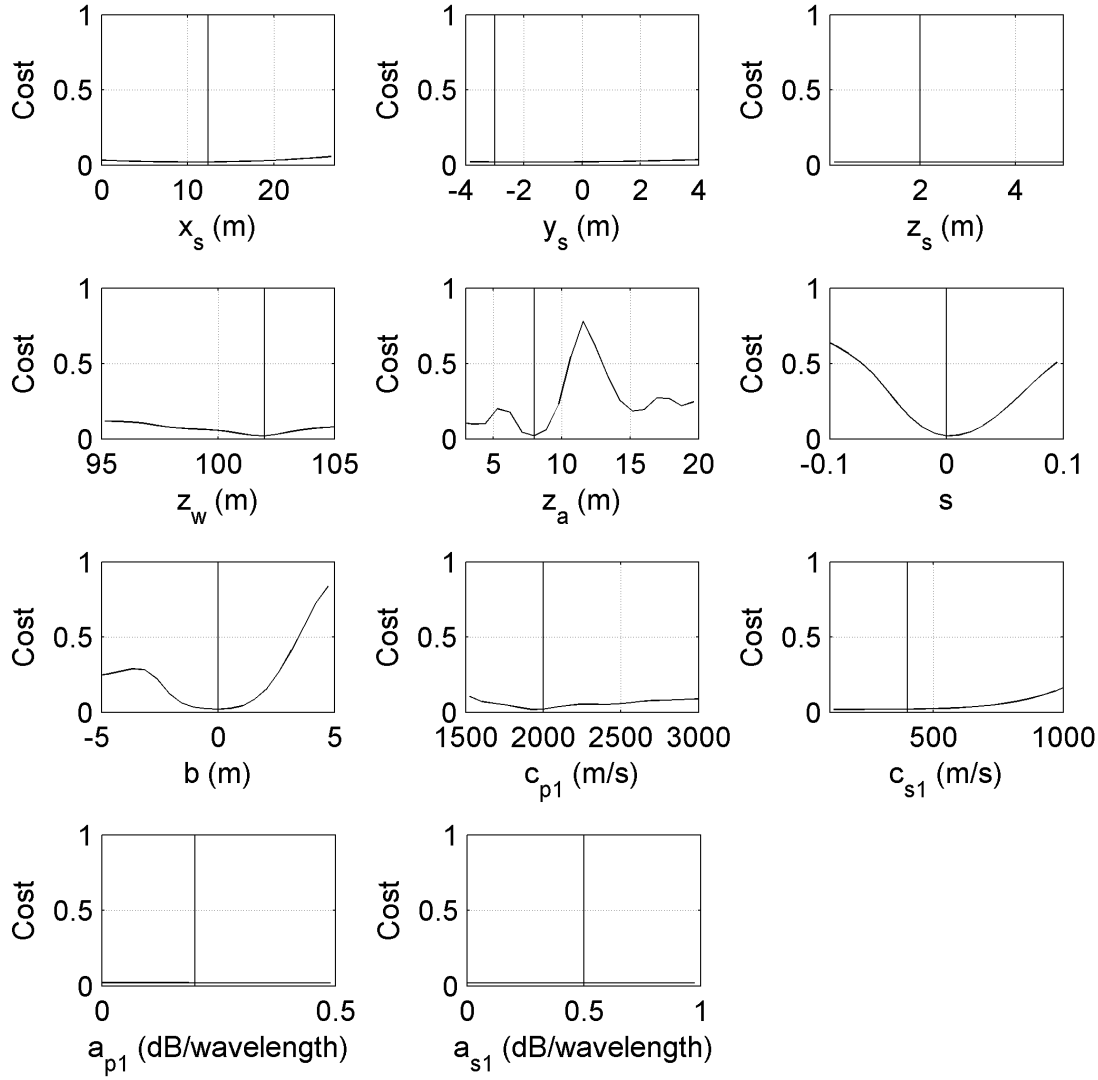

Figure 6.4 Parameter sensitivity plots for simulated data with half-space seabed and the vessel in the array endfire direction. In each case the vertical solid line is the true parameter value.

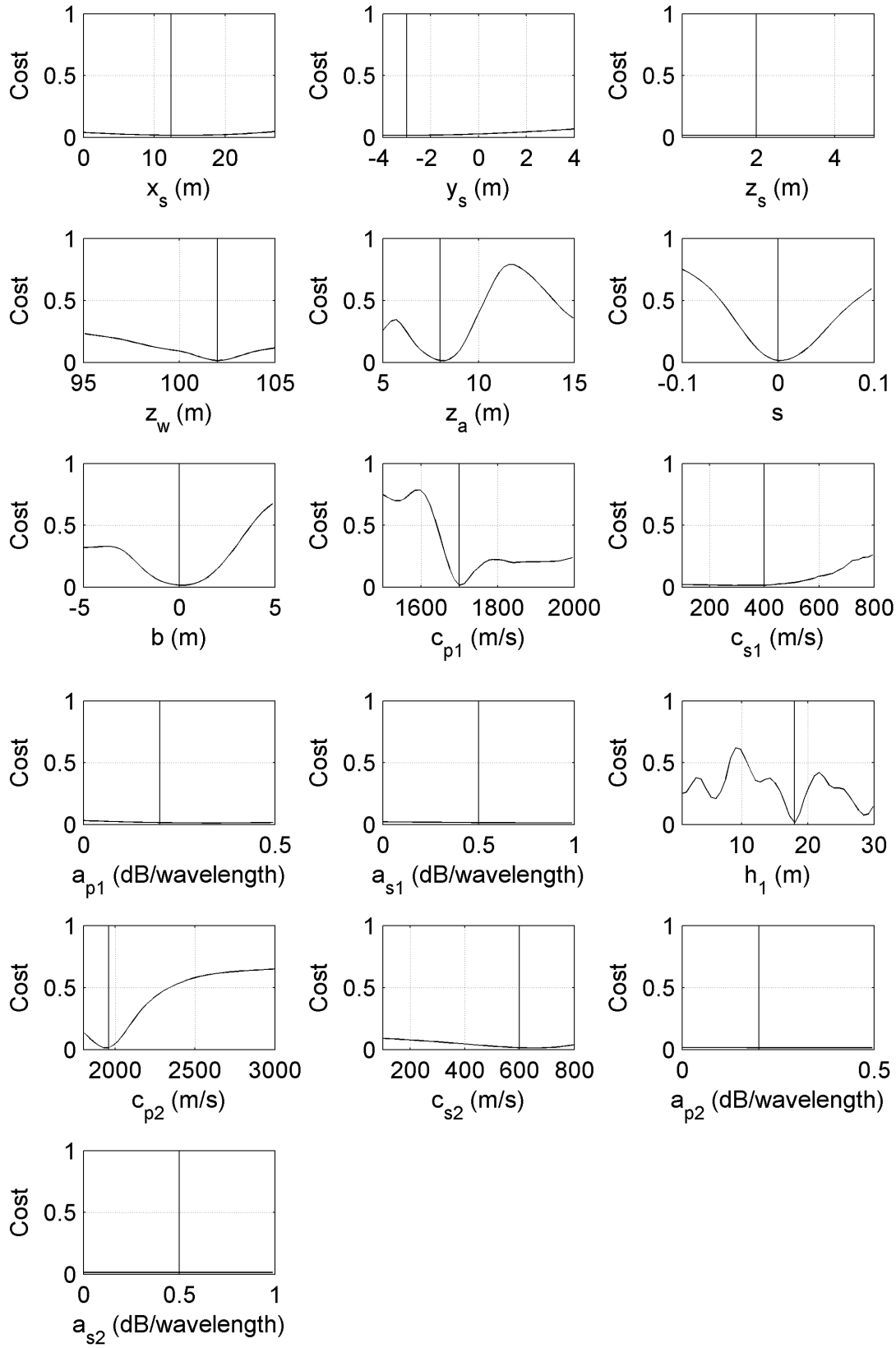

Figure 6.5 Parameter sensitivity plots for simulated data with layered seabed and the vessel in the array endfire direction. In each case the vertical solid line is the true parameter value.

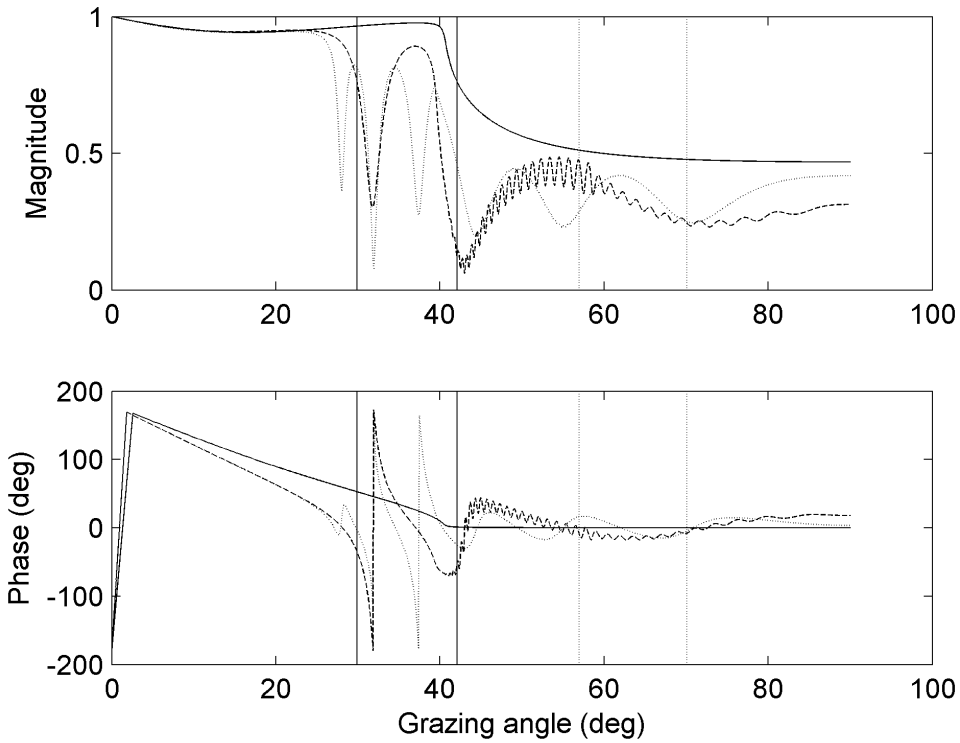

Figure 6.6 Magnitude and phase of seabed reflection coefficient versus grazing angle for the seabeds used to generate simulated data. Solid curve is half-space seabed, broken curve is layered seabed at 96 Hz, and dotted curve is half-space seabed at 213 Hz. Vertical solid lines delimit the range of bottom bounce grazing angles subtended by the array for the endfire simulation, and the vertical dotted lines delimit the range of grazing angles for the broadside simulation.

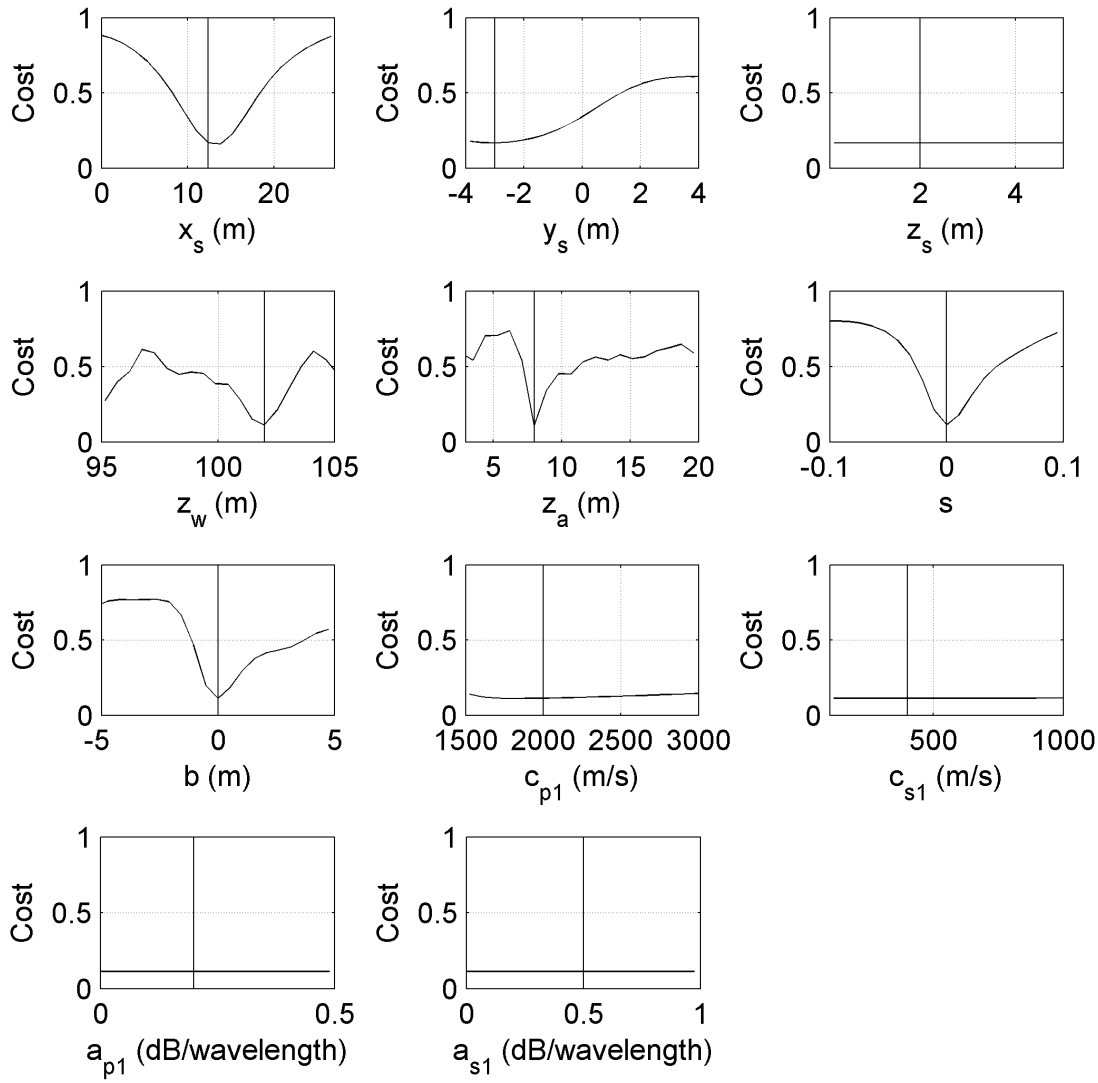

Figure 6.7 Parameter sensitivity plots for simulated data with half-space seabed and the vessel in the array broadside direction. In each case the vertical solid line is the true parameter value.

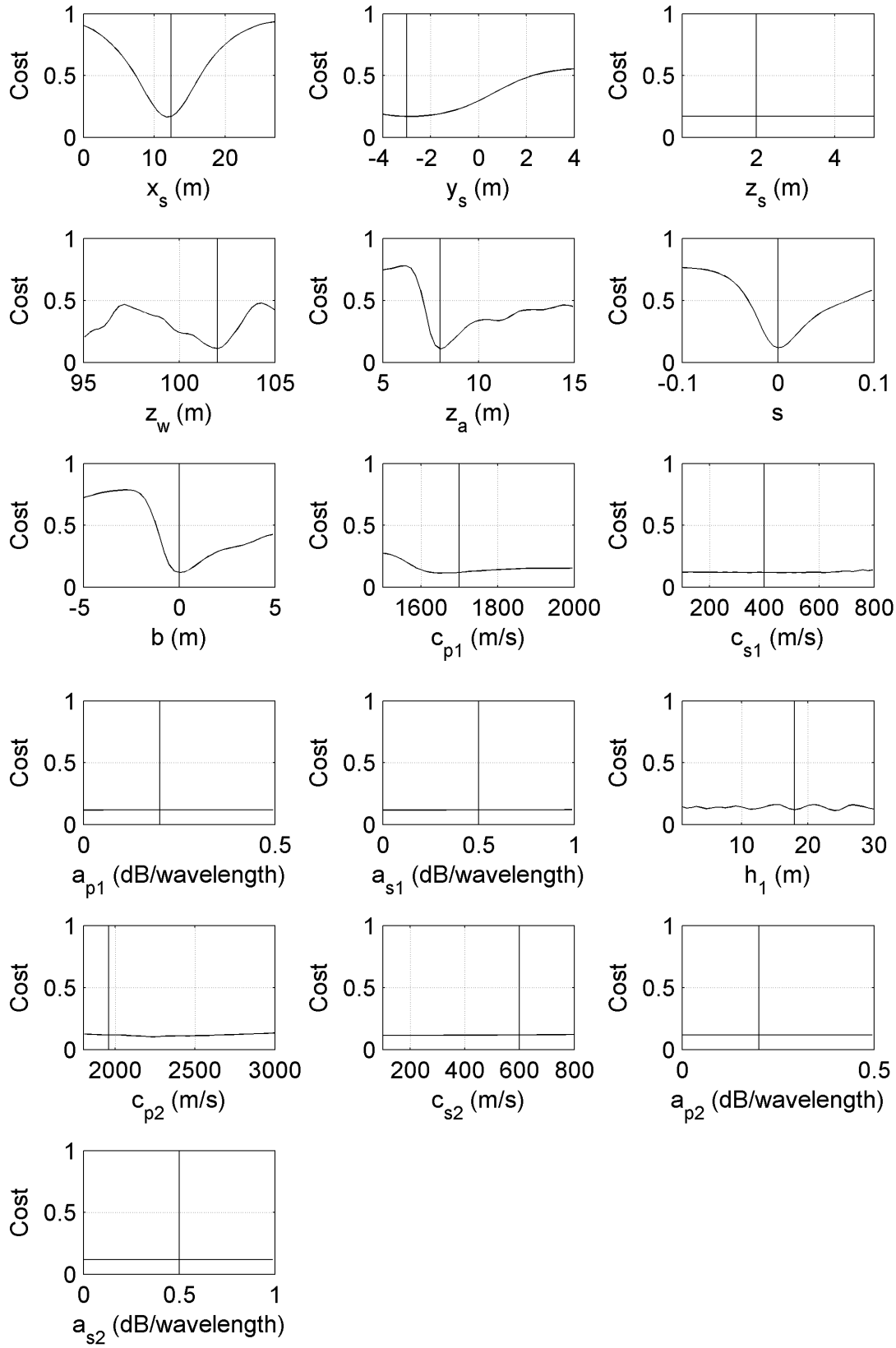

Figure 6.8 Parameter sensitivity plots for simulated data with layered seabed and the vessel in the array broadside direction. In each case the vertical solid line is the true parameter value.

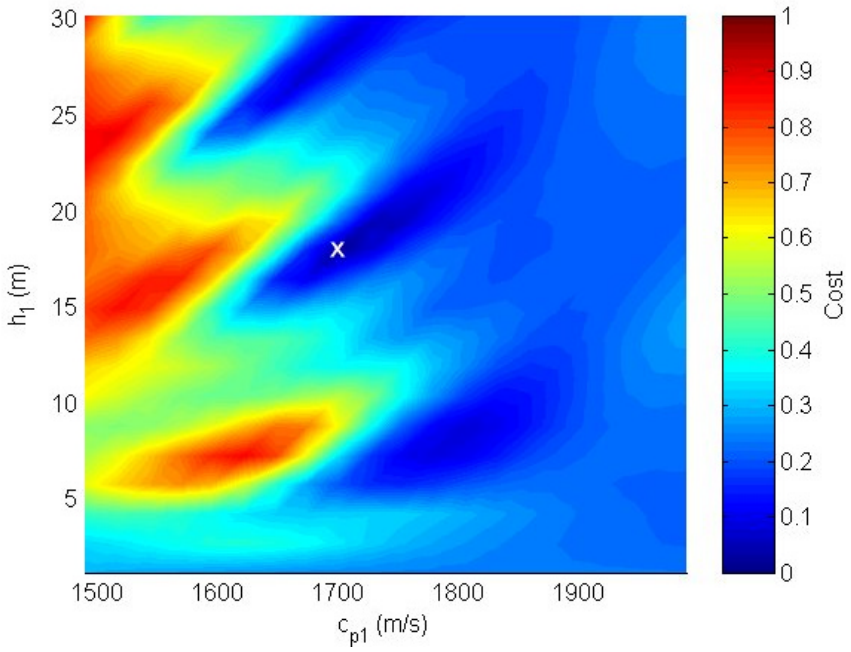

Figure 6.9 Cost as a function of top seabed layer thickness (h_1) and compressional wave speed (c_{p1}) for simulated data with the vessel in the array endfire direction. White cross shows true parameter values.

6.2.6 Overall procedure

The results of the parameter sensitivity tests suggested the following procedure, which was then applied to the matched-field inversion of the field data:

1. A simple beamformer, which assumed spherical spreading, was applied to the array data with the vessel broadside to the array. The minimum white noise (MWN) beamformer was used for this purpose (see Section 7.2.2.1).

2. The beamformer output was used to choose four spectral lines that appeared to emanate from the same location on the vessel.

3. Matched-field inversion was carried out at these frequencies for a time interval when the vessel was in the array endfire direction in order to determine z_w, z_a, s, b, and either c_{p1} and c_{s1} for a half-space seabed, or c_{p1}, h_1 and c_{p2} for a layered seabed. This was done using nominal values for the other parameters.

4. The Gibbs sampler was then used to determine the uncertainties and ambiguities in these parameter estimates.

5. An inversion was then carried out for a time interval when the vessel was in the array broadside direction. This was done with the seabed parameters fixed at the values determined in steps 3 and 4, but with x_s, z_w, z_a, s and b allowed to vary.

The nominal values and search ranges for the various parameters are given in tables 6.3 to 6.5, and Table 6.6 lists the frequencies and time intervals used for each serial.

Table 6.3 Geometric parameter ranges for matched-field inversion

Parameter	**Parameter range**		**Units**	**Determined from**
	Endfire	**Broadside**		
z_w	Tidal corrected charted depth +/- 3 m	Tidal corrected charted depth +/- 3 m	m	Charted bathymetry corrected for tide as measured by Department of Transport tide gauge located in Fremantle Harbour.
z_a	3 to 20	3 to 20	m	From transient hydrophone depth determinations (Section 5.1)
s	Serial 1A and 1C: 0 to 0.1 Serial 1D: -0.1 to 0.1	Serial 1A and 1C: 0 to 0.1 Serial 1D: -0.1 to 0.1	-	
b	-5 to 5	-5 to 5	m	
x_s	13.5	0 to 27	m	Endfire – amidships Broadside – limits of vessel
y_s	-3.1	-3.1	m	Approx. location of port side of hull
z_s	-1.76	-1.76	m	50% of vessel draft

Table 6.4 Half-space seabed parameter ranges for matched-field inversion

Parameter	Parameter range		Units	Determined from
	Endfire	**Broadside**		
c_{p1}	1550 to 4000	Endfire result	ms^{-1}	Typical sediment properties Jensen et al. (2000, Chapter 1)
c_{s1}	100 to 2000	Endfire result	ms^{-1}	
a_{p1}	0.2	0.2	dB/λ	
a_{s1}	0.5	0.5	dB/λ	

Table 6.5 Layered seabed parameter ranges for matched-field inversion

Parameter	Parameter range		Units	Determined from
	Endfire	**Broadside**		
c_{p1}	1540 to 2000	Endfire result	ms^{-1}	Typical sediment properties Jensen et al. (2000, Chapter 1)
c_{s1}	400	400	ms^{-1}	Hoffman (2002)
a_{p1}	0.2	0.2	dB/λ	
a_{s1}	0.5	0.5	dB/λ	
h_1	0.1 to 35	Endfire result	m	
c_{p2}	2000 to 4500	Endfire result	ms^{-1}	Typical sediment properties Jensen et al. (2000, Chapter 1)
c_{s2}	600 to 2000	Endfire result	ms^{-1}	
a_{p2}	0.2	0.2	dB/λ	
a_{s2}	0.5	0.5	dB/λ	

Table 6.6 Frequencies and time intervals used for inversions

Serial	1A	1C	1D
Frequencies (Hz)	95, 106, 116, 224	94, 117, 157, 226	72, 124, 170, 229
Endfire inversion time interval (hours UTC)	5.342 to 5.347	6.032 to 6.037	6.382 to 6.387
Broadside inversion time interval (hours UTC)	5.378 to 5.383	6.057 to 6.062	6.408 to 6.413

6.3 Results

The results of the endfire inversions for the three processed manoeuvres are summarised in Table 6.7, and the parameter marginal probability distributions computed by the Gibbs sampler are plotted in figures 6.10 to 6.15. Note that the inverted parameter values did not always correspond to the peaks in the probability distributions because the cost function used in the SA inversion equally weighted all four frequencies whereas a frequency dependent weighting (the denominator in Equation 6.9) was applied when calculating the probability distributions.

The inverted values for the water depth, array depth, and array slope were very similar for the two seabed models and these parameters tended to have probability distributions with well-defined single peaks. The probability distribution of the array bow also had a single well-defined peak, but this was somewhat broader than for the other geometric parameters, leading to larger discrepancies between the inverted values for the two seabed models. Plots of the vertical-plane array shapes obtained using the two seabed models were very similar (see Figure 6.16).

The half-space seabed inversions for serials 1A and 1D produced shear speeds that were unrealistically high compared to the inverted compressional sound speeds (see Table 6.7). In all three half-space cases the marginal probability density of the compressional sound speed had a single, well-defined peak (see figures 6.10 to 6.12), but the probability density of the shear speed had two broad, flat areas of similar height, separated by a dip, implying that the inverted shear speeds were poorly localised and ambiguous. The results for serials 1A and 1C were very similar with a compressional wave speed of around 2200 ms^{-1}, implying a partially consolidated seabed, whereas the Serial 1D results gave a compressional wave speed of 1734 ms^{-1} which is more typical of medium to coarse sand (Hamilton 1972). The shear speed results were less definitive but did imply a lower shear speed for Serial 1D than for the other two serials, which was consistent with the compressional speed results.

The layered seabed model produced slightly better fits to the measured data (i.e. slightly lower final costs) than the half-space seabed model (see Table 6.7), but again resulted in unrealistically high shear speeds in the lower half-space. The marginal probability density distributions (figures 6.13 to 6.15) showed that the lower half-space shear speed was poorly localised, but this time there were no dips between the

low speed and high speed regions. In all three cases the layer thickness probability distribution had a sharp peak at around 2 to 3 metres but for Serial 1D there was another peak of slightly greater magnitude corresponding to a layer thickness of 35 m. For serials 1A and 1C the layer and compressional sound speeds were poorly localised but had maximum probabilities at the upper end of their allowed range (2000 ms^{-1}) whereas the lower half-space compressional sound speeds had probability maxima close to the bottom of their allowed range, which was also 2000 ms^{-1}. These results therefore implied that there was little if any compressional wave velocity contrast across the interface between the sediment layer and the lower half-space. The results for Serial 1D were slightly different with a definite probability maximum corresponding to a layer compressional wave speed of 1760 ms^{-1}. As shown in Figure 4.19, the location of Serial1D was approximately 350 m northeast of the location of Serial 1C, and 900 m northeast of the location of Serial 1A.

Table 6.7 Endfire inversion parameter estimates for half-space and layered seabeds. Numbers in brackets are parameters that were fixed during the inversion.

Parameter	**Serial 1A**		**Serial 1C**		**Serial 1D**	
	Half-space	**Layered**	**Half-space**	**Layered**	**Half-space**	**Layered**
z_w (m)	103.6	103.6	100.9	101.5	98.5	97.7
z_a (m)	10.5	9.9	7.6	7.9	5.8	5.9
s	0.051	0.047	0.037	0.035	-0.001	-0.008
b (m)	0.22	1.07	0.23	-0.13	1.42	1.12
c_{p1} (ms^{-1})	2001	1666	2370	2000	1550	1760
c_{s1} (ms^{-1})	1786	(400)	773	(400)	1947	(400)
h_1 (m)	-	2.3	-	3.2	-	3.0
c_{p2}	-	2052	-	2349	-	2518
c_{s2}	-	1518	-	1404	-	1644
Final cost	0.546	0.510	0.412	0.407	0.415	0.404

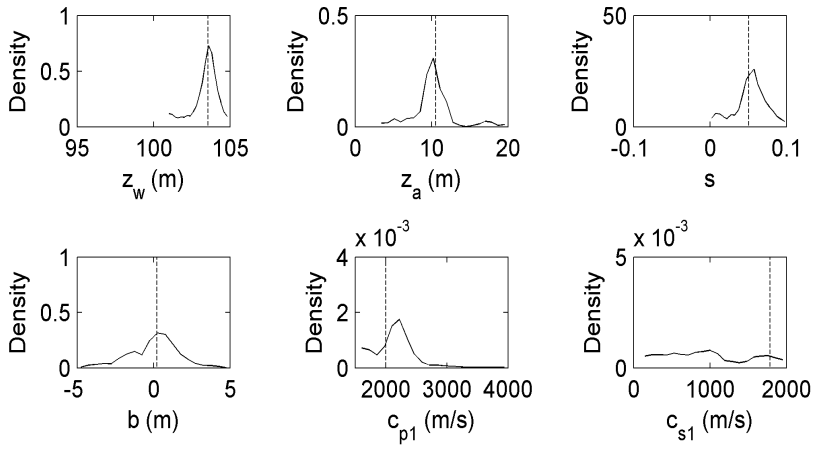

Figure 6.10 Parameter marginal probability density distributions for Serial 1A with a half-space seabed and the vessel in the array endfire direction. Broken vertical lines are inverted parameter values.

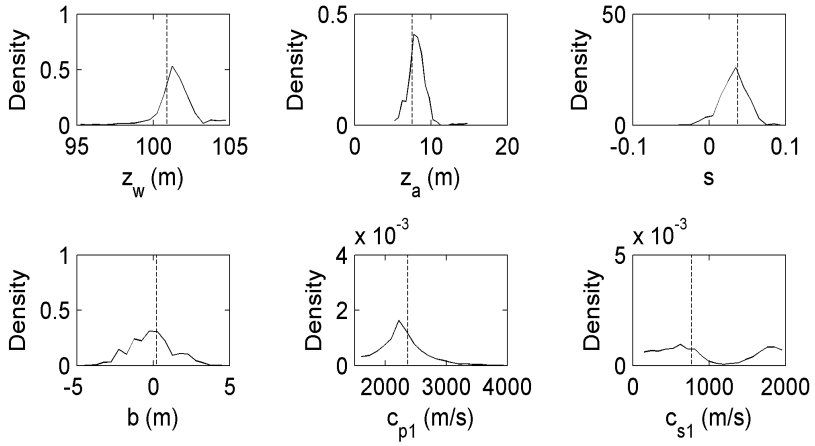

Figure 6.11 As for Figure 6.10 but Serial 1C.

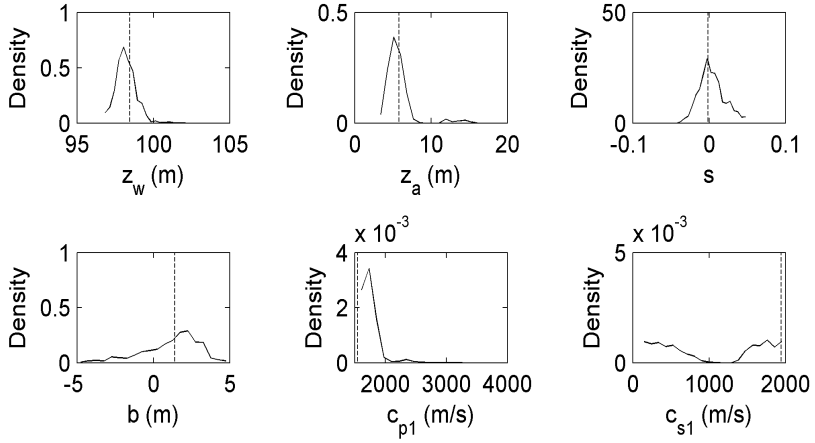

Figure 6.12 As for Figure 6.10 but Serial 1D.

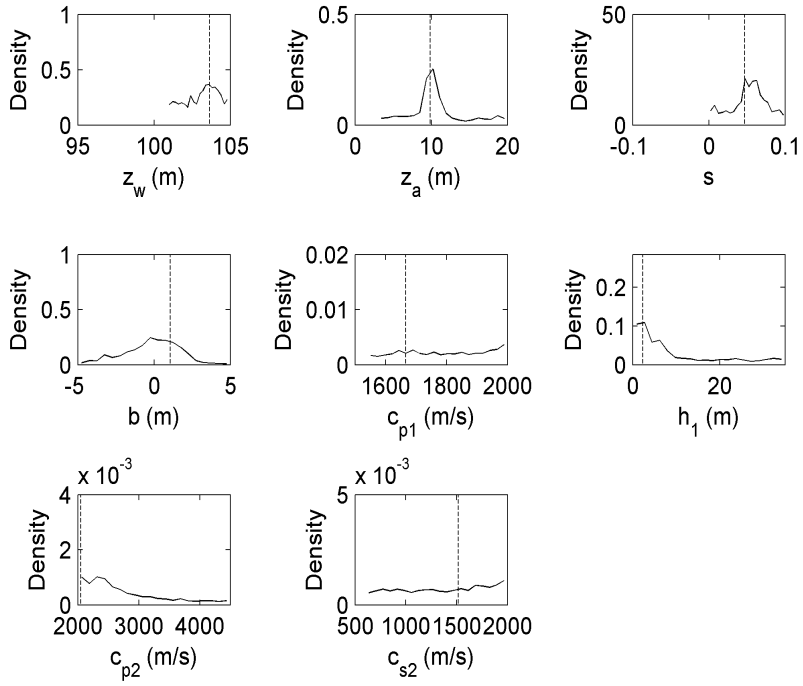

Figure 6.13 Parameter marginal probability density distributions for Serial 1A with a layered seabed and the vessel in the array endfire direction. Broken vertical lines are inverted parameter values.

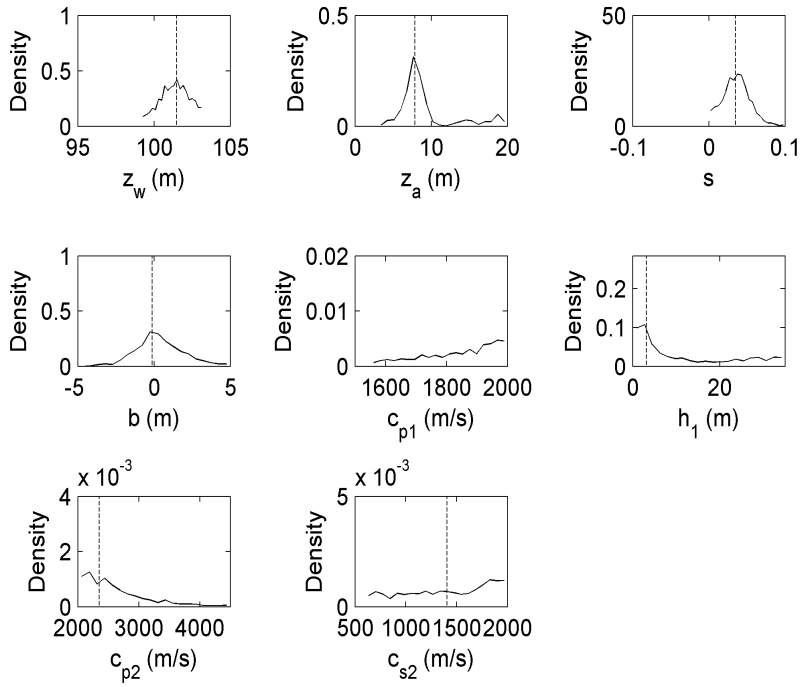

Figure 6.14 As for Figure 6.13 but Serial 1C.

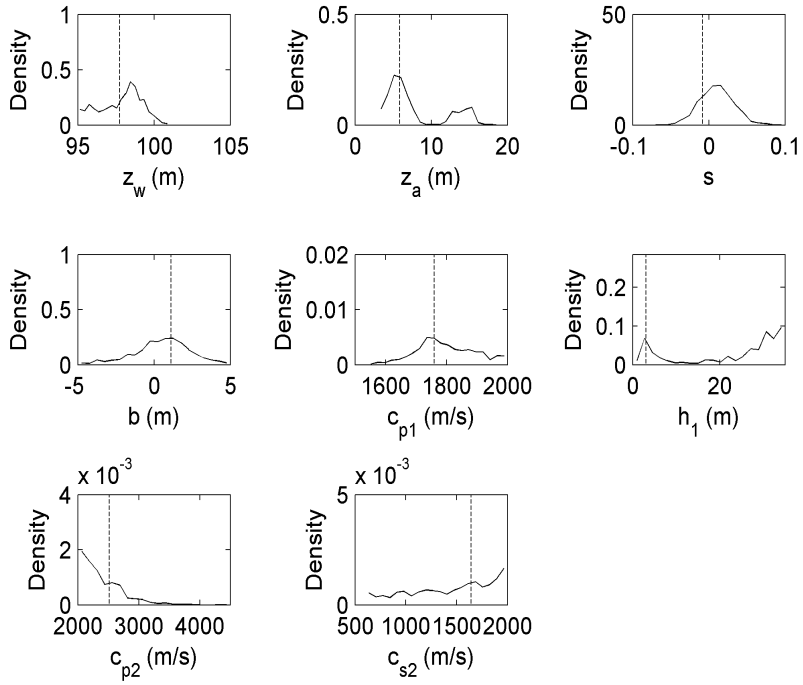

Figure 6.15 As for Figure 6.13 but Serial 1D.

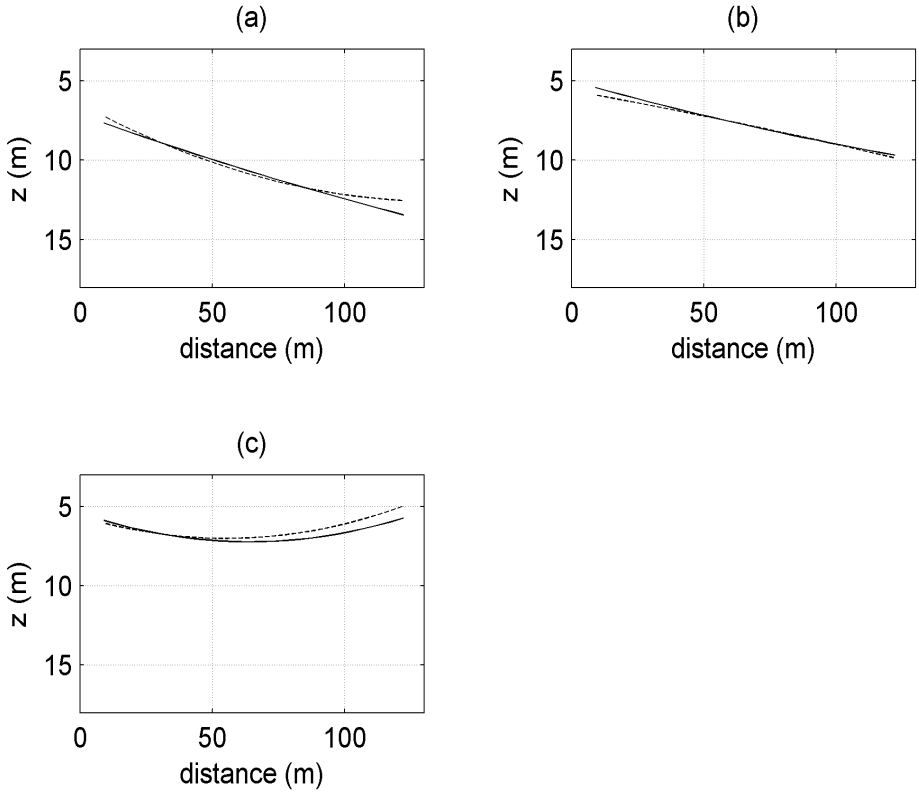

Figure 6.16 Hydrophone depth plotted against distance along the array as determined by matched-field inversion with the tow-vessel in the array endfire direction. (a) Serial 1A, 5.345 h; (b) Serial 1C, 6.035 h; and (c) Serial 1D, 6.385 h. Solid line is result assuming half-space seabed, broken line is result assuming layered seabed.

The results of the endfire inversions, combined with what is known about the geology of the seabed in the area (Collins 1988), implied that a reasonable model for the seabed was a partially consolidated sediment with a compressional sound speed of 2200 ms^{-1} overlain, in the case of Serial 1D, with a 3 m thick layer of sand with a compressional sound speed of 1760 ms^{-1}. The resultant geoacoustic models are fully specified in Table 6.8 and shown schematically in Figure 6.17.

The shear speed, compressional attenuation and shear attenuation of the sand layer, which were not available from the inversion results, were taken from Table 1.3 of Jensen et al. (2000) whereas the density was computed from the compressional sound speed using the method described in Section 6.2.5.

For the lower half-space the higher shear speed results were rejected on physical grounds, and the estimate of 640 ms^{-1} was arrived at by considering the shapes of the marginal probability density curves for serials 1A and 1C with the half-space seabed model, together with the published results for sediments of similar compressional sound speeds given in Jensen et al. (2000). Compressional and shear attenuations were obtained from the same reference, and the density was again computed from the compressional sound speed.

This geoacoustic model had strong similarities to the geoacoustic model given in Hoffman (2002) and shown in Figure 6.3. The main difference is that the matched-field inversion results implied a much thinner (Serial 1D), or non-existent (serials 1A and 1C) sand layer than the 18 m layer Hoffman inferred from his results. The basement layer in Hoffman's model was too deep (415 m) to influence the sound field at the frequencies used in the matched-field inversion.

The results of carrying out SA inversions for time periods when the tow-vessel was in the array broadside direction are given in Table 6.9. To generate these results the seabed parameters were fixed at the values specified in Table 6.8 and only the array geometric parameters and water depth were allowed to vary. These results indicated that the array was deeper and inclined more steeply at broadside for Serial 1A than it was for the other two serials, which was to be expected given that Serial 1A was carried out at a lower speed and involved a tighter turn than the other two serials, resulting in greater sinkage of the negatively buoyant array.

Inversions for the water depth and array geometric parameters were also carried out for time intervals centred on the times of the transient signals described in chapters 4 and 5. These inversions were carried out using the deterministic downhill inversion method, using the endfire inversion results as the starting points for the shots immediately before and after, then these results as the starting points for the next nearest shots and so on. The inverted vertical plane array shapes are plotted together with the transient results in figures 6.18 to 6.20 in order of increasing time. The endfire and broadside array shapes have also been included so that these plots provide a sequence of array shapes through each manoeuvre. In most cases the agreement between the transient and matched-field results was excellent. The largest discrepancies (Serial 1A, Shot 9, see Figure 6.18 (h)) occurred in a situation where all hydrophones were at a similar range from the vessel, thus providing relatively poor geometry for matched-field inversion.

Table 6.8 Final geoacoustic seabed model parameters.

Parameter	Value	How determined
c_{p1} (ms^{-1})	1760	Layered seabed inversion for Serial 1D.
c_{s1} (ms^{-1})	$110\tilde{z}^{0.3}$ where $\tilde{z}$ is depth below water-sediment interface (m)	Table 1.3, Jensen et al. (2000), sand.
r_1 (kgm^{-3})	2090	From c_{p1} (see Section 6.2.5).
a_{p1} (dB/λ)	0.8	Table 1.3, Jensen et al. (2000), sand.
a_{s1} (dB/λ)	2.5	
h_1 (m)	Serials 1A, 1C: 0 m Serial 1D: 3.0 m	Layered seabed and half-space probability densities (see discussion).
c_{p2} (ms^{-1})	2200	Half-space probability densities for serials 1A and 1C.
c_{s2} (ms^{-1})	640	Half-space probability densities for serials 1A and 1C and consideration of Table 1.3, Jensen et al. (2000), see discussion.
r_2 (kgm^{-3})	2170	From c_{p2} (see Section 6.2.5).
a_{p2} (dB/λ)	0.4	Table 1.3, Jensen et al. (2000), sediments with similar compressional wave speeds.
a_{s2} (dB/λ)	1.0	

Table 6.9 Broadside inversion parameter estimates obtained with the seabed parameters fixed at the values specified in Table 6.8.

Parameter	Serial 1A	Serial 1C	Serial 1D
x_s (m)	11.3	12.1	8.2
z_w (m)	103.4	102.0	97.7
z_a (m)	13.1	7.5	7.2
s	0.074	0.043	0.044
b (m)	0.70	-0.65	0.31
Final cost	0.292	0.327	0.335

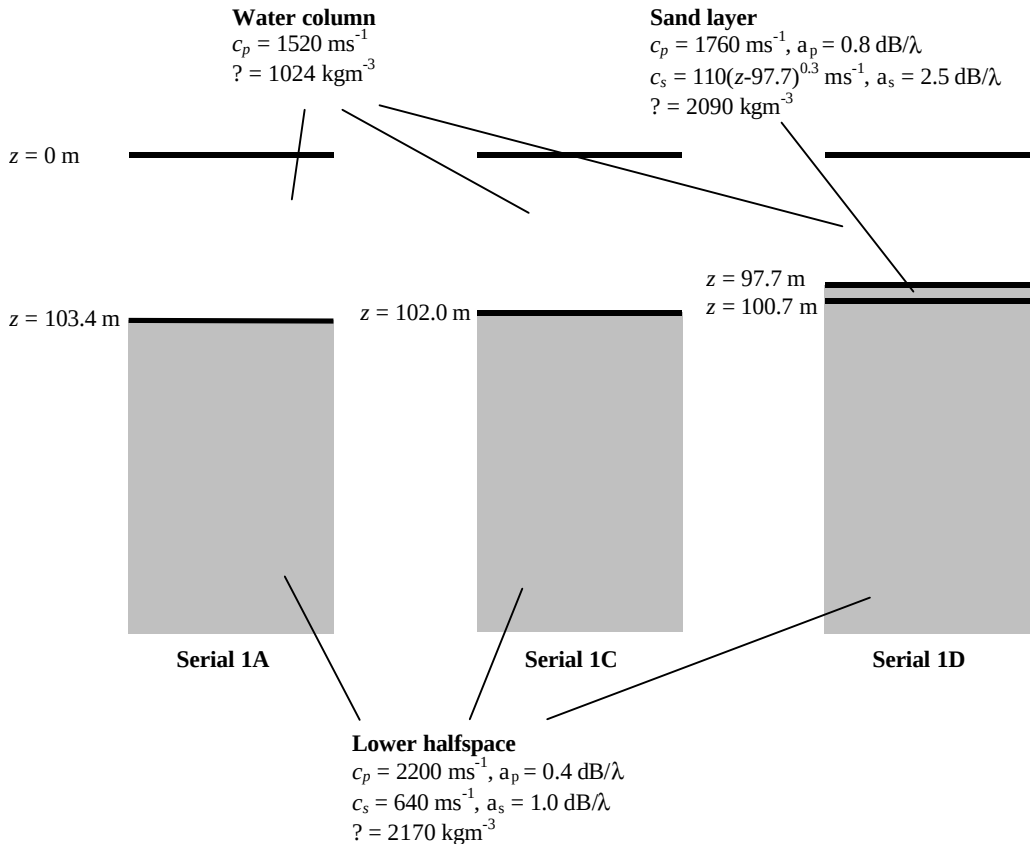

Figure 6.17 Schematic diagrams of final seabed models. Water depths are from broadside inversions.

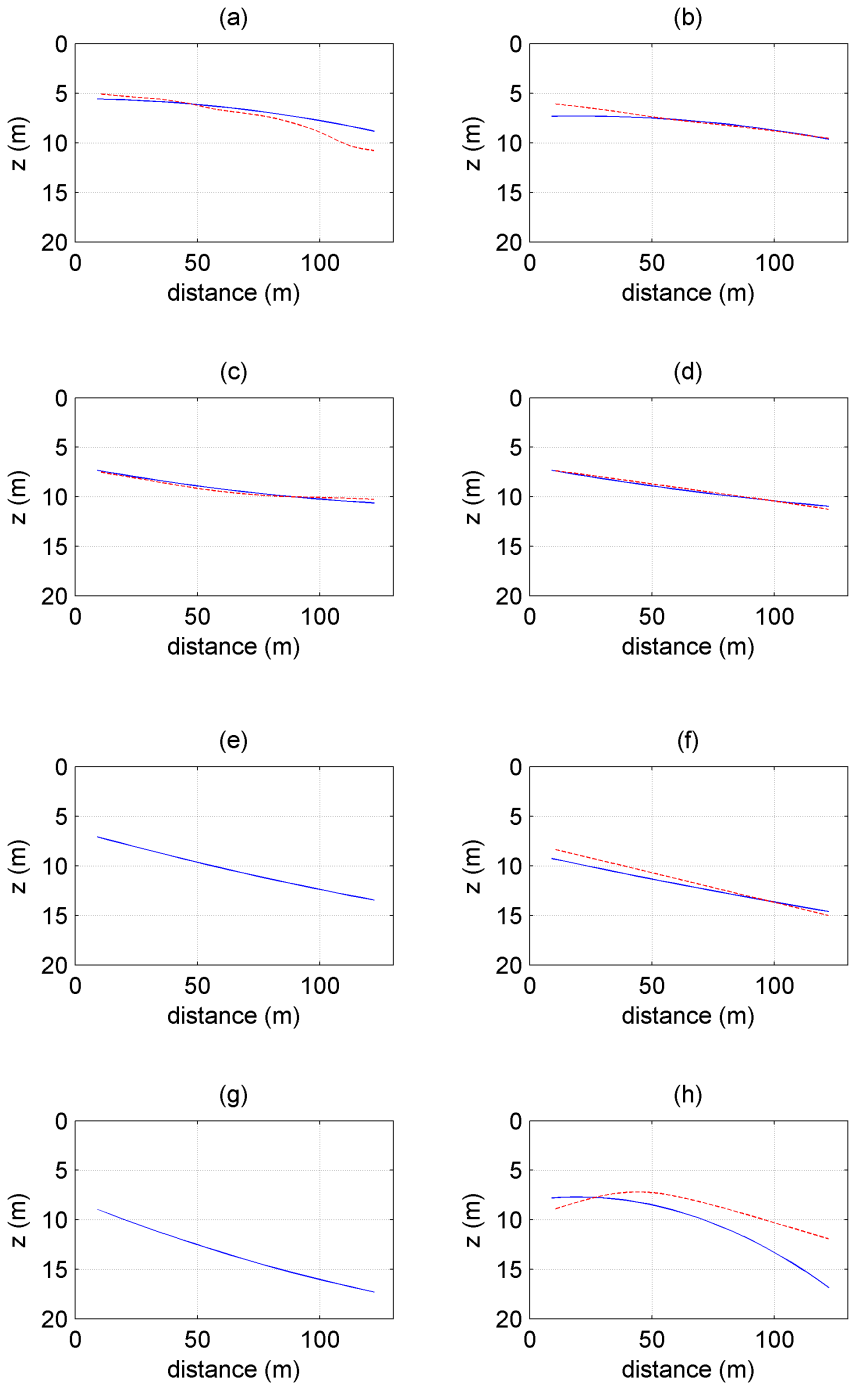

Figure 6.18 Array depth plotted against distance from the head of the acoustic section for a number of times during Serial 1A. Solid blue line is inversion result, broken red line is result from transient data (where available). (a) Shot 2, 5.257 h; (b) Shot 3, 5.275 h; (c) Shot 4, 5.297 h; (d) Shot 5, 5.317 h; (e) tow-vessel at endfire, 5.345 h; (f) Shot 7, 5.362 h; (g) tow-vessel at broadside, 5.380 h, (h) Shot 9, 5.409 h.

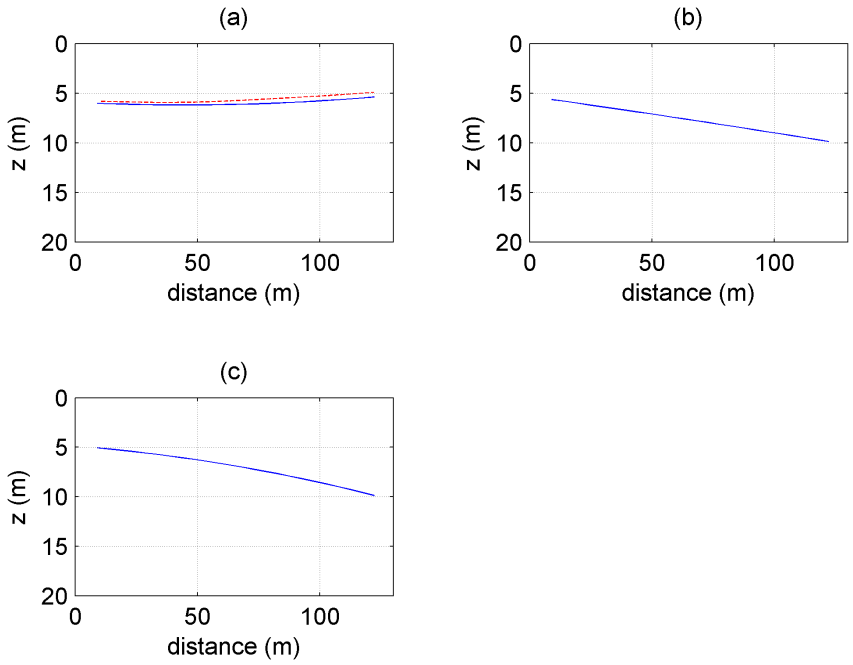

Figure 6.19 Array depth plotted against distance from the head of the acoustic section for a number of times during Serial 1C. Solid blue line is inversion result, broken red line is result from transient data (where available). (a) Shot 2, 5.952 h; (b) endfire, 6.035 h; (c) broadside, 6.060 h.

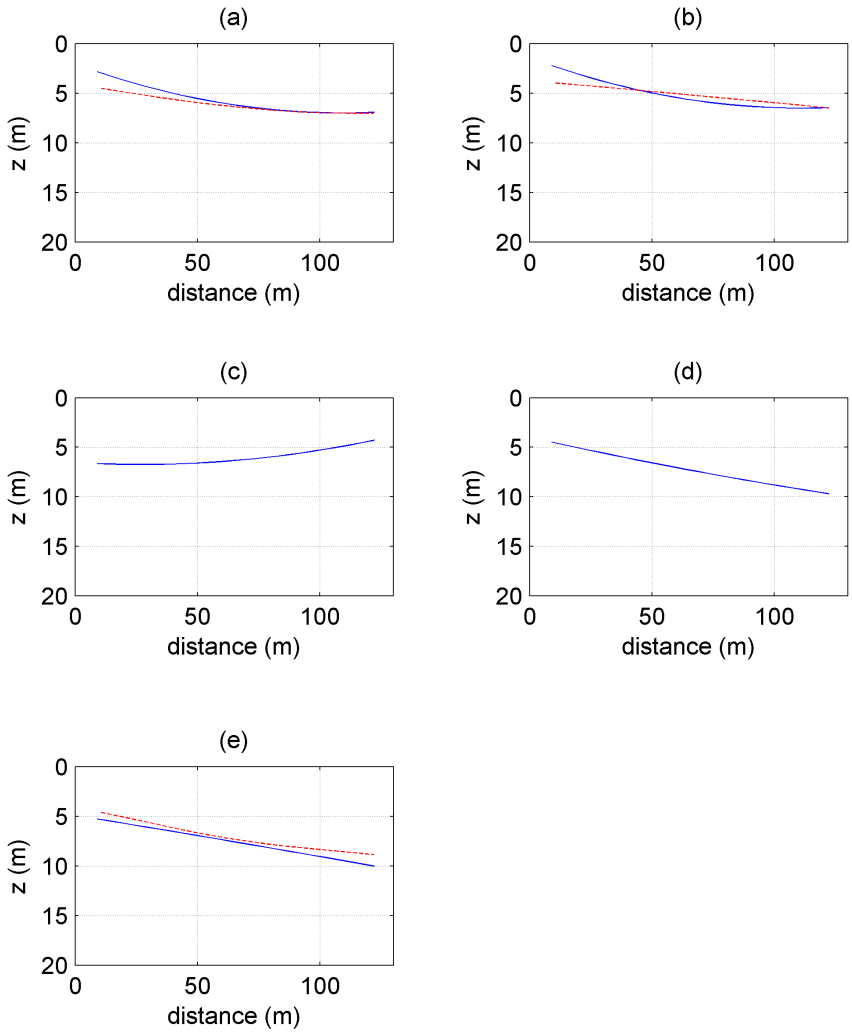

Figure 6.20 Array depth plotted against distance from the head of the acoustic section for a number of times during Serial 1D. Solid blue line is inversion result, broken red line is result from transient data (where available). (a) Shot 3, 6.340 h; (b) Shot 4, 6.359 h; (c) endfire, 6.385 h, (d) broadside, 6.410 h, (e) Shot 6, 6.415 h.

6.4 Summary

A matched-field inversion technique was developed based on a combination of simulated annealing and Gibbs sampling. This technique was then used to determine geoacoustic models of the seabed appropriate to the three processed serials and also to determine vertical plane array shapes at a number of different times. There was excellent agreement between the array shapes computed using this method and those estimated using transient signals as described in Chapter 5.

7 Array-processing

This chapter deals with the application of array-processing techniques to the acoustic signals received by the towed-array hydrophones. To achieve the aims of this project it was necessary to develop array-processing algorithms to localise acoustic sources on the tow-vessel and determine their amplitudes, and also to estimate the far-field signature of the vessel. Algorithms covering all of these aspects are dealt with in this chapter.

A review of relevant literature is given in Section 7.1 followed, in Section 7.2, by detailed descriptions of the implemented algorithms, which included several different beamformers and a regularised inversion processor. The algorithms were initially evaluated using simulated data (Section 7.3.1) and then applied to field data (Section 7.3.2). Section 7.4 provides a brief summary of the main results of the chapter.

7.1 Literature Review

Array-processing techniques for towed arrays usually assume that the array remains straight and that the sources of interest are sufficiently far away that their positions relative to the array change slowly compared to the averaging time required to compute the array output. The first assumption is violated when the tow vessel manoeuvres and the second assumption is violated when the array is used to track a nearby source that is moving rapidly. Both assumptions are violated when the towed array is used to image sources on the tow-vessel during a manoeuvre because of the distortion of the array and the relative motion of the array and tow-vessel.

Array-processing techniques have been an active field of research for many years with a consequent extensive literature, and so this review cannot hope to be exhaustive. To provide the necessary background standard array-processing techniques are covered, including both beamforming (Section 7.1.1) and high-resolution angle of arrival estimation techniques (Section 7.1.2). A number of newer methods are reviewed in sections 7.1.3 (inverse beamforming), 7.1.4 (matched-field processing), and 7.1.5 (model based processing), while array-processing techniques specific to sources in the acoustic near-field of the array are discussed in Section 7.1.6. Finally Section 7.1.7 reviews array-processing for moving arrays (primarily

passive synthetic techniques) and the small number of papers that deal with distorting arrays.

7.1.1 Beamforming

An excellent summary of beamforming techniques can be found in VanVeen & Buckle (1988).

For an array of N hydrophones, the beamformer output at angular frequency w is given by:

$$y(w) = \mathbf{w}^H \mathbf{x}(w) \qquad \textbf{(7.1)}$$

where:

$\mathbf{x}(w)$ is an N element vector of sensor outputs at angular frequency w,

w is an N vector of complex weights, and

the superscript H denotes the Hermitian transpose (complex conjugate of the transpose).

The response of the beamformer to a plane wave of angular frequency w incident from angle q is:

$$y(q,w) = \mathbf{w}^H \mathbf{a}(q,w) \qquad \textbf{(7.2)}$$

where:

a is the vector of array sensor outputs (the so-called steering vector), and

$y(q,w)$ is the beamformer output. (The beam pattern is given by $|y(q,w)|^2$)

Note that **a** is considered a function of w to allow discussion of broadband beamformers. Note also that **w** and **a** may both have a length greater than the number of sensors with the additional elements corresponding to time delayed sensor outputs. This is particularly the case for broadband beamformers.

The steering vector is given by:

$$\mathbf{a}(q,w) = \begin{bmatrix} 1 & e^{jwt_2(q)} & \dots & e^{jwt_N(q)} \end{bmatrix}^H \qquad \textbf{(7.3)}$$

where t_i is the propagation delay between the signal arriving at element 1 and at element i.

Two different broadband beamforming architectures are given in this reference. In the first the output of each sensor is Fourier transformed (either explicitly using an FFT or via finite impulse response (FIR) filters) and the outputs for each frequency are combined across the sensors using appropriate weights. The second is the classical delay and add beamformer where delays are used to steer the beam and real weights are used for beam shaping. Both of these can be represented by the above model with an appropriate choice of weights and signal vectors.

The authors classify beamformers as either "data independent" or "statistically optimum".

7.1.1.1 *Data independent beamformers*

Here the weights are fixed and do not depend on the array output. A common choice to steer the array to angle q_0 and frequency w_0 is:

$$\mathbf{w} = \mathbf{T}_a \mathbf{a}(q_0, w_0) \qquad \textbf{(7.4)}$$

Where $\mathbf{T}_a$ is a diagonal matrix of taper weights. See Harris (1978) for a comparison of a large number of tapering functions. This method is known variously as a conventional beamformer or a Bartlett beamformer.

A technique of general data independent design is given which minimises the squared error between the actual and desired response at Q points (q_i, w_i), i.e.

$$\min_{\mathbf{w}} \left| \mathbf{A}^H \mathbf{w} - \mathbf{y}_d \right|^2 \qquad \textbf{(7.5)}$$

where:

$\mathbf{A} = \left[\mathbf{a}(q_1, w_1), \quad \mathbf{a}(q_2, w_2) \quad \ldots \quad \mathbf{a}(q_Q, w_Q) \right]$ is called the steering matrix, and

$\mathbf{y}_d = \left[y_d(q_1, w_1), \quad y_d(q_2, w_2) \quad \ldots \quad y_d(q_Q, w_Q) \right]^H$ is a vector of desired responses.

The solution is:

$$\mathbf{w} = \left(\mathbf{A}\mathbf{A}^H \right)^{-1} \mathbf{A}\mathbf{y}_d \qquad \textbf{(7.6)}$$

Note, however, that if A is ill-conditioned (the steering vectors span a space of dimension < *N*, where *N* is the length of $\mathbf{w}$), then a weight vector with a very large norm, corresponding to a large white noise response, can result.

An alternative algorithm for determining the array weights required to achieve a desired beampattern is given in Tseng & Griffiths (1992). This paper formulates the problem as a constrained minimisation problem where the aim is to minimise the beamformer output power for a dense set of sources covering the angle range of interest, subject to the following constraints:

1. unity gain in the look direction,
2. first derivative of the gain with respect to angle equal to zero in the look direction, and
3. the peak levels of all sidelobes within the angle range of interest equal to a specified value.

The first two constraints guarantee a peak in the look direction and the third allows control of the sidelobe levels. However, the third constraint also makes it necessary to solve the problem using an iterative algorithm, as the angles at which the peaks in the sidelobes occur vary as the weights are adjusted. This is unlikely to be a problem in practice as convergence is achieved within a few iterations in the examples given in Tseng & Griffiths (1992).

7.1.1.2 *Statistically optimum beamforming.*

Here the weights are chosen so that the beamformer output contains a minimum contribution from noise and/or signals arriving from other than the desired direction. A number of techniques are discussed including the multiple sidelobe canceller (MSC), use of a reference signal, maximisation of signal to noise ratio, and linearly constrained minimum variance beamforming (LCMV). Of these the most useful appears to be the LCMV, which also includes the commonly used minimum variance distortionless response (MVDR) beamformer.

LCMV minimises the variance of the array output given the constraint that the response for a particular direction and frequency should be a complex constant, g. If g=1, the MVDR beamformer results. The resulting weight vector is given by Equation 7.7. For clarity the dependence on angular frequency has been omitted in what follows.

$$\mathbf{w} = g^{*} \frac{\mathbf{R}_x^{-1}\mathbf{a}(q)}{\mathbf{a}^H(q)\mathbf{R}_x^{-1}\mathbf{a}(q)} \qquad \textbf{(7.7)}$$

where:

$\mathbf{R}_x = \mathrm{E}\{\mathbf{x}\mathbf{x}^H\}$ is the spatial autocorrelation matrix of the sensor outputs. Here $\mathrm{E}\{\ \}$ denotes expectation. $\mathbf{R}_x$ is also referred to in the literature as the array cross-spectral matrix and as the array autocovariance matrix.

LCMV can be generalised to more than one constraint. In this case the constraint equations are written

$\mathbf{C}^H\mathbf{w} = \mathbf{f}$.

Here **C** is the constraint matrix (N x L) and **f** is the response vector (L x 1) where L is the number of constraints. In this case the optimum weight vector is

$$\mathbf{w} = \mathbf{R}_x^{-1}\mathbf{C}\left(\mathbf{C}^H\mathbf{R}_x^{-1}\mathbf{C}\right)^{-1}\mathbf{f} \qquad \textbf{(7.8)}$$

Different types of constraints can be specified including: point constraints, derivative constraints, and eigenvector constraints. The generalised sidelobe canceller (GSC) is an alternative formulation of the LCMV beamformer and has some implementation advantages. The weight vector for the GSC is

$$\mathbf{w} = \mathbf{w}_0 - \mathbf{C}_n\mathbf{w} \qquad \textbf{(7.9)}$$

with

$\mathbf{w}_0 = \mathbf{C}\left(\mathbf{C}^H\mathbf{C}\right)^{-1}\mathbf{f}$

$\mathbf{w}_n = \left(\mathbf{C}_n{}^H\mathbf{R}_x\mathbf{C}_n\right)^{-1}\mathbf{C}_n^H\mathbf{R}_x\mathbf{w}_0$

Here $\mathbf{C}_n$ is an N x (N-L) matrix that is orthogonal to **C**. It may be obtained from **C** by Gram-Schmidt orthogonalization, QR decomposition or singular value decomposition.

A generalised adaptive formulation of the statistically optimum beamforming algorithms is given which applies to MSC, Maximum SNR, and LMCV (GSC variant). Either block adaption or continuous (recursive) adaption can be used. For block adaption a block of data is used to calculate the sample covariance matrix and any other required statistics, which are then used in the formulae for the appropriate algorithm. For recursive adaption an iterative recursion relation, such as least-mean-

square (LMS) or recursive least squares (RLS) attempts to converge the weight vector to its optimum value over time. See VanVeen & Buckle (1988) for formulae.

Partially adaptive beamforming is also discussed in VanVeen & Buckle (1988). This attempts to reduce the dimensionality of the problem in order to reduce the computational load when there are many weights.

A limitation of statistically optimum beamforming techniques is that they assume a perfect knowledge of the spatial autocorrelation matrix $\mathbf{R}_x$ which must, in practice, be replaced by the sample autocorrelation matrix which is computed by an average over K snapshots:

$$\hat{\mathbf{R}} = \frac{1}{K}\sum_{k=1}^{K}\mathbf{x}_k\mathbf{x}_k{}^H \qquad \textbf{(7.10)}$$

where $\mathbf{x}_k$ is the array output vector for snapshot k.

The degree to which $\hat{\mathbf{R}}$ approximates $\mathbf{R}_x$ depends on the available integration time, which is limited by the requirement that both the noise and signal fields be statistically stationary over this time. As discussed in Nuttall & Wilson (Nuttall & Wilson 2000) this requirement is often not met for arrays operating at low frequencies, resulting in a significant degradation in beamformer performance.

Various techniques have been proposed to overcome the limitations imposed by finite integration time. The simplest is to diagonally load the autocorrelation matrix to obtain:

$$\mathbf{R}_x \approx \hat{\mathbf{R}} + e\mathbf{I} \qquad \textbf{(7.11)}$$

where e is an appropriately chosen positive constant. This method is shown in Cox et al. (1987) to be equivalent to placing a constraint on the gain of the beamformer when the noise is spatially white.

Another approach is to combine averaging in time (as in Equation 7.10) with averaging across a narrow band of frequencies. In order to perform the averaging in frequency it is necessary to correct for the variation of phase shift with frequency for a constant look direction. This is done by using the so-called steered covariance matrix (STCM) (Krolik & Swingler 1989, Swingler 1999):

$$\mathbf{R}_{STCM}(q) = \sum_{m=1}^{M} \mathbf{T}_m(q)^H \hat{\mathbf{R}}(f_m)\mathbf{T}_m(q) \qquad \textbf{(7.12)}$$

where $\mathbf{T}_m(q)$ is a diagonal matrix which transforms the received signals so that a source of frequency f_m located at angle q would give a result with zero phase shift. In other words, if the array was only illuminated by this source,

$$\mathbf{z}_m = \mathbf{T}_m(q)^H \mathbf{x}_m \qquad \textbf{(7.13)}$$

would be a vector of real numbers.

If $\mathbf{R}_{STCM}(q)$ is used in place of $\mathbf{R}_x$, the MVDR beamformer becomes the steered minimum variance (STMV) beamformer with weights given by:

$$\mathbf{w} = \frac{\mathbf{R}_{STCM}(q)^{-1}\mathbf{1}}{\mathbf{1}^H \mathbf{R}_{STCM}(q)^{-1}\mathbf{1}} \qquad \textbf{(7.14)}$$

where $\mathbf{1}$ represents a column vector of ones.

Note that the STMV beamformer requires the computation of a different covariance matrix (and its inverse) for each look direction, resulting in considerably more computational overhead than the MVDR beamformer.

Another limitation of statistically optimum beamformers is their sensitivity to interference from sources that are coherent with sources in the desired look direction, which can result in cancellation of the desired signal. In the case of uniform line arrays spatial averaging has been used to reduce this sensitivity at the expense of reduced angular resolution (Raghunath & Reddy 1992). This involves dividing the array into a number of overlapping sub-arrays of equal size and computing a covariance matrix by averaging the covariance matrices of the individual sub-arrays.

The problem of compensating statistically optimum beamformers for high bearing rate targets has been considered by Yang (2003). The issue here is that the target motion further reduces the number of snapshots available for estimating the array covariance matrix and consequently degrades the performance of the beamformer, especially its ability to detect low-level targets in the presence of strong interferers. The approach taken by Yang (2003) is to use a rotating coordinate frame to track the change in signal bearing, thus allowing much longer integration times. However, this presupposes that the bearing rate can be estimated in advance, or that sufficient

computational resources are available to carry out a search over possible bearing rates.

7.1.1.3 Broadband beamformers

Broadband beamforming can be carried out in either the time domain or the frequency domain. The frequency domain method involves Fourier transforming the output of each sensor and then applying a narrowband beamforming algorithm to each frequency bin.

Time domain broadband beamforming is commonly used in applications such as teleconferencing where the array output signal is required in real-time. A popular architecture is shown in Figure 7.1(a) (adapted from VanVeen & Buckle 1988) in which each sensor output is sampled via a filter that provides the required frequency-dependent time delays and amplitude shading. The filters are usually implemented as finite impulse response (FIR) filters (Figure 7.1(b)), which have tap weights (the w_k in Figure 7.1(b)) that can be altered to steer the array and adjust the beam pattern.

The array weight determination techniques discussed in Section 7.1.1.1 that are based on fitting a desired beam pattern can be generalised to the broadband case. See for example Jun et al. (2002). A discussion of other techniques that can be used to determine the filter weights is given in Section 7.1.6.

Broadband data dependent beamformers have also been developed based on the STMV beamformer described in the previous section. An example is given in Kim et al. (2002) which operates by dividing the frequency range of interest into a number of sub-bands and then applying the STMV beamformer to each sub-band.

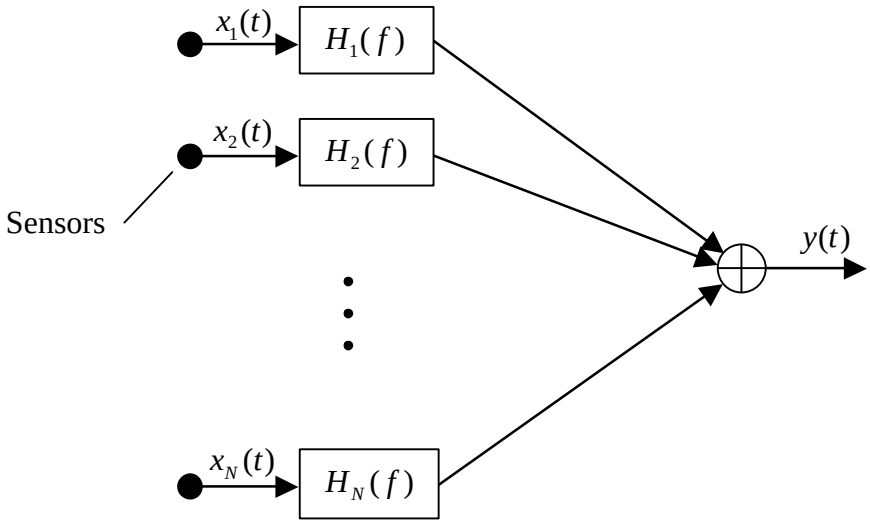

(a)

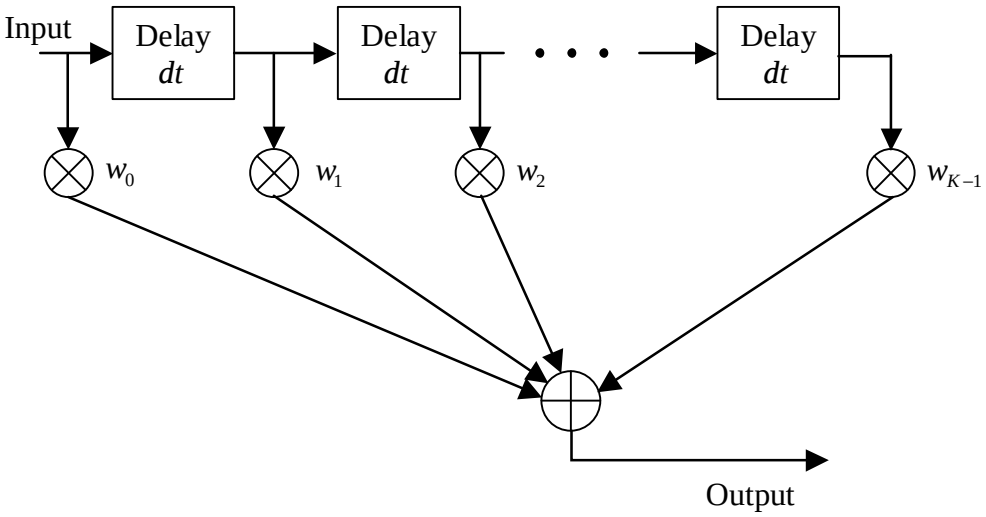

(b)

Figure 7.1 Schematic diagrams of (a) time domain broadband beamformer, and (b) finite impulse response (FIR) filter

7.1.2 High-resolution direction of arrival estimation

An excellent review of these techniques is given in Krim & Veberg (1996).

The starting point is the assumption that Q signals impinge on an array of N sensors from directions $q_1,...,q_Q$. The array output is therefore:

$$\mathbf{x} = \mathbf{A}(q)\mathbf{s} + \mathbf{n} \qquad \textbf{(7.15)}$$

where:

$\mathbf{A}(q) = \left[\mathbf{a}(q_1),...\mathbf{a}(q_Q)\right]$ is the steering matrix $(N \times Q)$,

$\mathbf{s} = \left[s_1,...,s_Q\right]^T$ is the signal vector $(Q \times 1)$, and

$\mathbf{n}$ is a noise vector $(N \times 1)$

The spatial covariance matrix is

$$\mathbf{R}_x = E\left\{\mathbf{x}(t)\mathbf{x}^H(t)\right\} = \mathbf{A}E\left\{\mathbf{s}(t)\mathbf{s}^H(t)\right\}\mathbf{A}^H + E\left\{\mathbf{n}(t)\mathbf{n}^H(t)\right\} = \mathbf{A}\mathbf{P}\mathbf{A}^H + s^2\mathbf{I} \qquad \textbf{(7.16)}$$

The last form of the equation makes the assumption that the noise is uncorrelated between sensors with variance s^2 (i.e. it is spatially white).

Note that the form of $\mathbf{R}_x$ is:

$$\mathbf{R}_x = \begin{bmatrix} x_1x_1^* & x_1x_2^* & \cdots & x_1x_N^* \\ x_2x_1^* & x_2x_2^* & & \\ \vdots & & \ddots & \\ x_Nx_1^* & & & x_Nx_N^* \end{bmatrix}$$

The covariance matrix can be factorised into its spectral factorisation:

$$\mathbf{R}_x = \mathbf{U}\Lambda\mathbf{U}^H \qquad \textbf{(7.17)}$$

Here:

$\mathbf{U}$ is a unitary matrix (i.e. its inverse is its Hermitian transpose), and $\Lambda = diag\{l_1, l_2,..., l_N\}$ is a diagonal matrix of real eigenvalues ordered such that $l_1 \geq l_2 \geq ... \geq l_N > 0$.

Any vector orthogonal to $\mathbf{A}$ is an eigenvector of $\mathbf{R}_x$ with eigenvalue s^2.

There are $N - Q$ such vectors because the columns of $\mathbf{A}$ span the Q element signal subspace of the total N element vector space. Note that the other eigenvalues of $\mathbf{R}_x$ are all larger than s^2.

The spectral factorisation can be partitioned into signal and noise components as follows:

$$\mathbf{R}_x = \mathbf{U}_s \Lambda_s \mathbf{U}_s{}^H + \mathbf{U}_n \Lambda_n \mathbf{U}_n{}^H \qquad \textbf{(7.18)}$$

where:

Λ_s contains all the eigenvalues greater than s^2, and

Λ_n contains all the eigenvalues equal to s^2.

Note that although $\mathbf{U}$ is unitary, so that $\mathbf{U}\mathbf{U}^H = \mathbf{I}$, this is not the case for $\mathbf{U}_s$ or $\mathbf{U}_n$

The projection operators onto the noise and signal subspaces are:

$$\Pi = \mathbf{U}_s \mathbf{U}_s{}^H = \mathbf{A}(\mathbf{A}^H\mathbf{A})^{-1}\mathbf{A}^H \qquad \textbf{(7.19)}$$

and

$$\Pi^{\perp} = \mathbf{U}_n \mathbf{U}_n{}^H = \mathbf{I} - \mathbf{A}(\mathbf{A}^H\mathbf{A})^{-1}\mathbf{A}^H \qquad \textbf{(7.20)}$$

In practice $\mathbf{R}_x$ is not usually known and the sample covariance matrix has to be used in its place (see Equation 7.10).

7.1.2.1 The multiple signal classification (MUSIC) algorithm

This is one of the best-known high-resolution direction of arrival estimation algorithms. The steps in the MUSIC algorithm are:

1. Obtain an estimate of the spatial covariance matrix, $\hat{R}$
2. Determine the eigenvalues and eigenvectors of $\hat{R}$ and separate the eigenvectors into the signal and noise eigenvectors (The signal eigenvectors are those with the Q highest eigenvalues).
3. Form the orthogonal projection onto the noise subspace: $\hat{\Pi}^{\perp} = \hat{\mathbf{U}}_n \hat{\mathbf{U}}_n{}^H$
4. The MUSIC spatial spectrum is then:
   $$P_M(q) = \frac{\mathbf{a}^H(q)\mathbf{a}(q)}{\mathbf{a}^H(q)\hat{\Pi}^{\perp}\mathbf{a}(q)}$$
   and this peaks in the direction of arrival.

This works because the noise eigenvectors are orthogonal to **A**, and consequently:

$$\mathbf{U}_n{}^H \mathbf{a}(q) = 0,\ q \in \{q_1,...,q_M\}$$

This means that the denominator of P_M goes to zero when $q \in \{q_1,...,q_M\}$.

The MUSIC algorithm has much better angular resolution than the beamforming methods and its angular resolution improves as the length of the data sequence increases and/or the signal to noise ratio increases.

Note that MUSIC does not work when coherent signals are present with different directions of arrival although techniques are available to reduce this problem at the expense of other aspects of the algorithm performance. (See Krim & Veberg 1996 for details.)

7.1.2.2 Parametric methods

Deterministic maximum likelihood (DML)

This method assumes a vector of Q deterministic signals

$$\mathbf{s}(t) = [s_1(t),...,s_Q(t)]^T$$

and spatially white, circularly symmetric noise with variance s^2. (A complex random process is circularly symmetric if its real and imaginary parts are identically distributed and have a skew-symmetric cross-variance.) Defining:

$\mathbf{A}^+ = (\mathbf{A}^H\mathbf{A})^{-1}\mathbf{A}^H$ (pseudo inverse of A)

$\Pi_A = \mathbf{A}\mathbf{A}^+$

$\Pi_A^\perp = \mathbf{I} - \Pi_A$

Then the DOA estimates are obtained by finding the set of M angles that minimise the following function with respect to the M arrival directions:

$$\hat{q}_{DML} = \arg\left\{\min_q (Tr(\Pi_A^\perp \hat{\mathbf{R}}))\right\} \qquad \textbf{(7.21)}$$

Importantly, the signals can then be estimated from:

$$\mathbf{s}(t) = \mathbf{A}^+\mathbf{x}(t) \qquad \textbf{(7.22)}$$

and the noise variance from:

$$\hat{s}^2 = \frac{1}{N} Tr(\Pi_A^\perp \hat{\mathbf{R}}) \qquad \textbf{(7.23)}$$

Stochastic maximum likelihood (SML)

This method works in a similar way but treats the signal as Gaussian rather than deterministic. The signal covariance matrix, the noise variance and the directions of arrival are outputs from the algorithm, but again a Q-dimensional search is required.

Other parametric methods

Several parametric subspace or subspace fitting methods are also described. These include signal subspace fitting (SSF), weighted subspace fitting (WSF), and noise subspace fitting (NSF). WSF in particular gives similar results to SML but at reduced computational cost.

For uniform line arrays (ULAs) the A matrix has a special form and a number of other algorithms are available. These include Root-MUSIC, ESPIRIT, IQML and Root-WSF. Root-MUSIC has similar asymptotic properties to MUSIC but behaves significantly better for small samples. Root-WSF is a very efficient algorithm for performing the WSF optimisation problem for uniform line arrays and appears to be one of the best algorithms for these arrays. Note that far-field sources are also assumed.

Reduced dimension beam-space processing

The idea here is to reduce the dimension of the problem by transforming the original array data to a smaller dimension subspace before applying the above algorithms. This is achieved by effectively narrowing the field of view of the array by a preliminary beamforming step, the output of which is given by:

$$\mathbf{z} = \mathbf{T}^H \mathbf{x} \qquad \textbf{(7.24)}$$

where the columns of $\mathbf{T}$ are chosen as appropriate steering vectors. The above algorithms are then applicable with $\mathbf{a}$ replaced by $\mathbf{T}^H\mathbf{a}$ and s^2 by $s^2\mathbf{T}^H\mathbf{T}$. This technique can improve the performance of high-resolution techniques such as MUSIC as well as offering computational advantages.

Anderson (1993) presents an algorithm for determining $\mathbf{T}$ which allows high-resolution direction of arrival estimation methods to be applied in beam-space with

the same accuracy as if they were applied directly to the original sensor data. The method of determining $\mathbf{T}$ is as follows:

1. Specify a d element vector of design directions covering the expected range of arrival directions q_a to q_b : $\mathbf{?} = [q_a, q_a + dq, q_a + 2dq, \cdots, q_b - dq, q_b]^T$ where dq is the beamwidth (angle between 3dB points).
2. Form the matrix $[\mathbf{A}(\mathbf{?})\ \mathbf{D}(\mathbf{?})]$ and calculate its singular value decomposition $\mathbf{USV}^H$ (Press et al. 1988, Chapter 2). Here $\mathbf{A}(\mathbf{?})$ is the steering matrix (see Equation 7.15) and $\mathbf{D}(\mathbf{?}) = [\mathbf{d}(q_1), \cdots \mathbf{d}(q_d)]$ with $\mathbf{d}(q_j) = \frac{\partial}{\partial q_j}\mathbf{a}(q_j), \quad j = 1, \cdots, d$.
3. The required transformation matrix is then given by $\mathbf{T} = \mathbf{U}$.

Note, however, that the derivation assumes spatially uncorrelated noise and stochastic signals, and that the DOA estimation algorithm's performance is severely degraded in the presence of sources close to but outside the range of expected directions. The paper uses the WSF algorithm, but appears to be applicable to most high-resolution algorithms.

7.1.2.3 *Broadband direction of arrival estimation methods*

Krim & Veberg (1996) mention three methods of applying high-resolution direction of arrival estimation algorithms to broadband sources.

The simplest is to narrowband filter via an FFT and then apply one of the narrowband algorithms described above at each frequency. The results can then be combined by some form of averaging. The primary disadvantage of this method is that the averaging is incoherent and consequently does not fully exploit the information inherent in the signal.

This limitation is overcome by a technique put forward by Wang & Kaveh (1985) called the coherent signal-subspace method (CSM). The basic idea is to apply a transformation of the same form as Equation 7.13 to the array output at each frequency. The transformation matrices, $\mathbf{T}(f_j)$, are chosen so as to meet the criterion:

$$\mathbf{T}^H(f_j)\mathbf{A}(f_j) = \mathbf{A}(f_0) \qquad \textbf{(7.25)}$$

where:

f_0 is the receiver centre frequency.

The correlation matrices, $\mathbf{R}_z(f_j)$, formed from the transformed array outputs can then be coherently averaged across frequency to produce $\hat{\mathbf{R}}_z$, which is used in an algorithm such as MUSIC to obtain the directions of arrival.

One of the subtleties of implementing this algorithm is that the transformation matrices depend on the direction of arrival so a preliminary beamforming step is required in order to obtain a preliminary estimate of this. Wang & Kaveh (1985) give various methods for determining appropriate transformation matrices (which are not unique) but the methods given in Hung & Kaveh (1988) result in unitary transformation matrices, which have better noise performance. These are given by:

$$\mathbf{T}(f_j) = \mathbf{U}(f_j)\mathbf{V}^H(f_j) \qquad \textbf{(7.26)}$$

where:

$\mathbf{U}(f_j)$ and $\mathbf{V}(f_j)$ are the left and right singular vectors of $\mathbf{A}(f_j)\mathbf{A}^H(f_0)$ which may be obtained by singular value decomposition (Press et al. 1988, Chapter 2).

A time domain implementation of CSM is described in Sivanand & Kaveh (1991).

Successful application of CSM relies heavily on the initial arrival angle estimate, which causes problems in practice. To overcome this several alternative methods of determining the transformation matrices $\mathbf{T}(f_j)$ have been proposed and are summarised in Bourennane & Bendjama (2002). The most promising appears to be to use:

$$\mathbf{T}(f_j) = \mathbf{V}_s(f_0)\mathbf{V}_s{}^H(f_j) \qquad \textbf{(7.27)}$$

where

$\mathbf{V}_s(f_j) = \left[\mathbf{v}_1(f_j), \mathbf{v}_2(f_j), \cdots, \mathbf{v}_Q(f_j)\right]$ and the $\mathbf{v}_m(f_j)$ are the eigenvectors corresponding to the Q largest eigenvalues of the covariance matrix $\mathbf{R}_x(f_j)$. Bourennane & Bendjama (2002) go on to develop a broadband direction of arrival estimation algorithm based on higher order statistics, which has less dependence on

assumptions about the noise and signal correlation properties than the other methods described.

An alternative method for combining information across frequencies is the steered covariance matrix (STCM) method described in Section 7.1.1.2.

Another wideband method discussed in Krim & Veberg (1996) is described in detail in Su & Morf (1986). This method models each source using an auto regressive moving average (ARMA) finite-difference model and estimates the poles of the resulting source spectra from the array output data. A narrowband technique is then applied at the poles to determine the corresponding directions of arrival.

Ottersten & Kailath (1990) present an algorithm that combines the ARMA modal decomposition technique with the ESPIRIT narrowband algorithm to provide a narrowband direction of arrival estimation method that is less sensitive to array geometry errors than the algorithm described by Su & Morf (1986). Note that this algorithm assumes that the array is comprised of two identical sub-arrays, the relative locations of which are known.

7.1.3 Inverse beamforming

Inverse beamforming refers to a technique for estimating the directionality of the acoustic field directly from the spatial correlation between array element pairs, followed by specific target tracking algorithms. There are two methods for determining the directionality of the acoustic field which are referred to as the Fourier integral method (FIM) and the Fourier series method (FSM).

Derivations of the FIM and FSM methods are given in Nuttall & Wilson (1991) for a uniform line array and for planar and volumetric arrays. A useful summary of the line array case is given in Wilson (1995), some performance results are described in Solomon et al. (2000), and an adaptive extension to the technique is described in Donald et al. (2000). FIM and FSM give very similar results and FIM is generally preferred because of its greater computational efficiency.

Most work has been done on the line array version of FIM, which has been demonstrated to give results superior to conventional beamforming in real ocean environments. The technique also compares favourably to MVDR and high-resolution methods, especially in low signal to noise ratio conditions. Note that FIM

and FSM apply only to plane waves, although Nuttall & Wilson (1991) state that they are attempting to extend them to spherical wavefronts.

FIM and FSM are two different computational schemes for inverting the following integral equation (called the inverse beamforming, or IBF integral equation)

$$R_x(j,k,f_i) = \int_0^p FIM(q, f_i) e^{i\mathbf{k}.(\mathbf{r}_j - \mathbf{r}_k)} dq \qquad \textbf{(7.28)}$$

where

$R_x(j,k,f_i)$ is the covariance matrix element between hydrophones j and k in frequency bin i.

$FIM(q, f_i)$ is the acoustic field plane wave density as a function of bearing q and frequency f_i

k is the acoustic wave vector

$\mathbf{r}_p$ is the position vector of hydrophone p.

Note that this is the 2D version of the IBF equation, the analogous 3D equation is given in Nuttall & Wilson (1991).

The FIM solution for an equally spaced line array of N elements is given by:

$$FIM(q, f) = \frac{1}{2N-1} \sum_{p=-(N-1)}^{N-1} R_x(p, f) e^{i2ppfd\cos(q)/c} \qquad \textbf{(7.29)}$$

where

$$R_x(p, f) = \frac{1}{N-|p|} \sum_{n=0}^{N-1-p} R_x(n, n+p, f)$$

The FIM beam pattern has a narrower main lobe than the conventional beamformer (CBF), by a factor of about 0.68, and has both positive and negative sidelobes. In the case of FIM the negative sidelobes represent a negative response to incident sound intensity (rather than pressure) and account for FIM's superior detection capability compared to CBF in the low SNR case (about 3dB). In a high SNR environment, however, the relatively high absolute levels of the sidelobes can cause masking of other, lower intensity sources.

Solomon et al. (2000) used a weighted version of FIM, called WFIM, which reduces the sidelobe levels at the expense of broadening the main beam by introducing a Hanning weighting function:

$$FIM(q, f) = \frac{1}{2N-1} \sum_{p=-(N-1)}^{N-1} w_p R_x(p, f) e^{i2ppfd\cos(q)/c}$$

with

$$w_p = 1 - \cos(2pk/N)$$

7.1.4 Matched-field processing

The array-processing techniques discussed so far take no account of the effect of the propagation environment on the array response. As pointed out in Wilson & Veenhuis (1997) multipath propagation in the shallow water environment can result in a significant degradation in the performance of these techniques, even for relatively short, horizontal arrays. Degradation occurs for arrivals off broadside because of the phase change introduced by modal interference. This phase change is a function of range and is not well represented as a plane wave front. Another way of looking at it is that rays with different grazing angles (horizontal wavenumbers) coming from the same azimuth have different wavenumber components along the array, except at broadside.

Matched-field processing (MFP) is a term that encompasses algorithms that have been developed to account for propagation effects, and indeed to exploit what is known about the environment to obtain more information about the source than would be possible in a free-field situation. For example it is often possible to obtain the depth and range of a source using a single vertical line array. MFP has been a very active field of research over the last decade with a consequent extensive literature so this review has been restricted to a few key papers that provide overviews of the field.

Porter (1993) is a very readable paper that provides a concise overview of ray, wavenumber integration, normal mode and PE models, together with a good introductory description of matched-field processing which is described in terms of modified beamforming.

The basic idea is to form the array output according to:

$$P(r,z) = \frac{\mathbf{a}^H \mathbf{R}_x \mathbf{a}}{\mathbf{a}^H \mathbf{a} \mathbf{x}^H \mathbf{x}} \qquad \textbf{(7.30)}$$

where:

$P(r,z)$ is known as the matched-field ambiguity function and is expected to peak at the true range and depth of the source,

$\mathbf{a}(r,z)$ is the acoustic field vector that would be received on the array due to a source at (r,z). This is the equivalent of the usual plane-wave steering vector but incorporates the complete information about the waveguide, and is usually computed using a standard acoustic propagation model.

$\mathbf{x}$ is the actual field vector received on the array, and

$\mathbf{R}_x = \mathrm{E}\{\mathbf{x}\mathbf{x}^H\}$ is the covariance matrix.

An excellent review of matched-field processing theory and experiment is given in Baggeroer et al. (1993). Theory is presented including "conventional MFP" which is essentially the method covered by Porter (above), and adaptive MFP which is based on the minimum variance distortionless response (MVDR) (or Capon) beamformer described in Section 7.1.1.2. The adaptive method is shown to have significantly lower sidelobes than the conventional method but is more sensitive to environmental mismatch.

MFP has primarily been used for source localisation in a known environment although there has also been some work on using MFP to determine environmental parameters where the source location is known, a method referred to as matched-field tomography.

Another area of research has been in determining both the source position and some environmental parameters. An example is given in Candy & Sullivan (1989) in which simulated data from a horizontal towed array is used to estimate normal mode wavenumbers and amplitudes. Their method can use various standard beamforming techniques, including conventional, MVDR, and what looks like a variant of MUSIC, to estimate the horizontal wavenumber spectrum, from which the normal modes are picked out. A mode vector is then formed and the phases of the elements

of the autocorrelation matrix of this mode vector are used to estimate the source range.

Many variations and extensions of matched-field processing have been proposed, including applications to tracking moving sources. Two notable papers on this last topic are Fawcett & Maranda (1993) in which a single measure is derived that combines the good tracking performance of matched-field processing near end-fire of a horizontal line array with the good performance of target motion analysis near broadside, and Fialkowski et al. (2001) in which a method of averaging ambiguity surfaces along a track is proposed that gives improved performance compared to computing individual ambiguity surfaces.

7.1.5 Model based array-processing

In this context model based processing refers to the application of the state-space techniques developed for the study of linear dynamic systems to array-processing. The following steps are required:

1. Express the problem in either continuous or discrete state-space form, with the states of the system representing the unknown parameters of the problem, and
2. Use a standard technique such as a Kalman-Bucy filter (continuous) or Kalman filter (discrete) to solve for the states.

The Kalman filter was discussed in Chapter 5, and for more detail see Grewel & Andrews (1993).

Candy & Sullivan (1992) present a state-space based method for estimating normal mode shapes and amplitudes from noisy vertical array data. Note that the method still requires knowledge of the top and bottom boundary conditions, although it is possible to deal with a depth-dependent sound velocity profile. The method is based on expressing the separated range and depth differential equations in state-space form, and using these equations as the dynamic model for a Kalman filter that combines a continuous dynamic model with a discrete observation equation. This dynamic model propagates the system state in range and depth, not in time. The system states are the modal functions and their differentials with respect to the vertical coordinate, and the observation equation links the pressure measurements to these states.

The same authors extend the approach further in a number of later papers including Candy & Sullivan (1994), in which efficient numerical techniques are developed for dealing with large arrays, and Candy & Sullivan (1996) which presents an algorithm for estimating the waveguide parameters.

Model based techniques for localising an acoustic source in a waveguide are given in Candy & Sullivan (1995) (narrowband source) and Candy & Sullivan (1998) (broadband source). Candy & Sullivan (1997) applies model based processing to the problem of bearing estimation from a moving towed array. The method achieves bearing angle accuracies similar to synthetic aperture techniques (see Section 7.1.7.1), despite there being no explicit beamforming structure specified.

7.1.6 Near-field sources

The beamforming techniques and many of the high-resolution techniques discussed above can be adapted to the situation where the sources are too close to the array for the plane-wave assumption to be valid simply by replacing the steering vector, $\mathbf{a}(q,w)$, with $\mathbf{a}(\mathbf{r},w)$, the response of the array to a source at position $\mathbf{r}$, thus effectively focusing the array at the source location. For example, Sahin & Miller (1999) apply a near-field version of the MUSIC algorithm to the localisation of electromagnetic scatterers and Yuen & Friedlander (1998) investigate the performance of an ESPIRIT-like algorithm for near-field source localisation.

When beamforming in the near-field the primary complication is the determination of the array weights (or filter coefficients for a broadband array) required to obtain the desired beam pattern. This is straightforward in the far-field case where the beam pattern and the array weights are related via a spatial Fourier transform (Carey & Moseley 1991), and many standard weighting functions are available (Harris 1978). In the near-field case, however, it is necessary to use more sophisticated techniques.

Greening & Foster (2000) discuss simulated annealing methods for obtaining optimum element spacing in sparse linear arrays and also both simulated annealing and a simpler heuristic technique for determining optimum weighting to apply to the sensor elements to achieve a specified beam pattern. Although intended for the

design of far-field beam patterns the techniques described are equally applicable to the near-field case.

The heuristic technique is applied to linear arrays where the sensor positions are known, but should be simple to extend to the distorted array case. The basic idea is to adjust the weights so as to minimise the maximum difference between the actual and desired beam patterns.

The hydrophone weight for sensor i at iteration n is given by $w_i^{(n)}$, then if q_n is the direction to the worst sidelobe (i.e. largest level), then

$$w_i^{(n+1)} = w_i^n - e\sum_l w_l^{(n)} \cos(k(x_i - x_l)\sin(q_n)) \qquad \textbf{(7.31)}$$

Here e is a (small) control parameter, k is the wavenumber, and x_p is the position of hydrophone p. The weights are normalised before proceeding to the next iteration.

Note that the iteration is designed to suppress (i.e. reduce the weights of) hydrophones that add in-phase in the sidelobe direction while enhancing hydrophones that add out of phase.

An algorithm based on simulated annealing is presented in Trucco (2002) for the design of broadband beamformers. In this case the algorithm determines the element positions and weights required to obtain the desired beam pattern while minimising the number of elements.

Kennedy et al. (1998) presents a technique for designing near-field, broadband, beamformers with a specified beam pattern. The procedure is to transform the specified near-field beam pattern to an equivalent far-field beam pattern and then design the array weights so as to achieve the pattern. The beamformer architecture comprises a filter on each array element followed by a summation, and the algorithm gives the required frequency response of each element's filter. The filters were implemented in the time domain using FIR design techniques.

An example is given of the design of a beamformer with a near-field response consisting of a Chebyshev beam pattern, which is invariant over an octave. The beamformer was implemented using a linear, unequally spaced, array of

microphones. Several algorithms for determining the element filter coefficients to obtain the desired response are also given.

In Kennedy et al. (1999) a method of designing a near-field beamformer that is computationally simpler than Kennedy et al. (1998) is presented. The procedure is as follows:

1. Specify the desired beam pattern at distance r.
2. Determine the weights that will give the complex conjugate of this beam pattern in the far-field.
3. Using these weights compute the corresponding near-field beam pattern at distance r.
4. Determine the weights that would give the complex conjugate of this beam pattern in the far-field. These weights will then give the desired beam pattern in the near-field.

The main limitation of the technique is that the beam pattern must be defined on the surface of a sphere.

Nordholm et al. (1998) describe another method of synthesising a broadband near-field beamformer. This method uses the same beamformer structure as in Kennedy et al. (1998), but directly computes the FIR filter coefficients using numerical optimisation. The method seems very general but is likely to be computationally intensive.

Abhayapala et al. (1999) propose a noise model for near-field beamformers which assumes an isotropic distribution of sources at a specified radius from the array. This model is then used to design a beamformer based on maximising the ratio of the signal power to the total noise power, resulting in a form of near-field statistically optimum beamformer.

7.1.7 Application to a moving, distorting array

7.1.7.1 Moving arrays

The bulk of the passive array-processing literature dealing with moving arrays is concerned with source localisation using a horizontal line array that is being towed

in a straight line at a constant speed. The aim is to exploit the additional bearing resolution obtainable from the "synthetic aperture" swept by the array. These techniques are known as passive synthetic aperture (PASA) processing and differ from the commonly used radar and active sonar synthetic aperture processing because PASA techniques have to cope with source signals of unknown centre frequency and limited temporal and spatial coherence.

Early attempts at PASA applied similar processing methods to active synthetic aperture processing and encountered limitations due to phase errors introduced by the medium and limited source coherence. Despite this there were successful applications to experimental data (eg Yen & Carey 1989).

A major step forward was the introduction of the algorithm that appears in Stergiopoulos (1989). This method uses the phase correlation between different hydrophones that are in the same location in successive sample periods to correct for phase fluctuations in the signal and environment, resulting in a very robust approach.

In Stergiopoulos (1990) the same technique is applied to the bearing estimation problem and it is also shown that the method achieves the Cramer Rao lower bound (the theoretical statistical variance in the bearing estimate). An alternative algorithm based on a maximum likelihood estimator is also described.

Sullivan et al. (1992) is the editorial for a special issue of the IEEE Journal of Oceanic Engineering devoted to synthetic aperture processing in acoustics. The editorial provides a very useful introduction to the subject and describes PASA as being like the processing used in conventional beamforming but with the incoherent averaging of beamformer outputs at successive snapshots being replaced by a coherent averaging process.

The authors make the point that PASA processing trades temporal gain for spatial gain and has no inherent advantage in terms of array gain compared to conventional array-processing where the noise field is isotropic. PASA can, however, give considerable improvements in bearing resolution and, for anisotropic noise, or where there are interfering sources close to the desired source PASA can give significant detection gains. When estimating both the bearing and frequency of a source PASA gives slightly worse results than using the same array in a stationary configuration,

but if either frequency or bearing is known the other parameter can be estimated more accurately than for a stationary array.

In the special issue Williams & Harris (1992) present a brief summary of a number of different techniques applicable to synthetic aperture sonar processing including both beamforming and Doppler processing techniques. Issues concerned with resolving bearing and source frequency ambiguities by manoeuvring are also discussed.

Other papers in the special issue, or published shortly afterwards, have explored the limitations of these algorithms and PASA in general (Edelson & Sullivan 1992, Edelson & Tufts 1992, and Fawcett 1993), introduced new algorithms (Nuttall 1992, Stergiopoulos & Urban 1992b, and Yen 1992), and applied the techniques to experimental data (Stergiopoulos & Urban 1992a).

Already mentioned in Section 7.1.5, Sullivan & Candy (1997) apply model-based processing to the problem of bearing estimation from a moving towed array. Basically the idea is to parameterise the problem (in this case frequency and bearing of two far-field sources) and then use a Kalman filter to estimate the parameters based on the measured time series at the hydrophones. The method achieves bearing angle accuracies similar to the synthetic aperture techniques described above, despite there being no explicit beamforming structure specified.

7.1.7.2 Moving, distorting arrays

Felisberto & Jesus (1996) discuss towed array beamforming using the estimated shape of the array during manoeuvres. Array shape was estimated from six compasses, six tilt-meters and two pressure gauges using a simple interpolation scheme. The array was also instrumented with accelerometers but these weren't used.

Beamforming was carried out in the frequency domain using an approximate delay and sum beamformer (i.e. a conventional time-domain beamformer) which was derived from the exact delay and sum beamformer by assuming an equal hydrophone spacing in the x direction (along the array), but allowing an offset in the y (crosswise) direction.

The authors state that in a comparative study the approximate beamformer was indistinguishable from the exact beamformer near broadside and a maximum error of 5 dB occurred at angles near endfire.

Field results are given showing a comparison of beamforming assuming a straight array to beamforming using the approximate beamformer and the array deformation determined from the heading sensors. Unfortunately these two sets of results are plotted in a different way, which makes comparison difficult. The results do, however, show an improvement in the ability of the array to resolve left-right ambiguity when it is distorted in shape.

Two recent papers deal with the application of statistically optimum (adaptive) beamforming to towed arrays as they distort during manoeuvres. In both cases the array is assumed to be distorting slowly enough that its shape can be assumed constant during the time it takes to accumulate one snapshot of data. Gerstoft et al. (2003) make use of the broadband nature of the particular signals used in their experiment to allow the computation of the steered covariance matrix (see Section 7.1.1.2, Equation 7.12), and subsequently the beamformer output, from a single snapshot of data.

Greening & Perkins (2002), derive a form of the MVDR beamformer (Section 7.1.1.2) that can be applied to narrowband data. In their approach each element of the weight vector, w_n, is considered to be the product of a time independent weight, b_n, and the time varying steering vector element, a_n. Minimising the array output subject to a constraint of unity gain in the look direction then yields the following formula for the vector of time independent weights:

$$\mathbf{b} = \frac{\mathbf{P}^{-1}\mathbf{1}}{\mathbf{1}^H \mathbf{P}^{-1}\mathbf{1}} \qquad \textbf{(7.32)}$$

where:

$\mathbf{P} = \mathrm{E}\{\mathbf{a}^H \mathbf{x}\mathbf{x}^H \mathbf{a}\}$ and $\mathbf{1}$ is a column vector of ones. The beamformer output power is then given by:

$$\Pi = \frac{1}{\mathbf{1}^H \mathbf{P}^{-1}\mathbf{1}} \qquad \textbf{(7.33)}$$

Gorban (2000) is a highly theoretical paper developing formulae for maximum likelihood estimators for moving, distorting, antennae. This paper considers the case

of an antenna moving sufficiently slowly that it can be considered stationary over short time periods and maximum likelihood estimators are then developed for deterministic and stochastic signals in the case of spatially uncorrelated noise and spatially uncorrelated noise with a single interferer.

There are two steps to the process:

1. carry out spatial processing over each time interval (using the signal Green's function to include propagation effects), and
2. form a weighted sum of the results of 1, either coherently, in the case of deterministic signals, or incoherently in the case of stochastic signals. In the deterministic case the complex signal spectrum is used as the weight whereas in the incoherent case the signal power spectrum is used.

If the noise includes a local interferer then the MLE processor takes the form of a sidelobe canceller where a beam is formed in the direction of the interferer and a proportion of this beam's output is subtracted from the main beam output before carrying out the summation over time periods.

For uncorrelated noise the SNR for the moving and stationary antennae are the same whereas for correlated noise the moving antenna can give superior results, but this depends on the details of the scenario.

The formulae given in the reference assume a lot of prior information about the signal, noise, and medium characteristics and aren't practical to implement in the form in which they are given. They are, however, useful for understanding general concepts and justifying specific approaches.

7.2 Implemented Algorithms

The array-processing algorithms chosen for implementation are described in detail in the following subsections. They included a simple time-domain, data independent beamformer, both data independent and data dependent frequency domain beamformers, and a deterministic maximum likelihood processor. The maximum likelihood processor operated in the frequency domain and solved for the amplitude distribution of a hypothetical array of acoustic sources at specified locations on the vessel. All of these algorithms required appropriate adaptations so that they could be applied to the near-field, moving, distorting array scenario considered here.

7.2.1 Beamformer architectures

From plots of the hydrophone positions relative to the tow-vessel given in Section 5.2.4.2 it was apparent that the velocity of the array relative to the vessel at broadside was approximately 2.5 m/s during Serial 1A, and 4.0 m/s during Serials 1C and 1D. Dealing with this relative motion was therefore an important consideration when deriving beamforming algorithms that could be used to image the noise sources on the tow-vessel. Several different architectures were considered to deal with this problem. The first was the time-domain delay and sum beamformer shown in Figure 7.2. In this architecture the time delay is continually adjusted to keep the beam focused on the desired point on the vessel. Fourier transforming the output of the beamformer then provides frequency domain information. Note that the beamformer shown in Figure 7.2 produces an output for a single focal point and has to be replicated for each additional focal point.

In principle this architecture has the advantage that the motion of the hydrophones can be compensated exactly in cases where the direct path dominates the received energy. Generating the required time delays, which vary with time, requires non-uniform re-sampling (i.e. interpolation) of the signal from each hydrophone, which introduces errors unless the sample rate is very high. Each combination of hydrophone and focal point results in a time delay that is a unique function of time and therefore requires a different re-sampling, resulting in a high computational load. Another disadvantage of this method is that control of the beam shape is only possible using simple amplitude weighting of the hydrophones, although the weights

can be time-varying. It is also difficult to adapt this method to deal with situations where significant amounts of received energy arrives via indirect paths, as in these cases the phases of the received signals are not well represented by simple frequency independent delays.

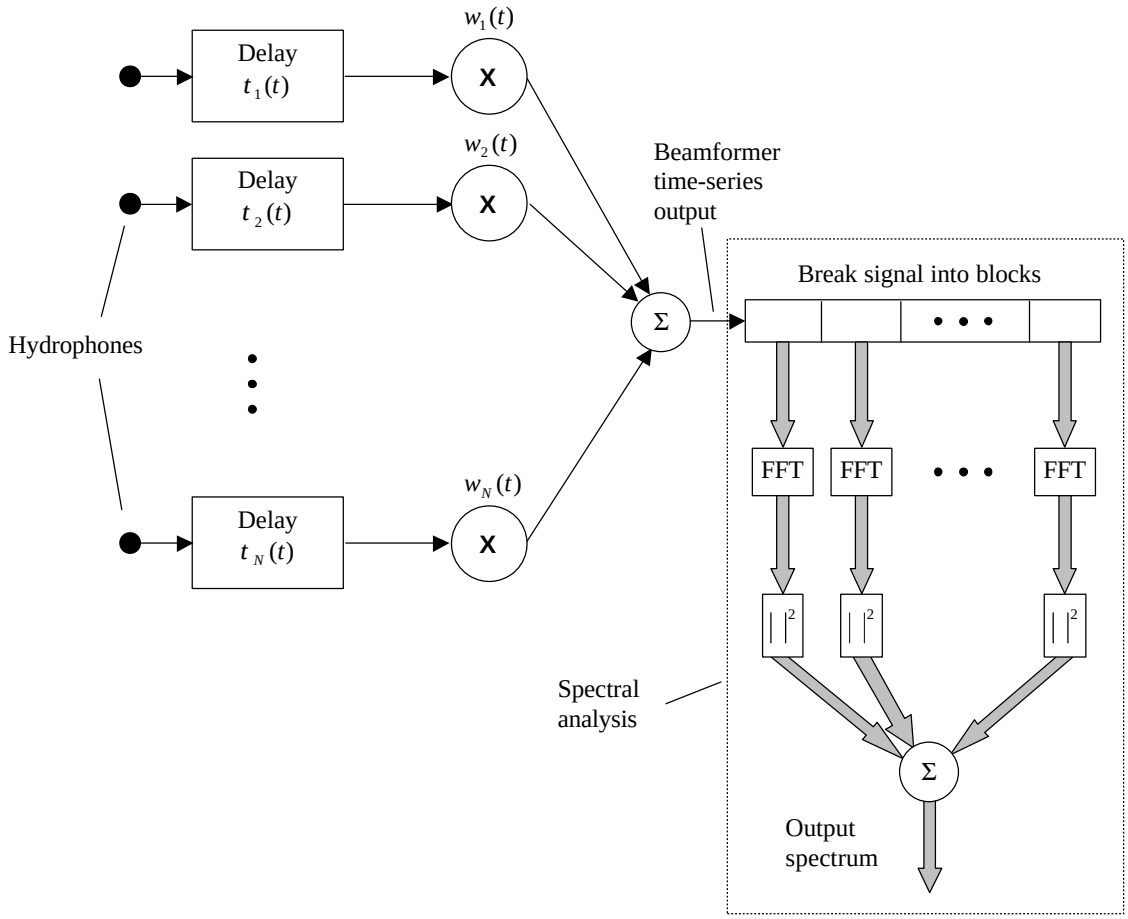

Figure 7.2 Block diagram of delay and sum time-domain beamformer

The architecture shown in Figure 7.3 (again for a single beam) provides better control over the beam pattern and also has the potential to compensate for propagation effects by incorporating a finite impulse response (FIR) filter in the signal path from each hydrophone. This is effectively the broadband time-domain beamformer discussed in Section 7.1.1.3 with the addition of a time-varying delay to minimise the required number of FIR filter taps. In this case the FIR filters are required to perform both beam shaping and the removal of propagation effects and are time-varying because the propagation effects vary with hydrophone position. The filters can be designed using the techniques described in Section 7.1.1.3 with the

steering vectors used in the calculation computed using an appropriate propagation model. An alternative approach to filter design is to recognize that the filters perform the same function as channel equalisers in a communication system and then to use standard equaliser design procedures (see for example Mulgrew & Cowan 1988 or Haykin 1996). Note that a new filter design is required for each time-step, leading to a very high computational load. In practice this can be somewhat reduced by computing the filter weights at longer intervals and interpolating.

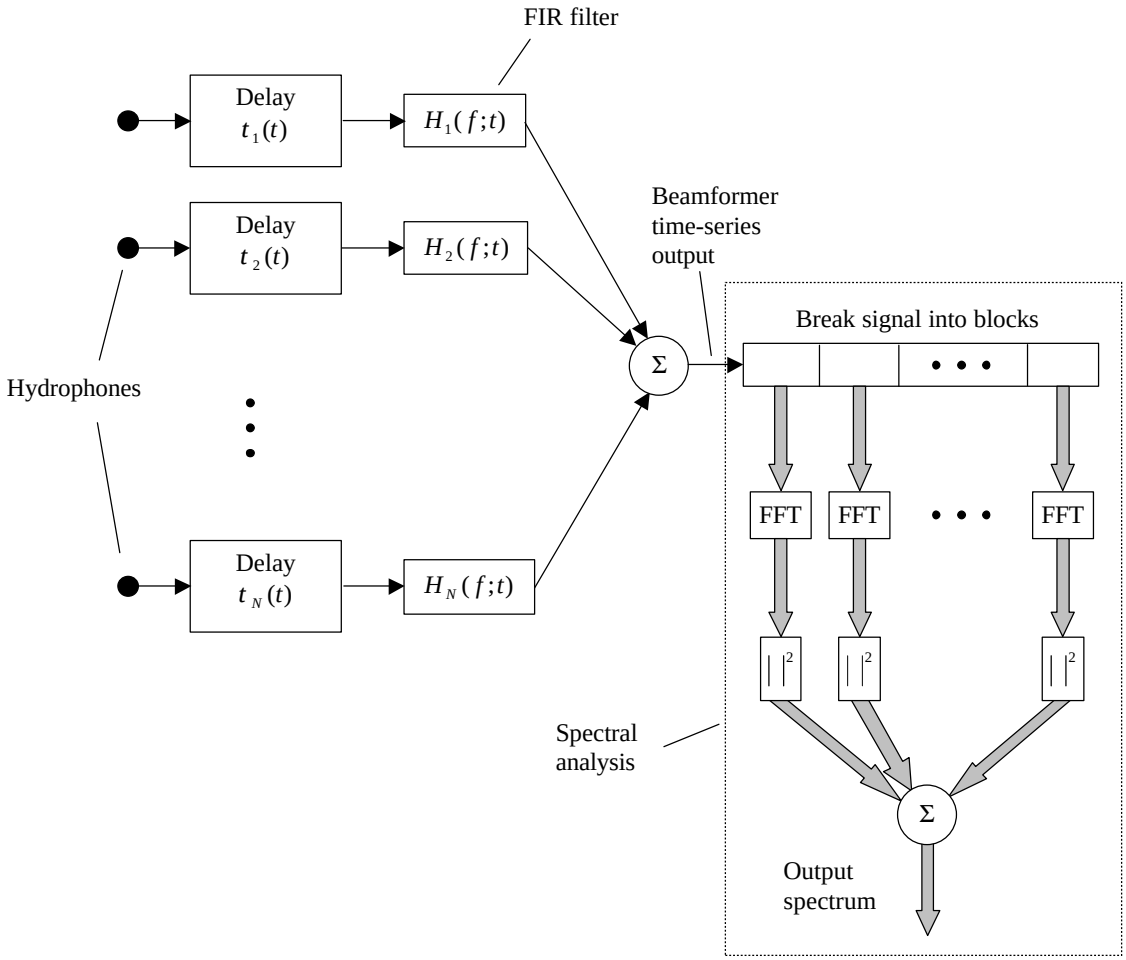

Figure 7.3 Block diagram of FIR filter time-domain beamformer

A frequency-domain beamformer architecture is shown in Figure 7.4. The acoustic data from each sensor is broken into short segments (termed snapshots), each snapshot is Fourier transformed into the frequency domain, and then the different sensor outputs are combined in a beamformer. The final stage is to incoherently sum the beamformer outputs from the different blocks. This beamformer produces an output spectrum at a number of focal points.

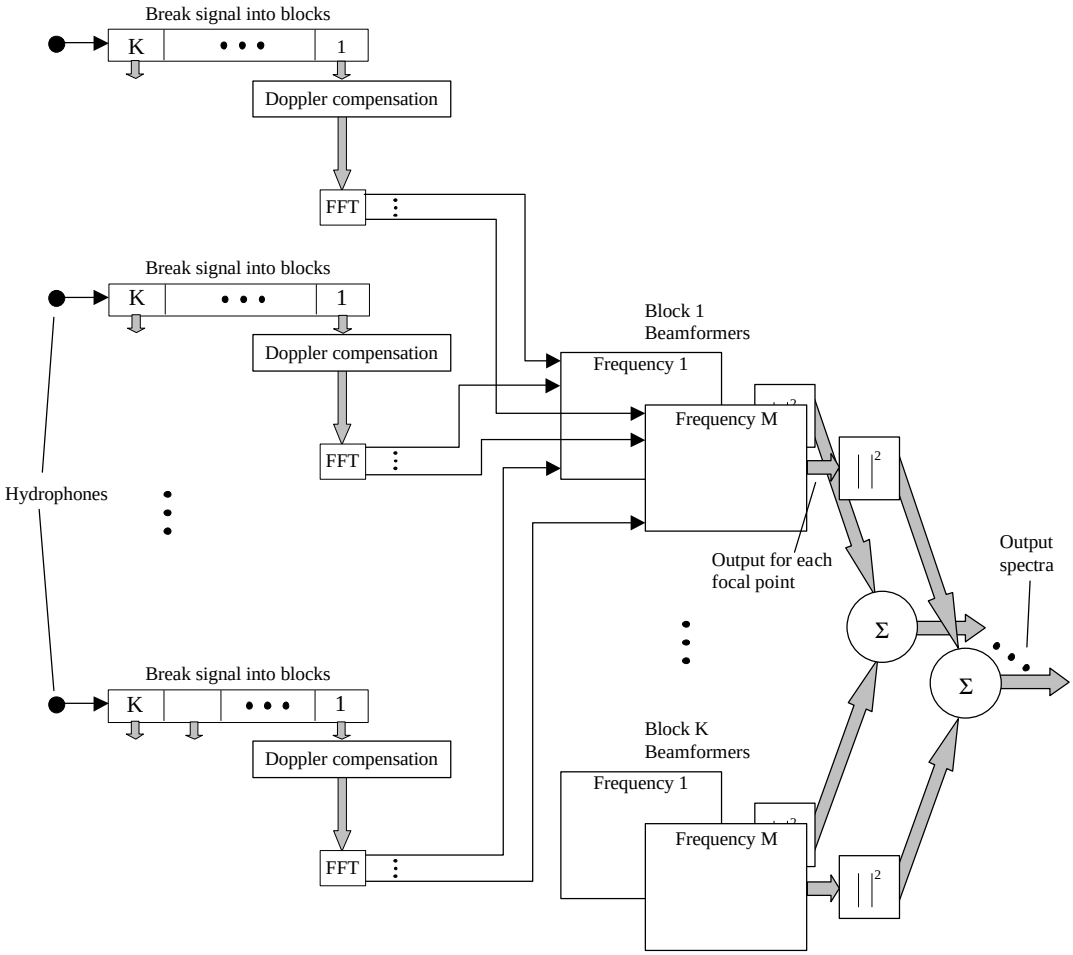

Figure 7.4 Block diagram of Doppler compensated frequency-domain beamformer

Near-field frequency domain beamformers usually require that the relative radial motion of the array and source be much less than a wavelength over the duration of a snapshot, which places an upper limit on the snapshot length and therefore a lower limit on the frequency resolution. Re-sampling the signal from each block to compensate for the hydrophone motion before Fourier transforming the data reduces this problem and is the function of the Doppler compensation blocks shown in Figure 7.4. The aim is to re-sample the signal in such a way that the samples are the same as those that would have been recorded if the hydrophone had been stationary.

Consider a stationary source transmitting an acoustic pressure signal $p_0(t)$. Ignoring the influence of boundary reflections, the received pressure at a hydrophone at slant-range $r(t)$ is:

$$p(r(t),t) = \frac{p_0\left(t - \frac{r(t)}{c_0}\right)}{r(t)} \qquad \textbf{(7.34)}$$

For a stationary receiver at range r_0 we have:

$$p(r_0,t) = \frac{p_0\left(t - \frac{r_0}{c_0}\right)}{r_0} \qquad \textbf{(7.35)}$$

If L samples of this signal are taken at times $t_l = \frac{l}{f_s}$, $l \in \left\{\frac{-L}{2} \cdots \frac{L}{2} - 1\right\}$ where f_s is the sampling frequency, the result for the stationary receiver is:

$$p_l(r_0) = \frac{p_0\left(\frac{l}{f_s} - \frac{r_0}{c_0}\right)}{r_0} \qquad \textbf{(7.36)}$$

For a moving receiver with the range changing linearly with time according to $r(t) = r_0 + vt$ we have:

$$p(r(t),t) = \frac{p_0\left(t\left(1 - \frac{v}{c_0}\right) - \frac{r_0}{c_0}\right)}{r_0 + vt} \qquad \textbf{(7.37)}$$

If this signal is sampled at times $t_l' = \frac{l}{f_s'}$, $l \in \left\{\frac{-L}{2} \cdots \frac{L}{2} - 1\right\}$, the result for the moving receiver is:

$$p_l(r(t)) = \frac{p_0\left(\frac{l}{f_s'}\left(1 - \frac{v}{c_0}\right) - \frac{r_0}{c_0}\right)}{r_0 + vt_l'} \qquad \textbf{(7.38)}$$

Assuming $\left|vt_l'\right| << r_0$, equations 7.36 and 7.38 will be equal providing the arguments of p_0 are equal. This requirement leads to:

$$f_s' = f_s\left(1 - \frac{v}{c_0}\right) \qquad \textbf{(7.39)}$$

This form of Doppler compensation is inexact for the following reasons:

1. The rate of change of range will not be constant during a snapshot.

2. Errors are introduced by ignoring the scaling of the signal with changing range.
3. Doppler compensation is carried out for a single focal point, and will be inaccurate for focal points well away from this. In principle each focal point could be individually Doppler compensated, but this would lead to a very high computational load.
4. Doppler is correctly compensated for the direct path signal between the source and receiver and will be not be correct for signals that contain significant energy that has travelled by other paths.

After consideration of the various merits of these three beamformer architectures it was decided to concentrate on the Doppler compensated frequency-domain beamformer as offering the best compromise between accuracy and execution time. A simple time-domain delay and sum beamformer was also implemented for comparison purposes. The FIR filter time-domain beamformer was not implemented because, although it potentially offered the most accurate results, its computational requirements were considered to be too severe.

7.2.2 Frequency-domain beamformer theoretical development

Having decided to use the frequency-domain beamformer architecture shown in Figure 7.4 the next task was to develop appropriate algorithms for determining the array weight vectors. To this end two data independent beamformers and one data dependent beamformer were derived.

7.2.2.1 Data independent beamformers

The data independent beamformers were derived using a least-squares fit to a desired beam pattern in a manner similar to the technique described in 7.1.1.1. A constraint of unity gain for a source at the focal point was also included and, in order to avoid excessive sidelobe levels outside the design range, a penalty was placed on the output of the beamformer when only spatially white noise of unit variance is present at the sensors. The white noise output of the beamformer is proportional to $|\mathbf{w}|^2$ where $\mathbf{w}^H$ is the weight vector applied to the array elements. Expressed mathematically the problem was therefore to minimise Equation 7.40 (cf. Equation 7.5) with respect to $\mathbf{w}$ subject to the constraint $\mathbf{w}^H\mathbf{a}_0 = 1$, where $\mathbf{a_0}$ is the steering

vector corresponding to the desired focal point. Note that each element of the steering vector was the expected response of the corresponding hydrophone to a source of unit amplitude located at the focal point, and was computed using an appropriate propagation model. Steering vectors were calculated at the central time of the snapshot under consideration.

$$\min_{\mathbf{w}}\left(\left|\mathbf{A}^H\mathbf{w}-\mathbf{y}_d\right|^2+b\left|\mathbf{w}\right|^2\right) \qquad \textbf{(7.40)}$$

Here **A** is the array steering matrix, which had columns comprising the steering vectors for the various focal points at which the desired array response was defined. The desired response of the array to a source at each of these points is given in the column vector $\mathbf{y}_d$, and b is a positive scalar that determines the trade-off between fitting the desired array response and minimising the white-noise gain.

This problem was solved using the well-known method of Lagrange multipliers (Haykin 1996, Appendix C), which required the following minimisation:

$$\min_{\mathbf{w},l}\left(\left|\mathbf{A}^H\mathbf{w}-\mathbf{y}_d\right|^2+b\left|\mathbf{w}\right|^2+l\left(\mathbf{w}^H\mathbf{a}_0-1\right)\right) \qquad \textbf{(7.41)}$$

where l is a scalar parameter that is determined as part of the minimisation.

After some manipulation (see Appendix D), which involved equating the derivatives of Equation 7.41 with respect to **w** and l to zero, the following solution was derived:

$$\mathbf{w}=\mathbf{M}^{-1}\left(\mathbf{A}\mathbf{y}_d-\left(\frac{\mathbf{a}_0^H\mathbf{M}^{-1}\mathbf{A}\mathbf{y}_d-1}{\mathbf{a}_0^H\mathbf{M}^{-1}\mathbf{a}_0}\right)\mathbf{a}_0\right) \qquad \textbf{(7.42)}$$

where:

$$\mathbf{M}=\mathbf{A}\mathbf{A}^H+b\mathbf{I}$$

Taking the limit of Equation 7.42 as $b\to\infty$ yielded the weight vector that minimised the beamformer output in the case of insonification by white noise, subject to unity gain for a source at the focal point. For this case:

$$\mathbf{w}=\frac{\mathbf{a}_0}{\mathbf{a}_0^H\mathbf{a}_0} \qquad \textbf{(7.43)}$$

In the remainder of this thesis this is referred to as the Minimum White Noise (MWN) Beamformer.

Another special case of Equation 7.42 occurs if the desired array response is zero for all steering vectors specified in $\mathbf{A}$. In this case $\mathbf{y}_d = \mathbf{0}$ and we have:

$$\mathbf{w} = \frac{\mathbf{M}^{-1}\mathbf{a}_0}{\mathbf{a}_0^H \mathbf{M}^{-1}\mathbf{a}_0}. \qquad \textbf{(7.44)}$$

This is referred to in what follows as the Least Squares Minimum Constrained (LSMC) Beamformer.

For comparison purposes it was more convenient to use a normalised form of the white noise gain weighting factor which was achieved by defining $b' = \frac{b}{\max(\mathrm{diag}(\mathbf{A}^H\mathbf{A}))}$ and specifying the beamformer in terms of b' rather than b.

7.2.2.2 *Data dependent beamformer*

The data dependent beamformer was based on the Minimum Variance Distortionless Response (MVDR) beamformer described in Section 7.1.1.2. The derivation of the MVDR beamformer (see Jensen et al. 2000 Section 10.3.2) relies on the assumption that the steering vectors, and hence array weights, are independent of time so that

$$\mathrm{E}\{\mathbf{w}^H\mathbf{x}\mathbf{x}^H\mathbf{w}\} = \mathbf{w}^H\,\mathrm{E}\{\mathbf{x}\mathbf{x}^H\}\mathbf{w} = \mathbf{w}^H\mathbf{R}_x\mathbf{w} \qquad \textbf{(7.45)}$$

where $\mathbf{x}$ is the array output vector at the frequency under consideration and $\mathrm{E}\{\ \}$ is the expectation operator. This assumption is not valid in the dynamic near-field case because the required weight vector is different for each snapshot and multiple snapshots are required to obtain a reasonable estimate of $\mathbf{R}_x$. This is a similar problem to that dealt with in Greening & Perkins (2002) for the far-field case (see Section 7.1.7.2), but a different method of solution was required here because of the geometry involved.

A transformation was applied to the array output vector as follows:

$$\mathbf{z}_i = \mathbf{T}_i\mathbf{x}_i \qquad \textbf{(7.46)}$$

where the subscript i represents the snapshot number and $\mathbf{T}_i$ is the diagonal transformation matrix:

$$\mathbf{T}_i = \begin{bmatrix} a_{1,i}/a_{1,1} & & \\ & \ddots & \\ & & a_{N,i}/a_{N,1} \end{bmatrix}. \qquad \textbf{(7.47)}$$

Here $a_{n,i}$ is the n^{th} element of the steering vector for the desired focal point at the midpoint of snapshot i. The effect of this transformation was to produce the same output at snapshot i for a source at the focal point as would have been produced if the array had stayed at the position it was in at the midpoint of the first snapshot. The effective steering vector and required weight vector were therefore constant and the beamformer output power could be computed using the usual MVDR formula:

$$\Pi = \frac{1}{\mathbf{a}_1^H \hat{\mathbf{R}}_z^{-1} \mathbf{a}_1} \qquad \textbf{(7.48)}$$

where $\mathbf{a}_1$ is the steering vector for the desired focal point at the midpoint of the first snapshot and $\hat{\mathbf{R}}_z$ is an estimate of the covariance matrix of $\mathbf{z}$ given by:

$$\hat{\mathbf{R}}_z = \frac{1}{K}\sum_{i=1}^{K} \mathbf{z}_i \mathbf{z}_i^H + e\mathbf{I}. \qquad \textbf{(7.49)}$$

Here K is the number of snapshots and e is a positive number that controls the amount of diagonal loading. As described in Section 7.1.1.2, diagonal loading reduced the number of snapshots required to obtain a useable covariance matrix estimate. The effectiveness of e in stabilising the covariance matrix depended on its size relative to the magnitude of the transformed array output vector, $\mathbf{z}_i$, and it was therefore more convenient to use the normalised parameter e' defined by:

$$e' = \frac{e}{\text{mean}\left(\text{diag}\left(\frac{1}{K}\sum_{i=1}^{K} \mathbf{z}_i \mathbf{z}_i^H\right)\right)} \qquad \textbf{(7.50)}$$

Note that because the transformation matrices used to calculate $\mathbf{z}_i$ were different for different focal points, $\hat{\mathbf{R}}_z$ also depended on the focal point and a separate matrix inversion had to be carried out for each one.

This beamformer is referred to as the Dynamic MVDR (DMVDR) beamformer in what follows.

The implementation of the DMVDR beamformer required a slightly different architecture to that shown in Figure 7.4, as a single beamformer block computed the

total output power summed over all snapshots at a given frequency without the need for the additional squaring and summing operations shown in the figure.

7.2.2.3 Regularised inversion processor

The regularised inversion (RI) processor was based on modelling the acoustic field emitted by the tow-vessel as being due to a set of point sources at known locations. The processor then solved for the vector of source complex amplitudes that produced the closest match (in a least squares sense) between the measured and predicted hydrophone outputs.

Mathematically this was similar to the far-field DML processor described in Section 7.1.2.2 with the signal vector, $\mathbf{s}$, now consisting of the complex amplitudes of the sources, and with the far-field steering matrix replaced by its near-field equivalent. The forward problem was:

$$\mathbf{x} = \mathbf{A}\mathbf{s} + \mathbf{n} \qquad \textbf{(7.51)}$$

where $\mathbf{n}$ is a noise vector. Minimising $(\mathbf{x} - \mathbf{A}\mathbf{s})^H (\mathbf{x} - \mathbf{A}\mathbf{s})$ with respect to $\mathbf{s}$ resulted in the well-known least squares solution:

$$\mathbf{s} = (\mathbf{A}^H \mathbf{A})^{-1} \mathbf{A}^H \mathbf{x} \qquad \textbf{(7.52)}$$

In some circumstances the matrix $\mathbf{A}^H\mathbf{A}$ became ill-conditioned and the matrix inversion could not be computed accurately. This happened whenever there were two or more combinations of source amplitudes that produced an acoustic field that fitted the measured data equally well. For example the matrix was singular if the number of sources exceeded the number of hydrophones and, even if this was not the case, became progressively less well conditioned as the separation between sources reduced below the conventional resolution of the array.

To address this problem and produce a more robust processor the method of regularised linear inversion was used. This is described in detail in Press et al. (1993), but briefly the idea is to find the source vector that minimises $(\mathbf{x} - \mathbf{A}\mathbf{s})^H (\mathbf{x} - \mathbf{A}\mathbf{s}) + g\mathbf{s}^H \mathbf{B}^H \mathbf{B}\mathbf{s}$, where g is a positive scalar used to adjust the relative weight given to the minimisation of the two terms and $\mathbf{B}$ is a coefficient matrix that determines what property of the source vector is to be minimised. If $\mathbf{B}$ was an identity matrix the effect was to minimise $\mathbf{s}^H\mathbf{s}$, which was proportional to the mean square source amplitude, whereas setting

$$\mathbf{B} = \begin{bmatrix} -1 & 1 & & & \\ & -1 & 1 & & \\ & & \ddots & \ddots & \\ & & & -1 & 1 \end{bmatrix} \qquad \textbf{(7.53)}$$

(elements not shown are zero) resulted in the minimisation of the differences between the amplitudes of adjacent sources.

The resulting solution for the source vector was:

$$\mathbf{s} = \left(\mathbf{A}^H\mathbf{A} + g\mathbf{B}^H\mathbf{B}\right)^{-1}\mathbf{A}^H\mathbf{x} \qquad \textbf{(7.54)}$$

g is usually chosen empirically so as to give a fit to the measured data that is consistent with the expected noise levels. To make this parameter independent of the relative magnitudes of the terms in the **A** and **B** matrices it was convenient to specify it in terms of a normalised parameter, g', which was related to g by:

$$g = g' \frac{\mathrm{tr}(\mathbf{A}^H\mathbf{A})}{\mathrm{tr}(\mathbf{B}^H\mathbf{B})} \qquad \textbf{(7.55)}$$

where tr represents the trace of the matrix.

A major difference between this processor and the various beamforming methods described above was that it inverted for the set of source amplitudes that would generate an acoustic field consistent with the array data, whereas the beamformers focussed on one point at a time and attempted to determine the acoustic power being emitted from the focal point while ignoring the effects of sources in other locations.

A further advantage of this processor was that the fitted source amplitude distribution could be used directly to compute the equivalent far-field source level and horizontal beam pattern of the vessel. It was straightforward to show (see Appendix D) that the equivalent far-field source pressure due to the combined set of Q sources was given by:

$$p_s(q) = \sum_{j=1}^{Q} s_j e^{-ik(x_j \cos q + y_j \sin q)} \qquad \textbf{(7.56)}$$

where the sources are located at (x_1, y_1), (x_2, y_2), etc. and q is the angle from the positive X axis. $p_s(q)$ is the pressure amplitude 1 metre from a source at the origin that would have produced the same far-field pressure at azimuth q as the hypothetical source array.

This processor was applied to the data to compute both the source amplitude distribution and the equivalent far-field source pressure amplitude for each snapshot and then in each case the results were incoherently combined to give an RMS value. The RMS amplitude for source q was computed from:

$$\bar{s}_q = \sqrt{\frac{1}{K}\sum_{i=1}^{K} s_{q,i} s_{q,i}^*} \qquad \textbf{(7.57)}$$

where K is the number of snapshots and $s_{q,i}$ is the complex source amplitude for source q estimated using data from snapshot i. The RMS far-field source pressure was calculated using:

$$\bar{p}_s(q) = \sqrt{\frac{1}{K'(q)}\sum_{i=1}^{K'(q)} p_s^{(i)}(q)\, p_s^{(i)*}(q)} \qquad \textbf{(7.58)}$$

where $p_s^{(i)}$ is the equivalent far-field source pressure estimated using data from snapshot i. The source amplitude distribution computed using data from a given snapshot was used to compute the far-field source pressure for the range of angles subtended by the array at all sources. This angular range changed from snapshot to snapshot as the array moved, and consequently the number of snapshots averaged, K', was a function of angle.

7.2.3 Implementation issues

7.2.3.1 Computation of steering vectors

All of the beamforming algorithms described above require the computation of the array steering vector for each frequency, snapshot and focal point. Each element of the steering vector was the expected response of the corresponding hydrophone to a unit amplitude continuous source of the appropriate frequency located at the focal point. Three different methods of computing the steering vectors were implemented:

1. Spherical spreading – this included only the direct path signal. For snapshot j, the steering vector element corresponding to hydrophone n was given by $a_{n,j} = \frac{e^{ikr_{n,j}}}{r_{n,j}}$ where $r_{n.j}$ is the slant range between the focal point and the hydrophone at the central time of the snapshot. Here $k = 2pf / c_0$ is the

wavenumber corresponding to frequency f and sound speed c_0, and $i = \sqrt{-1}$.

2. Lloyd mirror – this included the effects of both the direct and surface reflected paths, in which case $a_{n,j} = \frac{e^{ikr_{n,j}}}{r_{n,j}} - \frac{e^{ikr'_{n,j}}}{r'_{n,j}}$ where $r'_{n.j}$ is the slant range between the surface reflected image of the focal point and the hydrophone.

3. Fast-Field – this included the effects of all propagation paths for a specified acoustic environment. The fast-field program SCOOTER (Porter 1999) was run for the specified environment at each required frequency to generate a file containing a table of the received complex amplitude as a function of range and depth for each frequency. Each steering vector element was then generated by interpolating the appropriate table to the actual range and depth of the hydrophone. Methods for using the measured data to determine an appropriate acoustic environment to use in this calculation were discussed in Chapter 6.

7.2.3.2 Methods for combining array elements

The array used in the experiment described in Chapter 4 consisted of 60 hydrophones arranged in four octaves and by using various combinations of hydrophones it was possible to obtain four different 24-element equally spaced arrays. This process involved averaging the signals from two or more adjacent hydrophones and therefore some way of calculating the effective steering vector of the resulting combination was required. Two methods of doing this were implemented:

1. Each steering vector element was computed using the mean positions of the hydrophones making up the corresponding array element. This method was simple and fast but had the disadvantage that it did not compensate for the directionality of the array element caused by combining hydrophones.

2. The steering vector for all 60 hydrophones was computed and then the elements corresponding to the hydrophones that were combined to make up each array element were averaged, resulting in the required 24 element

steering vector. This method was slower than 1 because it required the computation of more steering vector elements but had the advantage of inherently including directionality effects.

7.2.3.3 Hydrophone directionality

The hydrophones used in the array were themselves made up of a number of elements, with the lower frequency hydrophones containing more elements, and hence being longer, than the higher frequency hydrophones. The hydrophones were therefore directional, an effect which became significant when the frequency was high enough that the wavelength was comparable to the hydrophone length.

To obtain the best possible spatial resolution it was desirable to use the largest possible array aperture at all frequencies, which in turn meant using the relatively long, low frequency hydrophones that were located near the extremities of the array, even at high frequencies. It was therefore necessary to compensate for the directionality of these hydrophones, and two different methods of achieving this were implemented.

1. Each hydrophone was treated as being made up of a number of pseudo-elements, which were evenly spread over the true length of the physical hydrophone. The computed steering vector elements for these pseudo-elements were then averaged to give the resulting steering vector element for the entire hydrophone. Pseudo-elements were used instead of the physical hydrophone elements in order to reduce the required number of steering vector element calculations. The pseudo-element spacing was chosen to be 0.5 m, which was approximately a third of a wavelength at 1 kHz.

2. Each hydrophone was considered to be a straight, continuous, line receiver. The theoretical response of the continuous line receiver in the direction of the focal point (Urick 1983, Chapter 3) was then used to compute an amplitude-weighting factor, which was multiplied by the calculated steering vector element. This approach was also extended to include the directionality effects introduced by combining hydrophones by using the appropriate directional response formula for a linear array of line elements (Urick 1983, Chapter 3).

The pseudo-element method had the advantage of compensating accurately for directionality effects even in situations where significant energy was arriving by indirect paths, but was slow because of the large number of steering vector elements that had to be calculated. The beam pattern method was much faster (by a factor of about 6) but potentially less accurate where strong multi-path signals existed.

7.3 Results

7.3.1 Application to simulated signals

The beamformer algorithms described in the previous section were tested with the same simulated hydrophone signals used to test the matched-field inversion algorithms and also with simulated signals that only included the direct path signals. The simulated signals included a source with similar characteristics and the same position as the UW30 source, and a machinery noise source. Details of the simulation parameters were given in Chapter 6.

The results of applying the various beamformers to the simulated data sets are shown below. The time-domain beamformer weighted the signal from each array element in proportion to its distance from the focal point. The LSMC beamformer was run with a normalised white noise gain weighting factor $b' = 1$, which was found to give a good compromise between beam width and excessive sidelobe levels outside the design region. The DMVDR beamformer was run with a relative diagonal loading factor $e' = 0.1$ and operated on five snapshots at a time. These parameters were found to give good results with the simulated data. In all cases the processing bandwidth was 1 Hz, giving a snapshot duration of 1 second.

Figure 7.5 shows the results of applying the four different beamformers to all 60 hydrophones at the UW30 source frequencies. The simulated data used here included only the direct path signal.

The time-domain and MWN beamformers weighted the output of each hydrophone in proportion to its distance from the focal point and therefore over-emphasised the central portion of the array, which contained the highest density of hydrophones. The resulting beam patterns were very broad, especially at the lower frequencies, leading to poor source localisation. The LSMC beamformer localised the source much better, but not as well as the DMVDR beamformer, which produced a single, sharply defined peak close to the true source location. Note that all three frequency-domain beamformers had a peak output 0.5 m to the left of the true source location whereas the time-domain beamformer peaked at the true source location. This was a consequence of using the hydrophone positions at the mid-point of each snapshot in the steering vector calculations rather than the mean hydrophone positions over the

snapshot. The two were only equivalent when the apparent velocities of the hydrophones relative to the vessel were constant.

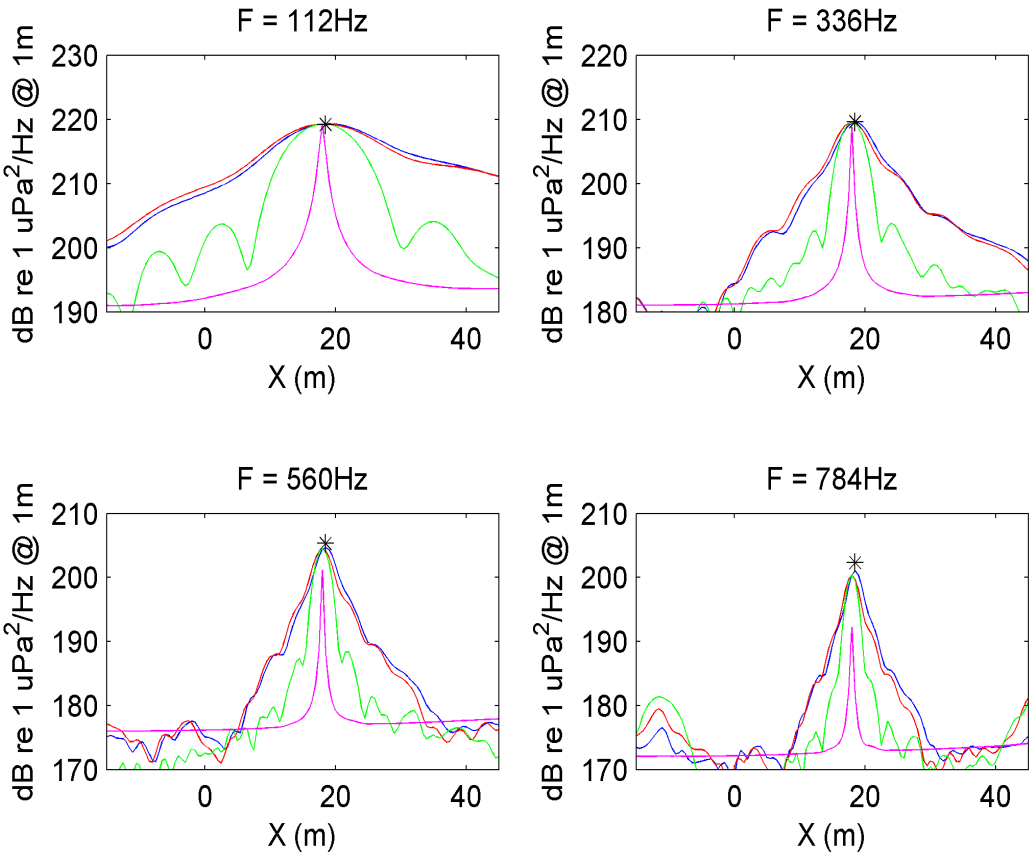

Figure 7.5 Results of applying different beamformers to simulated data (direct path only). Beamformers use all 60 hydrophones and the frequency-domain beamformers include Doppler correction. Blue, time-domain; red, MWN; green, LSMC; and magenta, DMVDR. Asterisks show true source positions and levels.

Errors in the source level estimates produced by the different beamformers are tabulated in Table 7.1 as a function of frequency. At the lower frequencies the beamformer estimates were very accurate, but the beamformers tended to underestimate the true source level as the frequency increased. The time-domain beamformer performed best in this regard, with a maximum error of only 1.3 dB at 784 Hz, whereas the DMVDR performed much worse than the others, underestimating the source level by 4.2 dB at 560 Hz and 10.2 dB at 784 Hz. In the case of the time-domain beamformer these errors were due to interpolation errors, whereas the frequency-domain beamformers suffered from errors due to the approximations inherent in the Doppler compensation process.

Table 7.1 Differences between peak beamformer output and true source level (dB) for simulated, direct path data.

Beamformer	**112 Hz**	**336 Hz**	**560 Hz**	**784 Hz**
Time-domain	+0.1	-0.1	-0.7	-1.3
MWN	+0.1	-0.1	-0.9	-2.0
LSMC	+0.1	-0.1	-0.9	-2.0
DMVDR	0.0	-0.7	-4.2	-10.2

Figure 7.6 shows the results of applying time-domain, MWN, LSMC and DMVDR beamformers to the equally spaced, 24-element X octave array, which was the lowest frequency equally spaced array and used all hydrophones in various combinations.

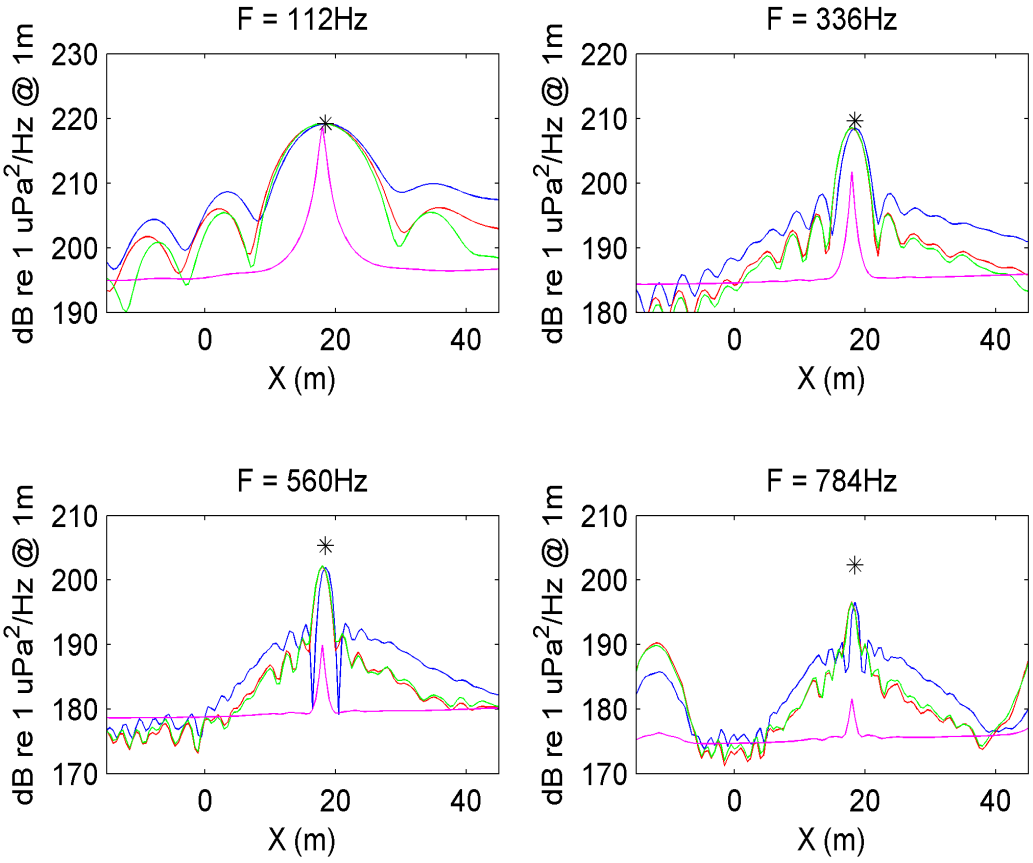

Figure 7.6 Results of applying different beamformers to simulated data (direct path only). Beamformers use X octave hydrophones and the frequency-domain beamformers include Doppler correction. Blue, time-domain; red, MWN; green, LSMC; and magenta, DMVDR. Asterisks show true source positions and levels.

The time-domain, MWN and LSMC beamformers all produced very similar results, but all significantly under-estimated the source level at the higher frequencies. This was due to the array element steering vectors being calculated using the mean positions of the component hydrophones, which took no account of the resulting array element directionality. The degradation in the performance of the DMVDR beamformer was much more significant than for the other beamformers.

Note that at 784 Hz the beamformer outputs were showing the effects of spatial aliasing, giving rise to the 10 dB increase in the height of the peak at –10 m. At this frequency the array element spacing (approx 5 m) was much larger than the wavelength (1.9 m) but his effect did not show up at lower frequencies, despite the normal $l/2$ minimum spacing criterion being violated, because of the small field of view under consideration.

As can be seen in Figure 7.7, compensating for the array element directionality by using the means of the steering vector elements for the individual hydrophones, or by weighting the steering vector elements with the theoretical beam patterns of the combined hydrophones, improved the estimate of source level at the higher frequencies. The beam pattern method implicitly assumed the individual hydrophones were directional, whereas the combined steering vector method did not, which accounts for the slight differences between the results obtained with these two methods.

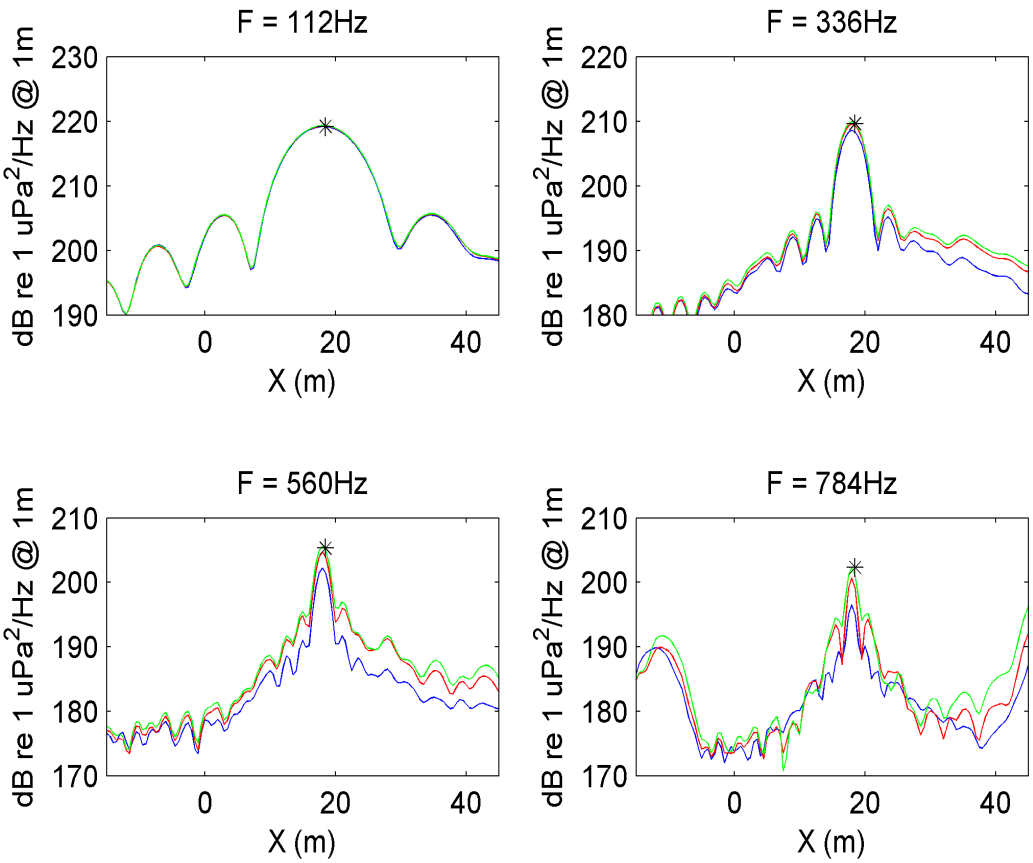

Figure 7.7 Results of applying LSMC beamformer to X octave hydrophones with different methods of computing combined steering vectors. Blue, mean position with omni hydrophones; red, mean steering vector with omni hydrophones; green, theoretical beam pattern of combined hydrophones.

Figure 7.8 shows how turning off Doppler compensation affected the outputs of the LSMC and DMVDR beamformers. This made very little difference to the results at 112 Hz and 336 Hz but degraded the beam patterns and source level estimates more as the frequency increased. The output of the DMVDR beamformer was affected much more than the LSMC beamformer, which was in keeping with the well-known high modelling error sensitivity of data dependent beamformers (Cox et al. 1987).

As can be seen from Figure 7.9, the location on the vessel of the focal point chosen for Doppler compensation had almost no effect on the LSMC beamformer output. This was not surprising given the small size of the vessel compared to the length of the array.

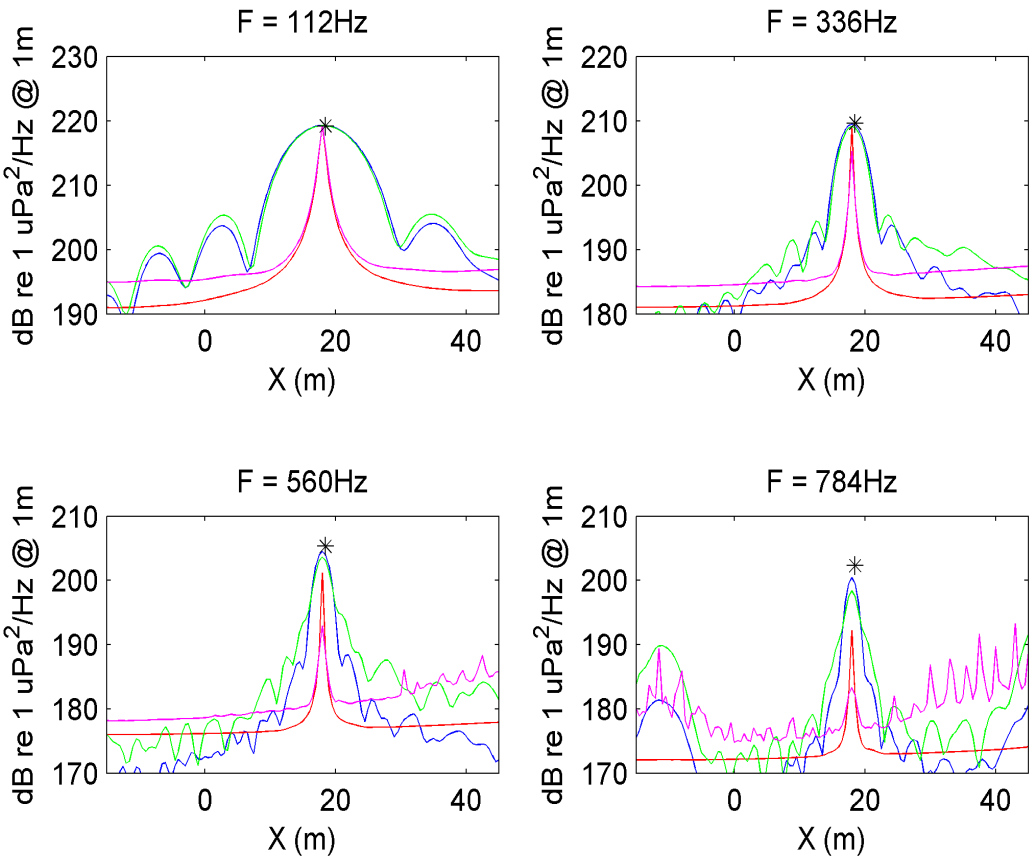

Figure 7.8 Effect of Doppler compensation on LSMC and DMVDR beamformers (All hydrophones, simulated direct path data). Blue, LSMC compensated; red, DMVDR compensated; green, LSMC uncompensated; magenta, DMVDR uncompensated. Asterisks show true source positions and levels.

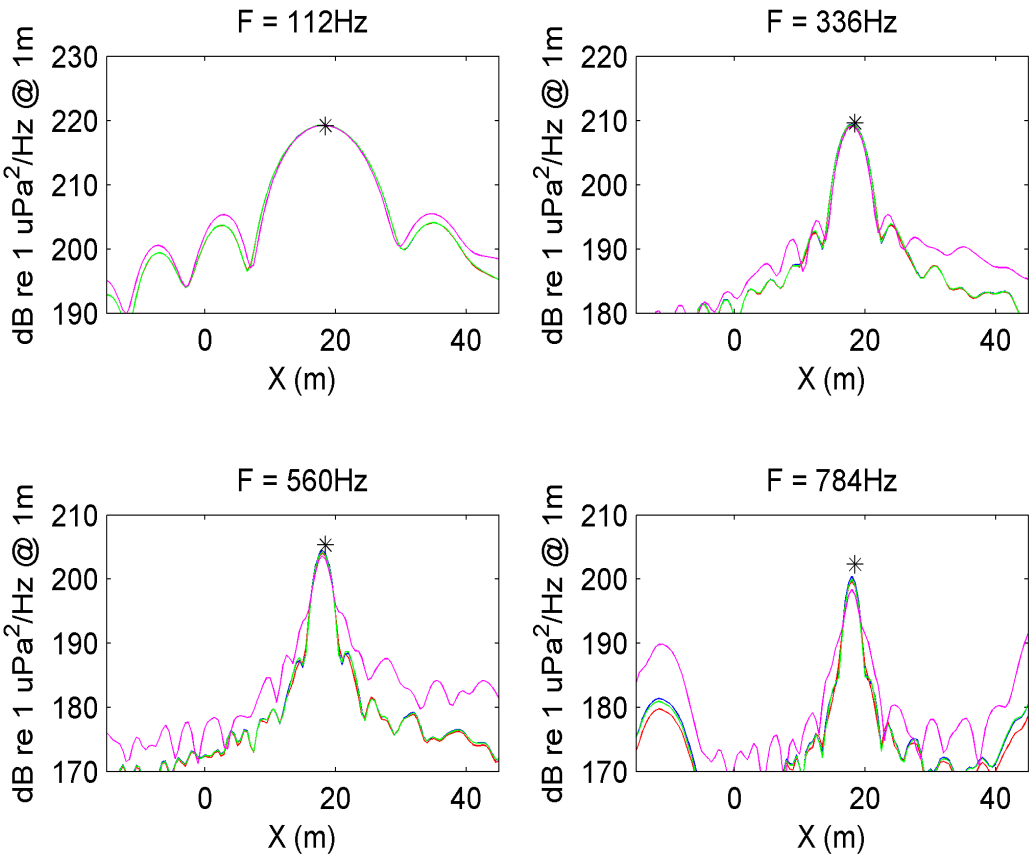

Figure 7.9 Sensitivity of Doppler compensation to location of compensated focal point for (LSMC beamformer, all hydrophones, direct path only). Blue, compensated at X=18.5 m (true source position); red, compensated at X=0 m (stern of vessel); green, compensated at 27 m (bow of vessel); magenta, uncompensated. Asterisk shows source position and level.

The effects of applying the LSMC and DMVDR beamformers to simulated data calculated using the wavenumber integration method are shown in Figure 7.10, and the corresponding source level estimate errors are tabulated in Table 7.2. Large errors in source level estimates and significant degradations of the beam patterns occurred when the steering vectors used by the beamformers were calculated assuming spherical spreading.

Using the fast-field method to compute the steering vectors significantly improved the results, particularly in the case of the LSMC beamformer, which then produced source level estimates only slightly less accurate than in the direct path only case. Also tabulated (but not plotted) are the source level estimate errors when the Lloyd mirror propagation model was used to compute the steering vectors. This method went a long way towards correcting the errors that occurred when spherical

spreading was assumed, but was not as accurate as the fast-field method at low frequencies. Again, the DMVDR beamformer produced significantly worse source level estimates than the LSMC beamformer.

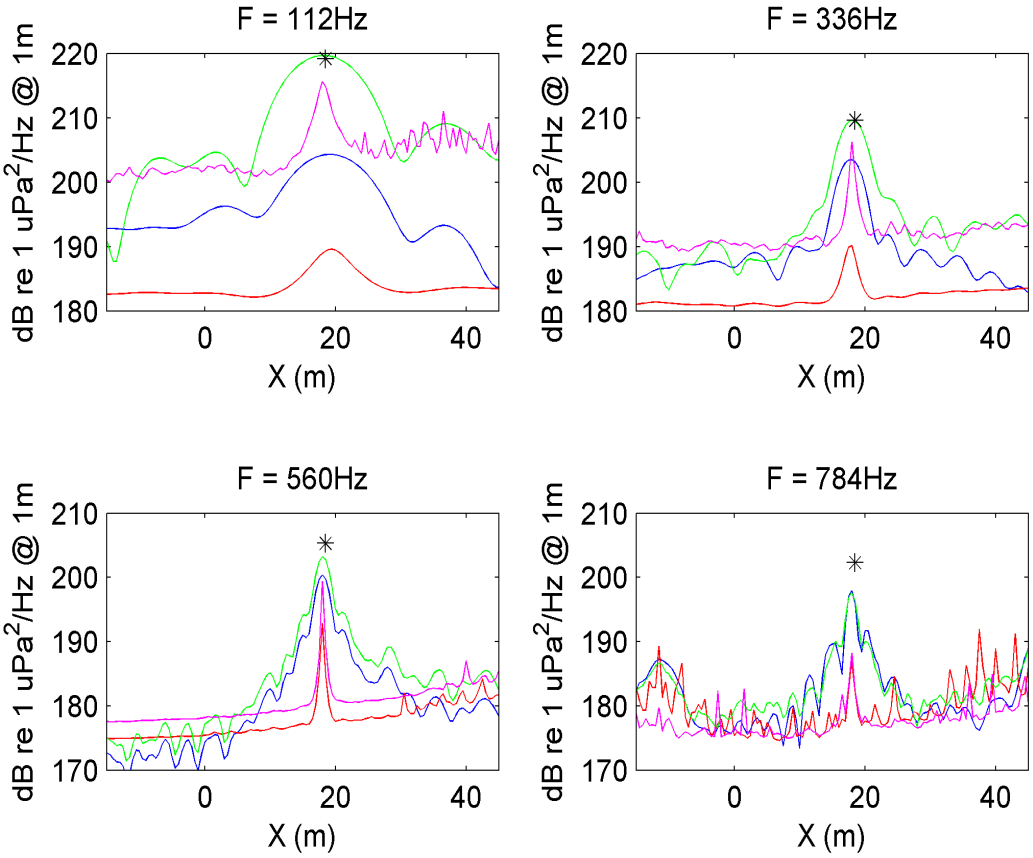

Figure 7.10 Comparison between beamformer outputs where simulated data includes propagation effects (all hydrophones). Blue, LSMC assuming spherical spreading; red, DMVDR assuming spherical spreading; green, LSMC beamformer using true transfer function; magenta, DMVDR using true transfer function. Asterisk shows source position and level.

Table 7.2 Differences between peak beamformer output and true source level (dB) for acoustic data simulated using wavenumber integration method.

Beamformer	**Steering vector calculation method**	**112 Hz**	**336 Hz**	**560 Hz**	**784 Hz**
LSMC	Spherical spreading	-14.9	-6.1	-5.0	-4.4
DMVDR		-29.7	-19.5	-12.6	-15.5
LSMC	Lloyd mirror	+2.1	+1.3	-1.8	-3.8
DMVDR		-11.3	-10.7	-5.6	-14.1
LSMC	Fast-field	+0.5	-0.1	-2.2	-4.7
DMVDR		-3.6	-3.5	-5.9	-14.1

The effect of adding a random error to the hydrophone Y coordinates was investigated and the results are shown in Figure 7.11, which plots the change in beamformer peak output level against the root mean square hydrophone position error. The errors were zero mean Gaussian and uncorrelated between hydrophones. Errors were only added to the Y coordinate because the array was aligned predominantly in the X direction and therefore relative errors in the hydrophone X coordinates, which were physically constrained by the array, were expected to be much smaller then the relative errors in the Y coordinates. It can be seen from the plot that the data for all frequencies gave similar results when the position error was plotted in wavelengths. For RMS position errors greater than 0.5 wavelengths the beamformer had defocused completely and the estimation errors were fairly constant. A quadratic fit to the data over the range 0 to 0.4 wavelengths gave the following formula for the estimation error:

$$Err = 0.322 - 13.2\left(\frac{Y_{RMS}}{l}\right) - 68.8\left(\frac{Y_{RMS}}{l}\right)^2 \quad \text{(dB)} \qquad \textbf{(7.59)}$$

where Y_{RMS} is the root mean square error in the hydrophone Y coordinate and l is the acoustic wavelength.

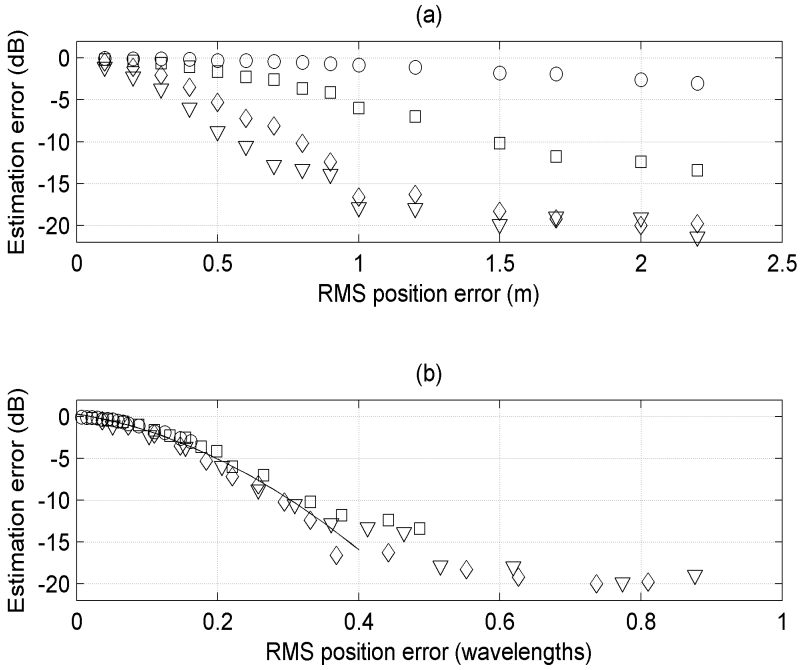

Figure 7.11 (a): LSMC beamformer source spectral level estimation error as a function of hydrophone Y coordinate RMS position error. Circles, 112 Hz; squares, 336 Hz; diamonds, 560 Hz, triangles, 784 Hz. (b): as for (a) but horizontal scale is normalised by acoustic wavelength. Solid line is quadratic line of best fit. Estimation errors are relative to source spectral level with no hydrophone position error.

Figure 7.12 compares the results obtained using the LSMC beamformer to the source amplitude distributions computed using the RI processor (Section 7.2.2.3). RI results are shown for hypothetical source arrays extending from -15 m to 45 m (the same range as the beamformer focal points) and from 0 to 27 m (the physical length of the vessel), and results are shown for both magnitude regularisation $(\mathbf{B} = \mathbf{I}, g' = 0.1)$ and slope regularisation ($\mathbf{B}$ as given in Equation 7.53, $g' = 5$). The value of g' only weakly affected the result and in each case it was chosen so as to give a reasonable source distribution without unduly increasing the mismatch between the measurements and modelled data.

There were strong similarities between the shapes of the LSMC beamformer outputs and the computed source amplitude distributions, but there were also substantial offsets between them. These offsets were due to the different normalisations implicit in the two methods: the LSMC beamformer was normalised so that its output gave the correct magnitude for a single point source located at the focal point, whereas the

RI processor gave the amplitudes of an array of point sources that together would have produced the measured field.

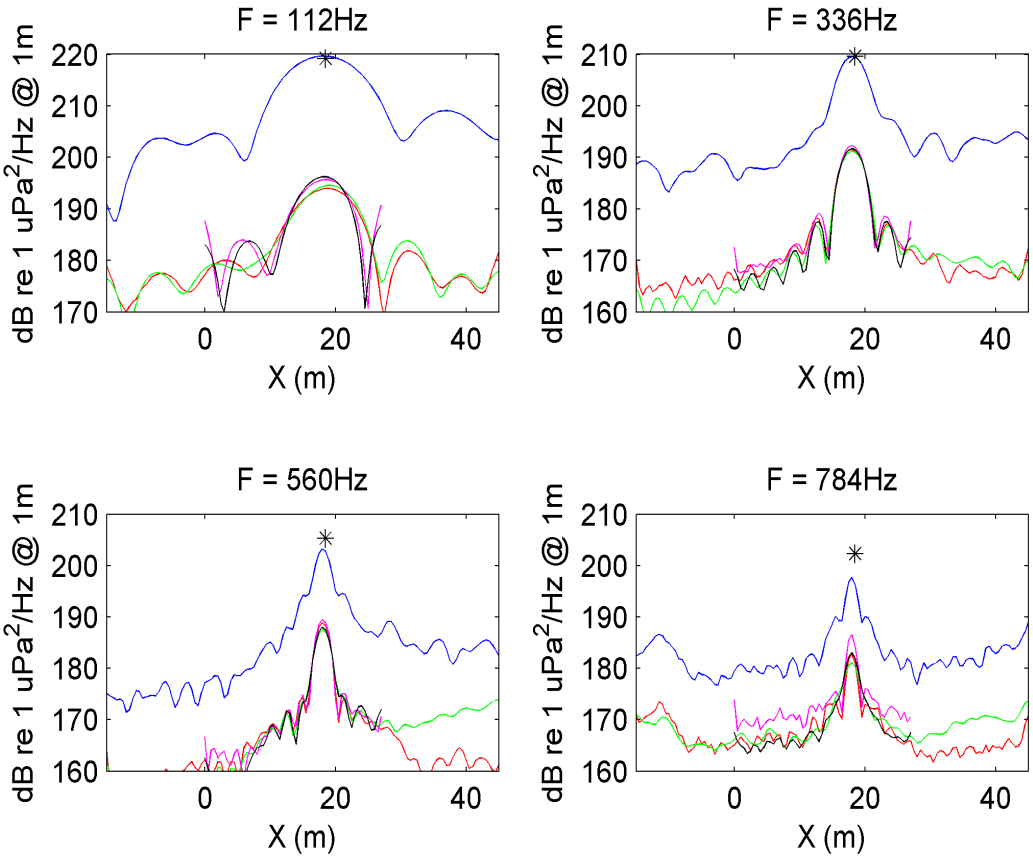

Figure 7.12 Comparison between LSMC beamformer output (blue) and source amplitude distributions computed using the RI processor. Red and green, sources distributed from -15 m to +45 m; magenta and black, sources distributed from 0 m to +27 m. In both cases source spacing was 0.5 m. Red and magenta, regularised using magnitude $(g'=0.1)$; green and black, regularised using slope $(g'=5)$. Calculation used all hydrophones, simulated data included propagation effects, and both algorithms used true transfer function.

The differences between the source amplitude distributions obtained using the two different regularisation methods appeared minor in Figure 7.12, but the corresponding far-field source levels computed from these distributions showed noticeable differences at some angles at the higher frequencies (see Figure 7.13). The source amplitude distributions also showed truncation effects at the ends. These effects were most noticeable at the lower frequencies and where the sources were distributed over the shorter interval (0 to 27 m).

From Figure 7.13 it is apparent that the computed far-field source levels agreed extremely well with the expected values at 112 Hz and 336 Hz and also conformed

well to the expected omnidirectional beam pattern. Larger errors occurred at the higher frequencies, with the source levels being underestimated by similar amounts to those obtained with the LSMC beamformer, and with the levels showing more variation with angle as the frequency increased.

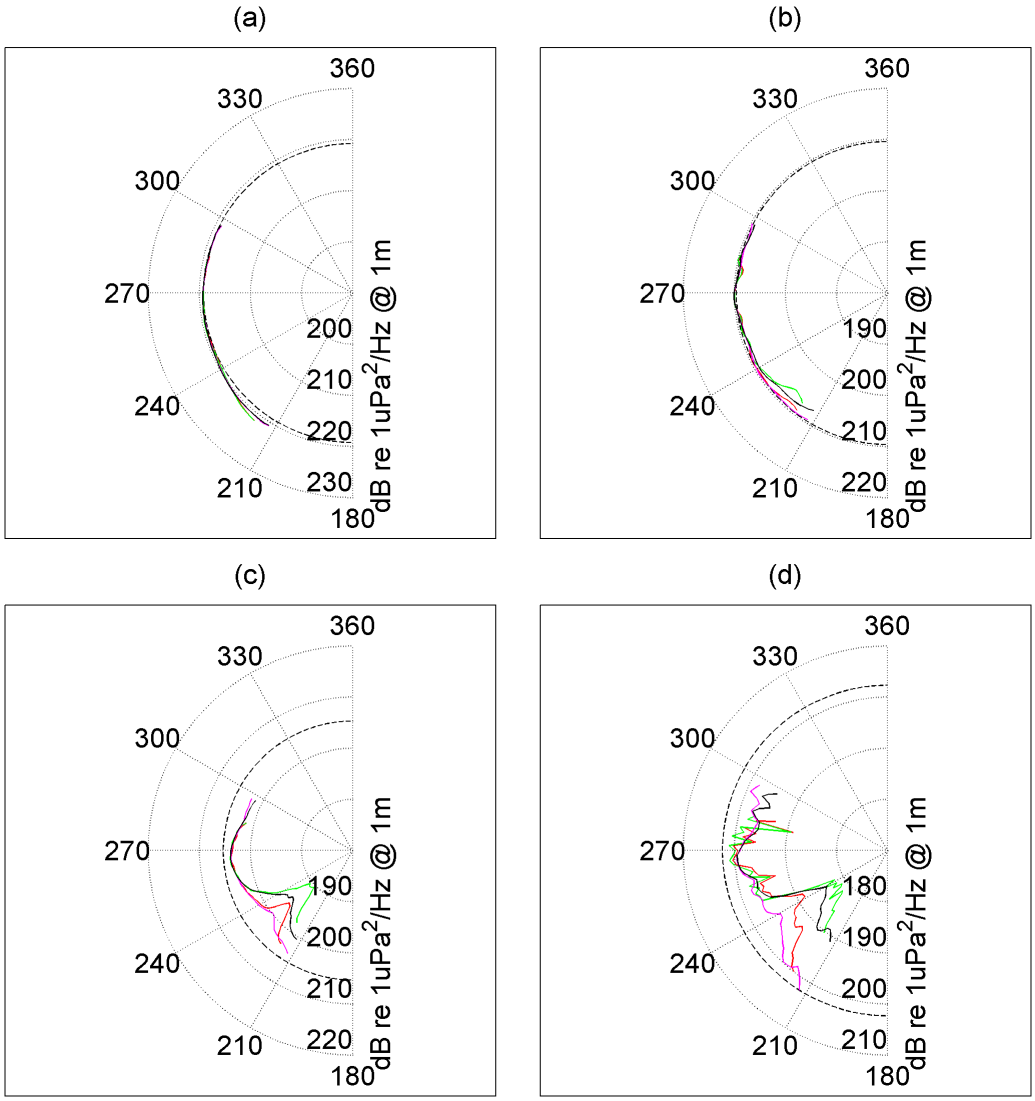

Figure 7.13 Equivalent far-field source levels computed using RI processor at (a) 112 Hz, (b) 336 Hz, (c) 560 Hz and (d) 784 Hz. Line colours and other parameters are as per Figure 7.12. In each case the broken black line is the true source level, and angles of 180° and 360° correspond to the stern and bow of the tow-vessel respectively.

The results plotted in Figure 7.14 were computed using simulated data that included shallow water propagation effects. Failure to include those effects when carrying out the array-processing markedly degraded the computed equivalent far-field beampattern.

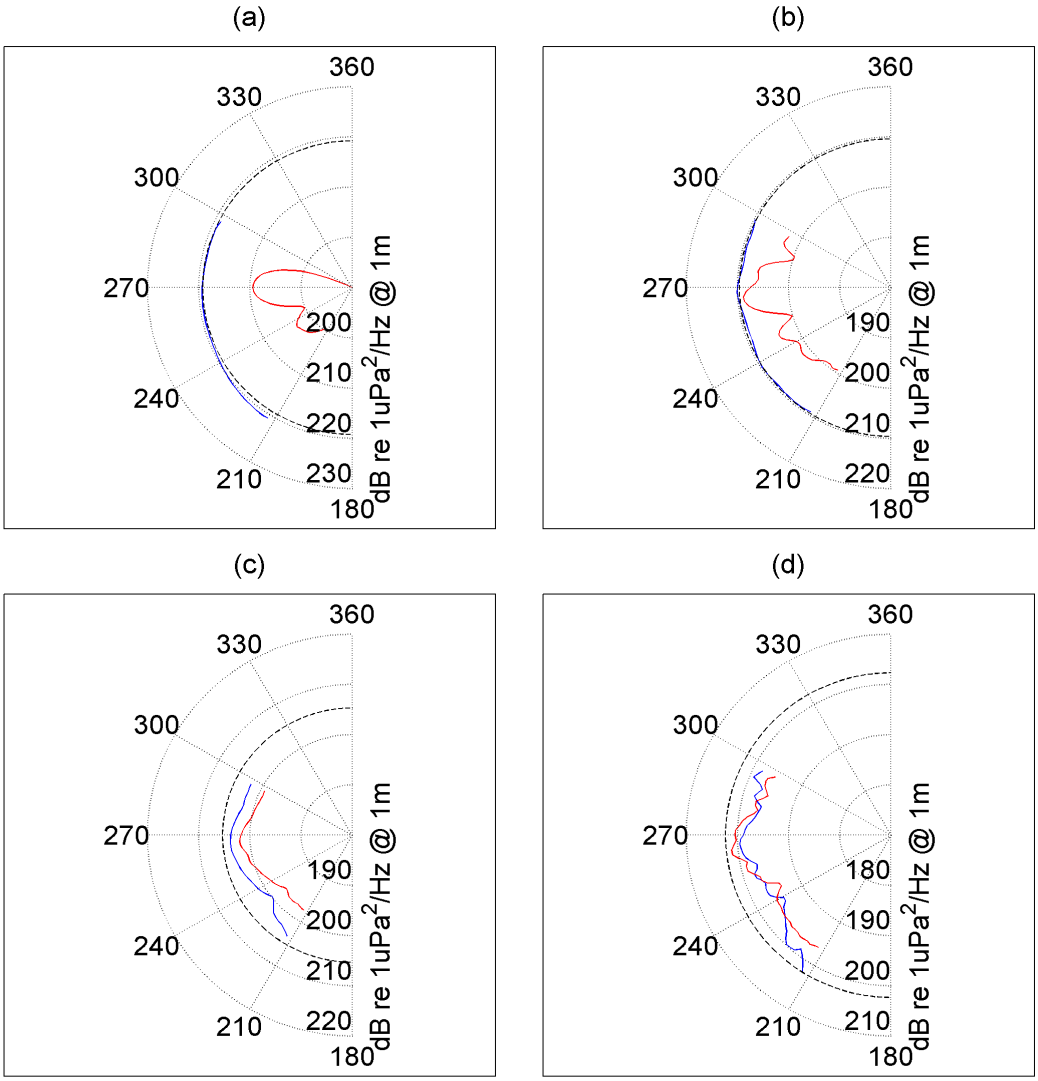

Figure 7.14 Equivalent far-field source levels at (a) 112 Hz, (b) 336 Hz, (c) 560 Hz and (d) 784 Hz. Simulation data included propagation effects. Blue, result using true transfer function; red, result assuming spherical spreading. Source array was from 0 to 27 m at 0.5 m intervals, and calculation used magnitude regularisation.

7.3.2 Application to field data

Figure 7.15 shows the results of applying the LSMC beamformer to the measured field data for three different manoeuvres: serials 1A, 1C and 1D. In each case the beamformer was applied over an 18 second time interval centred on the time at which the vessel was in the array broadside direction. The LSMC beamformer was run with a normalised white-noise gain weighting factor $b' = 1$, and the snapshot length was 1 s, which gave a processing bandwidth of 1 Hz. All 60 hydrophones

were used in the calculation and corrections were made for hydrophone directionality using the beam pattern method (Section 7.2.3.3). The geoacoustic models and vertical-plane array shapes obtained from the matched-field inversion described in Chapter 6 were used in the computation of the steering vectors. The transfer functions were calculated using the fast-field program SCOOTER with a sea surface roughness of 0.5 m RMS, which corresponded to the measured significant wave height of 2 m. The results plotted in the figure are for the frequencies emitted by the UW30 sound source, the position and source level of which are shown in each plot by an asterisk with an error bar indicating the uncertainty in the source level calibration.

There was excellent agreement between the position estimates obtained from the three manoeuvres at 112 Hz, and the Serial 1A results showed well-defined peaks at the correct locations at all frequencies. The results at the higher frequencies for serials 1C and 1D had broader, less well-defined peaks than the Serial 1A results but still produced source level estimates close to the correct values.

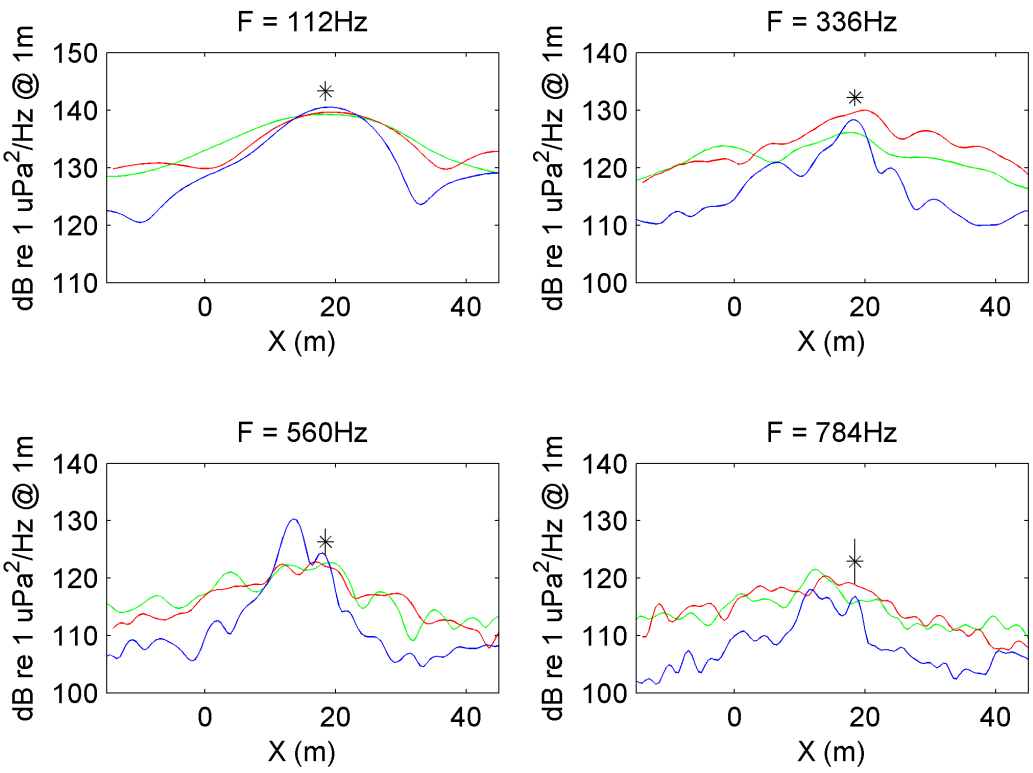

Figure 7.15 Comparison of LSMC beamformer outputs at broadside for serials 1A (blue), 1C (red) and 1D (green)

A comparison between the results of applying the DMVDR beamformer and the LSMC beamformer to the measured data from Serial 1A at the UW30 frequencies is shown in Figure 7.16. Various combinations of diagonal loading and numbers of snapshots were tried in order to optimise the performance of the DMVDR beamformer, and the results plotted here, which were the best obtained, were computed using a relative diagonal loading factor $e' = 0.1$ and all 18 snapshots.

As can be seen from the figure the performance of the DMVDR beamformer was in all cases inferior to the LSMC beamformer. Results were particularly poor when the pseudo-element method was used to correct for hydrophone directionality, which gave rise to spurious sharp peaks in the beamformer output.

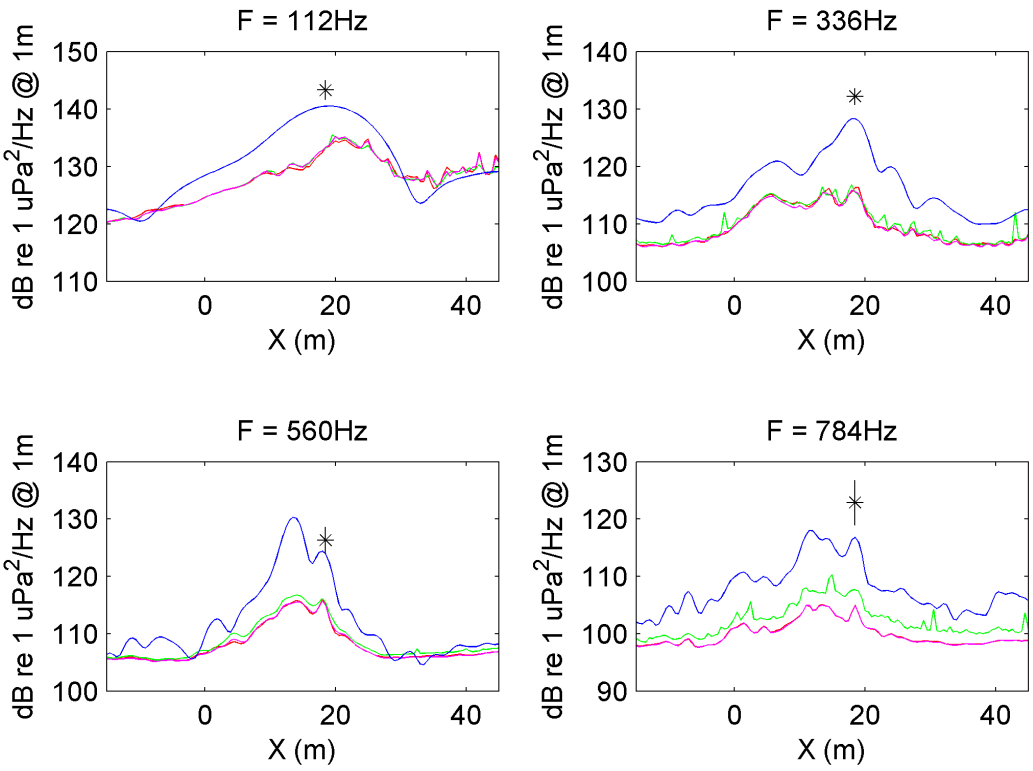

Figure 7.16 Comparison of LSMC and DMVDR beamformer results for Serial 1A. Blue, LSMC beamformer, directional hydrophones (pseudo-element); red, DMVDR beamformer, omni hydrophones; green, DMVDR beamformer, directional hydrophones (pseudo-element); magenta, DMVDR beamformer, directional hydrophones (beam pattern).

Figure 7.17 shows a comparison between the LSMC beamformer output and the source amplitude distributions computed using the RI processor for Serial 1A data at

the UW30 source frequencies. The results were similar to those obtained with simulated data, with the RI processor source amplitude distributions having similar shapes to the beamformer results, but lower levels. As mentioned previously, the lower levels produced by the RI processor were due to the different normalisation used by this processor. This effect will be discussed more fully in the next chapter. The truncation effects at the ends of the source array were more pronounced with the field data than they were with the simulated data, particularly when the source array extended over the smaller range (0 to 27 m).

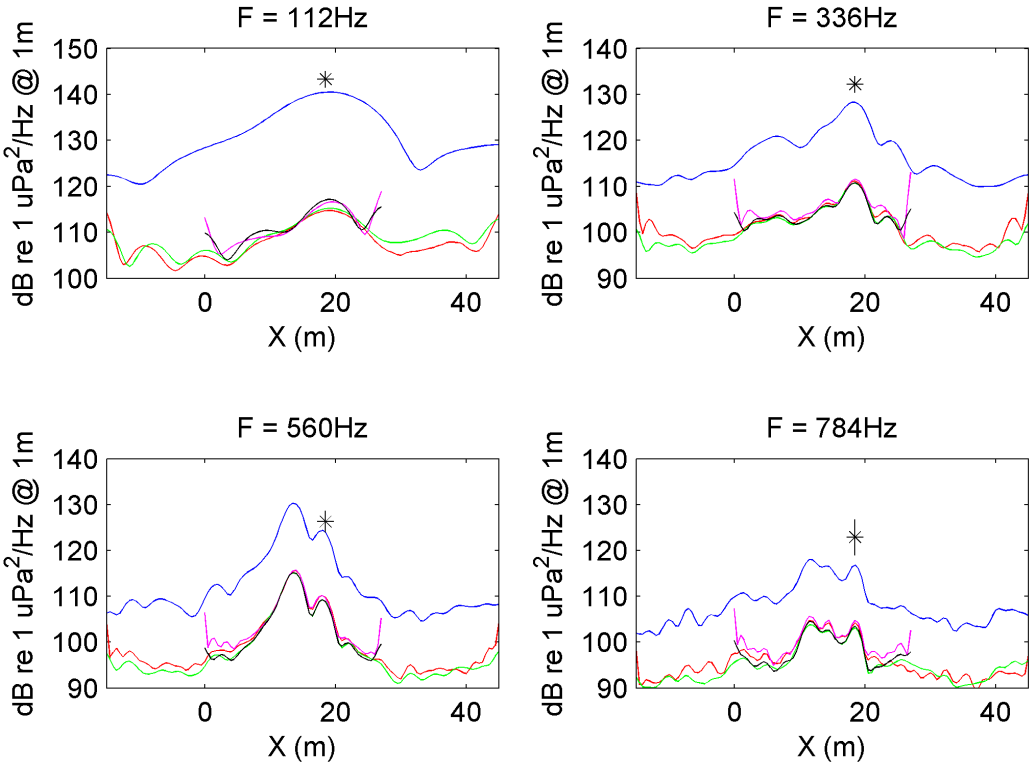

Figure 7.17 Comparison between LSMC beamformer output (blue) and source amplitude distributions computed using the RI processor and 18 seconds of data from Serial 1A. Red and green, sources distributed from -15 m to +45 m; magenta and black, source array extended from 0 m to +27 m. In both cases the source spacing was 0.5 m. Red and magenta, regularised using magnitude $(g' = 0.1)$; green and black, regularised using slope $(g' = 5)$. Calculation used all hydrophones and included hydrophone directionality (beam pattern).

The equivalent far-field source levels corresponding to these amplitude distributions are plotted in Figure 7.18. At each frequency the results were very similar near the centre of the beam pattern but differed towards either end.

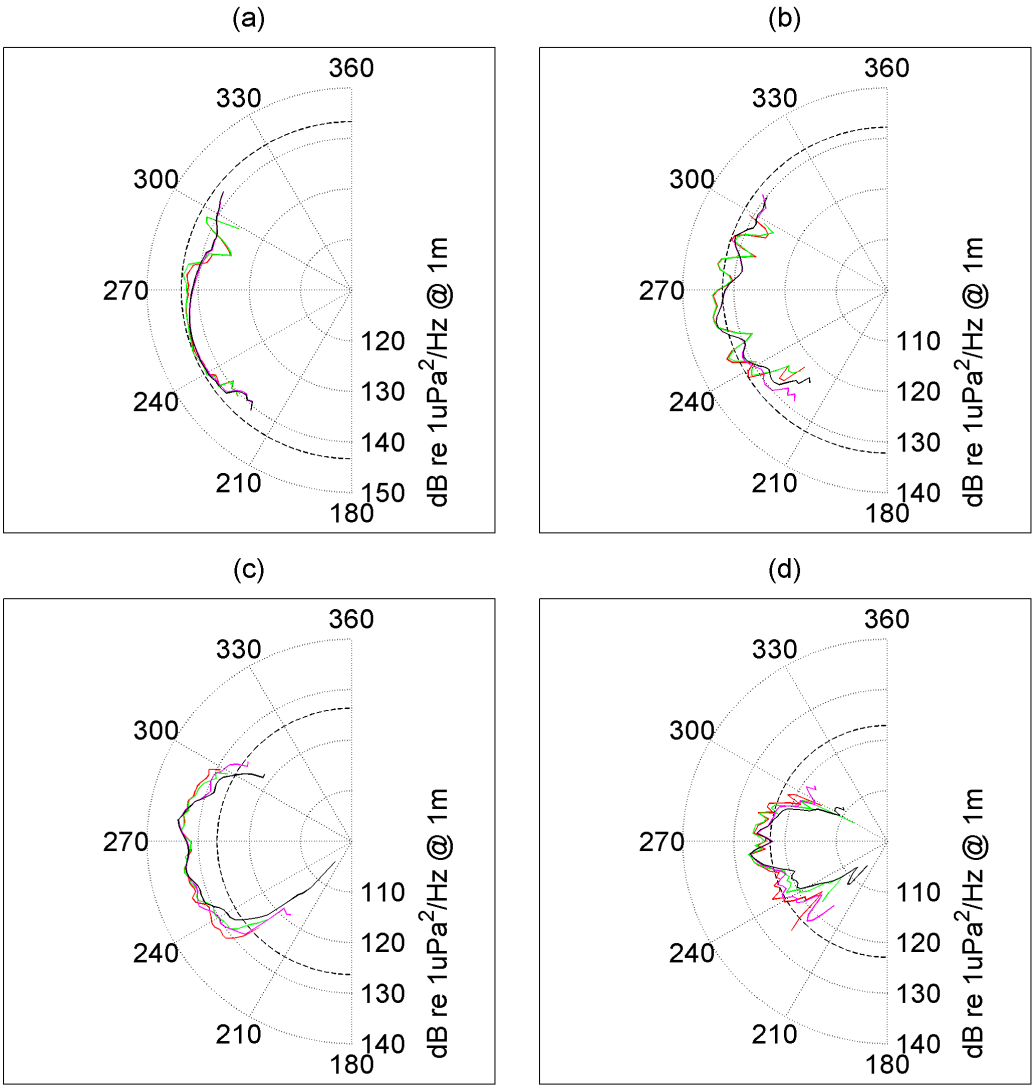

Figure 7.18 Equivalent far-field source levels computed using 18 seconds of data and RI processor at (a) 112 Hz, (b) 336 Hz, (c) 560 Hz and (d) 784 Hz. Line colours and other parameters are as per Figure 7.17. In each case the broken black line is the UW30 source level, and angles of 180° and 360° correspond to the stern and bow of the tow-vessel respectively.

It was possible to compute the equivalent far-field source levels over a wider range of angles by using data from a longer time period. Figure 7.19 compares the equivalent far-field source levels obtained using 108 s of data from Serial 1A to those obtained using 18 s of data. The results were consistent over the range of angles common to the two time periods. An arc corresponding to the source level of the UW30 is also plotted in Figure 7.19 for each frequency. This arc corresponds to the expected radiation pattern from the source in the absence of the ship's hull. In reality the close proximity of the hull would have introduced some directionality into the source radiation pattern and this is discussed in more detail in the next chapter.

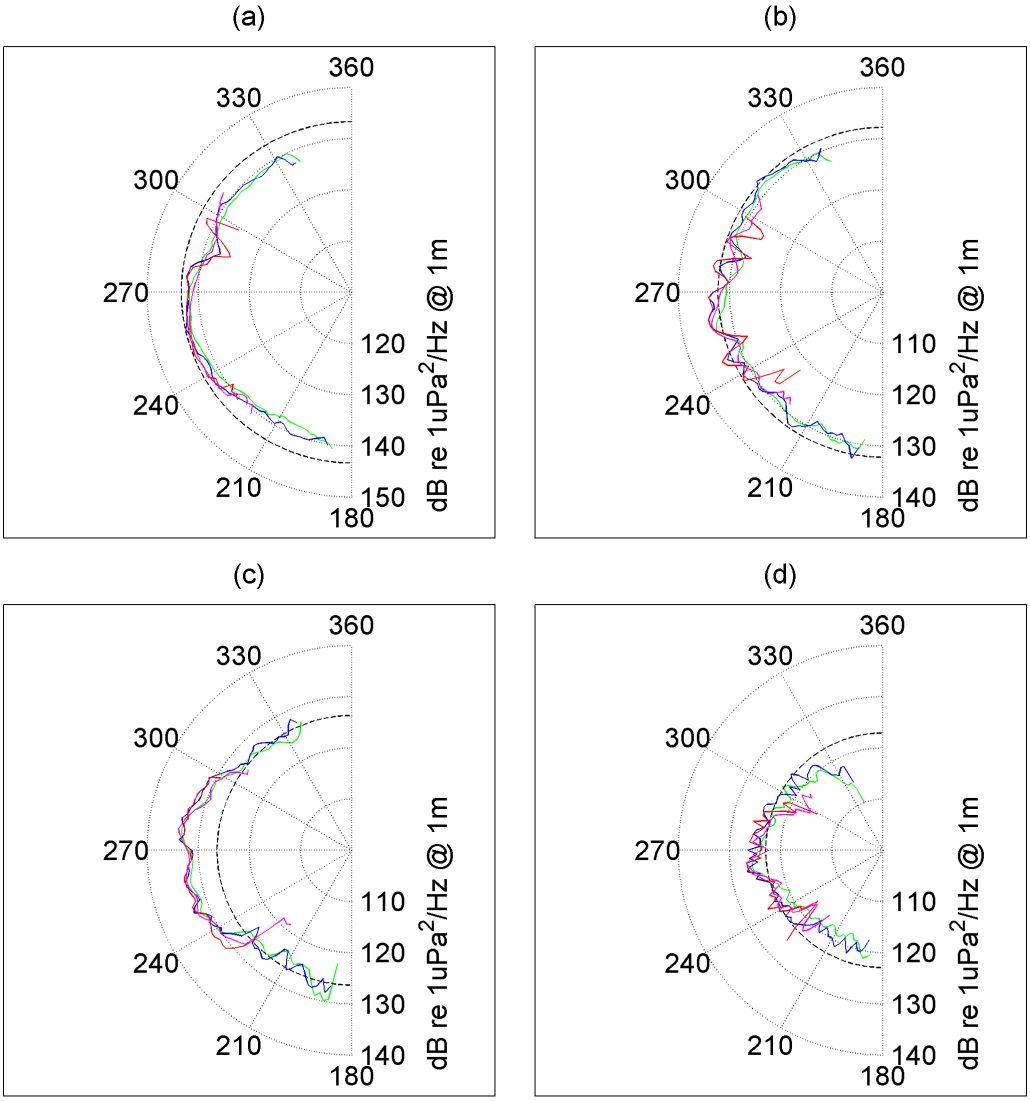

Figure 7.19 Comparison between Serial 1A equivalent far-field source levels computed using 18 seconds of data (red and magenta) and 108 seconds of data (blue and green) at (a) 112 Hz, (b) 336 Hz, (c) 560 Hz and (d) 784 Hz. Sources were distributed over: -15 to 45 m (blue and red); 0 to 27 m (green and magenta). All results calculated using magnitude regularisation.

Equivalent far-field source levels computed using the data from serials 1C and 1D are compared to the Serial 1A results in Figure 7.20. Similar results were obtained for all three serials at 112 Hz but there was more variation at the higher frequencies, particularly 784 Hz.

A detailed discussion of these results will be given in the next chapter.

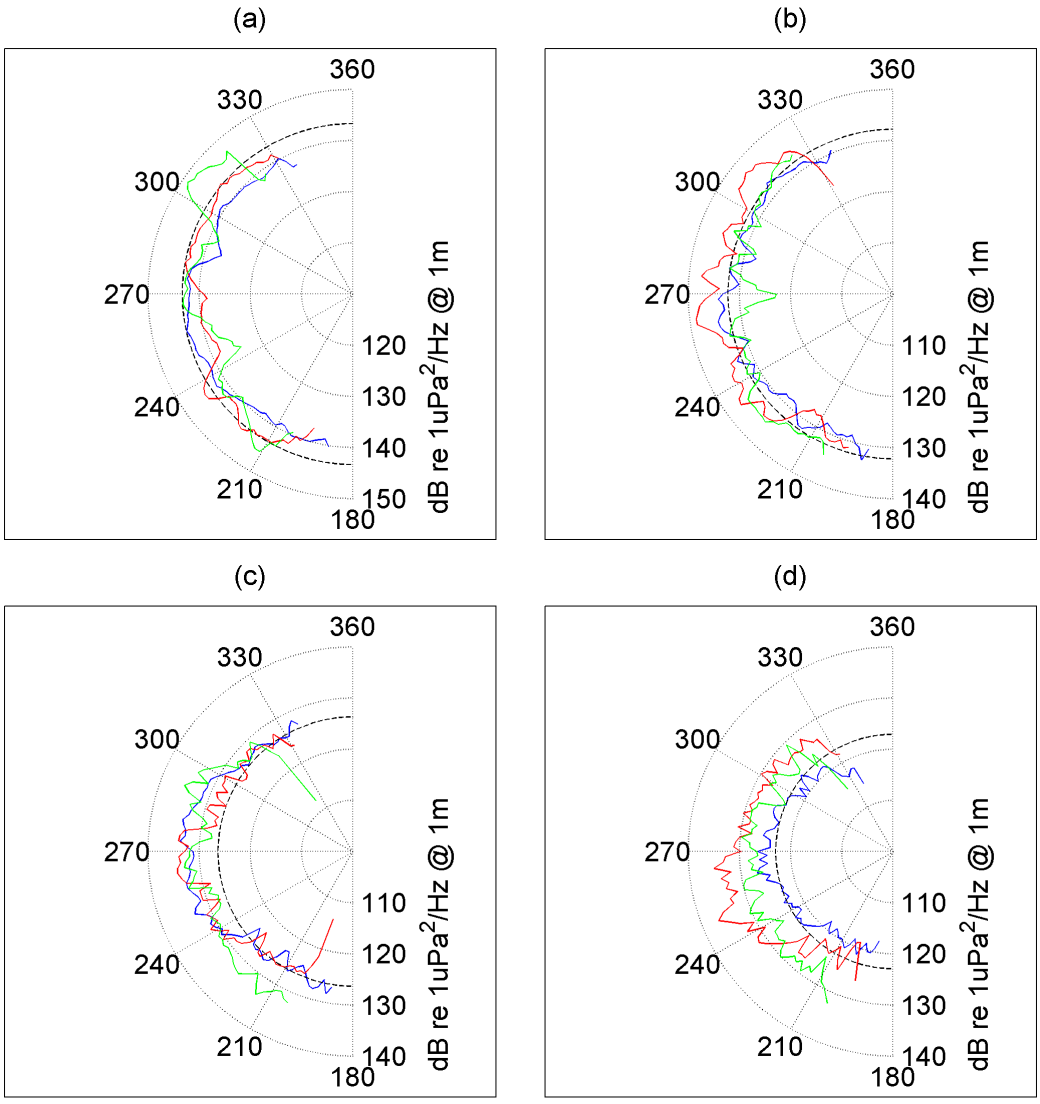

Figure 7.20 Comparison between equivalent far-field source levels at (a) 112 Hz, (b) 336 Hz, (c) 560 Hz and (d) 784 Hz computed using data from Serial 1A (blue), Serial 1C (red) and Serial 1D (green). Serial 1A result used 108 seconds of data. Serial 1C and 1D results used 72 seconds of data. Sources distributed over -15 to 45 m, magnitude regularisation.

Plots of the output of the LSMC beamformer over the frequency range 1 Hz to 1000 Hz are given in Figure 7.21 for the three serials. Processing parameters were the same as those described above for the results shown in Figure 7.15. The profile of the vessel is also plotted to scale in the appropriate location, but note that these plots represent the sound being emitted from the port side of the vessel. Plots of the same data over smaller frequency ranges are given in figures 7.22 to 7.25.

For all three serials, highest levels over the entire frequency range occurred in the region of the vessel's engine room. The Serial 1A results also indicated that some

energy was being emitted at a location corresponding to the vessel's propeller, particularly at higher frequencies. This was not apparent in the results from the other two serials, but may have been obscured by higher noise levels.

During Serial 1A only the starboard propeller was being driven, with the port engine out of gear and idling, whereas during serials 1C and 1D both propellers were being driven. This presumably accounts for the rather different character of the Serial 1A results, which were dominated by many quite narrow spectral lines whereas the results for the other two serials contained fewer, broader lines.

Nominal engine revolutions were slightly different for each serial, which accounts for the observed changes in frequency of the prominent spectral lines. Full machinery details were given in Chapter 4, but for reference the main engine rotation rates were: Serial 1A, port 770 rpm, starboard 800 rpm; Serial 1C, both 775 rpm, and Serial 1D, both 750 rpm.

Below 10 Hz the results were dominated by non-acoustic noise, most likely hydrodynamic flow noise. This can be clearly seen from Figure 7.26, which is a plot of relative signal level as a function of location in the frequency-wavenumber plane. These results were computed using a 2 dimensional (time and space) Fourier transform of data from the X octave hydrophones. If the array had been straight the wavenumber in question would be the component of the wave vector in the direction parallel to the array. In this case the array was slightly bent so this simple interpretation is not valid, but it is still the case that acoustic signals must lie in a region delimited approximately by the two lines shown, which are given by $f = \pm \frac{c_0 k}{2p}$ where f is the frequency (Hz) c_0 is the sound speed (ms^{-1}) and k is the wavenumber (m^{-1}). This was clearly not the case below 10 Hz.

The equivalent far-field source levels of the vessel with aspect from the bow, computed from Serial 1A data using the RI processor at frequencies from 1 Hz to 1000 Hz, are plotted in figures 7.27 and 7.28. The processing bandwidth was 1 Hz, magnitude regularisation was used, and the sources were distributed from -15 to 45 m. These results indicate that the vessel noise was directional at most frequencies and that a distinct change in the character of the directional pattern occurred at around 300 Hz. Below this frequency the most prominent spectral lines tended to have a minimum at broadside and maxima directed more towards the bow and stern

of the vessel, whereas above 300 Hz the bulk of the energy was directed towards broadside.

A more complete discussion of these results will be given in Chapter 8.

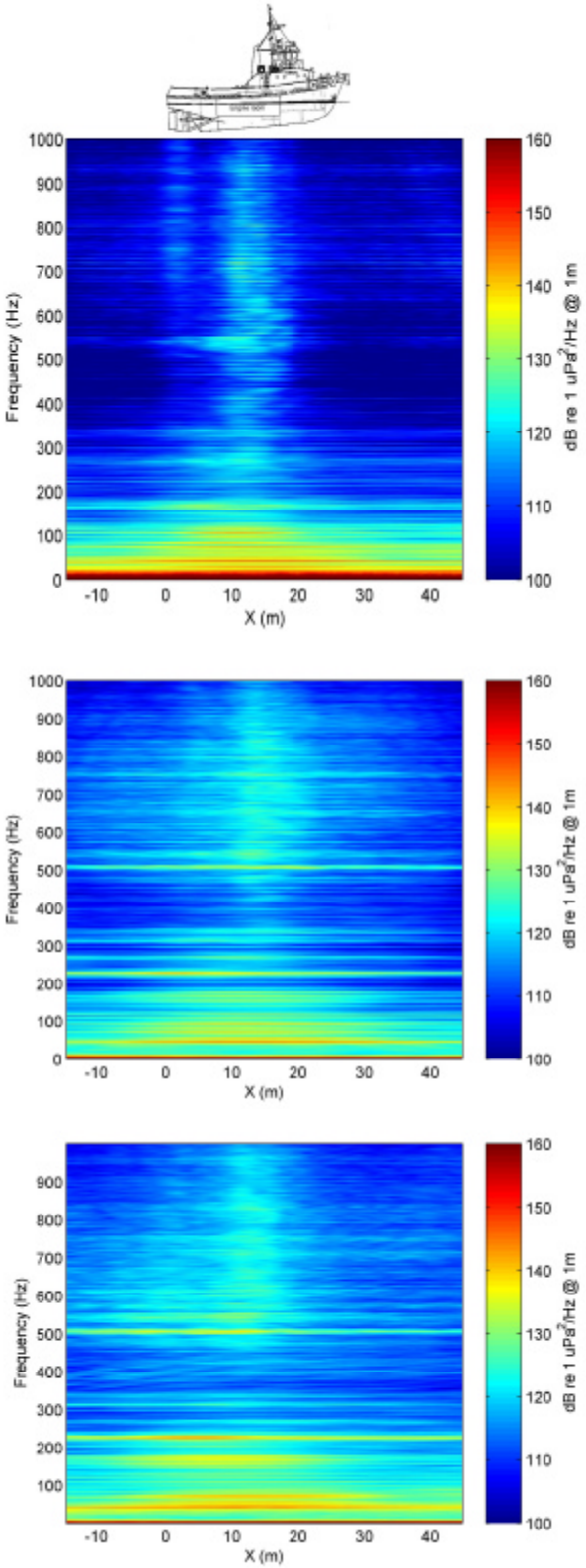

Figure 7.21 LSMC Beamformer outputs for frequencies from 1 to 1000 Hz. Top, Serial 1A; middle, Serial 1C; bottom, Serial 1D.

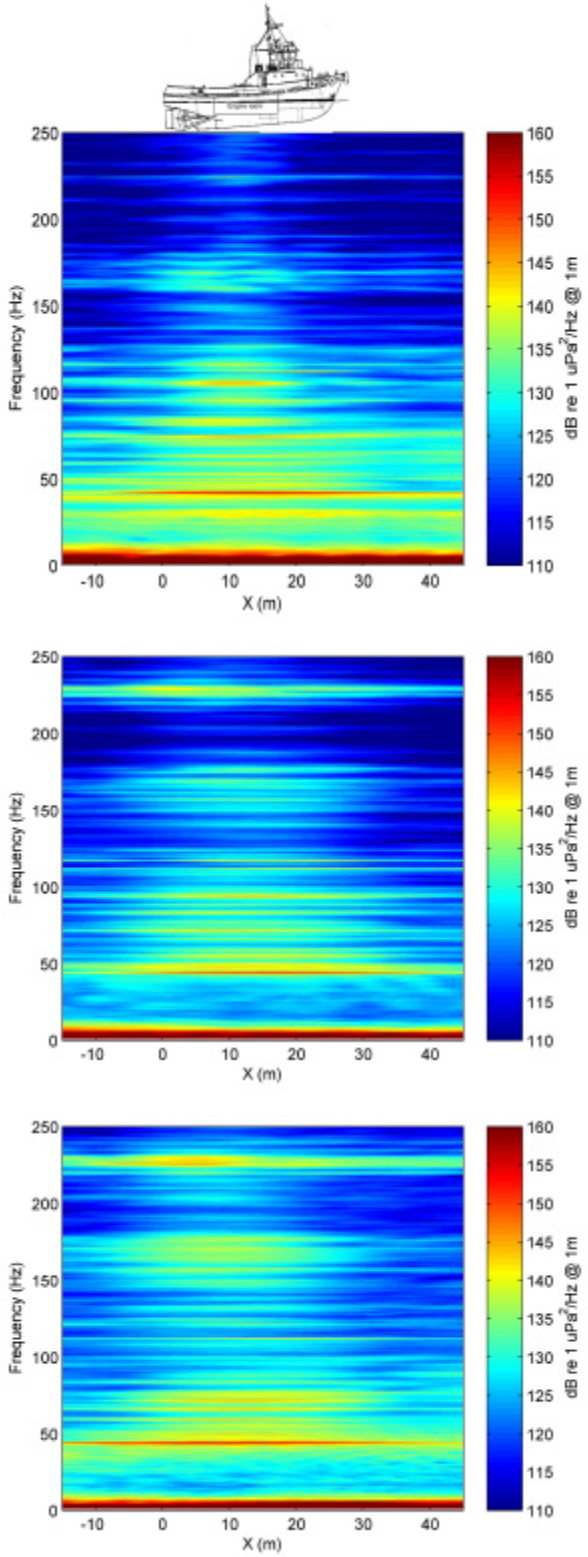

Figure 7.22 LSMC Beamformer outputs for frequencies from 1 to 250 Hz. Top, Serial 1A; middle, Serial 1C; bottom, Serial 1D.

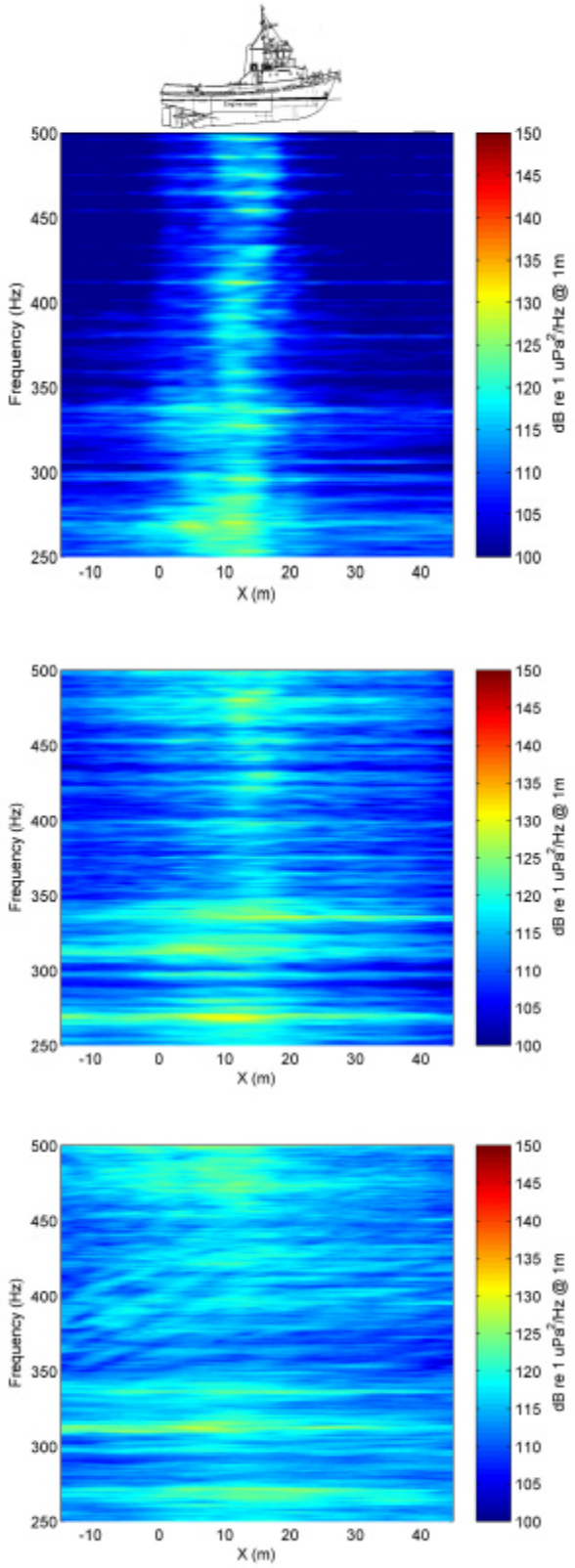

Figure 7.23 LSMC Beamformer outputs for frequencies from 250 to 500 Hz. Top, Serial 1A; middle, Serial 1C; bottom, Serial 1D.

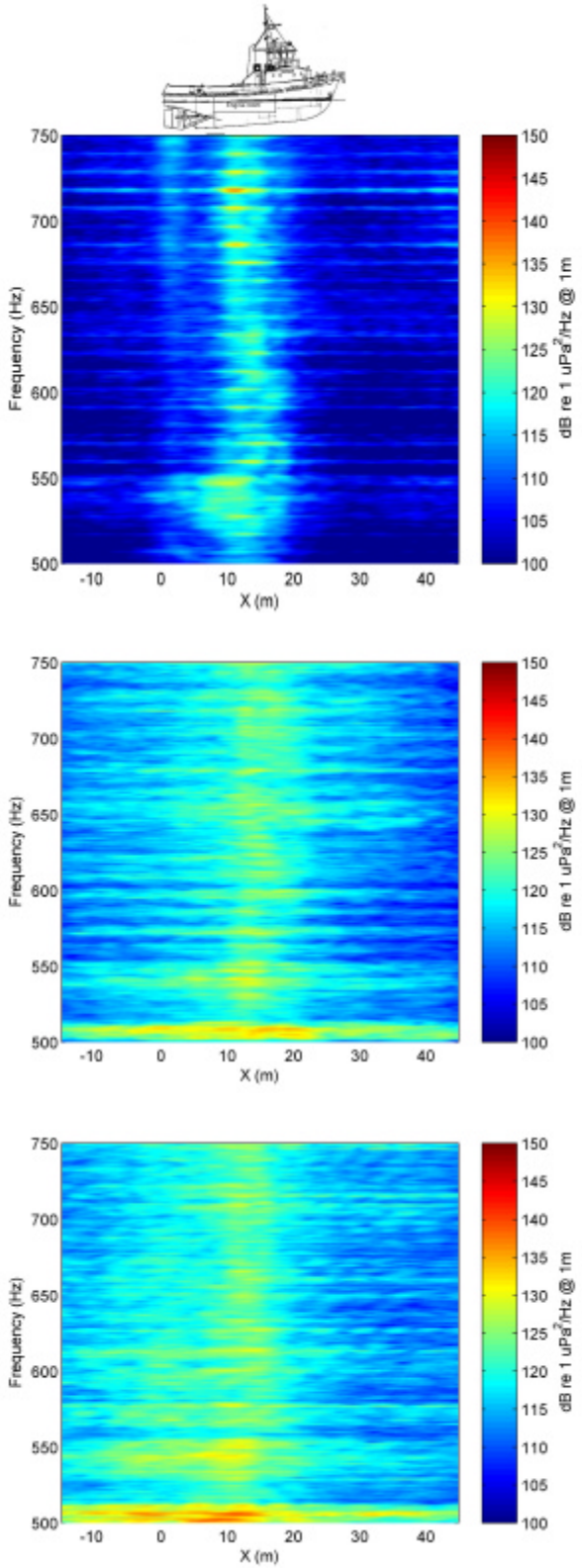

Figure 7.24 LSMC Beamformer outputs for frequencies from 500 to 750 Hz. Top, Serial 1A; middle, Serial 1C; bottom, Serial 1D.

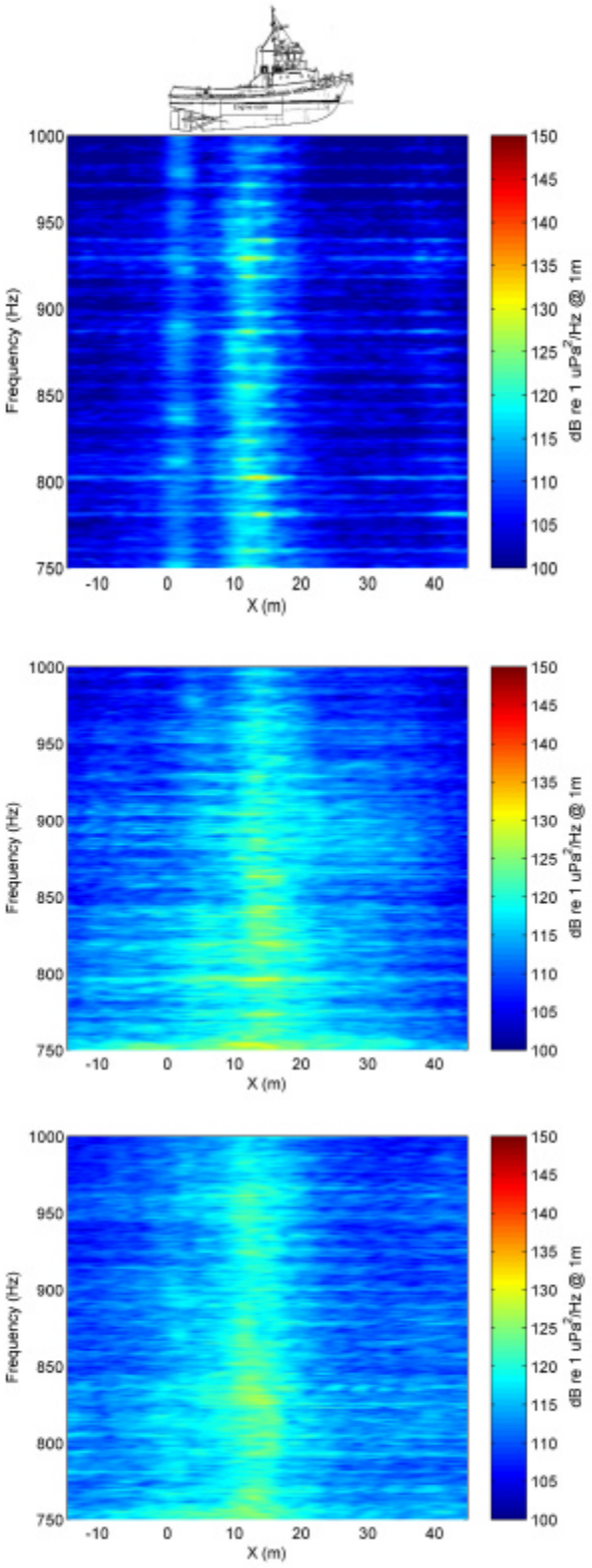

Figure 7.25 LSMC Beamformer outputs for frequencies from 750 to 1000 Hz. Top, Serial 1A; middle, Serial 1C; bottom, Serial 1D.

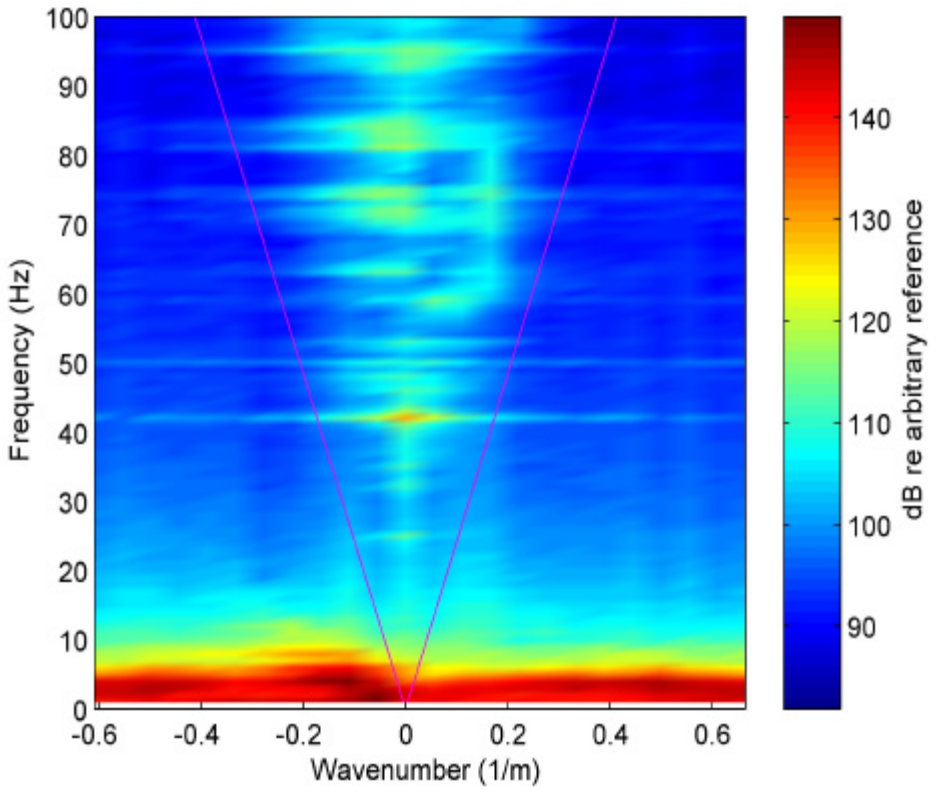

Figure 7.26 Frequency-wavenumber plot for Serial 1A field data computed using X octave hydrophones. Diagonal lines delimit the possible region for acoustic signals.

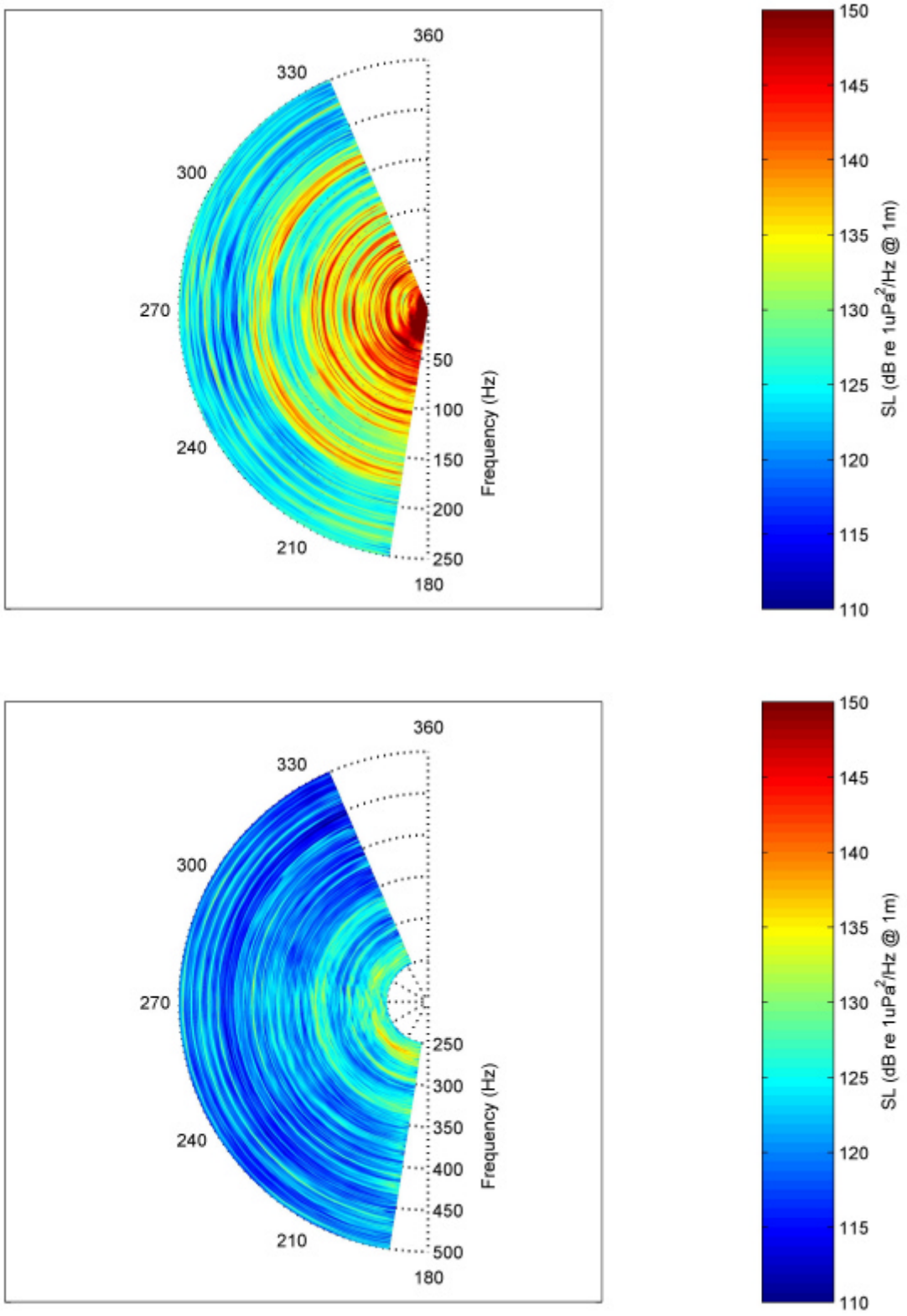

Figure 7.27 Equivalent far-field source levels for frequencies from 0 to 250 Hz (top) and 250 to 500 Hz (bottom). Computed using 108 seconds of data from Serial 1A and RI processor with magnitude regularisation. Angles of 180° and 360° correspond to the stern and bow of the tow-vessel respectively.

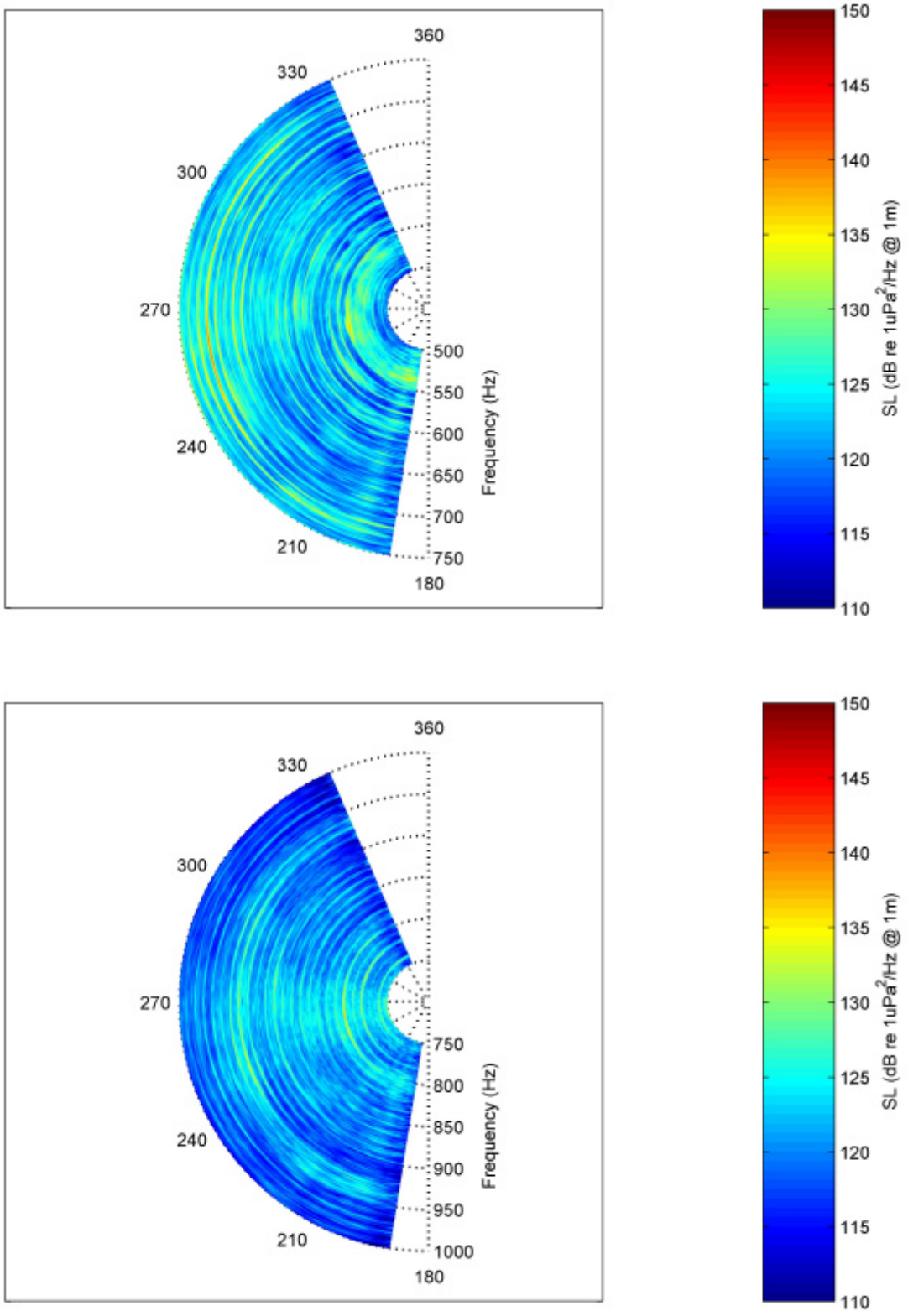

Figure 7.28 Equivalent far-field source levels for frequencies from 500 to 750 Hz (top) and 750 to 1000 Hz (bottom). Computed using 108 seconds of data from Serial 1A and RI processor with magnitude regularisation. Angles of 180° and 360° correspond to the stern and bow of the tow-vessel respectively.

7.4 Summary

A number of different array-processing algorithms were developed to localise acoustic sources on the tow-vessel, determine their amplitudes, and estimate the far-field signature of the vessel. Although time-domain beamformers seemed to offer most potential for dealing with the highly dynamic situation encountered in this project, the difficulty of modifying them to cope with time-varying acoustic transfer functions outweighed their potential advantages and attention was focussed on processing the array data in the frequency-domain. Three different algorithms were derived to do this: a data independent beamformer termed the LSMC beamformer, a data dependent beamformer, referred to as the DMVDR beamformer (which was obtained by modifying the well-known minimum variance distortionless response (MVDR) beamformer to deal with dynamic situations), and a method, referred to as the RI processor, based on the regularised inversion of the array data to obtain the complex amplitudes of a hypothesised set of sources. For all three algorithms a preliminary re-sampling of the signal, carried out to provide Doppler compensation, was found to improve the results.

All three algorithms performed well with simulated data, with the DMVDR beamformer providing the best source localisation but relatively poor source level estimates. However, the DMVDR beamformer's performance degraded significantly when it was applied to field data whereas the other two processors had similar performance with simulated and field data.

The LSMC beamformer was used to localise sources and determine their amplitudes at the frequencies emitted by the UW30 source for comparison with calibrated values. This beamformer was also used to obtain plots of the spatial distribution of energy radiated by the tow-vessel during the three processed serials over the frequency range 1 Hz to 1000 Hz.

Equivalent far-field source spectral levels were computed for the tow-vessel as a function of both azimuth and frequency using source amplitude distributions determined by the RI processor. Again results were calculated over the frequency range 1 Hz to 1000 Hz, with particular attention being paid to the UW30 source frequencies.

All of these results will be discussed in detail in the next chapter.

8 Discussion

The purpose of this chapter is to investigate the degree to which the algorithms developed in the preceding chapters succeeded in carrying out the following tasks:

1. localising underwater acoustic noise sources on the tow-vessel,
2. quantifying the strength of these sources, and
3. determining the resultant far-field acoustic signature of the tow-vessel.

Section 8.1 deals with the localisation of noise sources. Localisation results for the UW30 source are discussed and comparisons are made between the spatial positions of the various items of operating machinery, their expected spectral output, and the beamformer outputs.

The performance of the algorithms for determining the absolute amplitudes of acoustic sources are assessed in Section 8.2, which includes a detailed discussion of the various possible sources of error.

The application of these results to the computation of far-field vessel signatures is discussed in Section 8.3 and Section 8.4 deals with the feasibility of using these algorithms in an operational system. A summary of the main results of this chapter is given in Section 8.5.

8.1 Noise source localisation

Three array-processing techniques were applied to the field data in the previous chapter: the LSMC and DMVDR beamformers, and the RI processor. Of these, the LSMC beamformer produced the best source localisation results. This beamformer successfully localised the UW30 sound source at all frequencies using data from Serial 1A and successfully localised the 112 Hz fundamental in all three serials. The results for the higher frequencies for serials 1C and 1D were poorer and appeared to suffer from a lower signal to noise ratio than the equivalent Serial 1A results. The LSMC beamformer localisation results are summarised in Table 8.1 and discussed further below.

The DMVDR beamformer results for field data were generally quite poor and showed nowhere near the localisation performance obtained with this beamformer using simulated data. The DMVDR beamformer was based on the MVDR

algorithm, which has a well-documented high sensitivity to mismatch between reality and the propagation conditions and geometry assumed when calculating the steering vector (Cox et al. 1987). The MVDR beamformer is also known to perform poorly in the presence of correlated sources, which should not have been a problem when localising a point source such as the UW30, but could be a significant issue when attempting to localise machinery sources of substantial spatial extent. Considerable literature exists on ways of modifying the MVDR algorithm to reduce its sensitivity to mismatch and source correlation (see Jensen et al. 2000, Chapter 10, and VanVeen & Buckle 1988) and the references quoted therein) and the application of these techniques to the DMVDR beamformer may be a profitable topic for future research.

The source amplitude distributions produced by the RI processor were very similar in shape to the LSMC beamformer results but tended to have physically unrealistic increases in level at the ends. These increases in level occurred with both simulated and measured data although they were more pronounced in the latter case. The reason for these artefacts is unknown but it is likely that they arose because of a conflict between the finite length of the hypothetical source array and the smooth source amplitude distribution demanded by the regularisation procedure. It may have been preferable to model the vibration of the hull in terms of a sum of modes. The forward problem would then have been to compute the acoustic field due to these vibrations and the inverse problem would have been to determine the amplitude and phase of each mode. This approach was taken in Williams (1996) to obtain an expression for the vibration of the surface of a cylindrical shell from measurements of the acoustic field made along a semicircle in the far-field of the sources, but it would be awkward to apply it to a real ship because of the difficulty of determining the vibrational modes of such a complicated structure, especially in the absence of detailed knowledge of the vessel's construction.

A more promising approach may have been to represent the acoustic field as being due to a continuous line source with non-uniform amplitude given by a summation over an assumed set of orthogonal basis functions. The coefficients of the basis functions would then have been the parameters to be estimated. If the basis functions were chosen to be complex exponentials then this approach would have been equivalent to estimating the coefficients of the spatial Fourier transform of the

source amplitudes, rather than the source amplitudes themselves. This technique would have the advantage that the spatial resolution could be adjusted simply by adjusting the number of terms in the summation. By using only a few terms a well-determined set of equations would be obtained, with relatively poor spatial resolution but (unlike the implemented method) still retaining a smooth source amplitude distribution. Including more terms would improve the spatial resolution but the set of equations would become progressively less well determined. Further research along these lines is recommended.

Table 8.1 Summary of UW30 source location estimates obtained using LSMC beamformer.

Frequency (Hz)		112	336	560	784
True source location, m		18.5	18.5	18.5	18.5
1A	Estimated source location (error), m	19.0 (+0.5)	18.5 (0)	18.0 (-0.5)	18.5 (0)
1C	Estimated source location (error), m	19.5 (+1.0)	20.0 (+1.5)	17.0 (-1.5)	17.5 (-1.0)
1D	Estimated source location (error), m	18.5 (0)	18.0 (-0.5)	19.0 (+0.5)	19.5 - 22.0 (?)

The serials differed in several respects: the hydrophone CPA ranges were 80 m for Serial 1A, 110 m for Serial 1C, and 130 m for Serial 1D; the speed of the array relative to the vessel was 2.5 m/s during Serial 1A, and 4.0 m/s during Serials 1C and 1D; only the starboard engine was in gear during Serial 1A, whereas both engines were in gear during the other two serials; and the main engine rotation rates differed from serial to serial (see Chapter 4). The array was also shallower during serials 1C and 1D (mid-depth of 7.5 m and 7.2 m respectively) than it was in Serial 1A (mid-depth of 13 m). The sea state was similar for these three serials as evidenced by the RMS vessel roll, which was 3.9° for serials 1A and 1D, and 4.2° for Serial 1C.

Tests with simulated data have shown that beamformer degradation due to the motion of the array relative to the vessel was unlikely to have been the source of the poorer results obtained with data from Serials 1C and 1D, and that the problem was more likely to have been due to a lower signal to noise ratio. Possible reasons for the reduced signal to noise ratio will be discussed shortly.

Dr Darryl McMahon at the Defence Science and Technology Organisation carried out a harmonic analysis of the output of the leading array hydrophone, just before the start of each turn (McMahon 2002). This analysis detected harmonics due to the cylinder firing rates (CFRs) of the alternator and two main engines, as well as harmonics due to gear noise with fundamental frequencies equal to 0.418 times the corresponding main engine CFR. These results are plotted over the LSMC beamformer outputs for Serial 1A in figures 8.1 to 8.4. There was excellent correlation between the expected harmonic locations and the maxima in the beamformer output in both space and frequency. This occurred over the full frequency range of 0 to 1000 Hz, although at the higher frequencies slight shifts in frequency are apparent that were most probably due to the accumulation of slight errors in determining the fundamental frequencies. Some change in engine RPM between the two sets of measurements may also have occurred. Note also that the sound received by the array hydrophones was radiated by the hull from locations that depended not only on the positions of the various items of machinery but also on the vibration transmission paths and the response of the hull itself. Exact spatial correlation was therefore not expected.

Equivalent results for Serial 1C are plotted in figures 8.5 to 8.8, and showed good spatial and frequency domain correlations between the expected harmonic locations and the beamformer maxima up to a frequency of about 550 Hz. At frequencies above 500 Hz the beamformer maxima were less distinct than those in the equivalent Serial 1A plot due to an increase in background noise of ~10 dB, and also appeared to be spread more in space and frequency. The results for Serial 1D were very similar to those for Serial 1C and have not been plotted.

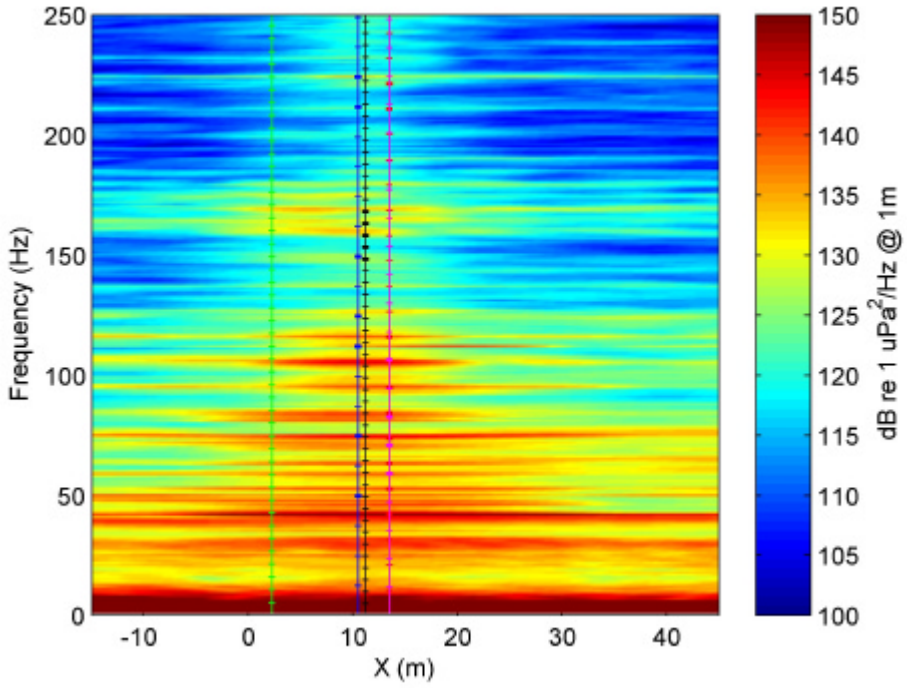

Figure 8.1 LSMC beamformer applied to Serial 1A data for frequency range 0 to 250 Hz. Vertical lines correspond to locations of centres of items of machinery: blue, alternator; magenta, main engines; black, gear boxes; green, propellers. Horizontal tick marks are at frequencies corresponding to expected harmonics: blue, alternator CFR; red, port engine CFR (out of gear); magenta, starboard engine CFR; black, starboard gearbox; green, starboard propeller blade rate. The UW30 source is clearly visible at x =18.5 m, and a frequency of 112 Hz.

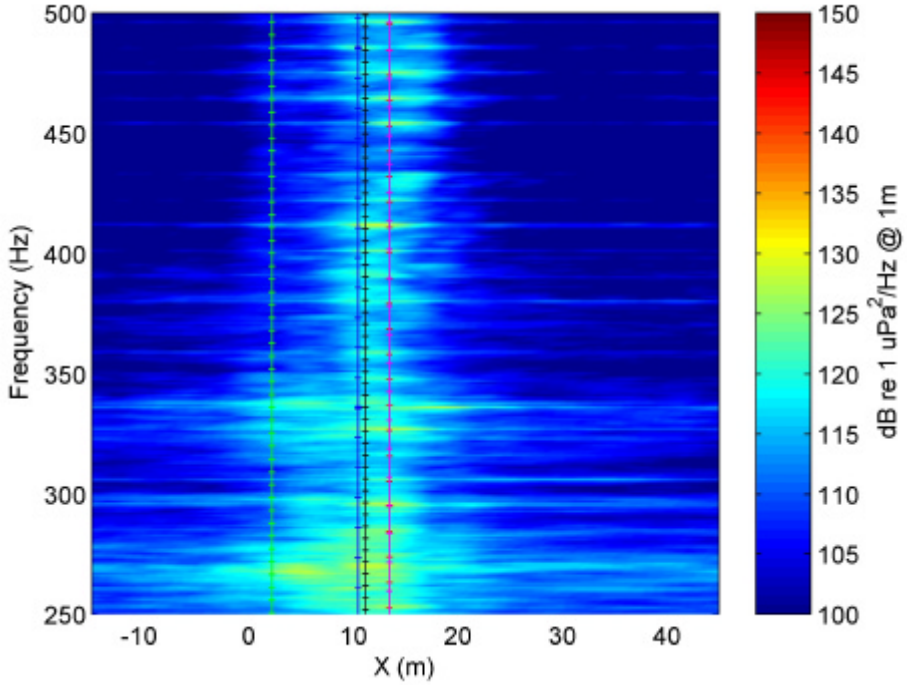

Figure 8.2 As for Figure 8.1 but for 250 to 500 Hz.

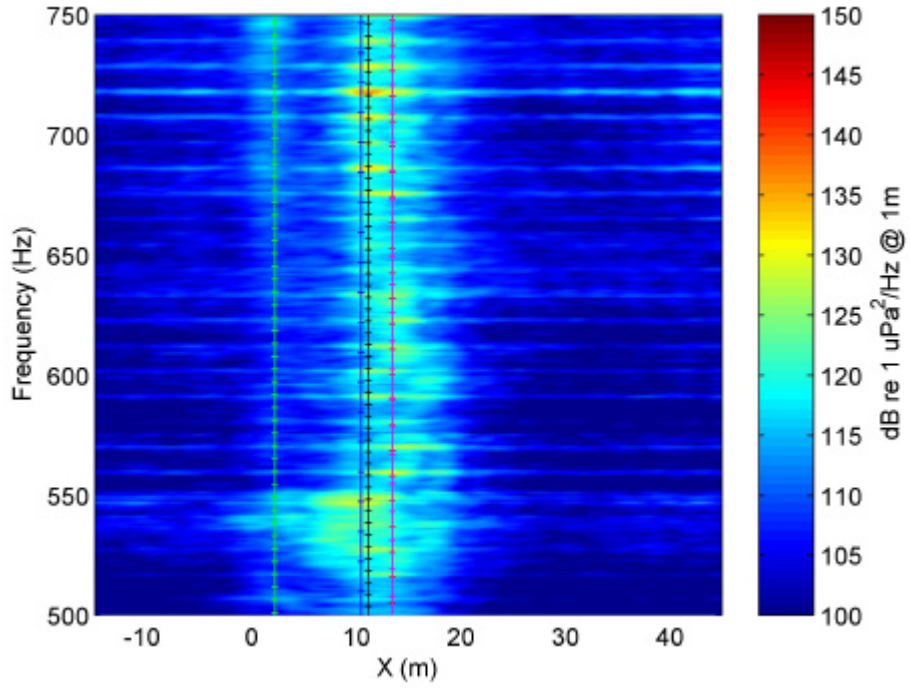

Figure 8.3 As for Figure 8.1 but for 500 to 750 Hz.

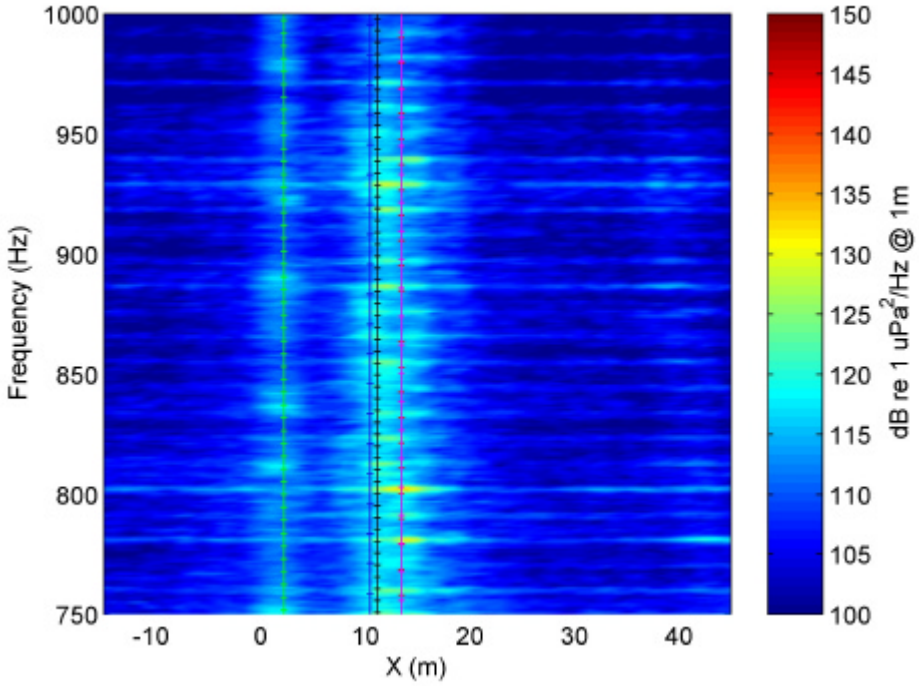

Figure 8.4 As for Figure 8.1 but for 750 to 1000 Hz.

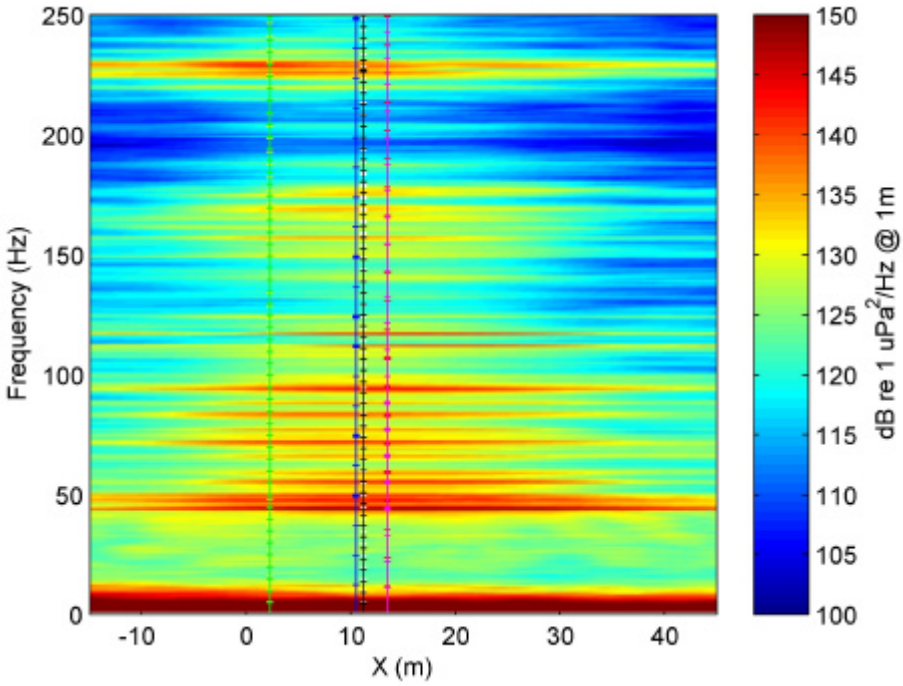

Figure 8.5 LSMC beamformer applied to Serial 1C data for frequency range 0 to 250 Hz. Vertical lines correspond to locations of centres of items of machinery: blue, alternator; magenta, main engines; black, gear boxes; green, propellers. Horizontal tick marks are at frequencies corresponding to expected harmonics: blue, alternator CFR; red, port engine CFR; magenta, starboard engine CFR; white, port gearbox; black, starboard gearbox; yellow, port propeller blade rate; green, starboard propeller blade rate. The UW30 source is clearly visible at X=18.5 m, and a frequency of 112 Hz.

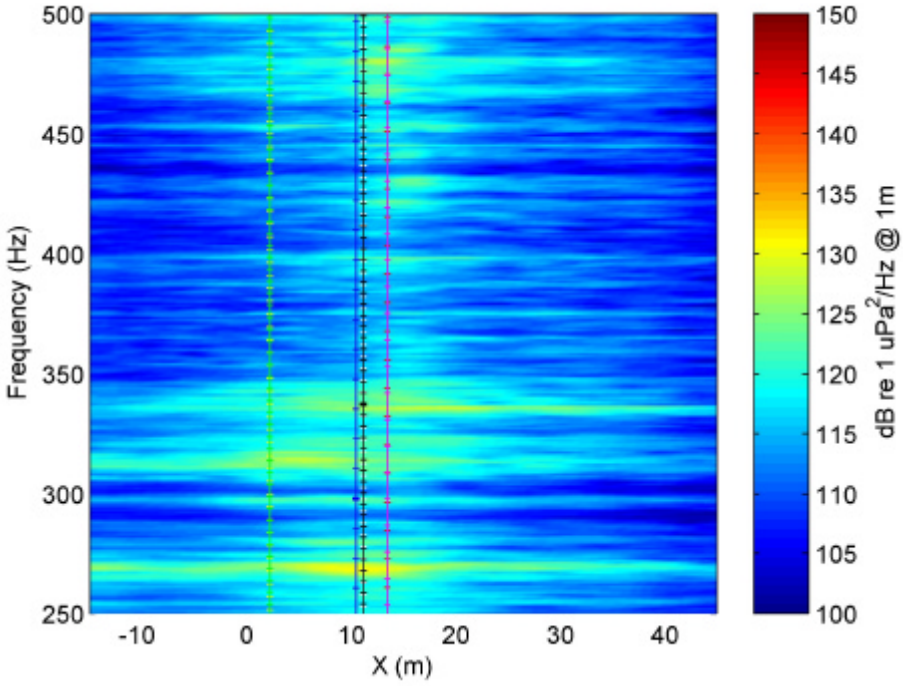

Figure 8.6 As for Figure 8.5 but 250 to 500 Hz.

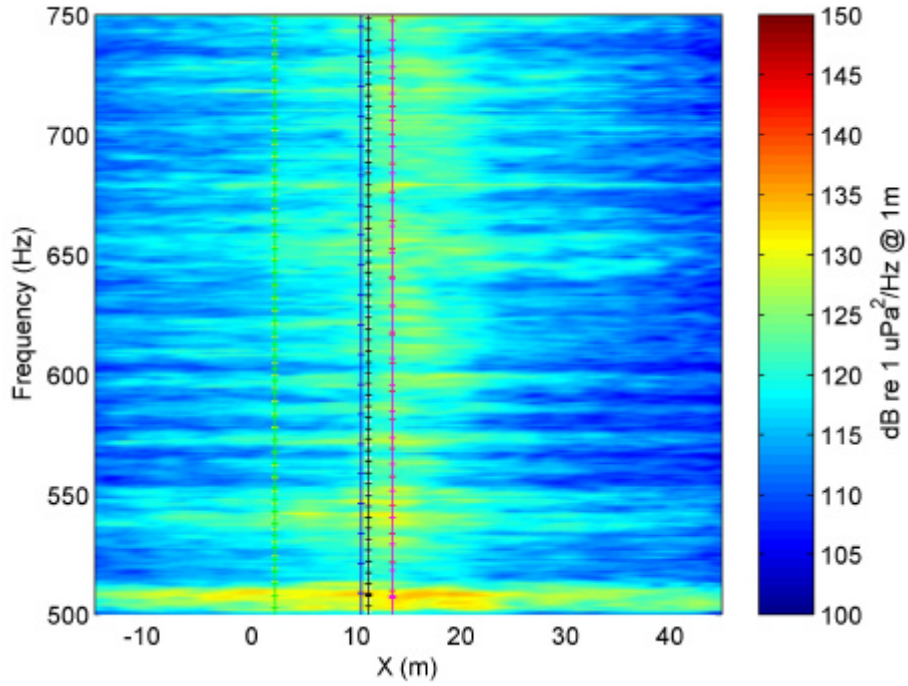

Figure 8.7 As for Figure 8.5 but 500 to 750 Hz.

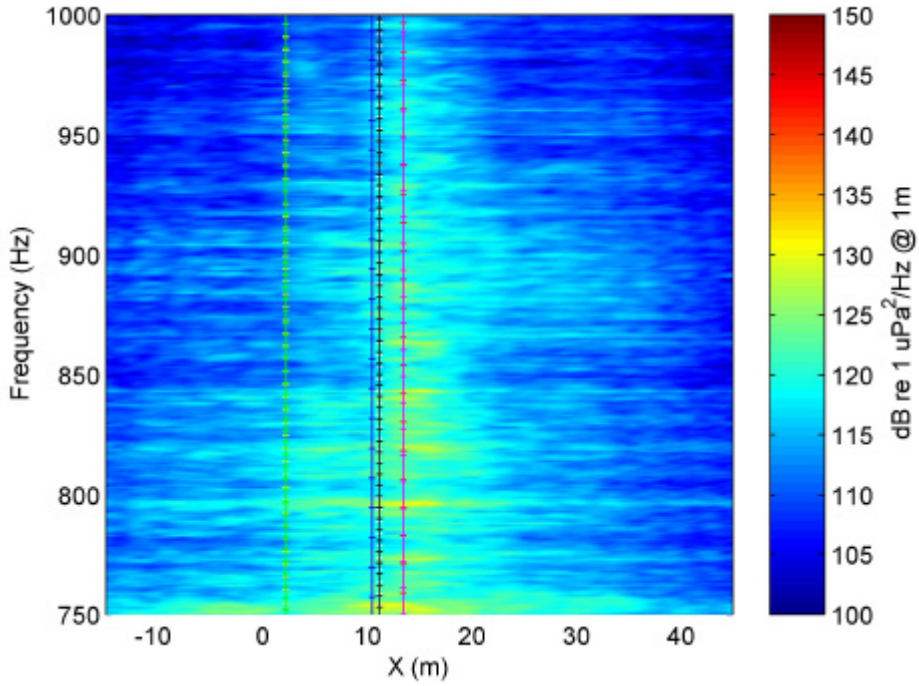

Figure 8.8 As for Figure 8.5 but 750 to 1000 Hz.

The poorer signal to noise ratio for Serial 1C was due primarily to the larger distances between the sources and hydrophones, and the shallower hydrophone depths. Plots of transmission loss versus range and depth, showing the regions

sampled by the array when computing the beamformer output for each serial, are given in figures 8.9 to 8.12. These plots were computed using the fast-field program, SCOOTER (Porter 1999), and show strong interference between the acoustic signals travelling by different paths. The transmission loss values shown in these plots were computed using the Serial 1A environment, but plots obtained using the environments for the other two serials showed very similar trends and differed only in the detail of the interference patterns. An effective overall transmission loss was computed for each serial and frequency. This was done by converting the transmission loss values within each rectangle to equivalent pressures (assuming a source level of 0 dB re 1 μPa @ 1 m), calculating the mean squared pressure over the rectangle, and then converting back to a transmission loss. The results of these calculations, which were carried out using the correct environment for each serial, are shown in Table 8.2. In order to provide the correct normalisation, the beamforming algorithm amplified each received signal, and consequently the associated noise, by an amount equivalent to the transmission loss. The numbers in brackets in the table therefore give an indication of the expected increase in beamformer output noise relative to Serial 1A at these frequencies, and agree well with what was seen in figures 8.1 to 8.8. This calculation provides a good indication of the expected noise increase but is inexact because in reality the hydrophones did not sample the rectangles uniformly.

The array was moving faster through the water during serials 1C and 1D than during Serial 1A, which would have led to an increase in flow noise. However, this mechanism would have primarily produced noise at low frequencies and is unlikely to have been a significant contributor to the increased high frequency noise seen here.

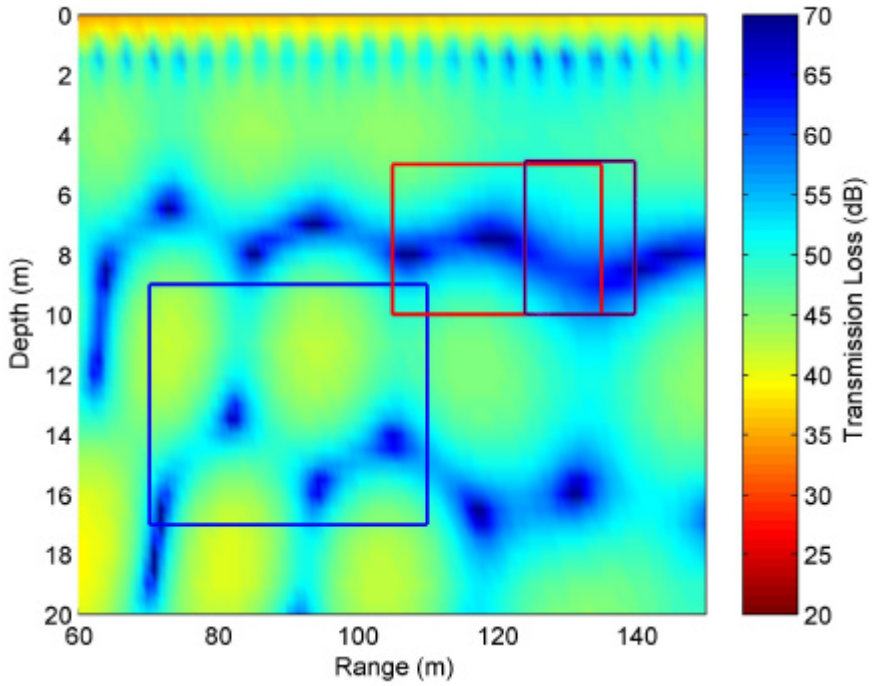

Figure 8.9 Transmission Loss vs. range and depth at 112 Hz for a 1.5 m deep source computed using SCOOTER and the Serial 1A environment. Rectangles show range-depth regions sampled by the array when computing beamformer outputs during serials 1A (blue), 1C (red) and 1D (black).

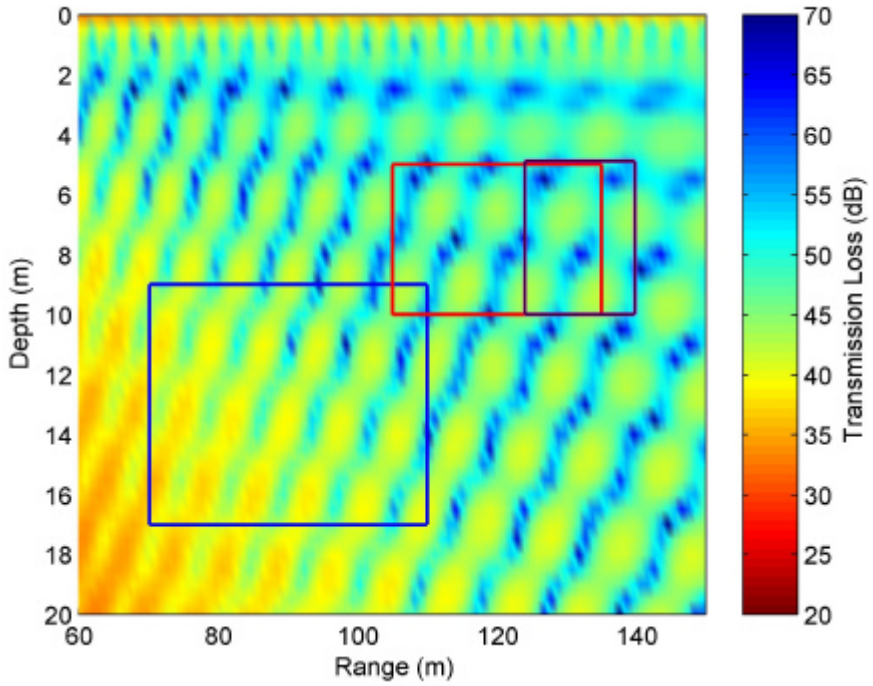

Figure 8.10 As for Figure 8.9, but for a frequency of 336 Hz.

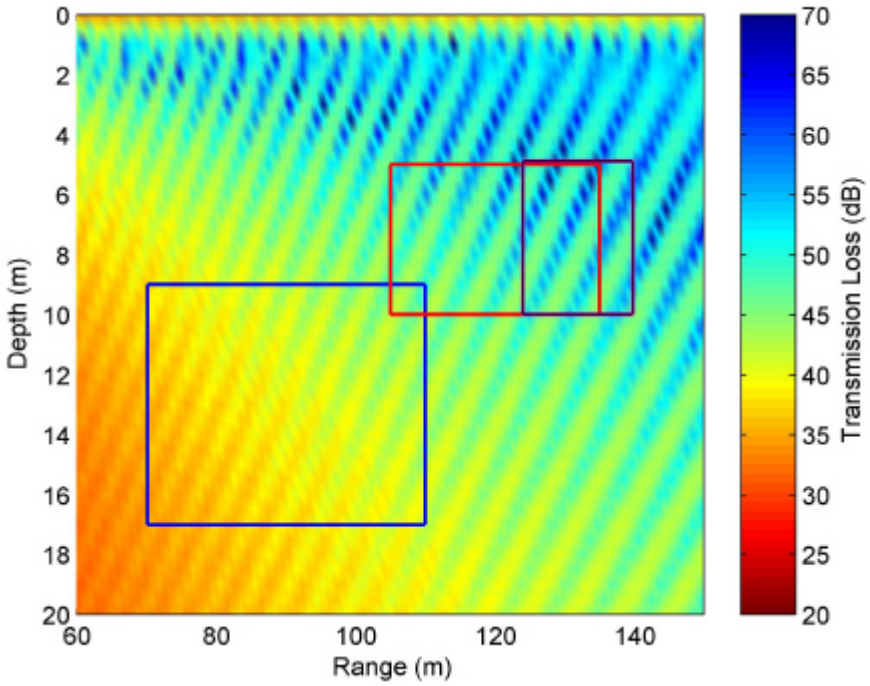

Figure 8.11 As for Figure 8.9, but for a frequency of 560 Hz.

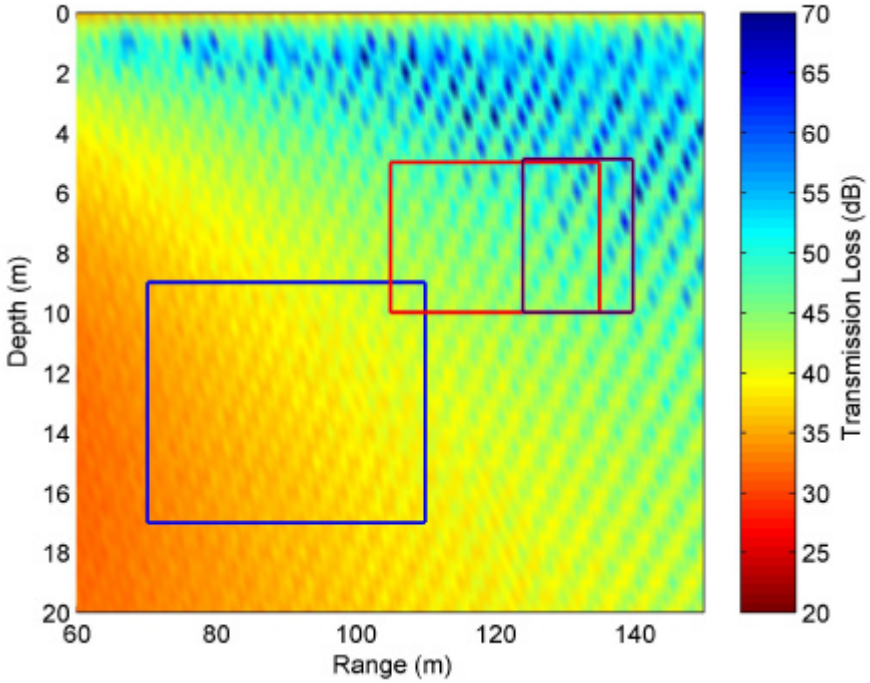

Figure 8.12 As for Figure 8.9, but for a frequency of 784 Hz.

Table 8.2 Effective transmission loss for each serial and frequency. Numbers in brackets are differences between these transmission losses and equivalent Serial 1A values.

	Frequency (Hz)			
Serial	112	336	560	784
1A	46.6 dB	42.0 dB	38.8 dB	36.8 dB
1C	51.8 dB (5.2 dB)	47.3 dB (5.3 dB)	47.0 dB (8.2 dB)	44.8 dB (8.0 dB)
1D	54.2 dB (7.6 dB)	47.6 dB (5.6 dB)	49.3 dB (10.5 dB)	46.2 dB (9.4 dB)

The beamformer outputs for serials 1C and 1D did not appear as well focussed as the Serial 1A results. There were a number of likely contributions to this:

1. The larger distances between the vessel and the array during serials 1C and 1D reduced the angle subtended by the array at the vessel and therefore degraded its spatial resolution. The beam pattern spreading caused by this mechanism was straightforward to quantify by assuming a point source at a specific location, computing the theoretical beamformer outputs for each snapshot, and incoherently averaging the results. The incoherent average of the theoretical output for beam q was calculated using

$$\hat{y}_q = \sqrt{\frac{\sum_{j=1}^{K} y_{q,j}^{*} y_{q,j}}{K}} \qquad \textbf{(8.1)}$$

where K is the number of snapshots, $y_{q,j} = \mathbf{w}_{q,j}^{H}\mathbf{a}_j$, $\mathbf{w}_{q,j}$ is the beamformer weight vector for beam q and snapshot j, and $\mathbf{a}_j$ is the steering vector for the assumed source location with the array at the appropriate position for snapshot j. The theoretical beamformer output computed by this method implicitly assumed an exact match between the computed steering vectors and reality. The results of applying this procedure to a point source at the UW30 source location are shown in Figure 8.13. The increased spreading of the main lobe was most noticeable at the lower two frequencies, but there

was an obvious increase in sidelobe levels at all frequencies, which would have led to an apparent increase in background noise.

2. Mismatch between the true and assumed acoustic environment (e.g. seabed geoacoustic properties, water depth, hydrophone depths), and approximations in the propagation calculations (see Section 8.2) would have tended to distort the beam shapes away from the theoretical beam shapes shown in Figure 8.13.

3. Some of the energy emitted by the tow-vessel would have been incoherently scattered from the rough sea surface. The scattered signals could not have been focussed by the beamformer because of the resulting random phase relationships between the signals received at the various hydrophones. The beamformer output noise was higher at frequencies corresponding to strong sources, which provided some evidence for this mechanism, although increased sidelobe levels caused by any of the other defocusing mechanisms mentioned above would have had a similar effect.

4. Errors in calculated hydrophone positions would have tended to defocus the beamformer at higher frequencies. These errors are likely to have been larger for the later two serials because of the greater distances from the tow-vessel and hence the tracking beacons. However, no independent evidence was available to test this.

In summary, source localisation was successful, with the results being consistent with all other available information. Degradations of the results at higher frequencies and larger source - hydrophone separations were apparent and were due primarily to the reduction in signal strength with increased range and reduced hydrophone depth caused by interference between the direct and surface reflected signal paths. The larger source-hydrophone separations also led to wider beamformer main lobe widths and higher sidelobe levels for serials 1C and 1D which would also have degraded the signal to noise ratio. A number of other mechanisms have been identified that may have contributed to this effect but have not been quantified.

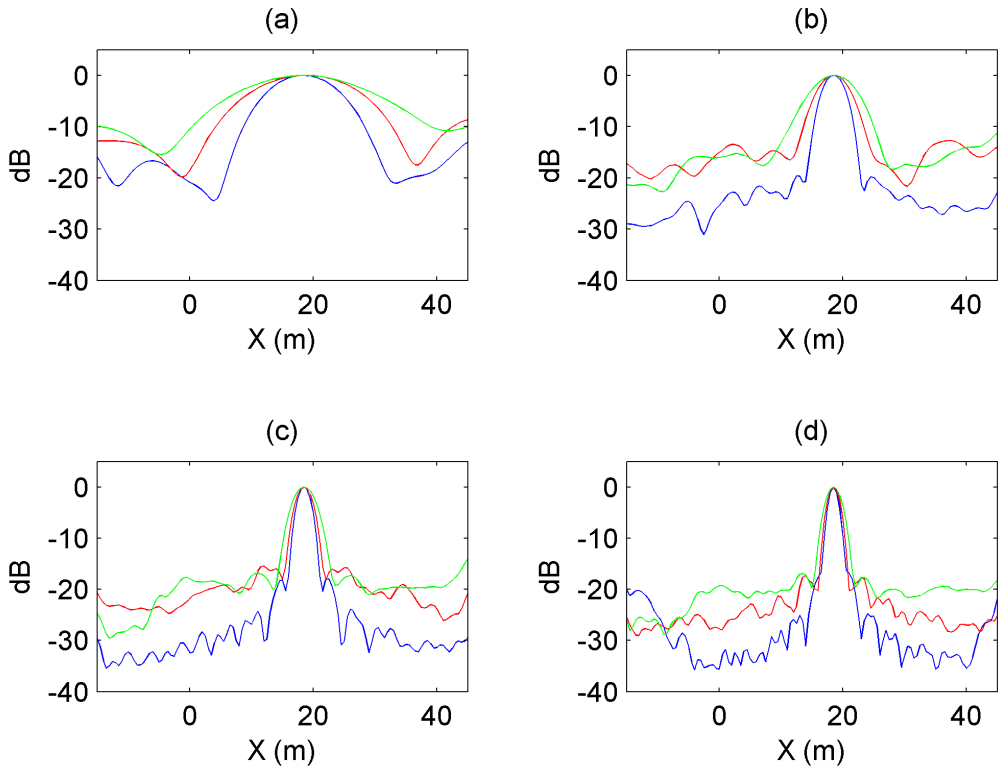

Figure 8.13 Comparison of theoretical beam patterns for serials 1A (blue), 1C (red) and 1D (green) at frequencies of (a) 120 Hz; (b) 336 Hz; (c) 560 Hz; and (d) 784 Hz. In each case beam is focussed at x = 18.5 m.

8.2 Quantifying acoustic source strength

Two different approaches to this issue were considered in the preceding chapter. In the first, several different beamforming algorithms were derived, with each algorithm normalised so that it produced the correct source spectral level for a single point source located at the focal point. The second approach, the RI processor, found the amplitudes of the point sources in a hypothesised array that produced the calculated acoustic field that best matched the measured hydrophone signals.

The beamforming algorithms had the advantage of allowing ready quantitative interpretation of the results from the UW30 source, which was a point source, but were more difficult to interpret for extended sources, such as machinery sources. The reason for this is that the beamformer output was the convolution of the beam pattern with the source amplitude distribution, and the beamformer output for a given focal point therefore included contributions from sources in other locations on the vessel.

By contrast the physical interpretation of the RI processor output was straightforward - it produced the combination of source amplitudes that best fitted the measured field at the array. However, as discussed in Chapter 7, the inversion for source amplitudes was not unique and therefore the RI processor used a regularisation procedure, which effectively produced the smoothest solution consistent with the measurements. This resulted in the UW30 point source being represented as a number of lower amplitude sources and having considerable spatial spread. The RI processor also suffered from truncation effects, which caused unrealistically high source amplitudes at either end of the hypothetical source array.

The beamforming algorithms were therefore preferable for obtaining source level estimates for point sources and, because of the lack of truncation effects, for looking at the relative intensities of spatially distributed sources, whereas the RI processor results were more appropriate for quantifying emissions from extended sources and estimating far-field signal levels.

The next two subsections consider the error sources inherent in these two approaches.

8.2.1 Beamformer estimation of UW30 source amplitudes

Two different beamforming algorithms were applied to field data (LSMC and DMVDR), and of these the LSMC beamformer produced the best source spectral level and source localisation results. The source spectral level estimates obtained with the LSMC beamformer at the frequencies emitted by the UW30 source are summarised in Table 8.3, from which it can be seen that the level estimates at the fundamental frequency of 112 Hz were all within 4.1 dB of the calibrated value, and varied by only 1.3 dB between serials. Results at the higher frequencies had slightly larger errors, with a maximum variation of 3.8 dB between serials (336 Hz), and a maximum deviation from the calibrated value of 6.8 dB (Serial 1D at 784 Hz).

Table 8.3 Summary of UW30 source spectral level estimates obtained using LSMC beamformer. Because the processing bandwidth was 1 Hz the estimated source spectral levels (dB re 1μPa^2/Hz @ 1 m) should be numerically equal to the corresponding calibrated source levels (dB re 1μPa @ 1 m).

Frequency (Hz)		112	336	560	784
Calibrated source level, dB re 1μPa @ 1 m		143.3	132.2	126.3	122.9
1A	Estimated source spectral level (error), dB re 1μPa^2/Hz @ 1 m	140.5 (-2.8)	128.3 (-3.9)	124.4 (-1.9)	116.8 (-6.1)
1C	Estimated source spectral level (error), dB re 1μPa^2/Hz @ 1 m	139.6 (-3.7)	129.9 (-2.3)	122.8 (-3.5)	119.2 (-3.7)
1D	Estimated source spectral level (error), dB re 1μPa^2/Hz @ 1 m	139.2 (-4.1)	126.1 (-6.1)	122.7 (-3.6)	116.1 (-6.8)

The mechanisms that may have accounted for the systematic errors between the source spectral levels estimated by the beamformer and the calibrated levels are discussed in the following subsections. A summary is provided in Table 8.7.

8.2.1.1 Towed array hydrophone calibration.

The towed array hydrophone calibration described in Section 5.3.10 had a number of significant shortcomings that could have produced large errors. Unfortunately the calibration exercise, which was carried out as part of a larger system test, was expensive and logistically complex, and there were insufficient resources to repeat it. The most significant shortcomings were as follows:

- The array that was calibrated was not the one used in the sea experiment, but a sister array of the same specification.
- Excluding the DA module hydrophones (which were found to have an unsatisfactory response and weren't used for array-processing), only two of the 60 hydrophones were calibrated, and these were both of the highest frequency (U) octave. None of the hydrophones in the X, Y or Z octaves were calibrated. Because of this the variation in sensitivity between hydrophones could not be determined.

- The calibration results were corrupted by interference from 50 Hz power-line signals and their harmonics.

Ignoring the potential sources of gross error and considering only the random errors apparent in Figure 4.17 and Figure 4.18 led to an estimated hydrophone calibration uncertainty of ±2 dB.

8.2.1.2 Source calibration.

The calibration of the UW30 source was described in detail in Section 5.3.4, and the uncertainties were estimated to be ±1.7 dB at 112 Hz, ±1.3 dB at 336 Hz, ±2.3 dB at 560 Hz, and ±3.9 dB at 784 Hz.

8.2.1.3 Time domain interpolation errors.

The results presented in Section 8.3.1 using simulated data showed that, even when the environment was known exactly and no noise was present there were errors in source spectral level estimates of -2.2 dB at 560 Hz and -4.7 dB at 784 Hz. The errors at 112 Hz and 336 Hz were insignificant. Cubic interpolation of the time-domain signal was carried out as part of the Doppler compensation algorithm and introduced errors at the higher frequencies. This effect is quantified in Figure 8.14, which was produced by generating sine waves at different frequencies and carrying out cubic interpolation to random times. The interpolation error was calculated by expressing the ratio of the mean square of the interpolated signal to the mean square of the original signal in decibels. The simulated hydrophone signals were generated using a 2 kHz sample rate whereas the measured hydrophone signals were originally sampled at 48 kHz and then down-sampled to 4 kHz before carrying out the array-processing. The frequency to sample rate ratios corresponding to the UW30 source frequencies and these two different sample rates are shown on the plot. It can be seen that time domain interpolation in the beamformer accounts for an error of -1.1 dB at 560 Hz and -2.5 dB at 784 Hz for simulated data but only -0.1 dB and -0.3 dB respectively for measured data. Generation of the simulated data also required interpolation, which is the most likely source of the remaining error in the simulation results.

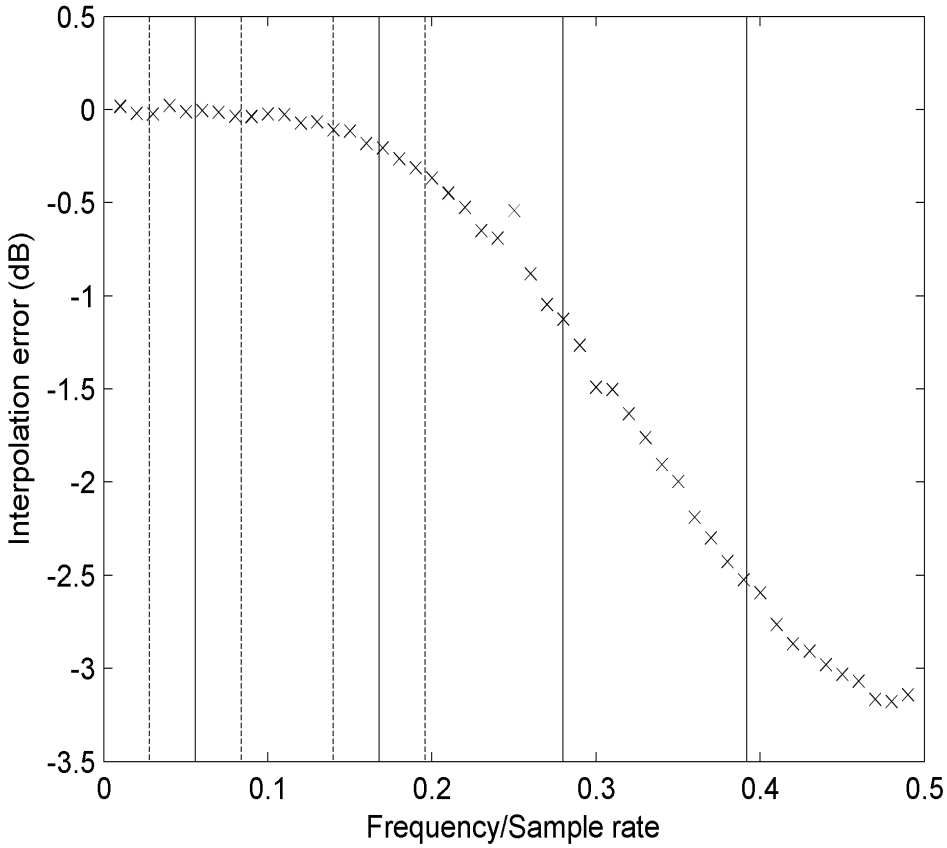

Figure 8.14 Crosses show interpolation error versus ratio of signal frequency to sampling rate. Solid vertical lines show the frequency/ sample rate ratios for the UW30 source frequencies for simulated data (2 kHz sample rate) and dotted lines show the corresponding ratios for field data (4 kHz sample rate).

8.2.1.4 *Spatial interpolation errors.*

Another potential source of error was the two-dimensional spatial interpolation required to calculate the steering vector elements. For each frequency the field was computed on a regular range-depth grid, which was then interpolated to the location of each hydrophone in order to obtain the steering vector elements. However, halving the grid spacing made no perceptible difference to the beamformer outputs, indicating that this source of error was insignificant.

8.2.1.5 *Scattering from the rough sea surface.*

SCOOTER, the program used to compute the transfer functions, had the capability to include sea surface roughness and this was used in the calculations. However, SCOOTER made the roughness correction by reducing the sea surface reflection coefficient according to the simple equation given in Equation 2.41 with its attendant assumptions of a Gaussian sea surface amplitude distribution, a Rayleigh parameter

less than 1 (i.e. a surface that isn't too rough compared to the wavelength, see Section 2.5), and no shadowing. Figure 8.15 plots contours of the Rayleigh parameter on the frequency - incidence angle plane and shows that the second criterion was met at all frequencies for the surface reflected path, but only at frequencies below 250 Hz for paths involving a bottom reflection. Some error due to this mechanism was therefore to be expected, but it could not be quantified because the true statistics of the sea surface elevation were unknown.

SCOOTER did not include a correction for incoherent scattering, which, as mentioned in Section 8.1, would have been be expected to appear as an increase in the beamformer output noise at frequencies corresponding to strong sources.

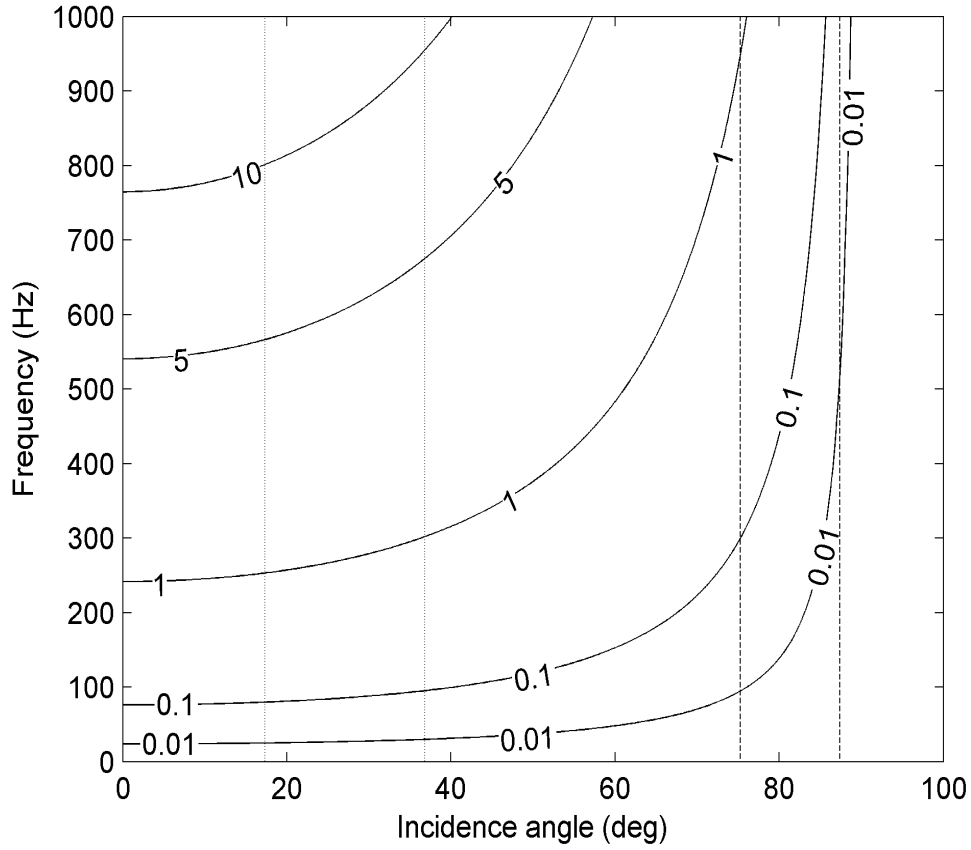

Figure 8.15 Contours of the Rayleigh roughness parameter, g, in the frequency - incidence angle plane. Incidence angles corresponding to surface reflected paths were in the region delimited by the vertical broken lines. Incidence angles corresponding to paths having one bottom reflection and one or two surface reflections were in the region delimited by the vertical dotted lines.

8.2.1.6 Acoustic source depth errors and source motion

The source spectral levels estimated by the beamformer were sensitive to the assumed source depth and this effect is shown in Figure 8.16. For comparison, the theoretical curves for a dipole source (i.e. including only the direct and surface reflected paths) are also shown.

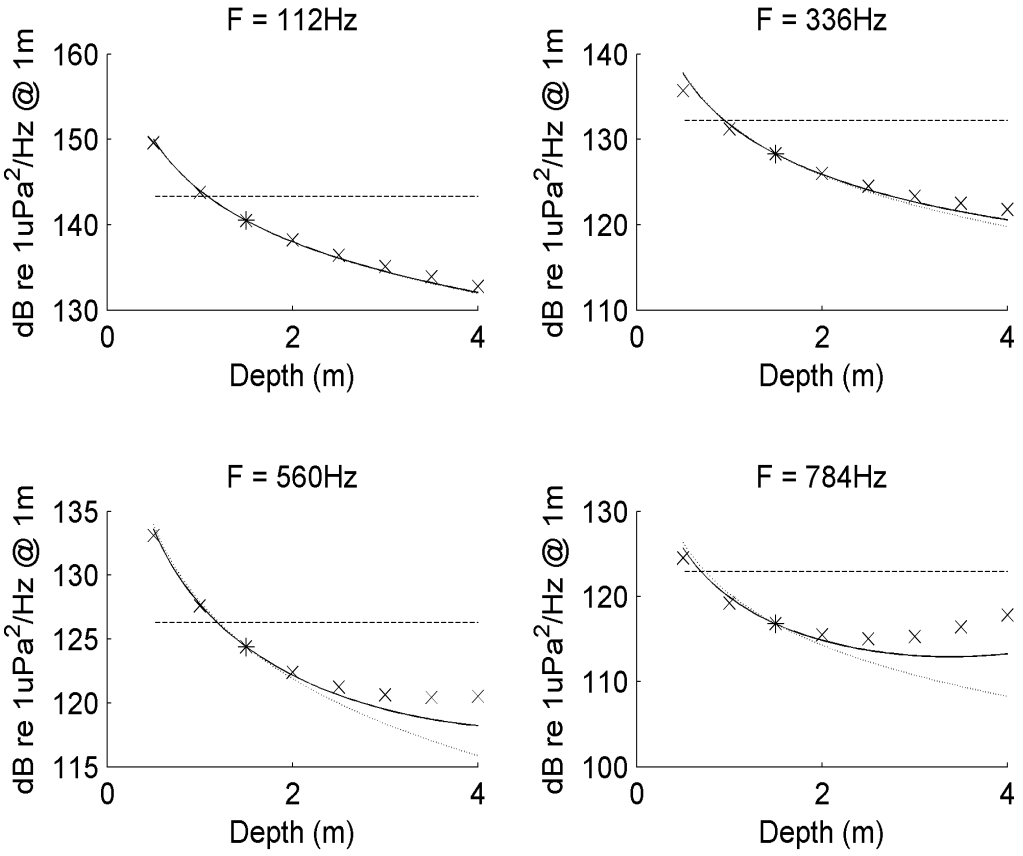

Figure 8.16 Plots of source spectral level versus assumed source depth for Serial 1A. Crosses are levels estimated by LSMC beamformer and asterisk is estimated level for measured source depth. Solid lines are theoretical curves for a dipole source and ignore seabed reflections. Dotted lines are results obtained by assuming received pressure is proportional to source depth. Horizontal broken lines are calibrated source levels.

It can be seen that the dipole model provided a good fit to the dependence of the beamformer's level estimates on assumed source depth for shallow source depths and low frequencies, but that there were significant deviations at the higher frequencies and larger source depths. The deviations were due to the effects of seabed reflections, which complicated the simple dipole dependence. The results indicated that the source would have had to have been 0.5 m shallower than the measured depth to account for the bulk of the discrepancy between the estimated and

calibrated levels at 112 Hz, 336 Hz and 560 Hz, and 0.8 m shallower to account for the discrepancy at 784 Hz. The source depth was measured with the vessel stationary alongside the dock in calm water and the source depth may have been different with the vessel underway at sea due to sinkage and trim effects. However, a personal communication from a naval architect has indicated that the source depth variations due to these effects are unlikely to have been greater than ±0.1 m (Gourlay 2003), which corresponds to source spectral level estimation uncertainties of ±0.5 dB at 784 Hz and ±0.6 dB at the other frequencies.

The effects of wind and turn induced roll were checked for Serial 1A by calculating the mean roll angle from the VRU output over the time period during which beamforming took place. This was measured by the VRU to be 0.4°, port side down, which would have corresponded to an insignificant source depth increase of 0.025 m.

Vessel motions, particularly roll and heave, resulted in dynamic changes in source depth. To quantify this, calculations were carried out based on the location of the source relative to the vessel centre line and assuming a Gaussian heave distribution with a standard deviation of 0.5 m (corresponding to the measured significant wave height of 2 m - vessel heave wasn't measured), and a Gaussian roll angle distribution with a standard deviation equal to the measured RMS roll angle of 4°. The results gave an expected source depth standard deviation of 0.56 m and an expected lateral source position standard deviation of 0.1 m, with no significant offset in the mean of either of these quantities from its nominal value.

To a first approximation a shallow dipole source produces a pressure signal at a shallow receiver that is proportional to the source depth (see Section 2.3). Figure 8.17 plots the received pressure computed using SCOOTER and incoherently averaged over the hydrophones, as a function of source depth. The vertical scale is normalised to the received pressure for a source depth of 1.5 m. It can be seen that the linear relationship was only a good approximation for source depths less than 2 m and that the deviations increased with increasing frequency. The effects of the dynamic changes in source depth were investigated by using a Gaussian random number generator to generate 1000 source depths with a mean of 1.5 m and a standard deviation of 0.56 m. The mappings obtained using SCOOTER and shown in Figure 8.17 were then interpolated to these source depths to give a set of relative

pressure values, and the root mean square pressure was calculated. This was found to be within +0.13 dB to -0.05 dB of the value computed using the mean source depth of 1.5 m.

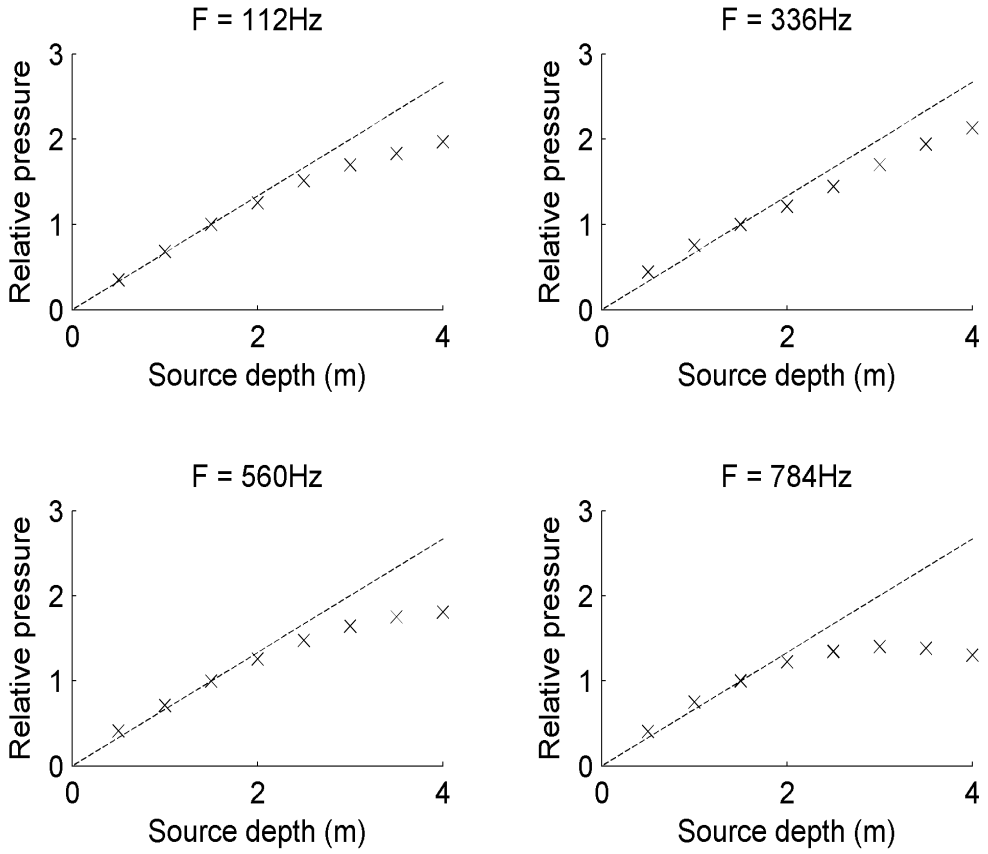

Figure 8.17 Received pressure computed using SCOOTER and incoherently averaged over the hydrophones as a function of source depth. The vertical scale is normalised to the received pressure for a source depth of 1.5 m.

The source motion would also have introduced a time varying Doppler shift into the signal, which would have resulted in frequency spreading. The frequency spread would have been greater for bottom bounce paths than for the direct and surface reflected paths because the source motion was predominantly vertical, and it is the component of the source velocity in the direction of propagation that determines the Doppler shift. Upper limits on the losses due to Doppler spreading were calculated by assuming vertical propagation, a vertical source motion of 0.56 m RMS, and converting to a velocity using a period of 10 seconds, which was the mean period measured by the Rottnest Waverider buoy. The resultant vertical velocity of 0.35 ms^{-1} RMS was then used to compute the RMS Doppler shift as a function of

frequency. For each frequency, a Gaussian random number generator was used to generate 10,000 samples of a random variable with a standard deviation equal to the computed RMS Doppler shift and a mean equal to the frequency under consideration. This was used to sample the effective frequency domain weighting function of the Fourier transform used to perform frequency analysis of the received signals, which is given by (Poularikas 1999 Chapter 3)

$$W(f) = \frac{\sin(p(f - f_c)/df)}{p(f - f_c)/df} \qquad \textbf{(8.2)}$$

where f_c is the centre frequency of the frequency bin (Hz) and df is the analysis bandwidth (1 Hz). The worst-case error due to Doppler spreading was then calculated from the mean square of the samples of $W(f)$, i.e.

$$Err = 10 * \log\left(\frac{1}{N}\sum_{j=1}^{N} W_i^2\right) \quad \text{(dB)} \qquad \textbf{(8.3)}$$

where N is the number of samples (10,000). The results are given in Table 8.4, and are again small with the largest error at any of the UW30 source frequencies being -0.43 dB at 784 Hz. (The worst-case error at the maximum analysis frequency of 1000 Hz was -0.67 dB.)

Table 8.4 Worst-case Doppler spreading loss due to vertical source motion

Frequency (Hz)	112	336	560	784
Spreading error (dB)	-0.01	-0.08	-0.22	-0.43

8.2.1.7 *Reflections from the tow-vessel's hull.*

The UW30 source was mounted close to the vessel's hull and reflections from the hull would be expected. The exact underwater shape of the vessel was not determined, but the distance between the source and hull is likely to have been between 0.5 m and 1.5 m. Because of the low frequencies and long wavelengths involved, a proper analysis of this effect would have required detailed numerical modelling using finite element and boundary element methods (Jensen et al. 2000) and this was not attempted. Instead, a simple calculation was carried out using

geometrical optics and modelling the hull as an 8 mm thick, air backed, infinite flat steel plate. The reflection coefficient of the plate was computed as a function of grazing angle using BOUNCE (Porter 1999), which gave a magnitude of 1.0 at all frequencies and grazing angles considered here, and a phase that varied between 53° (784 Hz, normal incidence) and 180° (grazing incidence, all frequencies). At 112 Hz the phase shift at normal incidence was 148°.

The far-field horizontal beam pattern of the combined source and hull reflected image was calculated at each frequency, and an estimate of the change in beamformer response as a function of source to hull separation was obtained by incoherently averaging the result over the horizontal angle range sampled by the array. The results, which are plotted in Figure 8.18, implied that hull reflections could have caused errors of as much as ±6 dB. This is likely to be a worst-case estimate as the curvature of the hull and diffraction effects were ignored, both of which would have reduced the strength of the reflected signal.

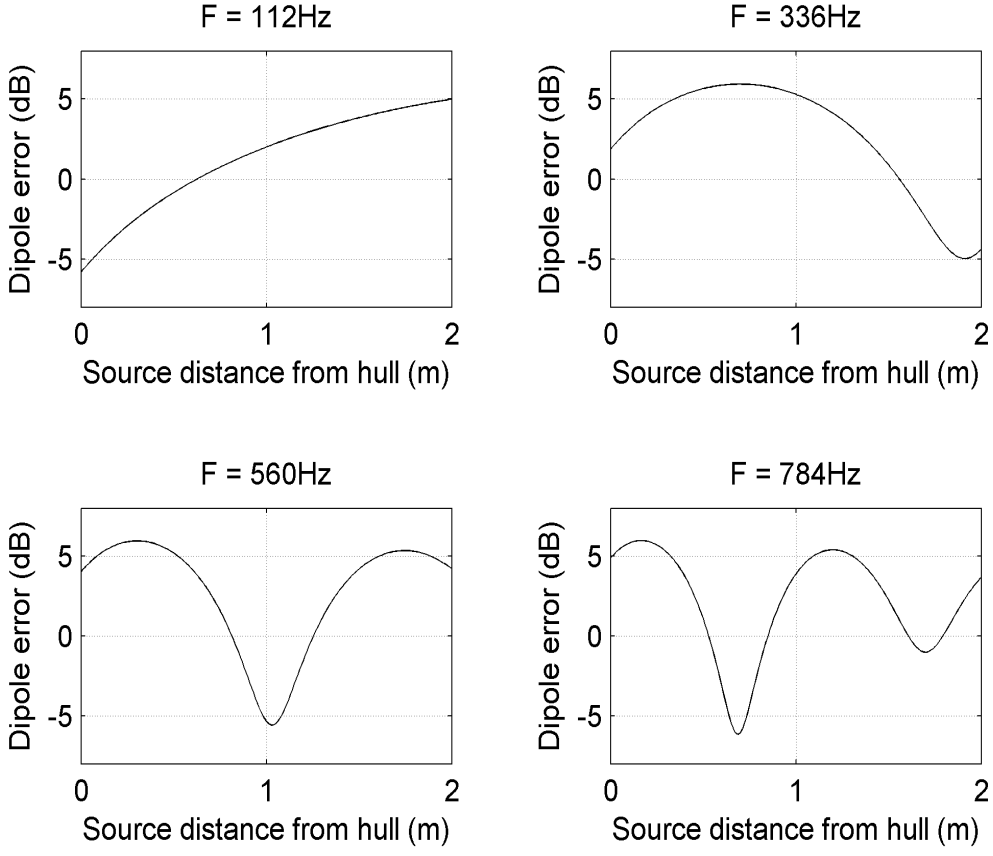

Figure 8.18 Error due to reflection from tow-vessel's hull as a function of source to hull separation

8.2.1.8 Environmental mismatch.

During this experiment energy reached the hydrophones via bottom reflected paths and therefore the seabed geoacoustic properties used in the beamformer calculations had an influence on the source spectral level determinations. The geoacoustic parameters used in the beamformer calculations, which were derived using matched field inversion as described in Chapter 6, were the best available, but the inverted parameters are unlikely to have matched reality exactly.

The sensitivities of the source spectral level estimates to the geoacoustic model were investigated by running the beamforming algorithm for each serial using a sand half-space seabed and a consolidated limestone half-space seabed and comparing the results to those obtained using the inverted seabeds. The sand and limestone seabeds were chosen as representing the softest and hardest seabeds likely to be encountered in the area of the experiment, and their geoacoustic parameters, which were obtained from Jensen et al. (2000), are given in Table 8.5. The results of this analysis, which are plotted in figures 8.19 to 8.21 and summarised in Table 8.6, demonstrate that the estimated source spectral levels were only weakly dependent on the seabed parameters. The dependence was weakest for Serial 1A data and for all serials the dependence reduced as the frequency increased. This was consistent with the expectation that the dependence of estimated source level on seabed properties would be greatest where the proportion of received energy due to bottom reflected paths was greatest. The shorter ranges and deeper hydrophone depths that occurred during Serial 1A resulted in stronger direct path signals and less complete destructive interference between the direct and surface reflected paths than for the other two serials, resulting in the bottom reflected paths being relatively less important. Similarly, the bottom reflected paths were more important at 112 Hz and 336 Hz than at the other frequencies because destructive interference between the direct and surface reflected paths was more complete at these lower frequencies.

From figures 8.19 to 8.21 it can also be seen that for all serials the beamformer output appeared better focussed at 112 Hz when the inverted seabed was used than when either of the other seabeds were used. The differences were small, but this provided further evidence that the inverted seabed models provided a good match to the actual acoustic propagation conditions, at least at 112 Hz.

Ignoring the seabed reflection altogether by using the Lloyd mirror propagation model severely degraded the focus of the beamformer at 112 Hz for all serials, and for Serial 1D the focus at 336 Hz was also degraded.

Table 8.5 Geoacoustic parameters for sand and limestone seabeds

Seabed	Sand	Limestone
Compressional wave speed, c_{p1} (ms^{-1})	1672	3000
Shear wave speed c_{s1} (ms^{-1})	180	1500
Density, r_1 (kgm^{-3})	1946	2460
Compressional wave attenuation, a_{p1} (dB/λ)	0.8	0.1
Shear wave attenuation, a_{s1} (dB/λ)	0.5	0.2

Table 8.6 Deviations of source spectral level estimates obtained using sand and limestone seabeds from those obtained using inverted seabeds (dB)

	Frequency (Hz)			
Serial	112	336	560	784
1A	+0.6 -0.9	+0.3 -0.2	+0.0 -0.0	+0.0 -0.0
1C	+2.5 -0.8	+0.9 -1.1	+0.6 -0.6	+0.1 -0.3
1D	+1.6 -2.0	+1.9 -0.9	+0.1 -0.3	+0.9 -0.0

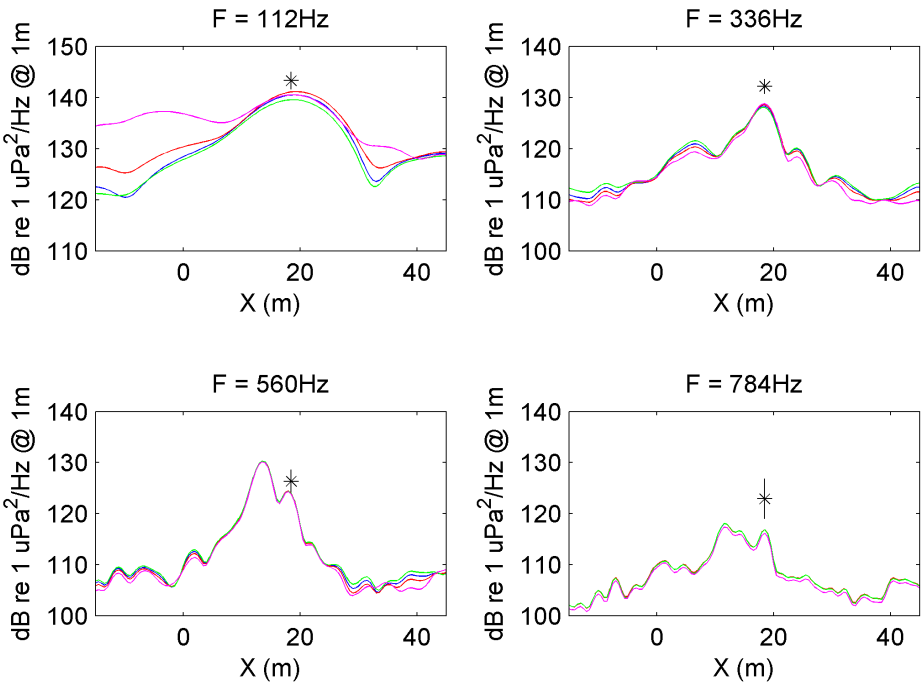

Figure 8.19 Comparison of Serial 1A LSMC beamformer outputs using different seabed models: Blue, inverted seabed; red, sand; green, limestone; magenta, no seabed.

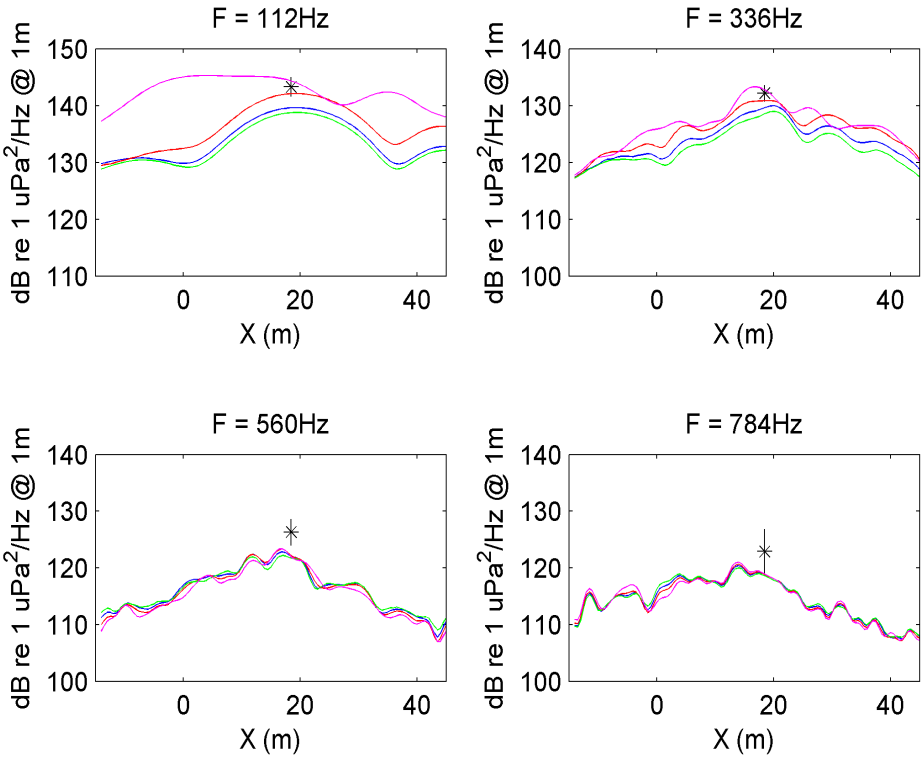

Figure 8.20 Comparison of Serial 1C LSMC beamformer outputs using different seabed models: Blue, inverted seabed; red, sand; green, limestone; magenta, no seabed.

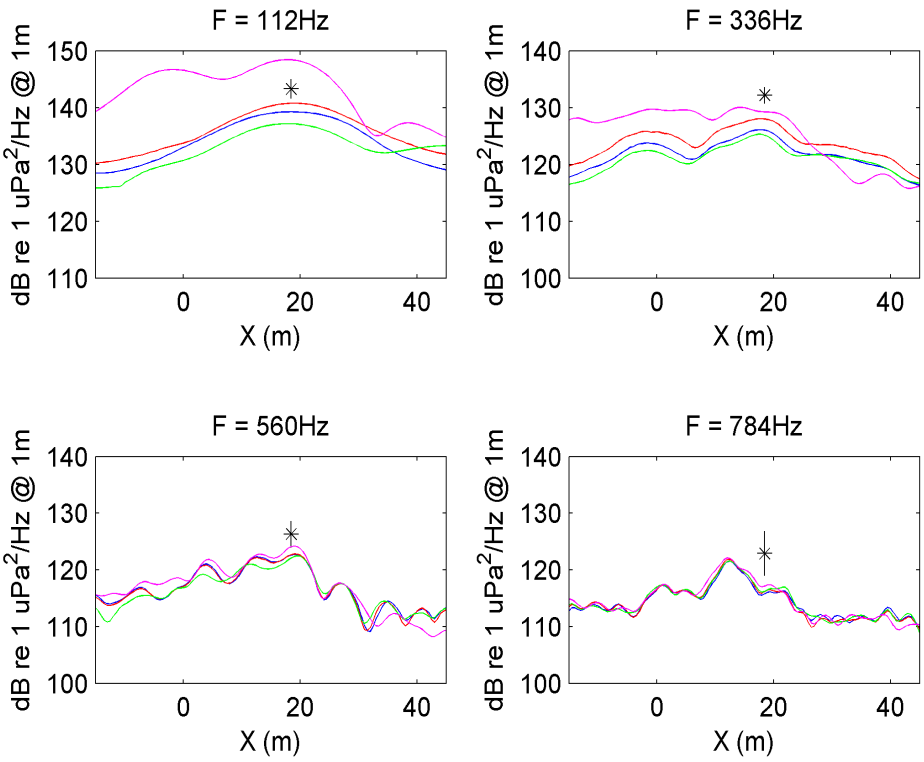

Figure 8.21 Comparison of Serial 1D LSMC beamformer outputs using different seabed models: Blue, inverted seabed; red, sand; green, limestone; magenta, no seabed.

8.2.1.9 *Doppler correction error*

The Doppler compensation algorithm described in Section 7.2.1 provided accurate compensation for the direct acoustic path, but not for the bottom reflected paths. However, the results of the previous subsection showed that the bottom reflected paths were only significant for frequencies of 112 Hz and 336 Hz, and the simulated data results described in Section 7.3.1 showed that ignoring the Doppler shift altogether resulted in negligible errors at these frequencies. Therefore this mechanism would not have contributed significant errors.

8.2.1.10 *Interference from machinery noise.*

The Serial 1A results plotted in Figure 8.19 showed clearly resolved machinery noise peaks at 560 Hz and 784 Hz. Energy from these machinery sources would have increased the levels of the peaks corresponding to the UW30 source. Limits on the size of this effect were obtained by using the beamformer plots in Figure 8.19 to estimate the range of possible machinery noise contributions at the UW30 location. These noise estimates were then incoherently subtracted from the level of the peak

corresponding to the UW30 source. The resulting corrections ranged from 1.6 dB to 0.8 dB at 560 Hz and from 1.3 dB to 0.9 dB at 784 Hz. These corrections reduced the estimated source spectral levels, slightly increasing the discrepancies between the estimated and calibrated values compared to those given in Table 8.3.

8.2.1.11 *Hydrophone positioning errors*

There were no independent sources of data available to check the accuracy of the dynamic hydrophone localisation results described in Chapter 5, and the best that could be done was to apply the beamformer using hydrophone positions computed using the two different Kalman filter dynamic models (local and global). The results obtained were very similar, with the maximum change being 0.5 dB for Serial 1D at 784 Hz, and in all other cases being 0.3 dB or less. This result supports the conclusion reached in Chapter 5 that the computed hydrophone positions were virtually independent of the dynamic model during the time period used for beamforming.

The effect on the source spectral level estimates of offset errors in the position of the array as a whole are shown in Figure 8.22. Results are plotted for offsets in the hydrophone Y coordinates, corresponding to changes in the distance between the vessel and the array, and offsets in hydrophone depths. Offsets in the Hydrophone X coordinates shifted the positions of the beamformer peaks by corresponding amounts but did not affect the estimated source levels. The fact that the Serial 1A beamformer peaks corresponding to the UW30 source occurred within ±0.5 m of the correct position is strong evidence that the hydrophone X positions were determined to at least the same level of accuracy.

Figure 8.22 shows that the estimated source spectral levels depended only weakly on the Y hydrophone offset. The position fixing geometry was such that the Y position of the array was more accurately determined than the X position, which implied that the Y offset would have been less than ±0.5 m and therefore the associated source level estimation error would have been less than ±0.5 dB.

The dependence of the estimated source spectral levels on the hydrophone Z coordinate offset was stronger than for the Y coordinate, especially at 112 Hz, where significant defocusing occurred as the array was moved away from its estimated depth. (112 Hz results were not plotted for depth offsets of +3 m and +4 m because

the beamformer output was defocused to such an extent that a peak value could not be determined.) This result reflected the fact that significant changes in the acoustic field occurred more rapidly for changes in depth than for changes in range (see Figure 8.9). The stronger dependence at 112 Hz was due to the spatial scale of the major fluctuations in the field being similar to the vertical extent of the array, so that a change in depth made a significant change to the relative phases of the signals at the hydrophones. At the higher frequencies the destructive interference between the direct and surface reflected paths was less complete and therefore the bottom reflected paths contributed relatively less energy, resulting in smaller amplitude fluctuations in the field. These fluctuations also occurred over depth and range scales much smaller than the depth and range spanned by the array and their effects tended to be averaged out.

Array depth was determined using matched-field inversion as described in Chapter 6. Gibbs sampler results given in Section 6.3 indicated that the uncertainty in array depth was approximately ±1.5 m which would correspond to a source spectral level uncertainty of ±2 dB.

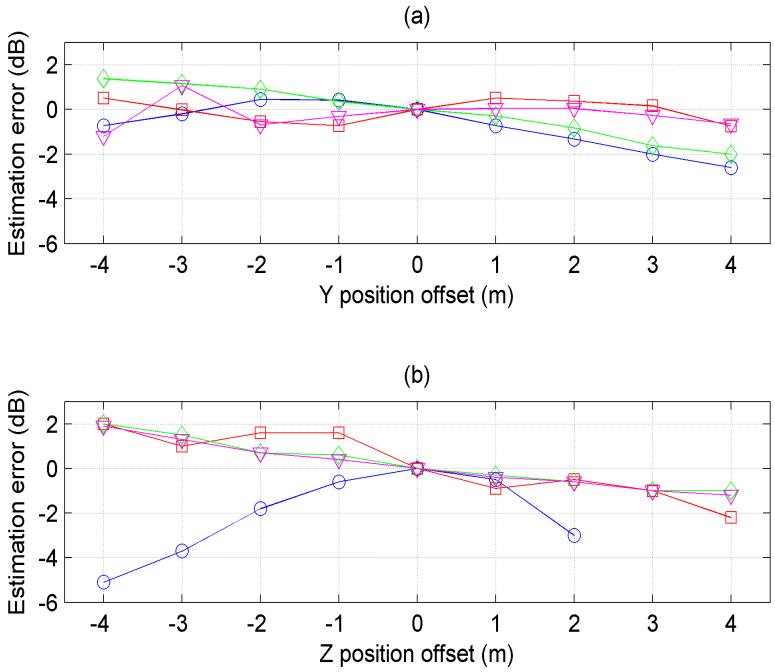

Figure 8.22 Source spectral level estimation error versus array position offset in (a) the Y direction and (b) the Z direction for Serial 1A. Blue, 112 Hz; red, 336 Hz; green, 560 Hz; magenta, 784 Hz.

The effects of spatially uncorrelated Gaussian random errors in hydrophone Y and Z coordinates are shown in Figure 8.23. Introducing random errors into the hydrophone Y coordinates had an effect on the source spectral level estimates similar to that seen with simulated data (see Section 7.3.1), with a 0.5 m RMS position error resulting in estimation errors of -0.34 dB at 112 Hz, -2.8 dB at 336 Hz, -2.5 dB at 560 Hz, and -6.3 dB at 784 Hz. These results were to be expected given that the beamforming algorithms relied on an accurate knowledge of the relative phases of the signals arriving at the different hydrophones. The absolute phase of the field changed rapidly with range (due to the $e^{ik_r r_h}$ dependence in Equation 2.38), whereas the relative phase of the field at the various hydrophones changed slowly when they were all translated in range together. Random changes in the Y coordinate altered the relative ranges from the focal points to the hydrophones, which had a much greater effect on the relative signal phases than when the coordinates were all offset by the same amount. The higher the frequency, the greater the phase shift due to a given range change, and therefore the larger the effect.

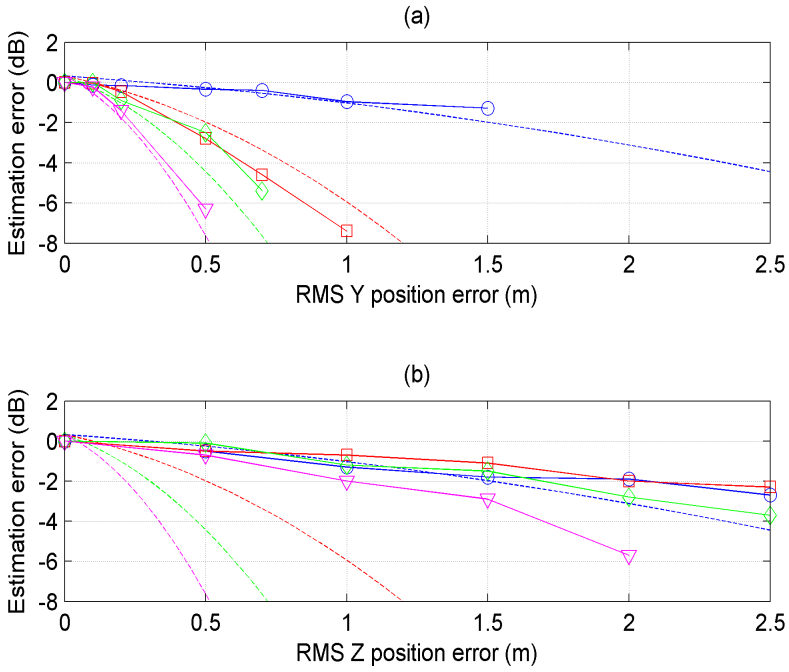

Figure 8.23 Source spectral level estimation error versus root mean square of hydrophone position error in (a) the Y direction and (b) the Z direction. Solid lines and symbols are measured data, broken lines correspond to the quadratic fit to simulated data with Y coordinate errors given in Equation 7.59. Blue, 112 Hz; red, 336 Hz; green, 560 Hz; magenta, 784 Hz.

Random errors in the hydrophone Z coordinates had a much weaker effect on the source level estimates than Y coordinate errors at all frequencies except 112 Hz. Again this was to be expected, in this case because Z coordinate changes affected the relative signal phases indirectly via vertical variations in the absolute phase of the acoustic field, and the phase varied much more slowly with depth than with range.

The true sizes of the random errors in the hydrophone Y and Z coordinates are unknown, as are their spatial and temporal statistics. The analysis carried out here has assumed spatially uncorrelated errors whereas the curvature constraints used in the position fixing algorithms would most probably have led to correlated errors. However, it is seems possible that random errors in the Y coordinate could have been large enough to cause significant source level estimation errors.

8.2.1.12 *Summary of error mechanisms*

A summary of the various error mechanisms described in the preceding subsections and their contributions to the overall uncertainty in source level estimation for Serial 1A is given in Table 8.7. The limits on the estimation error were obtained by summing the individual dB uncertainties at each frequency and represent the worst-case uncertainty, corresponding to a situation in which all error sources caused errors in the same direction. The expected estimation error was obtained by taking the mean of the positive and negative limits for each error mechanism and summing. The uncertainty with uncorrelated error sources was obtained by taking the square root of the sum of the squares of half the difference between the positive and negative limits. This last calculation is valid if the errors due to the different error mechanisms are uncorrelated.

The differences between the estimated and calibrated source spectral levels (see Table 8.3) were much smaller than the estimation error limits listed here, but were consistent with the uncertainty estimated assuming uncorrelated error sources.

The largest single contributor (±6 dB) was the uncertainty associated with the reflection of the UW30 source signals from the vessel's hull. This was a consequence of the less than ideal location of the UW30 source, which was brought about by the practical and financial constraints of the sea experiment, and would not have contributed to the uncertainties in estimating the levels of sound radiated by the vessel itself. Removing this uncertainty from the error budget resulted in

uncertainties of ±6 dB (worst case) and ±3 dB (uncorrelated errors) for vessel noise source level estimates. The computed uncertainties due to tow-vessel reflections are also likely to be overestimates because they were calculated using simple ray theory and the effects of diffraction were ignored.

The uncertainties in the hydrophone calibrations and array depth, each of which contributed ±2 dB to the total could be reduced to negligible levels in a practical system by properly calibrating the hydrophones and by using an array with functioning pressure sensors to measure depth. The sensitivity to array depth would also be reduced if the array were towed deeper. Such a system would therefore be expected to be able to determine the source level of point sources to better than ±2 dB, although this figure doesn't allow for the effects of the approximations inherent in the rough surface scattering model or random errors in hydrophone coordinates.

Table 8.7 Summary of source spectral level estimation error mechanisms and uncertainties for Serial 1A

Mechanism	**Resulting uncertainty (dB)**				**Comments**
	112 Hz	**336 Hz**	**560 Hz**	**784 Hz**	
Hydrophone calibration	±2	±2	±2	±2	Gross errors could have been much larger
Time domain interpolation	0	0	-0.1	-0.3	
Spatial interpolation	0	0	0	0	
Rough surface scattering	?	?	?	?	
Mean source depth	±0.6	±0.6	±0.6	±0.5	
Dynamic source depth changes - depth effect	+0.13 to -0.05	+0.13 to -0.05	+0.13 to -0.05	+0.13 to -0.05	
Dynamic source depth changes (Doppler spreading)	+0 to -0.01	+0 to -0.08	+0 to -0.22	+0 to -0.43	
Reflections from tow-vessel's hull	±6 dB	±6 dB	±6 dB	±6 dB	
Environmental mismatch	+0.6 to -0.9	+0.3 to -0.2	0	0	
Doppler correction error	0	0	0	0	
Machinery noise interference	0?	0?	+0.8 to +1.6	+0.9 to +1.3	Machinery sources were not identified at 112 Hz and 336 Hz but could have been present.
Array Y coordinate offset	±0.5	±0.5	±0.5	±0.5	
Array Z coordinate offset	±2	±2	±2	±2	
Hydrophone Y coordinate random error	?	?	?	?	Unknown, but possibly significant
Hydrophone Z coordinate random error	?	?	?	?	Unknown, but unlikely to be significant
Limits on estimation error	**+11.8 to -12.1**	**+11.5 to -11.4**	**+12.7 to -10.7**	**+12.1 to -10.9**	
Expected estimation error	**-0.1**	**+0.1**	**+1.0**	**+0.6**	
Uncertainty with uncorrelated error sources	**±6.7**	**±6.7**	**±6.7**	**±6.7**	

8.2.2 RI processor source amplitude distributions

As described above, the output of the RI processor was easier to interpret than the output of the beamformer when dealing with spatially extended sources such as machinery sources, but was corrupted by truncation effects at the ends.

The output of the RI processor depended on the spacing between adjacent sources in the assumed hypothetical source array, because this determined the number of point sources representing a given physical source. Halving this spacing doubled the number of sources and halved their amplitude, resulting in a change in the level of each source of -6 dB. This should be borne in mind when interpreting the results of Section 7.3.2 which were computed using a source spacing of 0.5 m.

The error sources listed in Table 8.7 applied to the RI processor to the same extent that they applied to the LSMC beamformer, and as pointed out in the preceding section, the largest error source, reflections from the tow-vessel's hull, would not have contributed to uncertainties in mechanical noise source level estimates. In addition, the non-uniqueness of the inversion for the source amplitude distribution resulted in the RI processor output also depending to some extent on the method of regularisation used. For example, changing from magnitude regularisation to slope regularisation resulted in the amplitude peaks at the UW30 source location changing by +0.5 dB at 112 Hz, -0.5 dB at 336 Hz, -1.0 dB at 560 Hz, and -1.1 dB at 784 Hz (Serial 1A data, sources distributed from -15 m to +45 m).

8.3 Determination of far-field vessel signature

In Section 7.3.2 equivalent far-field source spectral levels of the tow vessel were presented for the three processed serials at the UW30 source frequencies (see Figure 7.20). The equivalent source spectral levels were a combination of both machinery noise and the signal from the UW30 source, and changes in machinery state between the serials could therefore have affected the result. This appears to have been the case at 784 Hz, which showed the biggest variation between serials. Levels at 112 Hz and 560 Hz were consistent between serials, but it was difficult to tell whether the variations between levels at 336 Hz were due to real changes in machinery noise or statistical fluctuations.

Uncertainties in the equivalent far-field source spectral levels included the various systematic error sources discussed in the previous section and also random

fluctuations from snapshot to snapshot due to noise. This latter effect is quantified in Figure 8.24, which shows the resulting 68% confidence intervals for the equivalent far-field source spectral levels for Serial 1A. These were calculated by computing the standard deviation of the N_{avg} source amplitude estimates at each azimuth and dividing by $\sqrt{N_{avg}}$ to give the standard deviation of the mean.

Consideration of the equivalent far-field source spectral level plots (Figure 7.20) and the LSMC beamformer results for Serial 1A (Figure 7.15) led to the observations and conclusions summarised in Table 8.8.

A procedure that is often used to determine the acoustic signature of a vessel as a function of azimuth is to run the vessel past a stationary hydrophone and then compute the azimuth of the hydrophone relative to the vessel as a function of time. The effect of the changing range must be removed by the use of an appropriate propagation model. With minor modification this procedure was also applicable to the data collected for this project and was much simpler and less computationally intensive than the method based on the RI processor described in the previous chapter. It did, however, have several serious disadvantages. These are illustrated in Figure 8.25, which compares equivalent far-field source spectral levels computed using the RI processor and the procedure described in Chapter 7 to those computed using a single hydrophone (Hydrophone 30).

The single hydrophone results were not only noisier, but also contained two different types of artefacts: radial lines caused by transients that are visible between azimuths of 200° and 250°, and U shaped lines that don't conform to circular arcs. The latter were due to interference nulls in the acoustic transfer functions and arose because the computation of the equivalent source level involved dividing by the transfer function and consequently received noise was over-emphasised wherever a null in the transfer function occurred.

Table 8.8 Conclusions from analysis of Serial 1A field data at UW30 source frequencies.

Frequency	**Beamformer**	**Equivalent far-field source spectral levels**	**Conclusion**
112 Hz	Single peak at UW30 location was 2.8 dB below expected source spectral level.	Varied between expected UW30 source spectral level near broadside to 5 dB below this.	UW30 source dominated at this frequency. Variation with angle may have been due to interference between direct path signal and reflection from vessel hull.
336 Hz	Peak at UW30 location was 3.9 dB below expected source spectral level. Peak sat on a broad plateau extending from X=5 m to X=23 m.	Levels were similar to UW30 source spectral levels at all angles but were more variable than at other frequencies.	Plateau was probably due to machinery noise, which contributed significantly to the far-field signature because of its large spatial extent.
560 Hz	Peak at UW30 location was 1.9 dB below expected source spectral level. Well defined peak 6 dB higher than this at X=13.5 m.	UW30 source spectral levels were exceeded over the range 240° to 300°. Outside this range the level is similar to the UW30 source spectral level.	Peak at X-13.5 m was due to machinery noise, which was directional at this frequency and dominated the UW30 source over the angular range 240° to 300°.
784 Hz	Peak at UW30 location 6.1 dB below expected source spectral level. 1.5 dB higher, broad peak at X=11.5 m.	Level is similar to or slightly exceeds UW30 source spectral level at all angles.	Far-field signal was dominated by machinery noise.

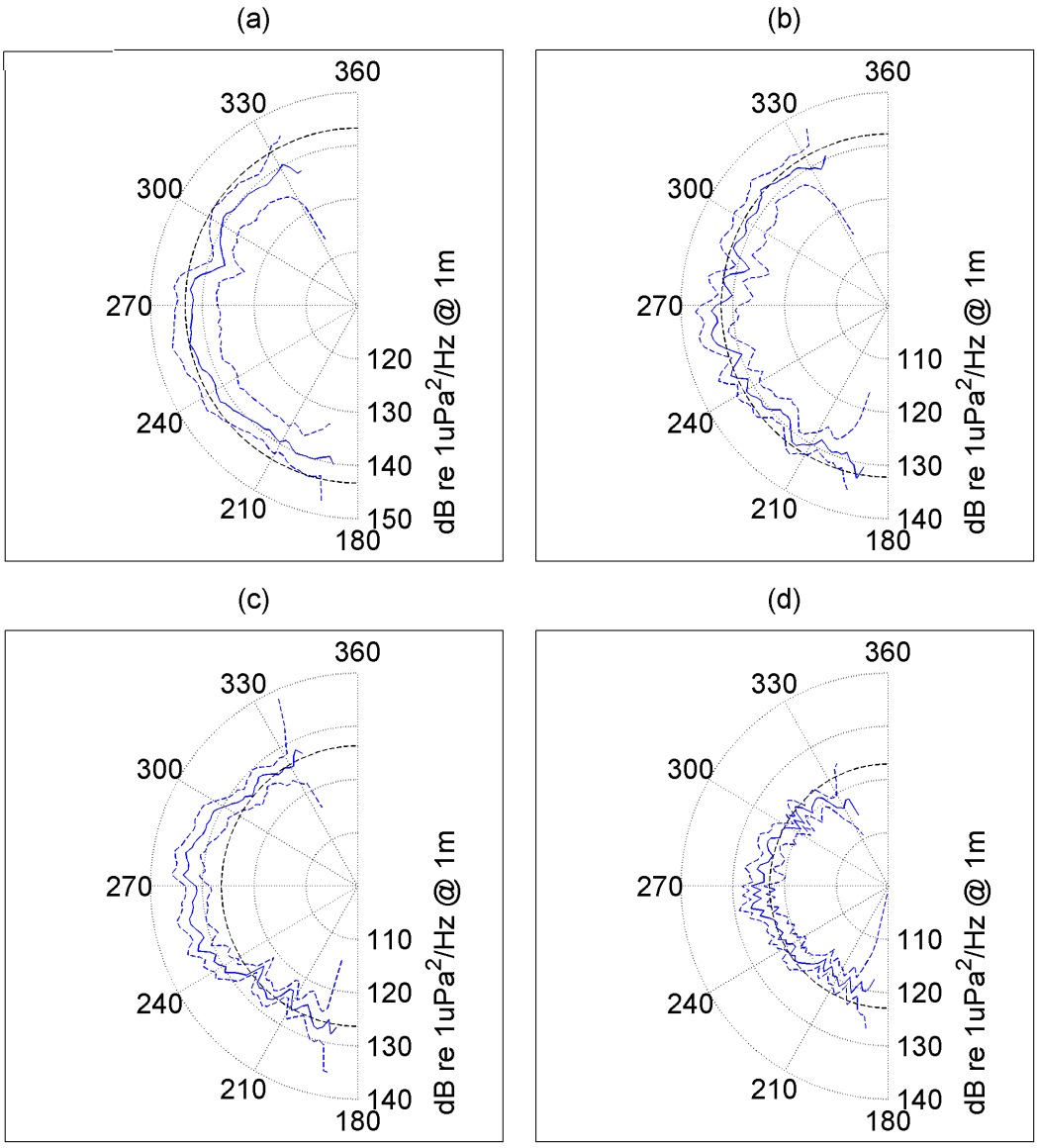

Figure 8.24 Equivalent far-field source levels plotted against azimuth at (a) 112 Hz, (b) 336 Hz, (c) 560 Hz and (d) 784 Hz computed using data from Serial 1A. Regions between broken blue lines are 68% confidence regions based on statistical fluctuations between snapshots. Broken black lines are calibrated UW30 source levels.

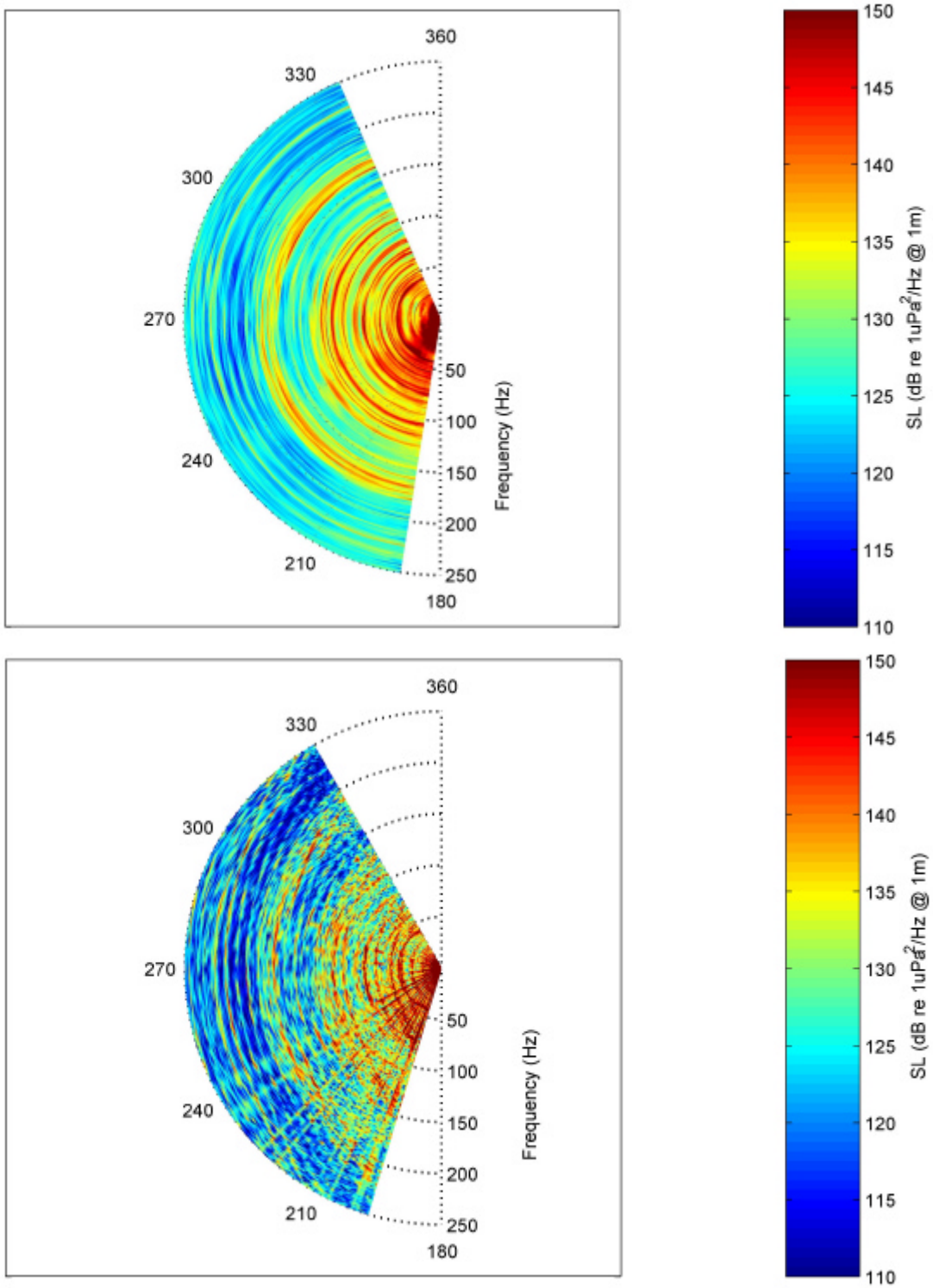

Figure 8.25 Equivalent far-field source levels for frequencies from 0 to 250 Hz computed using RI processor (top) and computed using hydrophone 30 only (bottom).

By contrast, the RI processor exploited the directional gain of the array to only include signals originating from the vicinity of the tow-vessel and in addition the field at a given azimuth was sampled by all 60 hydrophones and therefore at a

number of different depths and ranges, averaging out the effects of the interference nulls. Although the same averaging effect could have been achieved by carrying out the single hydrophone computation for each of the 60 hydrophones in the array and then averaging the results, this would still have admitted noise and interference coming from sources not associated with the tow-vessel. The RI processor also allowed an explicit transformation between measurements made at any range from the tow-vessel and its equivalent far-field signature, whereas the single hydrophone method relied on the measurements being made far enough from the vessel that near-field effects were unimportant.

The main disadvantage of the RI processor was the amount of computation time required to compute the source amplitude distributions. The computations required to produce the results plotted in figures 8.27 and 8.28, which were carried out at 1 Hz intervals from 1 to 1000 Hz and used 108 seconds of data, took over 80 hours on a 720 MHz Pentium III processor. However, no attempt was made to optimise the algorithm and the implementation of a few simple strategies would have drastically reduced the time required. For example:

- Making the number of sources and the source spacing a function of frequency rather than using the same source spacing at all frequencies. An investigation of the effect of source spacing on the computed far-field response showed that the source spacing had a negligible effect on the results providing it was less than 0.5 wavelengths. Fewer sources could therefore have been used at lower frequencies.

- Using fewer, more widely spaced, hydrophones at lower frequencies than at higher frequencies, rather than using all hydrophones at all frequencies.

- Not processing every block of data. The rate of change of azimuth was greatest near broadside and reduced progressively either side of this. The computational load could therefore have been reduced by selecting blocks centred a constant azimuth interval apart rather than processing every block.

- Ignoring the seabed reflections at higher frequencies. It was shown in Section 8.2.1.8 that seabed reflections had little effect on the results at frequencies of 560 Hz and above. It would therefore be possible to ignore

seabed reflections at these higher frequencies, vastly simplifying the calculation of the acoustic transfer functions.

The source amplitudes computed by the RI processor for mechanical noise sources depended on the assumed source depth in the same manner as the LSMC beamformer estimates of the UW30 source spectral levels (see Section 8.2.1.6). Consequently the equivalent far-field source levels were also functions of the assumed source depth. This was not a problem for the UW30 source, which was at a known depth, but the effective depths of the mechanical noise sources were unknown. The effect of changing the source depth can be determined from curves such as those shown in Figure 8.16 although to a first approximation the source amplitude is inversely proportional to the assumed source depth (dotted line in Figure 8.16).

Unfortunately no independent data were available to confirm the far-field vessel signature results produced by the RI processor and it is recommended that such a study be carried out in the future, together with a more detailed investigation of the effects of different hypothetical source arrays and regularisation techniques.

8.4 Implementation feasibility

This work has focussed on the development of methods of localising and quantifying tow-vessel acoustic emissions in a situation where all processing was carried out after the event and there was no requirement for generating results in real-time. Therefore very little effort has been put into optimising the various algorithms for speed. For an operational system to be useful it would have to generate results within minutes of a manoeuvre being carried out, and it would be necessary to take the algorithms described in this thesis and develop them to the point where this was feasible.

However, many of the difficulties and complexities that were encountered in this project were due to the fact that the tow-vessel was a surface vessel, and consequently the noise sources were very close to the sea surface, and that the experiment was carried out in shallow water. These two factors combined to make reflections from the seabed an important contributor to the acoustic field at the hydrophones and necessitated the use of fast-field integration techniques and

interpolation of the resultant field in order to compute the array steering vectors. This in turn made it necessary to carry out geoacoustic inversion in order to adequately characterise the acoustic properties of the seabed. All of this took a large amount of computation time. In deep water the situation would be very much simpler as, over the short ranges considered here, refraction could be ignored and the propagation from a source modelled as simple spherical spreading from the source and a sea surface reflected image. For a deeply submerged submarine in deep water the situation would be simpler still as only the direct path signal would be of importance.

The next few subsections discuss each of the steps that led to the final source level estimates and the associated practical issues. Suggestions on how each step could be optimised are also provided.

8.4.1 Hydrophone tracking

The hydrophone tracking method used here utilised a set of sophisticated tracking beacons located on the tow-vessel and involved active transmissions from the beacons and replica correlation of the received signals at each hydrophone. The tracking system was able to compute a subset of the beacon-hydrophone ranges in real time but the remainder were computed after the event. In order to allow real-time tracking of the array it would be necessary to reduce the number of beacon-hydrophone combinations, which could be done by only tracking a selection of the hydrophones. This could be achieved without significant loss of accuracy or reliability by tracking only a few of the closely spaced U and Z octave hydrophones. The positions of the remainder could then be interpolated from these locations.

The Kalman smoother based hydrophone tracking algorithm described in Section 5.2 is not a limiting factor as it ran slightly slower than real-time and would run faster if the number of hydrophones used in the calculation were reduced.

A more serious consideration for future systems is that the tracking beacon frequencies were outside the normal operating frequency range of the array and that it was only possible to use this tracking method because the array used analog signal processing and the filters in the array's signal conditioner did not roll off rapidly at high frequencies. Modern digital arrays contain high-order anti-alias filters and digitally sample the signal at the hydrophone, making it impossible to receive signals

at frequencies above the array's maximum intended frequency of operation. Reducing the operating frequencies of the beacons would allow their signals to be received by the array hydrophones but generating the required signal levels at the lower frequencies would require larger, more expensive transducers and the range measurement accuracy would be reduced. There is also the danger that the beacon frequency spectra would start to overlap the frequency range of interest for the noise radiated by the vessel, although the directional gain of the array should allow the beacon signals to be separated from those from other sources.

Coming up with a practical method of tracking the hydrophones in a modern digital array is likely to be the biggest challenge in implementing an operational system. These arrays are usually outfitted with a number of pressure sensors, which would solve the vertical plane positioning problem, and a number of heading sensors, that would give some measure of array orientation and shape. An approach worthy of investigation would be to combine the information from these sensors with navigation data from the tow-vessel, a hydrodynamic model such as the one described in Appendix A, and ranging data from a single active beacon mounted on the tow-vessel and operating at the upper end of the array's frequency response.

It is notable that, as shown in Section 8.2.1.10 the sensitivity of the results to random errors in the hydrophone positions is much greater than their sensitivity to offsets in the array position. This implies that more error will be acceptable in the array position than in the array shape.

8.4.2 Matched-field inversion

The matched-field inversion techniques described in Chapter 6 required many hours of computation time and a great deal of prior knowledge and intuition in order to obtain physically realistic solutions. They are a long way from being something that is practical to implement in an operational system.

Having said this, it was shown in Section 8.2.1.8 that the source level estimation results depended only weakly on the seabed model and that in fact seabeds ranging from a sand half-space to a limestone half-space produced only small differences. This implies that a general knowledge of the geoacoustic properties of the seabed, such as would be obtained from knowledge of the geology of the area, would suffice in most cases. In deeper water, or with deeper sources (such as on a submarine) the

relative contribution of the seabed reflected paths would be further reduced and the properties of the seabed would become irrelevant.

8.4.3 Beamforming and inversion for source amplitudes

The LSMC beamformer algorithm derived in Chapter 7 was found to produce very good results when applied to the field data, and the techniques used to compensate for array shape, array motion, and complex propagation conditions were successful. The cost of all this was a beamformer that required a lot of computation time - about 10 hours to compute the results for one manoeuvre over the full frequency range of 1 Hz to 1000 Hz using 18 seconds of data. This computational requirement could be reduced significantly by using strategies similar to those recommended for the RI processor in Section 8.3:

- Making the focal point spacing a function of frequency rather than using the same focal points at all frequencies.
- Using fewer, more widely spaced, hydrophones at lower frequencies than at higher frequencies, rather than using all hydrophones at all frequencies.
- Ignoring the seabed reflections at higher frequencies.

The computational load was dominated by the computation of the acoustic transfer functions and their interpolation to the required hydrophone locations. As mentioned above, this would be reduced substantially in situations where the seabed reflections could be ignored and therefore the transfer functions could be calculated using simple formulae.

These strategies will not reduce the computational load to the levels achieved by the highly optimised beamformers used for far-field beamforming with straight, equally spaced line arrays because of the inherent complications in dealing with moving, distorting arrays and near-field processing. It may therefore be necessary to use high speed parallel processors or to be selective about the frequencies to be processed if near real-time performance is to be achieved.

These comments apply equally to the RI processor, which required a similar computational effort to the LSMC beamformer to process the same amount of data.

8.4.4 Computation of equivalent far-field source spectral levels and predicting the vessel's signature in other environments

The computation of the equivalent far-field source spectral levels shown at the end of Chapter 7 was trivial once the source amplitude distribution was calculated and only took a few minutes.

Equivalent far-field source spectral levels can be used to predict the vessel's acoustic signature in any other acoustic environment simply by running an acoustic propagation model appropriate to the environment of interest and using the computed transmission loss together with the source spectral level to determine the received spectral level.

The main practical issue is the effect of the assumed source depth on the results. This is primarily an issue for surface vessels because of the strong dependence of source strength on source depth near the sea surface and would be much less important for a submerged submarine.

It was shown in Section 8.2.1.6 that for shallow sources the relationship between assumed source depth and source level is only weakly dependent on the acoustic environment. When predicting the acoustic field in other environments the effect of changing the assumed source depth on the estimated source level would therefore tend to be cancelled by the effect of the source depth change on the transmission loss, resulting in a field that was approximately independent of the assumed source depth. For example, if the assumed source depth was halved the calculated source amplitude would approximately double (the source spectral level would increase by 6 dB). However, the transmission loss from the shallower source to the receiver would be 6 dB greater than from the deeper source, resulting in the same level at the receiver. Figure 8.26 shows how the transmission loss at 112 Hz was affected by changing the source depth from 2 m to 1 m, resulting in a shift of 6 dB at all ranges. These simple relationships break down progressively as the frequency and source depth increase resulting in a greater dependency of the received level on the assumed source depth.

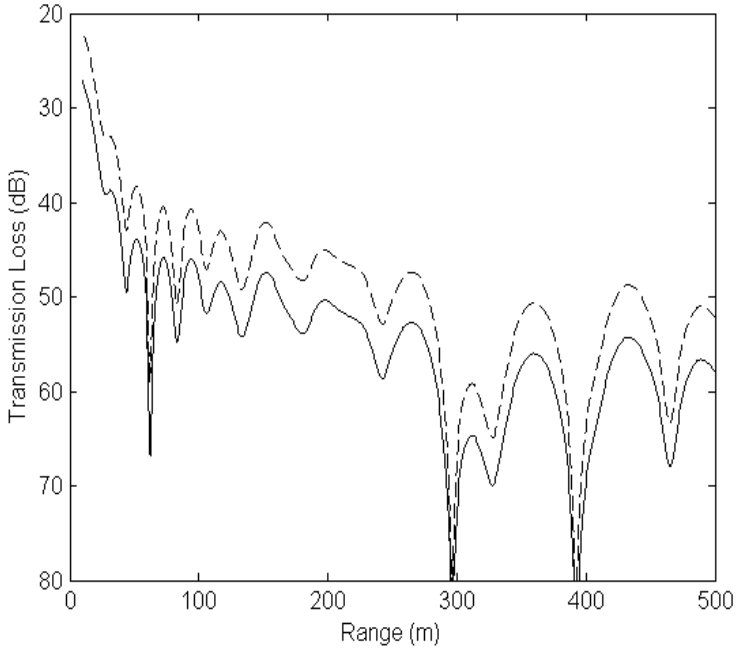

Figure 8.26 Transmission loss versus range at 112 Hz computed using SCOOTER for the Serial 1A environment. Source depths were 1 m (solid line) and 2 m (broken line). The receiver depth was 12 m.

8.4.5 Tow-vessel manoeuvrability

A serious practical consideration is whether a given tow-vessel is sufficiently manoeuvrable when towing the array to perform a manoeuvre that will bring the array into the required geometry for beamforming. A first estimate can be obtained simply by assuming that the array follows in the vessel's wake but this will be pessimistic because in reality the array will cut inside the vessel track which will result in the acoustic section of the array coming further forward relative to the tow-vessel than would otherwise be the case. The hydrodynamic model described in Appendix A can be used for a more accurate assessment.

8.5 Summary

Source localisation was successful with the UW30 source being localised to within ±0.5 m at all frequencies for Serial 1A and within ±1 m at 112 Hz for all serials. The poorer performance at the higher frequencies for the second two serials was consistent with the expected decrease in signal to noise ratio due to larger source - hydrophone separations and shallower hydrophone depths, and the reduction in beamformer spatial resolution at longer range. The beamformer outputs at other

frequencies agreed well with the known locations and frequency spectra of various items of machinery.

At 112 Hz the estimated levels of the UW30 source obtained during three different manoeuvres were all within 4.1 dB of the calibrated value, and varied by only 1.3 dB between manoeuvres. Results at the higher frequencies had slightly larger errors, with a maximum variation of 3.8 dB between serials, and a maximum deviation from the calibrated value of 6.8 dB. The largest potential source of error in the estimates of the UW30 source levels was identified as being the effect of the close proximity of the vessel's hull to the source, although this was not accurately quantified. This would not be a cause of error when measuring the levels of internal machinery sources.

The estimated levels were only weakly dependent on the seabed geoacoustic properties and the remaining errors were dominated by the uncertainties in the hydrophone calibrations and array depth, which could be reduced to negligible levels in a practical system by properly calibrating the hydrophones and by using an array with functioning pressure sensors to measure depth. The sensitivity to array depth would also be reduced if the array were towed deeper.

Accurate determination of the array shape was found to be much more critical than the determination of the distance of the array as a whole from the vessel, with random errors of only 0.2 wavelengths RMS in the hydrophone positions leading to an error of -5 dB in the estimated source spectral level (at 784 Hz this corresponded to an error of 0.39 m RMS). By contrast, changes in the distance between the array and the vessel of ±4 m were found to produce changes in source level estimates of less than ±2 dB.

It was estimated that source levels could be measured to an accuracy of ±2 dB using a system with properly calibrated hydrophones and depth sensors, providing the array shape was determined with sufficient accuracy.

The computed equivalent far-field vessel source levels appeared to be physically reasonable and were a major improvement over what could be achieved with a single hydrophone, but no independent measurements were available to check these results.

Of the various implementation issues discussed in Section 8.4 the most pressing is the development of a method of tracking the array hydrophones that could be used with digital arrays and minimises the requirement for acoustic beacons.

9 Conclusions and Recommendations

9.1 Conclusions

The work described in this thesis has demonstrated the feasibility of using a towed array to localise acoustic sources on the tow-vessel and to determine their absolute amplitudes. This was successful even in the difficult case of a surface vessel operating in shallow water and would be much more straightforward in deep water and particularly in the case of an array being towed by a submerged submarine.

An acoustic simulation was developed that allowed the signals received by a moving array of hydrophones to be accurately simulated in a variety of environments (see Chapter 3). The acoustic simulation had a great deal of flexibility and included the provision of a number of different types of acoustic sources and the capability of dealing with a variety of acoustic environments. It incorporated a method of computing the signals in environments with fluid half-space seabeds that was considerably faster than the full fast-field solution but just as accurate, even at low frequencies. Data generated by this simulation was then used for testing array-processing algorithms.

A field experiment was carried out in which a 27 m tug towing a 60-hydrophone array performed a number of U-turn manoeuvres (see Chapter 4). This took place in the acoustically difficult situation of a shallow water (100 m water depth) environment with sources located close to the sea surface, and the recorded data formed the basis of the extensive analyses carried out in the subsequent chapters.

Hydrophone localisation algorithms were developed for processing transient signals from imploding sources deployed from a second vessel and for dynamic tracking of the hydrophones using acoustic beacons mounted on the tow-vessel (see Chapter 5). The transient data provided snapshots of the array shape in the vertical and horizontal planes although there were some ambiguities in horizontal plane shape due to only a single transient source being used. The dynamic tracking algorithm had to deal with a large number of dropouts in the range data due to the directionality of the array hydrophones at the high frequencies used by the tracking beacons. Despite this the algorithm was successful in producing robust array tracks and array shapes, especially over the critical period when the vessel was broadside on to the

array and the geometry was optimum for beamforming. The transient and dynamic hydrophone localisation algorithms both incorporated hydrophone spacing constraints and a penalty on array curvature, which were found to be essential for producing good results.

The shallow water environment used for the sea experiment led to a requirement for information about the geoacoustic properties of the seabed. It was shown in Chapter 6 that sufficient information could be obtained by matched-field inversion of data from the first part of the manoeuvre, when the tow-vessel was in the array endfire direction, by using frequencies corresponding to prominent vessel noise spectral lines. The matched-field inversion process was also used successfully to determine the vertical plane array shape, providing a means of obtaining this information at times when no transient data were available. Vertical plane array shapes determined using matched-field inversion agreed well with those obtained from transient data. The matched-field inversion process was, however, extremely time consuming and required a lot of trial and error in order to produce good results. It is unlikely to be practical to implement this in an operational system in the near future.

A number of different array-processing algorithms were developed to deal with the data from the rapidly moving, distorting, towed array and the performance of three of these was investigated in detail using both simulated and field data (see Chapter 7). Although time-domain beamformers seemed to offer the most potential for dealing with this highly dynamic situation, the difficulty of modifying them to cope with time-varying acoustic transfer functions outweighed their potential advantages and attention was focussed on processing the array data in the frequency-domain. Three different algorithms were derived to do this: a data independent beamformer termed the LSMC beamformer, a data dependent beamformer, referred to as the DMVDR beamformer (which was obtained by modifying the well-known minimum variance distortionless response (MVDR) beamformer to deal with dynamic situations), and a method, referred to as the RI processor, based on the regularised inversion of the array data to obtain the complex amplitudes of a hypothesised set of sources. For all three algorithms a preliminary re-sampling of the signal, carried out to provide Doppler compensation, was found to improve the results.

All three algorithms performed well with simulated data, with the DMVDR beamformer providing the best source localisation but relatively poor source level

estimates. However, the DMVDR beamformer's performance degraded significantly when it was applied to field data whereas the other two processors had similar performance with simulated and field data. Source spectral level estimates were obtained with the LSMC beamformer at the frequencies emitted by a calibrated source mounted on the tow-vessel (112 Hz, 336 Hz, 560 Hz and 784 Hz). At 112 Hz the estimated levels obtained during three different manoeuvres were all within 4.1 dB of the calibrated value, and varied by only 1.3 dB between manoeuvres. Results at the higher frequencies had slightly larger errors, with a maximum variation of 3.8 dB between serials, and a maximum deviation from the calibrated value of 6.8 dB. The LSMC beamformer succeeded in localising the calibrated source to within 1 m of its true position at 112 Hz for all three manoeuvres, and source localisation was accurate to within ±0.5 m at all frequencies for the first manoeuvre which involved the closest approach of the array to the vessel (a minimum range of 80 m). The RI processor was not as useful as the LSMC beamformer for estimating the amplitude of the calibrated source, but provided results that could readily be used to determine the equivalent far-field source levels of the vessel as a whole. The RI processor suffered from truncation effects at the ends of the hypothetical source array, but otherwise provided source localisation accuracies equivalent to those achieved with the LSMC processor.

Estimated source levels and amplitude distributions were found to be relatively insensitive to seabed parameters providing the parameters were within a range covering half-spaces varying from sand to limestone. The importance of reflections from the seabed would be further diminished if measurements were carried out in deeper water, particularly if the vessel and hydrophones were deeper than they were in this experiment, making it likely that an approximate knowledge of the acoustic reflectivity would suffice for most practical applications of this technique. If, in addition, the array were outfitted with depth sensors so that its vertical plane shape could be determined without resorting to acoustic techniques, there would be no need to include matched-field inversion as part of the analysis procedure.

A detailed analysis of error sources was carried out in Chapter 8 from which it was determined that an operational system with properly calibrated hydrophones and depth sensors on the array should be able to determine acoustic source levels to within ±2 dB providing its hydrophones could be tracked with sufficient accuracy.

Accurate determination of the array shape was found to be much more critical than the determination of the distance of the array as a whole from the vessel, with random errors of only 0.2 wavelengths RMS in the hydrophone positions leading to an error of -5 dB in the estimated source spectral level (at 784 Hz this corresponded to an error of 0.39 m RMS). By contrast, changes in the distance between the array and the vessel of ±4 m were found to produce changes in source level estimates of less than ±2 dB.

Far-field source level estimates were obtained using the complex source amplitudes produced by the RI processor. The results seemed reasonable and were superior to those obtained with a single hydrophone, but there was no independent field data available to check them. Therefore, this method has only been validated with simulated data. There are also a number of outstanding issues regarding the RI processor that would be worthy of investigation and these are detailed in Section 9.2.3.

Overall then, this project was successful in achieving its aims and proved that determining the locations and amplitudes of acoustic sources on a vessel using its own towed array was possible. During the sea experiment described in this thesis a second vessel was used to deploy transient sources, but the transient data only provided a useful crosscheck and was not essential to generating the final results. All the essential information was obtained from data recorded on the tow-vessel itself, including the required information about the seabed properties, and consequently fully autonomous measurements have also been demonstrated. The equivalent far-field signature of the tow-vessel was computed from this data, and although these results have not been verified with comparable field data, it is highly likely that this represents a viable technique for fully autonomous acoustic signature measurement.

The practical aspects of turning the algorithms described here into an operational method of acoustic signature measurement were considered in Chapter 8, with the main issue being to devise a method of tracking the hydrophones that will work with digitally sampled arrays and that minimises the requirement for acoustic beacons. This issue, and other possible avenues of further research that have arisen in the course of this project are considered in the following recommendations for further work.

9.2 Recommendations for further work

9.2.1 Hydrophone tracking

To facilitate the practical application of this technique it will be necessary to develop methods of hydrophone tracking suitable for use with digital arrays and to minimise the requirement for acoustic tracking beacons. In particular, this effort should be directed towards combining information from array heading and depth sensors with vessel navigation data and a hydrodynamic model of the array to minimise the reliance on acoustic tracking. Constraints on hydrophone spacings and array curvature will almost certainly be required and it will be necessary to utilise at least one acoustic source at a known position on the tow-vessel in order to remove the accumulated effects of unknown environmental effects such as currents. It may be possible to use a simple tone-burst source, allowing approximate ranges to the array hydrophones to be computed, and then obtain an accurate array shape by adjusting the hydrophone positions so as to provide the sharpest possible image of the source. Ferguson (1990) may provide a useful guide here.

9.2.2 Matched field inversion

The best recommendation here is to try to avoid having to do it! Matched-field inversion is a very time consuming process and is unlikely to be practical in an operational system for quite some time. Having said this, the following are worthy of investigation:

- Modifying the forward propagation model to include rough surface effects. This would be straightforward to do but was not attempted because scattering effects were expected to be unimportant at the relatively low frequencies used for the inversion.

- Combining data from multiple array positions in order to get a greater range of bottom incidence angles to use in the inversion. This should reduce the number of ambiguous solutions and result in a more accurate determination of the seabed geoacoustic parameters, but would require a significant increase in computational effort. The inverted vertical plane array shape was relatively insensitive to the seabed parameters so it should be possible to reduce the computational requirements by inverting for the array shape for

each snapshot first (array shape will in general be time varying), and then use the combined snapshots to invert for the seabed parameters.

9.2.3 Array-processing

There are many different array-processing algorithms described in the literature and there was only time to investigate a small subset in the course of this project. Even for these there are outstanding questions. Some of the more promising lines of investigation are as follows:

- Carry out a thorough investigation of the RI processor and other related inversion techniques. In particular:
  - Investigate the causes of the truncation effects seen in the source amplitude distributions and try to find ways of eliminating them.
  - Devise a robust method of determining the regularisation weights to replace the ad hoc method used here.
  - Investigate alternative regularisation methods not considered here. The aim would be to find a method that would result in point sources being represented by single hypothetical sources and distributed sources by multiple hypothetical sources, rather than point sources being smeared out as they are with the current method. Maximum entropy regularisation (Press et al. 1993) has been used with success in image reconstruction and would be worth investigating, but it may be too computationally intensive for this application.
  - Investigate using information from multiple snapshots in a single source distribution inversion rather than inverting each snapshot independently. To avoid problems with incoherent sources this would have to be set up in such a way that the source amplitudes and phase differences between sources remained the same from snapshot to snapshot but the absolute phase was allowed to vary.
  - Try using a spatial Fourier transform representation of the source amplitude distributions and inverting for the spatial frequency coefficients rather than individual source amplitudes. This would allow

control of the spatial resolution by varying the number of coefficients in the inversion while always maintaining smooth source distributions.

- Implement the methods for reducing the computational requirements of the RI processor and LSMC beamformer listed in the Chapter 8 and look for other methods of optimising the algorithms to allow near real-time computation.
- Investigate the DMVDR beamformer in order to determine the cause of its poor performance when applied to field data and see if this can be addressed by using some of the methods that have been applied to the MVDR and other data dependent beamformers in order to reduce their sensitivity to correlated sources and modelling errors.
- Carry out further investigations of the time-domain beamformer:
  - Determine whether beam shapes can be improved for non-equally spaced arrays simply by weighting the hydrophone elements in inverse proportion to their spatial density.
  - Look for efficient ways of implementing an FIR filter time-domain beamformer in order to compensate for changes in the acoustic transfer functions as the array moves.
- Investigate other data independent beamformers, eg. by applying constraints on maximum sidelobe peak levels over design range, or an additional zero derivative constraint in the look direction.
- Assess whether eigenspace beamformers (eg. MUSIC) can be made sufficiently robust against modelling errors to be applied to this problem.
- Investigate the application of passive synthetic aperture techniques to this problem in order to improve spatial resolution and reduce the number of required hydrophones. There are significant difficulties in going down this path given the relatively wide bandwidths and therefore short coherence times of many machinery noise sources and the problem that source frequencies are not known precisely. It may be possible to circumvent these problems using the passive synthetic array techniques described in Section **7.1.7.1**, in which case the payoffs could be substantial.

Appendix A. Towed Array Hydrodynamic Simulation

A hydrodynamic simulation was written in Matlab to allow the positions of the hydrophones in the towed array to be estimated during manoeuvres of the tow-vessel. The aim of the simulation was to provide hydrophone tracks that could be used for testing tracking algorithms. The aim was not to compute exact positions for an operational system.

The theoretical basis for the simulation is presented in Section A.1 and the values chosen for the various parameters and the reasons for choosing them are described in Section A.2. The results of a series of tests of the simulation are described in Section A.3 which also includes a discussion of the effects of various parameters on the path taken by the array.

A.1 Theory

The simulation used a two-dimensional lumped mass model for the towed array and was a modified version of that described in Ranmuthugala & Gottschalk (1993). The following changes were made to the model described in this reference:

- The model was modified to operate in the horizontal plane, rather than a vertical plane (the towed array was assumed neutrally buoyant).
- The model described in Ranmuthugala & Gottschalk (1993) was for a two-part tow consisting of a cable running from the tow-vessel to a depressor and a second cable, attached to the first above the depressor, leading to a towed body. Their method was modified so as to be appropriate to a single cable, although the properties of the cable were allowed to vary along its length.
- The numerical integration scheme described in the reference was found to be unstable for long simulation times and consequently the equations were re-cast in a form that could be integrated using a standard differential equation solver.
- Damping was added to the stretching of the cable to remove unrealistic length-wise oscillations.

The geometry used for the model is shown in Figure A.1. The towed array was modelled as a series of n nodes containing the array mass, connected together by

mass-less springs. Here M_i (kg) is the mean of the masses of array segments *i-1* and *i* and is assumed located at node *i* with coordinates x_i, y_i (m). This mass is acted on by the tensions $\mathbf{T}_i$ and $\mathbf{T}_{i-1}$ (N) and by the hydrodynamic drag force, $\mathbf{Fd}_i$ (N). The drag force was determined as the mean of the drag force vectors on the two attached segments, each of which was characterised by a component normal to the segment, Fdn_i, and a component tangential to the segment, Fdt_i. Note that node 1 was the free (aft) end of the array and that an array with *n* segments was towed from node *n+1*.

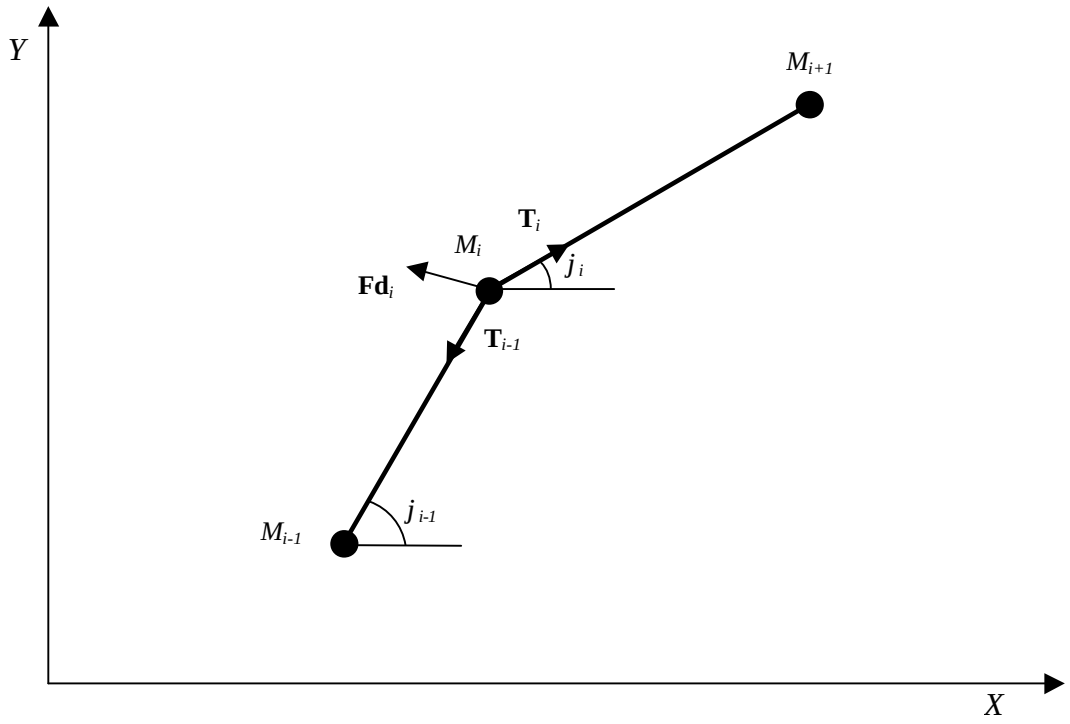

Figure A.1 Lumped mass cable model

The hydrodynamic forces on the cable segments that were proportional to the cable accelerations were modelled as added mass terms in the directions tangential, $a_{t,i}$, and normal, $a_{n,i}$, to the cable. After the appropriate coordinate transformations were applied the resulting equation of motion for node *i* was:

$$\ddot{\mathbf{X}}_i = \mathbf{M}_i^{-1}\mathbf{F}_i \qquad \textbf{(A.1)}$$

where

$\mathbf{X}_i = \begin{bmatrix} x_i \\ y_i \end{bmatrix}$ is the node position vector, and

$\mathbf{M}_i = \begin{bmatrix} I_i & -K_i \\ -K_i & J_i \end{bmatrix}$ is the mass matrix for the node, with

$$I_i = M_i + 0.5\left(a_{n,i}\sin^2 f_i + a_{t,i}\cos^2 f_i + a_{n,i-1}\sin^2 f_{i-1} + a_{t,i-1}\cos^2 f_{i-1}\right),$$

$$J_i = M_i + 0.5\left(a_{t,i}\sin^2 f_i + a_{n,i}\cos^2 f_i + a_{t,i-1}\sin^2 f_{i-1} + a_{n,i-1}\cos^2 f_{i-1}\right),$$

$$K_i = -0.5\left\{(a_{t,i} - a_{n,i})\sin f_i \cos f_i + (a_{t,i-1} - a_{n,i-1})\sin f_{i-1}\cos f_{i-1}\right\}.$$

$\mathbf{F}_i = \begin{bmatrix} F_{x,i} \\ F_{y,i} \end{bmatrix}$ is the vector of forces acting on the node, with

$$F_{x,i} = T_i\cos f_i - T_{i-1}\cos f_{i-1} - 0.5\left(Fdn_i\sin f_i + Fdn_{i-1}\sin f_{i-1}\right) + 0.5\left(Fdt_i\cos f_i + Fdt_{i-1}\cos f_{i-1}\right)$$

and

$$F_{y,i} = T_i\sin f_i - T_{i-1}\sin f_{i-1} + 0.5\left(Fdn_i\cos f_i + Fdn_{i-1}\cos f_{i-1}\right) + 0.5\left(Fdt_i\sin f_i + Fdt_{i-1}\sin f_{i-1}\right)$$

The normal and tangential hydrodynamic drag forces were given by

$$Fdn_i = -0.5C_{dn}\rho_0 D_i l_i v_{n,i}\left|v_{n,i}\right| \qquad \textbf{(A.2)}$$

and

$$Fdt_i = -0.5C_{dt}\rho_0 \pi D_i l_i v_{t,i}\left|v_{t,i}\right| \qquad \textbf{(A.3)}$$

where

C_{dn} is the normal drag coefficient (non-dimensional), which is defined by Equation A.2 and depends on the cross-sectional shape of the cable and the flow conditions (see next section),

C_{dt} is the tangential drag coefficient (non-dimensional), which is defined by Equation A.3 and depends on the cable roughness and flow conditions (see next section),

ρ_0 is the density of the fluid (kg.m^{-3}),

D_i is the diameter of the cable segment (m),

l_i is the length of the cable segment (m),

$v_{n,i}$ is the component of the mean velocity of the segment normal to the segment (ms^{-1}) and

$v_{t,i}$ is the component of the mean velocity of the segment tangential to the segment (ms^{-1}).

Note that equations A.2 and A.3 assume that the fluid is stationary.

The mean velocities of each segment were calculated from the velocities of the nodes at either end of the segment with the application of an appropriate coordinate rotation as follows:

$$v_{t,i} = \frac{(\dot{x}_i + \dot{x}_{i+1})}{2}\cos f_i + \frac{(\dot{y}_i + \dot{y}_{i+1})}{2}\sin f_i \qquad \textbf{(A.4)}$$

and

$$v_{n,i} = \frac{(\dot{y}_i + \dot{y}_{i+1})}{2}\cos f_i - \frac{(\dot{x}_i + \dot{x}_{i+1})}{2}\sin f_i \qquad \textbf{(A.5)}$$

The tension in cable segment *i* was related to the coordinates and velocities of the nodes on either end of the segment by

$$T_i = A_i E_i \left(\frac{l_i}{l_{0i}} - 1 \right) + \frac{a_i A_i}{l_{0i}} \dot{l}_i \qquad \textbf{(A.6)}$$

where

A_i is the cross-sectional area of the cable segment (m^2),

E_i is the Young's modulus of the cable segment (Pa),

l_{0i} is the unstretched length of the cable segment (m),

a_i is the damping coefficient for cable extension (Pa.s).

If

$dx_i = x_{i+1} - x_i$, and

$dy_i = y_{i+1} - y_i$,

then

$l_i = \sqrt{dx_i^2 + dy_i^2}$, and

$$\dot{l}_i = \frac{dx_i}{l_i} d\dot{x}_i + \frac{dy_i}{l_i} d\dot{y}_i .$$

In order to solve equations A.5 and A.6 the problem was set up as a set of 4*n* simultaneous first-order differential equations as follows. (*n* is the number of cable nodes):

$$\dot{x}_i = v_{x,i}, \; i = 1 \ldots n$$

$$\dot{y}_i = v_{y,i}, \; i = 1 \ldots n$$

$$\dot{v}_{x,i} = \begin{cases} f_{x1}(x_i, x_{i+1}, y_i, y_{i+1}, v_{x,i}, v_{x,i+1}, v_{y,i}, v_{y,i+1}), \; i = 1 \\ f_x(x_{i-1}, x_i, x_{i+1}, y_{i-1}, y_i, y_{i+1}, v_{x,i-1}, v_{x,i}, v_{x,i+1}, v_{y,i-1}, v_{y,i}, v_{y,i+1}, t), \; i = 2 \ldots n \end{cases} \quad \textbf{(A.7)}$$

$$\dot{v}_{y,i} = \begin{cases} f_{y1}(x_i, x_{i+1}, y_i, y_{i+1}, v_{x,i}, v_{x,i+1}, v_{y,i}, v_{y,i+1}), \; i = 1 \\ f_y(x_{i-1}, x_i, x_{i+1}, y_{i-1}, y_i, y_{i+1}, v_{x,i-1}, v_{x,i}, v_{x,i+1}, v_{y,i-1}, v_{y,i}, v_{y,i+1}, t), \; i = 2 \ldots n \end{cases}$$

Here the functions f_{x1}, f_x, f_{y1}, and f_y were obtained from Equation A.1. Note that node *n*+1 was the tow-point and the position and velocity of this node formed the dynamic inputs to the cable.

A.2 Selection of simulation parameters

The simulation was tested using a towed-array model consisting of a tow-cable, a forward vibration isolation module (VIM), an acoustic section, and an aft vibration isolation module. A set of simulation parameters was adopted using reasonable values from the literature as discussed below. These parameters were used for a reference simulation and the sensitivity of the simulation to each parameter was checked by varying each in turn. The parameters and their reference values are shown in Table A.1.

Table A.1 Parameters for reference simulation

	Tow-cable	**Forward VIM**	**Acoustic section**	**Aft VIM**
Overall section length (m)	200	100	300	50
Section diameter (m)	0.01	0.05	0.05	0.05
Segment length	25	25	25	25
Number of segments in section	8	4	12	2
Young's modulus (Pa)	7.8×10^{10}	1×10^{9}	1×10^{9}	1×10^{9}
Tension damping coefficient (Pa.s)	1×10^{9}	2×10^{8}	2×10^{8}	2×10^{8}
Normal drag coefficient	0.7	0.7	0.7	0.7
Tangential drag coefficient	2.5×10^{-3}	2.5×10^{-3}	2.5×10^{-3}	2.5×10^{-3}
Normal added mass (kg)	= mass of displaced fluid	= mass of displaced fluid	= mass of displaced fluid	= mass of displaced fluid
Tangential added mass	0	0	0	0

The simulation assumed that the towed array was made up of a number of straight segments, each bounded by the nodes at which the masses were lumped. The segment lengths were chosen as a reasonable compromise between simulation accuracy and computational speed.

Young's moduli for the array sections were not critical parameters as they predominantly affected only the static stretch of the array. Low values were found to speed execution of the simulation as larger time-steps could be used, but they were also found to introduce significant longitudinal oscillations of the array. The oscillations were removed by including a damping force proportional to the rate of stretch of the array. The values shown in the table were found to give a good compromise between execution speed and static stretch.

Tension damping coefficients were chosen so as to be just large enough to remove the longitudinal oscillations. Increasing them further only served to reduce the simulation time step and hence slow the simulation.

As will be seen from the comparisons between simulation runs given in the next section, the tangential and normal drag coefficients were the most critical parameters in determining the array shape through the manoeuvre. The values of these coefficients are well established for smooth, rigid cylinders subject to either pure normal flow or pure axial flow (Hoerner 1965), but are less certain for flow aligned at an arbitrary angle to the axis of the cylinder. The main complication is the effect of Reynolds number, which is a dimensionless quantity that represents the ratio of mechanical forces to viscous forces and can be defined either in terms of the length or diameter of the cylinder as follows:

$Re_l = \frac{U_0 l}{n} \approx U_0 l \times 10^6$ is the length dependent Reynolds number,

$Re_d = \frac{U_0 D}{n} \approx U_0 D \times 10^6$ is the diameter dependent Reynolds number,

U_0 is the flow speed (m/s)

l is the length of the cylinder (m)

D is the diameter of the cylinder (m), and

n is the kinematic viscosity of the fluid ($\approx 1 \times 10^{-6}$ m^2/s for water).

For a cylinder subject to flow normal to its axis the normal drag coefficient is approximately constant at a value of 1.2 for $100 < \mathrm{Re}_d < \sim 10^5$. Between Reynolds numbers of 10^5 and 10^6 the drag coefficient drops dramatically to a value that depends on the roughness of the cylinder but could be as low as 0.3. The exact value of Re_d at which the transition occurs also depends on the roughness of the cylinder, with the transition generally occurring at lower Reynolds numbers for rougher cylinders. To put this in context, for a 50 mm diameter array section a flow speed of 5 m/s (10 knots) corresponds to $Re_d = 2.5 \times 10^5$.

According to Hoerner & Borst (1975) for a cylinder at a small angle of attack to the flow the normal drag coefficient is in the range 0.7 to 1.2 with the smaller values

corresponding to higher flow speeds. Hoerner & Borst state that there is some uncertainty as to the appropriate Reynolds number to use for defining this transition.

A value of 0.7 was chosen as the reference normal drag coefficient but the effect of increasing the value to 1.2 was also investigated.

There was uncertainty associated with the tangential drag coefficient, not least because of the unknown roughness of the array surface. Hoerner (1965) gave a formula for the tangential drag coefficient of a smooth cylinder subject to axial flow that depended on the length dependent Reynolds number and the length to diameter ratio of the cylinder.

$$C_{dt} = \frac{0.074}{Re_l^{0.2}} + 0.0016\frac{l}{DRe_l^{2/5}},\ Re_l < 10^6$$

(A.8)

$$C_{dt} = \frac{0.455}{(\log_{10} Re_l)^{2.58}} + 0.0016\frac{l}{DRe_l^{2/5}},\ 10^6 < Re_l < 10^9$$

A problem with applying Equation A.8 to the towed array was deciding what length of cylinder to use as this affected both the Reynolds number and the resulting drag coefficient. This is illustrated in Figure A.2 for a 0.05 m diameter cylinder and a flow speed of 5 m/s. A tangential drag coefficient value of 2.5×10^{-3} was chosen as being consistent with a cylinder length equal to the segment length of 25 m. The effect of doubling this value was also tested.

The added mass of a cylinder undergoing uniform acceleration in a direction normal to its axis is simply equal to the mass of the fluid displaced by the cylinder Chakrabarti (1994). No reference was found for the added mass for axial acceleration of the cylinder (tangential added mass) so this parameter was varied in the simulation from a reference value of zero to the mass of the displaced fluid.

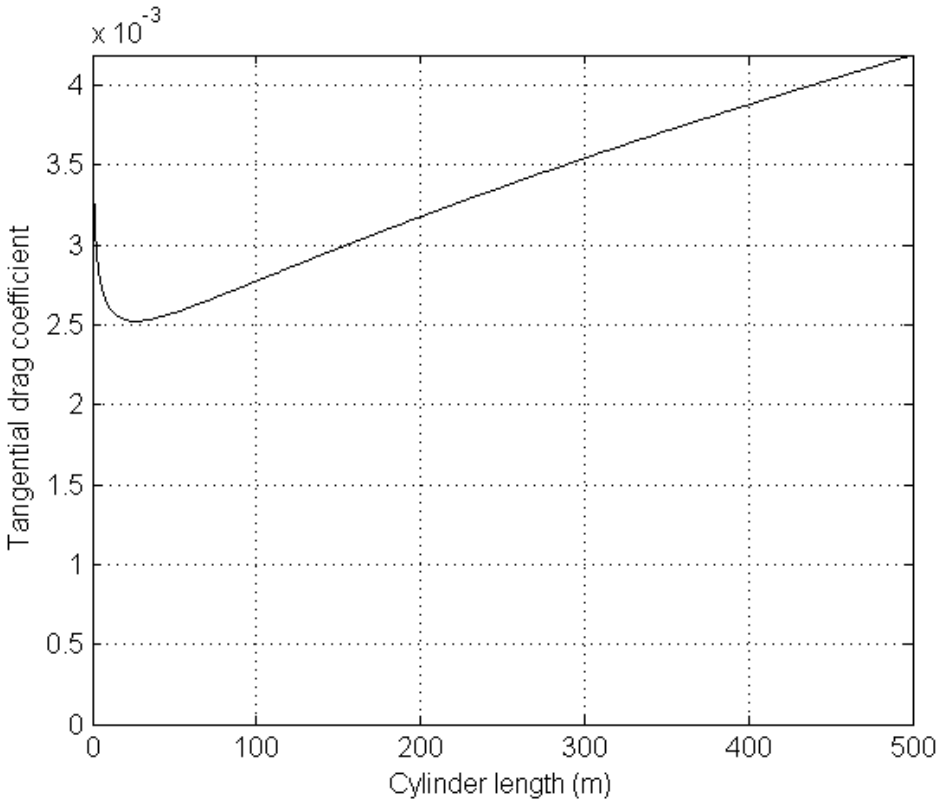

Figure A.2 Effect of cylinder length on tangential drag coefficient for a smooth cylinder subject to axial flow. Cylinder diameter = 0.05 m, flow speed = 5 ms^{-1}.

A.3 Simulation results and discussion

Results for a simulated 150 m radius U-turn manoeuvre at 5 m/s are plotted in Figure A.3 and Figure A.4. The simulation was run with the reference cable parameters given in Table A.1 for a simulated time of 300 seconds, starting with the vessel at (0,0), heading north at a speed of 5 m/s with the towed array streaming directly behind.

These results demonstrated that the path of the towed array was far more sensitive to the tangential and normal drag coefficients than it was to any of the other parameters. It was also apparent that the relative values of the two drag coefficients was the important factor as doubling both of them resulted in a far smaller change in array path than altering either individually. Having said this, the array paths were still qualitatively very similar over the range of drag coefficients tested (see Figure A.5 and Figure A.6).

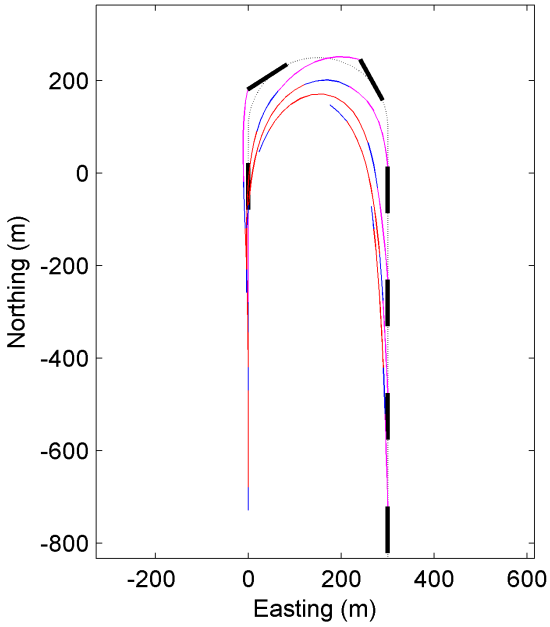

Figure A.3 Position of vessel (thick black line) and towed array (thin line). Dotted line is vessel track. Vessel is initially heading north at an easting of 0 m. Simulated using the reference parameters for 150 m radius U-turn manoeuvre at 5 m/s. Colours delineate array sections.

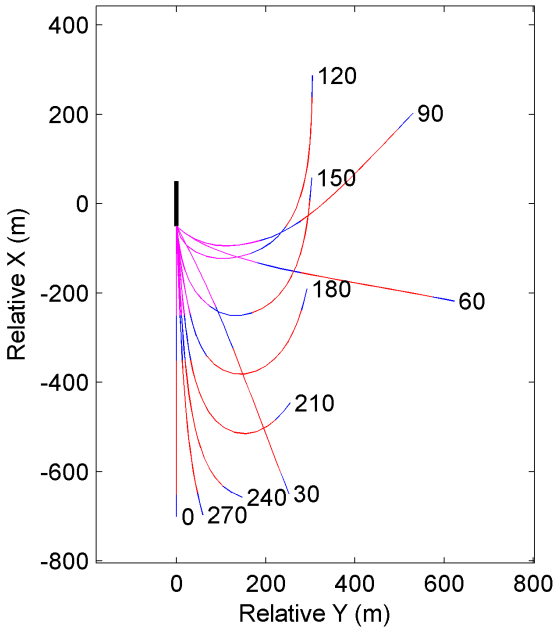

Figure A.4 Position of towed array (thin lines) relative to vessel (thick black line) calculated for the same manoeuvre and parameters as Figure A.3. Numbers are seconds after start of simulation.

The effects of changing various simulation parameters were tested and the results are summarised in Table A.2.

Table A.2 Change in node positions due to variation of simulation parameters.

Parameter varied	**Reference value**	**Comparison value**	**Maximum node position change (m)**
Segment length	25 m	12.5 m	1.7
Normal drag coefficient	0.7	1.2	46.4
Tangential drag coefficient	2.5×10^{-3}	5×10^{-3}	75.3
Normal added mass (kg)	= mass of displaced fluid	0	3.5
Tangential added mass	0	= mass of displaced fluid	1.5
Normal drag coefficient and tangential drag coefficient (ratio kept constant)	0.7 2.5×10^{-3}	1.4 5×10^{-3}	4.1
Vessel speed	5 m/s	0.5 m/s	0.4

It was at first surprising that the vessel speed had little effect on the array path. The reason why the simulation results were virtually independent of vessel speed was that the drag force was proportional to the square of the speed and, as the tension was due primarily to the drag force, it was also proportional to the square of the speed. Consequently the overall force on each node and thus the acceleration of the node was proportional to the square of the vessel speed, which was exactly what was required to achieve a constant turn radius. In reality the drag coefficients are a function of Reynolds number and hence speed, rather than being constant as was assumed here, and the path of a real towed array would therefore be expected to depend on the tow speed.

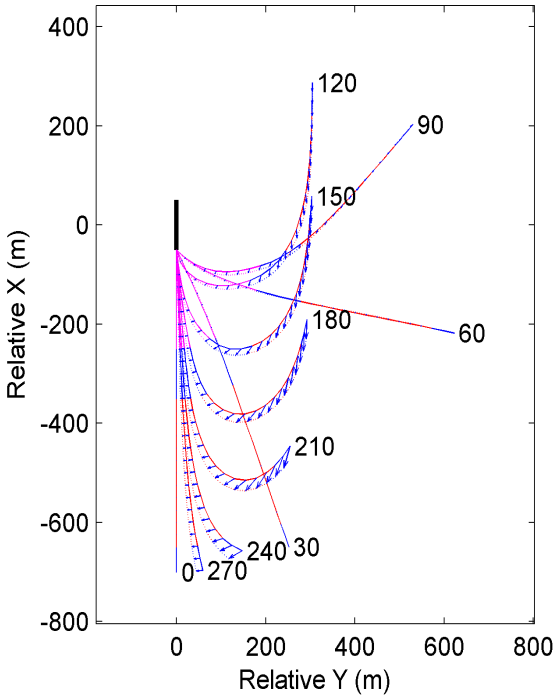

Figure A.5 Effect of increasing normal drag coefficient from 0.7 to 1.2. Arrows point from reference solution to solution with increased drag coefficient.

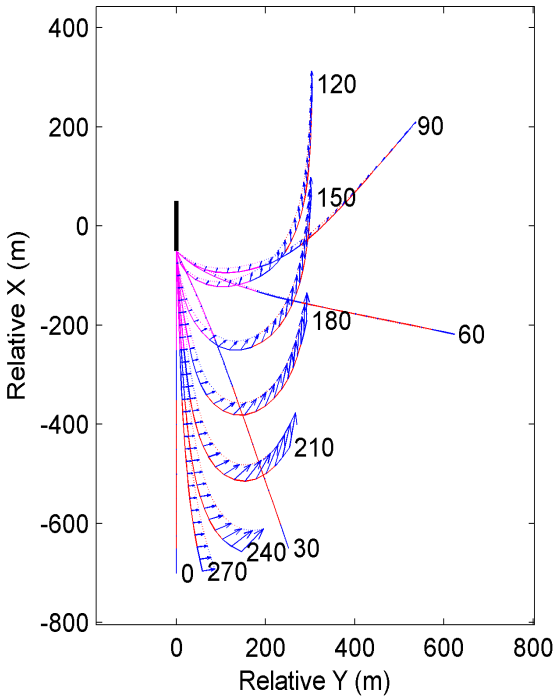

Figure A.6 Effect of increasing tangential drag coefficient from 2.5×10^{-3} to 5×10^{-3}. Arrows point from reference solution to solution with increased drag coefficient.

Appendix B. Hydrophone transient localisation plots

This appendix contains plots of the towed array shapes determined from the transient source field data. See Chapter 5 for a full explanation. Horizontal plane array shapes are given in figures B.1 to B.12 and vertical plane shapes in figures B.13 to B.22.

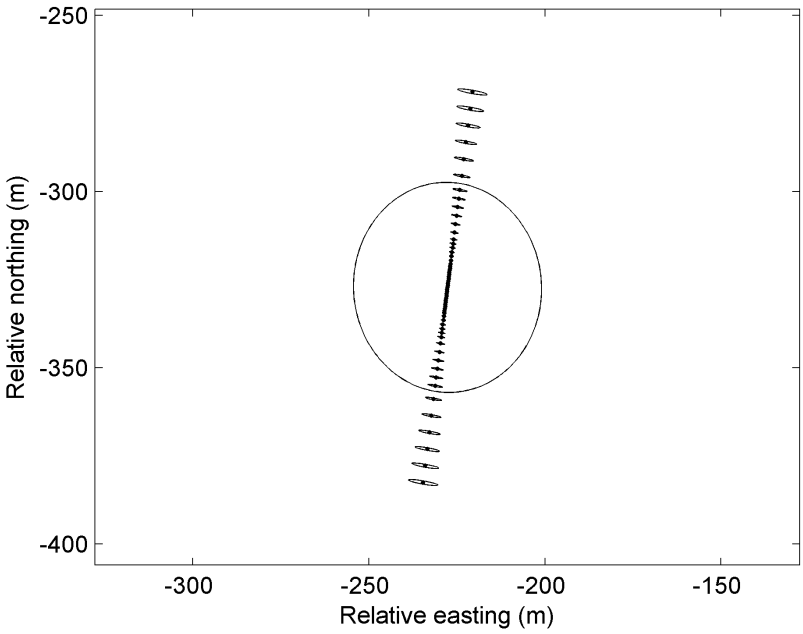

Figure B.1 Serial 1A, Shot 1 (5.238 h) horizontal plane array shape. Large ellipse is 68.3% uncertainty region for overall array position. Ellipses on individual hydrophones are 68.3% uncertainty regions for relative positions. Source was at (0, 0).

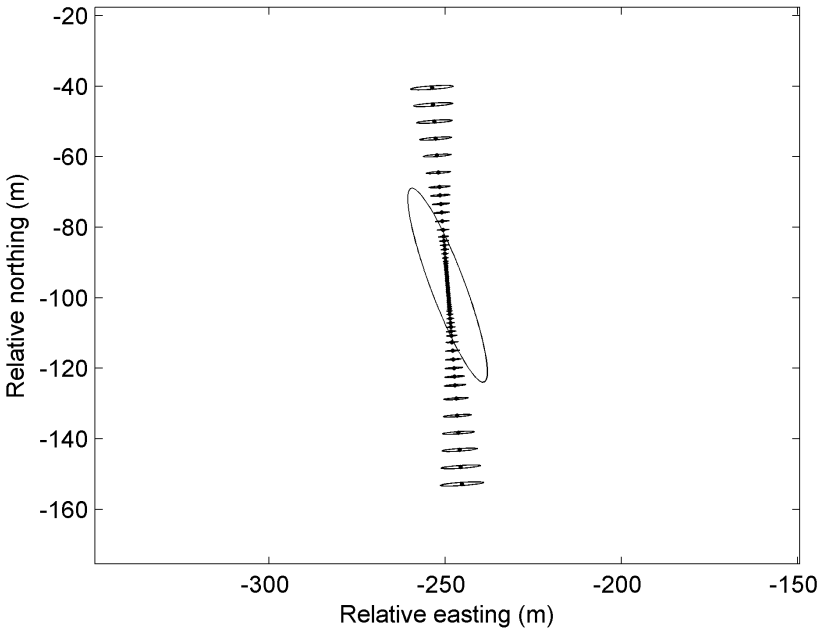

Figure B.2 As for Figure B.1 but for Serial 1A, Shot 3 (5.275 h).

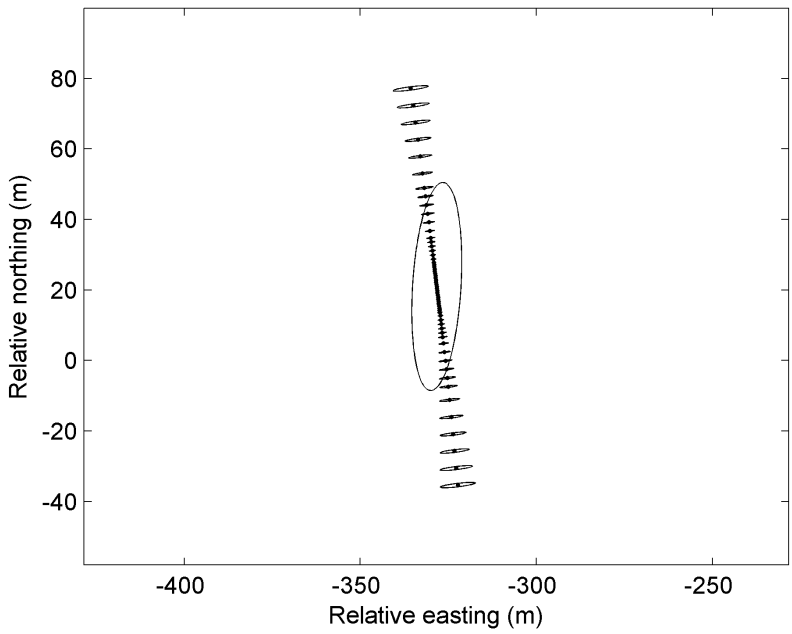

Figure B.3 As for Figure B.1 but for Serial 1A, Shot 4 (5.296 h).

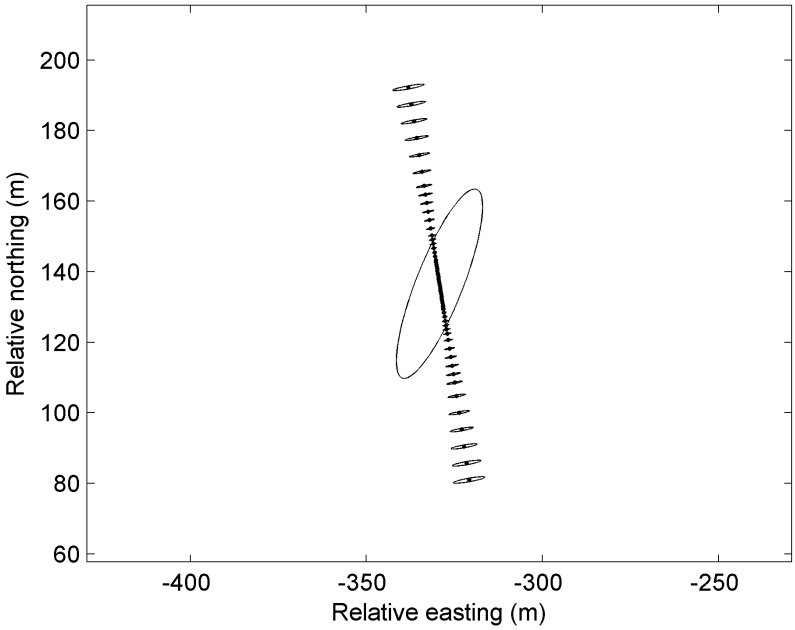

Figure B.4 As for Figure B.1 but for Serial 1A, Shot 5 (5.316 h).

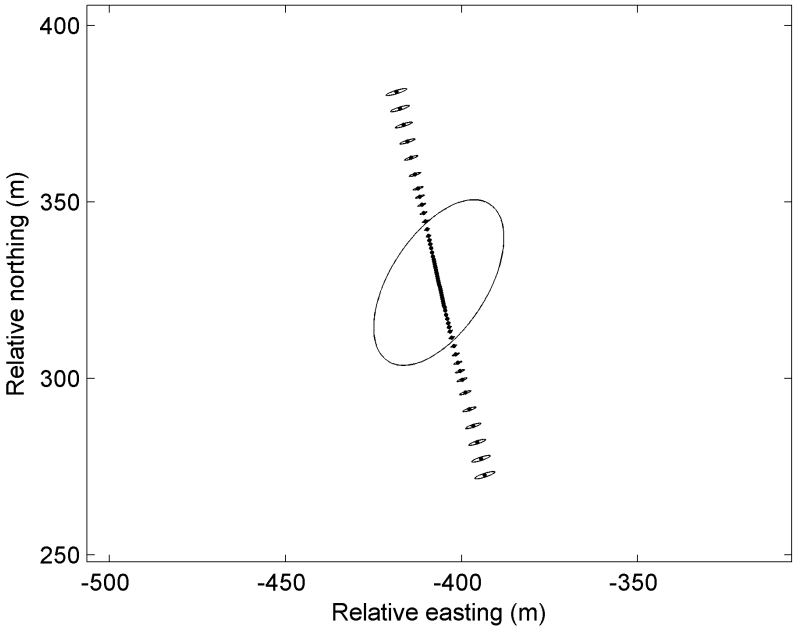

Figure B.5 As for Figure B.1 but for Serial 1A, Shot 7 (5.363 h).

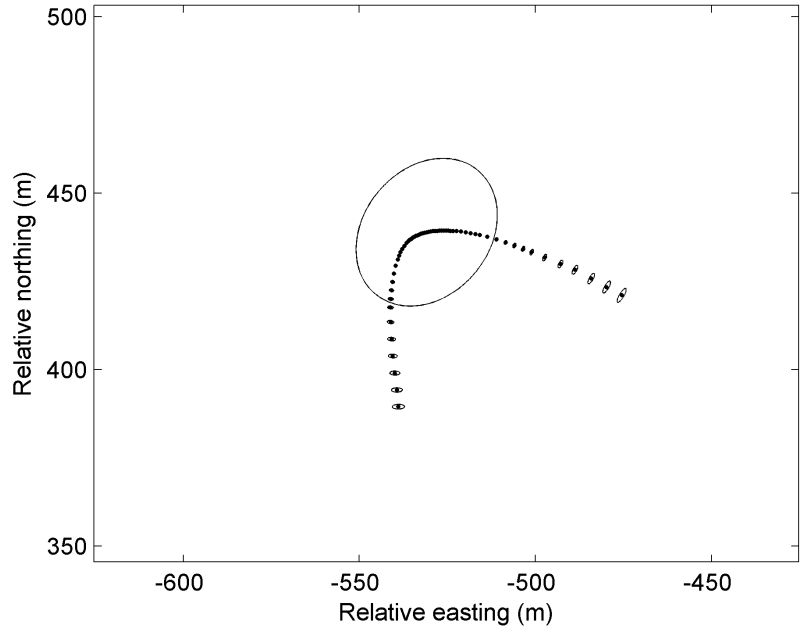

Figure B.6 As for Figure B.1 but for Serial 1A, Shot 9 (5.409 h).

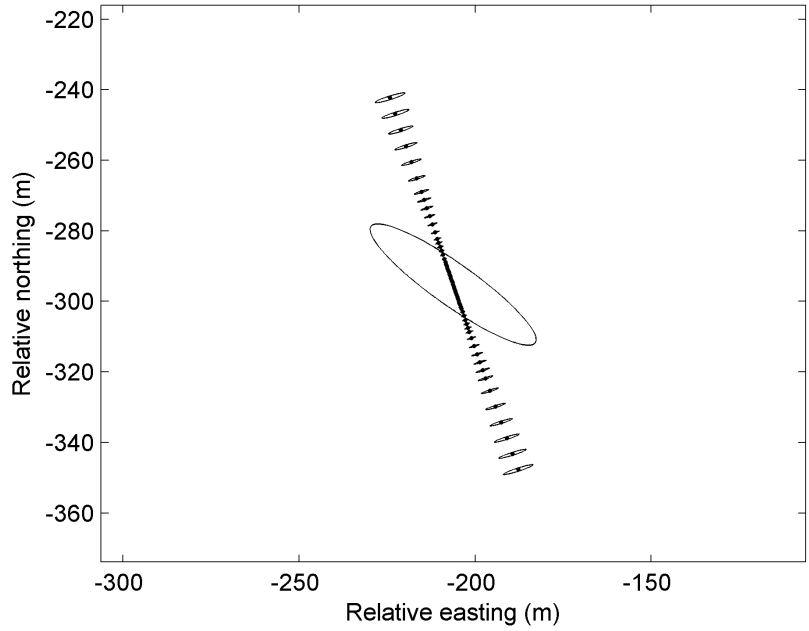

Figure B.7 As for Figure B.1 but for Serial 1C, Shot 2 (5.952 h).

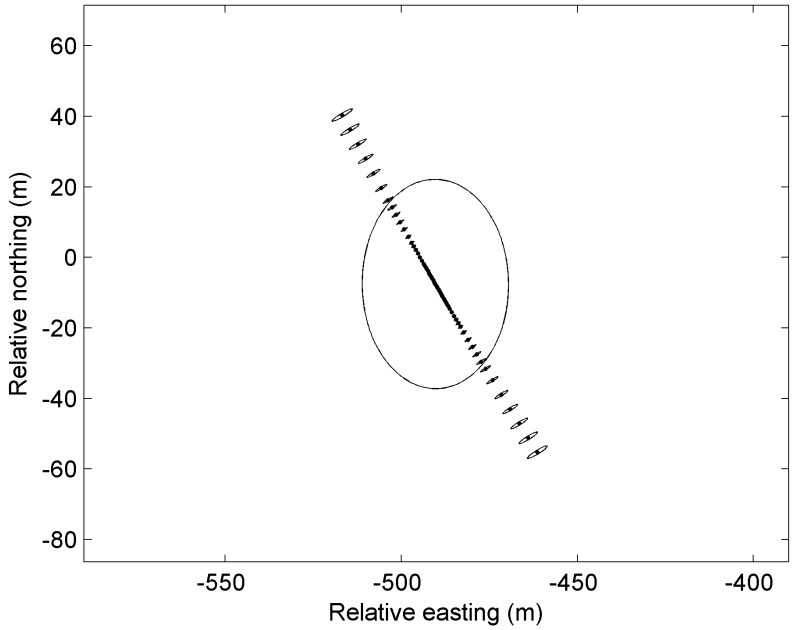

Figure B.8 As for Figure B.1 but for Serial 1C, Shot 3 (5.992 h).

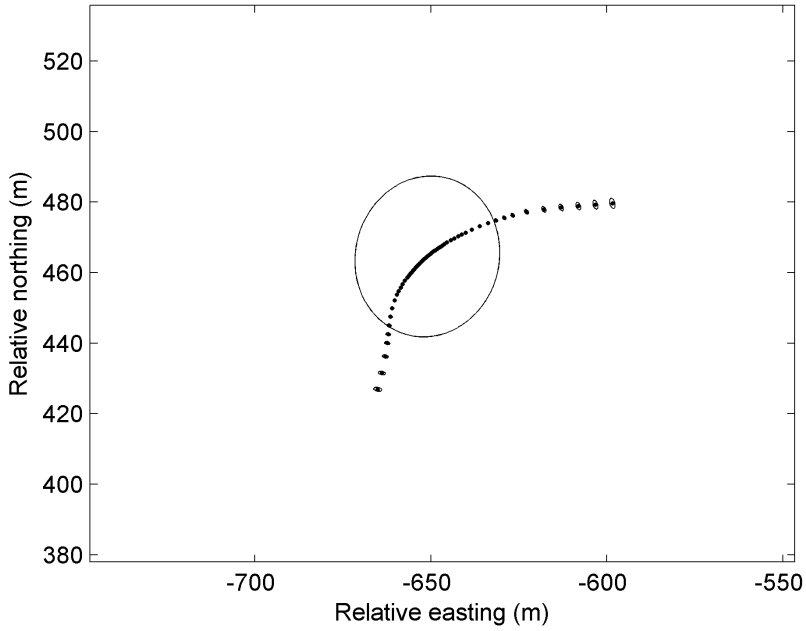

Figure B.9 As for Figure B.1 but for Serial 1C, Shot 6 (6.087 h).

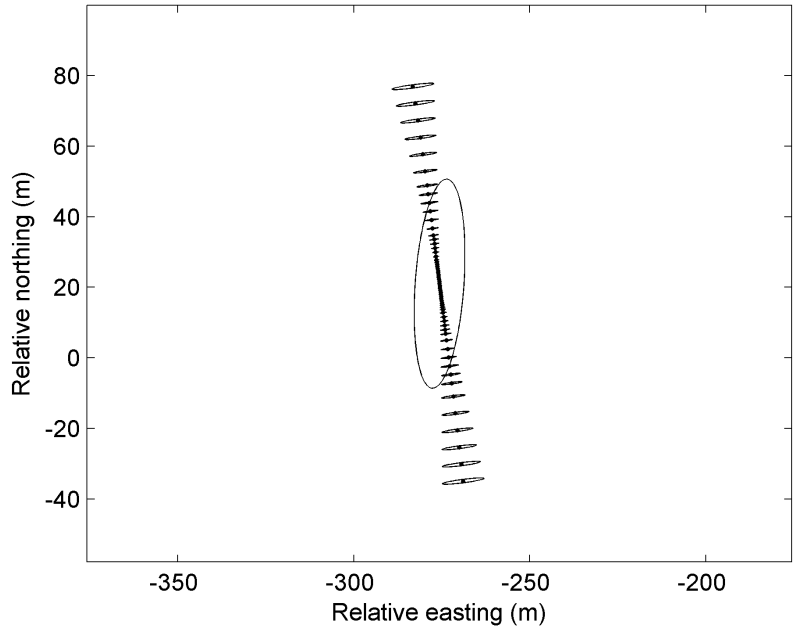

Figure B.10 As for Figure B.1 but for Serial 1D, Shot 3 (6.340 h).

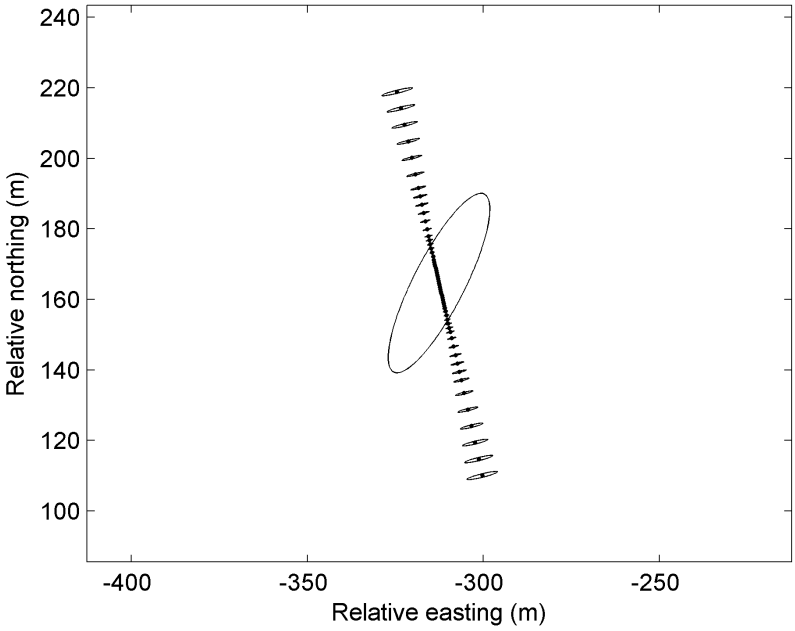

Figure B.11 As for Figure B.1 but for Serial 1D, Shot 4 (6.359 h).

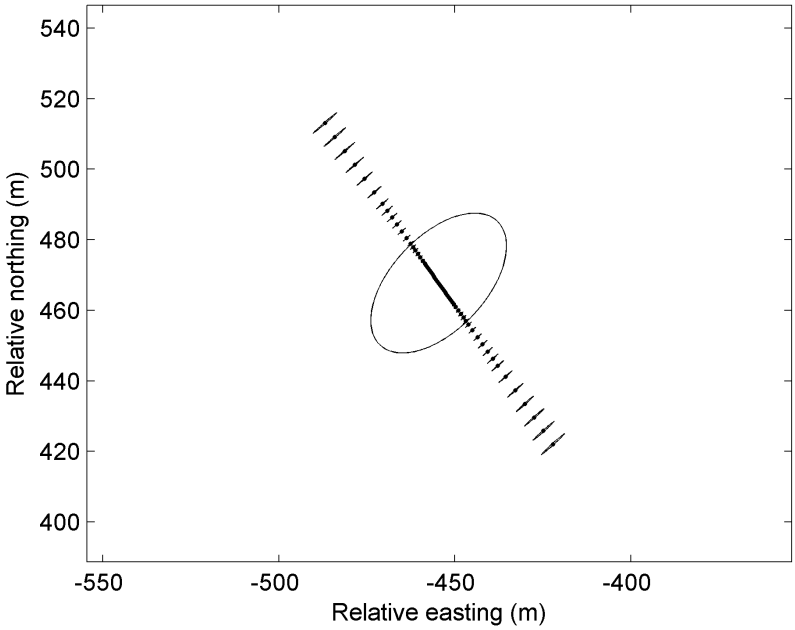

Figure B.12 As for Figure B.1 but for Serial 1D, Shot 6 (6.415 h).

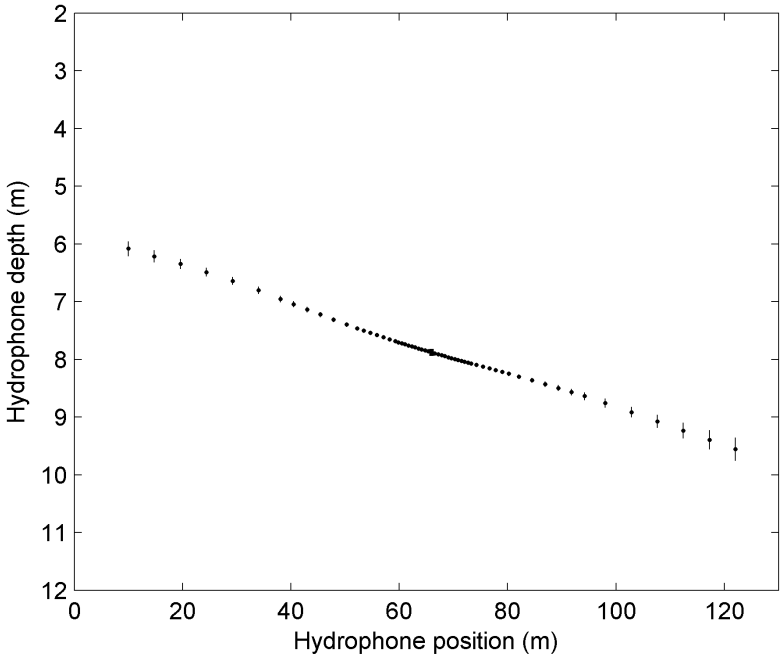

Figure B.13 Serial 1A, Shot 3 (5.275 h) vertical plane array shape. Central error bar is 68.3% uncertainty region for absolute array depth, other error bars are 68.3% uncertainty regions for relative hydrophone depths.

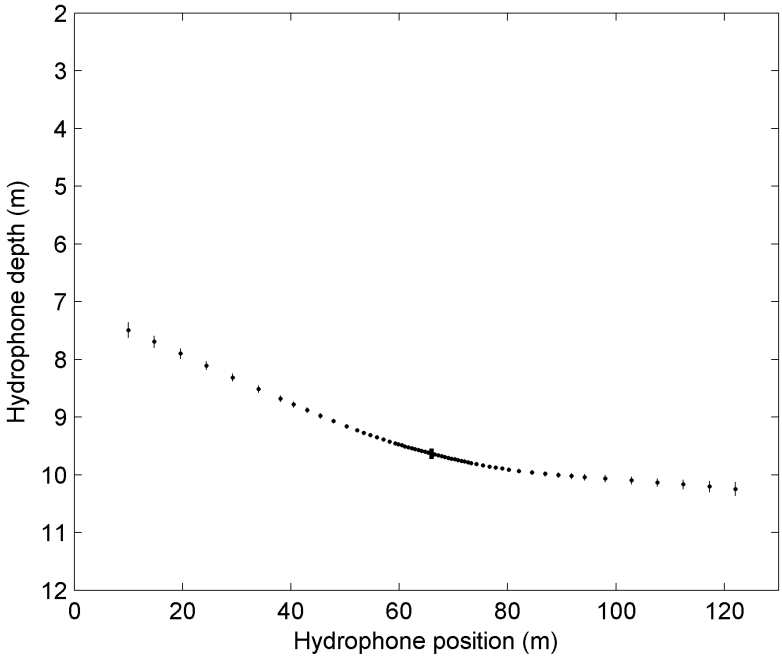

Figure B.14 As for Figure B.13 but for Serial 1A, Shot 4 (5.296 h).

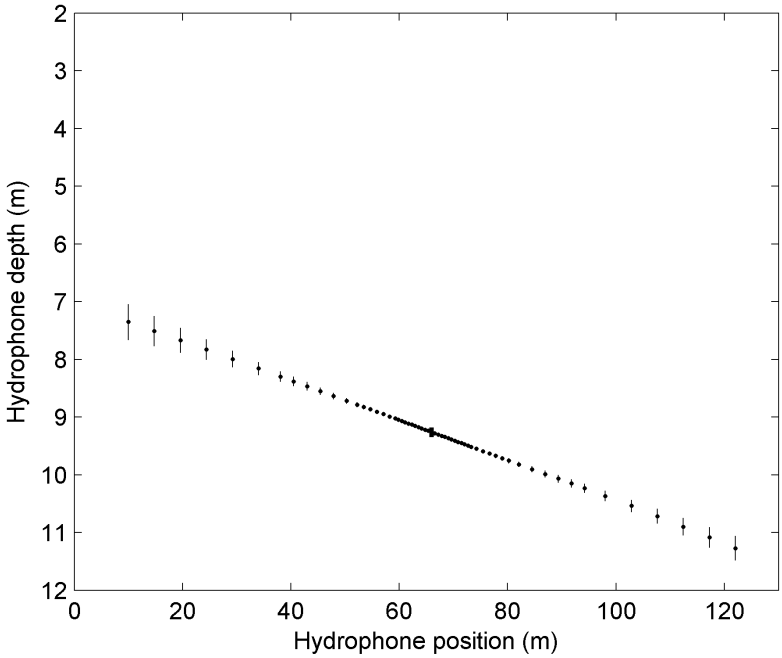

Figure B.15 As for Figure B.13 but for Serial 1A, Shot 5 (5.316 h).

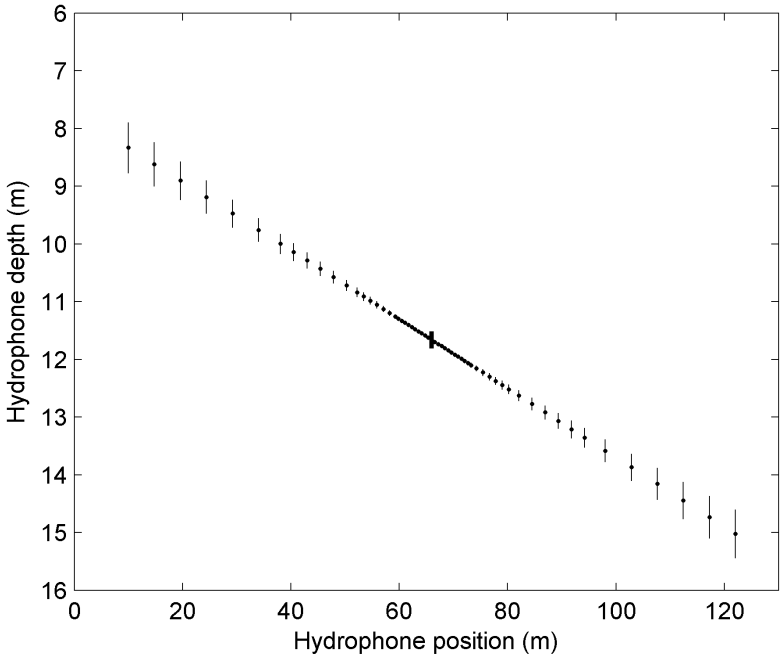

Figure B.16 As for Figure B.13 but for Serial 1A, Shot 7 (5.363 h).

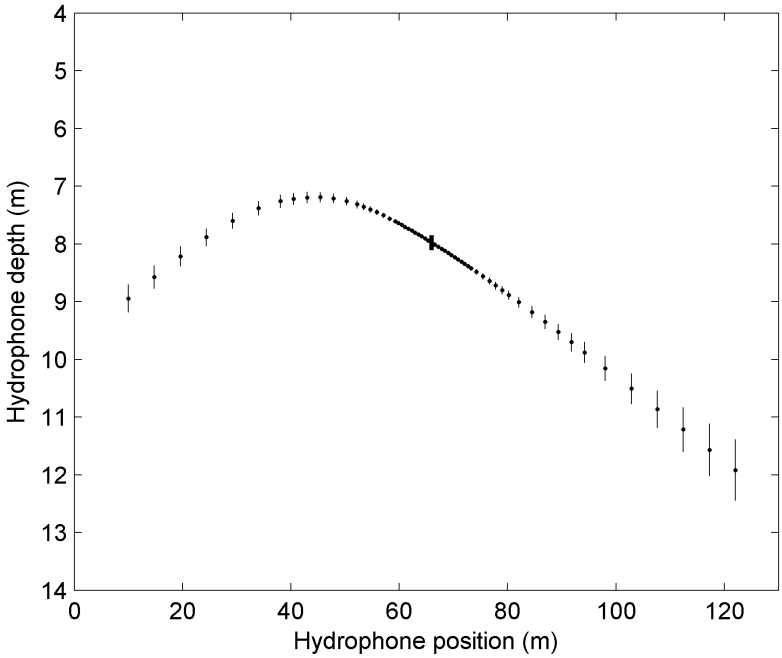

Figure B.17 As for Figure B.13 but for Serial 1A, Shot 9 (5.409 h).

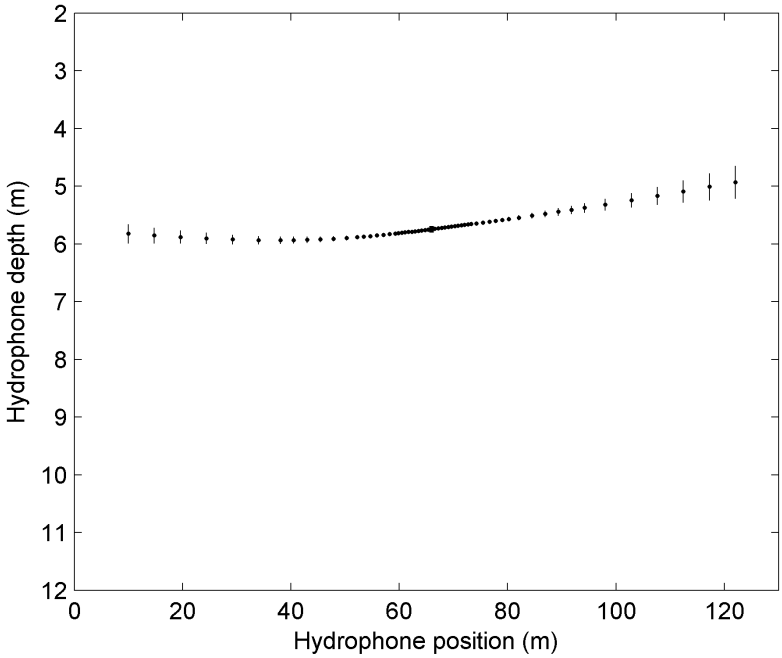

Figure B.18 As for Figure B.13 but for Serial 1C, Shot 2 (5.952 h).

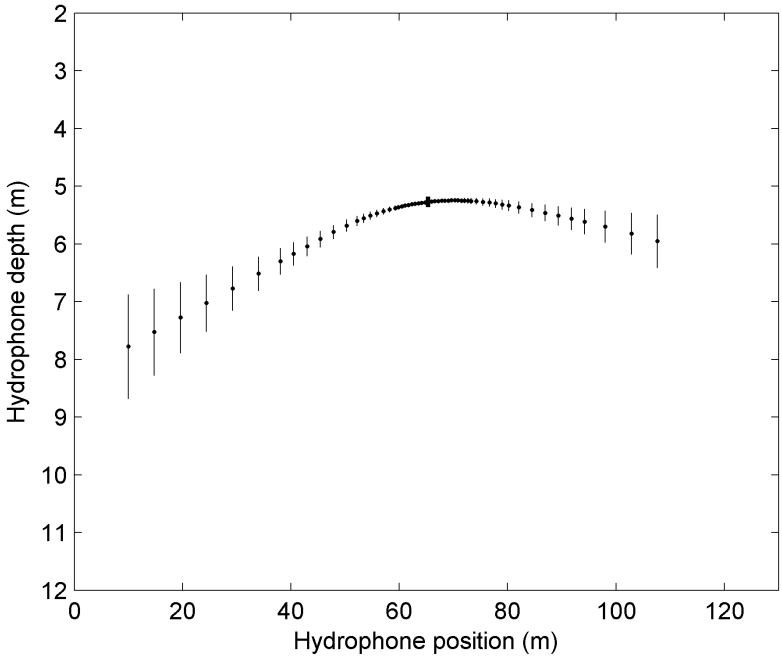

Figure B.19 As for Figure B.13 but for Serial 1C, Shot 6 (6.087 h).

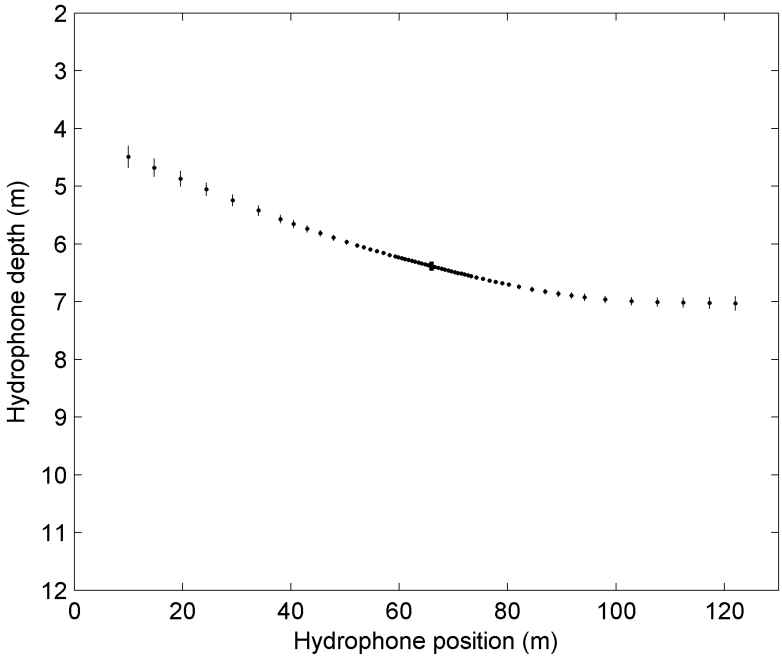

Figure B.20 As for Figure B.13 but for Serial 1D, Shot 3 (6.340 h).

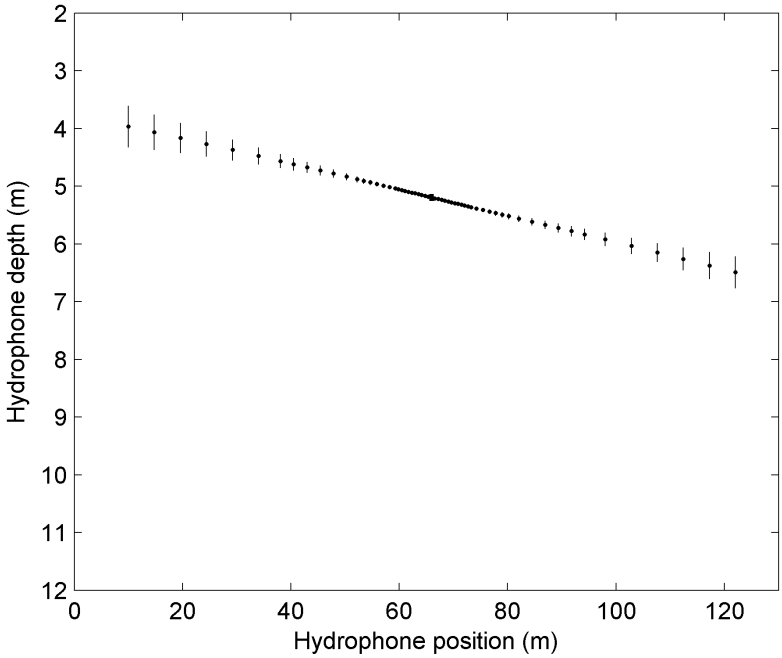

Figure B.21 As for Figure B.13 but for Serial 1D, Shot 4 (6.359 h).

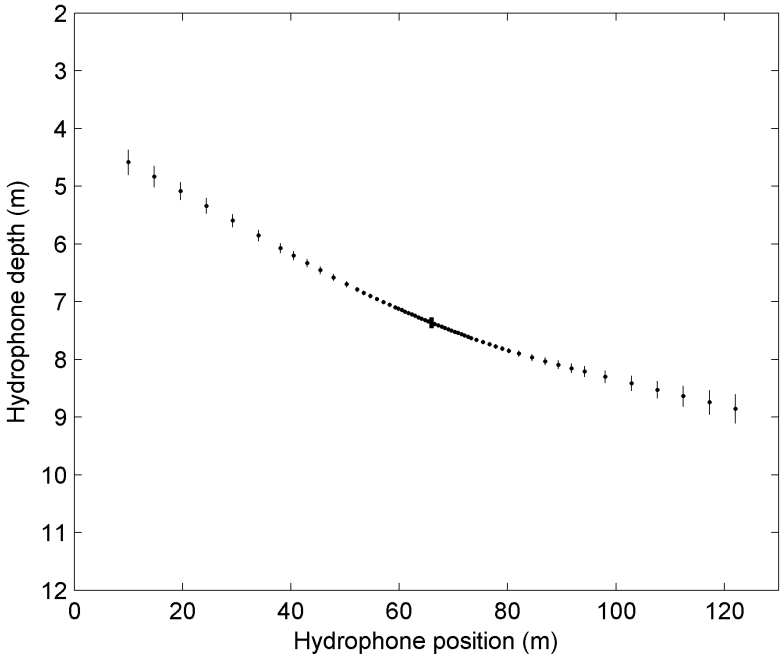

Figure B.22 As for Figure B.13 but for Serial 1D, Shot 6 (6.415 h).

Appendix C. Derivation of global coordinate dynamic model

This appendix details the derivation of the position dynamic equation for a dynamic model that assumes constant acceleration in a fixed global coordinate system.

Using the standard equations for transformation of coordinates in a plane (Spiegel 1968):

$$x_{k+1} = \left(X_{k+1} - X_{0,k+1}\right)\cos q_{k+1} + \left(Y_{k+1} - Y_{0,i+1}\right)\sin q_{k+1} \qquad \textbf{(C.1)}$$

and

$$y_{k+1} = -\left(X_{k+1} - X_{0,k+1}\right)\sin q_{k+1} + \left(Y_{k+1} - Y_{0,i+1}\right)\cos q_{k+1} \qquad \textbf{(C.2)}$$

where:

X, Y are the global coordinates of a hydrophone (X is northing, Y is easting),

X_0, Y_0 are the global coordinates of the origin of the tow-vessel coordinate system (i.e. the tow-point),

x, y are the coordinates of the hydrophone in tow-vessel coordinates

q is the vessel heading (radians clockwise from north), and

the subscript k refers to the time-step.

Substituting the global reference frame constant acceleration dynamic equations:

$$\dot{X}_{k+1} = \dot{X}_k + dt\ddot{X}_k + \frac{dt^2}{2}\dddot{X}_k, \qquad \textbf{(C.3)}$$

and

$$\ddot{X}_{k+1} = \ddot{X}_k + dt\dddot{X}_k \qquad \textbf{(C.4)}$$

into Equation C.1:

$$\begin{aligned} x_{k+1} = &\left(X_k + dt\dot{X}_k + dt^2\ddot{X}_k/2 + dt^3\dddot{X}_k/6 - X_{0,k+1}\right)\cos q_{k+1} + \cdots \\ &\left(Y_k + dt\dot{Y}_k + dt^2\ddot{Y}_k/2 + dt^3\dddot{Y}_k/6 - Y_{0,k+1}\right)\sin q_{k+1} \end{aligned} \qquad \textbf{(C.5)}$$

Defining dq such that $q_{i+1} = q_i + dq$, using the standard trigonometric angle sum formulae, making the assumption that dq is sufficiently small that $\sin dq \approx dq$ and $\cos dq \approx 1$, and using a first order Taylor expansion for the vessel motion: $X_{0,k+1} = X_{0,k} + dt\dot{X}_{0,k}$ and $Y_{0,k+1} = Y_{0,k} + dt\dot{Y}_{0,k}$ gives:

$$
\begin{aligned}
x_{k+1} = {} & \left(X_k - X_{0,k+1}\right)\left(\cos q_k - dq \sin q_k\right) + \ldots \\
& \left(dt\left(\dot{X}_k - \dot{X}_{0,k}\right) + dt^2 \ddot{X}_k / 2 + dt^3 \dddot{X}_k / 6\right)\cos q_{k+1} + \cdots \\
& \left(Y_k - Y_{0,k+1}\right)\left(\sin q_k + dq \cos q_k\right) + \ldots \\
& \left(dt\left(\dot{Y}_k - \dot{Y}_{0,k}\right) + dt^2 \ddot{Y}_k / 2 + dt^3 \dddot{Y}_k / 6\right)\sin q_{k+1}
\end{aligned}
\qquad \textbf{(C.6)}
$$

A little manipulation yields:

$$
\begin{aligned}
x_{k+1} = {} & \left(X_k - X_{0,k}\right)\cos q_k + \left(Y_k - Y_{0,k}\right)\sin q_k + \ldots \\
& dq\left(-\left(X_k - X_{0,k}\right)\sin q_k + \left(Y_k - Y_{0,k}\right)\cos q_k\right) + \ldots \\
& \left(dt\left(\dot{X}_k - \dot{X}_{0,k}\right) + dt^2 \ddot{X}_k / 2 + dt^3 \dddot{X}_k / 6\right)\cos q_{k+1} + \ldots \\
& \left(dt\left(\dot{Y}_k - \dot{Y}_{0,k}\right) + dt^2 \ddot{Y}_k / 2 + dt^3 \dddot{Y}_k / 6\right)\sin q_{k+1}
\end{aligned}
\qquad \textbf{(C.7)}
$$

The final step is to substitute equations C.1 and C.2 into Equation C.7 to eliminate X and Y, giving:

$$
\begin{aligned}
x_{k+1} = {} & x_k + dq y_k + \ldots \\
& \left(dt\left(\dot{X}_k - \dot{X}_{0,k}\right) + dt^2 \ddot{X}_k / 2 + dt^3 \dddot{X}_k / 6\right)\cos q_{k+1} + \ldots \\
& \left(dt\left(\dot{Y}_k - \dot{Y}_{0,k}\right) + dt^2 \ddot{Y}_k / 2 + dt^3 \dddot{Y}_k / 6\right)\sin q_{k+1}
\end{aligned}
\qquad \textbf{(C.8)}
$$

The derivation of the corresponding equation in the y direction is completely analogous and gives:

$$
\begin{aligned}
y_{k+1} = {} & y_k - dq x_k - \ldots \\
& \left(dt\left(\dot{X}_k - \dot{X}_{0,k}\right) + dt^2 \ddot{X}_k / 2 + dt^3 \dddot{X}_k / 6\right)\sin q_{k+1} + \ldots \\
& \left(dt\left(\dot{Y}_k - \dot{Y}_{0,k}\right) + dt^2 \ddot{Y}_k / 2 + dt^3 \dddot{Y}_k / 6\right)\cos q_{k+1}
\end{aligned}
\qquad \textbf{(C.9)}
$$

Treating $q, dq, \dot{X}_0$ and $\dot{Y}_0$ as exactly known quantities, and $\dddot{X}$ and $\dddot{Y}$ as noise terms allows the dynamic model to be expressed in matrix form as:

$$
\tilde{\mathbf{x}}_{k+1} = \mathbf{F}_k \tilde{\mathbf{x}}_k + \mathbf{B}_k \mathbf{u}_k + \mathbf{G}_k \mathbf{e}_k
\qquad \textbf{(C.10)}
$$

where

$$
\begin{aligned}
\tilde{\mathbf{x}} = \big[& x_1 \quad \cdots \quad x_N \quad \dot{X}_1 \quad \cdots \quad \dot{X}_N \quad \ddot{X}_1 \quad \cdots \quad \ddot{X}_N \cdots \\
& y_1 \quad \cdots \quad y_N \quad \dot{Y}_1 \quad \cdots \quad \dot{Y}_N \quad \ddot{Y}_1 \quad \cdots \quad \ddot{Y}_N \big]^T
\end{aligned}
\qquad \textbf{(C.11)}
$$

is the state vector. Here lower case letters represent tow-vessel coordinates and capital letters represent global coordinates.

$$
\mathbf{u}_k = \begin{bmatrix} \dot{X}_0 \\ \dot{Y}_0 \end{bmatrix},
$$

$$
\mathbf{e}_k = \left[\dddot{X}_1 \quad \cdots \quad \dddot{X}_N \quad \dddot{Y}_1 \quad \cdots \quad \dddot{Y}_N \right]^T,
$$

$$\mathbf{F}_k = \begin{bmatrix} \mathbf{I} & \Phi_{1,2} & \Phi_{1,3} & \Phi_{1,4} & \Phi_{1,5} & \Phi_{1,6} \\ \mathbf{Z}_3 & \mathbf{I} & \Phi_{2,3} & \mathbf{Z}_3 & \mathbf{Z}_3 & \mathbf{Z}_3 \\ \mathbf{Z}_3 & \mathbf{Z}_3 & \mathbf{I} & \mathbf{Z}_3 & \mathbf{Z}_3 & \mathbf{Z}_3 \\ \Phi_{4,1} & \Phi_{4,2} & \Phi_{4,3} & \mathbf{I} & \Phi_{4,5} & \Phi_{4,6} \\ \mathbf{Z}_3 & \mathbf{Z}_3 & \mathbf{Z}_3 & \mathbf{Z}_3 & \mathbf{I} & \Phi_{5,6} \\ \mathbf{Z}_3 & \mathbf{Z}_3 & \mathbf{Z}_3 & \mathbf{Z}_3 & \mathbf{Z}_3 & \mathbf{I} \end{bmatrix}, \qquad \textbf{(C.12)}$$

$$\mathbf{B}_k = \begin{bmatrix} -\mathbf{v}_1 & -\mathbf{v}_2 \\ \mathbf{z}_1 & \mathbf{z}_1 \\ \mathbf{z}_1 & \mathbf{z}_1 \\ \mathbf{v}_2 & -\mathbf{v}_1 \\ \mathbf{z}_1 & \mathbf{z}_1 \\ \mathbf{z}_1 & \mathbf{z}_1 \end{bmatrix}, \text{ and} \qquad \textbf{(C.13)}$$

$$\mathbf{G}_k = \begin{bmatrix} \mathbf{G}_{1,1} & \mathbf{G}_{1,2} \\ \mathbf{G}_{2,1} & \mathbf{Z}_3 \\ \mathbf{G}_{3,1} & \mathbf{Z}_3 \\ \mathbf{G}_{4,1} & \mathbf{G}_{4,2} \\ \mathbf{Z}_3 & \mathbf{G}_{5,2} \\ \mathbf{Z}_3 & \mathbf{G}_{6,2} \end{bmatrix}. \qquad \textbf{(C.14)}$$

In these equations:

$\mathbf{I}$ is the $N \times N$ identity matrix,

$\mathbf{Z}_3$ is an $N \times N$ matrix of zeros,

$\Phi_{1,2} = \Phi_{4,5} = dt \cos q_{k+1} \mathbf{I}$,

$\Phi_{1,3} = \Phi_{4,6} = \frac{dt^2 \cos q_{k+1}}{2} \mathbf{I}$,

$\Phi_{1,4} = -\Phi_{4,1} = dq \mathbf{I}$,

$\Phi_{1,5} = -\Phi_{4,2} = dt \sin q_{k+1} \mathbf{I}$,

$\Phi_{1,6} = -\Phi_{4,3} = \frac{dt^2 \sin q_{k+1}}{2} \mathbf{I}$, and

$\Phi_{2,3} = \Phi_{5,6} = dt \mathbf{I}$,

$\mathbf{v}_1$ is the $N \times 1$ vector $\begin{bmatrix} dt \cos q_{k+1} & \cdots & dt \cos q_{k+1} \end{bmatrix}^T$,

$\mathbf{v}_2$ is the $N \times 1$ vector $\begin{bmatrix} dt \sin q_{k+1} & \cdots & dt \sin q_{k+1} \end{bmatrix}^T$,

$\mathbf{z}_1$ is an $N \times 1$ vector of zeros,

$$\mathbf{G}_{1,1} = \mathbf{G}_{4,2} = \frac{dt^3}{6} \cos q_{k+1} \mathbf{I},$$

$$\mathbf{G}_{1,2} = -\mathbf{G}_{4,1} = \frac{dt^3}{6} \sin q_{k+1} \mathbf{I},$$

$\mathbf{G}_{2,1} = \mathbf{G}_{6,2} = dt\mathbf{I}$, and

$$\mathbf{G}_{3,1} = \mathbf{G}_{5,2} = \frac{dt^2}{2} \mathbf{I} \quad .$$

Appendix D. Array-processing derivations

This appendix derives two of the equations discussed in Chapter 7: the data independent beamforming algorithm and the equation used to convert source amplitude distributions to equivalent far-field source pressures.

See Chapter 7 for background information and symbol definitions.

D.1 Derivation of data independent beamforming algorithm

The array weight vector is obtained by carrying out the following minimisation, with respect to $\mathbf{w}$ and l :

$$\min_{\mathbf{w},l}\left(\left|\mathbf{A}^H\mathbf{w}-\mathbf{y}_d\right|^2 + b\left|\mathbf{w}\right|^2 + l\left(\mathbf{w}^H\mathbf{a}_0 - 1\right)\right) \qquad \textbf{(D.1)}$$

The function to be minimised may be expressed as:

$$\begin{aligned} F &= \left(\mathbf{A}^H\mathbf{w}-\mathbf{y}_d\right)^H\left(\mathbf{A}^H\mathbf{w}-\mathbf{y}_d\right) + b\mathbf{w}^H\mathbf{w} + l\left(\mathbf{w}^H\mathbf{a}_0 - 1\right) \\ &= \left(\mathbf{w}^H\mathbf{A}-\mathbf{y}_d^H\right)\left(\mathbf{A}^H\mathbf{w}-\mathbf{y}_d\right) + b\mathbf{w}^H\mathbf{w} + l\left(\mathbf{w}^H\mathbf{a}_0 - 1\right) \\ &= \mathbf{w}^H\mathbf{A}\mathbf{A}^H\mathbf{w} - \mathbf{w}^H\mathbf{A}\mathbf{y}_d - \mathbf{y}_d^H\mathbf{A}^H\mathbf{w} + \mathbf{y}_d^H\mathbf{y}_d + b\mathbf{w}^H\mathbf{w} + l\left(\mathbf{w}^H\mathbf{a}_0 - 1\right) \end{aligned} \qquad \textbf{(D.2)}$$

Differentiate Equation D.2 with respect to the weight vector and equate to zero:

$$\frac{\partial F}{\partial \mathbf{w}} = \begin{bmatrix} \dfrac{\partial F}{\partial w_1} \\ \vdots \\ \dfrac{\partial F}{\partial w_N} \end{bmatrix} = 2\mathbf{A}\mathbf{A}^H\mathbf{w} - 2\mathbf{A}\mathbf{y}_d + 2b\mathbf{w} + l\,\mathbf{a}_0 = 0\,. \qquad \textbf{(D.3)}$$

Rearrange to give:

$$\left(\mathbf{A}\mathbf{A}^H + b\mathbf{I}\right)\mathbf{w} = \mathbf{A}\mathbf{y}_d - \frac{l}{2}\mathbf{a}_0\,. \qquad \textbf{(D.4)}$$

Let $\mathbf{M} = \mathbf{A}\mathbf{A}^H + b\mathbf{I}$ and solve for $\mathbf{w}$:

$$\mathbf{w} = \mathbf{M}^{-1}\left(\mathbf{A}\mathbf{y}_d - \frac{l}{2}\mathbf{a}_0\right) \qquad \textbf{(D.5)}$$

which implies:

$$\mathbf{a}_0^H\mathbf{w} = \mathbf{a}_0^H\mathbf{M}^{-1}\left(\mathbf{A}\mathbf{y}_d - \frac{l}{2}\mathbf{a}_0\right). \qquad \textbf{(D.6)}$$

Now differentiate Equation D.2 with respect to l and equate to zero:

$$\frac{\partial F}{\partial l} = \mathbf{w}^H\mathbf{a}_0 - 1 = 0 \qquad \textbf{(D.7)}$$

so

$$\mathbf{w}^H \mathbf{a}_0 = \mathbf{a}_0^H \mathbf{w} = 1. \qquad \textbf{(D.8)}$$

Substitute Equation D.8 for the left hand side of Equation D.6 giving

$$1 = \mathbf{a}_0^H \mathbf{M}^{-1} \left(\mathbf{A}\mathbf{y}_d - \frac{l}{2}\mathbf{a}_0 \right) \qquad \textbf{(D.9)}$$

which may be solved for $\frac{l}{2}$ to yield:

$$\frac{l}{2} = \frac{\mathbf{a}_0^H \mathbf{M}^{-1} \mathbf{A}\mathbf{y}_d - 1}{\mathbf{a}_0^H \mathbf{M}^{-1} \mathbf{a}_0} \qquad \textbf{(D.10)}$$

Finally, substitute for $\frac{l}{2}$ in Equation D.5

$$\mathbf{w} = \mathbf{M}^{-1} \left(\mathbf{A}\mathbf{y}_d - \left(\frac{\mathbf{a}_0^H \mathbf{M}^{-1} \mathbf{A}\mathbf{y}_d - 1}{\mathbf{a}_0^H \mathbf{M}^{-1} \mathbf{a}_0} \right) \mathbf{a}_0 \right) \qquad \textbf{(D.11)}$$

In the limit, as $b \to \infty$, $\mathbf{M} \to b\mathbf{I}$, and

$$\begin{aligned} \mathbf{w} &= \lim_{b \to \infty} \left(\frac{1}{b} \left(\mathbf{A}\mathbf{y}_d - \left(\frac{\frac{\mathbf{a}_0^H \mathbf{A}\mathbf{y}_d}{b} - 1}{\frac{\mathbf{a}_0^H \mathbf{a}_0}{b}} \right) \mathbf{a}_0 \right) \right) \\ &= \lim_{b \to \infty} \left(\frac{\mathbf{A}\mathbf{y}_d}{b} - \frac{1}{b} \left(\frac{\mathbf{a}_0^H \mathbf{A}\mathbf{y}_d - b}{\mathbf{a}_0^H \mathbf{a}_0} \right) \mathbf{a}_0 \right) \\ &= \frac{\mathbf{a}_0}{\mathbf{a}_0^H \mathbf{a}_0} \end{aligned} \qquad \textbf{(D.12)}$$

D.2 Derivation of equivalent far-field source pressure

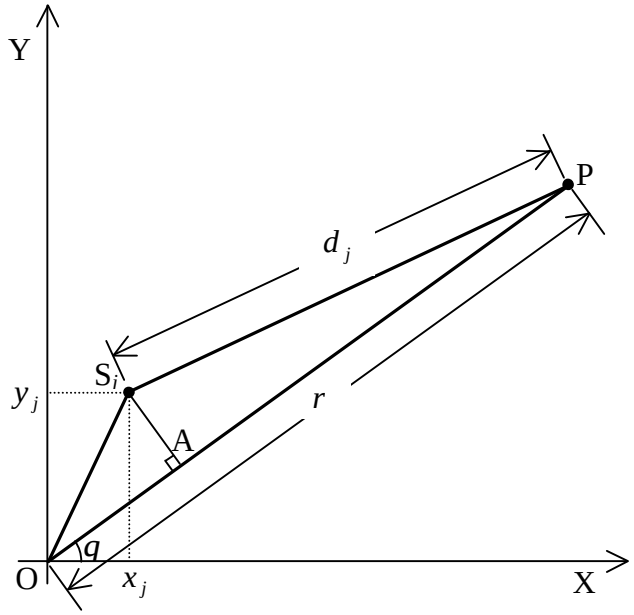

Figure D.23 Geometry for derivation of equivalent far-field pressure

Consider a point source, S_j, located at (x_j, y_j) and a receiver at P, a distance r from the origin in direction q (see Figure D.23). Assuming spherical spreading, the received pressure at P, due to source S_j is then:

$$p_j(r,q) = \frac{s_j}{d_j} e^{ikd_j} \qquad \textbf{(D.13)}$$

where s_j is the complex pressure due to the source at a distance of 1 metre and k is the wavenumber. If this source was replaced by a source at the origin that produced a pressure amplitude of $p_{s,j}$ at a distance of 1 metre, the pressure at P would be:

$$p_j(r,q) = \frac{p_{s,j}}{r} e^{ikr} \qquad \textbf{(D.14)}$$

Combining these two equations and rearranging terms gives the following expression for the amplitude of an equivalent source at the origin:

$$p_{s,j} = \frac{rs_j}{d_j} e^{ik(d_j - r)} \qquad \textbf{(D.15)}$$

In the limit as $r \to \infty$, $\frac{r}{d_j} \to 1$, and $r - d_j \to x_j \cos q + y_j \sin q$, the latter following from simple geometry. This leads to:

$$p_{s,j}(q) = s_j e^{-ik(x_j \cos q + y_j \sin q)} \qquad \textbf{(D.16)}$$

Summing over all Q sources then gives the amplitude of the pressure 1 metre from a source at the origin that would produce the same far-field pressure in direction q as the actual source distribution:

$$p_s(q) = \sum_{j=1}^{Q} s_j e^{-ik(x_j \cos q + y_j \sin q)} \qquad \textbf{(D.17)}$$

References

Abhayapala, T. D., Kennedy, R. A. & Williamson, R. C. 1999, 'Noise modeling for nearfield array optimization', *IEEE Signal Processing Letters,* vol. 6, no. 8, pp. 210-212.

Anderson, S. 1993, 'On optimal dimension reduction for sensor array signal processing', *Signal Processing,* vol. 30, pp. 245-256.

Arveson, P. T. & Vendittis, D. J. 2000, 'Radiated noise characteristics of a modern cargo ship', *Journal of the Acoustical Society of America,* vol. 107, no. 1, pp. 118-129.

Baggeroer, A. B., Kuperman, W. A. & Mikhalevsky, P. N. 1993, 'An overview of matched field methods in ocean acoustics', *IEEE Journal of Oceanic Engineering,* vol. 18, no. 4, pp. 401-424.

Battle, D. J., Gerstoft, P., Kuperman, W. A., Hodgkiss, W. S. & Siderius, M. 2003, 'Geoacoustic inversion of tow-ship noise via near-field matched-field processing', *IEEE Journal of Oceanic Engineering,* vol. in press.

Bourennane, S. & Bendjama, A. 2002, 'Locating wide band acoustic sources using higher order statistics', *Applied Acoustics,* vol. 63, pp. 235-251.

Brekovskikh, L. & Lysanov, Y. 1982, *Fundamentals of ocean acoustics,* Springer-Verlag, Berlin-Heidelberg.

Brekovskikh, L. M. 1960, *Waves in layered media,* Academic Press, New York.

Caiti, A., Jesus, S. M. & Kristensen, A. 1996, 'Geoacoustic seafloor exploration with a towed array in a shallow water area of the Strait of Sicily', *IEEE Journal of Oceanic Engineering,* vol. 21, no. 4, pp. 355-366.

Candy, J. V. 1988, *Signal processing: the modern approach,* McGraw-Hill.

Candy, J. V. & Sullivan, E. J. 1989, 'Model-based passive ranging', *Journal of the Acoustical Society of America,* vol. 85, no. 6, pp. 2472-2480.

Candy, J. V. & Sullivan, E. J. 1992, 'Ocean acoustic signal processing: A model-based approach', *Journal of the Acoustical Society of America,* vol. 92, no. 6, pp. 3185-3201.

Candy, J. V. & Sullivan, E. J. 1994, 'Model-based processing for a large aperture array', *IEEE Journal of Oceanic Engineering,* vol. 19, no. 4, pp. 519-528.

Candy, J. V. & Sullivan, E. J. 1995, 'Passive localisation in ocean acoustics: a model based approach', *Journal of the Acoustical Society of America,* vol. 98, no. 3, pp. 1455-1471.

Candy, J. V. & Sullivan, E. J. 1996, 'Model-based identification: An adaptive approach to ocean-acoustic processing', *IEEE Journal of Oceanic Engineering,* vol. 21, no. 3, pp. 273-289.

Candy, J. V. & Sullivan, E. J. 1998, 'Broadband model-based processing for shallow ocean environments', *Journal of the Acoustical Society of America,* vol. 104, no. 1, pp. 275-287.

Carey, W. M. & Moseley, W. B. 1991, 'Space-time processing, environmental-acoustic effects', *IEEE Journal of Oceanic Engineering,* vol. 16, no. 3, pp. 185-301.

Cato, D. H. 1995, *Ambient sea noise prediction curves - Australian waters (1995),* personal communication received.

Chakrabarti, S. K. 1994, *Hydrodynamics of offshore structures,* Computational Mechanics Publications, Southampton, Boston.

Chapman, N. R. & Lindsay, C. E. 1996, 'Matched-field inversion for geoacoustic model parameters in shallow water', *IEEE Journal of Oceanic Engineering*, vol. 21, no. 4, pp. 347-354. Retrieved: October 1996, from

Collins, L. B. 1988, 'Sediments and history of the Rottnest Shelf, southwest Australia: a swell-dominated, non-tropical carbonate margin', *Sedimentary Geology*, vol. 60, pp. 15-49.

Collins, M. D. & Fishman, L. 1995, 'Efficient navigation of parameter landscapes', *Journal of the Acoustical Society of America*, vol. 98, no. 3, pp. 1637-1644.

Collins, M. D., Kuperman, W. A. & Schmidt, H. 1992, 'Nonlinear inversion for ocean-bottom properties', *Journal of the Acoustical Society of America*, vol. 92, no. 5, pp. 2770-2783.

Cox, H., Zeskind, R. M. & Owen, M. M. 1987, 'Robust adaptive beamforming', *IEEE transactions on Acoustics, Speech and Signal Processing*, vol. 35, no. 10, pp. 1365-1375.

Cross, P. A. 1983, *Advanced least squares applied to position-fixing*, Department of Land Surveying, North East London Polytechnic, Working paper no. 6.

Cross, P. A. & Prichett, C. H. 1986, 'A Kalman filter for real-time positioning during geophysical surveys at sea', *XVIII FIG Congress, Toronto*.

Donald, J. B., Nuttall, A. & Wilson, J. H. 2000, 'Adaptive beamforming (AIBF) for noise and interference suppression', *Undersea Defence Technology Pacific 2000*, Sydney, Australia, 24-26 February 2000, pp. 192-199.

Dosso, S. E. 2002, 'Quantifying uncertainty in geoacoustic inversion. I. A fast Gibbs sampler approach', *Journal of the Acoustical Society of America*, vol. 111, no. 1, pp. 129-142.

Dosso, S. E., Fallat, M. R., Sotirin, B. J. & Newton, J. L. 1998, 'Array element localization for horizontal arrays via occams inversion', *Journal of the Acoustical Society of America*, vol. 104, no. 2 Part 1, pp. 846-859.

Dosso, S. E. & Nielsen, P. L. 2002, 'Quantifying uncertainty in geoacoustic inversion. II. Application to broadband, shallow-water data', *Journal of the Acoustical Society of America*, vol. 111, no. 1, pp. 143-159.

Dosso, S. E. & Riedel, M. 2001, 'Array element localisation for towed marine seismic arrays', *Journal of the Acoustical Society of America*, vol. 110, no. 2, pp. 955-966.

Dosso, S. E. & Wilmut, M. J. 2002a, 'Effects of incoherent and coherent source spectral information in geoacoustic inversion', *Journal of the Acoustical Society of America*, vol. 112, no. 4, pp. 1390-1398.

Dosso, S. E. & Wilmut, M. J. 2002b, 'Quantifying data information content in geoacoustic inversion', *IEEE Journal of Oceanic Engineering*, vol. 27, no. 2.

Dosso, S. E., Wilmut, M. J. & Lapinski, A.-L. S. 2001, 'An adaptive-hybrid algorithm for geoacoustic inversion', *IEEE Journal of Oceanic Engineering*, vol. 26, no. 3, pp. 325-336.

Duncan, A. J. & Savage, M. 2002, *Calibration of UW-30 underwater loudspeaker*, Centre for marine Science and Technology, Curtin University of Technology, C2002-18.

Edelson, G. S. & Sullivan, E. J. 1992, 'Limitations of the overlap-correlator method imposed by noise and signal characteristics', *IEEE Journal of Oceanic Engineering*, vol. 17, no. 1, pp. 30-39.

Edelson, G. S. & Tufts, D. W. 1992, 'On the ability to estimate narrow-band signal parameters using towed arrays', *IEEE Journal of Oceanic Engineering*, vol. 17, no. 1, pp. 48-61.

Etter, P. C. 1996, *Underwater acoustic modelling - principles, techniques and applications*, 2nd edn, Chapman & Hall, London.

Fawcett, J. A. 1993, 'Synthetic aperture processing for a towed array and a moving source', *Journal of the Acoustical Society of America*, vol. 94, no. 5, pp. 2832-2837.

Fawcett, J. A. & Maranda, B. H. 1993, 'A hybrid target motion analysis/matched-field processing localisation method', *Journal of the Acoustical Society of America*, vol. 94, no. 3, pp. 1363-1371.

Felisberto, P. & Jesus, S. M. 1996, 'Towed-array beamforming during ship's manoeuvring', *IEE Proceedings: Radar, Sonar and Navigation*, vol. 143, no. 3, pp. 210-215.

Ferguson, B. G. 1990, 'Sharpness applied to the adaptive beamforming of acoustic data from a towed array of unknown shape', *Journal of the Acoustical Society of America*, vol. 88, no. 6, pp. 2695-2701. Retrieved: December 1990, from

Fialkowski, L. T., Perkins, J. S., Collins, M. D., Nicholas, M., Fawcett, J. A. & Kuperman, W. A. 2001, 'Matched-field source tracking by ambiguity surface averaging', *Journal of the Acoustical Society of America*, vol. 110, no. 2, pp. 739-746.

Gerstoft, P. 1994, 'Inversion of seismoacoustic data using genetic algorithms and a posteriori probability distributions', *Journal of the Acoustical Society of America*, vol. 95, no. 2, pp. 770-782.

Gerstoft, P., Hodgkiss, W. S., Kuperman, W. A., Song, H., Siderius, M. & Nielsen, P. L. 2003, 'Adaptive beamforming during a turn', *IEEE Journal of Oceanic Engineering*, vol. 28, no. 1, pp. 44-54. Retrieved: January 2003, from

Gerstoft, P. & Mecklenbrauker, C. F. 1998, 'Ocean acoustic inversion with estimation of a posteriori probability distributions', *Journal of the Acoustical Society of America*, vol. 104, no. 2, pp. 808-819. Retrieved: August 1998, from

Ghiotto, A. 2002, *DSTO IPA Narama Towed Array Trial #2*, Nautronix Ltd, Fremantle, 162-500-018.

Gillard, C. A., Thomson, D. J. & Heard, G. J. 2002, 'Matched-field geoacoustic inversion using bayesian estimation', *Acoustics 2002 - Innovation in acoustics and vibration*, ed. Zander, A., Australian Acoustical Society, Adelaide, Australia, 13-15 November 2002, pp. 372-381.

Gorban, I. I. 2000, 'Space-time signal processing for moving antennae', *Advances in Engineering Software*, vol. 31, pp. 119-125.

Gourlay, T. 2003, *Tammar squat/trim*, personal communication received 12 June 2003.

Gray, D. A., Anderson, B. D. O. & Bitmead, R. R. 1993, 'Towed array shape estimation using Kalman filters-theoretical models', *IEEE Journal of Oceanic Engineering*, vol. 18, no. 4, pp. 543-56.

Gray, L. M. 1981, 'Investigation into modeling and measurement of propeller cavitation source strength at blade rate on merchant vessels', *Propellers '81*, Society of Naval Architects and Marine Engineers, Virginia Beach, Virginia, USA, pp. 165-179.

Gray, L. M. & Greeley, D. S. 1980, 'Source level model for propeller blade rate radiation for the world's merchant fleet', *Journal of the Acoustical Society of America*, vol. 67, no. 2, pp. 516-522.

Greening, M. V. & Foster, S. 2000, 'Optimal linear sparse arrays', *Undersea Defence Technology Pacific 2000*, Sydney, Australia, 24-26 February 2000, pp. 150-154.

Greening, M. V. & Perkins, J. E. 2002, 'Adaptive beamforming for nonstationary arrays', *Journal of the Acoustical Society of America*, vol. 112, no. 6, pp. 2872-2881. Retrieved: December 2002, from

Grewel, M. S. & Andrews, A. P. 1993, *Kalman filtering: theory and practice*, Prentice-Hall, Englewood Cliffs, New Jersey.

Hall, M. 2002, *Sound-speed density relationships*, personal communication received August 2002.

Hamilton, E. L. 1972, 'Compressional-wave attenuation in marine sediments', *Geophysics*, vol. 37, pp. 284-310.

Hamilton, E. L. 1978, 'Sound velocity-density relations in sea-floor sediments and rocks', *Journal of the Acoustical Society of America*, vol. 63, no. 2, pp. 366-377.

Harris, F. J. 1978, 'On the use of windows for harmonic analysis with the discrete Fourier transform', *Proceedings of the IEEE*, vol. 66, no. 1, pp. 51-83.

Haykin, S. 1996, *Adaptive filter theory*, 3rd edn, Prentice-Hall, New Jersey.

Heine, J. C. 1982, 'Acoustic source characteristics of merchant ships', *SACLANTCEN conference proceedings No 32 - Underwater Ambient Noise*, SACLANTCEN, San Bartolomeo, Italy, 11-14 May 1982, pp. 2.1-2.16.

Hermand, J.-P. 1999, 'Broad-band geoacoustic inversion in shallow water from waveguide impulse response measurements on a single hydrophone: theory and experimental results', *IEEE Journal of Oceanic Engineering*, vol. 24, no. 1, pp. 41-66.

Hermand, J.-P. & Gerstoft, P. 1996, 'Inversion of broad-band multitone acoustic data from the Yellow Shark summer experiments', *IEEE Journal of Oceanic Engineering*, vol. 21, no. 4, pp. 324-346. Retrieved: October 1996, from

Hodgkiss, W. S., Ensberg, D. E., Murray, J. J., D'Spain, G. L., Booth, N. O. & Schey, P. W. 1996, 'Direct measurement and matched-field inversion approaches to array shape estimation', *IEEE Journal of Oceanic Engineering*, vol. 21, no. 4, pp. 393-401. Retrieved: October 1996, from

Hoerner, S. F. 1965, *Fluid-dynamic drag*, Hoerner Fluid Dynamics, Brick Town, New Jersey.

Hoerner, S. F. & Borst, H. V. 1975, *Fluid-dynamic lift*, Hoerner Fluid Dynamics, Brick Town, New Jersey.

Hoffman 2002, *Geoacoustic model for a site offshore from Perth, Western Australia*, personal communication received March 2002.

Hung, H. & Kaveh, M. 1988, 'Focussing matrices for coherent signal-subspace processing', *IEEE transactions on Acoustics, Speech and Signal Processing*, vol. 36, no. 8, pp. 1272-1281.

ICSM 1998, *Geocentric Datum of Australia Technical Manual*, Intergovernmental Committee on Surveying and Mapping, PO Box 2, Belconnen ACT 2616, Australia.

Jensen, F. B., Kuperman, W. A., Porter, M. B. & Schmidt, H. 2000, *Computational ocean acoustics*, Springer-Verlag, New York.

Jun, B. D., Kim, D. Y., Lim, J.-S., Song, J.-i. & Sung, K.-M. 2002, 'Design of broadband beamformer for passive sonar arrays', *Undersea Defence Technology Korea 2002*, Nexus, Cheju Island, Korea, 8-10 October 2002.

Kennedy, R. A., Abhayapala, T. D. & Ward, D. B. 1998, 'Broadband nearfield beamforming using a radial beampattern transformation', *IEEE Transactions on Signal Processing*, vol. 46, no. 8, pp. 2147-2156.

Kennedy, R. A., Ward, D. B. & Abhayapala, T. D. 1999, 'Nearfield beamforming using radial reciprocity', *IEEE Transactions on Signal Processing*, vol. 47, no. 1, pp. 33-40.
Keys, R. G. 1981, 'Cubic convolution interpolation for digital image processing', *IEEE transactions on Acoustics, Speech and Signal Processing*, vol. 29, no. 6, pp. 1153-1160.
Kim, J.-S., Park, G.-T., Lee, J.-H., Kim, I.-I. & Lee, K.-K. 2002, 'MVDR method using subband decomposition for high frequency resolution in passive sonar system', *Undersea Defence Technology Korea 2002*, Nexus, Cheju Island, Korea, 8-10 October 2002.
Krim, H. & Veberg, M. 1996, 'Two decades of array signal processing research: the parametric approach', In *IEEE signal processing magazine*, pp. 67-94.
Krolik, J. & Swingler, D. 1989, 'Multiple broad-band source location using steered covariance matrices', *IEEE transactions on Acoustics, Speech and Signal Processing*, vol. 37, no. 10, pp. 1481-1494.
Latorre, R. 1981, 'Propeller tip vortex cavitation noise inception', *Propellers '81*, Society of Naval Architects and Marine Engineers, Virginia Beach, Virginia, USA, pp. 319-333.
Lindsay, C. E. & Chapman, N. R. 1993, 'Matched field inversion for geoacoustic model parameters using adaptive simulated annealing', *IEEE Journal of Oceanic Engineering*, vol. 18, no. 3, pp. 224-231. Retrieved: July 1993, from
Loeser, H. T. 1992, *Sonar Engineering Handbook*, Peninsula Publishing, Los Altos, California.
Mathews, D. N., Hall, M. V., Jessup, B. L., Mentjox, J. & Formby, P. 2000, 'Accurate measurement of ship acoustic signatures in shallow water', *Underwater Defence Technology Pacific 2000*, Sydney, Australia, 24-26 February 2000, pp. 14-17.
Matusiak, J. 1992, 'Broadband noise of the cavitation of marine propellers: generation and collapse of the free bubbles downstream of the fixed cavitation', *Nineteenth Symposium on Naval Hydrodynamics*, National Academy Press, Seoul, Korea, 1994, pp. 701-714.
McMahon, D. 2002, *Harmonic analysis of Tammar machinery noise*, personal communication received August 2002.
Medwin, H. & Clay, C. S. 1998, *Fundamentals of acoustical oceanography*, Academic Press, San Diego, USA.
Mulgrew, B. & Cowan, C. F. N. 1988, *Adaptive filters and equalisers*, Kluwer Academic Publishers.
Nordholm, S. E., Rehbock, V., Teo, K. L. & Nordebo, S. 1998, 'Chebyshev optimization for the design of broadband beamformers in the near field', *IEEE Transactions on Circuits & Systems II Analog & Digital Signal Processing*, vol. 45, no. 1, pp. 141-143.
Nuttall, A. H. 1992, 'The maximum likelihood estimator for acoustic synthetic aperture processing', *IEEE Journal of Oceanic Engineering*, vol. 17, no. 1, pp. 26-29.
Nuttall, A. H. & Wilson, J. H. 1991, 'Estimation of the acoustic field directionality by use of planar and volumetric arrays via the Fourier series method and the Fourier integral method', *Journal of the Acoustical Society of America*, vol. 90, no. 4, pp. 2004-2019.
Nuttall, A. H. & Wilson, J. H. 2000, 'Adaptive beamforming at very low frequencies in spatially coherent, cluttered noise environments with low signal-to-noise ratio

and finite averaging times', *Journal of the Acoustical Society of America,* vol. 108, no. 5, pp. 2256-2265.
Ogilvy, J. A. 1991, *Theory of wave scattering from random rough surfaces,* Institute of Physics Publishing, Bristol.
Ottersten, B. & Kailath, T. 1990, 'Direction-of-arrival estimation for wide-band signals using the ESPIRIT algorithm', *IEEE transactions on Acoustics, Speech and Signal Processing,* vol. 38, no. 2, pp. 317-327.
Pekeris, C. L. 1948, *Theory of propagation of explosive sound in shallow water,* Geological Society of America, Memoir 27.
Plumpton, N. G. & Tindle, C. T. 1989, 'Saddle point analysis of the reflected acoustic field', *Journal of the Acoustical Society of America,* vol. 85, no. 3, pp. 1115-23.
Porter, M. B. 1993, 'Acoustic models and sonar systems', *IEEE Journal of Oceanic Engineering,* vol. 18, no. 4, pp. 425-437.
Porter, M. B. 1999, 'Acoustic toolbox (atPII_f95)'.
Porter, M. B. & Bucker, H. P. 1987, 'Gaussian beam tracing for computing ocean acoustic fields', *Journal of the Acoustical Society of America,* vol. 82, no. 4, pp. 1349-1359.
Poularikas, A. D. 1999, *The handbook of formulas and tables for signal processing,* CRC Press.
Press, W. H., Flannery, B. P., Teukolsky, S. A. & Vetterling, W. T. 1988, *Numerical recipes in C,* Cambridge University Press, Cambridge.
Press, W. H., Flannery, B. P., Teukolsky, S. A. & Vetterling, W. T. 1993, *Numerical recipes in C, the art of scientific computing, 2nd Edition,* 2 edn, Cambridge University Press.
Raghunath, K. J. & Reddy, V. U. 1992, 'Finite data performance analysis of MVDR beamformer with and without spatial smoothing', *IEEE Transactions on Signal Processing,* vol. 40, no. 11, pp. 2726-2736.
Ranmuthugala, S. D. & Gottschalk, S. A. 1993, 'Dyamic simulation of a two part underwater tow', *Offshore Australia 93*.
Rauch, H. E., Tung, F. & Striebel, C. T. 1965, 'Maximum likelihood estimates of linear dynamic systems', *American Institute of Aeronautics and Astronautics (AIAA) Journal,* vol. 3, pp. 1445-1450.
Richardson, M. D. & Briggs, K. B. 1993, 'On the use of acoustic impedance values to determine sediment properties', *Proceeding of the Institute of Acoustics,* vol. 15, no. 2, pp. 15-24.
Riley, J. L. & Gray, D. A. 1993, 'Towed array shape estimation using Kalman filters-experimental investigations', *IEEE Journal of Oceanic Engineering,* vol. 18, no. 4, pp. 572-81.
Ross, D. 1987, *Mechanics of Underwater Noise,* Peninsula Publishing, Los Altos.
Sahin, A. & Miller, E. L. 1999, 'Electromagnetic scattering-based array processing methods for near-field object characterisation', *Journal of Electromagnetic Waves and Applications,* vol. 13, pp. 1209-1236.
Siderius, M. & Nielsen, P. L. 2002, 'Range-dependent seabed characterisation by inversion of acoustic data from a towed receiver array', *Journal of the Acoustical Society of America,* vol. 112, no. 4, pp. 1523-1535. Retrieved: October 2002, from
Sivanand, S. & Kaveh, M. 1991, 'Focusing filters for coherent direction finding', *IEEE Transactions on Signal Processing,* vol. 39, no. 2, pp. 437-445.

Solomon, I. S. D., Knight, A. J., Liebing, D. F. & Faulkner, S. B. 2000, 'Sonar beamforming using the fourier integral method', *Undersea Defence Technology Pacific 2000*, Sydney, Australia, 24-26 February 2000, pp. 182-186.
Spiegel, M. R. 1968, *Mathematical handbook*, McGraw-Hill.
Stergiopoulos, S. 1989, 'Extended towed array processing by an overlap correlator', *Journal of the Acoustical Society of America*, vol. 86, no. 1, pp. 158-171.
Stergiopoulos, S. 1990, 'Optimum bearing resolution for a moving towed array and extension of its physical aperture', *Journal of the Acoustical Society of America*, vol. 87, no. 5, pp. 2128-2140.
Stergiopoulos, S. & Urban, H. 1992a, 'An experimental study in forming a long synthetic aperture at sea', *IEEE Journal of Oceanic Engineering*, vol. 17, no. 1, pp. 62-72.
Stergiopoulos, S. & Urban, H. 1992b, 'A new passive synthetic aperture technique for towed arrays', *IEEE Journal of Oceanic Engineering*, vol. 17, no. 1, pp. 16-25.
Su, G. & Morf, M. 1986, 'Modal decomposition signal subspace algorithms', *IEEE transactions on Acoustics, Speech and Signal Processing*, vol. 34, no. 3, pp. 585-602.
Sullivan, E. J. & Candy, J. V. 1997, 'Space-time array processing: the model-based approach', *Journal of the Acoustical Society of America*, vol. 102, no. 5, pp. 2809-2820.
Sullivan, E. J., Carey, W. M. & Stergiopoulos, S. 1992, 'Editorial for special issue on synthetic aperture processing', *IEEE Journal of Oceanic Engineering*, vol. 17, no. 1, pp. 1-7.
Swingler, D. 1999, 'A low-complexity MVDR beamformer for use with short observation times', *IEEE Transactions on Signal Processing*, vol. 47, no. 4, pp. 1154-1160.
Szu, H. & Hartley, R. 1987, 'Fast simulated annealing', *Physics Letters A*, vol. 122, no. 3,4, pp. 157-162.
Tietze, U. & Schenk, C. 1991, *Electronic circuits, design and applications*, Springer-Verlag, Heidelberg.
Tindle, C. T. 1983, 'Ray calculations with beam displacement', *Journal of the Acoustical Society of America*, vol. 73, no. 5, pp. 1581-6.
Tindle, C. T. & Bold, G. E. J. 1981, 'Improved ray calculations in shallow water', *Journal of the Acoustical Society of America*, vol. 70, no. 3, pp. 813-19.
Tindle, C. T. & Deane, G. B. 1985, 'Sound propagation over a sloping bottom using rays with beam displacement', *Journal of the Acoustical Society of America*, vol. 78, no. 4, pp. 1366-1374.
Tindle, C. T. & Plumpton, N. G. 1990, 'Attenuation in a saddle-point analysis of the reflected acoustic field', *Journal of the Acoustical Society of America*, vol. 87, no. 1, pp. 135-141.
Trucco, A. 2002, 'Weighting and thinning wide-band arrays by simulated annealing', *Ultrasonics*, vol. In press.
Tseng, C.-Y. & Griffiths, L. J. 1992, 'A simple algorithm to achieve desired patterns for arbitrary arrays', *IEEE Transactions on Signal Processing*, vol. 40, no. 11, pp. 2737-2746.
Uhlmann, J. 1996, *Covariance Intersection*, Available: [http://www.ait.nrl.navy.mil/people/uhlmann/covint.html].
Urick, R. J. 1983, *Principles of underwater sound*, 3rd edn, Peninsula Publishing, Los Altos, California.

VanVeen, B. D. & Buckle, K. M. 1988, 'Beamforming: a versatile approach to spatial filtering', In *IEEE Acoustics, Speech and Signal Processing Magazine*, pp. 4-24.

Walpole, R. E. & Myers, R. H. 1985, *Probability and statistics for engineers and scientists*, 3rd edn, Macmillan.

Wang, H. & Kaveh, M. 1985, 'Coherent signal-subspace processing for the detection and estimation of angles of arrival of multiple wide-band sources', *IEEE transactions on Acoustics, Speech and Signal Processing*, vol. 33, no. 4, pp. 823-831.

Westwood, E. K. 1989a, 'Complex ray methods for acoustic interaction at a fluid-fluid interface', *Journal of the Acoustical Society of America*, vol. 85, no. 5, pp. 1872-84.

Westwood, E. K. 1989b, 'Ray methods for flat and sloping shallow-water waveguides', *Journal of the Acoustical Society of America*, vol. 85, no. 5, pp. 1885-94.

Westwood, E. K. 1992, 'Broadband modeling of the three-dimensional penetrable wedge', *Journal of the Acoustical Society of America*, vol. 92, no. 4, pt.1, pp. 2212-22.

Westwood, E. K. & Tindle, C. T. 1987, 'Shallow water time-series simulation using ray theory', *Journal of the Acoustical Society of America*, vol. 81, no. 6, pp. 1752-61.

Westwood, E. K. & Vidmar, P. J. 1987, 'Eigenray finding and time series simulation in a layered-bottom ocean', *Journal of the Acoustical Society of America*, vol. 81, no. 4, pp. 912-924.

Williams, E. G. 1996, 'Imaging the sources on a cylindrical shell from far-field pressure measured on a semicircle', *Journal of the Acoustical Society of America*, vol. 99, no. 4 Part 1, pp. 2022-2032.

Williams, R. & Harris, B. 1992, 'Passive synthetic aperture processing techniques', *IEEE Journal of Oceanic Engineering*, vol. 17, no. 1, pp. 8-15.

Wilson, J. H. 1995, 'Applications of inverse beamforming theory', *Journal of the Acoustical Society of America*, vol. 98, no. 6, pp. 3250-3261.

Wilson, J. H. & Veenhuis, R. S. 1997, 'Shallow water beamforming with small aperture, horizontal, towed arrays', *Journal of the Acoustical Society of America*, vol. 101, no. 1, pp. 384-394.

Winder, A. & Loda, C. J. 1981, *Space-time information processing*, Peninsula Publishing, Los Altos, California.

Yang, T. C. 2003, 'Motion compensation for adaptive horizontal line array processing', *Journal of the Acoustical Society of America*, vol. 113, no. 1, pp. 245-260. Retrieved: January 2003, from

Yang, T. C. & Yates, T. W. 1996, 'Acoustic inversion of bottom reflectivity and bottom sound-speed profile', *IEEE Journal of Oceanic Engineering*, vol. 21, no. 4, pp. 367-376. Retrieved: October 1996, from

Yen, N.-c. 1992, 'A circular passive synthetic array: an inverse problem approach', *IEEE Journal of Oceanic Engineering*, vol. 17, no. 1, pp. 40-47.

Yen, N.-c. & Carey, W. M. 1989, 'Application of synthetic-aperture processing to towed-array data', *Journal of the Acoustical Society of America*, vol. 86, no. 2, pp. 754-765.

Yuen, N. & Friedlander, B. 1998, 'Performance analysis of higher order ESPIRIT for localisation of near-field sources', *IEEE Transactions on Signal Processing*, vol. 46, no. 3, pp. 709-719.